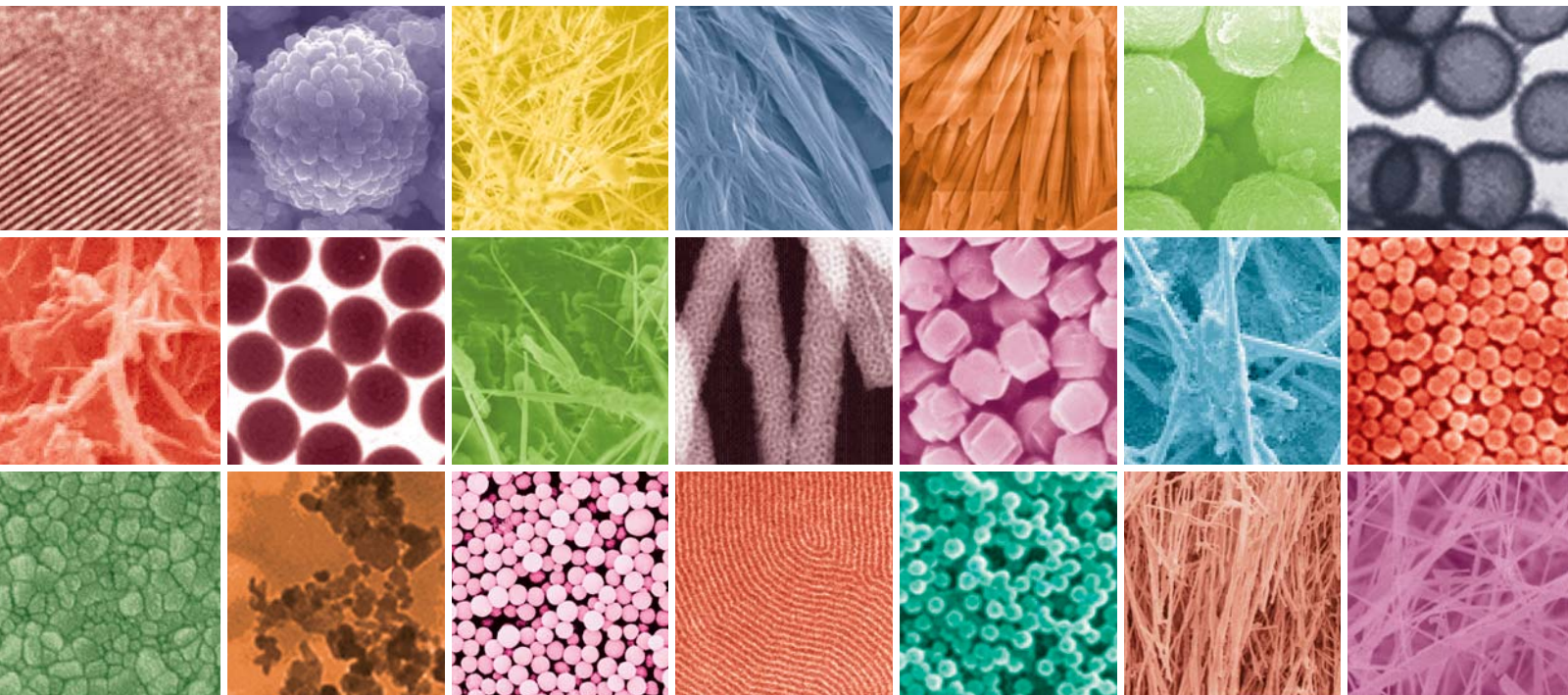# Nanostructures for Medicine and Pharmaceuticals

Guest Editors: Xing-Jie Liang, Donglu Shi, and Daxiang Cui

Nanostructures for Medicine and Pharmaceuticals

Nanostructures for Medicine and Pharmaceuticals

Guest Editors: Xing-Jie Liang, Donglu Shi, and Daxiang Cui

Editorial Board

Contents

Editorial

Nanostructures for Medicine and Pharmaceuticals

Xing-Jie Liang,[1] Anil Kumar,[1] Donglu Shi,[2, 3] and Daxiang Cui[4]

[1] CAS Key Laboratory of Biomedical Effects of Nanomaterial and Nanosafety, National Center for Nanoscience and Technology of China, Beijing, China
[2] The Institute for Advanced Materials and Nano Biomedicine, Tongji University, Shanghai 200092, China
[3] School of Electronic and Computing Systems, College of Engineering and Applied Science, University of Cincinnati, Cincinnati, OH 45221, USA
[4] Institute of Micro/Nano Science and Technology, Shanghai Jiao Tong University, Shanghai, China

Correspondence should be addressed to Xing-Jie Liang, liangxj@nanoctr.cn

The rapid developments in nanostructured materials and nanotechnology will have profound impact in many areas of biomedical applications including delivery of drugs and biomolecules, tissue engineering, detection of biomarkers, cancer diagnosis, cancer therapy, and imaging. This field is expanding quickly, and a lot of work is ongoing in the design, characterization, synthesis, and application of materials, for controlling shape and size at nanometer scale to develop highly advanced materials for biomedical application and even to design better pharmaceutical products. In recent years, novel nanostructure with multifunctionalities has been focused on the use of *nanostructures toward solving problems of biology and medicine.*

The main scope of this special issue is to demonstrate the latest achievement of nanotechnology and its application in nanomedicine particularly in new approaches for drug delivery such as targeted drug delivery system, nanostructure for drug storage, nanomaterials for tissue engineering, medical diagnosis and treatment, and generation of new kinds of materials from biological sources. Therefore, many critical issues in nanostructured materials, particularly their applications in biomedicine, must be addressed before clinical applications. This special issue devotes several review and research articles encompassing various aspects of nanomaterials for medicine and pharmaceuticals.

We have invited colleagues from worldwide who have been exploring their research in biomedical applications of nanomaterials for design of medicine and pharmaceuticals.

The paper by S. M. Christensen et al. focuses on the applications of various nanostructures and nanodevices in clinical diagnostics and detection of important biological molecules. They have introduced some basic techniques of micro-/nanoscale fabrication that have enabled reproducible production of nanostructures. In the same section, the paper by A. Kumar et al. has broadly mentioned the significant properties of gold playing an important role for the diagnosis of cancer and HIV. S. Jin et al. emphasized the application of quantum dots in biological imaging, and H. Yim et al. mentioned magnetic-resonance-imaging- (MRI-) based contrast agents and multifunctional materials for diagnosis and therapy.

The following section covers the nanomaterials used for pharmaceutical drug delivery and tissue engineering in which C.-W. Li et al. investigated the self-emulsifying drug delivery systems (SEDDSs). Another author has synthesised the starch-chitosan hydrogel, prepared by using the oxidation method, while some papers discussed polybutylcyanoacrylate for oral delivery. One paper mentioned PMAA- (poly(methacrylic acid)-) coated gelatin nanoparticles encapsulated with fluorescent dye for cell imaging. Some papers discuss clay-based polyurethane nanocomposite as local triamcinolone acetonide delivery system. J. Ali et al. mentioned "*Fabrication of coated-collagen electrospun PHBV nanofiber film by plasma method and its cellular study.*" Z. Yang et al. have investigated optimization and preparation of amphotericin *B Cubosomes* for an oral delivery. In the same section, some of papers discuss the delivery of siRNA and its current challenges for cancer therapy. P. He et al. mentioned toxicity of TiO_2 nanopowder, and another paper discusses "*Mechanical properties of chitosan-starch composite*

filled hydroxyapatite micro- and nanopowders for biological applications." F. Li et al. investigated the gene delivery in drug-resistant A2780/DDP ovarian cancer cell line via magnetofection.

In another session, X. Junzheng et al. mentioned "*Biodistribution study of ^{60}Co–Co graphitic-shell nanocrystals in vivo.*" X. Cheng et al. studied about "*Characterization of multiwalled carbon nanotubes dispersing in water and association with biological effects,*" and C. Riggio et al. comprehensively described the nanooncology and its clinical applications for cancer therapy. In the final section, Z.-S. Chen et al. mentioned the synthesis of nanoparticles from microorganisms and their applications, W. Zhang et al. studied "*The effect of superhydrophobic surface of titanium on Staphylococcus aureus adhesion,*" and Th. S. Dhahi et al. demonstrated the "*Fabrication of lateral polysilicon gap of less than 50 nm using conventional lithography.*"

In summary, the development of novel nanoplatform for the diagnosis and treatment of disease would continue to remain an area of great attention in the field of nanomedicine. In this special issue, we do hope some covered aspects will also provide some interesting information to the readers and researchers to design better pharmaceutical products for human welfare.

Acknowledgments

Xing-Jie Liang
Anil Kumar
Donglu Shi
Daxiang Cui

Review Article

Nanostructures for Medical Diagnostics

Md. Motasim Bellah,[1,2] Shawn M. Christensen,[3] and Samir M. Iqbal[1,2,4,5]

[1] Department of Electrical Engineering, University of Texas at Arlington, Arlington, TX 76011, USA
[2] Nanotechnology Research and Teaching Facility, University of Texas at Arlington, Arlington, TX 76019, USA
[3] Department of Biology, University of Texas at Arlington, Arlington, TX 76010, USA
[4] Joint Graduate Committee of Bioengineering Program, University of Texas at Arlington, Arlington, TX 76010, USA
[5] Department of Bioengineering, University of Texas at Arlington, Arlington, TX 76010, USA

Correspondence should be addressed to Samir M. Iqbal, smiqbal@uta.edu

Nanotechnology is the art of manipulating materials on atomic or molecular scales especially to build nanoscale structures and devices. The field is expanding quickly, and a lot of work is ongoing in the design, characterization, synthesis, and application of materials, structures, devices, and systems by controlling shape and size at nanometer scale. In the last few years, much work has been focused on the use of nanostructures toward problems of biology and medicine. In this paper, we focus on the application of various nanostructures and nanodevices in clinical diagnostics and detection of important biological molecules. The discussion starts by introducing some basic techniques of micro-/nanoscale fabrication that have enabled reproducible production of nanostructures. The prospects, benefits, and limitations of using these novel techniques in the fields of biodetection and medical diagnostics are then discussed. Finally, the challenges of mass production and acceptance of nanotechnology by the medical community are considered.

1. Introduction

By definition, a nanostructure is an object that has at least one dimension equal to or smaller than 100 nanometers. There is a wide variety of nanostructures, such as nanoparticles, nanopores, nanorods, nanowires, nanoribbons, nanotubes, and nanoscaffolds. The most promising features of these structures are their size-dependent properties. For example, metallic nanoparticles exhibit tunable radiation and absorption wavelength depending on their aspect ratio [1] and coating [2]. These unique properties are attributed to the phenomenon called localized surface plasmon resonance (LPSR). Each particle can effectively produce photoluminescence equivalent to a million dye molecules. Additionally, they are photostable and do not suffer from photobleaching [3]. Owing to their superior optical properties, they can produce better signal over ordinary dye molecules. After coating with probe molecules, the optical properties of nanostructures allow the detection of specific target molecules.

Some nanostructured surfaces are known to be suitable for enhanced cell adhesion and proliferation [4, 5]. This is believed to stem from mimicking the actual nanofeatures of the living systems [6]. Carbon nanotubes exhibit exceptionally high current carrying capacity [7, 8]. They can be used to interconnect devices at very low dimensions where ordinary metals suffer from high contact resistance and electromigration. Electromigration limits the use of the most widely used interconnect metal, copper, at nano-scale. Nanowires are reported to be useful in different sensing techniques including electrical, electrochemical, optical, and mass-based approaches [9–12]. Usually nanowires show high resistance due to the surface scattering of carriers, but their resistance is strongly dependent on the species attached on the surface. If the immobilized species can selectively bind to a target, then it can detect an ultralow concentration of target species [13–15].

Early detection is very crucial for some diseases like cancer to provide better treatment. Early detection increases the probability of curing diseases and significantly improves
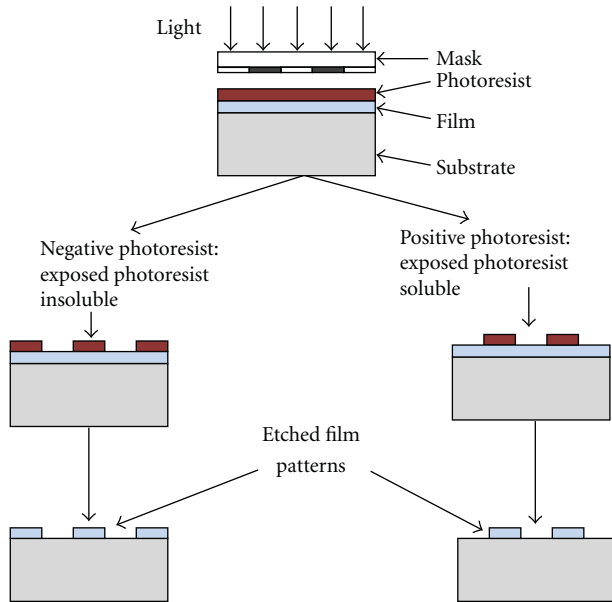
FIGURE 1: Photolithography using negative or positive photoresist.

the rate of mortality. Historically, it has been difficult to detect early or precancerous states due to unavailability of ultra-sensitive devices capable of detecting a multivariate disease like cancer. But now, such devices may be realizable using a large number of nanostructures on a single assay system [16, 17].

There are two different approaches for fabricating nanostructures irrespective of the field of applications: top down and bottom up.

In top-down approach, a bulk material is laterally patterned by a series of subtractive and additive steps. The basic fabrication steps in a top-down approach are (i) lithography, (ii) oxidation, (iii) etching, (iv) ion implantation, (v) diffusion, and (vi) deposition.

(i) Lithography: lithography is the process of transferring a pattern from a mask on to a substrate. Optical lithography, generally called photolithography, has been the workhorse of semiconductor industry. Newer techniques, called next-generation lithography (e.g., e-beam/ion-beam lithography, X-ray lithography, nanoimprint lithography, scanning probe lithography, interference lithography, nanotemplating, etc.) are more of experimental nature but are expected to replace photolithography. Photolithography requires a mask that contains the template features on it. A photosensitive material (photoresist) is spun cast on the substrates which undergoes changes in chemical composition when exposed optically to a specific wavelength of light through the mask. The exposed wafer is then developed in a solution (developer solution such as MF-319) to create the pattern. A typical photolithography process is shown in Figure 1 (adapted from [18]).

(ii) Oxidation: it is the formation of silicon dioxide (SiO_2) on a silicon substrate [18]. There are several techniques for growing SiO_2 on a silicon substrate; more common are thermal oxidation, plasma anodization, and wet anodization. Among these, thermal oxidation is used in large-scale integration of electronic devices. A silicon wafer is placed in a furnace and exposed to high temperature either with or without water vapor. There are thus two types of thermal oxides: oxides made via dry oxidation and oxides made via wet oxidation. In dry oxidation, a mixture of nitrogen and oxygen is pumped into the furnace (which is already at or above $1000°C$). At high temperature, silicon reacts with oxygen and a SiO_2 layer is grown. In wet oxidation, water vapor instead of oxygen is pumped into the chamber along with nitrogen. The growth rates of oxide in both cases depend on the temperature, pressure, orientation of the wafer, dopant species in the wafer, moisture content inside the chamber, presence of chlorine, and so forth. Thermally grown oxides are used as tunneling oxide, gate oxide in metal oxide field effect transistors (MOSFETs), dielectric material in capacitors, masking material against ion implantation and diffusion, passivation layer on the substrate, device isolating material, and so forth [18].

(iii) Etching: etching is a subtractive method that selectively removes material from the substrate. A mask pattern is first created on the layer to be etched. Then the etchant is introduced into the system. This can be done in dry or wet conditions, depending on the requirements. Wet etching offers a high etching rate, but it is mostly isotropic, which is sometimes not desired. On the other hand, dry etching is highly directional in nature but less selective compared to wet etching. Dry etching is preferred over wet etching where a high aspect ratio needs to be achieved. Almost every lithography step is followed by an etching step to create patterns.

(iv) Ion Implantation: ion implantation is a process in which energetic, charged atoms (or molecules) are directly introduced into the substrate. It is the process of introducing impurities in a controlled fashion. The distribution of the impurity atoms depend on the type of particles, their energy, and the orientation of the wafer with respect to the ion beam.

(v) Diffusion: diffusion is the spontaneous movement of particles toward a lower concentration region due to the concentration gradient. It is used to introduce dopants in crystal. It is a high temperature process.

(vi) Deposition: this process is used for putting uniform layers of materials onto substrates. It can be chemical vapor deposition (CVD) or physical vapor deposition (PVD), as depicted in Figure 2 [18]. In CVD the reactant species are introduced into the chamber. These react with each other and deposit a layer of one product material. The rest of the byproducts are usually gaseous and are pumped out of the chamber. CVD offers uniform, robust, and high throughput deposition of materials. It can be used to deposit a wide variety of materials, including Si_3N_4, SiO_2, Al, and W. PVD is a physical process where a target material may be vaporized using heat or an electron beam. The evaporated atoms or molecules are deposited on the surface of the substrate. No chemical reaction occurs in this process. Since there is no other material inside the chamber, PVD offers purer deposited films than CVD, but the throughput is lower for a PVD system [18].
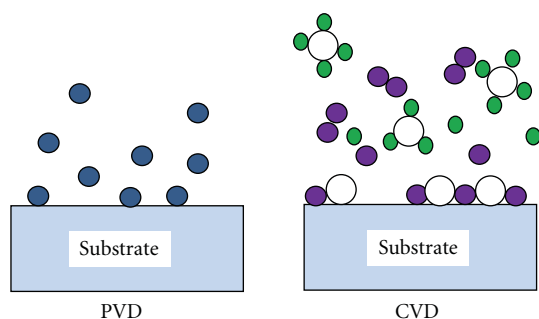
Figure 2: Chemical vapor deposition (CVD) and physical vapor deposition (PVD), adapted from [18].

The top-down approach can be used to fabricate a wide variety of devices with high reliability and high integrity; thus, this approach is common in the semiconductor device industry. Many of the novel nanostructures, like nanowires and nanopores, may be fabricated with top-down approaches [19–23]. Stern et al. reported nanowires fabricated by the top-down approach that were used to detect biological samples without any labeling [21]. Nanopores can be used to detect and measure biophysical properties of DNA, proteins and many other molecules passing through the nanopores [22, 24, 25].

The major advantages of the top-down approach are that a large number of features can be transferred onto a substrate from a mask by a single exposure and that single mask can be used many times. Successive masks can be aligned with high precision using alignment marks placed on the substrate. Owing to the parallel nature of the top-down approach, high density devices can be produced at mass-scale. In last few decades, advances in top-down fabrication has led to a monotonic decrease of device dimensions, thereby increasing the density of devices on a single chip. The immediate consequence has been significant reduction in cost per device.

However, at very small scales (less than 100 nm), the top-down approach has inherent limitations [26]. Optical lithography, which has been the key enabler of low cost mass production of micro-/nanodevices, is no longer suitable to fabricate structures below 100 nm. When the wavelength gets too small, conventional lenses cannot be used to focus light due to the high optical absorption [26]. New equipment would be required to focus the light, adding to production cost.

In bottom-up fabrication, the building blocks (e.g., the atoms or molecules) are brought in close proximity to form the desired structures. The assembling of the elementary blocks is usually manipulated by physical aggregation, chemical reaction, and use of templates [27]. Controlled chemical reactions are used to manipulate those blocks to self-assemble and make nanostructures such as nanotubes, nanoribbons, and quantum dots [28, 29]. There are two methods to achieve self-assembly: templating and nontemplating. Templating involves the interaction of biomacromolecules under the influence of a specific sequence, pattern, structure, external force, or spatial constraint. For

instance, cylindrical amphiphilic polymeric micelles may be used as templates to fabricate semiconducting nanotubes of cadmium sulphide. Semiconducting cadmium sulphide may be used to detect a DNA sequence via field effect transistor (FET) action [30]. In contrast, nontemplating is the formation of larger structures by individual atoms or molecules without external influence [31, 32]. For example, nontemplating can be used to form a variety of structures and shapes, including twins, tetramers, rods, triangles, and 3D arrays [32]. Self-assembly is a cost-effective and efficient technique that can be used to produce nanostructures and features below 100 nm [33].

The bottom-up approach accommodates a wide range of possibilities in the design and fabrication of molecular devices. The unique advantage of the bottom-up approach is the potential to assemble nanostructures where the top-down approach fails. Even with sophisticated photolithography, it is not easy to fabricate nanostructures at a size of a few nanometers. Self-assembly is an ideal approach in this case [34]. Nonetheless, one of the major challenges of this approach is to ensure predefined structures with precise shapes and sizes. Hierarchical design, which makes the top-down approach suitable for producing high density devices, is not yet feasible with the bottom-up approach.

2. Medical Applications of Nanostructures

Nanodiagnostics is defined as the use of nanotechnology for clinical diagnostic purposes [35, 36]. Recently, a wide variety of nanostructures has been tested in different diagnostics applications. Nanostructure-based diagnostics have the promise to offer higher sensitivity and specificity, allowing earlier detection of diseases [36]. The increased demand for sensitivity requires the occurrence of a diagnostically significant interaction between analyte molecules and signal-generating parts, thus enabling detection of a very low amount of analyte. Due to their increased sensitivity and selectivity, different nanostructure-based assays have opened new directions in diagnostics of pathogens and diseases in the last few years [36]. The novel and unique characteristics of nanostructure-based diagnostics have the potential to create point-of-care applications. The applications of different nanostructures in the field of diagnostic and detection are reviewed below.

2.1. Nanostructured Surfaces. Nanoscale topography is achieved on a substrate by using a number of techniques. Nanostructured or more precisely nanotextured surfaces show interesting properties. For example, nanotextured surfaces have been shown to enhance adsorption of cells and increase cell proliferation [37, 38]; nanopillars on a polyethylene glycol (PEG) surface patterned by UV-mediated capillary lithography have been shown to enhance the adsorption of proteins [39]. The nanopatterned surface in the latter case also enhanced the cell adhesion (heart fibroblasts of natal rat). The enhanced adhesion was explained in terms of the increased surface area, and the resulting increase in interactions between the cells and the functional group on the surface [39]. Antibody

(a)

(b)

(c)

(d)
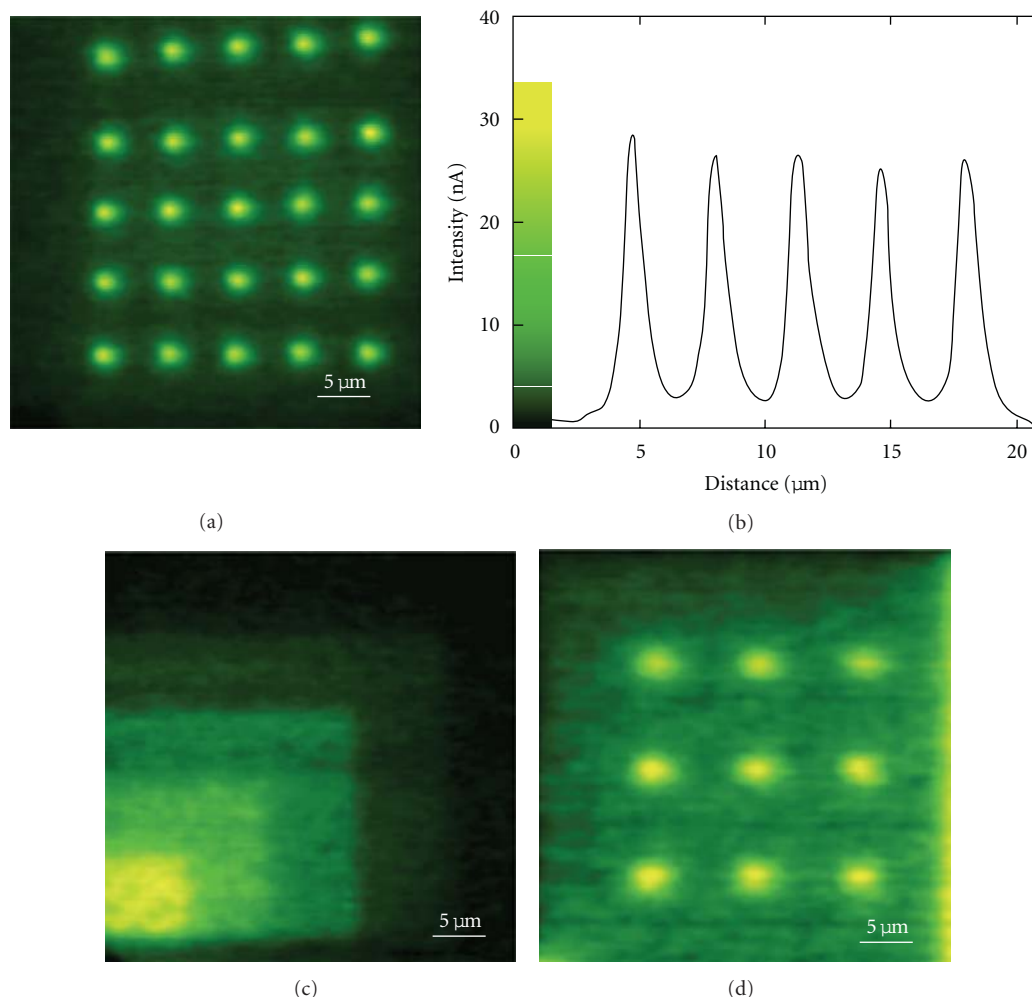
FIGURE 3: Fluorescence images of (a) biotinylated DNA deposited on to a streptavidin-coated glass surface; (b) intensity plot across the bottom row of (a); (c) pattern of biotinylated DNA square on top of another; (d) G-protein dots on a positively charged glass surface, reprinted with permission from [42]. Copyright 2002 American Chemical Society.

functionalized nanostructured surfaces have also been used to detect specific proteins or cells [40]. The increased adhesion has been shown to impart more sensitivity in the detection. Additionally, these structures are simple to fabricate and to reproduce. The structures are robust enough to remain stable upon exposure to solvents like water and ethanol [39].

Dip pen nanolithography (DPN) is a scanning probe lithography technique that can directly write patterns of molecules like modified oligonucleotides and mercapto-propyltrimethoxysilane (MPTMS) on silicon dioxide chips [41]. Fluorophore-labeled complementary and noncomplementary DNA molecules have been used to verify the specificity of the patterned molecules. The same array could be reused after rinsing with deionized (DI) water to assemble the modified complimentary DNA.

Andreas et al. reported a straightforward method to create patterns by direct writing of DNA and proteins on a glass surface by scanning ion conductance microscopy (SICM). Reportedly, their method possessed delivery control down to the single molecule level [42]. Fluorophore-labeled DNA and G protein were patterned on a glass surface, and images were taken as shown in Figure 3. These methods can be used to fabricate DNA and protein arrays [41, 42]. Antibodies and complementary DNA tagged with fluorophore or nanoparticles could be detected by these arrays. Though this nanopatterning technique is still at its nascent level, it shows the potential to possibly miniaturize certain medical diagnostic assays as this novel technique can utilize very small sample volumes to detect target molecules.

Recently, nanoarrays of monoclonal antibodies have been created by DPN to capture HIV p24 proteins from human plasma samples. AFM was used to determine the presence of p24 after capture. By adding anti-p24-modified gold nanoparticles which would selectively bind to the p24 spot, a detection limit of 0.025 pg/mL was achieved. This detection level is much better than the 5 pg/mL limit of conventional enzyme-linked immunosorbent assay (ELISA) [43].

A capacitor is an electrical device that is formed when an insulating material is sandwiched between two electrode

plates. When the gap between two plates is a few nanometers, it can be called a nanocapacitor. The capacitance can be determined from the plate area, the distance between plates, and the dielectric properties of the insulating medium. The working principle of a nanocapacitor-based biodetection device is simple: if some target molecule selectively could be attached onto a dielectric material, it would change the dielectric constant of the material appreciably, and the change in capacitance would be significant. This change could be measured electrically, allowing detection of the target molecules. The main advantage of this method is that it does not require any prior labeling of the sample. The only requirement is that there should be a minimum concentration of target molecules present in the sample sufficient to create appreciable change in capacitance. Kang et al. developed transparent nanocapacitors that were used to monitor dielectric and optical dynamic behavior of biomolecules. They used planar nanogap capacitors with 50 nm gaps, fabricated using silicon nanolithography [44]. The nanogap was created by in-plane sacrificial oxide etching. The single stranded DNA (ssDNA) was immobilized on the electrode surface. When the target DNA hybridized with the probe DNA, the dielectric property changed, resulting in a change in capacitance. The permittivity changed upon hybridization, which implied that the capacitance changed accordingly [44]. Permittivity was significantly increased in the case of hybridization, allowing detection of complimentary DNA. A large two-dimensional array of such nanocapacitors can be used for label-free measurement of nucleic acid targets with high sensitivity.

2.2. Nanoparticles. Nanoparticles are ultrafine particles with at least one of the diameters (major or minor axis) less than 100 nm [45]. There is a wide variety of nanoparticles depending on their shapes, materials, and sizes. The most common shapes of nanoparticles are sphere, rod, prism, dot, star, and so forth. Nanoparticles can be synthesized from metals or polymers [46, 47]. Among metallic nanoparticles, gold nanoparticles (GNPs) are used extensively for many applications and especially in bioassays [46]. There are several techniques to produce GNPs. Most commonly, GNPs are synthesized by chemical reduction of a precursor compound of gold in the presence of a capping agent (such as $AuClO_4$) [48]. This capping agent is able to bind to the GNP surface, blocking its growth beyond the nanometer range and stabilizing the colloid in a particular solvent. This method is commonly used to produce spherical GNPs [48]. Temperature, reducing agent, capping agent, and reaction time are the experimental parameters to control the shape and size of the GNPs [49].

Quantum dots (QDs) and GNPs can be used to develop immunoassays to detect pathogens and DNA sequence [50]. Used as fluorophores, these nanoparticles can produce six orders of magnitude stronger emission intensity than conventional dyes. Properties like high photostability, single-wavelength excitation and size-tunable emission make QDs and GNPs very suitable for imaging purposes [51]. GNPs have also been widely used in optical detection systems due to their very high absorption coefficients [52]. The

optical properties of GNPs and QDs (such as absorption coefficient, refractive index, color, etc.) can be explained from a phenomenon called surface plasmon resonance (SPR). The emission bands of NPs and QDs strongly depend on their shapes rather than sizes and are not perturbed by refractive index of the surrounding medium [52].

GNPs can be detected by optical absorption, Raman scattering, fluorescence, magnetic/atomic force microscopy, and electrical resistance measurements. The availability of these various detection methods makes GNPs useful markers [53]. GNPs with attached DNA and Raman-active dyes have been shown to assemble on a sensor surface to detect the presence of complementary DNA target. Surfaces patterned with multiple DNA strands have the potential to detect different DNA sequences simultaneously [36].

Zhang et al. demonstrated a quantum dot-fluorescence-resonance-energy- transfer (QD-FRET) based nanosensor. In the presence of target DNA, the reporter probe and the capture probes were sandwiched as shown in Figure 4 [54]. The assembly was then attached to the QD with the help of a capture probe. When this complex was excited with a laser source, it emitted two characteristic wavelengths: one for the QD and one for the reporter molecule. In the absence of the target molecule, there was emission only from QD. However, if the target was present, then emissions from QD and reporter molecules both were detected [54].

For separation-free DNA hybridization detection, molecular beacons are the most widely used biomolecules. A background noise comparison between the QD-FRET-based nanosensor and the molecular beacon is presented in Figure 5. From Figure 5(a) it can be seen that the background fluorescent signal kept increasing with the increase of probe concentration, whereas the QD-FRET-based nanosensor showed almost zero noise irrespective of the probe concentration. Comparison of detection sensitivity, defined as the ratio of the fluorescent burst after and before introducing the targets is shown in Figure 5(b). At every level of target concentration, the nanosensor showed higher responsivity. The nanosensor showed almost 100-fold higher responsivity than the molecular beacon at a target concentration of 0.96 nM. Also, this QD-based sensor had the sensitivity as low as 4.8 fM, which is 10,000 times lower than that achieved by the molecular beacons [54]. The QD-based sensing technique shows promise in the detection of oligonucleotides, proteins and polypeptides. The main advantages of the platform are that it produces results in real time and at the single molecule level; therefore, it can be used to study molecular interactions with high temporal and spatial resolution [54].

An electrical resistance measurement system can also be used to detect the hybridization between the probe and target molecules. In one report, capture strands of DNA were attached in between electrode gap first, then the GNP-modified probing strands were dispensed on the surface [50]. A mixture of silver nitrate and hydroquinone was used to enhance the conductivity of the gap. When the target strands were present in the sample solution, they hybridized to the capture strands and GNP probes onto the surface, and the resistance kept reducing as the time went by [50]. It was

(a)

(b)

(c)
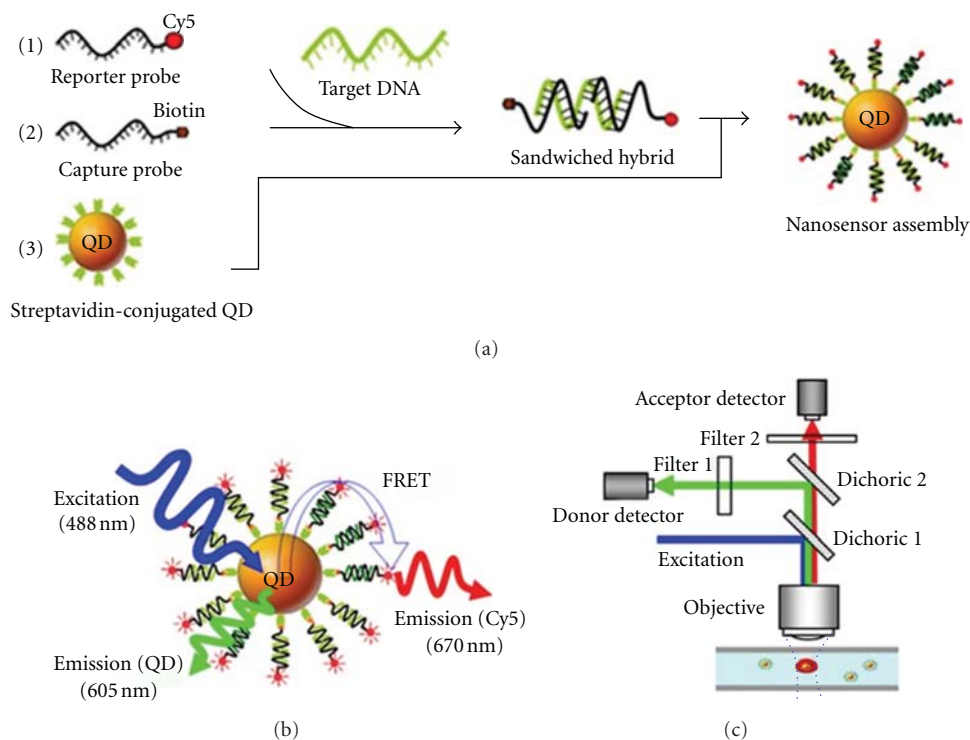
FIGURE 4: Schematic diagram of single-QD-based DNA nanosensors: (a) functionalized QD in the presence of target molecules; (b) mechanism of fluorescence emission from Cy5 upon illumination. It is caused by FRET between Cy5 acceptors and a QD donor; (c) experimental setup, reprinted by permission from Nature Publishing Group: Nature Materials [54], copyright 2005.

(a)

(b)
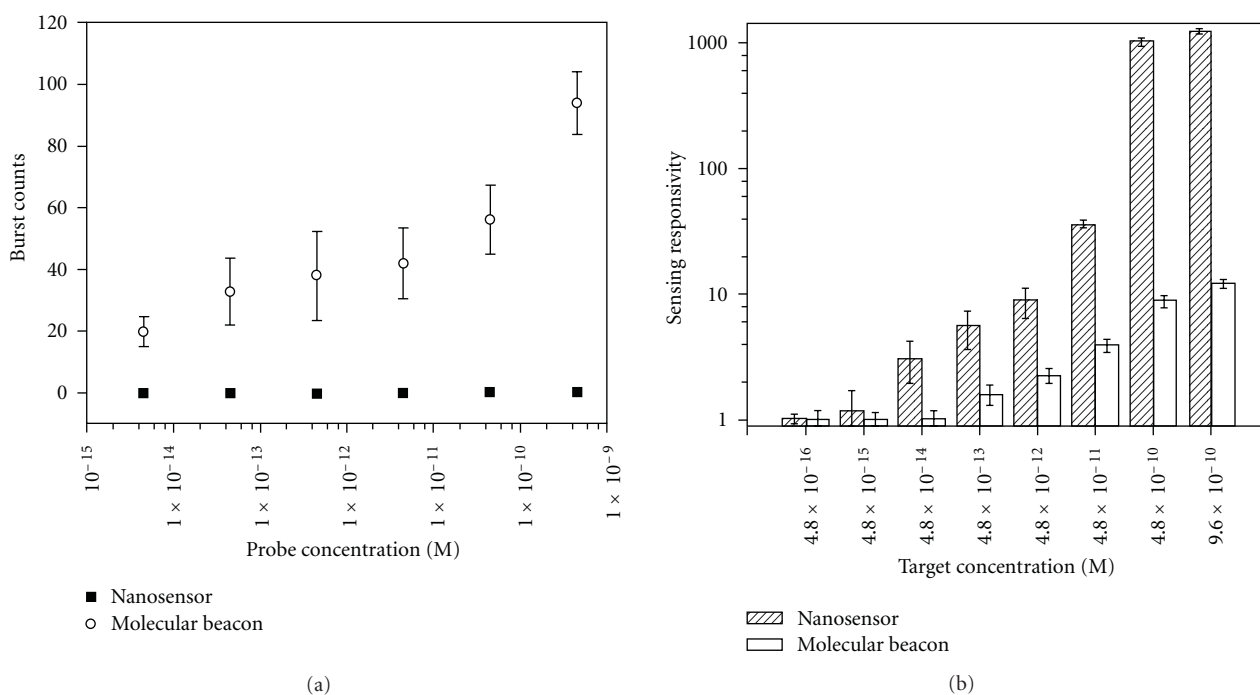
FIGURE 5: Performance of QD-based nanosensor. (a) Fluorescent burst counts versus probe concentration plot for QD-based nanosensors and molecular beacons. The concentration ratio of the Cy5-labelled reporter probe and the biotinylated capture probe was 1 : 1, and the Cy5/QD ratio was maintained at 24 in all experiments. The molecular beacons were Cy5-5-CGACC CCTGC CACGG TCTGA GA GGTCG-3-BHQ-2 (stems are underlined). Measurement time was 100 s. (b) Sensing responsivity versus target concentration plot for nanosensors and molecular beacons. Concentrations of receptor, capture probe, and molecular beacon were all 4.8×10^{-10} M and concentration of QD was 2×10^{-11} M, reprinted by permission from Nature Publishing Group: Nature Materials [54], copyright 2005.
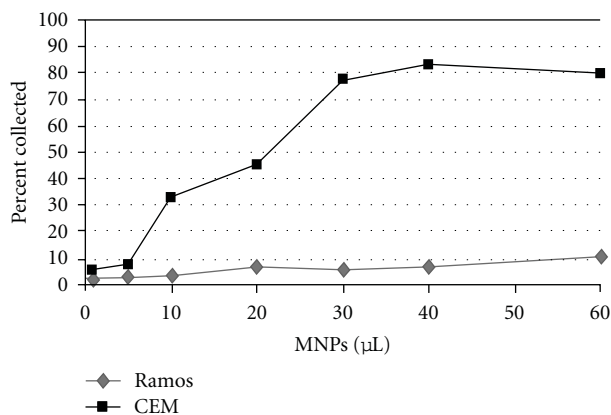
FIGURE 6: Extraction efficiency of magnetic nanoparticles (MNPs) between target (CCRF-CEM cells are actually CCL-119 T-cell) and control cells (Ramos cells are CRL-1596, B-cell), reprinted with permission from [55], Copyright 2006 American Chemical Society.

reported that this method could detect 50 nM to 500 fM of DNA by adjusting silver enhancement time [50]. This method showed 10 times more sensitivity and 10^6 times more specificity over current genomic detection systems [50].

Recently, Herr et al. reported that a novel two nanoparticles assay can be used to extract and detect acute leukemia cells rapidly [55]. They used aptamer modified magnetic and fluorescent nanoparticles simultaneously. First, magnetic nanoparticles extracted the target cells from the sample solution, and subsequently fluorescent nanoparticles enhanced the sensitivity of the detection. The magnetic extraction efficiency for the target cells was well above that for control cells, as shown in Figure 6. To improve the sensitivity even further, fluorescent nanoparticles were used with the magnetic nanoparticles. To compare the fluorescent enhancement capabilities of dye-doped nanoparticles over aptamer conjugated fluorescent dye, individual dye (Rubpy) probes were linked with the aptamer in order to be immobilized on target cells. Equal amounts of magnetic and Rubpy nanoparticles were incubated with target cells and then washed three times by magnetic extraction. The sensitivity of dye-doped nanoparticles was at least 100 times higher than that for the aptamer conjugated fluorescent dye, as shown in Figure 7. The simultaneous use of two different aptamer-conjugated nanoparticles on the same target enhanced the selectivity significantly. Only magnetic extraction separated a good number of target cells from control cells, but due to nonspecific binding, some control cells were also retained in the extracted solution, as shown in Figure 8. Simultaneous incorporation of the fluorescent nanoparticles along with the magnetic extraction enhanced the selectivity even further, which is much desired for practical applications. Very high sensitivity is always required to analyze a real sample due to the low ratio of target cells to other cells.

Recently, Lee et al. have also reported multimodal probing of tumor cells using iron oxide nanoparticles with thermally crosslinked polymer shells [56]. They synthesized triblock polymer (poly(3-(trimethoxysilyl) propyl methacrylate-r-PEG methyl ether methacrylate)), denoted as poly(TMSMA-r-PEGMA), for coating the iron oxide nanoparticles. Figure 9 shows the coating and crosslinking of the polymer on the surface of nanoparticles. The thermally crosslinked superparamagnetic iron oxide nanoparticles were denoted as TCL-SPION. The N-hydroxysuccinimide-activated carboxylic acid group provided active sites for the further conjugation of fluorescent dyes (such as near-infrared dyes) for optical imaging and cancer-specific ligands [57]. $Si(OCH_3)_3$ group provided the bonding to iron oxide and the crosslinking of the polymer shells and PEG for biocompatibility [56].

Magnetic resonance imaging (MRI) showed the tumor as a hyperintense area in T_2-weighted images, as shown in Figure 10(a) with a red arrow and a dashed circle before the injection of the Cy5.5 TCL-SPION. At 3.5 hours after the injection, MRI showed a decrease in signal, implying the accumulation of the SPION within tumor region. This decrease in signal was sufficient for a radiologist to detect the tumor with high confidence. *In vivo* fluorescence images of the same mouse at similar time points were also taken, as shown in Figure 10(b). The pseudo-color-adjusted optical images showed a relatively intense fluorescence signal exclusively in the tumor area (red arrow in Figure 10(b)) at 3.5 h postinjection time. This result perfectly agreed with the MR imaging results. The *in vivo* T_2 MR and near-infrared (NIR) fluorescent imaging of tumor-bearing mice after the intravenous injection of the Cy5.5 conjugated multimodal probes revealed that the probes were accumulated at the tumor site due to enhanced permeation and retention effect. This dual imaging technique ensured the detection of tumors with good confidence.

In order to investigate further, *ex vivo* NIR fluorescent images of several organs and tumors were taken. They indicated that the highest fluorescence intensity was observed in the tumor region. When the free Cy5.5 dye without nanoparticles was intravenously injected into a tumor-bearing mouse as a control experiment, only a faint fluorescence signal was observed in the tumor [56].

2.3. Nanopores. A nanopore is a nanoscale channel or hole in a freestanding membrane. Solid-state nanopores were originally inspired from reports of biological transmembrane proteins being used as nanopores and nanoscale detectors. For example, the alpha-hemolysin (HL) channel was used to detect small molecules of single stranded nucleic acids in the seminal paper by Kasianowicz et al. [58]. More recently, Clarke et al. have shown that a modified HL nanopore (as shown in Figure 11) can be used to distinguish individual DNA mononucleotides [59]. As a mononucleotide base passes through the pore, the ionic current is modulated in a more or less base-specific manner. Pulse depth is a measure of how strongly the base interacts with the pore and depth of pulse distribution is used to discriminate among different bases. Although a given DNA base (e.g., dAMP) does not yield a uniform pulse depth, the pulse distribution is largely distinguishable between the four DNA bases, as shown in Figure 12(b). There is some degree of overlap between consecutive distributions that can introduce

(a)

(b)

(c)

- ■ RuBpy dye
- ■ RuBpy NPs
- ■ Cells alone
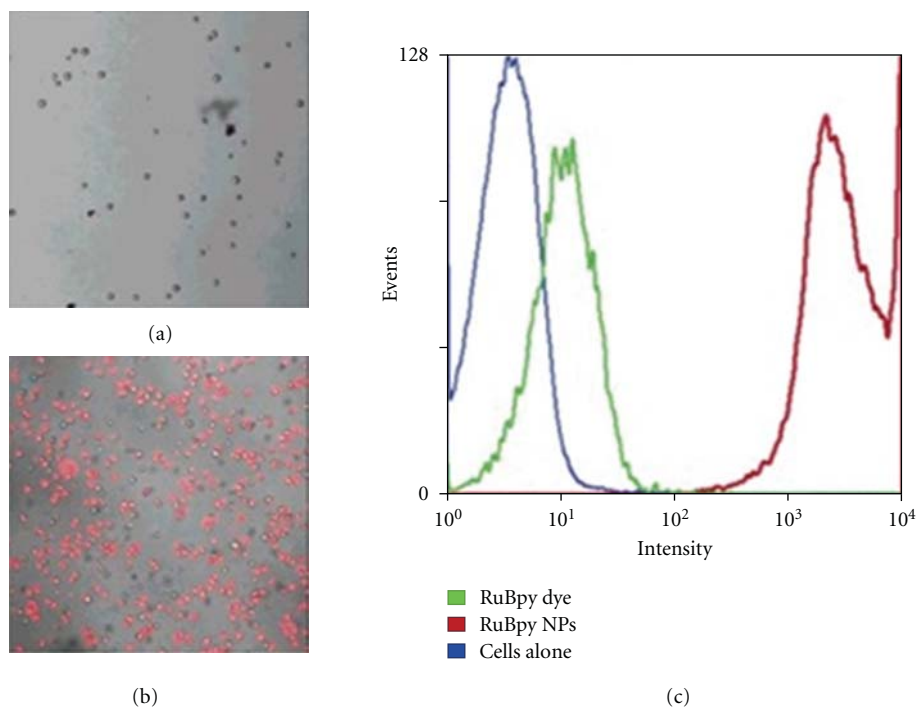
FIGURE 7: Fluorescence images of extracted cells after 5 min incubation followed by three magnetic washes with (a) Rubby dye-aptamer conjugates (40 μM) and (b) Rubby nanoparticle-aptamer conjugates (0.5 nM). (c) Comparative plots between dye-labeled cells and NP-labeled cells by flow cytometric analysis, reprinted with permission from [55], Copyright 2006 American Chemical Society.

(a)

(b)

(c)

- ■ Ramos cells
- ■ CEM cells
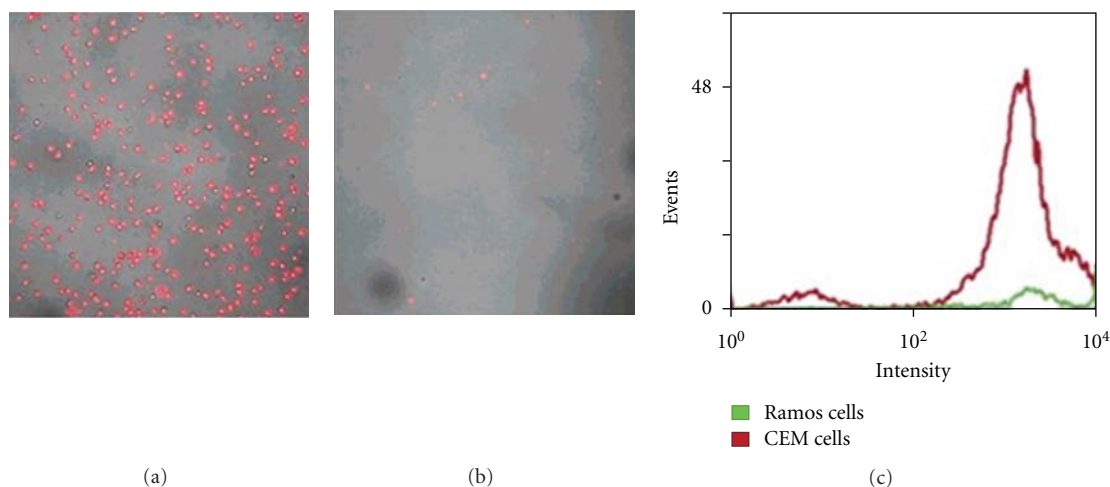
FIGURE 8: (a) Sample from target cells, (b) sample extracted from control cells, and (c) flow cytometric comparison between target and control signal after 5 min incubation followed by three magnetic washes with magnetic and fluorescent nanoparticles, reprinted with permission from [55], Copyright 2006 American Chemical Society.

detection errors. A mutant HL and a covalently attached adapter protein (am$_6$amPDP$_1$ CD), however, can enhance the base discrimination, thereby reducing errors (see the current pulses and histograms in Figure 12) [59].

Figure 13 shows that each of four DNA mononucleotides had characteristic pore current distribution. The four distributions were centered around four distinct current levels; that is, signals from each base were separable. This method was capable of discriminating between the four DNA

nucleotides (dAMP, dTMP, dCMP, and dGMP) with over 99% confidence under optimal operating condition [59].

Such reports show the potential of nanopores toward the ultimate goal of direct sequencing of single molecules of DNA. A reliable, low-cost DNA sequencing can have a profound effect on genome research. DNA sequence information can provide useful information about an individual's genetic makeup that might put someone at increased risk for certain diseases like cancer. Apart from medical applications,

(a)

Carboxyl TCL-SPION

Crosslinked polymeric shell

(b)

Carboxyl TCL-SPION

Amino TCL-SPION

Cy5.5 TCL-SPION

	Carboxyl TCL-SPION	Amino TCL-SPION	Cy5.5 TCL-SPION
Size (DLS)	25.6 ± 2.7 nm	32.6 ± 3.7 nm	31.9 ± 4.6 nm
Zeta potential	-30.5 mV	-1.34 mV	-25.13 mV

(c)
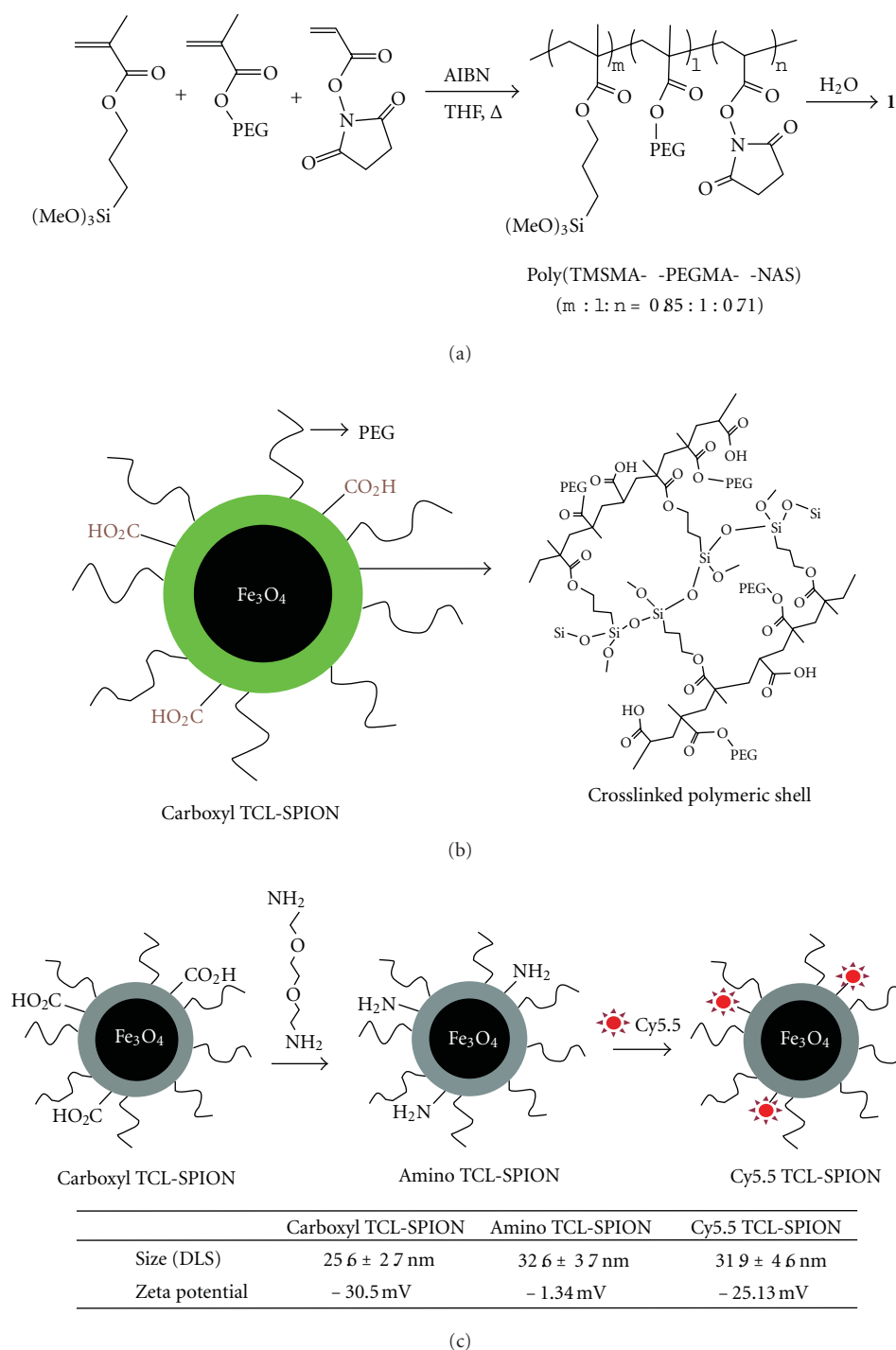
FIGURE 9: (a) Method of synthesis of poly (TMSMA-r-PEGMA-r-NAS); (b) schematic representation of carboxyl TCL-SPION crosslinking between polymer layers after heat treatment; and (c) amino and Cy5.5 TCL-SPION with different size and zeta potential, reprinted with permission from [56]. Copyright 2007, American Chemical Society.

there are many other application areas, such as agriculture, security, defense, and evolutionary biology, where genomic information is useful [33].

Solid-state nanopores (also called artificial nanopores) are made using many types of membrane materials (silicon, SiO_2, and Si_3N_4) and by opening the orifice using a num-ber of different approaches. A recent review on solid-state nanopores used for nucleic acid detection succinctly describes various approaches [25]. The paper delineates both the advances and the many remaining hurdles. Although focused on nucleic acid analysis, this paper lays out advancements that have been achieved through last 15 years and

Pre (0 h)   Pre (0 h)

3.5 h   3.5 h

(a)   (b)
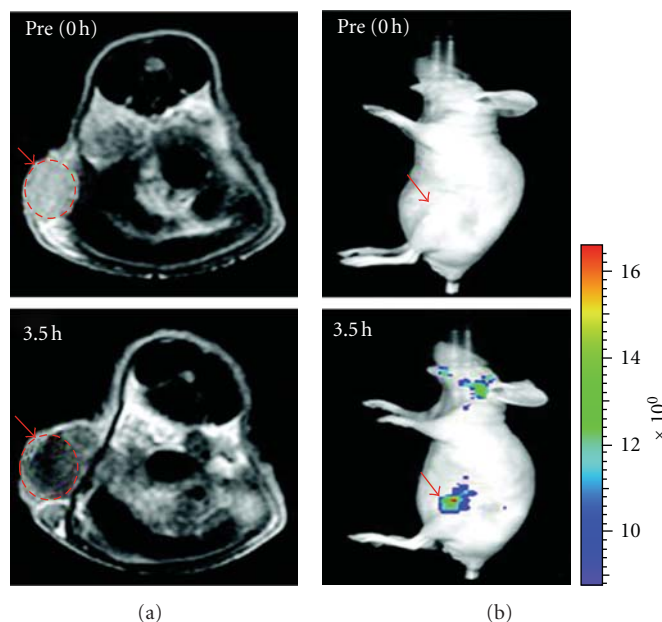
FIGURE 10: (a) T_2-weighted MR images (TR/TE of 4200 ms/102 ms) taken after 0 and 3.5 h of injection of 14.7 mg Fe/kg in PBS of Cy5.5 TCL-SPION at the level of tumor (320 mm³). The allograft tumor region is dashed with red circle. (b) Fluorescence images of the same mouse under same condition. An exposure time of 1 s and a Cy5.5 filter channel were used. The scale on the right indicates the relative fluorescence intensity, reprinted with permission from [56]. Copyright 2007, American Chemical Society.

M113R
T115C
T117C
G119C (2.6 Å)
N121C (2.9 Å)
N123C (10.3 Å)
T125C (13.5 Å)

N139Q
G137C (7 Å)
L135C (9.1 Å)
G133C (17 Å)

9.2 Å   N139Q
         L135C

(a)   (b)
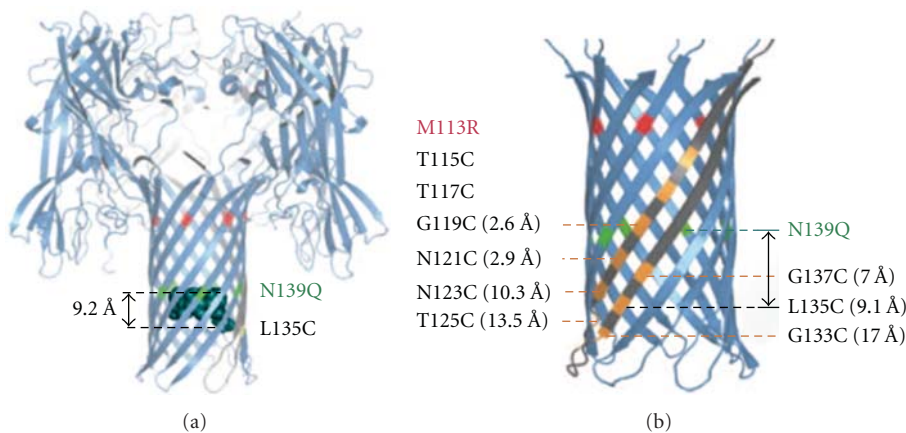
FIGURE 11: (a) Structure of the WT (M113R/N139Q)$_6$ (M113R/N139Q/L135C)$_1$ mutant (cartoon view) showing the covalent attachment of cyclodextrin at position 135 (space filling model), the glutamines at residue 139, and the vertical distance between the secondary hydroxyls and the disulphide bond of the cyclodextrin. (b) barrel structure showing the location of arginines (at position 113) and the cysteines in the mutants. Single letter standard amino acid code was used to describe the mutants, reprinted by permission from Nature Publishing Group: Nature Nanotechnology [59], copyright 2009.

clearly defines challenges that have impeded applications of nanopore sensors in general. Most important challenges include needs for high spatial resolution, algorithms for complex analysis and severe lack of chemical engineering approaches for nanopores towards selective and sensitive detection. A recent book has also appeared that describes the whole range of nanopore fabrication approaches as well as targets of detection [24].

One such fabrication approach used polydimethylsiloxane (PDMS), a common polymer used to create microfluidic channels and microscale devices (Figure 14) [60]. The

nanoscale device was created by sealing a PDMS mold containing two reservoirs connected by a pore with a glass cover slip. It was then filled with an ionic solution. The potential across the pore was measured at constant applied current by using a four-point technique. When DNA molecules were passed through the pore, they partially blocked the flow of ions, giving a downward spike in the current profile, as shown in Figure 15. Each downward peak corresponded to a single DNA molecule passing through the pore. No current dip was observed in the absence of DNA. By tweaking the pore sizes to slightly larger dimensions, it is

(a)

(b)
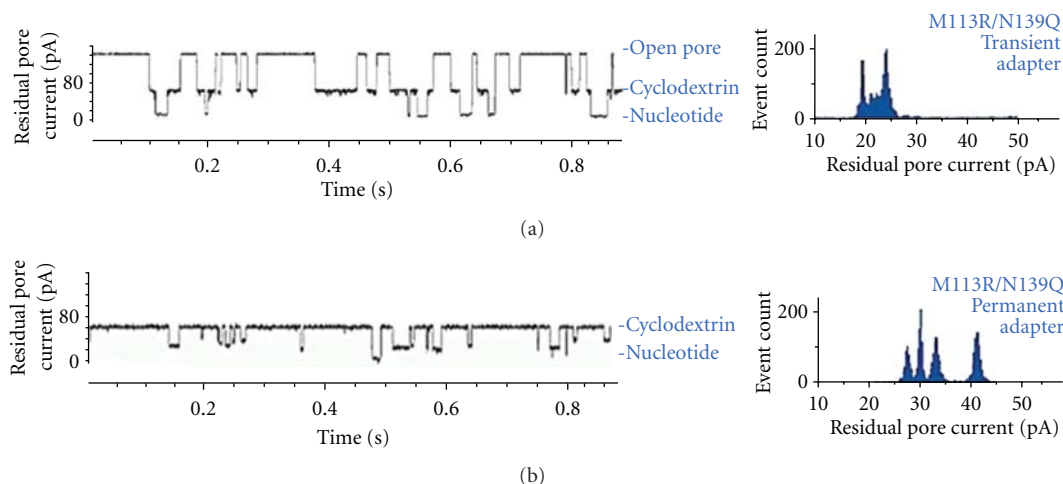
Figure 12: Comparison of recording from single channel of permanent and transient adapters. (a) The WT-(M113R/N139Q)$_7$ HL pore illustrating transient adapter binding (40 mM am7 CD) and nucleotide detection. Nucleotide binding events histogram for residual current. (b) Corresponding data for the WT-(M113R/N139Q)$_6$ (M113R/N139Q/L135C)$_1$ mutant with a covalently bonded am$_6$amPDP$_1$ CD, allowing continuous nucleotide detection and enhanced nucleotide discrimination. The traces were recorded under the parameter set up of 800 mM KCl, 25 mM Tris HCl, pH 7.5, at +160 mV in the presence of 10 μM dGMP, 10 μM dTMP, 10 μM dAMP, and 10 μM dCMP, reprinted by permission from Nature Publishing Group: Nature Nanotechnology [59], copyright 2009.

(a)

(b)
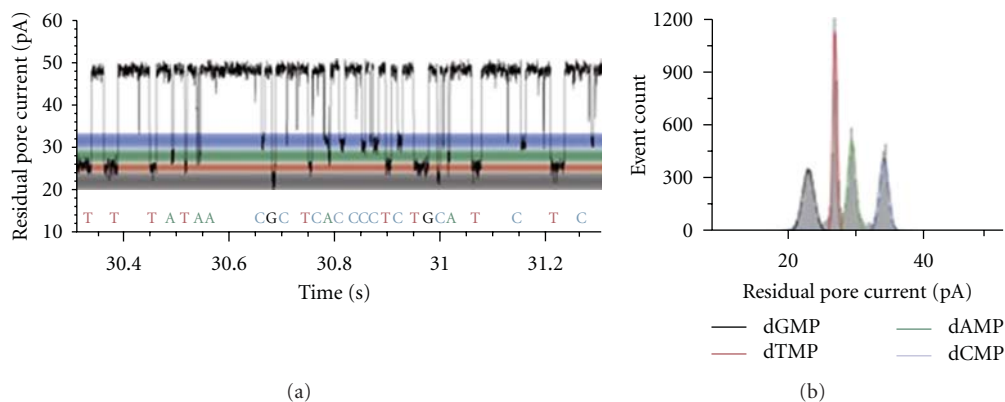
Figure 13: Distribution of nucleotide event with the permanent adapter. (a) Single-channel recording from the WT-(M113R/N139Q)$_6$(M113R/N139Q/L135C)$_1$-am$_6$amPDP$_1$ CD pore showing dGMP, dTMP, dAMP, and dCMP discrimination with a Gaussian fits. (b) Corresponding residual current histogram of nucleotide binding events, including Gaussian fits. Data acquired under the condition of 400 mM KCl, 25 mM Tris HCl, pH 7.5, at +180 mV in the presence of 10 μM dGMP, 10 μM dTMP, 10 μM dAMP, and 10 μM dCMP, reprinted by permission from Nature Publishing Group: Nature Nanotechnology [59], copyright 2009.

also possible to detect viruses or proteins [61, 62]. Covalently attaching probe molecules to the pore wall have allowed such devices to detect specific target species [61].

Specific target detection is also possible by measuring the change in size of a chemically functionalized colloid upon binding target molecules [60]. Saleh and Sohn reported an antibody-antigen-binding detection system based on a PDMS nanopore [22]. They functionalized the surface of colloidal particles with biocompatible material. When the particle passed through the pore, it left a signature of current blockade depending on its size. A particle with larger diameter took more time to pass and created higher dips in the current profile [22]. Antibody was specifically bound to the colloid surface, increasing its diameter. The increased size of the particle resulted in higher resistance in the current flow. Size-dependent discrimination was based on the translocation time and the current dip. Therefore, this device had the potential to detect an antigen corresponding to the antibody attached to the colloid surface by comparing the difference in the current profile [22]. This technique was used to detect presence of *Streptococcus* group A. The sensitivity of detection was compared to that of a standard latex agglutination assay, and it was found that the former method was an order of magnitude more sensitive than the agglutination assay. It was also four times faster [22].

Nanopore-based detection systems require small sample volumes and can count and distinguish among a variety of different biological molecules in a complex mixture using
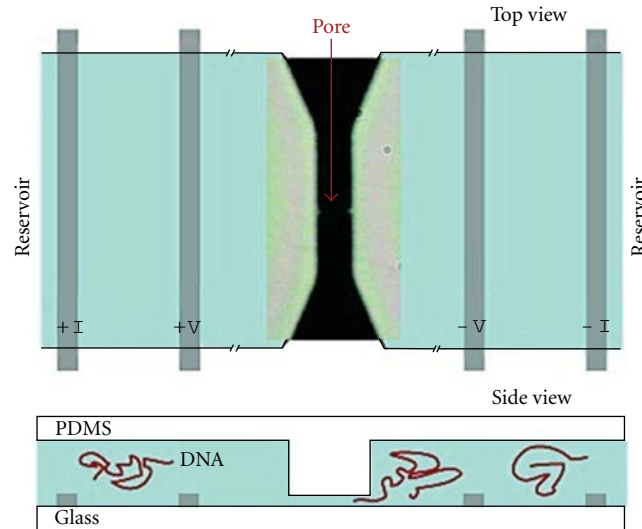
FIGURE 14: Top and side views of the nanopore device consisting of two 5 μm deep reservoirs connected by a lateral pore of 3 μm length and 200 nm diameter, reprinted with permission from [60], Copyright 2003 American Chemical Society.
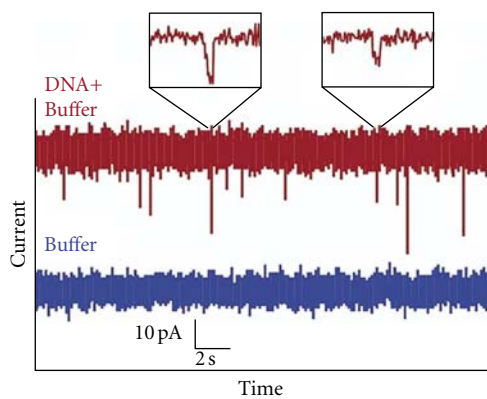
FIGURE 15: Current versus time plot of buffer solution (lower trace) and buffer with -phage DNA molecules (upper trace) upon application of 0.4 V across the pore. Every dip in current profile represents a DNA molecule passing through the pore. The pulse widths are typically 2–10 ms in duration and are well resolved, as shown in the insets. The variations in peak height are attributed to the different conformation of each molecule, reprinted with permission from [60], Copyright 2003 American Chemical Society.

simple electronic measurements. The cost-effectiveness, simplicity, speed, and versatility of nanopore assays is poised to expedite the development of molecular diagnostics [23].

2.4. Carbon Nanotubes. A carbon nanotube (CNT) is an allotrope of graphite. Carbon atoms are hexagonally connected in a CNT lattice. CNTs can be visualized as single or multiple graphite sheets rolled to form a cylindrical structure. Depending on the number of sheets, there are two types of CNTs: single wall carbon nanotubes (SWCNTs) and multiwall carbon nanotubes (MWCNTs). These are also classified as armchair, zigzag, and chiral based on the orientation of atoms on the sheet with respect to the axes. Depending on how carbon atoms are oriented on the CNT

surface, their electronic, chemical, and mechanical properties can change. Armchair CNTs are preferred to be used as electrodes in biosensors [63].

Li et al. developed a DNA microarray system which contained sensing pads constructed from assembled MWCNTs that were built into a matrix within a silicon nitride template, as shown in Figure 16 [64]. The open ends of nanotubes acted as nanoelectrodes. By combining such a nanoelectrode platform with Ru(bpy)32+-mediated guanine oxidation, target oligonucleotides at few attomoles could be detected with this method. The sensitivity could be further improved by increasing the number of nanotubes in one cluster. It was reported that the system was capable of providing fast, cheap, and simple molecular diagnostic solutions for medical and field uses [64]. In a recent study, Wang et al. showed that CNTs coated with alkaline phosphatase (ALP) enzymes as labels amplified the signal-to-noise ratio [65]. The CNTs were modified with oligonucleotides that were complementary to half of the target DNA sequence.

Magnetic microparticles modified with oligonucleotides complementary to the other half of the target DNA sequence were used. As shown in Figure 17, while there was target DNA present in the sample, a sandwich of magnetic nanoparticles-target-CNT was formed which was magnetically separated from the assay [65]. R-naphthyl phosphate was added to the extract in order to detect the ALP-modified CNTs. The presence of ALP in the mixture changed the R-naphthyl phosphate into R-naphthol, which was detected by the CNT-modified electrodes using a method called chronopotentiometric stripping. Reportedly, this method could detect very low concentrations of DNA (54 attomoles) [65].

2.5. Nanowires. A nanowire is a rodlike structure with diameter on the order of a few nanometers and an unconstrained length. Self-limiting oxidation has been used to fabricate silicon nanowires [66, 67]. To create an array, a silicon-on-insulator (SOI) wafer was patterned and etched as shown
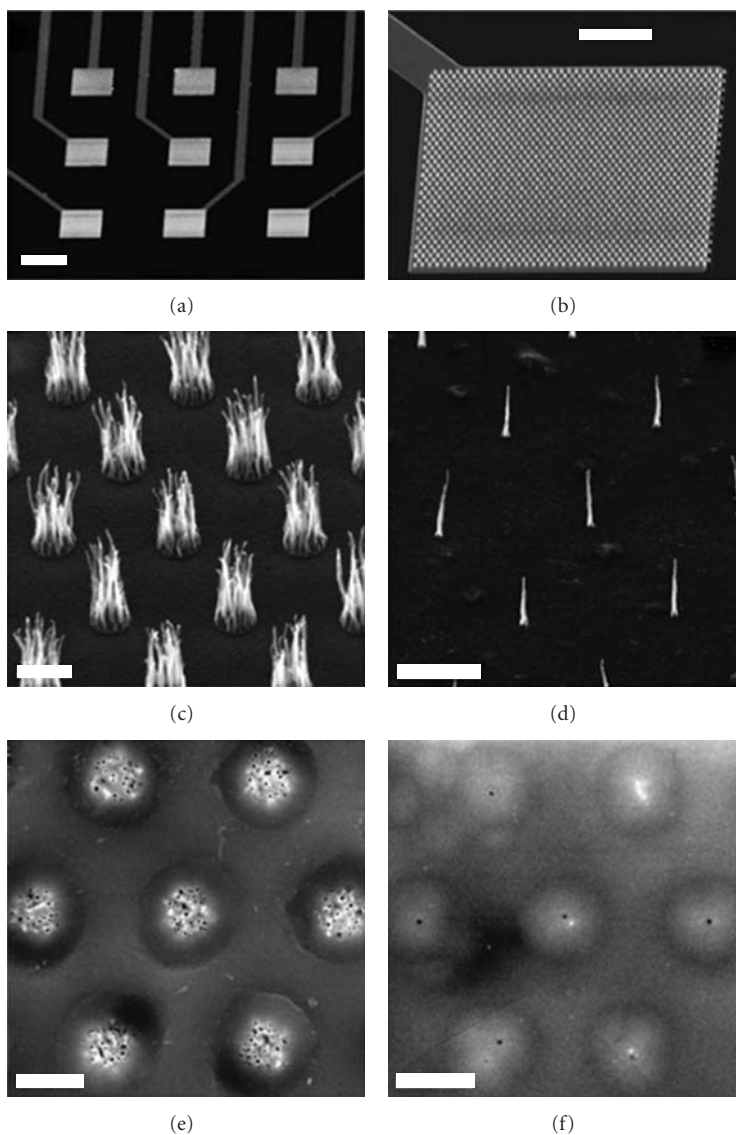
FIGURE 16: SEM micrographs of (a) 3×3 Ni electrode array, (b) array of MWCNT bundles on an electrode pad, (c) and (d) array of MWCNTs on Ni spots patterned by UV-lithography and e-beam lithography, respectively, (e) and (f) the surface of polished MWCNT array electrodes grown on 2 μm and 200 nm spots, respectively. 45° perspective view was used for (a–d) and (e-f) were top views. The scale bars for (a), (b), (c), (d), (e), and (f) are 200, 50, 2, 5, 2, and 2 μm, respectively, reprinted with permission from [64], Copyright 2003 American Chemical Society.

in Figure 18 [15]. The fin structures were further oxidized and stripped of the oxide layer to realize the nanowires. A metallization step was followed to establish contact to the nanowires. Isolation of electrodes from each other and from the substrate was provided by using an oxide and buried oxide layer, respectively. An encapsulation was used to isolate all electrical contacts from the aqueous solution [15].

Gao et al. reported a method of DNA detection using silicon nanowires. Peptide nucleic acid (PNA) probes were immobilized onto the nanowire surfaces by silane chemistry, as shown in Figure 19 [15]. The PNA probes were allowed to hybridize with target DNA. Hybridization, in turn, induced a change in the resistance of the nanowires. The use of PNA over DNA gave twofold advantages: bonding strength

of PNA-DNA is higher than that of a DNA-DNA pair due to the absence of negatively charged phosphate groups in PNA, and resistance change due to nonspecific binding of DNA was less in the case of PNA probes [68, 69]. The calibration curve was plotted as shown in Figure 20 [15]. The relationship between relative change in resistance and the logarithm of DNA concentration was approximately linear over a range of 1 nM to 0.1 fM. The relative error associated with the detection method described was less than 25% [70]. Hahm and Lieber also reported similar sensitivity of silicon nanowire sensor to detect DNA, albeit with high background noise [71].

Signal strength must be enhanced to make these silicon nanowire sensors as practical devices. Nanowire-based
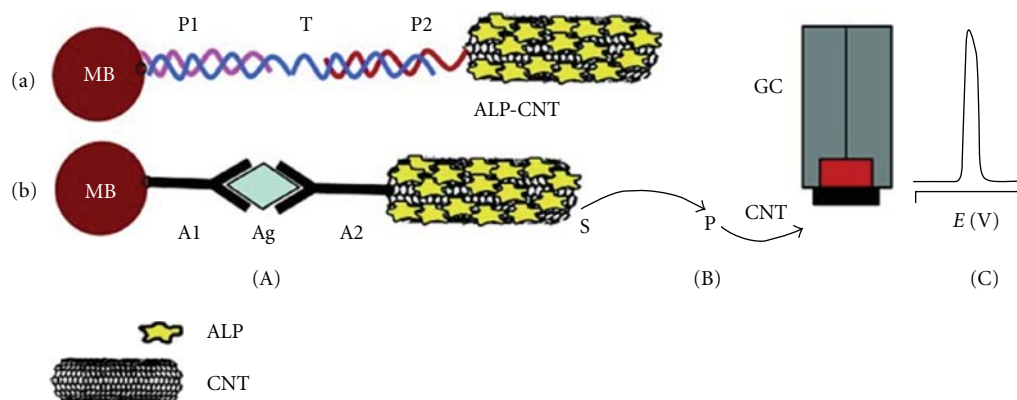
FIGURE 17: (A) Schematic illustration of capture of the alkaline-phosphate-(ALP-) coated CNT tags to the streptavidin-modified magnetic beads by (a) a sandwich DNA hybridization (b) Ab-Ag-Ab interaction. (B) Enzymatic reaction. (C) Electrochemical detection of the product produced from enzymatic reaction at the CNT-modified glassy carbon electrode, reprinted with permission from [65], Copyright 2001 American Chemical Society. MB: magnetic beads; P1: DNA probe 1, T: DNA target, P2: DNA probe 2, AB1: first antibody, Ag: antigen, Ab2: secondary antibody, S and P: substrate and product, respectively; GC: glassy carbon electrode, and CNT: carbon nanotube layer.
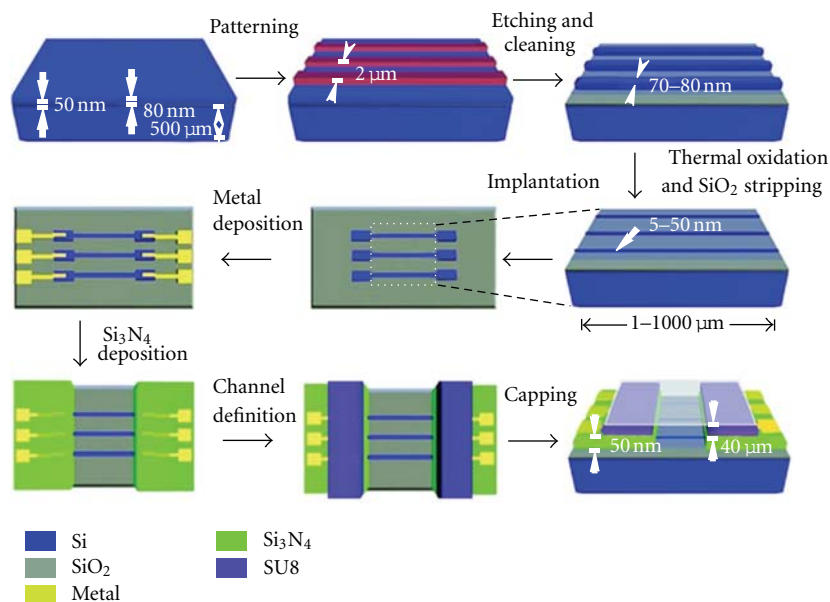
FIGURE 18: Schematic illustration of the fabrication process of Silicon nanowire arrays with fluidic channels, reprinted with permission from [15], Copyright 2007 American Chemical Society.

detection methods can be used for multiplexed bioanalysis [72–74]. Semiconductor nanowire-based FETs can be used to provide ultrasensitive label-free detection of biomolecular interactions [75]. Electrical conductance is the parameter to be monitored to detect binding events occurring on the nanowire surface.

A PNA-modified nanowire was used as FET to selectively detect specific DNA molecules [71]. The high sensitivity was attributed to the small diameter of the nanowires. The binding of the target molecules on the surface of nanowires caused accumulation or depletion of charges, which led to a change in the channel conductance. This technique also has been used to detect proteins, ions, and viruses with high sensitivity [75–77].

The same group developed silicon nanowire FETs with control nanowires in the same assay that gave a way to eliminate false-positive results [78]. Reportedly, a femto-molar concentration of protein markers was repeatedly detected with the device. The nanowire array provided highly selective and sensitive multiplexed detection of prostate-specific antigen (PSA), PSA-a1-antichymotrypsin, carcinoembryonic antigen, and mucin-1, all biomarkers for cancer [78]. Using an undiluted serum sample, they achieved a detection limit of 0.9 pg/mL. Telomerase activity was also monitored by using nucleic acid functionalized real-time nanowire assays. The capability of multiplexed real-time monitoring of protein biomarker and telomerase activity with high sensitivity and selectivity is very important
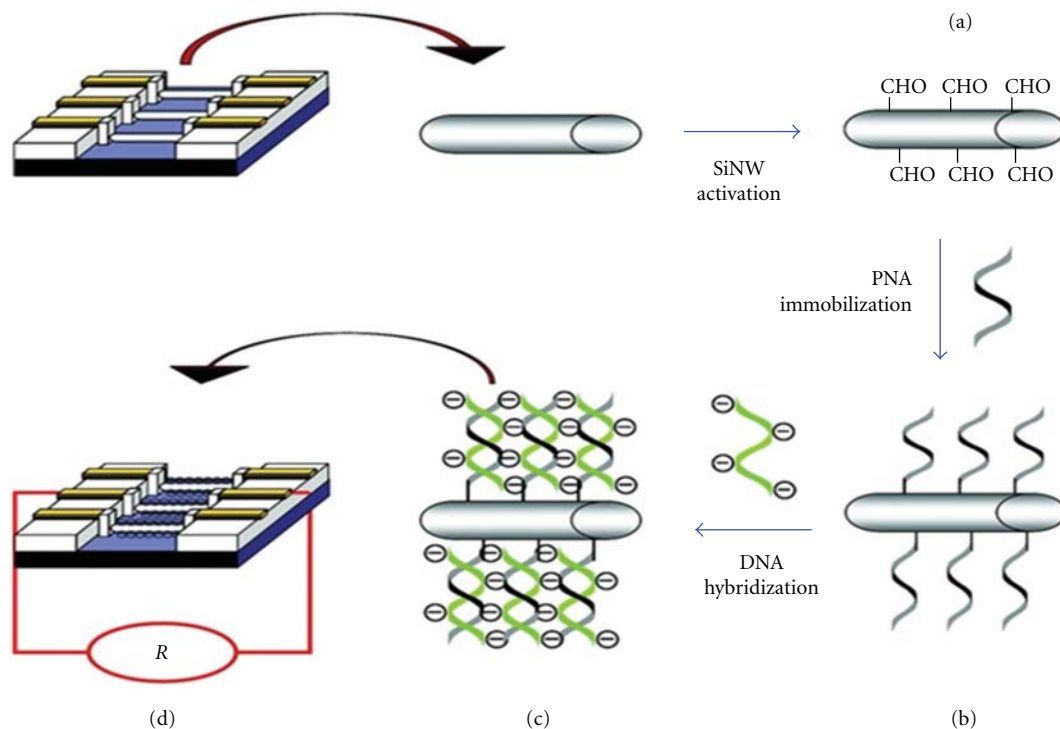
FIGURE 19: Operating principle of the silicon nanowire array biosensor for DNA detection, reprinted with permission from [15]. Copyright 2007 American Chemical Society.
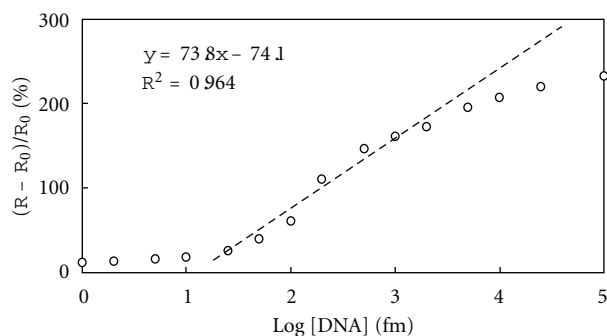
FIGURE 20: Calibration profile for target oligonucleotides detection with a linear fit (Operating condition 60 min hybridization at 50°C), reprinted with permission from [15]. Copyright 2007 American Chemical Society.

clinically to diagnose cancer early and then to monitor disease progression [78].

Barcoded metallic nanowires, synthesized by template electrodeposition of multiple metal segments, were reported to have the potential to be used as suspension array to detect protein and nucleic acid simultaneously [73, 74]. Multiplexed detection of biothreat simulants, including protein, spore, and viral targets were reported with high sensitivities using metallic nanowires array [79]. The detection limit of this assay could be scaled by reducing the total number of barcoded nanowires. Sha et al. reported that their barcoded nanowires system was capable of performing 30 different

assays simultaneously to determine the genotypes of single-nucleotide polymorphisms (SNPs) [80].

Very recently, Chua et al. developed a silicon nanowire array-based assay that was capable of providing ultrasensitive, label-free electrical detection of a cardiac biomarker in real time. This assay proved itself to be effective to detect ultralow concentrations of a target protein in a biological analyte solution, even in the presence of a high total protein concentration. The high specificity, selectivity, and swift response time from this method serves the need of medical diagnostic systems for point-of-care applications to provide early and accurate indication of cardiac cellular necrosis [81].

Nanowire-based detection systems provide a flexible multiplexing scheme to detect biomolecules simultaneously. They offer ultrasensitive electrical detection without any labeling, which is the prime requirement to develop a portable, low-power microchip-based device that can process multiplexed data from many individual sensors. The use of such devices would not be limited to clinical environments; they could be used outside the clinical environment where availability of medical facilities is limited.

2.6. Nanosheets.

A nanosheet is a single- or multilayer two-dimensional array of atoms or molecules. Graphene is a flat monolayer of carbon atoms arranged in a two-dimensional honeycomb crystal structure [82]. It is a basic building block for graphitic materials of all other dimensionalities. High thermal conductivity ($\sim$5000 W/m K) [83], high specific surface area, high electron mobility (250,000 cm^2/Vs) [84], easily achievable biocompatibility, and exceptional thermal

stability make it a material of choice for fabricating electrochemical immunosensors [82, 85–88].

Wang et al. reported that graphene oxide nanosheets (GO-nS) could be used to probe *in vivo* cellular interactions [89]. These nanosheets could be used as DNA cargo and sensing platforms. The unique interaction between GO-nS and DNA molecules was exploited to produce an aptamer/GO-nS complex, which was used as a real-time biosensing platform in living cells. In the experiments, they used a fluorescently tagged ATP-binding aptamer (FAM-aptamer) to elucidate the use of GO-nS as (i) a sensing platform with high fluorescence quenching efficiency for realizing real-time *in vivo* target monitoring, (ii) DNA transporter into living cells, and (iii) efficient protection of oligonucleotides from enzymatic cleavage [89]. ATP was targeted because it is of medical interest. ATP is a central molecule involved in cellular metabolism and bioenergetics. Figure 21 shows the schematic illustration of the experiment. FAM-Aptamer was loaded onto GO-nS. The FAM florescence was quenched by the GO-nS in the GO-nS bound state. In the presence of ATP, ATP-aptamer complexes formed and released from the GO-nS. The released ATP-aptamer complexes were detectable by the FAM fluorescence [89].

In order to investigate the sensing performance of the aptamer/GO-nS complex, *in vitro* ATP detection was carried out first. Initially, fluorescent quenching was observed due to the fluorescent resonance energy transfer (FRET) between FAM and GO-nS. When ATP was present in the solution, it bound to the aptamer, thus releasing the FAM from the GO-nS surface. The released FAM showed the fluorescence activity. Figure 22 shows the fluorescence intensity upon the presence of different amounts of ATP in the solution. It indicates that aptamer-FAM/GO-nS complex had high sensitivity and a wide detection range, from $10\,\mu$M to 2.5 mM, for *in vitro* ATP sensing [89]. The specificity of this complex was also good. Only ATP showed an obvious fluorescence recovery up to 85.7%, whereas none of cytidine triphosphate (CTP), guanosine triphosphate (GTP), or thymidine triphosphate (TTP) showed any substantial fluorescence recovery. The good selectivity and sensitivity of the aptamer/GO-nS nanocomplex predicted its potential use for intracellular ATP monitoring in living cells [89].

For *in vivo* analysis, mice epithelial cells (JB6 Cl 41-5a) were chosen. It was seen that only the aptamer-FAM/GO-nS had a significantly higher uptake rate than random DNA/GO-nS or GO-nS alone or aptamer-FAM alone. The GO-nS not only helped to transport the DNA into the cell but also protected it from the enzymatic cleavage.

Figure 23 shows a comparative picture of cellular ATP probing done by aptamer-FAM/GO-nS (g–l) and random DNA/GO-nS (a–f). As time elapsed, the amount of fluorescent signal increased in the case of aptamer-FAM/GO-nS, which showed that the ATP-aptamer duplex was formed; hence, fluorescence was recovered. But for random DNA/GO-nS, no significant increase of fluorescence was observed, which confirmed the hypothesis that GO-nS helped to deliver the aptamer inside the cell and released the aptamer for target detection [89].
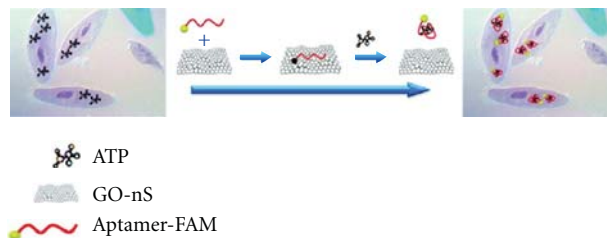
FIGURE 21: Schematic representation of in situ molecular probing inside living cells using aptamer/GO-nS nanocomplex, reprinted with permission from [89]. Copyright 2010, American Chemical Society.
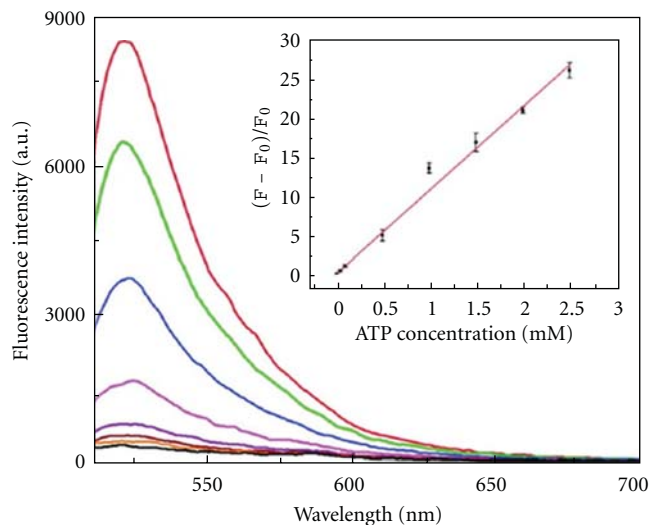
FIGURE 22: Fluorescence emission spectra of ATP aptamer-FAM quenched (100 nM) with $3\,\mu$g/mL GO-nS (black bottom line) and fluorescence recovery by addition of ATP with a concentration range from $10\,\mu$M to 2.5 mM (from bottom to top). Inset: linear fit between relative fluorescence intensity and ATP concentration. Given that F_0 and F are the fluorescence intensity without and with the presence of ATP, respectively, reprinted with permission from [89]. Copyright 2010, American Chemical Society.

3. Major Challenges with the Use of Nanostructures

Over the last decade or so, many synthesized nanostructures with at least one dimension in the 1–100 nm range have been created and used to exhibit fascinating physicochemical properties [90, 91]. In addition to their small sizes, these nanostructures have large surface-to-volume ratios and very high reactivities compared to their bulk counterparts. Their very small size allows them to cross many boundaries with ease (e.g., across cell membranes). They can efficiently bind to biological molecules and species such as DNA, RNA, PNA, proteins, and viruses. Owing to the novel properties of nanoscale structures, they have been examined for their potential to be incorporated into various devices, such as sensors, immunoassays, transistors, drug and gene delivery carriers, virus inhibitors, and DNA and protein immobilizers [16, 21, 22, 41, 44, 53, 59, 65, 81, 92–94].
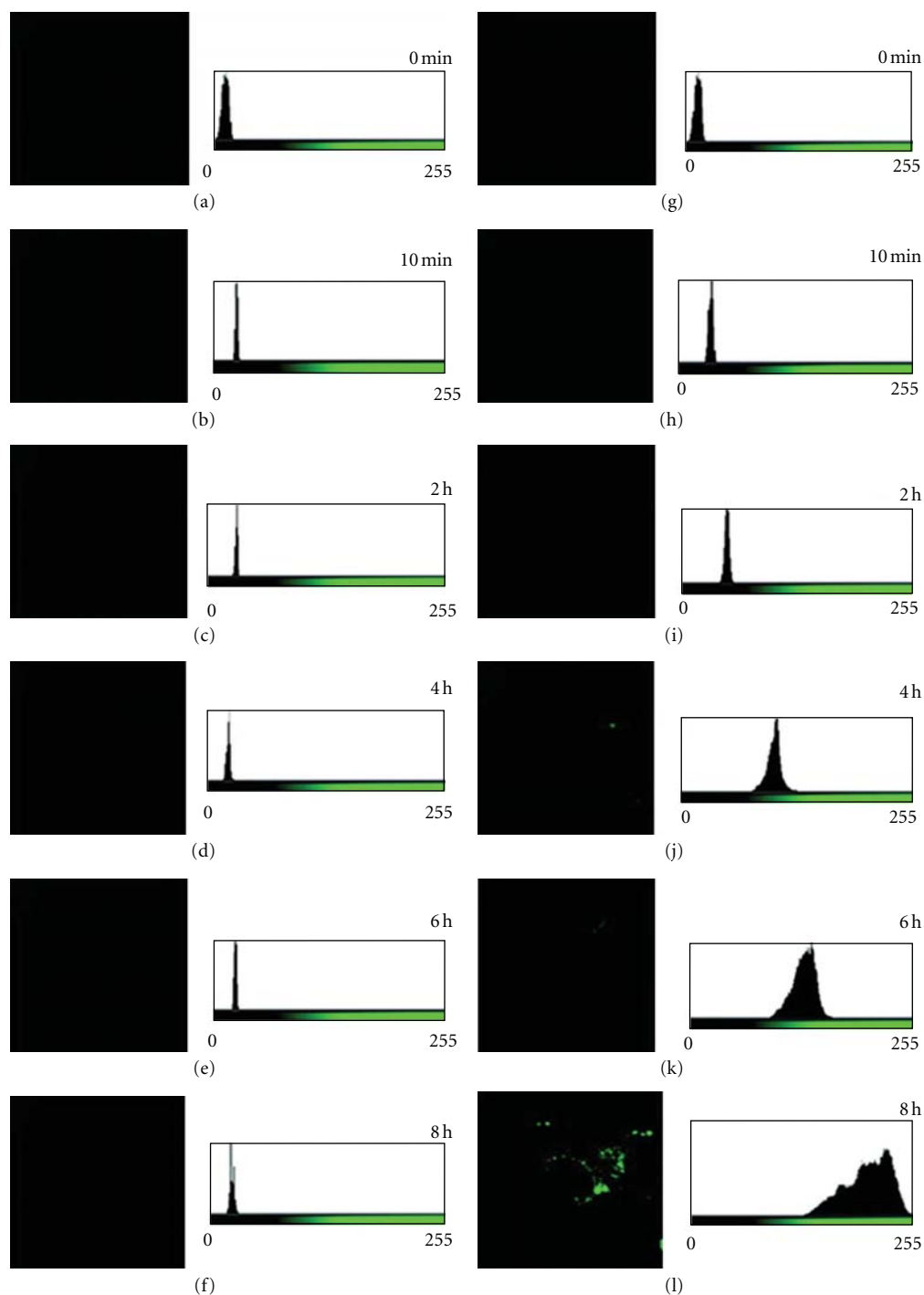
FIGURE 23: Real-time monitoring of JB6 cells cultured with random DNA-FAM/GO-nS (a–f) and aptamer-FAM/GO-nS (g–l) for 8 h at 37°C. Images were captured every 2 h using a wide-field microscopy every 2 h. Colored bar indicates the fluorescent intensity, reprinted with permission from [89]. Copyright 2010, American Chemical Society.

Although nanodevices have indeed demonstrated great potential, enthusiasm is tempered by the fact that reproducing devices with such dimensions is still a challenge. In addition, short- and long-term toxicological effects of nanoparticles and nanostructures in biological systems are largely unknown. Nanostructures have been reported to produce pulmonary inflammation [95]. They can also reach other organs by passing through the lung epithelium and can reach interstitial tissues [95, 96]. These effects have been shown to be more prevalent in species such as dogs and primates than in rodents [97].

Studies have shown carbon nanotubes to be cytotoxic. They can induce granulomas in the lungs of laboratory animals [98]. *In vitro* studies have demonstrated that

single-wall nanotubes can generate reactive oxygen species in human keratinocytes and human bronchial epithelial cells, indicating that oxidative stress is one of the predominant mechanisms of their acute toxicity [99, 100]. Oxidative stress was identified as the participating mechanism of Ag nanoparticles toxicity in an *in vitro* study with BRL-3A liver cells, supporting the previous notion [101]. Nanoparticles made of metals and metallic oxides such as copper, cobalt, titanium, and silicon oxide have also been shown to have inflammatory and toxic effects on cells [98].

Another *in vitro* study showed that metal nanoparticles disrupted proliferation, damaged cell membranes, and initiated apoptosis in C18-4 and germ-line stem cells [102]. After intraperitoneal administration, fullerenes have been shown to distribute throughout the embryo and yolk sac of mice 18 hours after injection, and they crossed the placental barrier [103]. Rhodamine-labeled silica-coated magnetic nanoparticles passed the blood-testis barrier and aggregated in the seminiferous epithelium where spermatogenesis takes place. After penetration into seminiferous epithelium, the nanoparticles got incorporated into the developing germ cells and eventually became part of mature sperms [104].

Asharani et al. showed that multiwalled CNTs damaged DNA in mouse embryonic stem (ES) cells [105]. In another study it was shown that multiwalled CNTs could accumulate and induce apoptosis in mouse ES cells and activated the tumor suppressor protein p53 within two hours of exposure [106]. The above studies indicate that nanostructures could potentially impact human health by producing oxidative stress, altering DNA, or producing phenotypic damage to the cells.

A necessary step, therefore, is accurately determining nanostructures' properties of interest and understanding their interactions with relevant biological systems. Detailed characterization of such a wide variety of novel structures and their modified versions is required to assess the toxicity or any other threat they may possess. Various synthesis techniques of nanostructures produce a wide variety of structures with different physical characteristics such as size, morphology, surface chemistry, and biological coatings. In a biological context, we need to understand the impacts of these variations in order to improve the existing methods in terms of quality, control, and safety issues. Further studies are required to develop more precise fabrication techniques and to determine the appropriate modifications that will resolve the safety issues.

4. Conclusion

In this review article, we have discussed fabrication techniques of different nanostructures. We have also discussed the applications of these structures in the fields of medical diagnostics. The promise of increased sensitivity and speed with reduced cost and labor makes nanostructure-based assays an appealing alternative to current diagnostic techniques. The potential uses of nanostructures in medical diagnostics are numerous, although some important challenges to implementation exist. Aside from the technical difficulties of nanostructure fabrication, there are serious concerns about nanostructure toxicity and that toxicity may vary depending on the physical characteristics of each new particle type. Further research is required to evaluate and solve these issues. If the issues can be overcome, the high sensitivity, specificity, reduced cost, portability, and reusability of nanostructures will make nanostructures important medical diagnostics tools.

References

[1] X. Huang, I. H. El-Sayed, W. Qian, and M. A. El-Sayed, "Cancer cell imaging and photothermal therapy in the near-infrared region by using gold nanorods," *Journal of the American Chemical Society*, vol. 128, no. 6, pp. 2115–2120, 2006.

[2] P. K. Jain and M. A. El-Sayed, "Universal scaling of plasmon coupling in metal nanostructures: extension from particle pairs to nanoshells," *Nano Letters*, vol. 7, no. 9, pp. 2854–2858, 2007.

[3] P. K. Jain, X. Huang, I. H. El-Sayed, and M. A. El-Sayed, "Noble metals on the nanoscale: optical and photothermal properties and some applications in imaging, sensing, biology, and medicine," *Accounts of Chemical Research*, vol. 41, no. 12, pp. 1578–1586, 2008.

[4] L. Zhang and T. J. Webster, "Nanotechnology and nanomaterials: promises for improved tissue regeneration," *Nano Today*, vol. 4, no. 1, pp. 66–80, 2009.

[5] H. Shen, X. Hu, J. Bei, and S. Wang, "The immobilization of basic fibroblast growth factor on plasma-treated poly(lactide-co-glycolide)," *Biomaterials*, vol. 29, no. 15, pp. 2388–2399, 2008.

[6] J. Carpenter, D. Khang, and T. J. Webster, "Nanometer polymer surface features: the influence on surface energy, protein adsorption and endothelial cell adhesion," *Nanotechnology*, vol. 19, no. 50, Article ID 505103, 2008.

[7] S. Moon, W. Song, N. Kim et al., "Current-carrying capacity of double-wall carbon nanotubes," *Nanotechnology*, vol. 18, no. 23, Article ID 235201, 2007.

[8] J. G. Park, S. Li, R. Liang, X. Fan, C. Zhang, and B. Wang, "The high current-carrying capacity of various carbon nanotube-based buckypapers," *Nanotechnology*, vol. 19, no. 18, Article ID 185710, 2008.

[9] F. Patolsky, B. P. Timko, G. Zheng, and C. M. Lieber, "Nanowire-based nanoelectronic devices in the life sciences," *MRS Bulletin-Materials Research Society*, vol. 32, no. 2, pp. 142–149, 2007.

[10] K. Kerman, M. Saito, E. Tamiya, S. Yamamura, and Y. Takamura, "Nanomaterial-based electrochemical biosensors for medical applications," *TrAC—Trends in Analytical Chemistry*, vol. 27, no. 7, pp. 585–592, 2008.

[11] S. E. Brunker, K. B. Cederquist, and C. D. Keating, "Metallic barcodes for multiplexed bioassays," *Nanomedicine*, vol. 2, no. 5, pp. 695–710, 2007.

[12] L. G. Carrascosa, M. Moreno, M. Alvarez, and L. M. Lechuga, "Nanomechanical biosensors: a new sensing tool," *TrAC—Trends in Analytical Chemistry*, vol. 25, no. 3, pp. 196–206, 2006.

[13] Y. J. Seo, J. Lim, E. H. Lee et al., "Base pair opening kinetics study of the aegPNA: DNA hydrid duplex containing a site-specific GNA-like chiral PNA monomer," *Nucleic Acids Research*, vol. 39, no. 16, pp. 7329–7335, 2011.

[14] J. B. Raoof, R. Ojani, S. M. Golabi, E. Hamidi-Asl, and M. S. Hejazi, "Preparation of an electrochemical PNA biosensor

for detection of target DNA sequence and single nucleotide mutation on p53 tumor suppressor gene corresponding oligonucleotide," *Sensors and Actuators, B: Chemical*, vol. 157, no. 1, pp. 195–201, 2011.

[15] Z. Gao, A. Agarwal, A. D. Trigg et al., "Silicon nanowire arrays for label-free detection of DNA," *Analytical Chemistry*, vol. 79, no. 9, pp. 3291–3297, 2007.

[16] J. Fritz, M. K. Baller, H. P. Lang et al., "Translating biomolecular recognition into nanomechanics," *Science*, vol. 288, no. 5464, pp. 316–318, 2000.

[17] M. Ferrari, "Cancer nanotechnology: opportunities and challenges," *Nature Reviews Cancer*, vol. 5, no. 3, pp. 161–171, 2005.

[18] S. Wolf and R. N. Tauber, *Silicon Processing for the VLSI Era: Process Technology*, vol. 1, Lattice Press, Sunset Beach, Calif, USA, 1986.

[19] D. Xia, D. Li, Z. Ku, Y. Luo, and S. R. J. Brueck, "Top-down approaches to the formation of silica nanoparticle patterns," *Langmuir*, vol. 23, no. 10, pp. 5377–5385, 2007.

[20] D. Li, J. T. McCann, Y. Xia, and M. Marquez, "Electrospinning: a simple and versatile technique for producing ceramic nanofibers and nanotubes," *Journal of the American Ceramic Society*, vol. 89, no. 6, pp. 1861–1869, 2006.

[21] E. Stern, J. F. Klemic, D. A. Routenberg et al., "Label-free immunodetection with CMOS-compatible semiconducting nanowires," *Nature*, vol. 445, no. 7127, pp. 519–522, 2007.

[22] O. A. Saleh and L. L. Sohn, "Direct detection of antibody-antigen binding using an on-chip artificial pore," *Proceedings of the National Academy of Sciences of the United States of America*, vol. 100, no. 3, pp. 820–824, 2003.

[23] K. K. Jain, "Nanodiagnostics: application of nanotechnology in molecular diagnostics," *Expert Review of Molecular Diagnostics*, vol. 3, no. 2, pp. 153–161, 2003.

[24] S. M. Iqbal and R. Bashir, Eds., *Nanopores: Sensing and Fundamental Biological Interactions*, Springer, New York, NY, USA, 2011.

[25] B. M. Venkatesan and R. Bashir, "Nanopore sensors for nucleic acid analysis," *Nature Nanotechnology*, vol. 6, no. 10, pp. 615–624, 2011.

[26] V. Balzani, "Nanoscience and nanotechnology: a personal view of a chemist," *Small*, vol. 1, no. 3, pp. 278–283, 2005.

[27] N. A. Ochekpe, P. O. Olorunfemi, and N. C. Ngwuluka, "Nanotechnology and drug delivery part 1: background and applications," *Tropical Journal of Pharmaceutical Research*, vol. 8, no. 3, pp. 265–274, 2009.

[28] S. Rauf, A. Glidle, and J. M. Cooper, "Production of quantum dot barcodes using biological self-assembly," *Advanced Materials*, vol. 21, no. 40, pp. 4020–4024, 2009.

[29] S. A. E. Valentin, A. Filoramo, A. Ribayrol et al., "Self-assembly fabrication of high performance carbon nanotubes based FETs," *Materials Research Society Symposium Proceedings*, vol. 772, pp. 201–207, 2003.

[30] T. Liu, C. Burger, and B. Chu, "Nanofabrication in polymer matrices," *Progress in Polymer Science*, vol. 28, no. 1, pp. 5–26, 2003.

[31] P. Hyman, R. Valluzzi, and E. Goldberg, "Design of protein struts for self-assembling nanoconstructs," *Proceedings of the National Academy of Sciences of the United States of America*, vol. 99, no. 13, pp. 8488–8493, 2002.

[32] D. Shu, W. D. Moll, Z. Deng, C. Mao, and P. Guo, "Bottom-up assembly of RNA arrays and superstructures as potential parts in nanotechnology," *Nano Letters*, vol. 4, no. 9, pp. 1717–1723, 2004.

[33] D. D. Majumder, R. Banerjee, C. Ulrichs, I. Mewis, and A. Goswami, "Nano-materials: science of bottom-up and top-down," *The Institution of Electronics and Telecommunication Engineers*, vol. 24, no. 1, pp. 9–25, 2007.

[34] M. Shimomura and T. Sawadaishi, "Bottom-up strategy of materials fabrication: a new trend in nanotechnology of soft materials," *Current Opinion in Colloid and Interface Science*, vol. 6, no. 1, pp. 11–16, 2001.

[35] K. K. Jain, "Applications of nanobiotechnology in clinical diagnostics," *Clinical Chemistry*, vol. 53, no. 11, pp. 2002–2009, 2007.

[36] K. K. Jain, "Nanotechnology in clinical laboratory diagnostics," *Clinica Chimica Acta*, vol. 358, no. 1-2, pp. 37–54, 2005.

[37] D. C. Miller, A. Thapa, K. M. Haberstroh, and T. J. Webster, "Endothelial and vascular smooth muscle cell function on poly(lactic-co-glycolic acid) with nano-structured surface features," *Biomaterials*, vol. 25, no. 1, pp. 53–61, 2004.

[38] Y. Wan, M. A. I. Mahmood, N. Li et al., "Nanotextured substrates with immobilized aptamers for cancer cell isolation and cytology," *Cancer*, vol. 118, no. 4, pp. 1145–1154, 2012.

[39] P. Kim, D. H. Kim, B. Kim et al., "Fabrication of nanostructures of polyethylene glycol for applications to protein adsorption and cell adhesion," *Nanotechnology*, vol. 16, no. 10, pp. 2420–2426, 2005.

[40] K. P. S. Dancil, D. P. Greiner, and M. J. Sailor, "A porous silicon optical biosensor: detection of reversible binding of IgG to a protein A-modified surface," *Journal of the American Chemical Society*, vol. 121, no. 34, pp. 7925–7930, 1999.

[41] L. M. Demers, D. S. Ginger, S. J. Park, Z. Li, S. W. Chung, and C. A. Mirkin, "Direct patterning of modified oligonucleotides on metals and insulators by dip-pen nanolithography," *Science*, vol. 296, no. 5574, pp. 1836–1838, 2002.

[42] A. Bruckbauer, L. Ying, A. M. Rothery et al., "Writing with DNA and protein using a nanopipet for controlled delivery," *Journal of the American Chemical Society*, vol. 124, no. 30, pp. 8810–8811, 2002.

[43] K.-B. Lee, E.-Y. Kim, C. A. Mirkin, and S. M. Wolinsky, "The use of nanoarrays for highly sensitive and selective detection of human immunodeficiency virus type 1 in plasma," *Nano Letters*, vol. 4, no. 10, pp. 1869–1872, 2004.

[44] H. K. Kang, J. Seo, D. D. Carlo, Y. K. Choi, and L. P. Lee, "Planar nanogap capacitor arrays on quartz for optical and dielectric bioassays," in *Proceedings of the Micro Total Analsysis Systems*, pp. 697–700, Squaw Valley, Calif, USA, 2003.

[45] C. Buzea, I. I. Pacheco, and K. Robbie, "Nanomaterials and nanoparticles: sources and toxicity," *Biointerphases*, vol. 2, no. 4, 55 pages, 2007.

[46] E. Boisselier and D. Astruc, "Gold nanoparticles in nanomedicine: preparations, imaging, diagnostics, therapies and toxicity," *Chemical Society Reviews*, vol. 38, no. 6, pp. 1759–1782, 2009.

[47] Y. Fu, P. Li, T. Wang et al., "Novel polymeric bionanocomposites with catalytic Pt nanoparticles label immobilized for high performance amperometric immunoassay," *Biosensors and Bioelectronics*, vol. 25, no. 7, pp. 1699–1704, 2010.

[48] A. D. McFarland, C. L. Haynes, C. A. Mirkin, R. P. van Duyne, and H. A. Godwin, "Color my nanoworld," *Journal of Chemical Education*, vol. 81, no. 4, p. 544, 2004.

[49] P. Baptista, E. Pereira, P. Eaton et al., "Gold nanoparticles for the development of clinical diagnosis methods," *Analytical and Bioanalytical Chemistry*, vol. 391, no. 3, pp. 943–950, 2008.

[50] S. J. Park, T. A. Taton, and C. A. Mirkin, "Array-based electrical detection of DNA with nanoparticle probes," *Science*, vol. 295, no. 5559, pp. 1503–1506, 2002.

[51] H. M. E. Azzazy, M. M. H. Mansour, and S. C. Kazmierczak, "Nanodiagnostics: a new frontier for clinical laboratory medicine," *Clinical Chemistry*, vol. 52, no. 7, pp. 1238–1246, 2006.

[52] P. K. Jain, K. S. Lee, I. H. El-Sayed, and M. A. El-Sayed, "Calculated absorption and scattering properties of gold nanoparticles of different size, shape, and composition: applications in biological imaging and biomedicine," *Journal of Physical Chemistry B*, vol. 110, no. 14, pp. 7238–7248, 2006.

[53] L. M. Liz-Marzán, "Tailoring surface plasmons through the morphology and assembly of metal nanoparticles," *Langmuir*, vol. 22, no. 1, pp. 32–41, 2006.

[54] C. Y. Zhang, H. C. Yeh, M. T. Kuroki, and T. H. Wang, "Single-quantum-dot-based DNA nanosensor," *Nature Materials*, vol. 4, no. 11, pp. 826–831, 2005.

[55] J. K. Herr, J. E. Smith, C. D. Medley, D. Shangguan, and W. Tan, "Aptamer-conjugated nanoparticles for selective collection and detection of cancer cells," *Analytical Chemistry*, vol. 78, no. 9, pp. 2918–2924, 2006.

[56] H. Lee, K. Y. Mi, S. Park et al., "Thermally cross-linked superparamagnetic iron oxide nanoparticles: synthesis and application as a dual imaging probe for cancer in vivo," *Journal of the American Chemical Society*, vol. 129, no. 42, pp. 12739–12745, 2007.

[57] A. Moore, Z. Medarova, A. Potthast, and G. Dai, "In vivo targeting of underglycosylated MUC-1 tumor antigen using a multimodal imaging probe," *Cancer Research*, vol. 64, no. 5, pp. 1821–1827, 2004.

[58] J. J. Kasianowicz, E. Brandin, D. Branton, and D. W. Deamer, "Characterization of individual polynucleotide molecules using a membrane channel," *Proceedings of the National Academy of Sciences of the United States of America*, vol. 93, no. 24, pp. 13770–13773, 1996.

[59] J. Clarke, H. C. Wu, L. Jayasinghe, A. Patel, S. Reid, and H. Bayley, "Continuous base identification for single-molecule nanopore DNA sequencing," *Nature Nanotechnology*, vol. 4, no. 4, pp. 265–270, 2009.

[60] O. A. Saleh and L. L. Sohn, "An artificial nanopore for molecular sensing," *Nano Letters*, vol. 3, no. 1, pp. 37–38, 2003.

[61] J. D. Uram, K. Ke, A. J. Hunt, and M. Mayer, "Submicrometer pore-based characterization and quantification of antibody-virus interactions," *Small*, vol. 2, no. 8-9, pp. 967–972, 2006.

[62] A. Han, M. Creus, G. Schürmann et al., "Label-free detection of single protein molecules and protein-protein interactions using synthetic nanopores," *Analytical Chemistry*, vol. 80, no. 12, pp. 4651–4658, 2008.

[63] R. H. Baughman, A. A. Zakhidov, and W. A. de Heer, "Carbon nanotubes—the route toward applications," *Science*, vol. 297, no. 5582, pp. 787–792, 2002.

[64] J. Li, H. T. Ng, A. Cassell et al., "Carbon nanotube nanoelectrode array for ultrasensitive DNA detection," *Nano Letters*, vol. 3, no. 5, pp. 597–602, 2003.

[65] J. Wang, G. Liu, and M. R. Jan, "Ultrasensitive electrical biosensing of proteins and DNA: carbon-nanotube derived amplification of the recognition and transduction events," *Journal of the American Chemical Society*, vol. 126, no. 10, pp. 3010–3011, 2004.

[66] H. I. Liu, D. K. Biegelsen, F. A. Ponce, N. M. Johnson, and R. F. W. Pease, "Self-limiting oxidation for fabricating sub-5 nm silicon nanowires," *Applied Physics Letters*, vol. 64, no. 11, pp. 1383–1385, 1994.

[67] N. Singh, A. Agarwal, L. K. Bera et al., "High-performance fully depleted silicon nanowire (diameter 5 nm) gate-all-around CMOS devices," *IEEE Electron Device Letters*, vol. 27, no. 5, pp. 383–386, 2006.

[68] T. Ratilainen, A. Holmén, E. Tuite, P. E. Nielsen, and B. Nordén, "Thermodynamics of sequence-specifc binding of PNA to DNA," *Biochemistry*, vol. 39, no. 26, pp. 7781–7791, 2000.

[69] M. Egholm, O. Buchardt, L. Christensen et al., "PNA hybridizes to complementary oligonucleotides obeying the Watson-Crick hydrogen-bonding rules," *Nature*, vol. 365, no. 6446, pp. 566–568, 1993.

[70] J. J. Schmidt and C. D. Montemagno, "Using machines in cells," *Drug Discovery Today*, vol. 7, no. 9, pp. 500–503, 2002.

[71] J. I. Hahm and C. M. Lieber, "Direct ultrasensitive electrical detection of DNA and DNA sequence variations using nanowire nanosensors," *Nano Letters*, vol. 4, no. 1, pp. 51–54, 2004.

[72] B. He, T. J. Morrow, and C. D. Keating, "Nanowire sensors for multiplexed detection of biomolecules," *Current Opinion in Chemical Biology*, vol. 12, no. 5, pp. 522–528, 2008.

[73] S. R. Nicewarner-Pena, R. G. Freeman, B. D. Reiss et al., "Submicrometer metallic barcodes," *Science*, vol. 294, no. 5540, pp. 137–141, 2001.

[74] C. D. Keating and M. J. Natan, "Striped metal nanowires as building blocks and optical tags," *Advanced Materials*, vol. 15, no. 5, pp. 451–454, 2003.

[75] F. Patolsky, G. Zheng, and C. M. Lieber, "Nanowire-based biosensors," *Analytical Chemistry*, vol. 78, no. 13, pp. 4260–4269, 2006.

[76] Y. Cui, Q. Wei, H. Park, and C. M. Lieber, "Nanowire nanosensors for highly sensitive and selective detection of biological and chemical species," *Science*, vol. 293, no. 5533, pp. 1289–1292, 2001.

[77] F. Patolsky, G. Zheng, and C. M. Lieber, "Fabrication of silicon nanowire devices for ultrasensitive, label-free, real-time detection of biological and chemical species," *Nature Protocols*, vol. 1, no. 4, pp. 1711–1724, 2006.

[78] G. Zheng, F. Patolsky, Y. Cui, W. U. Wang, and C. M. Lieber, "Multiplexed electrical detection of cancer markers with nanowire sensor arrays," *Nature Biotechnology*, vol. 23, no. 10, pp. 1294–1301, 2005.

[79] B. H. T. Jeffrey, F. Y. S. Chuang, M. C. Kao et al., "Metallic striped nanowires as multiplexed immunoassay platforms for pathogen detection," *Angewandte Chemie—International Edition*, vol. 45, no. 41, pp. 6900–6904, 2006.

[80] M. Y. Sha, I. D. Walton, S. M. Norton et al., "Multiplexed SNP genotyping using nanobarcode particle technology," *Analytical and Bioanalytical Chemistry*, vol. 384, no. 3, pp. 658–666, 2006.

[81] J. H. Chua, R. E. Chee, A. Agarwal, S. M. Wong, and G. J. Zhang, "Label-free electrical detection of cardiac biomarker with complementary metal-oxide semiconductor-compatible silicon nanowire sensor arrays," *Analytical Chemistry*, vol. 81, no. 15, pp. 6266–6271, 2009.

[82] A. K. Geim and K. S. Novoselov, "The rise of graphene," *Nature Materials*, vol. 6, no. 3, pp. 183–191, 2007.

[83] A. A. Balandin, S. Ghosh, W. Bao et al., "Superior thermal conductivity of single-layer graphene," *Nano Letters*, vol. 8, no. 3, pp. 902–907, 2008.

[84] K. I. Bolotin, K. J. Sikes, Z. Jiang et al., "Ultrahigh electron mobility in suspended graphene," *Solid State Communications*, vol. 146, no. 9-10, pp. 351–355, 2008.

[85] Y. Song, K. Qu, C. Zhao, J. Ren, and X. Qu, "Graphene oxide: intrinsic peroxidase catalytic activity and its application to glucose detection," *Advanced Materials*, vol. 22, no. 19, pp. 2206–2210, 2010.

[86] B. Su, J. Tang, J. Huang et al., "Graphene and nanogold-functionalized immunosensing interface with enhanced sensitivity for one-step electrochemical immunoassay of -fetoprotein in human serum," *Electroanalysis*, vol. 22, no. 22, pp. 2720–2728, 2010.

[87] Z. Zhong, W. Wu, D. Wang et al., "Nanogold-enwrapped graphene nanocomposites as trace labels for sensitivity enhancement of electrochemical immunosensors in clinical immunoassays: carcinoembryonic antigen as a model," *Biosensors and Bioelectronics*, vol. 25, no. 10, pp. 2379–2383, 2010.

[88] D. Du, Z. Zou, Y. Shin et al., "Sensitive immunosensor for cancer biomarker based on dual signal amplification strategy of graphene sheets and multienzyme functionalized carbon nanospheres," *Analytical Chemistry*, vol. 82, no. 7, pp. 2989–2995, 2010.

[89] Y. Wang, Z. Li, D. Hu, C. T. Lin, J. Li, and Y. Lin, "Aptamer/graphene oxide nanocomplex for in situ molecular probing in living cells," *Journal of the American Chemical Society*, vol. 132, no. 27, pp. 9274–9276, 2010.

[90] V. L. Colvin, "The potential environmental impact of engineered nanomaterials," *Nature Biotechnology*, vol. 21, no. 10, pp. 1166–1170, 2003.

[91] E. Oberdörster, "Manufactured nanomaterials (fullerenes, C60) induce oxidative stress in the brain of juvenile largemouth bass," *Environmental Health Perspectives*, vol. 112, no. 10, pp. 1058–1062, 2004.

[92] J. M. Nam, C. S. Thaxton, and C. A. Mirkin, "Nanoparticle-based bio-bar codes for the ultrasensitive detection of proteins," *Science*, vol. 301, no. 5641, pp. 1884–1886, 2003.

[93] T. A. Taton, C. A. Mirkin, and R. L. Letsinger, "Scanometric DNA array detection with nanoparticle probes," *Science*, vol. 289, no. 5485, pp. 1757–1760, 2000.

[94] T. L. Lasseter, W. Cai, and R. J. Hamers, "Frequency-dependent electrical detection of protein binding events," *Analyst*, vol. 129, no. 1, pp. 3–8, 2004.

[95] A. Nemmar, A. Delaunois, B. Nemery et al., "Inflammatory effect of intratracheal instillation of ultrafine particles in the rabbit: role of C-fiber and mast cells," *Toxicology and Applied Pharmacology*, vol. 160, no. 3, pp. 250–261, 1999.

[96] S. Utsunomiya, K. A. Jensen, G. J. Keeler, and R. C. Ewing, "Direct identification of trace metals in fine and ultrafine particles in the Detroit urban atmosphere," *Environmental Science and Technology*, vol. 38, no. 8, pp. 2289–2297, 2004.

[97] K. J. Nikula, K. J. Avila, W. C. Griffith, and J. L. Mauderly, "Sites of particle retention and lung tissue responses to chronically inhaled diesel exhaust and coal dust in rats and cynomolgus monkeys," *Environmental health perspectives*, vol. 105, supplement 5, pp. 1231–1234, 1997.

[98] K. A. D. Guzmán, M. R. Taylor, and J. F. Banfield, "Environmental risks of nanotechnology: national nanotechnology initiative funding, 2000–2004," *Environmental Science and Technology*, vol. 40, no. 5, pp. 1401–1407, 2006.

[99] C. Grabinski, S. Hussain, K. Lafdi, L. Braydich-Stolle, and J. Schlager, "Effect of particle dimension on biocompatibility of carbon nanomaterials," *Carbon*, vol. 45, no. 14, pp. 2828–2835, 2007.

[100] A. A. Shvedova, E. Kisin, A. Murray et al., "Exposure of human bronchial cells to carbon nanotubes caused oxidative stress and cytotoxicity," 2004.

[101] S. M. Hussain, K. L. Hess, J. M. Gearhart, K. T. Geiss, and J. J. Schlager, "In vitro toxicity of nanoparticles in BRL 3A rat liver cells," *Toxicology in Vitro*, vol. 19, no. 7, pp. 975–983, 2005.

[102] L. Braydich-Stolle, S. Hussain, J. J. Schlager, and M. C. Hofmann, "In vitro cytotoxicity of nanoparticles in mammalian germline stem cells," *Toxicological Sciences*, vol. 88, no. 2, pp. 412–419, 2005.

[103] T. Tsuchiya, I. Oguri, Y. N. Yamakoshi, and N. Miyata, "Novel harmful effects of [60] fullerene on mouse embryos in vitro and in vivo," *FEBS Letters*, vol. 393, no. 1, pp. 139–145, 1996.

[104] J. S. Kim, T. J. Yoon, K. N. Yu et al., "Toxicity and tissue distribution of magnetic nanoparticles in mice," *Toxicological Sciences*, vol. 89, no. 1, pp. 338–347, 2006.

[105] P. V. Asharani, N. G. B. Serina, M. H. Nurmawati, Y. L. Wu, Z. Gong, and S. Valiyaveettil, "Impact of multi-walled carbon nanotubes on aquatic species," *Journal of Nanoscience and Nanotechnology*, vol. 8, no. 7, pp. 3603–3609, 2008.

[106] S. M. Hussain, L. K. Braydich-Stolle, A. M. Schrand et al., "Toxicity evaluation for safe use of nanomaterials: recent achievements and technical challenges," *Advanced Materials*, vol. 21, no. 16, pp. 1549–1559, 2009.

Research Article

In Vitro Assessment of Antibacterial Activity and Cytocompatibility of Quercetin-Containing PLGA Nanofibrous Scaffolds for Tissue Engineering

Zhi-Cai Xing,[1] Wan Meng,[2] Jiang Yuan,[3] Sungmo Moon,[4] Yongsoo Jeong,[4] and Inn-Kyu Kang[1]

[1] *Department of Polymer Science and Engineering, Kyungpook National University, Daegu 702-701, Republic of Korea*
[2] *Department of Chemical Engineering, Yanbian University, Yanji 133002, China*
[3] *Jiangsu Key laboratory of Biofunctional Materials, College of Chemistry and Environmental Science, Nanjing Normal University, Nanjing 210097, China*
[4] *Materials Processing Division, Korea Institute of Materials Science, Changwon 641-010, Republic of Korea*

Correspondence should be addressed to Inn-Kyu Kang, ikkang@knu.ac.kr

Flavonoids, such as quercetin, have been reported to exhibit a wide range of biological activities related to their antioxidant capacity. The aim of this study was to investigate the protective effect of quercetin on cell adhesion, and the viability and proliferation of KB epithelial cells. Quercetin- (1, 5 wt%)-containing poly (l-lactide-co-glycolide) (PLGA) nanofibrous scaffolds (PLGA/Q 1, PLGA/Q 5) were prepared by electrospinning technique and their antibacterial properties were examined. Two types of bacteria strains, *Staphylococcus aureus* (SA) and *Klebsiella pneumoniae* (KP), were used to evaluate the antibacterial properties of the scaffolds. The results showed that the quercetin-containing PLGA nanofibrous scaffolds exhibited significant antibacterial effects against the two bacterial strains. KB epithelial cells were also used to evaluate the cytocompatibility of the scaffolds. From the results, it was found that the PLGA nanofibrous scaffolds with 1 wt% of quercetin had good cell compatibility. It is considered that the PLGA nanofibrous scaffolds with 1 wt% quercetin have potential to be used in tissue engineering.

1. Introduction

Dietary antioxidants, including polyphenolic compounds, are considered beneficial because of their potential protective role in the pathogenesis of multiple diseases associated to oxidative stress such as cancer, coronary heart disease, and atherosclerosis [1]. Flavonoids comprise a large group of naturally occurring low molecular weight polyphenolic compounds that are present in all plants [2]. Flavonoids, especially flavonols such as quercetin, have been reported to exhibit a wide range of biological activities [3], including anticarcinogenic, anti-inflammatory, and antiviral actions.

The flavonoid used in this study, quercetin, is one of the most abundant flavonol-type flavonoids present in several components of a human's diet such as vegetables, fruit, tea, and wine [3] with a well-characterized antioxidant activity *in vitro* [4, 5]. Quercetin exhibits a wide range of physiological and pharmacological activities relevant to human health, such as anticarcinogenic, anti-inflammatory, and antiviral actions [6, 7]. Many of these effects are supposed to be related to its antioxidant property. The mode of action for quercetin is scavenging free radicals through chelating divalent cations which inhibits some enzymes and protect the DNA damage. Therefore, quercetin may be considered as an effective attenuating factor for preventing various disorders caused by environmental contaminants [8–10].

Electrospun nanofiber matrices have been widely used for tissue regeneration of blood vessels [11, 12], skin [13, 14], cartilage [15, 16], bone [17, 18], and nerve [19]. Poly (l-lactide-co-glycolide) (PLGA) has been approved for several biomedical applications in humans and widely used as a scaffold material in tissue engineering [20–23]. PLGA nanofibers have been shown to promote the adhesion of interstitial and endothelial cells [24], the growth of fetal pulmonary cells

(a)

(b)

(c)

Figure 1: SEM micrographs of electrospun (a) PLGA, (b) PLGA/Q 1, and (c) PLGA/Q 5 nanofibrous scaffolds.

Figure 2: The fluorescence image of PLGA/Q 5 nanofibrous scaffolds.

were studied. Two types of bacterial strains, *Staphylococcus aureus* (SA) and *Klebsiella pneumoniae* (KP), were chosen to evaluate the antibacterial activity of the quercetin-containing PLGA nanofibrous scaffolds. Furthermore, *in vitro* cytotoxicity was examined by conducting tests on the scaffolds as well.

2. Materials and Methods

2.1. Preparation of Polymer Solution. Poly (l-lactide-co-gly-colide) (PLGA, polymer composition: $79:21 \sim 85:15$ molar ratio, Aldrich Chemical Co., USA) was dissolved in 1,1,1, 3,3,3,-hexafluoro-2-propanol (HFIP) with a concentration of 4 wt % and the solution was stirred overnight at room temperature to ensure complete dissolution. Then, certain amounts of quercetin dihydrate (Q, Sigma-Aldrich, USA) (1, 5 wt %) were mixed with the PLGA solution and stirred by magnetic stirrer for 24 h to obtain the PLGA/Q solution. The quercetin-containing PLGA nanofibrous scaffolds were named PLGA/Q 1 and PLGA/Q 5, respectively.

2.2. Electrospinning. The electrospinning experiments were done at room temperature and the apparatus for the electro-spinning was assembled based on a study done by Lee et al. [28]. The polymer solution was placed into a 10 mL glass syringe fitted with a needle (20 G). A clamp connected to a high voltage power supply that could supply a positive vol-tage from 0 to 50 kV was attached to the needle. A piece of aluminum foil was placed at a distance of 15 cm away from the needle tip. The polymer jets generated from the needle by high voltage flew to the collector and formed a nanofiber mesh. The polymer solutions were electrospun with a fixed mass flow rate of 1.0 mL/h and a voltage of 10 kV. Finally, the electrospun samples were dried overnight at 40°C to remove the solvent. The morphologies of the electrospun nanofibers were observed by field emission scanning electron micro-scope (FE-SEM S-4300, Hitachi, Japan) and the fluorescence images of the electrospun nanofibers (PLGA/Q 5) were obtained using a fluorescence microscope (Carl zeiss, Ger-many).

[25] and porcine chondrocytes [26]. Our previous study [27] showed that the silver-containing PLGA nanofibrous scaf-folds inhibited the proliferation of *Staphylococcus aureus* (SA) and *Klebsiella pneumoniae* (KP) bacteria, without exhi-biting any *in vitro* cell cytotoxicity. However, to date, no report has yet been published showing the antibacterial activ-ity and cytotoxicity of quercetin-containing PLGA nano-fibrous scaffolds using the electrospinning technique.

In this study, the antibacterial and biological properties of the quercetin-containing PLGA nanofibrous scaffolds

(a) (b)

FIGURE 3: Effect of the quercetin on the formation of inhibition zones: (a) *Staphylococcus aures* and (b) *Klebsiella pneumonia*.

2.3. Antibacterial Assessment. For the zone of inhibition screening test for antibacterial activity, *Staphylococcus aureus* (SA 6538) and *Klebsiella pneumoniae* (KP 4352) were cultivated in a nutrient broth for 24 h in a CO_2 incubator. Afterwards, diluted bacteria suspensions collected from each vial were spread onto nutrient broth agar plate. After that, the PLGA/Q 1 and PLGA/Q 5 nanofibrous mats were each placed onto a lawn *Staphylococcus aureus* and *Klebsiella pneumoniae* on the agar plates and incubated overnight at 37°C. The zone of inhibition formed around the nanofibrous mats was observed against the two microorganisms.

2.4. Quercetin Release. The quercetin release test was done by immersing the PLGA/Q 5 nanofibrous scaffold ($4 \times 4 \, cm^2$, 0.02 g) into distilled water (5 mL, pH 7.2) for different periods of time. The amount of quercetin released from the sample was measured by UV-visible spectra (JASCO V-650).

2.5. Cell Attachment. In order to examine the interaction of the nanofibrous scaffolds with KB epithelial cells, circular nanofibrous scaffolds were fitted in a 24-well culture dish and subsequently immersed in a DMEM medium containing 10% fetal bovine serum (FBS) (Gibco, Japan) and 1% penicillin G-streptomycin (Gibco, Japan). To the scaffolds, 1 mL of the cell solution (3×10^4 cells/cm^2) was added and incubated in a humidified atmosphere of 5% CO_2 at 37°C for 4 h. After incubation, the supernatant was removed, washed twice with PBS, and fixed in a 2.5% glutaraldehyde aqueous solution for 20 min. The sample sheet was then dehydrated, dried in a critical point drier, and finally sputter-coated with gold. The surface morphology of the samples was then observed with FE-SEM.

2.6. Cell Proliferation. The proliferation of KB epithelial cells was determined using a colorimetric immunoassay, enzyme-linked immunosorbent assay (ELISA). The ELISA method was based on the measurement of 5-bromo-2-deoxyuridine (BrdU), which was incorporated during DNA synthesis. The ELISA was done according to the manufacturer's instructions (Roche Molecular Biochemicals).

2.7. Cell Viability. A standard live/dead assay [29] was used to image cell survival, adhesion, and spatial organization. KB epithelial cells were collected by centrifugation and then were incubated in calcein-AM (1 mM in DMSO) and propidium iodide (PI, 1.5 mM in H_2O) solution for 15 min. Cells with compromised membranes exhibited red-fluorescence from the intercalation of the propidium iodide into the DNA double helix. Cells with intact cell membranes were able to use nonspecific cytosolic esterases to convert nonfluorescent calcein-AM into bright green-fluorescent calcein. Cells were observed under a fluorescence microscope using a band-pass filter (Nikon Eclipse E600-POL, Japan).

3. Results and Discussion

3.1. Surface and Morphology of Nanofibers. Figure 1 shows SEM images of the electrospun nanofibers from 4 wt% PLGA solutions with different amounts of quercetin (0, 1, and 5 wt %). It was observed that the diameter distribution of the PLGA nanofibers did not change when the quercetin was added to the PLGA solution (Figure 1). Figure 2 shows the fluorescence images of quercetin which randomly dispersed through the PLGA nanofibrous scaffold.

3.2. Antibacterial Activity. For the zone of inhibition screening test for the antibacterial activity, PLGA/Q 1 and PLGA/Q 5 nanofibrous scaffolds were placed onto a lawn of organisms on an agar plate and incubated for 24 h. After incubation, antibacterial responses were observed in both test cases. The bactericidal activity displayed a good zone of inhibition, that is, the region in which the bacterial species were unable to propagate around the PLGA/Q fiber mats (Figure 3). In addition, the growth inhibition rate of the bacteria increased a little with an increase in quercetin content (Figure 3). This is attributed to trace amounts of quercetin released from the fiber, which attached to the bacteria and inhibited nucleic acid synthesis, cytoplasmic membrane function and energy metabolism [30].

The antibacterial activity of the scaffolds is based on the role of the quercetin that was embedded in the surface of the scaffold or released from the scaffold. Therefore, in this study,
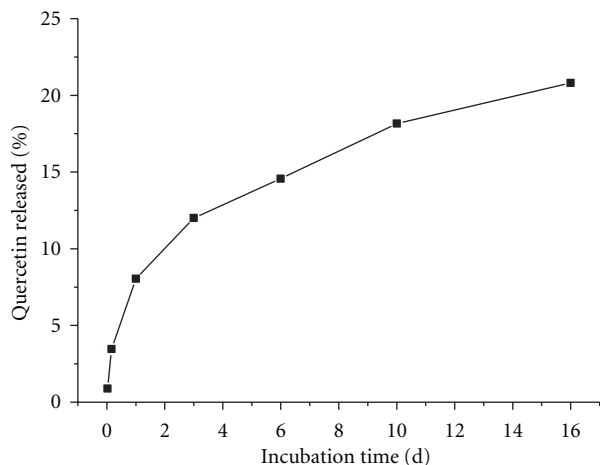
FIGURE 4: The percentage of quercetin released from PLGA/Q 5 nanofibrous scaffolds as a function of the immersion time.

the amount of quercetin released from the PLGA/Q 5 nanofibrous scaffold was calculated using UV-visible spectra. As shown in Figure 4, the percentage of released quercetin gradually increased with an increase in incubation time, and it reached 20.8% after 16 days of incubation. Rapid release of quercetin from PLGA/Q 5 is probably due to the high surface area of the nanofibrous scaffold. The released quercetin from the nanofibrous scaffold showed a high inhibitory effect on the growth of bacteria and killed the microorganisms, as seen in Figure 3.

3.3. In Vitro Cell Compatibility. As seen in Figure 5, KB epithelial cells were attached on the surface of three different scaffolds, and the number of cells attached on the surface of the PLGA nanofibrous scaffolds (Figure 5(a)) was not much different from those the quercetin-containing PLGA nanofibers (Figures 5(b) and 5(c)). The cells formed monolayers on the surface of the PLGA and PLGA/Q 1 nanofibrous scaffolds (Figures 6(a) and 6(b)) after 3 days of incubation. However, the monolayers were partially observed when the cells were cultured on the surface of the PLGA/Q 5 nanofibrous scaffolds (Figure 6(c)). Comparable results for differences in proliferation behavior, expressed as the amount of newly synthesized DNA, are shown in Figure 7. The cell proliferation on the quercetin-containing PLGA nanofibrous scaffolds (PLGA/Q 5) was significantly lower ($P < 0.05$) than that on the PLGA nanofibrous scaffolds (Figure 7) due to the antioxidant property of quercetin. The viability of cells cultured for 7 days on the nanofibrous scaffolds was observed by using the live/dead assay and the results are shown in Figure 8. The fluorescence colors of cells cultured on the PLGA and PLGA/Q 1 were green, indicating good viability of the cells. However, a few dead cells were found in the case of the PLGA/Q 5 nanofibrous scaffolds, which emitted a red fluorescence.

Quercetin has been reported to be a potent inhibitor of lipoxygenase (LOX) and cyclooxygenase (COX) activities, sodium-potassium adenosine triphosphatase (Na-K-ATPase), protein kinase C (PKC), and various tyrosine kinases [31]. Through one or more of the above biochemical

(a)

(b)

(c)
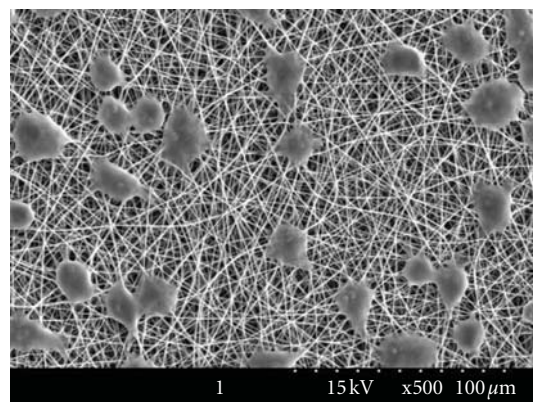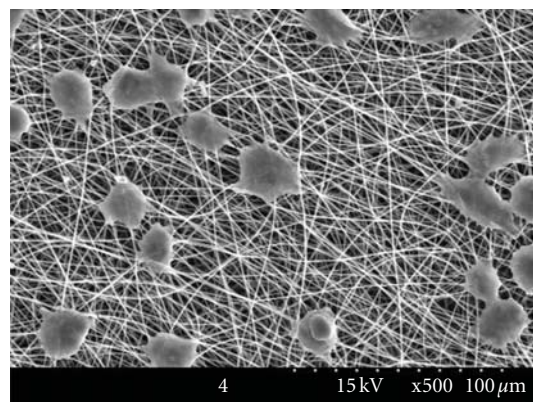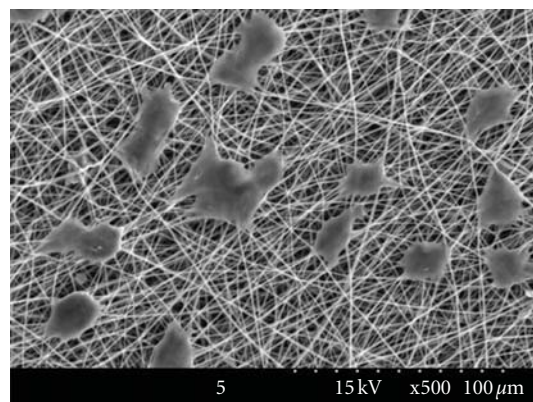
FIGURE 5: SEM images of KB epithelial cells cultured for 4 h on (a) PLGA, (b) PLGA/Q 1, and (c) PLGA/Q 5 nanofibrous scaffolds.

mechanisms, quercetin has been reported to protect against both chemically induced and spontaneously formed tumors in animals [31, 32] and arrest cell proliferation in a variety of transformed cell lines in culture [32–36]. Alía et al. [5] concluded that doses of quercetin significantly decreased HepG2 cell proliferation, which has been previously reported for other cancer cells *in vitro*, such as human adenocarcinoma [37], human promyelocytic leukemia [38, 39], human colon cancer [33, 34, 40], and murine hepatoma [41]. Still other investigators have found both preoxidant and antioxidant

(a)

(b)

(c)
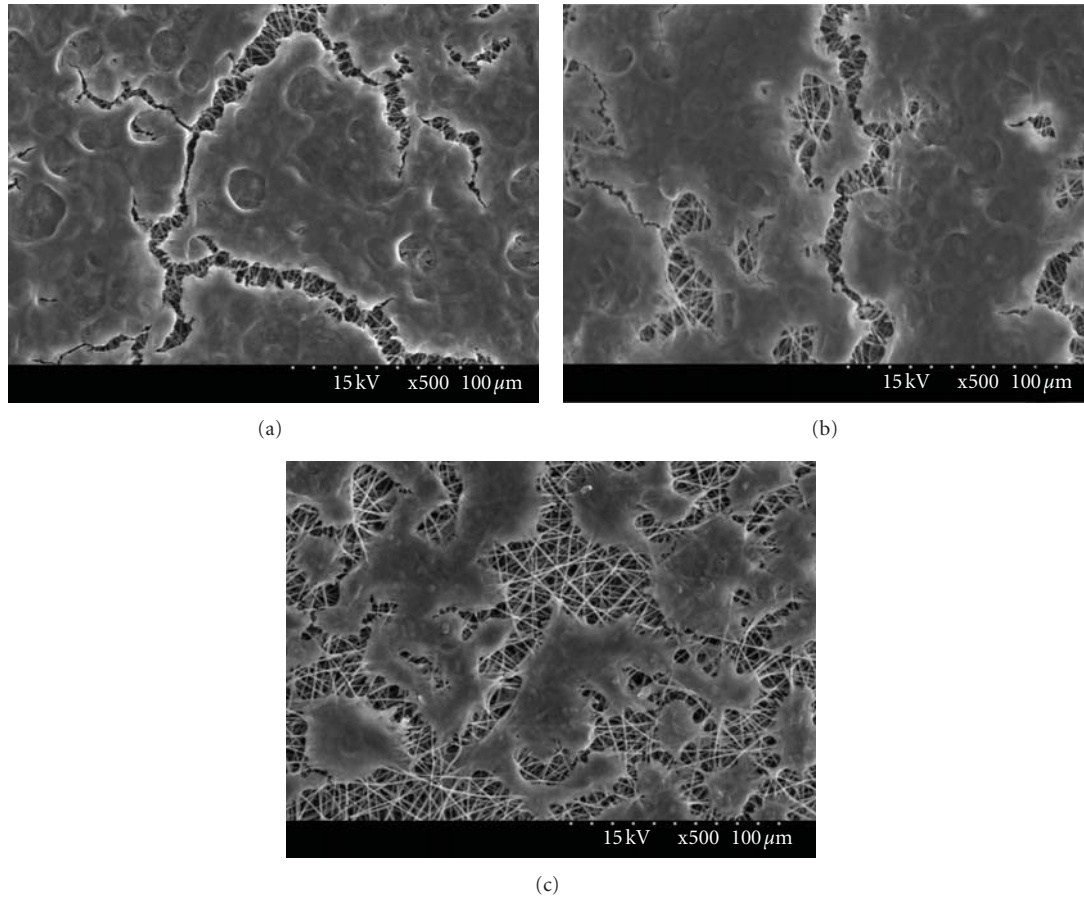
FIGURE 6: Morphology of KB epithelial cells incubated for 3 days on (a) PLGA, (b) PLGA/Q 1, and (c) PLGA/Q 5 nanofibrous scaffolds.
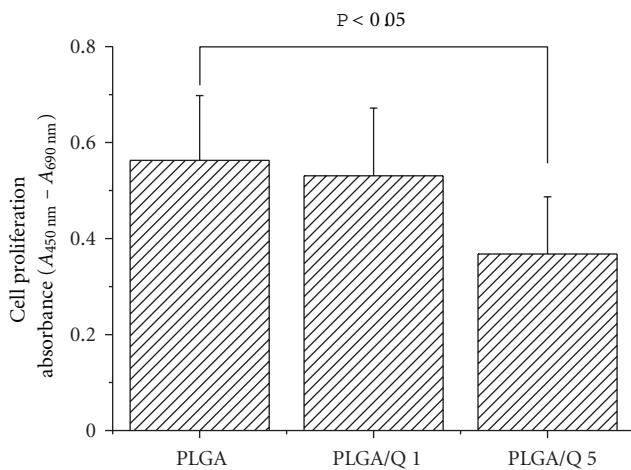
FIGURE 7: Proliferation of KB epithelial cells cultured for 3 days. Data are expressed as the means ± SD ($n = 6$) for the specific absorbance.

effects of quercetin depending on the concentrations used for experimentation [42]. In this study, the results showed that the quercetin-containing PLGA nanofibrous scaffolds affected the *in vitro* growth of the KB epithelial cells. Interestingly, the inhibitory effect of PLGA/Q 1 on the growth of KB epithelial cells was significantly low, indicating a lower activity or accessibility to the cultured cells. However, PLGA/Q 5 significantly reduced the proliferation of KB epithelial cells (Figure 7) due to the cytotoxic effect of the quercetin.

4. Conclusions

Quercetin-containing PLGA nanofibers were successfully prepared using an electrospinning technique and were characterized by SEM and fluorescence microscope. The results demonstrated that the nanofibers electrospun at maximum conditions were straight and that quercetin was distributed throughout the fibers. Finally, the PLGA nanofibrous scaffolds with 1 wt % of quercetin (PLGA/Q 1) inhibited the proliferation of *Staphylococcus aureus* (SA) and *Klebsiella pneumoniae* (KP) bacteria, without any *in vitro* cell cytotoxicity from the scaffolds. If these results can be confirmed *in vivo*, the PLGA/Q 1 nanofibrous scaffolds may be applicable for use in total joint arthroplasty particularly due to its effect against multiresistant bacteria.

(a)

(b)

(c)
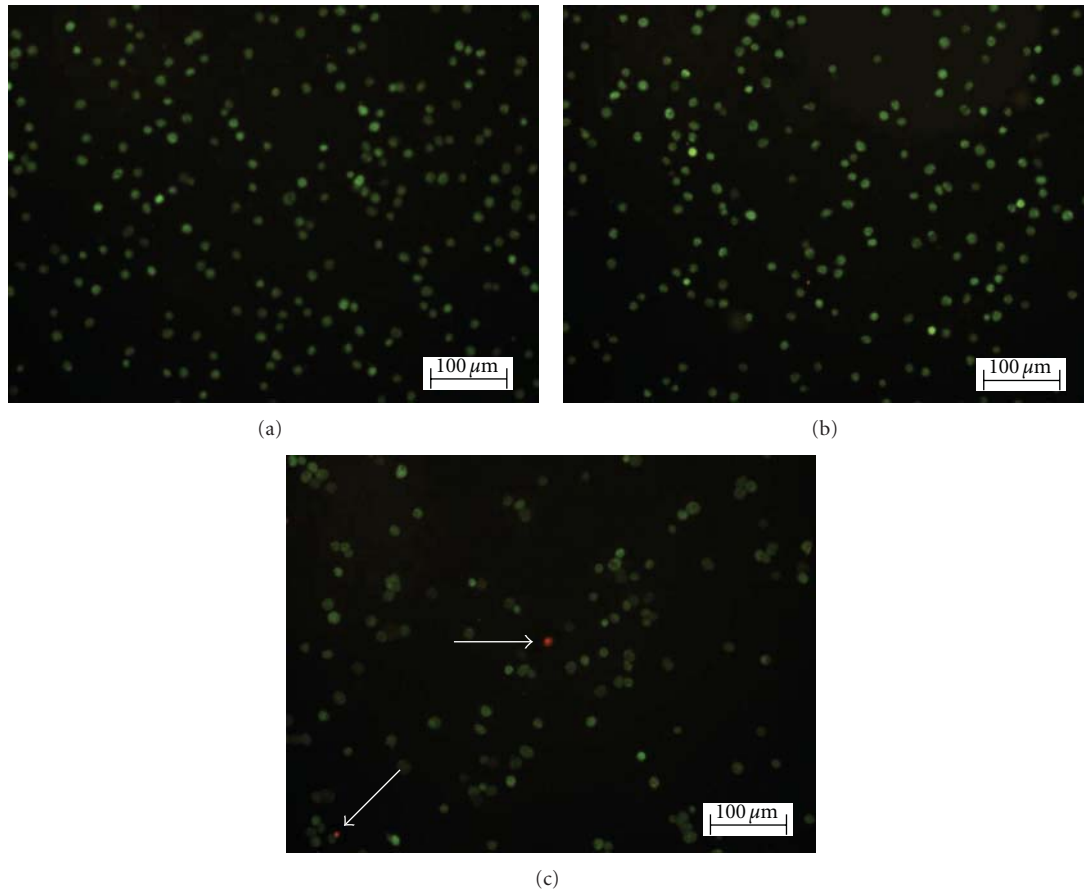
FIGURE 8: Fluorescence microscopic images of KB epithelial cells cultured for 7 days on (a) PLGA, (b) PLGA/Q 1, and (c) PLGA/Q 5 nanofibrous scaffolds.

Acknowledgments

References

[1] M. R. Peluso, "Flavonoids attenuate cardiovascular disease, inhibit phosphodiesterase, and modulate lipid homeostasis in adipose tissue and liver," *Experimental Biology and Medicine*, vol. 231, no. 8, pp. 1287–1299, 2006.

[2] L. Bravo, "Polyphenols: chemistry, dietary sources, metabolism, and nutritional significance," *Nutrition Reviews*, vol. 56, no. 11, pp. 317–333, 1998.

[3] M. G. L. Hertog and P. C. H. Hollman, "Potential health effects of the dietary flavonol quercetin," *European Journal of Clinical Nutrition*, vol. 50, no. 2, pp. 63–71, 1996.

[4] R. L. Prior, "Fruits and vegetables in the prevention of cellular oxidative damage," *American Journal of Clinical Nutrition*, vol. 78, supplement 3, pp. 570S–578S, 2003.

[5] M. Alía, R. Mateos, S. Ramos, E. Lecumberri, L. Bravo, and L. Goya, "Influence of quercetin and rutin on growth and antioxidant defense system of a human hepatoma cell line (HepG2)," *European Journal of Nutrition*, vol. 45, no. 1, pp. 19–28, 2006.

[6] J. P. Brown, "A review of the genetic effects of naturally occurring flavonoids, anthraquinones and related compounds," *Mutation Research*, vol. 75, no. 3, pp. 243–277, 1980.

[7] M. A. Read, "Flavonoids: naturally occurring anti-inflammatory agents," *American Journal of Pathology*, vol. 147, no. 2, pp. 235–237, 1995.

[8] K. Kuriyama, T. Kitamura, R. Yokoi et al., "Evaluation of testicular toxicity and sperm morphology in rats treated with methyl methanesulphonate (MMS)," *Journal of Reproduction and Development*, vol. 51, no. 5, pp. 657–667, 2005.

[9] Y. L. Mi and C. Q. Zhang, "Protective effect of quercetin on aroclor 1254-induced oxidative damage in cultured chicken spermatogonial cells," *Toxicological Sciences*, vol. 88, no. 2, pp. 545–550, 2005.

[10] U. Kaindl, I. Eyberg, N. Rohr-Udilova, C. Heinzle, and B. Marian, "The dietary antioxidants resveratrol and quercetin protect cells from exogenous pro-oxidative damage," *Food and Chemical Toxicology*, vol. 46, no. 4, pp. 1320–1326, 2008.

[11] S. H. Lee, B. S. Kim, S. H. Kim et al., "Elastic biodegradable poly(glycolide-co-caprolactone) scaffold for tissue engineering," *Journal of Biomedical Materials Research A*, vol. 66, no. 1, pp. 29–37, 2003.

[12] Z. Ma, M. Kotaki, T. Yong, W. He, and S. Ramakrishna, "Surface engineering of electrospun polyethylene terephthalate (PET) nanofibers towards development of a new material for blood vessel engineering," *Biomaterials*, vol. 26, no. 15, pp. 2527–2536, 2005.

[13] J. Venugopal and S. Ramakrishna, "Biocompatible nanofiber matrices for the engineering of a dermal substitute for skin regeneration," *Tissue Engineering*, vol. 11, no. 5-6, pp. 847–854, 2005.

[14] M. S. Khil, D. I. Cha, H. Y. Kim, I. S. Kim, and N. Bhattarai, "Electrospun nanofibrous polyurethane membrane as wound dressing," *Journal of Biomedical Materials Research B*, vol. 67, no. 2, pp. 675–679, 2003.

[15] X. Wang, I. C. Um, D. Fang, A. Okamoto, B. S. Hsiao, and B. Chu, "Formation of water-resistant hyaluronic acid nanofibers by blowing-assisted electro-spinning and non-toxic post treatments," *Polymer*, vol. 46, no. 13, pp. 4853–4867, 2005.

[16] I. C. Um, D. Fang, B. S. Hsiao, A. Okamoto, and B. Chu, "Electro-spinning and electro-blowing of hyaluronic acid," *Biomacromolecules*, vol. 5, no. 4, pp. 1428–1436, 2004.

[17] K. Fujihara, M. Kotaki, and S. Ramakrishna, "Guided bone regeneration membrane made of polycaprolactone/calcium carbonate composite nano-fibers," *Biomaterials*, vol. 26, no. 19, pp. 4139–4147, 2005.

[18] H. Yoshimoto, Y. M. Shin, H. Terai, and J. P. Vacanti, "A biodegradable nanofiber scaffold by electrospinning and its potential for bone tissue engineering," *Biomaterials*, vol. 24, no. 12, pp. 2077–2082, 2003.

[19] F. Yang, R. Murugan, S. Ramakrishna, X. Wang, Y. X. Ma, and S. Wang, "Fabrication of nano-structured porous PLLA scaffold intended for nerve tissue engineering," *Biomaterials*, vol. 25, no. 10, pp. 1891–1900, 2004.

[20] C. M. Agrawal and R. B. Ray, "Biodegradable polymeric scaffolds for musculoskeletal tissue engineering," *Journal of Biomedical Materials Research A*, vol. 55, no. 2, pp. 141–150, 2001.

[21] E. Behravesh, A. W. Yasko, P. S. Engel, and A. G. Mikos, "Synthetic biodegradable polymers for orthopaedic applications," *Clinical Orthopaedics and Related Research*, supplement 367, pp. S118–S125, 1999.

[22] K. A. Athanasiou, G. G. Niederauer, and C. M. Agrawal, "Sterilization, toxicity, biocompatibility and clinical applications of polylactic acid/polyglycolic acid copolymers," *Biomaterials*, vol. 17, no. 2, pp. 93–102, 1996.

[23] J. B. Lee, S. E. Kim, D. N. Heo, I. K. Kwon, and B. J. Choi, "In vitro characterization of nanofibrous PLGA/gelatin/hydroxyapatite composite for bone tissue engineering," *Macromolecular Research*, vol. 18, no. 12, pp. 1195–1202, 2010.

[24] T. A. Telemeco, C. Ayres, G. L. Bowlin et al., "Regulation of cellular infiltration into tissue engineering scaffolds composed of submicron diameter fibrils produced by electrospinning," *Acta Biomaterialia*, vol. 1, no. 4, pp. 377–385, 2005.

[25] M. J. Mondrinos, S. Koutzaki, E. Jiwanmall et al., "Engineering three-dimensional pulmonary tissue constructs," *Tissue Engineering*, vol. 12, no. 4, pp. 717–728, 2006.

[26] H. J. Shin, C. H. Lee, I. H. Cho et al., "Electrospun PLGA nanofiber scaffolds for articular cartilage reconstruction: mechanical stability, degradation and cellular responses under mechanical stimulation in vitro," *Journal of Biomaterials Science, Polymer Edition*, vol. 17, no. 1-2, pp. 103–119, 2006.

[27] Z. C. Xing, W. P. Chae, M. W. Huh et al., "In vitro antibacterial and cytotoxic properties of silver-containing poly(L-lactide-co-glycolide) nanofibrous scaffolds," *Journal of Nanoscience and Nanotechnology*, vol. 11, no. 1, pp. 61–65, 2011.

[28] K. H. Lee, H. Y. Kim, Y. J. Ryu, K. W. Kim, and S. W. Choi, "Mechanical behavior of electrospun fiber mats of poly(vinyl chloride)/polyurethane polyblends," *Journal of Polymer Science B*, vol. 41, no. 11, pp. 1256–1262, 2003.

[29] A. Alhadlaq, J. H. Elisseeff, L. Hong et al., "Adult stem cell driven genesis of human-shaped articular condyle," *Annals of Biomedical Engineering*, vol. 32, no. 7, pp. 911–923, 2004.

[30] T. P. T. Cushnie and A. J. Lamb, "Antimicrobial activity of flavonoids," *International Journal of Antimicrobial Agents*, vol. 26, no. 5, pp. 343–356, 2005.

[31] M. Lipkin, B. Reddy, H. Newmark, and S. A. Lamprecht, "Dietary factors in human colorectal cancer," *Annual Review of Nutrition*, vol. 19, pp. 545–586, 1999.

[32] G. G. Duthie, S. J. Duthie, and J. A. M. Kyle, "Plant polyphenols in cancer and heart disease: implications as nutritional antioxidants," *Nutrition Research Reviews*, vol. 13, no. 1, pp. 79–106, 2000.

[33] G. Agullo, L. Gamet, C. Besson, C. Demigne, and C. Remesy, "Quercetin exerts a preferential cytotoxic effect on active dividing colon carcinoma HT29 and Caco-2 cells," *Cancer Letters*, vol. 87, no. 1, pp. 55–63, 1994.

[34] F. O. Ranelletti, R. Ricci, L. M. Larocca et al., "Growth-inhibitory effect of quercetin and presence of type-II estrogen-binding sites in human colon-cancer cell lines and primary colorectal tumors," *International Journal of Cancer*, vol. 50, no. 3, pp. 486–492, 1992.

[35] M. Richter, R. Ebermann, and B. Marian, "Quercetin-induced apoptosis in colorectal tumor cells: possible role of EGF receptor signaling," *Nutrition and Cancer*, vol. 34, no. 1, pp. 88–99, 1999.

[36] R. L. Singhal, Y. Albert Yeh, N. Prajda, E. Olah, G. W. Sledge, and G. Weber, "Quercetin down-regulates signal transduction in human breast carcinoma cells," *Biochemical and Biophysical Research Communications*, vol. 208, no. 1, pp. 425–431, 1995.

[37] G. Scambia, F. O. Ranelletti, P. B. Panici et al., "Quercetin potentiates the effect of adriamycin in a multidrug-resistant MCF-7 human breast-cancer cell line: p-glycoprotein as a possible target," *Cancer Chemotherapy and Pharmacology*, vol. 34, no. 6, pp. 459–464, 1994.

[38] T. B. Kang and N. C. Liang, "Studies on the inhibitory effects of quercetin on the HL-60 leukemia cells," *Biochemical Pharmacology*, vol. 54, no. 9, pp. 1013–1018, 1997.

[39] S. Uddin and M. A. Choudhry, "Quercetin, a bioflavonoid, inhibits the DNA synthesis of human leukemia cells," *Biochemistry and Molecular Biology International*, vol. 36, no. 3, pp. 545–550, 1995.

[40] S. M. Kuo, "Antiproliferative potency of structurally distinct dietary flavonoids on human colon cancer cells," *Cancer Letters*, vol. 110, no. 1-2, pp. 41–48, 1996.

[41] C. W. Chi, Y. F. Chang, Y. R. Ou et al., "Effect of quercetin on the in vitro and in vivo growth of mouse hepatoma cells," *Oncology Reports*, vol. 4, no. 5, pp. 1021–1024, 1997.

[42] A. Robaszkiewicz, A. Balcerczyk, and G. Bartosz, "Antioxidative and prooxidative effects of quercetin on A549 cells," *Cell Biology International*, vol. 31, no. 10, pp. 1245–1250, 2007.

Review Article

Gold Nanoparticles: Promising Nanomaterials for the Diagnosis of Cancer and HIV/AIDS

Anil Kumar,[1] Bhargavi Mazinder Boruah,[2] and Xing-Jie Liang[1]

[1] CAS Key Laboratory for Biomedical Effects of Nanoparticles and Nanosafety, National Center for Nanoscience and Nanotechnology,
Chinese Academy of Sciences, Beijing 100190, China
[2] CAS Key Laboratory of Pathogenic Microbiology and Immunology, Institute of Microbiology, Chinese Academy of Sciences,
Beijing 100101, China

Correspondence should be addressed to Xing-Jie Liang, liangxj@nanoctr.cn

Gold nanoparticles (*Au*NPs) are currently playing a significant role for human welfare in the field of clinical diagnosis as well as several biomedical applications. More and more research shows that *Au*NPs-based technologies are becoming promising approaches in cancer research and AIDS treatment. In this paper, we have focused mainly on the exploitation of unique and characteristic properties of *Au*NPs such as surface plasmon resonance (SPR), surface enhance Raman scattering (SERS), magnetic properties (MRI), and fluorescence behavior shown upon conjugation with biological and biocompatible ligands. These properties find wide prevalence in biodiagnostics like plasmon-based labeling and imaging, enzyme-linked immunosorbant assay (ELISA), and electrochemical-based methods that can pave the way for developing novel techniques towards diagnosis and therapy of cancer and human immunodeficiency virus/acquired immunodeficiency syndrome (HIV/AIDS).

1. Why Nanoparticles for Biomedical Applications?

In contrast to a majority of micro- and macroparticles, nanoparticles (NPs) contain highly significant properties such as molecular fluorophores which make them ideal for biodiagnostic applications. The characteristic properties earmarked for NPs are their (a) small size (1–100 nm) and correspondingly large surface-to-volume ratio, (b) physical and chemical properties that can be tuned depending upon the requirements of size, composition, and shape (e.g., gold nanoparticles), (c) quantitive and qualitative target-binding properties, and (d) high robustness shown by some of the nanostructure materials [1]. The size of NPs plays an indispensable role in the field of nanobiotechnology which makes them suitable for all biological applications. They offer various advantages over a bulk structure; their characteristic properties make them more ideal. The physical and chemical properties of NPs can have significant effect on the overall function such as target-binding event. In the present research scenario, a number of research and publications are focussing on the tunable physicochemical properties of materials to synthesize highly advanced materials and to boost their robustness. Applications of NPs in biological sciences have a long history as NPs have been used in bioconjugation with peptides, proteins, and DNA and also with some other biological molecules as cellular delivery, labeling, and imaging agents [2, 3]. Specifically the size, shape, and absorptive and light-scattering properties of some materials exhibit different phenomenon when a beam of light is incident on the surface molecules, which in turn make these materials ideal for multiplexed analyte detection for biological moieties [4–7]. Past few years have seen growth in nanomaterial engineering like the construction of nanowires, nanofibers, and nanotubes which can control the different ways to achieve the target analytes [8]. Additionally, in the present era, methods and techniques for engineering materials such as surface modification, size control, and patterning have reached advances to such a point which now allows generation of very high nanoscale materials for arrays of biomacromolecules and small molecules on surfaces [9–12].

To sum up, engineering the NPs in different directions and ability to tailor the physicochemical properties have

together given a right way to make the materials more advanced and highly robust for the binding affinities of various biomolecules and drug targets [13–16] as well as for the diagnosis and treatment of diseases like cancer and HIV.

2. Role of Gold Nanoparticles in Nanobiotechnology

Gold (*Au*) is unique compared to other metals because of its resistance to tarnishing. According to the earliest records, use of *Au* for medical purposes can be traced back to the Chinese civilization in 2500 BC, and after that, several ancient cultures have utilized *Au*-based materials for medicinal purpose for the treatment of a variety of diseases such as smallpox, skin ulcers, measles, and syphilis [17]. In today's era of nanotechnology, gold nanoparticles (*Au*NPs) have been used for the treatment of diseases like rheumatoid arthritis, and so forth, while considerable research is currently going on for unveiling potential anticancer and antimicrobial and biodiagnostic applications of *Au*-based materials and compounds for clinical applications [18].

In the recent years, nanotechnology has attracted most of the scientific community concerning the applications of nanotechnology in medicine. One particularly exciting field of research involves the use of *Au*NPs for the diagnosis of cancer. *Au*NPs find significant exploitations in biomedical field due to (i) their comparative chemical stability, making them less hazardous, (ii) simple and straightforward synthesis and fabrication process, and (iii) genuine biocompatibility and noninterference with other labeled biomaterials (e.g., antibody and other biomarkers) [15, 19]. Furthermore, the advancement of nanotechnology has led researchers to generate nanostructures that can be conjugated to several kinds of biological molecules, including hormones and antibodies, which can reach targeted cells expressing the receptors [20–22]. Colloidal *Au* has been playing an important role for curing various diseases although the exact mechanism of action is still poorly understood. Today, the applications of *Au*NPs are increasing day by day in pharmaceutical sciences for human welfare. It can be used to understand more about the nature of diseases like cancer and HIV by providing significant target with nanovehicles [23].

3. Unique Properties of Gold Nanoparticles for Diagnostic Purpose

The past two decades have seen rapid changes in the fictionalization of NPs from the point of view of applications such as physiochemical properties, material size, shape, structure morphology, and detailed structural chemistry of the materials [24]. The combination of unique optical, electronic, and magnetic properties exhibited at nanoscale level can be exploited in a systematic manner to design more advanced materials and might be possible to attract the NPs more into the biological field (Figure 1) [1, 4, 25, 26]. Herein, we have reviewed the unique properties of *Au*NPs which make them the ultimate nanoscale materials for diagnostic purposes.

3.1. Tuning the Optical Properties of Gold for Biodiagnosis. The size-dependent absorbance of *Au*NPs was explored to demonstrate how alloying affects the chemical stability of NPs and also how composition, size, and nanostructure can be employed to adjust the optical properties [27, 28]. The absorbance and scattering properties of *Au*NPs can be tuned in accordance with their size parameter [29–32]. NPs less than 20 nm show only their surface plasma resonance (SPR), but scattering properties of such materials is negligible. In the case of large NPs (20–80 nm), the scattering properties of the materials increase [33]. The spherical *Au*NPs are colloidal in solution and appear red in color with SPR band positioned at 520 nm depending upon the size, shape, refractive index of surrounding media, and on the interparticle distance of the NPs (Figure 2) [33–36]. The large *Au*NPs show relatively high-scattering properties making them more applicable for biomedical applications, whereas those having relatively high-absorption properties are widely used in colorimetric detection of analytes as well as for biological analysis by changing refractive index of *Au*NP's environment [37]. Similarly, the use of *Ag-Au* alloy-NPs has shown very distinct optical properties and allows for improved detection of biological interactions by novel phenomenon like localized surface plasmon resonance (LSPR) and coupled plasma mass spectrometry (CPMS) [38–40]. LSPR provides an excellent way to improve the sensitivity of plasmon-based bioassays, paving the way for single molecule-based detection and clinically relevant method for diagnostics [40]. Besides detecting biomolecular interaction systems, SPR can also be used to identify interactions involving synthetic receptors like ionophores and imprinted polymers [41]. The use of ionophores as the receptor on the sensor allows the quantitative and specific detection of ionic species molecules [42], while the use of imprinted polymers allows the replacement of antibodies for the quantitative and specific detection of small molecules [43].

3.2. Gold Nanoparticles and Surface Plasmon Resonance (SPR). Surface plasmon resonance (SPR) is a phenomenon occurring at the metal surface when a beam of light is incident on the surface of the molecules at a particular angle and distance (typically in case of gold (*Au*) and silver (*Ag*) metals or spherical NPs). It is well known that size and thickness of materials play an important role at the metal surface; the SPR phenomenon results in a gradual reduction in intensity of the reflected light. By measuring the appropriate exquisite sensitivity of SPR to the refractive index of the surrounding medium on to the metal surface, it is possible to measure accurately the adsorption and scattering of molecules on the metal surface and their targeted specific ligands [45]. Nowadays, the most common and fundamental application of biosensing SPR instruments is the determination of affinity parameters for biomolecular interactions [45]. The last twenty years have seen tremendous development of SPR and its usage in biomedical applications related to diagnostics and therapy. This technique holds utility not only for measurement in real-time kinetics of ligand-receptor interactions but also in screening of lead compound identification in pharmaceutical drug development as well as in detection of

Surface plasmon resonance
- Ligand-receptor interaction
- DNA hybridization
- Antibody characterization
- Epitope mapping
- Label-free immunoassay
- Screening of lead compound
- Identification of disease biomarker

Surface plasmon resonance
- Single-molecule detection
- Actual biological system and catalysis analytical assay
- *In situ* ambient analysis
- Protein and nucleic acid biosensors
- Protein characterization studies

Magnetic resonance properties
- MRI
- CT-MRI
- MRI-contrast agent
- Diagnosis of malignant and solid tumors
- Bimodal contrast agents

Fluorescence properties
- Imaging
- Analytical genomic and proteomic studies
- Drug screening
- Immunological assay
- Identification of reactive oxygen species (ROS)

FIGURE 1: Unique properties of *Au*NPs along with their applications in clinical diagnosis and different biological studies.

(a)

(b)
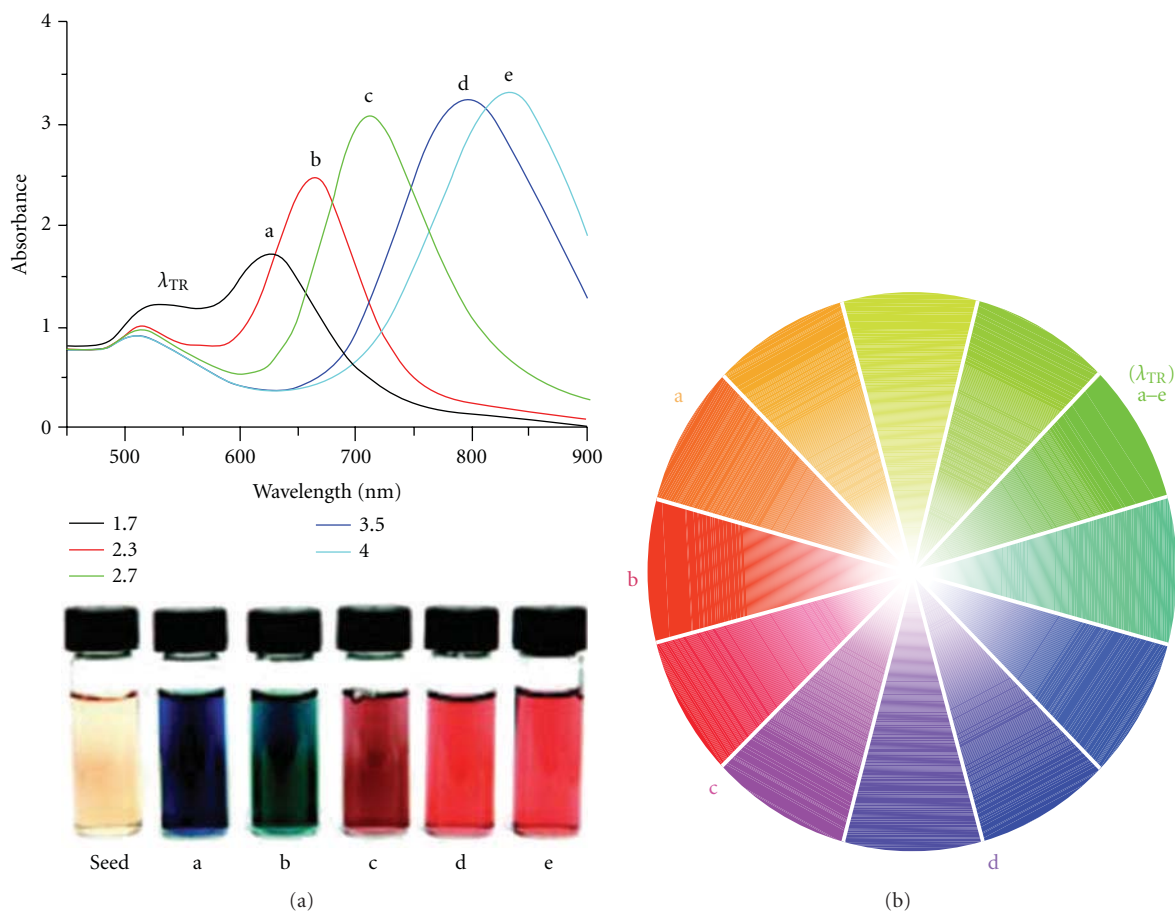
FIGURE 2: Tunable optical properties of gold nanorods (*Au*NRs) with absorptions at visible and near-infrared wavelengths region. (a) Optical absorption spectra of *Au*NRs with different aspect ratios and composition (a–e). (b) Color wheel representing of *Au*NRs labeled a–e, TR = transverse resonance. *(Reprinted with permission from John Wiley and Sons, [44]).*

Biologically-targeted ligands on recognition sites →

Free gold nanoparticles   Binding of targeted molecules changes the refractive index of surrounding medium which results in change of color from red to purple
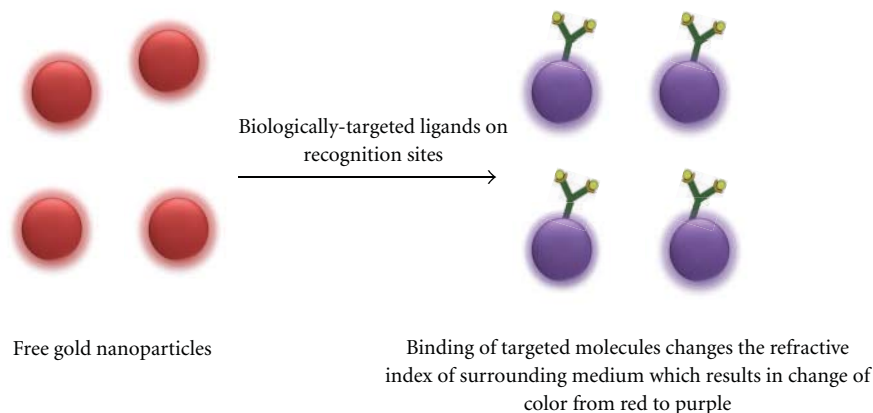
FIGURE 3: SPR phenomenon of *Au*NPs bound to antibodies or targeted sites leading to color change.

small molecules [46], DNA hybridization [47–50], enzyme-substrate interactions [51], antibody characterization [52, 53], studying antigen-antibody interaction [54–56], characterization of antibody orientations [57], epitope mapping [58, 59], protein conformational studies [60], and label-free immunoassays [61–63]. Boisselier and Astruc [64] have reviewed the significance of the *Mie theory* and highlighted the fundamentals which depict that the particle morphology such as spherical or nonspherical, various shapes (rods, prisms, triangles, tetrapods, dogbones, cubes, and shells) as well as physical properties of the metal surfaces influences the frequency variation of the plasmon bands. The same phenomenon was observed in the case of *Au*NPs specially in the case of gold nanorods (*Au*NRs) [65] which exhibited two plasmon bands, one band corresponding to oscillations along the length of the *Au*NRs (longitudinal plasmon band) and the other along the width of the *Au*NRs (transverse plasmon band). *Au*NRs exhibit plasmon bands at different wavelength—one around 500 and the other at 1600 nm. Thus, it is possible to synthesize *Au*NRs with suitable ratio, so that they correspond to commercial lasers (e.g., 360 nm, 785 nm, and 1064 nm). If the shift of the plasmon band is towards the IR region, *Au*NRs allow obtaining a penetration into living tissues that is comparatively deeper than visible light with less background fluorescence [66, 67]. The strong dependence of SPR phenomenon has made *Au*NRs attractive candidates for colorimetric sensors, photothermal therapy, gene therapy, imaging, and various bioassay applications [65, 68]. *Au*NPs also change color from red to purple in response to refractive index change in the vicinity of NP surface. Antibodies can be easily attached to the NPs and when the specific analytes bind to the antibodies, the interaction leads to colour changes in proportion to analyte concentration (Figure 3).

3.3. Magnetic Resonance Properties of AuNPs for MRI.
The new era of molecular imaging, *in vivo* characterization, and measurement of biological processes at cellular and molecular level aims at quantifying molecular changes associated with the onset and development of pathological states, thereby, providing early diagnosis and prognosis of diseases like

cancer. The imaging of cells, cellular and subcellular structures, requires imaging agents of high relaxivity and density endowed with targeting ability to specific cellular receptors. *Au*NPs are especially attractive for imaging and therapy due to their SPR, enhanced light scattering, and absorption. In the field of MRI, *Au*NPs can be used as a template agent in place of Gadolinium (*Gd*) chelates for use as MRI contrast agents due to their high sensitivity [73, 74] and also in clinical diagnosis [75, 76]. Cho et al. [77] investigated the core-shell structured iron-gold (Fe-*Au*) NPs prepared by reverse micelle method, and their potential applications as magnetic resonance (MR) contrast agents. The average NP size is 19 nm, and the materials show high relaxivity and magnetising properties.

Alric et al. [95] reported to have designed *Au*NPs for MRI where materials exhibit high relaxivity ($r = 586 \, \text{nM}^{-1}\text{s}^{-1}$ as compared to $3.0 \, \text{nM}^{-1}\text{s}^{-1}$ for Gd), rendering them very attractive as contrast agents for MRI. Another group has reportedly encapsulated *Au* cores within a multilayered organic shell composed of *Gd* chelates bound to each other through disulfide bonds. The presence of *Gd* ions entrapped in the organic shell results in contrast enhancement, whereas the *Au* core provides a strong X-ray absorption. The study reveals that these particles are suited for dual modality imaging and circulate freely in the blood vessels without undesirable accumulation in the organ system such as lungs, spleen, and liver. PEG-coated iron oxide gold is a type of core-shell nanoparticles (PEG-*Au*IONs), measuring approximately 25 nm in diameter, which reveals high specificity to solid tumors as they accumulate mostly within the tumor mass along with low nonspecific accumulation in the liver and spleen. These results suggest PEG-*Au*IONs as promising MRI contrast agents for diagnosis of malignant tumors including pancreatic cancer [96]. Nasiruzzaman Sk Md et al. [97] investigated the *Au*NPs coated by *Gd*-chelate (GdL *Au*) as a potential CT/MRI Bimodal contrast agent. MRI signaling requires strong magnetic properties of materials for defined use in biodiagnostic purposes.

3.4. Fluorescence Behavior of Gold Nanoparticles.
Fluorescence-based assays and detection techniques are among

the most highly sensitive and popular biological tests in clinical diagnosis. *Au*NPs show excellent behavior of antiphotobleaching under the presence of strong light illumination. Despite low quantum yields, *Au*NPs exhibit strong native fluorescence under relatively high excitation energy state. A new fluorescence method has been developed for cell imaging, when the cells stained with *Au*NPs are illuminated with strong light, the fluorescence of *Au*NPs on cell membrane or inside cells can be collected for cell imaging [98]. Lee et al. [99] investigated *Au* nanoprobes immobilized with fluorescein-hyaluronic acid (HA) conjugates which are fabricated and utilized for monitoring intracellular reactive oxygen species (ROS) generation in live cells via NP surface energy transfer. An adhesive molecule, dopamine, is used to robustly end-immobilize HA onto the surface of *Au*NPs for securing intracellular stability against glutathione which allows rapid and specific detection of intracellular ROS by emitting strong fluorescence-recovery signals. The result suggests that fluorescent *Au* nanoprobe is usefully exploited for real-time intracellular ROS detection and antioxidant screening assay and has exciting potential for various biomedical applications as a new class of ROS imaging probes.

Recently, Coto-Garcia et al. [100] reviewed about the *Au*NPs as fluorescent labels for optical imaging and sensing for analytical genomics and proteomics, with particular emphasis on the outlook for different strategies of using NPs for bioimaging and quantitative bioanalytical applications. Fluorescence resonance energy transfer (FRET) is a spectroscopic technique whereby the excitation energy of the donor electron is transferred to the acceptor via an induced-dipole movement interaction [64]. Depending upon this technique, *Au*NP-based FRET monitors DNA hybridization, and DNA cleavage by nucleobases after hybridization has been developed by varying the DNA length. The distance between *Au*NP and Cy3 dye was systematically varied between 3 and 100 nm, and 50% quenching efficiency was observed even at 25 nm separation [101]. Large molecules such as proteins can be sensed with 20 nm *Au*NPs stabilized by Cy5.5-Gly-Po-Leu-Gly-Val-Arg-Gly-Cys-(amide) showing selectivity for a matrix metalloprotease served as fluorescent imaging probe for *in vivo* drug screening and protease activity [102]. You et al. [103] reported the use of a fluorescent polymer to decode the response produced by nanomolar concentrations of proteins by selective *Au*NP-protein affinities. Other groups employed *Au*NPs as fluorescence quenchers for the detection of the protein cardiac troponin [T(cTnT)] by its simultaneous interaction with two different antibodies, one attached to *Au*NP and the other labeled with fluorescent dyes [104].

4. Current Clinical Diagnosis Using Gold Nanoparticles

Diagnosis and treatment of cancer in nascent stages are of great importance because of the widespread occurrence of the disease, high death rate, and the frequency of reoccurrence even after treatment. According to cancer statistics 2010 done by American Cancer Society, estimated new cancer cases were 1,529,560 and 569,490 death in both males and females in the US [105]. However, the exact survival rate

of cancer patients is heavily dependent on early diagnosis [106]. Hence, developing technologies applicable for the sensitivity detection of cancer at the initial stages has always been one of the most pressing issues in diagnosis [107]. Diagnostics is an area where nanotechnology, particularly using *Au*, has the ability to revolutionize the way of dealing with the disease. *Au*-based NPs are the perfect raw materials for robust, rapid diagnostic testing to detect cancer and HIV. The minute quantities required make it inexpensive, whilst its stability, sensitivity, and reproducibility as well as high-quality supplies give manufacture guarantee due to which it is already commercially available. The unique properties of *Au*NPs offer various advantages which are currently being studied in exciting fields of academic research due to which potential products are now heading towards the market. However, current methods of cancer diagnosis and treatment are costly and can have adverse side effects to the body organs. *Au*NPs offer an inexpensive and significant route to targeting only cancerous cells, leaving healthy cells untouched without doing any harm [108]. The unique light absorption and emission and scattering properties of *Au*NPs have made them the most studied entities during recent years in cancer diagnostics [108]. Biomarkers related to cancer cells and optical contrast agents provide excellent signal sources from cancer tissues to detect them from complex environment. Most of the larger *Au*NPs make them promising probes for cancer detection based on imaging because of their scattering properties. Cancer cells are targeted with antibody *Au*NPs by selectively binding antigens. For example, cervical epithelial cancer cells (SiHa cells) that overexpress the transmembrane glycoprotein and epithelial growth factor receptor (EGFR) were imaged by immunotargeted *Au*NPs for the early stage of prostate cancer detection [78]. Biomarkers have been employed for the early cancer screening and diagnosis [109, 110]. The recent major developments in the diagnosis of cancer are summarized in Table 1. However, low concentrations of these biomarkers in the complex environment lose their effects often making it difficult to detect the specificity and target. Baptista et al. [111] have demonstrated three approaches for diagnosis of cancer based on *Au*NPs, namely, (i) colorimetric sensing for specific DNA hybridization, depending upon inter-*Au*NP distance for the detection of specific nucleic acid sequences in biological samples, (ii) surface functionalization with different coating materials resulting in highly selective nanoprobes, and (iii) electrochemical-based methods for signal enhancement detection. On the basis of these three methods, clinical diagnosis has been emphasized to applications of cancer and HIV/AIDS using *Au*NPs.

4.1. Bioconjugation on AuNPs Surface for Diagnosis of Cancer. *Au*NPs make promising probes for cancer detection based on immunotargeting of antibody-*Au*NP-labelled cancer cells. SiHa cells, a type of cancer cell line, overexpressing the transmembrane glycoprotein, epithelial growth factor receptor (EGFR), can be imaged by immunotargeted *Au*NPs in case of pericervical cancer [78]. *Au*NPs can be modified with PEG and covalently conjugated with monoclonal antibody (MAb), Herceptin (HER), that enables recognition of breast

Table 1: Current application of *Au*NPs in cancer diagnosis and their advantages.

AuNPs: size and functionalization	Conjugated/Targeted	Type of cancer	Techniques/Methods	Advantages	Ref.
25 nm	anti-EGFR	Precervical cancer	Illumination microscopy, combined with novel contrast agents	Powerful tool for detecting cellular and molecular changes	[78]
PEG-modified *Au*NPs	Herceptin (HER)	Breast cancer cells	Molecular imaging	Promising imaging technique for early detection of cancer	[79]
15 nm	anti-EGFR	Oral cancer	SERS	Saliva-based assay for early diagnosis of oral cancer	[80]
60–80 nm pegylated	ScFv (single-chain variable fragment)	Head-and-neck	SERS	Optical and EM probes for tumor detection	[81]
Au nanorods	anti-EGFR	Oral squamous cell carcinoma	SERS	Bioimaging and cancer biodiagnostics	[82]
45 nm * 15 nm *Au* nanorod	Her-2/neu antigen	Prostate cancer detection	Contrast photoacoustic imaging	Visual tool for molecular and structural information	[83]
15 nm	F19 monoclonal antibodies	Pancreatic adenocarcinoma	Light scattering, size exclusion chromatography, and TEM	Novel labeling method	[84]
20 nm	Aptamer	Leukemia and lymphoma	Spectroscopic method	Early and accurate detection of cancer	[85]
Oval shaped (14 nm length and 18 nm width)	anti-HER2/c erb-2 antibody and aptamers	Breast cancer	Colorimetric and two-photon scattering	Rapid and highly sensitive	[86]
*Au*NPs (size not known)	Tag-PC-3	Prostate cancer	Photoacoustic waves	Detect single cells under flow condition	[87]
Au functionalized with PEG (90 nm)	EGF-ligand and tag Raman receptor	Circulation tumor	SERS	New clinical tool for management of patients with SCCHN	[69]
15 ± 2 nm	anti-CA15-3-HRP antibody	Breast cancer	ELISA	Cancer biomarker detection	[88]
20 nm	cationic protein kinase C (PKC-alpha) peptide	Breast cancer	GNP-based colorimetric assay	Initial screening during cancer diagnosis	[89]
100 to 150 nm	anticarcinoembryonic antibody	Cancer	ELISA	Early diagnosis of cancer	[90]
30 nm (±10)−150.5 (±30.4) nm	ENO1 antibody	Lung cancer	Electrochemical-based immune sensor	Quantitative tests protein and cancer biomarkers	[19]
15 nm	Functionalized glassy carbon electrode (GCE)	Lung and liver cancer, drug-sensitive leukemia cells, and drug-resistant leukemia	Electrochemical and contact angle measurements	Rapid identification and highly sensitive detection for cancer	[70]

TABLE 1: Continued.

AuNPs: size and functionalization	Conjugated/Targeted	Type of cancer	Techniques/Methods	Advantages	Ref.
Hollow Au nanospheres (thicknes 45–12 and 15–5 nm)	pAb and mAb anti-CEA antibodies,	MCF7 cells	SERS immunoassay technique	Novel immunoassay technique	[91]
35 nm	anti-EGFR	Oral epithelial living cancer	SPR	Useful molecular biosensor	[92]
Au DENPs	folic acid (FA), and fluorescein isothiocyanate (FI)	Epithelial cancer	Imaging	Imaging and therapeutics	[93]
20 nm	Heparin-DOPA coated	Liver cells-specific CT imaging	Imaging	Potential CT imaging	[94]

AuNps: Au nanoparticles, EGFR: endothelial growth factor receptor, HER: human epidermal growth factor receptor, Her2: human epidermal growth factor receptor 2, EGF: endothelial growth factor, ScFv: single-chain variable fragment, SERS: surface enhance Raman scattering, SPR: surface plasmon resonance, TEM: tanning electron microscope, SCCHN: squamous cell carcinoma of the head and neck, ELISA: enzyme-linked immunosorbant assay, ENO1: alpha-enolase, GCE: glassy carbon electrode, pAb: polyclonal antibody, mAb: monoclonal antibody, Au DENPs: AuNPs-capped dendrimers, PEG: poly ethylene glycol, DOPA: 3,4-dihydroxy-phenylalanine, CT: computed tomography, CA15-3-HRP: signaling antibody anti-CA15-3-HRP (horseradish peroxidase), PC-3: prostate cancer cells, CEA: carcinoembryonic antigen.
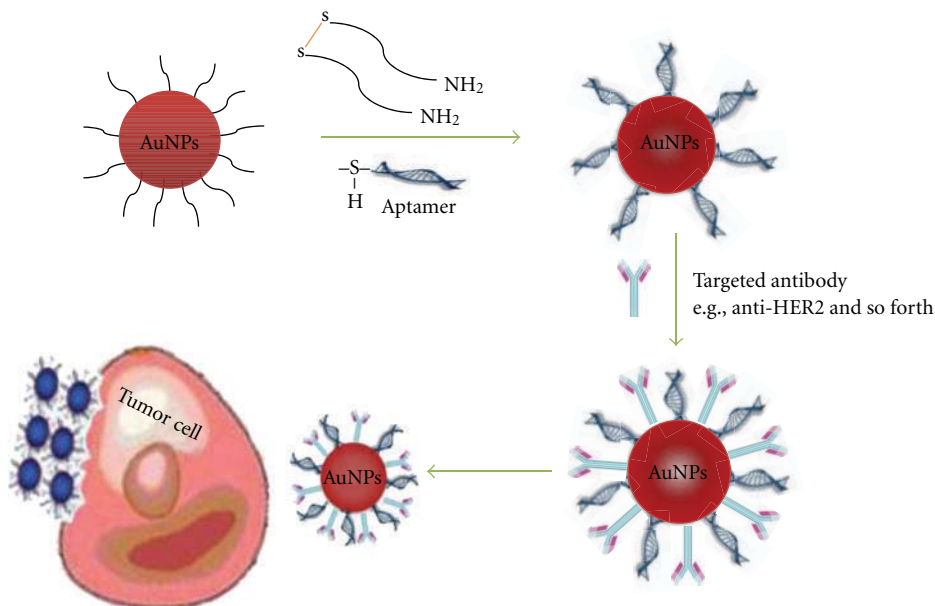
FIGURE 4: Schematic representation of the synthesis of monoclonal anti-HER2 antibody and S6 RNA aptamer-conjugated oval-shaped *Au*NPs (steps one and two). Third step shows schematic representation of multifunctional oval-shaped *Au*NP-based sensing of the breast cancer cell lines.

cancer cells expressing their highly specific tumor-associated antigens and poly(ethylene glycol) (PEG) which obscure particles against the reticuloendothelial system in the body [79]. The stability and functionality of Herceptin-polyethylene glycol *Au* nanorods (Her-PEG *Au*NRs) were demonstrated *in vitro* in the presence of blood as well as *in vivo* in nude mice model for breast cancer. The study showed successful accumulation of functionalized *Au*NRs within HER2/neu overexpressing breast tumors in tumor-bearing nude mice, thus, providing a novel imaging technique for early detection of cancer. Kah et al. [80] reported colloidal *Au*NPs conjugated to antiepidermal growth factor receptor (EGFR) for imaging. They have developed a self-assembled surface-enhanced-Raman-scattering- (SERS-) active *Au*NPs monolayer film as a biosensing surface using a simple drop-dry method. *Au*NPs could elicit an optical contrast to discriminate between cancerous and normal cells and their conjugation with antibodies allowed them to map the expression of relevant biomarkers for molecular imaging under confocal reflectance microscopy. Large optical enhancements can be achieved under *in vivo* conditions for tumor detection using biocompatible and nontoxic NPs based on pegylated *Au* and surface-enhanced Raman scattering (SERS) properties of NPs. These PEGylated SERS NPs were considerably brighter than semiconductor quantum dots with light emission in the near-infrared region. When conjugated to tumor-targeting ligands such as single-chain variable fragment (ScFv) antibodies, the conjugated NPs were able to target tumor biomarkers such as epidermal growth factor receptors on human cancer cells and in xenograft tumor models [81].

4.2. Diagnosis of Cancer by Colorimetric Assay. Direct-visualization/detection of cancer cells using *colorimetric assay* has

been currently progressing fast due to their simplicity and versatility [112]. *Au*NPs-conjugated aptamer has been shown to easily assemble on cell membrane surface for spectral changes, providing direct visualization of cancer cells. Cell-SELEX aptamers have been generated for leukemia, lymphoma, lung cancer, and liver cancer, suggesting that the assays could work out for the detection of these diseases [85]. Recently, Lu et al. [86] have demonstrated a label-free, fast, and highly sensitive multifunctional oval-shaped *Au*NPs based on simple colorimetric and highly sensitive two-photon scattering assay for the selective detection of breast cancer (Figure 4). When oval-shaped *Au*NPs were mixed with breast cancer SK-BR-3 cell line, a distinct color change occurred, and two-photon scattering intensity was increased by about thirteen times. The method was clearly able to detect the cancerous from noncancerous cells and also distinguished it from other breast cancer cell lines that express low levels of HER2.

Melanin, a natural light absorber in melanoma cells, has been reported to induce photoacoustic waves for tumor cell detection for nonpigmented prostate cancer cell line (PC-3). The nonpigmented tumor cells such as breast, prostate, and lung cancers lack intrinsic pigmentation and thus do not generate photoacoustic waves for detection [87]. Utilizing this method on prostate cancer cell line (PC-3), the photoacoustic response over the wavelengths (470–570 nm) can be determined by tagging them with *Au*NPs. A new approach for SERS using *Au*NPs tags can be used for direct measurement of targeted CTCs (circulating tumor cells) in the presence of white blood cells (Figure 5). *Au*NPs-tagged Raman receptors conjugated with epidermal growth factor (EGF) peptides successfully identified CTCs in the peripheral blood of 19 patients with squamous cell carcinoma of

(a)

(b)

(c)
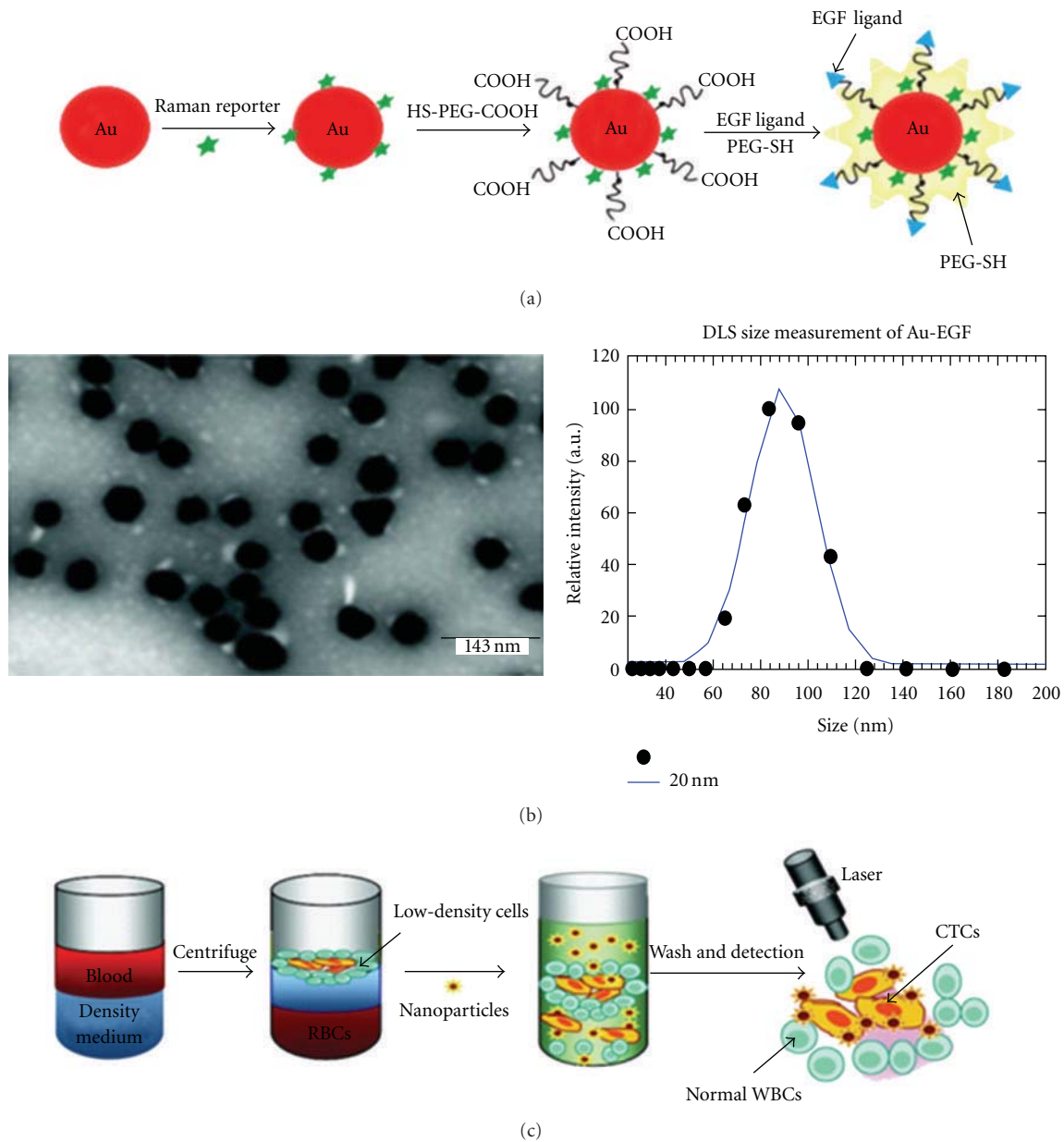
FIGURE 5: Schematic design of EGF-SERS NPs for labeling and detection of CTCs. (a) Raman-encoded, PEG-stabilized, and EGF-peptide-functionalized SERS nanoparticle. (b) TEM image and DLS measurement of modal system after preparation. (c) Assay principle of CTC detection from whole blood using EGF-SERS nanoparticles. (Reprinted with permission from author, [69]).

the head and neck (SCCHN), within a range of 1–720 CTCs per milliliter of whole blood [69].

4.3. Detection of Cancer Using Immunoassay and Electrochemical-Based Method. AuNPs can be used as carriers in optical-based enzyme-linked immunosorbent assay (ELISA) for the analysis of important biomarkers present in blood samples for the treatment of breast cancer. The assay adopting AuNPs as an enhancer resulted in higher sensitivity and shorter assay time when compared to classical method [88]. Kang et al. [89] have developed a noncrosslinking aggregation mechanism with a cationic protein-kinase-C- (PKC-α-) specific

peptide substrate, which is used as a coagulant of AuNPs with anionic surface. As phosphorylation occurs, the PKC suppressed AuNPs aggregation resulting in red color formation. But in case of nonphosphorylation, the color of the GNP solution changed from red to blue, indicating particle aggregation. Zhou et al. [90] developed a stable AuNPs-layer- (GNPL-) modified high-binding ELISA plate method for the representative biomarker carcinoembryonic antigen (CEA) detection. They demonstrated that GNPL markedly amplified the ELISA signal and significantly improved the limit of detection (LOD) and holds great promise in clinical applications for the early diagnosis of cancer. He et al. [70]
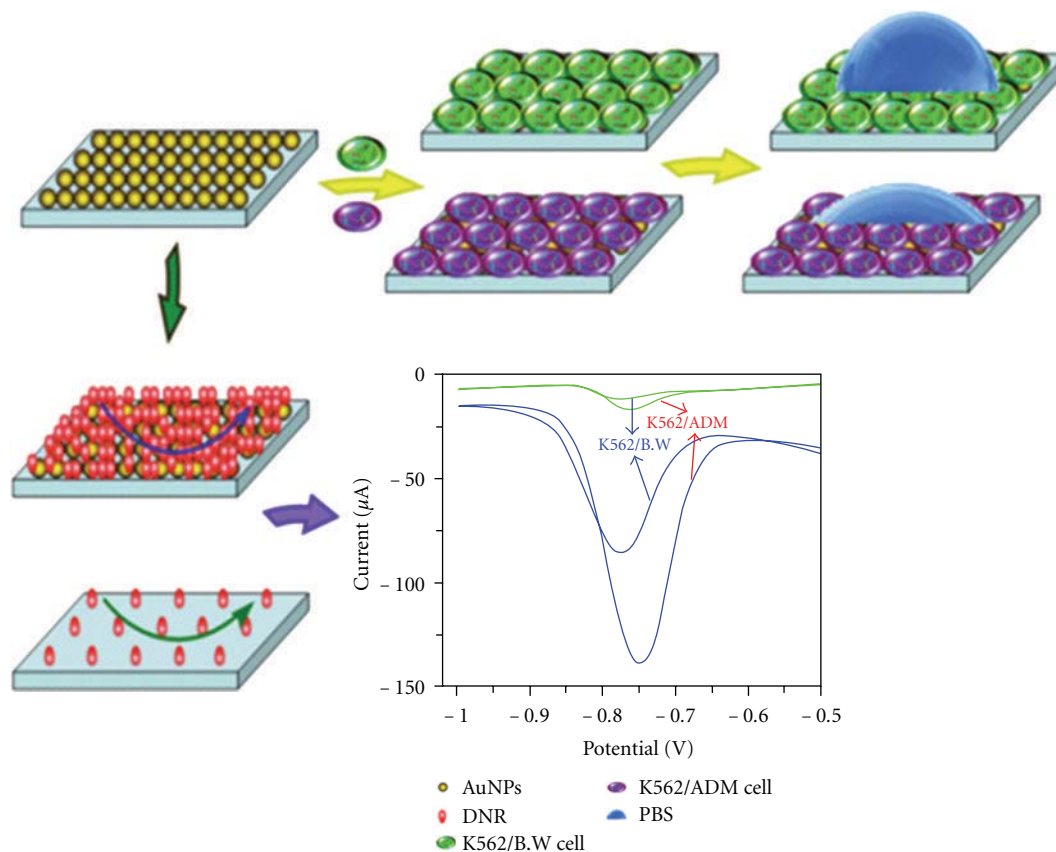
FIGURE 6: Schematic representation of electrochemical and contact angle detection of cancer cells based on functionalized GNPs-GCE interface. *(Reprinted with permission from Elsevier, [70]).*

demonstrated *Au*NPs-modified interface for distinguishing different cancer cells, including lung cancer, liver cancer, drug-sensitive leukemia K562/B.W cells, and drug-resistant leukemia K562/ADM cells by using electrochemical and contact angle measurements (**Figure 6**). In another report, Chon et al. [91] developed a quick and reproducible surface-enhanced-Raman-scattering- (SERS-) based immunoassay technique, using hollow *Au* nanospheres (HGNs) and magnetic beads for immunoanalysis of cancer markers.

4.4. Diagnosis of Cancer by Imaging and Microscopy Techniques. In the field of optical imaging techniques, photoacoustic tomography, multiphoton plasmon resonance microscopy, optical coherence microscopy, and third-harmonic microscopy are promising new techniques for the diagnosis of cancer [113]. A general approach for the targeting and imaging of cancer cells using dendrimer-entrapped *Au*NPs (*Au* DENPs) was found to be able to covalently link with targeting molecules and imaging ligands. *In vitro* studies have shown that FA- (folic-acid-) and FI- (fluorescein-isothiocyanate-) modified *Au* DENPs can specifically bind to KB cells (a human epithelial carcinoma cell line) that overexpress high-affinity folate receptors, and they are internalized dominantly into lysosomes of target cells within 2 h. These findings suggest that *Au* DENPs may serve as general platform for cancer imaging and therapeutics [93]. Lin et al. [114] developed

optical-based diagnostic approach using *Au* core-shells NPs of different sizes by applying *Monte Carlo* models which gave extremely tunable optical resonance peak ranging from the near UV to the mid-IR wavelengths. This can well predict the effect of varying concentrations of nanoshells on tissue reflectance. Another simple and inexpensive technique is the dark-field microscopy which can be used for successful detection of cancerous cells. *Au*NPs conjugated with anti-EGFR antibodies immunotargeted two malignant epithelial cell lines, selected for optimal intense SPR using a white-light source from a conventional microscope, and resulted in a colored *Au*NP image with dark background [92].

4.5. Some New Approaches for Diagnosis of Cancer. A new dimension has been added in the diagnosis of cancer by Peng and his coworkers wherein they combined solid-phase microextraction with gas chromatography/mass spectrometry method for identifying volatile organic compounds acting as biomarkers for lung cancer [71]. The *Au* nanosensor can rapidly distinguish the breath of lung cancer patients from the breath of healthy individuals in an atmosphere of high humidity (**Figure 7**).

Breast cancer stem cells surface marker can be identified by applying a new approach for dual-mode sensing based on targeting, using pointer and signal enhancement using surface plasmon resonance (SPR) and surface-enhanced Raman

(i)   (ii)   (iii)   (iv)

2 cm   1 mm   100 nm   50 nm

(a)

Breath collection

Simulated breath

Application of the collected breath to the sensors array

(b)
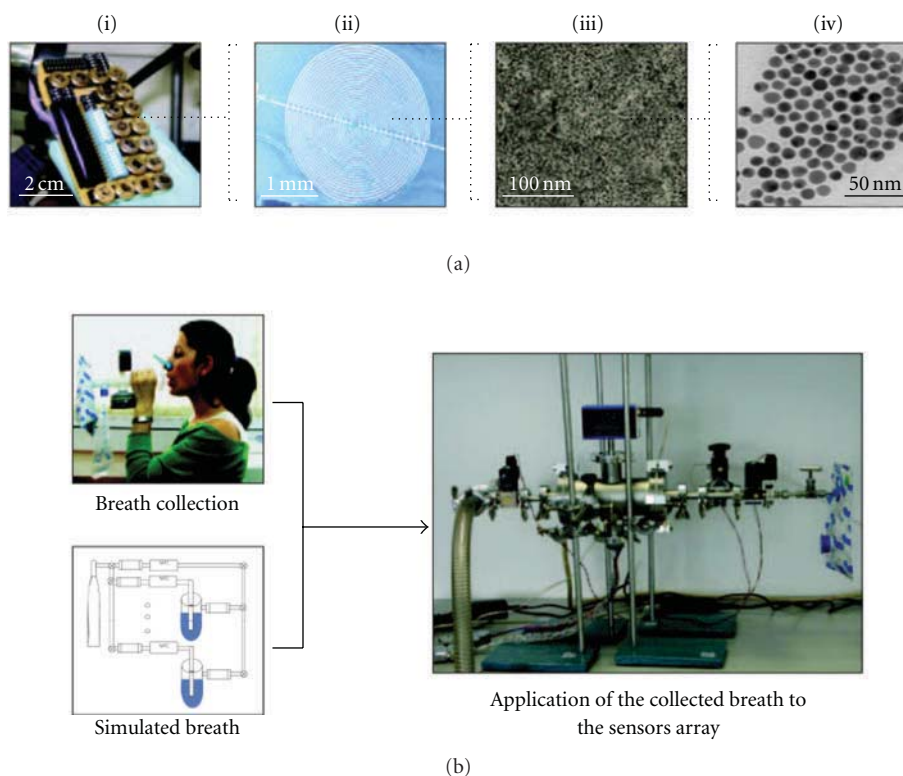
FIGURE 7: Breath testing as a method for detecting lung cancer. (a) (i) Array of chemiresistors, (ii) image of chemiresistor using scanning electron microscope (SEM), (iii) image of *Au*NPs film located between two adjacent electrodes using SEM, and (iv) transmission electron microscope (TEM) image of monolayer-capped *Au*NPs appearing as dark dots and the capping organic molecules as bright medium between the adjacent dots. The *Au*NPs in the films provide the necessary electrical conductivity, and the organic film component provides sites for the sorption of analyte molecules. (b) The exhaled breath (from patients) and simulated breath (mixture of representative VOCs at concentrations similar to those determined by GC-MS analysis of exhaled patient's breath) using the array of *Au*NPs sensors. *(Reprinted with permission from Nature Publishing Group, [71]).*

scattering (SERS) [115]. By applying these concepts, it was possible to detect the cell surface markers antigen, CD44 and CD24, in three breast cancer cell lines to identify subpopulation CD44$^+$/CD24$^-$ of cancer stem cells (CSCs).

5. Applications of Gold Nanoparticles for Diagnosis of HIV/AIDS

Inspite of tremendous research undertaken till date to find a cure, HIV/AIDS continues to wreck havoc upon mankind with no cure or preventive vaccine against it. According to the World Health Organisation (WHO), HIV infection in humans is considered to be at pandemic levels. Worldwide, over 33 million people are believed to be living with HIV, while 2 million population met AIDS-related death in 2008. However, many of these deaths may have been preventable if access to appropriate diagnostics and therapies method would have been possible.

Advances in nanotechnology have led to the development of *Au*NP-based biobarcode amplification assay (BCA), which can detect HIV-1 p24 antigen at very low concentration levels (0.1 pg/mL). The limit of detection was 10–15 pg/mL, and these results demonstrated that HIV-1 p24 BCA assay offers

100–150-fold enhancement in the detection limit over the traditional ELISA method. In the second set, they used the Europium-based NPs for immunoassay instead of *Au*NPs in the BCA assay to further simplify the detection method and decrease the incubation time. In this case, the lower limit of detection for HIV-1 p24 was 0.5 pg/mL. This universal labeling technology based on NPs and its application may provide a rapid and sensitive testing platform for clinical diagnosis for HIV [116].

Another technique that holds promise is the visual DNA microarray for simultaneous, sensitive, and specific detection of human immunodeficiency virus type-1 (HIV-1) based on *Au*-labelled silver staining and coupled with multiplex asymmetric polymerase chain reaction (PCR). The 5′-end amino-modified oligonucleotides were immobilized on glass surface, which were used as the capturing probes to bind the complementary biotinylated target DNA. When *Au*-conjugated streptavidins were introduced to the microarray for specific binding to biotin molecules, it gave rise to black image of microarray spots, which is the result of the formation of silver precipitate onto *Au*NPs and bound to streptavidins. A total of 169 clinical samples of HIV-1 and *T. pallidum* from infected patients were tested through this method. Overall, the results demonstrate that visual gene
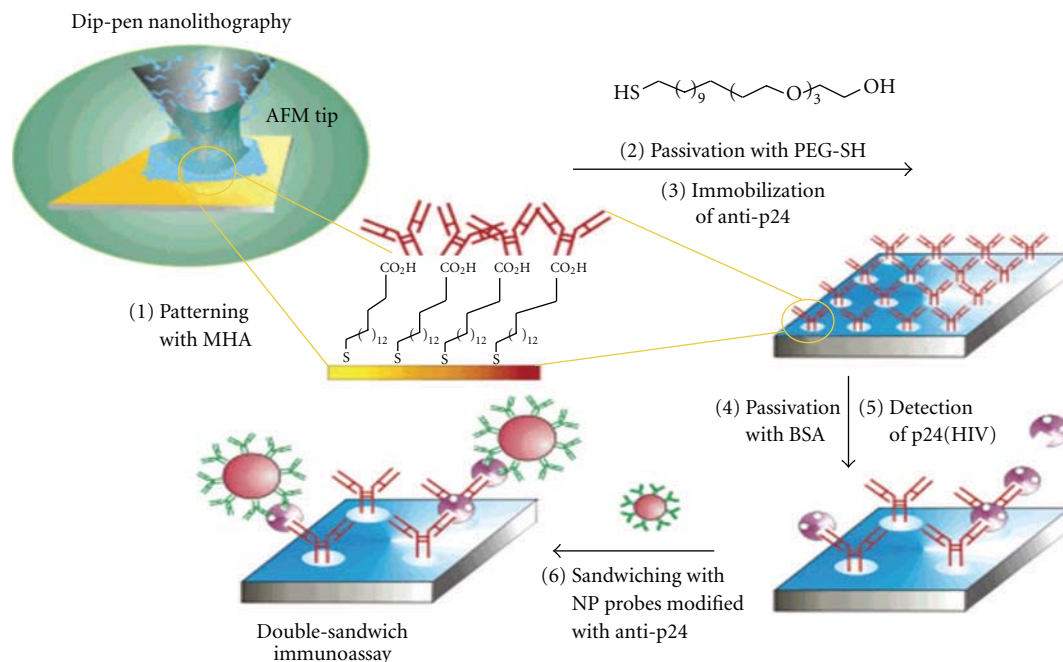
FIGURE 8: Illustration of the immunoassay model used in the detection of HIV-1 p24 antigen with anti-p24 antibody nanoarray. (1) patterning process, (2) and (3) passivated process of *Au* with PEG-SH, (4) and (5) Passivated with BSA and detection of p24(HIV), and (6) sandwich process with nanoprobe modified with p24 (HIV) *(Reprinted with permission from American Chemical Society, [72]).*

detection technique offers high sensitivity and specificity for the clinical applications in case of diseases like HIV [117].

Bowman et al. [118] documented the first ever application of small molecule, SDC-1721 (a derivative of the potent HIV inhibitor, TAK-779) coated with 2-nm *Au*NP-mercaptobenzoic acid, as effective inhibitors of HIV fusion. TAK-779 is a known CCR5 antagonist that serves as the main entry coreceptor for most commonly transmitted and infectious strains of HIV-1. In this way, TAK-779 inhibited HIV-1 replication with an IC 50 of 10 nM. Similarly, 2 nm *Au*NPs coated with multiple copies of an amphiphilic sulfate-ended ligand were developed which were able to bind the HIV envelope glycoprotein gp120 [119]. SPR results of *in vitro* HIV infection of T cells at nanomolar concentrations revealed high levels of inhibition. These results suggest the possibility of tailoring both sulfated ligands and other anti-HIV molecules on the same *Au* cluster, thus contributing to the development of anti-HIV therapeutics as well as for diagnosis purpose. Lee et al. [72] reported the application of nanometer-scale antibody array-based analysis to determine the human immunodeficiency virus type-1 (HIV-1) in blood samples. In this method, Dip-pen nanolithography (DPN) was used to generate nanoscale patterns of antibodies against the HIV-1 p24 antigen on *Au* surface. The HIV-1 p24 antigen in plasma sample was hybridized to the antibody array *in situ*, and the bound protein was hybridized to an *Au* antibody-functionalized nanoparticle probe for signal enhancement. The nanoarray features in the three-component sandwich assay were confirmed by atomic force microscopy (AFM). The amount of HIV-1 p24 antigen measure in plasma was less than 50 copies of RNA per mililiter of plasma (corresponding to 0.025 pg/mL) (Figure 8).

Mahmoud et al. [120, 121] have suggested the possibility of electrochemical detection of HIV type-1 protease (HIV-1 PR) using ferrocene- (Fc-) pepstatin-modified surfaces in picomolar level. In this experiment, they modified the *Au* electrode surface using *Au*NPs or thiolated single-walled carbon nanotubes/gold nanoparticles (SWCNT/*Au*NP). The thiol-terminated Fc-pepstatin was then self-assembled on such surfaces as confirmed by raman spectroscopy and scanning electron microscope (SEM) techniques. The exact interaction between the Fc-pepstatin-modified substrates and HIV-1 PR was studied by cyclic voltametry and electrochemical spectroscopy. The sensing electrode modified with thiolated SWCNTs/*Au*NPs showed remarkable detection and high sensitivity with an estimated detection limit of 0.8 picomolar (pM).

Darbha et al. [122] demonstrated a label-free, highly sensitive, rapid, easy, and reliable diagnosis of single-base-mismatch HIV-1 virus DNA by measuring the HRS (hyper-Rayleigh scatter) intensity from DNA-modified *Au*NRs. They provide higher multipolar contribution to nonlinear optical response (NLO) of *Au*NRs to approach this result. The advantages of this assay are (i) to use unmodified protein and DNA to probe them in solution by the HRS technique, (ii) it can be two orders of magnitude more sensitive than the usual colorimetric technique, and (iii) single-base-pair mismatches are easily detected.

6. Conclusion

It is clear that *Au*NPs offer various advantages over bulk structures; their characteristic properties make them ideal for diagnostic purpose and several biomedical applications.

A number of techniques applying with *Au*NPs such as surface chemistry mainly by conjugating them with biological molecules have been playing a great role in 21th century for the diagnosis and treatment of various diseases like cancer and HIV. Surface plasmon resonance (SPR) is significant for the absorption and scattering properties of *Au*NPs [123]. The last 20 years have seen tremendous development of SPR and its use in biomedical applications related to diagnostics and therapy. This technique applies not only for measuring real-time kinetics of ligand-receptor interactions, but also for the screening of lead compound identification in the pharmaceutical drug development, and for the detection of small molecules [54–68, 73–77, 95]. Modern and highly advanced spectroscopic techniques based upon SERS [124] provide a huge enhancement of the Raman signal, by a factor of ca. 10^{14}–10^{15}, allowing detection at the single-molecule level in pico/nanoconcentration [35]. The most promising applications of *Au*NPs in cancer are tumor detection, molecular imaging, multiplex diagnostic, and fluoroimmunoassay. All these together have boosted the immense potential of *Au*NPs and would shed light on various applications of biomedical field.

Currently, there is no cure, preventive vaccine, and appropriate diagnosis for HIV/AIDS. According to the World Health Organisation, HIV infection in humans is considered to be at pandemic level. Colloidal *Au* is suitable for long-term storage and, therefore, can be used in the typical African climate and in remote area. *Au*NP-based biobarcode amplification (BCA) assay can detect HIV-1 p24 antigen at levels as low as 0.1 pg/mL [116]. In the recent years, protein microarray detection strategies and Protein Chip System for parallel analysis of multitumor markers and its application in cancer detection have also been developed [125].

However despite rapid advancement in research, new cancer cases have been still increasing. Therefore, to attract the use of NPs more towards the biological field, new synthesis, fabrication, and characterization methods are needed for developing highly advanced NPs capable of use in sensitive and multiple detection methods with negligible toxicity.

To conclude, engineering the NPs in different directions and ability to tailor the physicochemical properties have together given a right way to make the material more advanced and highly robust for the binding affinities of various biomolecules and drug targets for the diagnosis and treatment of disease like cancer and HIV. In future, it might be possible to apply all these properties together and evolve new chemistry for synthesis of smart materials for diagnostic applications.

Acknowledgments

References

[1] N. L. Rosi and C. A. Mirkin, "Nanostructures in biodiagnostics," *Chemical Reviews*, vol. 105, no. 4, pp. 1547–1562, 2005.

[2] P. Baudhuin, P. vander Smissen, S. Beavois, and J. Courtoy, "Molecular interactions between colloidal gold, proteins, and living cells," in *Colloidal Gold: Principles, Methods, and Applications*, M. A. Hayat, Ed., vol. 1-2, Academic Press, 1989.

[3] X. J. Liang, C. Chen, Y. Zhao, L. Jia, and P. C. Wang, "Biopharmaceutics and therapeutic potential of engineered nanomaterials," *Current Drug Metabolism*, vol. 9, no. 8, pp. 697–709, 2008.

[4] P. Alivisatos, "The use of nanocrystals in biological detection," *Nature Biotechnology*, vol. 22, no. 1, pp. 47–52, 2004.

[5] R. C. Jin, Y. C. Cao, E. Hao, G. S. Metraux, G. C. Schatz, and C. A. Mirkin, "Controlling anisotropic nanoparticle growth through plasmon excitation," *Nature*, vol. 425, no. 6957, pp. 487–490, 2003.

[6] Y. G. Sun and Y. N. Xia, "Shape-controlled synthesis of gold and silver nanoparticles," *Science*, vol. 298, no. 5601, pp. 2176–2179, 2002.

[7] T. K. Sau and C. J. Murphy, "Room temperature, high-yield synthesis of multiple shapes of gold nanoparticles in aqueous solution," *Journal of the American Chemical Society*, vol. 126, no. 28, pp. 8648–8649, 2004.

[8] Y. Cui, Q. Wei, H. Park, and C. M. Lieber, "Nanowire nanosensors for highly sensitive and selective detection of biological and chemical species," *Science*, vol. 293, no. 5533, pp. 1289–1292, 2001.

[9] D. S. Ginger, H. Zhang, and C. A. Mirkin, "The evolution of dip-pen nanolithography," *Angewandte Chemie*, vol. 43, no. 1, pp. 30–45, 2004.

[10] K. Wadu-Mesthrige, S. Xu, N. A. Amro, and G. Y. Liu, "Fabrication and imaging of nanometer-sized protein patterns," *Langmuir*, vol. 15, no. 25, pp. 8580–8583, 1999.

[11] M. Z. Liu, N. A. Amro, C. S. Chow, and G. Y. Liu, "Production of nanostructures of DNA on surfaces," *Nano Letters*, vol. 2, no. 8, pp. 863–867, 2002.

[12] J. R. Kenseth, J. A. Harnisch, V. W. Jones, and M. D. Porter, "Investigation of approaches for the fabrication of protein patterns by scanning probe lithography," *Langmuir*, vol. 17, no. 13, pp. 4105–4112, 2001.

[13] C. A. Mirkin, R. L. Letsinger, R. C. Mucic, and J. J. Storhoff, "A DNA-based method for rationally assembling nanoparticles into macroscopic materials," *Nature*, vol. 382, no. 6592, pp. 607–609, 1996.

[14] M. Endo, Y. Katsuda, K. Hidaka, and H. Sugiyama, "Regulation of DNA methylation using different tensions of double strands constructed in a defined DNA nanostructure," *Journal of the American Chemical Society*, vol. 132, no. 5, pp. 1592–1597, 2010.

[15] L. J. Wang Yz Hb and X. J. Liang, "Current status of nanotechnology applied in biomedicine," *Acta Biophysica Sinica*, vol. 25, no. 3, pp. 168–174, 2009.

[16] R. J. Chen, Y. Zhang, D. Wang, and H. Dai, "Noncovalent sidewall functionalization of single-walled carbon nanotubes for protein immobilization," *Journal of the American Chemical Society*, vol. 123, no. 16, pp. 3838–3839, 2001.

[17] M. C. Daniel and D. Astruc, "Gold Nanoparticles: assembly, supramolecular chemistry, quantum-size-related properties, and applications toward biology, catalysis, and nanotechnology," *Chemical Reviews*, vol. 104, no. 1, pp. 293–346, 2004.

[18] K. S. Soppimath, G. V. Betageri, and M. H. Cho, "Nanostructures for cancer diagnostics and therapy," in *Biomedical Nanostructures*, K. Gonsalves, C. Halberstadt, C. Laurencin, and L. Nair, Eds., pp. 409–437, John Wiley & Sons, New York, NY, USA, 2008.

[19] J. A. A. Ho, H. C. Chang, N. Y. Shih et al., "Diagnostic detection of human lung cancer-associated antigen using a gold nanoparticle-based electrochemical immunosensor," *Analytical Chemistry*, vol. 82, no. 14, pp. 5944–5950, 2010.

[20] H. Devalapally, D. Shenoy, S. Little, R. Langer, and M. Amiji, "Poly(ethylene oxide)-modified poly(β-amino ester) nanoparticles as a pH-sensitive system for tumor-targeted delivery of hydrophobic drugs: part 3. Therapeutic efficacy and safety studies in ovarian cancer xenograft model," *Cancer Chemotherapy and Pharmacology*, vol. 59, no. 4, pp. 477–484, 2007.

[21] D. Shenoy, S. Little, R. Langer, and M. Amiji, "Poly(ethylene oxide)-modified poly(β-amino ester) nanoparticles as a pH-sensitive system for tumor-targeted delivery of hydrophobic drugs: part 2. In vivo distribution and tumor localization studies," *Pharmaceutical Research*, vol. 22, no. 12, pp. 2107–2114, 2005.

[22] O. C. Farokhzad, J. Cheng, B. A. Teply et al., "Targeted nanoparticle-aptamer bioconjugates for cancer chemotherapy in vivo," *Proceedings of the National Academy of Sciences of the United States of America*, vol. 103, no. 16, pp. 6315–6320, 2006.

[23] Gold for good, "Gold and nanotechnology in the age of innovation," http://www.gold.org/download/rs_archive/gold_and_nanotechnology_in_the_age_of_innovation.pdf#.

[24] C. Burda, X. Chen, R. Narayanan, and M. A. El-Sayed, "Chemistry and properties of nanocrystals of different shapes," *Chemical Reviews*, vol. 105, no. 4, pp. 1025–1102, 2005.

[25] E. Katz and I. Willner, "Integrated nanoparticle-biomolecule hybrid systems: synthesis, properties, and applications," *Angewandte Chemie*, vol. 43, no. 45, pp. 6042–6108, 2004.

[26] G. M. Whitesides, "The "right" size in nanobiotechnology," *Nature Biotechnology*, vol. 21, no. 10, pp. 1161–1165, 2003.

[27] J. Wilcoxon, "Optical absorption properties of dispersed gold and silver alloy nanoparticles," *Journal of Physical Chemistry B*, vol. 113, no. 9, pp. 2647–2656, 2009.

[28] P. N. Njoki, I. I. S. Lim, D. Mott et al., "Size correlation of optical and spectroscopic properties for gold nanoparticles," *Journal of Physical Chemistry C*, vol. 111, no. 40, pp. 14664–14669, 2007.

[29] I. O. Sosa, C. Noguez, and R. G. Barrera, "Optical properties of metal nanoparticles with arbitrary shapes," *Journal of Physical Chemistry B*, vol. 107, no. 26, pp. 6269–6275, 2003.

[30] S. Link, M. B. Mohamed, and M. A. El-Sayed, "Simulation of the optical absorption spectra of gold nanorods as a function of their aspect ratio and the effect of the medium dielectric constant," *Journal of Physical Chemistry B*, vol. 103, no. 16, pp. 3073–3077, 1999.

[31] S. Link and M. A. El-Sayed, "Simulation of the optical absorption spectra of gold nanorods as a function of their aspect ratio and the effect of the medium dielectric constant," *Journal of Physical Chemistry B*, vol. 109, no. 20, pp. 10531–10532, 2005.

[32] M. Losurdo, M. M. Giangregorio, G. V. Bianco et al., "Size dependence of the dielectric function of silicon-supported plasmonic gold nanoparticles," *Physical Review B*, vol. 82, no. 15, Article ID 155451, 25 pages, 2010.

[33] P. K. Jain, K. S. Lee, I. H. El-Sayed, and M. A. El-Sayed, "Calculated absorption and scattering properties of gold nanoparticles of different size, shape, and composition: applications in biological imaging and biomedicine," *Journal of Physical Chemistry B*, vol. 110, no. 14, pp. 7238–7248, 2006.

[34] K. S. Lee and M. A. El-Sayed, "Dependence of the enhanced optical scattering efficiency relative to that of absorption for gold metal nanorods on aspect ratio, size, end-cap shape, and medium refractive index," *Journal of Physical Chemistry B*, vol. 109, no. 43, pp. 20331–20338, 2005.

[35] C. Sonnichsen, B. M. Reinhard, J. Liphardt, and A. P. Alivisatos, "A molecular ruler based on plasmon coupling of single gold and silver nanoparticles," *Nature Biotechnology*, vol. 23, no. 6, pp. 741–745, 2005.

[36] J. Perez-Juste, I. Pastoriza-Santos, L. M. Liz-Marzan, and P. Mulvaney, "Gold nanorods: synthesis, characterization and applications," *Coordination Chemistry Reviews*, vol. 249, no. 17-18, pp. 1870–1901, 2005.

[37] K. Kneipp, H. Kneipp, and J. Kneipp, "Surface-enhanced raman scattering in local optical fields of silver and gold nanoaggregates—from single-molecule raman spectroscopy to ultrasensitive probing in live cells," *Accounts of Chemical Research*, vol. 39, no. 7, pp. 443–450, 2006.

[38] C. Zhang, Z. Zhang, B. Yu, J. Shi, and X. Zhang, "Application of the biological conjugate between antibody and colloid Au nanoparticles as analyte to inductively coupled plasma mass spectrometry," *Analytical Chemistry*, vol. 74, no. 1, pp. 96–99, 2002.

[39] X. Li, L. Jiang, Q. Zhan, J. Qian, and S. He, "Localized surface plasmon resonance (LSPR) of polyelectrolyte-functionalized gold-nanoparticles for bio-sensing," *Colloids and Surfaces A*, vol. 332, no. 2-3, pp. 172–179, 2009.

[40] W. P. Hall, S. N. Ngatia, and R. P. VanDuyne, "LSPR biosensor signal enhancement using nanoparticle-antibody conjugates," *Journal of Physical Chemistry C*, vol. 115, no. 5, pp. 1410–1414, 2011.

[41] P. Englebienne, *Immune and Receptor Assays in Theory and Practice*, CRC Press, Boca Raton, Fla, USA, 2000.

[42] S. Nishimura, T. Yoshidome, W. Kyuutoku, M. Mitsushio, and M. Higo, "Characteristics of a surface plasmon resonance sensor combined with a poly(vinyl chloride) film-based ionophore technique for metal ion analyses," *Analytical Sciences*, vol. 18, no. 3, pp. 267–271, 2002.

[43] A. Kugimiya and T. Takeuchi, "Surface plasmon resonance sensor using molecularly imprinted polymer for detection of sialic acid," *Biosensors & Bioelectronics*, vol. 16, no. 9–12, pp. 1059–1062, 2001.

[44] L. Tong, Q. Wei, A. Wei, and J. X. Cheng, "Gold nanorods as contrast agents for biological imaging: optical properties, surface conjugation and photothermal effects," *Photochemistry and Photobiology*, vol. 85, no. 1, pp. 21–32, 2009.

[45] P. Englebienne, A. Van Hoonacker, and M. Verhas, "Surface plasmon resonance: principles, methods and applications in biomedical sciences," *Spectroscopy*, vol. 17, no. 2-3, pp. 255–273, 2003.

[46] J. Matsui, K. Akamatsu, N. Hara et al., "SPR sensor chip for detection of small molecules using molecularly imprinted polymer with embedded gold nanoparticles," *Analytical Chemistry*, vol. 77, no. 13, pp. 4282–4285, 2005.

[47] A. J. Thiel, A. G. Frutos, and C. E. Jordan, "In situ surface plasmon resonance imaging detection of DNA hybridization to oligonucleotide arrays on gold surfaces," *Analytical Chemistry*, vol. 69, no. 24, pp. 4948–4956, 1997.

[48] L. K. Wolf, Y. Gao, and R. M. Georgiadis, "Kinetic discrimination of sequence-specific DNA-drug binding measured by surface plasmon resonance imaging and comparison to solution-phase measurements," *Journal of the American Chemical Society*, vol. 129, no. 34, pp. 10503–10511, 2007.

[49] C. E. Jordan, A. G. Frutos, A. J. Thiel, and R. M. Corn, "Surface plasmon resonance imaging measurements of DNA hybridization adsorption and streptavidin/DNA multilayer formation at chemically modified gold surfaces," *Analytical Chemistry*, vol. 69, no. 24, pp. 4939–4947, 1997.

[50] B. P. Nelson, T. E. Grimsrud, M. R. Liles, R. M. Goodman, and R. M. Corn, "Surface plasmon resonance imaging measurements of DNA and RNA hybridization adsorption onto DNA microarrays," *Analytical Chemistry*, vol. 73, no. 1, pp. 1–7, 2001.

[51] Y. Iwasaki, T. Horiuchi, and O. Niwa, "Detection of electrochemical enzymatic reactions by surface plasmon resonance measurement," *Analytical Chemistry*, vol. 73, no. 7, pp. 1595–1598, 2001.

[52] K. Matsumoto, A. Torimaru, S. Ishitobi et al., "Preparation and characterization of a polyclonal antibody from rabbit for detection of trinitrotoluene by a surface plasmon resonance biosensor," *Talanta*, vol. 68, no. 2, pp. 305–311, 2005.

[53] M. B. Medina, "Hygromycin B antibody production and characterization by a surface plasmon resonance biosensor," *Journal of Agricultural and Food Chemistry*, vol. 45, no. 2, pp. 389–394, 1997.

[54] C. S. Bich, M. Scott, A. Panagiotidis, R. J. Wenzel, A. Nazabal, and R. Zenobi, "Characterization of antibody-antigen interactions: comparison between surface plasmon resonance measurements and high-mass matrix-assisted laser desorption/ionization mass spectrometry," *Analytical Biochemistry*, vol. 375, no. 1, pp. 35–45, 2008.

[55] E. Kaganer, R. Pogreb, D. Davidov, and I. Willner, "Surface plasmon resonance characterization of photoswitchable antigen-antibody interactions," *Langmuir*, vol. 15, no. 11, pp. 3920–3923, 1999.

[56] G. J. Wegner, H. J. Lee, and R. M. Corn, "Characterization and optimization of peptide arrays for the study of epitope-antibody interactions using surface plasmon resonance imaging," *Analytical Chemistry*, vol. 74, no. 20, pp. 5161–5168, 2002.

[57] H. X. Chen, J. Huang, J. Lee, S. Hwang, and K. Koh, "Surface plasmon resonance spectroscopic characterization of antibody orientation and activity on the calixarene monolayer," *Sensors and Actuators B*, vol. 147, no. 2, pp. 548–553, 2010.

[58] B. Johne, "Epitope mapping by surface plasmon resonance in the BIAcore," *Molecular Biotechnology*, vol. 9, no. 1, pp. 65–71, 1998.

[59] V. Towne, Y. Wang, C. B. Oswald et al., "Epitope characterization of human papillomavirus type 16 virus-like particle through pair-wise antibody footprinting using surface plasmon resonance based biosensor technology," *Abstracts of Papers of the American Chemical Society*, vol. 228, pp. U201–U202, 2004.

[60] S. Chah, M. R. Hammond, and R. N. Zare, "Gold nanoparticles as a colorimetric sensor for protein conformational changes," *Chemistry and Biology*, vol. 12, no. 3, pp. 323–328, 2005.

[61] H. Z. Huang, P. Ran, and Z. Liu, "Signal enhancement of surface plasmon resonance-based immunoassays for the allergen detection," *Sensors and Actuators B*, vol. 131, no. 2, pp. 417–423, 2008.

[62] D. R. Shankaran and N. Miura, "Trends in interfacial design for surface plasmon resonance based immunoassays," *Journal of Physics D*, vol. 40, no. 23, pp. 7187–7200, 2007.

[63] W. M. Mullett, E. P. C. Lai, and J. M. Yeung, "Surface plasmon resonance-based immunoassays," *Methods*, vol. 22, no. 1, pp. 77–91, 2000.

[64] E. Boisselier and D. Astruc, "Gold nanoparticles in nanomedicine: preparations, imaging, diagnostics, therapies and toxicity," *Chemical Society Reviews*, vol. 38, no. 6, pp. 1759–1782, 2009.

[65] D. X. Cui and D. P. Yang, "Advances and prospects of gold nanorods," *Chemistry*, vol. 3, no. 12, pp. 2010–2022, 2008.

[66] S. Lal, S. E. Clare, and N. J. Halas, "Nanoshell-enabled photothermal cancer therapy: impending clinical impact," *Accounts of Chemical Research*, vol. 41, no. 12, pp. 1842–1851, 2008.

[67] A. Ben-Yakar, N. J. Durr, T. Larson, D. K. Smith, B. A. Korgel, and K. Sokolov, "Two-photon luminescence imaging of cancer cells using molecularly targeted gold nanorods," *Nano Letters*, vol. 7, no. 4, pp. 941–945, 2007.

[68] M. Hu, J. Chen, Z. Y. Li et al., "Gold nanostructures: engineering their plasmonic properties for biomedical applications," *Chemical Society Reviews*, vol. 35, no. 11, pp. 1084–1094, 2006.

[69] X. Wang, X. Qian, J. J. Beitler et al., "Detection of circulating tumor cells in human peripheral blood using surface-enhanced raman scattering nanoparticles," *Cancer Research*, vol. 71, no. 5, pp. 1526–1532, 2011.

[70] F. He, Q. Shen, H. Jiang et al., "Rapid identification and high sensitive detection of cancer cells on the gold nanoparticle interface by combined contact angle and electrochemical measurements," *Talanta*, vol. 77, no. 3, pp. 1009–1014, 2009.

[71] G. Peng, U. Tisch, O. Adams et al., "Diagnosing lung cancer in exhaled breath using gold nanoparticles," *Nature Nanotechnology*, vol. 4, no. 10, pp. 669–673, 2009.

[72] K. B. Lee, E. Y. Kim, C. A. Mirkin, and S. M. Wolinsky, "The use of nanoarrays for highly sensitive and selective detection of human immunodeficiency virus type 1 in plasma," *Nano Letters*, vol. 4, no. 10, pp. 1869–1872, 2004.

[73] E. A. Wallnofer, G. C. Thurner, A. A. Abdelmoez et al., "MRI molecular imaging with nanoparticles: a technical platform for early diagnosis of cancer," *International Journal of Clinical Pharmacology and Therapeutics*, vol. 49, no. 1, pp. 73–74, 2011.

[74] M. A. Hahn, A. K. Singh, P. Sharma, S. C. Brown, and B. M. Moudgil, "Nanoparticles as contrast agents for in-vivo bioimaging: current status and future perspectives," *Analytical and Bioanalytical Chemistry*, vol. 399, no. 1, pp. 3–27, 2011.

[75] L. Moriggi, C. Cannizzo, E. Dumas, C. R. Mayer, A. Ulianov, and L. Helm, "Gold nanoparticles functionalized with gadolinium chelates as high-relaxivity MRI contrast agents," *Journal of the American Chemical Society*, vol. 131, no. 31, pp. 10828–10829, 2009.

[76] C. Alric, R. Serduc, C. Mandon et al., "Gold nanoparticles designed for combining dual modality imaging and radiotherapy," *Gold Bulletin*, vol. 41, no. 2, pp. 90–97, 2008.

[77] S. J. Cho, B. R. Jarrett, A. Y. Louie, and S. M. Kauzlarich, "Gold-coated iron nanoparticles: a novel magnetic resonance agent for T 1 and T2 weighted imaging," *Nanotechnology*, vol. 17, no. 3, pp. 640–644, 2006.

[78] M. Rahman, M. Abd-El-Barr, V. MacK et al., "Optical imaging of cervical pre-cancers with structured illumination: an integrated approach," *Gynecologic Oncology*, vol. 99, no. 3, supplement 1, pp. S112–S115, 2005.

[79] M. Eghtedari, A. V. Liopo, J. A. Copland, A. A. Oraevsky, and M. Motamed, "Engineering of hetero-functional gold nanorods for the in vivo molecular targeting of breast cancer cells," *Nano Letters*, vol. 9, no. 1, pp. 287–291, 2009.

[80] J. C. Y. Kah, K. W. Kho, C. G. Lee et al., "Early diagnosis of oral cancer based on the surface plasmon resonance of gold nanoparticles," *International Journal of Nanomedicine*, vol. 2, no. 4, pp. 785–798, 2007.

[81] X. M. Qian, X. H. Peng, D. O. Ansari et al., "In vivo tumor targeting and spectroscopic detection with surface-enhanced Raman nanoparticle tags," *Nature Biotechnology*, vol. 26, no. 1, pp. 83–90, 2008.

[82] X. H. Huang, I. H. El-Sayed, W. Qian, and M. A. El-Sayed, "Cancer cells assemble and align gold nanorods conjugated to antibodies to produce highly enhanced, sharp, and polarized surface Raman spectra: a potential cancer diagnostic marker," *Nano Letters*, vol. 7, no. 6, pp. 1591–1597, 2007.

[83] A. Agarwal, S. W. Huang, M. O'Donnell et al., "Targeted gold nanorod contrast agent for prostate cancer detection by photoacoustic imaging," *Journal of Applied Physics*, vol. 102, no. 6, pp. 064701–064704, 2007.

[84] W. Eck, G. Craig, A. Sigdel et al., "PEGylated gold nanoparticles conjugated to monoclonal F19 antibodies as targeted labeling agents for human pancreatic carcinoma tissue," *ACS Nano*, vol. 2, no. 11, pp. 2263–2272, 2008.

[85] C. D. Medley, J. E. Smith, Z. Tang, Y. Wu, S. Bamrungsap, and W. Tan, "Gold nanoparticle-based colorimetric assay for the direct detection of cancerous cells," *Analytical Chemistry*, vol. 80, no. 4, pp. 1067–1072, 2008.

[86] W. T Lu, S. R. Arumugam, D. Senapati et al., "Multifunctional oval-shaped gold-nanoparticle-based selective detection of breast cancer cells using simple colorimetric and highly sensitive two-photon scattering assay," *ACS Nano*, vol. 4, no. 3, pp. 1739–1749, 2010.

[87] J. A. Viator, S. Gupta, B. S. Goldschmidt et al., "Gold nanoparticle mediated detection of prostate cancer cells using photoacoustic flowmetry with optical reflectance," *Journal of Biomedical Nanotechnology*, vol. 6, no. 2, pp. 187–191, 2010.

[88] A. Ambrosi, F. Airo, and A. Merkoci, "Enhanced gold nanoparticle based ELISA for a breast cancer biomarker," *Analytical Chemistry*, vol. 82, no. 3, pp. 1151–1156, 2010.

[89] J. H. Kang, Y. Asami, M. Murata et al., "Gold nanoparticle-based colorimetric assay for cancer diagnosis," *Biosensors and Bioelectronics*, vol. 25, no. 8, pp. 1869–1874, 2010.

[90] F. Zhou, L. Yuan, H. Wang, D. Li, and H. Chen, "Gold nanoparticle layer: a promising platform for ultra-sensitive cancer detection," *Langmuir*, vol. 27, no. 6, pp. 2155–2158, 2011.

[91] H. Chon, S. Lee, S. W. Son, C. H. Oh, and J. Choo, "Highly sensitive immunoassay of lung cancer marker carcinoembryonic antigen using surface-enhanced raman scattering of hollow gold nanospheres," *Analytical Chemistry*, vol. 81, no. 8, pp. 3029–3034, 2009.

[92] I. H. El-Sayed, X. Huang, and M. A. El-Sayed, "Surface plasmon resonance scattering and absorption of anti-EGFR antibody conjugated gold nanoparticles in cancer diagnostics: applications in oral cancer," *Nano Letters*, vol. 5, no. 5, pp. 829–834, 2005.

[93] X. G. Shi, S. Wang, S. Meshinchi et al., "Dendrimer-entrapped gold nanoparticles as a platform for cancer-cell targeting and imaging," *Small*, vol. 3, no. 7, pp. 1245–1252, 2007.

[94] I. C. Sun, D.-K. Eun, J. H. Na et al., "Heparin-coated gold nanoparticles for liver-specific CT imaging," *Chemistry*, vol. 15, no. 48, pp. 13341–13347, 2009.

[95] C. Alric, J. Taleb, G. Le Duc et al., "Gadolinium chelate coated gold nanoparticles as contrast agents for both X-ray computed tomography and magnetic resonance imaging," *Journal of the American Chemical Society*, vol. 130, no. 18, pp. 5908–5915, 2008.

[96] M. Kumagai, T. K. Sarmat, H. Cabral et al., "Enhanced in vivo magnetic resonance imaging of tumors by PEGylated iron-oxide-gold core-shell nanoparticles with prolonged blood circulation properties," *Macromolecular Rapid Communications*, vol. 31, no. 17, pp. 1521–1528, 2010.

[97] Nasiruzzaman Sk Md, H. K. Kim, J. A. Park, Y. Chang, and T. J. Kim, "Gold nanoparticles coated with Gd-chelate as a potential CT/MRI bimodal contrast agent," *Bulletin of the Korean Chemical Society*, vol. 31, no. 5, pp. 1177–1181, 2010.

[98] H. He, C. Xie, and J. Ren, "Nonbleaching fluorescence of gold nanoparticles and its applications in cancer cell imaging," *Analytical Chemistry*, vol. 80, no. 15, pp. 5951–5957, 2008.

[99] H. Lee, K. Lee, I. K. Kim, and T. G. Park, "Fluorescent gold nanoprobe sensitive to intracellular reactive oxygen species," *Advanced Functional Materials*, vol. 19, no. 12, pp. 1884–1890, 2009.

[100] A. M. Coto-Garcia, E. Sotelo-Gonzalez, M. T. Fernandez-Arguelles, R. Pereiro, J. M. Costa-Fernandez, and A. Sanz-Medel, "Nanoparticles as fluorescent labels for optical imaging and sensing in genomics and proteomics," *Analytical and Bioanalytical Chemistry*, vol. 399, no. 1, pp. 29–42, 2011.

[101] P. C. Ray, G. K. Darbha, A. Ray, J. Walker, and W. Hardy, "Gold nanoparticle based FRET for DNA detection," *Plasmonics*, vol. 2, no. 4, pp. 173–183, 2007.

[102] S. Lee, E. J. Cha, K. Park et al., "A near-infrared-fluorescence-quenched gold-nanoparticle imaging probe for in vivo drug screening and protease activity determination," *Angewandte Chemie*, vol. 47, no. 15, pp. 2804–2807, 2008.

[103] C. C. You, O. R. Miranda, B. Gider et al., "Detection and identification of proteins using nanoparticle-fluorescent polymer "chemical nose" sensors," *Nature Nanotechnology*, vol. 2, no. 5, pp. 318–323, 2007.

[104] S. Mayilo, M. A. Kloster, M. Wunderlich et al., "Long-range fluorescence quenching by gold nanoparticles in a sandwich immunoassay for cardiac troponin T," *Nano Letters*, vol. 9, no. 12, pp. 4558–4563, 2009.

[105] American Cancer Socity of research, "Cancer fact and figure," Health Policy, 2010, http://www.cancer.org/acs/groups/content/@nho/documents/document/acspc-024113.pdf.

[106] Y. E. Choi, J. W. Kwak, and J. W. Park, "Nanotechnology for early cancer detection," *Sensors*, vol. 10, no. 1, pp. 428–455, 2010.

[107] L. F. Cheow, S. H. Ko, S. J. Kim, K. H. Kang, and J. Han, "Increasing the sensitivity of enzyme-linked immunosorbent assay using multiplexed electrokinetic concentrator," *Analytical Chemistry*, vol. 82, no. 8, pp. 3383–3388, 2010.

[108] Y. Pellequer and A. Lamprecht, "Nanoscale cancer therapeutics," in *Nanotherapeutics: Drug Delivery Concepts in Nanoscience*, A. Lamprecht, Ed., pp. 93–124, Pan Stanford, Chicago, Ill, USA, 2009.

[109] Z. Fang, L. Soleymani, G. Pampalakis et al., "Direct profiling of cancer biomarkers in tumor tissue using a multiplexed nanostructured microelectrode integrated circuit," *ACS Nano*, vol. 3, no. 10, pp. 3207–3213, 2009.

[110] W. Yang, M. Yu, X. Sun, and A. T. Woolley, "Microdevices integrating affinity columns and capillary electrophoresis for multibiomarker analysis in human serum," *Lab on a Chip*, vol. 10, no. 19, pp. 2527–2533, 2010.

[111] P. Baptista, E. Pereira, P. Eaton et al., "Gold nanoparticles for the development of clinical diagnosis methods," *Analytical and Bioanalytical Chemistry*, vol. 391, no. 3, pp. 943–950, 2008.

[112] W. Zhao, M. A. Brook, and Y. Li, "Design of gold nanoparticle-based colorimetric biosensing assays," *ChemBioChem*, vol. 9, no. 15, pp. 2363–2371, 2008.

[113] X. Huang, P. K. Jain, I. H. El-Sayed, and M. A. El-Sayed, "Gold nanoparticles: interesting optical properties and recent applications in cancer diagnostics and therapy," *Nanomedicine*, vol. 2, no. 5, pp. 681–693, 2007.

[114] A. W. H. Lin, N. A. Lewinski, J. L. West, N. J. Halas, and R. A. Drezek, "Optically tunable nanoparticle contrast agents for early cancer detection: model-based analysis of gold nanoshells," *Journal of Biomedical Optics*, vol. 10, no. 6, 2005.

[115] K. Lee, V. P. Drachev, and J. Irudayaraj, "DNA-gold nanoparticle reversible networks grown on cell surface marker sites: Application in diagnostics," *ACS Nano*, vol. 5, no. 3, pp. 2109–2117, 2011.

[116] S. X. Tang and I. Hewlett, "Nanoparticle-based immunoassays for sensitive and early detection of HIV-1 capsid (p24) antigen," *The Journal of Infectious Diseases*, vol. 201, supplement 1, pp. S59–S64, 2010.

[117] J. F. Tang, L. Zhou, W. Gao, X. Cao, and Y. Wang, "Visual DNA microarrays for simultaneous detection of human immunodeficiency virus type-1 and Treponema pallidum coupled with multiplex asymmetric polymerase chain reaction," *Diagnostic Microbiology and Infectious Disease*, vol. 65, no. 4, pp. 372–378, 2009.

[118] M.-C. Bowman, T. E. Ballard, C. J. Ackerson, D. L. Feldheim, D. M. Margolis, and C. Melander, "Inhibition of HIV fusion with multivalent gold nanoparticles," *Journal of the American Chemical Society*, vol. 130, no. 22, pp. 6896–6897, 2008.

[119] P. Di Gianvincenzo, M. Marradi, O. M. Martinez-Avila, L. M. Bedoya, J. Alcami, and S. Penades, "Gold nanoparticles capped with sulfate-ended ligands as anti-HIV agents," *Bioorganic and Medicinal Chemistry Letters*, vol. 20, no. 9, pp. 2718–2721, 2010.

[120] K. A. Mahmoud, S. Hrapovic, and J. H. T. Luong, "Picomolar detection of protease using peptide/single walled carbon nanotube/gold nanoparticle-modified electrode," *ACS Nano*, vol. 2, no. 5, pp. 1051–1057, 2008.

[121] K. A. Mahmoud and J. H. T. Luong, "Impedance method for detecting HIV-1 protease and screening for its inhibitors using ferrocene-peptide conjugate/Au nanoparticle/single-walled carbon nanotube modified electrode," *Analytical Chemistry*, vol. 80, no. 18, pp. 7056–7062, 2008.

[122] G. K. Darbha, U. S. Rai, A. K. Singh, and P. C. Ray, "Gold-nanorod-based sensing of sequence specific HIV-1 virus DNA by using hyper-rayleigh scattering spectroscopy," *Chemistry*, vol. 14, no. 13, pp. 3896–3903, 2008.

[123] S. B. Lee, "Focus on nanoparticles for cancer diagnosis and therapeutics," *Nanomedicine*, vol. 2, no. 5, pp. 647–648, 2007.

[124] M. Y. Sha, H. Xu, S. G. Penn, and R. Cromer, "SERS nanoparticles: a new optical detection modality for cancer diagnosis," *Nanomedicine*, vol. 2, no. 5, pp. 725–734, 2007.

[125] S. Spisak and A. Guttman, "Biomedical applications of protein microarrays," *Current Medicinal Chemistry*, vol. 16, no. 22, pp. 2806–2815, 2009.

Research Article

Cytotoxicity Property of Nano-TiO$_2$ Sol and Nano-TiO$_2$ Powder

Pingting He, Jie Tao, Jianjun Xue, and Yulan Chen

College of Materials Science and Technology, Nanjing University of Aeronautics and Astronautics, Nanjing 210016, China

Correspondence should be addressed to Jie Tao, taojie@nuaa.edu.cn

A homogeneous and transparent titania (TiO$_2$) sol with nanosized anatase TiO$_2$ particles was prepared by hydrothermal synthesis method. The transmission electron microscope and X-ray diffraction were used to characterize the structure and morphology of particulates in the TiO$_2$ sol and purchased TiO$_2$ powder. The results show that the homogeneous anatase crystalline phase was formed and the size of the spindle-like particle in sol was about 20 nm in width and 150 nm in average length, and the particulates of the purchased powder were globular-like about 50 nm in diameter. In addition, a consistent set of in vitro experimental protocols was used to study the effects of nano-TiO$_2$ sol as prepared and nano-TiO$_2$ powder on mouse peritoneal macrophage. The cytotoxicity tests in vitro indicate that, with the increasing of TiO$_2$ sol concentration contaminated with the cells, the relative proliferation rate of macrophage cells was improved slightly after the cells contaminated for 24 h, but it reduced rapidly after contaminated for 48 h. The purchased nano-TiO$_2$ powder inhibited the growth of the cells obviously as cultivating with macrophage both for 24 h and 48 h.

1. Introduction

Manufactured nanoparticles (NPs) of titanium dioxide (TiO$_2$) have been widely used in many fields in the recent years [1–5]. During the production and application, nanoparticles will be contacted with organism inevitably. Thus, their potential toxicity gets more and more attention for human health.

Some research has shown that nanomaterials might have negative effects on the health of the organisms [6]. Mauderly et al. [7] observed pulmonary tumors in rats exposed to 2.5 mg/m^3 carbon black or 6.5 mg/m^3 burning products of diesel. Shvedova et al. [8] found free radicals, the accumulation of peroxide and reduction of antioxidant, and, hence, decreased cell activity and changed in the cell morphology and ultrastructure after exposure of Haca T in single-walled carbon nanotubes for 18 h. Oberdörster et al. [9] exposed rats to an environment containing 20 nm nanoparticles of polytetrafluoroethylene for 15 min and found that most of the rats died after 4 h of exposure in the air. Nevertheless, after exposure to an environment containing 130 nm of polytetrafluoroethylene particles, as the control group, were not affected. Therefore, it is essential to examine the biosafety of nanosized TiO$_2$ for the *in vivo* applications. However, data

from several research groups indicated that TiO$_2$ NPs had distinct risks to human health compared with their normal size counterparts [10–12]. TiO$_2$ NP toxicity has been studied with respect to reactive oxygen species (ROS) production and oxidative stress in mammalian studies [13, 14]. TiO$_2$ NPs induced oxidative damage to human bronchial epithelial cells [15] and to brain microglia [16]. However, some ecological studies showed that TiO$_2$ NP exposure in aquatic species caused oxidative damage-mediated effects [17–19]. Palomäki [20] explored immunological effects of five different nanomaterials on antigen presenting cells (APC) *in vitro*. TiO$_2$ and TiO$_2$-silica-induced dose-dependent cell death also in macrophages. Due to diverse effects on different nanomaterials on immune cells, it was suggested that each kind of new nanomaterial should be extensively studied *in vitro* and *in vivo* for risk assessment before they are used in final products.

In addition, with the rapid development of nanotechnology and the special properties of nanosized TiO$_2$, the application fields of nanomaterials are broadening remarkably in some cases. There are many ways to prepare nanotitania, such as sol-gel method, chemical precipitation process, hydrothermal synthesis, and magnetron sputtering technique. The advantages of sol-gel method include simplicity,

high-purity product and small particle size. However, it is very difficult to control the agglomeration of nanosized particles, resulting in the poor performance in final application. Therefore, it is of great significance to solve these problems.

In this study, a highly dispersed nanosized titania particle sol was prepared by conventional low-temperature synthesis method. The resulting sol is homogeneous, and the spindle-like particles are highly dispersed in the whole aqueous system. A consistent set of *in vitro* experimental protocols was used to study the effects of nano-TiO_2 sol as prepared and nano-TiO_2 powder on mouse peritoneal macrophage. The objective was to explore the relationship between the comparable properties with the viability response of macrophage treated *in vitro* with nano-TiO_2 colloid particles and nano-TiO_2 powder, to identify whether particle properties will impact cytotoxicity through altering intracellular oxidative conditions, and to compare the cytotoxicity degree induced by two typical different nano-TiO_2 particles at low treatment concentrations. Accordingly, cytotoxicity was sufficiently measured by the forms as follows. The relative proliferation rate, the cell morphology, the malondialdehyde (MDA), the lactate dehydrogenase (LDH), and the intracellular levels of glutathione (GSH) were determined, respectively.

2. Material and Methods

2.1. Preparation of Titania Sol. 1.1 mL of titanium chloride was added to 10 mL distilled water with ice bath. Aqueous ammonia (10%, in mass, the same below) was dropped into the solution with continual stirring (600 r/min) to form white $Ti(OH)_4$ precipitate until the pH value reached 9.0 [21]. After further stirring for another 0.5 h, the precipitates were washed with distilled water and centrifugally filtered for 5 min (4000 r/min). This cleaning process was repeated four times to remove the NH_4^+ and SO_4^{2-} byproducts formed in the reaction. Subsequently, 10 mL (30%) aqueous hydrogen peroxide were poured into the precipitates under constant stirring (400 rpm) to dissolve and disperse the products homogeneously, then the obtained solution was diluted with distilled water until the total volume reached 100 mL. The light yellow solution was added into a reactor and incubated at 120°C for 24 h. Finally, a transparent, homogeneous and light blue colloid as shown in Figure 1 was obtained.

2.2. Characterization of Nano-TiO_2. The dried-crystal powder from titania sol (NP1) and the nano-TiO_2 power (NP2) purchased from Huzheng Nano Technology was analyzed by X-ray powder diffraction (XRD) pattern obtained from D8-Advance X-ray diffractometer with CuKa radiation (λ = 0.15418 nm) with voltage of 40 kV and current of 30 mA in the region h = 10–90° with a step size of 0.04°.

The FT-IR spectra of the NP1 and NP2 were collected by Nexus 670 FT-IR spectrometry from the manufacturer of Thermo Nicolet Company and samples were dispersed in pressed KBr disks.

The TEM characterization of the NP1 and NP2 were carried out on an FEI-Techai 1200 instrument with 200 kV accelerating voltage.

Figure 1: Optical photographs of the sol.

2.3. In Vitro Culture Cell. Macrophage was collected from normal mouse and washed three times with phosphate-buffered solution (PBS) and modulated cell concentration to 1×10^6 cells·mL^{-1} with RPMI-1640 medium containing 10 units/mL penicillin, 10 units/mL streptomycin, and 10% fetal bovine serum (FBS) [22]. The collected cells in this manner were viable at least 95% by trypan blue dye exclusion test. The cells were seeded in a 96-well plate directly at a density of 2.0×10^4 cells per well in 200 μL culture medium, cultured 4 h later at 37°C under a 5% CO_2 atmosphere and humid chamber till adherent to the surface of the cell culture dish.

2.4. In Vitro Assay for Cytotoxic Activity of Nano-TiO_2

2.4.1. Cell Morphology Characterization. Photographs of the interaction of living cells with different concentrations of NP1 and NP2 for 24 h and 48 h were taken, respectively. The morphological microstructure (100×) was observed using an Olympus IX51 inverted fluorescence microscope.

2.4.2. Cell Viability Assay. After adherent to the surface of the cell culture dish, the supernatant substance were piped out and washed with PBS, and fresh RPMI-1640 medium with nano-TiO_2 NP1 and NP2 diluted to appropriate concentrations (2, 20, 60, and 100 μg·mL^{-1}) with the culture medium freshly was added into every well, respectively, and incubated for 24 h and 48 h separately. The wells in which cells were not treated with nanoparticles served as positive controls and that without cells but nanoparticles as negative controls in each group of experiments.

The cytotoxicity of NP1 and NP2 on macrophage was evaluated by MTT [3-(4,5-dimethylthiazol-2-yl)-2, 5-diphenyltetrazolium bromide] spectrophotometry. 20 μL MTT (5 mg·mL^{-1} in PBS solution) was added to each well treated with NP1 and NP2 and incubated at 37°C for 4 h in incubator thermostat (HEPA-class 100). The medium was
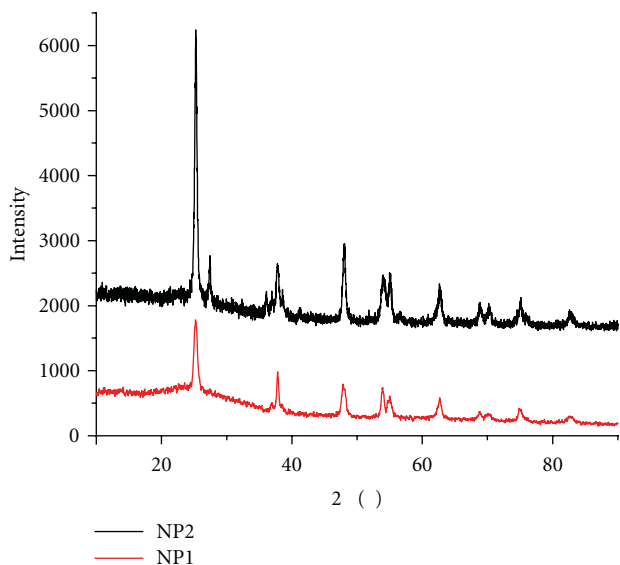
FIGURE 2: XRD pattern of NP1 and NP2.

FIGURE 3: IR spectrum of NP1 and NP2.

then removed from each well, and DMSO (150 μL) was added. The plates were then shaken at Micro Oscillator (Analysis Medical Instrument Factory of Shanghai) and the light absorptions of the formazan (the products of MTT reacted with succinate dehydrogenase and cytochrome C in mitochondria of macrophages) were measured at the wavelength of 490 nm using ELISA detector (BIORAD-Model 680, Japan). The effect of nanoparticles on macrophage proliferation was expressed as the percentage of cell viability compared with the controls or relative proliferation rate (RPR), which is calculated as the following formula:

$$\text{RPR}(\%) = \frac{A - A_N}{A_P - A_N} \times 100\%, \tag{1}$$

where A represents the absorbance of each different concentration group; A_N is the absorbance of negative control group; A_P is the absorbance of positive control group.

2.4.3. Enzymatic Activity Assay. Malondialdehyde (MDA) and glutathione (GSH) reagent kits (purchased from Jiancheng Bioengineering Co. Ltd, Nanjing, China) were employed to indicate the oxidative damage, lactate dehydrogenase (LDH) kit (Jiancheng Bioengineering Co. Ltd, Nanjing, China) to detect the integrity of cell membrane structural caused by nano-TiO₂. Macrophage cells were plated into twenty-four-well plates at a density of 1.0×10^6 cells per well in 2 mL culture medium and cultured 6 h before contaminated. Cells were treated with the nano-TiO₂ NP1 and NP2, respectively, at concentrations of 0, 2, 20, 60, and 100 μg·mL⁻¹ for 24 h and 48 h. Then, collected the macrophage cell supernatant and centrifuged (150× g, 10 min), then MDA, GSH, and LDH were, respectively, measured using the reagent kits according to the manufacturer's instructions, and the optical density (OD) was measured using a UV-visible spectrophotometer (UV-9200); the results
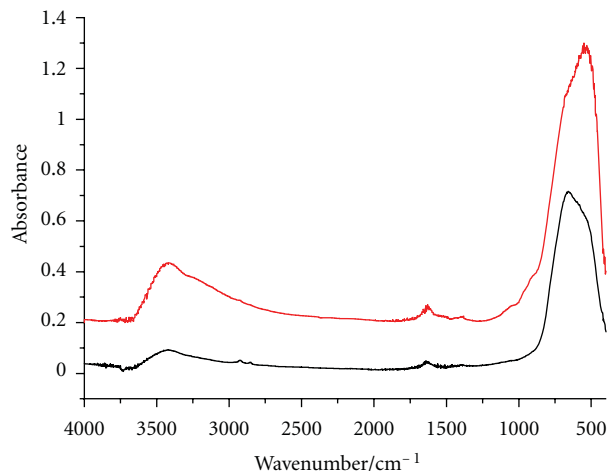
were expressed as percentage viability compared with the untreated controls.

2.5. Statistics Analysis. All experiments were performed in duplicate and repeated at least three times. The statistical significance of the data was expressed as mean ± SD. Statistical differences among groups were determined by one-way analysis of variance with SPSS 13.0.

3. Results and Discussion

3.1. Characterization of Titania Sol. The optical photographs of the sol are shown in Figure 1. The titania sol is light blue and transparent homogeneously. XRD pattern of the as-prepared nanophase TiO₂ sol (NP1) and nano-TiO₂ power (NP2) is shown in Figure 2. All diffraction peaks of NP1 can be assigned to anatase TiO₂, and the diffraction data are in good agreement with the JCPDS card for titania (JCPDS no. 73–1764). The five major peaks locate at about 25.2°, 37.8°, 47.9°, 54.0°, and 62.7° [23]. And most of the diffraction peaks of NP2 were in accordance with anatase TiO₂, but relatively small amounts of diffraction peaks were assigned to rutile.

Figure 3 shows the IR spectrum of the obtained anatase-TiO₂ particles in colloid and purchased nano-TiO₂ powder. In both of the IR spectra, a broad absorption band in the region 3000–3600 cm⁻¹ and the other absorption band in the region 1200–1700 cm⁻¹ are characteristic of the OH stretching vibrations (peak at 3421 cm⁻¹) and bending vibrations (peak at 1636 cm⁻¹) of free and hydrogen-bonded surface hydroxyl groups, respectively, [24, 25]. Molecules of water can strongly or weakly be attached to titania surface forming a number of OH stretching and bending vibrations. The vibration modes of anatase skeletal Ti-O-Ti bonds were observed in the range of 500–800 cm⁻¹ [26]. No other absorption band was observed in the midinfrared range.

Figures 4 and 5 show the TEM photographs of the sol and purchased nano-TiO₂ powder. Apparently, the particulates of the powder were globular-like, about 50 nm in diameter. The
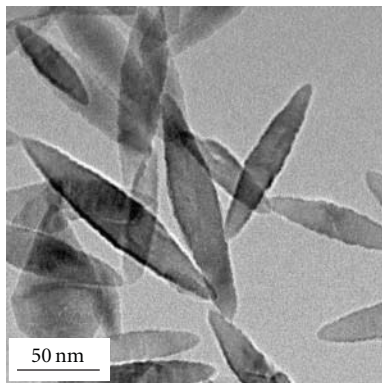
FIGURE 4: TEM photographs of the sol.
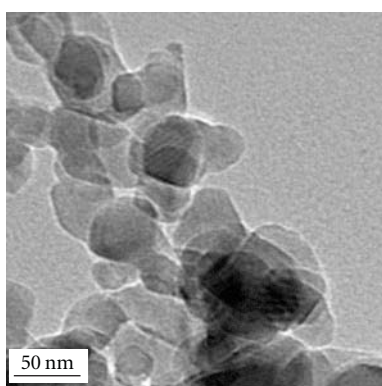
FIGURE 5: TEM photographs of the powder.

particles in the sol were spindle-like, about 20 nm in width and 150 nm in average length, are highly dispersed in the whole aqueous solution. All TiO_2 crystal structures consist of TiO_6^{2-} octahedra, which share edges and corners in different manners that result in forming different crystal phases. Octahedra in anatase share four edges and are arranged in zigzag chains along [221], while rutile octahedra share only two edges and form linear chains parallel to [001] [27]. According to this, the spindle-like particulates are formed in zigzag chains.

3.2. Cytotoxicity Evaluation

3.2.1. Morphologic Changes. Macrophage cells adhered to the plastic surface of the cell culture plate transparently and regularly in spindle shape before added nano-TiO_2 sol (NP1) and nano-TiO_2 powder (NP2) in suspension of PBS (see Figures 6(a) and 6(d), Figures 7(a), and 7(d)). But the particulates in sol were uptaken into the cytoplasm rapidly after added into the medium of macrophage cells for 24 h and 48 h, respectively, (see Figures 6(b) and 6(e)). Then the intracellular aggregated particulates of nano-TiO_2 resided mainly around the nuclear membrane, not in the cytoplasmic region. Some of the particulates of NP2 formed aggregates out of the cell, and some dispersed particulates entered into the cells and resided around the membrane (see

Figures 7(b) and 7(e)). Cell contraction and deformation in variational degree were observed with different concentration of the NP1 and NP2 in the culture medium. It suggested the reduced cell proliferation or cell activity and even cell death after 24 h and 48 h contamination with NP1 and NP2.

3.2.2. Relative Proliferation Rate of Macrophage Cells. The RPR of macrophage cells was used to evaluate the cytotoxicity of nano-TiO_2 sol (NP1) and nano-TiO_2 powder in suspension of PBS (NP2) according to the MTT assay data. The results were given in Table 1. The relative proliferation rate of macrophage cells improved slightly with the increase of concentration of NP1 after contaminated 24 h, but reduced rapidly after contaminated 48 h. It seemed that NP1 had some proliferative effect to macrophage cells in 24 h, but some apparent proliferation inhibition to macrophage cells after contaminated with NP1 in a longer time. And the relative proliferation rate of macrophage cells contaminated with NP2 reduced obviously both in 24 h and 48 h. It suggested that NP2 had apparent and instantaneous proliferation inhibition to macrophage cells.

With the variations of the contacted times and the concentration of NP1 and NP2, the relative proliferation rate of macrophage cells changed. As exogenous substances, nano-TiO_2 particulate in sol could stimulate growth of the macrophage cells during in a short time, thus, shows no apparently toxicity, but when it contacted with nano-TiO_2 sol continuously, most of them were taken up into the cells, even into the nucleus. It may be damaged the membrane or even made oxidative stress and interacted with a number of biological macromolecules, leading to the macrophage death. But in the same way as a foreign substance, the nano-TiO_2 particulate suspended in PBS (NP2) inhibited the growth of the macrophage cells instantly in 24 h and continuously in 48 h. The NP2 without surface treatment was easy to form aggregates outside the cells, which could make cells elicit an immune response and produce a large number of free radicals, leading to the decrease in the cell activity and even to death.

3.2.3. Enzymatic Activity Assay. MDA was an intermediate product of lipid peroxidation, which determined the degree of lipid peroxidation and cell damage indirectly. Normal organism keeps a dynamic balance through its own oxidase system on the free radical oxidation and antioxidant regulation. The lipid peroxidation level increased when the NP1 or NP2 acted with macrophage cells in 24 h and 48 h (see Table 2). But compared with the control group in the 24 h group, MDA content had no significant difference ($P > 0.05$), which suggested that there was no lipid peroxidation during the process of NP1 reacted with the macrophage cells in 24 h. In the 48 h group, MDA content indicated significant difference at 0.05 level or 0.01 level ($P < 0.05$, $P < 0.01$); consequently lipid peroxidation happened. As NP2 acted with macrophage cells, the lipid peroxidation level increased both in the 24 h and 48 h experimental groups. Furthermore, compared with the control groups, MDA content indicated significant difference at 0.05 level or 0.01 level ($P < 0.05$,
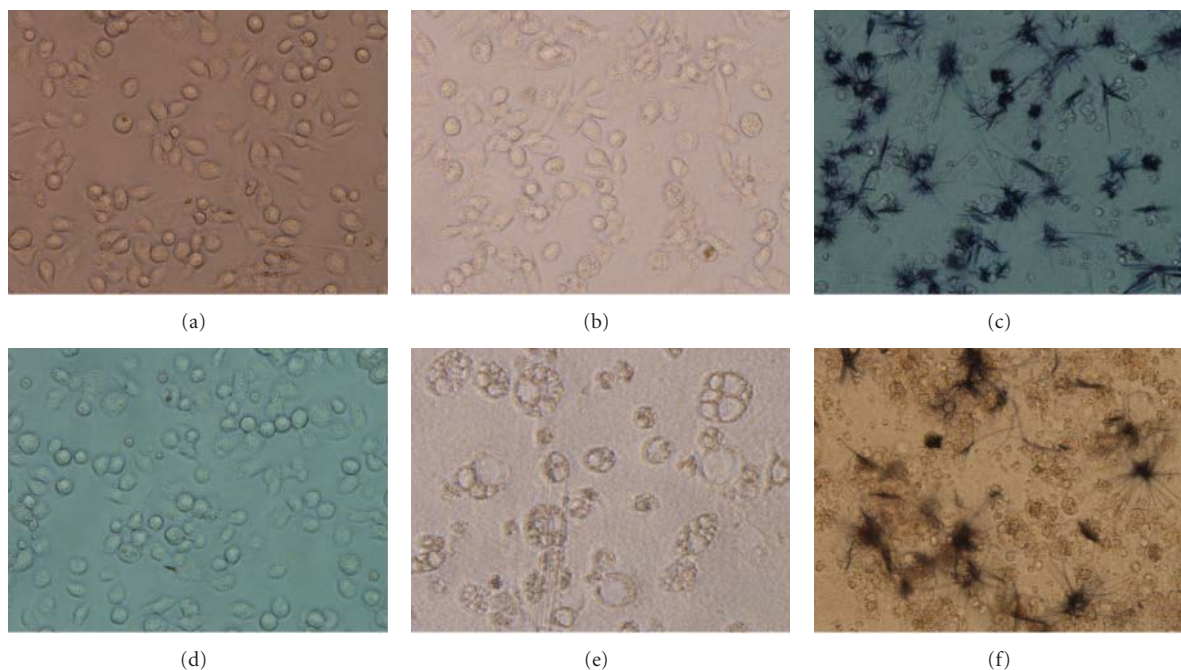
Figure 6: Morphology of macrophages before and after adding nano-TiO$_2$ sol with 24 h (a–c) and 48 h (d–f) (400×) (a, d) without nano-TiO$_2$ sol, (b, e) 60 μg·mL^{-1}, (c, f) 60 μg·mL^{-1} (after 4 hours incubated with MTT).
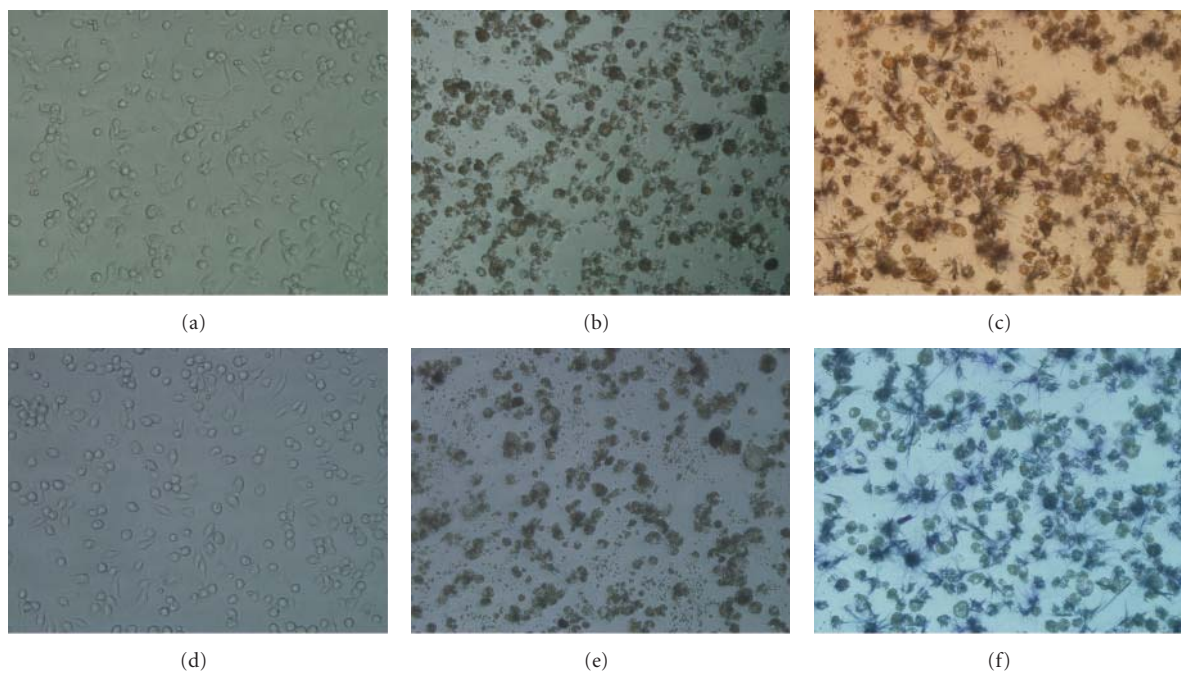
Figure 7: Morphology of macrophages before and after adding nano-TiO$_2$ powder in suspension of PBS with 24 h (a–c) and 48 h (d–f) (400×) (a, d) without nano-TiO$_2$, (b, e) 60 μg·mL^{-1}, (c, f) 60 μg·mL^{-1} (after 4 hours incubated with MTT).

$P < 0.01$). Therefore, NP2 caused the lipid peroxidation and even damaged the cells.

Glutathione (GSH) was an important oxidant in cells, and its primary function was to eliminate radicals. During the reaction, the glutathione might be oxidized to oxidized glutathione; consequently the antioxidant capacity of cells was depressed. This made for the maladjustment of redox reaction and the content of active oxygen increasing and impacted the viability of cells. Almost all GSH levels exhibited some changes after 24 h and 48 h exposure to NP1 or NP2 (see Table 2). Statistically GSH contents have significant difference ($P < 0.05$) and even extremely significant

Table 1: Result of macrophage toxicity by MTT assay.

Concentration of nano-TiO$_2$/mg·L^{-1}		0	2	20	60	100
NP1	Absorbance in 24 h	0.830	0.878	0.930	1.003	1.073
	Viability/%	100	106	112	121	129
NP2	Absorbance in 24 h	0.481	0.246	0.216	0.054	0.073
	Viability/%	100	51	45	11	15
NP1	Absorbance in 48 h	0.690	0.630	0.543	0.418	0.198
	Viability/%	100	91	79	61	29
NP2	Absorbance in 48 h	0.244	0.179	0.115	0.101	0.067
	Viability/%	100	73	47	42	27

Table 2: The content of MDA, LDH, and GSH in different concentrations of nano-TiO$_2$.

Time	TiO$_2$ (μg/mL)		0	2	20	60	100
24 h	NP1	MDA (nmol/mL)	0.40 ± 0.02	0.44 ± 0.05	0.54 ± 0.04	0.74 ± 0.05	1.18 ± 0.08
		LDH (U/L)	1222.22 ± 93.95	1132.62 ± 79.26	681.00 ± 55.95*	741.94 ± 38.77**	358.42 ± 14.12**
		GSH (mg/L)	7.25 ± 0.59	5.08 ± 0.32**	7.15 ± 0.75*	8.46 ± 0.49	10.66 ± 0.16*
	NP2	MDA (nmol/mL)	1.24 ± 0.03	2.11 ± 0.07**	4.26 ± 0.07**	3.27 ± 0.04**	4.33 ± 0.08**
		LDH (U/L)	738.10 ± 62.99	769.84 ± 49.56	1055.56 ± 49.56**	1150.80 ± 13.75**	1325.39 ± 59.92**
		GSH (mg/L)	8.11 ± 0.22	10.97 ± 0.38**	16.45 ± 0.38**	15.50 ± 0.46**	20.25 ± 0.63**
48 h	NP1	MDA (nmol/mL)	0.56 ± 0.04	1.11 ± 0.13	1.41 ± 0.14*	1.57 ± 0.23*	1.97 ± 0.15**
		LDH (U/L)	197.39 ± 15.92	424.58 ± 27.72	581.00 ± 32.21**	849.16 ± 29.56**	1009.31 ± 46.79**
		GSH (mg/L)	27.33 ± 1.09	21.85 ± 0.88	9.95 ± 0.16**	18.87 ± 0.93*	24.58 ± 0.31*
	NP2	MDA (nmol/mL)	0.94 ± 0.14	1.10 ± 0.14	4.06 ± 0.04**	2.13 ± 0.03**	3.11 ± 0.04**
		LDH (U/L)	854.38 ± 8.62	902.69 ± 12.42*	959.28 ± 4.78**	995.17 ± 6.32**	938.58 ± 10.42**
		GSH (mg/L)	6.37 ± 0.33	8.22 ± 0.25**	11.81 ± 0.19**	9.36 ± 0.25**	10.01 ± 0.41**

*$P < 0.05$, **$P < 0.01$ (of control).

difference ($P < 0.01$) compared with the control groups. After contaminated to the NP1 or NP2 for 24 h and 48 h at 2~100 μg·mL^{-1}, the GSH levels fluctuated compared with the control groups, which were not a dose-dependent change. In the final analysis, the GSH levels of the culture supernatant were affected by the quantity of radicals and the damaged degree of membrane. For the penetration of damaged membrane was increased, the intracellular GSH excreted into the extracellular so that the GSH levels of the culture supernatant changed and were not dose dependent markedly.

Lactate dehydrogenase (LDH) was an endoenzyme and could leak to the extracellular space as the membrane was damaged and its penetration was increased. So the Lactate dehydrogenase activity of the macrophage culture supernatant may be reflected the damaged degree of membrane. The NP1 and NP2 induced LDH leakage apparently from macrophage cells treated both for 48 h and 24 h, and LDH levels in cell medium were gradually elevated as particle concentrations increased (see Table 2). Also all of them were statistically significant different except the 2 μg·mL^{-1} groups compared with the control groups. In addition, the LDH levels of the macrophage treated with the NP1 for 24 h were not increased, which suggested that damages on the cellular membrane were not obvious. As the contacted time reached 48 h, the LDH levels were increased. Generally the NP2

damaged the cellular membrane obviously both in 24 h and 48 h.

In summary, in 24 h the NP2 had some inhibition on the growth of macrophage cells, while the NP1 had some stimulation on their proliferation to the macrophages superficially which could be seen as an immunostimulant characteristic actually. Within 48 h, both NP1 and NP2 inhibited the growth of macrophage cells significantly with the different concentrations and had some degree of cytotoxicity. The LDH test results indicated that the membrane of macrophage cells was damaged apparently contacted with the NP1 and NP2 for 48 h, but in 24 h the NP1 damages on the cellular membrane were not obvious while the NP2 damages were apparent. The variation regularity of LDH test results was in accordance with the one of relative proliferation rate of macrophage cells. The MDA and GSH test results suggested that the particulate could get through the membrane of macrophage cells and interact with some substances to damage the membrane, which resulted in oxidative stress, decreasing the activity of cells and even induced death. Overall, the MDA and GSH levels responded to the instant cytotoxicity in cells. And the LDH levels and the relative proliferation rate of cells represented the overall effect and continual cytotoxicity reaction. It suggested that the instant cytotoxicity primarily originated from the cellular internalization of foreign substance rather than physical

damage on the cellular membrane. Thus, with the toxicity of nanomaterials, size, shape, chemical composition, and other factors related to the mechanisms of cell toxicity still need further detailed study and discussion.

In contrast to the growing literatures on application of nanomaterials, the information about biological effects of nano-TiO$_2$ is insufficient, and the publications available on this topic are often controversial. We focused on nano-TiO$_2$ as examples of typical manufactured nanomaterials that are associated with environmental and occupational exposures. In the present study, we examined the effect of nano-TiO$_2$ sol and powder concentrations on macrophage cells. It is reasonable to suggest that, according to our results, more attention should be paid to the biosafety evaluation on the reactive metal oxide nanomaterials. Otherwise, the macrophage cells utilized in our study were primary cultured cells from mouse abdomen and could be genetically identical with normal cells *in vivo* while more sensitive to extraneous stimulating factors than cell lines. Though these qualities can help us achieve more practical results; the conclusions should be further tested *in vivo*.

4. Conclusions

A highly dispersed nanosized anatase TiO$_2$ particle sol was prepared with the conventional low-temperature synthesis method. The sol is transparent and homogeneous. The spindle-like particle size is about 20 nm in width and 150 nm in average length. Moreover, both the particulate in the sol and nano-TiO$_2$ powder purchased have some cytotoxicity to macrophage cell. The relative proliferation rate of macrophage cells improved slightly with the increasing in concentration of TiO$_2$ sol after contaminated 24 h, but the relative proliferation rate of cells reduced rapidly after contaminated with nano-TiO$_2$ sol in 48 h. The purchased nano-TiO$_2$ powder inhibited the growth of the cells obviously as cultivating with macrophage for 24 h and 48 h. The variation regularity of LDH test results was in accordance with the one of relative proliferation rate of macrophage cells. The MDA and GSH levels responded to the instant cytotoxicity in cells *in vitro*. According to our results, it is reasonable to suggest that more attention should be paid to the biosafety evaluation on the reactive metal oxide nanomaterials.

Acknowledgments

References

[1] C. Liu, "Research and development of nanopharmaceuticals in China," *Nano Biomedicine and Engineering*, vol. 1, no. 1, pp. 1–12, 2009.

[2] H. Li, Y. Zhang, and W. Huang, "Photoactivation of ion-exchangeable trititanate nanotubes modified by MS (M = Cd, Zn) nanoparticles," *Nano Biomedicine and Engineering*, vol. 1, no. 1, pp. 32–37, 2009.

[3] H. Yang, Z. Ge, C. Zou, and G. Shen, "Detection of nanobubbles at the TiO$_2$ Coatings—water interface," *Nano Biomedicine and Engineering*, vol. 1, no. 1, pp. 75–79, 2009.

[4] H. Li, Y. Zhang, and W. Huang, "Novel selective sensors based on TiO$_2$ nanotubes supported MS(TiO$_2$@MS, M=Cd, Zn) for their gas sensing properties," *Nano Biomedicine and Engineering*, vol. 2, no. 2, pp. 143–148, 2010.

[5] R. Wu, "Advance and prospect of nanoscale Chinese medicine," *Nano Biomedicine and Engineering*, vol. 2, no. 3, pp. 193–200, 2010.

[6] Y. Li, Z. Li, and X. Zhou, "Detection of nano Eu$_2$O$_3$ in cells and study of its biological effects," *Nano Biomedicine and Engineering*, vol. 2, no. 1, pp. 24–30, 2010.

[7] J. L. Mauderly, M. B. Snipes, E. B. Barr et al., "Pulmonary toxicity of inhaled diesel exhaust and carbon black in chronically exposed rats. Part I: neoplastic and nonneoplastic lung lesions," *Research Report (Health Effects Institute)*, no. 68, part 1, pp. 1–77, 1994.

[8] A. A. Shvedova, V. Castranova, E. R. Kisin et al., "Exposure to carbon nanotube material: assessment of nanotube cytotoxicity using human keratinocyte cells," *Journal of Toxicology and Environmental Health, Part A*, vol. 66, no. 20, pp. 1909–1926, 2003.

[9] G. Oberdörster, J. N. Finkelstein, C. Johnston et al., "Acute pulmonary effects of ultrafine particles in rats and mice," *Research Report (Health Effects Institute)*, no. 96, pp. 5–75, 2000.

[10] E. J. Park, J. Yi, K. H. Chung, D. Y. Ryu, J. Choi, and K. Park, "Oxidative stress and apoptosis induced by titanium dioxide nanoparticles in cultured BEAS-2B cells," *Toxicology Letters*, vol. 180, no. 3, pp. 222–229, 2008.

[11] Q. Rahman, M. Lohani, E. Dopp et al., "Evidence that ultrafine titanium dioxide induces micronuclei and apoptosis in syrian hamster embryo fibroblasts," *Environmental Health Perspectives*, vol. 110, no. 8, pp. 797–800, 2002.

[12] Y. Yu, W. Ren, and B. Ren, "Nanosize titanium dioxide cause neuronal apoptosis: a potential linkage between nanoparticle exposure and neural disorder," *Journal of Neurology Research*. http://www.ncbi.nlm.nih.gov/pubmed/18662496. In press.

[13] N. J. F. Dodd and A. N. Jha, "Titanium dioxide induced cell damage: a proposed role of the carboxyl radical," *Mutation Research*, vol. 660, no. 1-2, pp. 79–82, 2009.

[14] J. F. Reeves, S. J. Davies, N. J. F. Dodd, and A. N. Jha, "Hydroxyl radicals (∘OH) are associated with titanium dioxide (TiO$_2$) nanoparticle-induced cytotoxicity and oxidative DNA damage in fish cells," *Mutation Research*, vol. 640, no. 1-2, pp. 113–122, 2008.

[15] J. R. Gurr, A. S. S. Wang, C. H. Chen, and K. Y. Jan, "Ultrafine titanium dioxide particles in the absence of photoactivation can induce oxidative damage to human bronchial epithelial cells," *Toxicology*, vol. 213, no. 1-2, pp. 66–73, 2005.

[16] T. C. Long, N. Saleh, R. D. Tilton, G. V. Lowry, and B. Veronesi, "Titanium dioxide (P25) produces reactive oxygen species in immortalized brain microglia (BV2): implications for nanoparticle neurotoxicity," *Environmental Science and Technology*, vol. 40, no. 14, pp. 4346–4352, 2006.

[17] G. Federici, B. J. Shaw, and R. D. Handy, "Toxicity of titanium dioxide nanoparticles to rainbow trout (Oncorhynchus mykiss): gill injury, oxidative stress, and other physiological effects," *Aquatic Toxicology*, vol. 84, no. 4, pp. 415–430, 2007.

[18] A. Jemec, D. Drobne, M. Remškar, K. Sepčić, and T. Tišler, "Effects of ingested nano-sized titanium dioxide on terrestrial isopods (Porcellio scaber)," *Environmental Toxicology and Chemistry*, vol. 27, no. 9, pp. 1904–1914, 2008.

[19] R. Klaper, J. Crago, J. Barr, D. Arndt, K. Setyowati, and J. Chen, "Toxicity biomarker expression in daphnids exposed to manufactured nanoparticles: changes in toxicity with functionalization," *Environmental Pollution*, vol. 157, no. 4, pp. 1152–1156, 2009.

[20] J. Palomäki, P. Karisola, L. Pylkkänen, K. Savolainen, and H. Alenius, "Engineered nanomaterials cause cytotoxicity and activation on mouse antigen presenting cells," *Toxicology*, vol. 267, no. 1–3, pp. 125–131, 2010.

[21] H. Ichinose, M. Terasaki, and H. Katsuki, "Properties of peroxotitanium acid solution and peroxo-modified anatase sol derived from peroxotitanium hydrate," *Journal of Sol-Gel Science and Technology*, vol. 22, no. 1-2, pp. 33–40, 2001.

[22] D. L. Specter, R. D. Goldman, and L. A. Leinwand, *Cell Experimental Tutorials*, Science press, Beijing, China, 2001.

[23] D. Zhao, J. Zhou, and N. Liu, "Microstructure of copper modified attapulgite/nanotitania composite powders," *Kuei Suan Jen Hsueh Pao/ Journal of the Chinese Ceramic Society*, vol. 34, no. 7, pp. 792–795, 2006.

[24] J. A. Wang, R. Limas-Ballesteros, T. López et al., "Quantitative determination of titanium lattice defects and solid-state reaction mechanism in iron-doped TiO_2 photocatalysts," *Journal of Physical Chemistry B*, vol. 105, no. 40, pp. 9692–9698, 2001.

[25] Y. Zheng, E. Shi, S. Cui, W. Li, and X. Hu, "Hydrothermal preparation and characterization of brookite-type TiO_2 nanocrystallites," *Journal of Materials Science Letters*, vol. 19, no. 16, pp. 1445–1448, 2000.

[26] K. Lv, H. Zuo, J. Sun et al., "(Bi, C and N) codoped TiO_2 nanoparticles," *Journal of Hazardous Materials*, vol. 161, no. 1, pp. 396–401, 2009.

[27] M. Yan, F. Chen, J. Zhang, and M. Anpo, "Preparation of controllable crystalline titania and study on the photocatalytic properties," *Journal of Physical Chemistry B*, vol. 109, no. 18, pp. 8673–8678, 2005.

Research Article

Synthesis, Characterization, and Evaluation of Radical Scavenging Ability of Ellagic Acid-Loaded Nanogels

Gautam Behl,¹ Monal Sharma,² Saurabh Dahiya,³ Aruna Chhikara,¹ and Madhu Chopra²

¹ *Department of Chemistry, Dyal Singh College, University of Delhi, Lodhi Road, New Delhi 110003, India*
² *Dr. B. R. Ambedkar Center for Biomedical Research, University of Delhi, New Delhi 110007, India*
³ *Department of Anatomical Sciences and Neurobiology, University of Louisville School of Medicine, Louisville, KY 40292, USA*

Correspondence should be addressed to Aruna Chhikara, arunachhikara@gmail.com
and Madhu Chopra, mchopradu@gmail.com

Ellagic acid (EA), a potential antioxidant phytochemical has low aqueous solubility and bioavailability. In this paper, encapsulation of ellagic acid has been carried out into the biodegradable disulfide crosslinked poly (ethylene glycol) PEO-based nanogels synthesized via AGET (activator generated electron transfer) ATRP (atom transfer radical polymerization), and their radical scavenging ability was evaluated. The encapsulation of the EA was carried out at two drug loading percentages, that is, 10 and 20 wt.% of the nanogels. 1,1-Diphenyl-2-picryldrazyl (DPPH) assay was utilized in order to assess the radical scavenging ability of the ellagic acid-loaded nanogels. A drug-loading level of about 2.5 wt.% was achieved with encapsulation efficiency of about 25% at 10 wt.% of the EA w.r.t nanogels, which was found to increase to about 4.7 wt.% with decreased encapsulation efficiency of 23.5% as EA content was increased to 20wt.% of the nanogels. Ellagic acid loading was found to be accompanied with increase in the size of the nanogels from 144.6 ± 39.52 nm for neat nanogels to 217.8 ± 105.5 and 633 ± 160.1 nm at 2.5 and 4.7 wt.% drug loading level. The nanogels were found to be capable of scavenging radicals and biocompatible on human cervical cancer cell lines (HeLa cells) at appropriate concentrations.

1. Introduction

It is widely known that fruits and vegetables are rich in compounds which prevent cancer and are free radical scavengers. These compounds are generally phenolic acids with a single ring structure and flavonoids containing several hydroxyl groups associated with phenolic groups. Oxidative stress which is caused by an imbalance between the antioxidants and oxidants is responsible for many diseases including cancer [1]. EA, a naturally occurring polyphenolic compound, present in fruits and nuts such as blueberries, red raspberries, pomegranates, walnuts, and grape seeds, is very well known to possess antioxidant, anticarcinogenic, and antimutagenic properties [1–6]. Due to its low water solubility and permeability, EA falls under Class IV of the biopharmaceutic classification system [7, 8]. EA is not only insoluble in water (water solubility $\simeq 9.7\,\mu$g/mL) [9] but also difficult to solubilize in commonly used organic solvents which is a prerequisite for

a pharmaceutical entity to be formulated into a dosage form. Animal studies suggest that orally administered EA is poorly absorbed and its retention in the body is very low and hence therapeutic effects could not be achieved [10, 11]. The low oral bioavailability of EA can be attributed to its low aqueous solubility, metabolism in the gastrointestinal tract, irreversible binding to cellular DNA and proteins and first-pass effect [8, 12]. Hence, there is a strong need to develop an effective delivery carrier for EA, to achieve considerable therapeutic output.

Nanoparticles are a reliable option for the delivery of poorly water soluble drugs [7]. Recently, nanoemulsion-based formulation of poorly soluble anticancer drug Paclitaxel has been prepared showing enhanced anticell prolifeative capacity and apoptotic properties [13]. The aims for nanoparticle entrapment of drugs are enhanced delivery to or uptake by target cells and/or a reduction in the toxicity of the free drug to nontarget organs. For these aims, synthesis of

long-lived nanoparticles is needed [14]. Poly(ethylene glycol) particularly solves these problems owing to its prolonged presence in the blood circulation by inhibiting recognition and phagocytosis by the mononuclear phagocytic system [15]. In recent years, ATRP (atom transfer radical polymerization) has emerged as a very useful technique for the synthesis of biodegradable and biocompatible polymers for the delivery of therapeutic agents [16–20]. The technique has been known to be very useful for the synthesis of colloidal particles with halide end functionality which may be advantageous for further chain extension, formation of block copolymers and conjugation with bio-related molecules, resulting in the formation of polymer-biomolecule conjugates [21–24].

In this paper we report a simple method for the encapsulation of EA into the poly(ethylene glycol)-based disulfide crosslinked nanogels, by simply suspending them into a solution of EA in methanol with PEG-400 as cosolvent. The method is simple and does not require use of any stabilizer or surfactant and any complexation strategy used earlier [2, 7, 8]. The nanogels were synthesized via AGET ATRP in an inverse miniemulsion, which is a known technique for controlled polymerization with prepared polymer chains having polydispersity index (PDI) ≈ 1 [17, 18, 25]. The nanogels were synthesized by using poly(ethylene glycol) which is itself a biocompatible material and known to enhance the circulation lifetime in the blood and prevent opsonization of the particles [26, 27] ensuring that carrier will be retained in the body for the maximum possible time, in order to achieve enhanced therapeutic output. The disulfide crosslinker used here further adds biodegradability to the nanogels and is known to degrade in the presence of tripeptide glutathione present within the cells [17].

2. Materials and Methods

2.1. Materials. Ellagic acid was obtained from Sigma Aldrich. Poly(ethylene glycol) monomethylether with $M_n = 5000$ (PEO5000-OH) was used as received from Fluka. Poly (ethylene glycol) monomethacrylate (PEOMA526, $M_n = 526$ g/mol) was purchased from Sigma-Aldrich and purified according to the procedure reported earlier [25]. Copper (II) bromide (CuBr$_2$, 99%), 1, 3-dicyclohexylcarbodiimide (DCC, 99%) were used as received from Acros. Oligo (ethylene glycol) monomethyl ether methacrylate (OEOMA) molecular weight $M = 300$ g/mol, pendent EO units DP ≈ 5, was purchased from Aldrich and purified by passing it through a column filled with basic alumina to remove the inhibitor. 2-Bromo-2-methyl propionyl poly (ethylene glycol) monomethyl ether (PEO5000-Br) macroinitiator, dithiopropionyl poly (ethylene glycol) dimethacrylate (DMA) crosslinker, and tris [(2-pyridyl) methyl] amine (TPMA) ligand were synthesized according to the procedure reported earlier [16, 17, 28]. 2-Bromo-2-methylpropionic acid (98%), 4-dimethyl aminopyridine (DMAP, 99+%), 3, 3′-dithiopropionic acid, glutathione ethyl ester (reduced form), L-ascorbic acid (99+%), sorbitan monooleate (Span 80), cyclohexane (HPLC grade), MTT (3-(4,5-dimethyl-2-yl)-2,5-diphenyltetrazolium bromide), and DPPH were used as received from Aldrich. All other chemicals and reagents used were of analytical grade.

2.2. Methods

2.2.1. Characterization Methods. TEM micrographs were obtained on TECNAI G^2-30 U-TWIN FEI Company HR-TEM at 200 KV (University Science Instrumentation Center Facility, University of Delhi). Size distribution characterization of the nanogels was carried out on DLS (dynamic light scattering) by dispersing nanogels in cyclohexane using DLS; FAST Version 2.8.3.Alango Ltd (Lab facility of Prof. Subho Mozumdar, Dept. of Chemistry, University of Delhi). FTIR (Fourier fransform infrared) spectra of the nanogels were recorded using Perkin Elmer Spectrum BX Series instrument by the KBr disc method. ^{1}H NMR spectra were recorded on Bruker Avance II 400 MHz instrument (NMR facility, Institute of Nuclear Medicine & Allied Sciences, Defence Research and Development Organisation, New Delhi). EPR (electron paramagnetic resonance) spectra were recorded on JES-FA ESR spectrometer with settings: magnetic field, 336.5 ± 5 mT; power, 2 mW; modulation frequency, 9.435 GHz; amplitude, 1×1000; modulation width, 0.8 mT; sweep width, 10 mT; sweep time, 30 s. (JEOL LTD.) (University Science Instrumentation Center Facility, University of Delhi). UV-visible study was carried out on Perkin Elmer Lambda 25 spectrophotomer at ACBR.

2.2.2. Synthesis of (P (OEOMA)) Nanogels by AGET ATRP. Poly(oligoethylene glycol) monomethacrylate (P (OEOMA)) nanogels were synthesized by carrying out an AGET ATRP reaction in an inverse miniemulsion according to the procedure described earlier (**Figure 1**) [16, 17]. Briefly, OEOMA 300 (1.4 g, 4.67 mmol), PEO5000-Br (79.8 mg, 0.016 mmol), TPMA (2.3 mg, 0.008 mmol), CuBr$_2$ (1.7 mg, 0.008 mmol), and water (1.4 mL) were mixed in a 50 mL round bottom flask at room temperature, and 1.5 mol% DMA in aqueous solution was introduced. The resulting clear solution was then mixed with a solution of Span 80 (surfactant) (1.0 g) in cyclohexane (20 g), and the mixture was sonicated for 2 min in an ice bath at 0°C to form a stable inverse miniemulsion. The dispersion was transferred into a 50 mL Schlenk flask and then bubbled with nitrogen for 30 min. The flask was immersed in water bath preheated to 30°C, and then an argon-purged aqueous solution of ascorbic acid (0.005 mmol, 192 μL) was added via syringe to start polymerization. The polymerization was stopped after 2 h by exposing the reaction mixture to air. The resulting nanogel was purified by removal of the cyclohexane followed by addition of THF and the resulting heterogeneous mixture was stirred at room temperature for 5 h. The gels were separated by centrifugation (15, 000 rpm $\times$ 20 min) and decantation of the supernatant. THF was added and the same procedure was repeated twice. After the final wash, the precipitate was dried in a vacuum oven at 30°C for 2 h to yield the nanogels.

2.2.3. Degradation Study of the Nanogels in Presence of Glutathione. A degradation study of nanogels was performed in
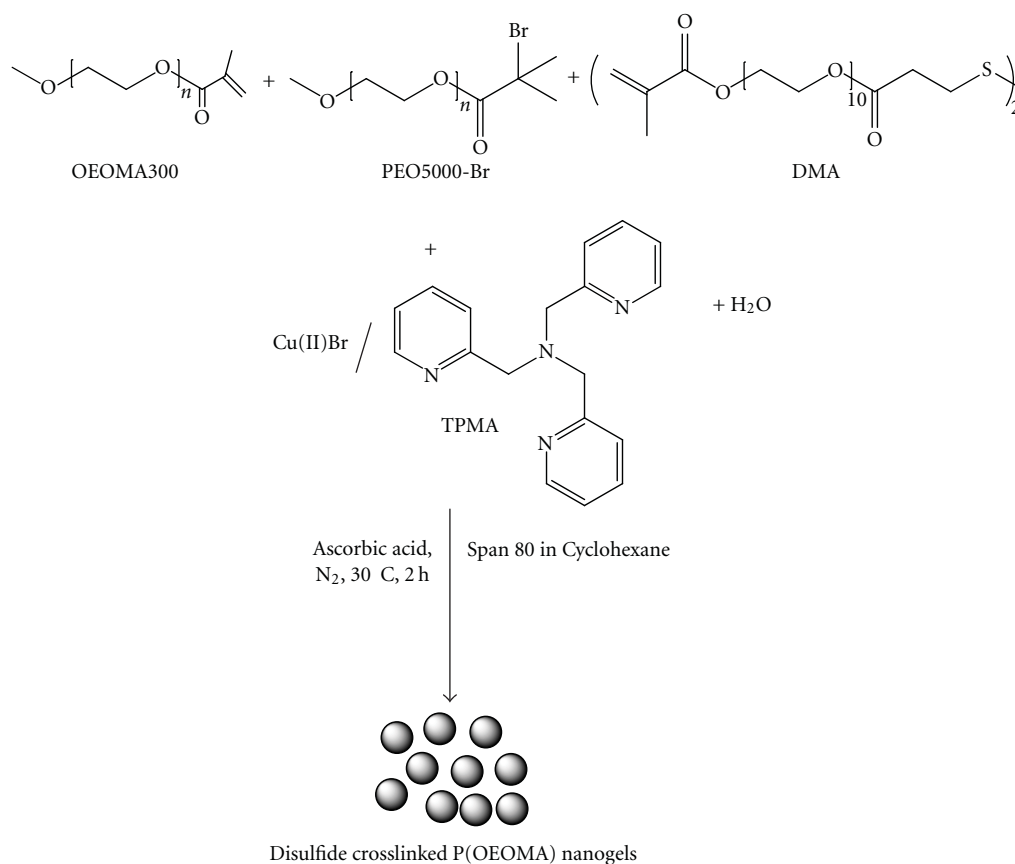
FIGURE 1: Schematic representation of the syntheses of P(OEOMA) nanogels via inverse miniemulsion ATRP.

the presence of glutathione according to the procedure reported earlier [17] with slight modification. Briefly, 20 mg of the nanogels were fully swollen in water (1.7 mL) for 3 days and then centrifuged to separate the gels (W1). The nanogels were then mixed with 10 wt.% (2 mg) and 20 wt.% of the glutathione in water (1.7 mL) and allowed to stir at room temperature for appropriate time and centrifuged (15000 rpm × 20 min) to separate the gels (W2). The extent of degradation was calculated from the equation in terms of weight fraction (W2/W1 × 100) of the nanogels remained. A control experiment was also carried out using similar conditions in the absence of glutathione.

2.2.4. Drug Loading. Required amount of nanogels was allowed to stir in methanol: poly(ethylene glycol) ($M_n = 400$) solution (2400 : 600 μL for every 1 mg of EA) for 5 days. At the end of this period, the contents were centrifuged to precipitate nanogels, which were washed repeatedly with methanol and dried in vacuum. The amount of drug loading was calculated indirectly by taking absorbance of the supernatant at 361 nm, and fitting the absorbance value in Beer-Lambert equation with predetermined extinction coefficient of EA.

2.2.5. DPPH Radical Scavenging Ability of the EA-Loaded Nanogels. DPPH radical scavenging activity of the EA-loaded

nanogels was determined by UV-visible spectrophotometric method and EPR spectroscopy according to the procedure reported earlier [29, 30] at predetermined concentrations with slight modifications. The results were expressed in terms of absorbance decay of DPPH at 517 nm and decrease in the height of EPR signal. About 100 μL of the suspension of EA-loaded nanogels in water was mixed with 900 μL of the DPPH (100 μM) in ethanol solution. The solution was mixed and incubated for 30 min at room temperature in dark. The absorbance of the final solution was recorded spectrophotometrically at a wavelength of 517 nm. For EPR study about 50 μL of the suspension of the drug-loaded nanogels was added to 150 μL of the ethanolic solution of DPPH (100 μM). After mixing vigorously for 10 s, the solution was transferred into a quartz capillary tube and its radical scavenging activity was measured in terms of peak height.

2.2.6. In Vitro Cytotoxicity of the EA-Loaded Nanogels. Cytotoxicity of the EA-loaded nanogels was determined by MTT assay as described elsewhere [31]. Briefly, the cells were grown in 96-well plates at a density of 5×10^4 cells/well. After 24 h, cells were washed with fresh medium and treated with neat and EA-loaded nanogels at varying concentrations. After 48 h of incubation, cells were rewashed and 50 μL of MTT (5 mg/mL) was added to each well and incubated for 4 h. Finally, 200 μL of DMSO was added to solubilize

(a)

(b)
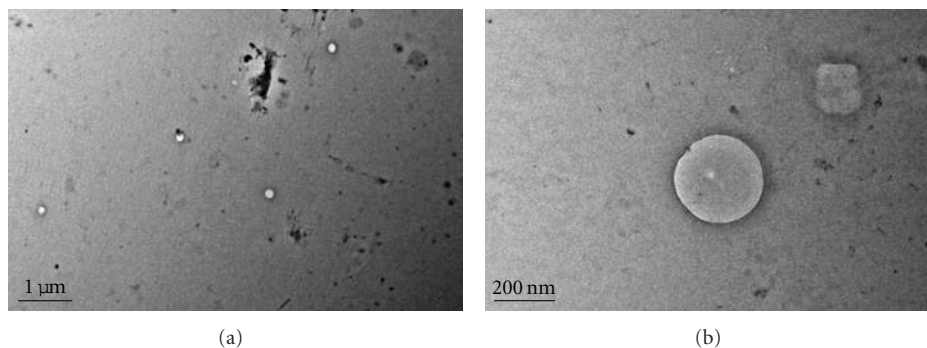
FIGURE 2: HR-TEM micrographs of the nanogels at 1 μm (a) and 200 nm (b) scale bar. Nanogels were suspended in water by sonication and then mounted on a carbon-coated TEM grid.

the formazan salt formed and the amount of formazan salt was determined by measuring the optical density (OD) at 540 nm using a GENios microplate reader (TECAN Austria GmbH, Grodig/Salzburg, Austria).

3. Results and Discussion

ATRP in an inverse miniemulsion enables the formation of uniformly crosslinked particles and gels with well-controlled polymer segments [16, 32–34]. This approach has become very useful for the preparation of biomaterials with many predeterminable site specific features, including uniform network, high loading efficiency of biomolecules or drugs, distributed halide end-group functionalities, and degradable interior [16]. Based on this method we synthesized P(OEOMA) nanogels in inverse miniemulsion, and their spherical morphology was revealed by TEM micrographs as shown in Figure 2.

The nanogels were insoluble in a number of solvents including THF and water, but when incubated with appropriate concentrations of glutathione they got degraded and became soluble in water. The extent of degradation was found to be dependent on the concentration of the glutathione as evident from Figure 3.

There was no degradation in the control setup, however, 78% of the nanogels degraded in the presence of 20 wt.% glutathione, comparable to the previously reported results [17]. Authors in this paper synthesized the nanogels via ATRP, a degradation study was carried out in the presence of tripeptide glutathione resulting in reduction of the disulfide group to the corresponding thiols making the water soluble byproducts. Our approach was based on the use of these disulfide crosslinked nanogels as biodegradable carriers, as these groups add biodegradability to the nanogels [32, 35] in the presence of glutathione within the cells [36]. The results obtained here confirm that the nanogels were crosslinked with disulfide crosslinker and their excretion from the body would be easier after their degradation in the presence of glutathione.

A wide variety of drugs can be delivered using nanoparticulate carriers via a number of routes. Size of the nanoparticles is very crucial for their uptake via any route. For oral
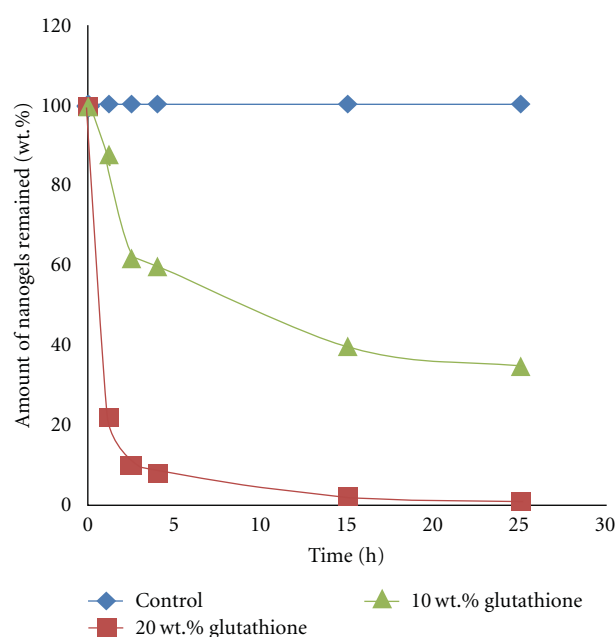
FIGURE 3: Degradation of the nanogels in terms of weight fraction of the nanogels remained in the presence of different concentrations of glutathione with time.

TABLE 1: DLS data of the nanogels dispersed in cyclohexane at 30°C.

	Drug-loaded nanogels (wt %)	D_{av}* (nm)
Neat nanogels	—	144.6 ± 39.52
	2.5	217.8 ± 105.5
	4.7	633 ± 160.1

* D_{av} is average diameter ± standard deviation.

route where the lymphatic uptake of the nanoparticles by the Payer's patches in the GALT (gut-associated lymphoid tissue) is of major interest, the optimum size ranges from less than 1 μm to 5 μm. Whereas for intravenous delivery it becomes smaller than 5 μm [37]. Here in our case, DLS measurement of the nanogels revealed a size distribution of about 144.6 ± 39.52 nm (Figure 4 and Table 1) within the prescribed limits comparable to the size obtained earlier [16, 17].

(a)

(b)

(c)
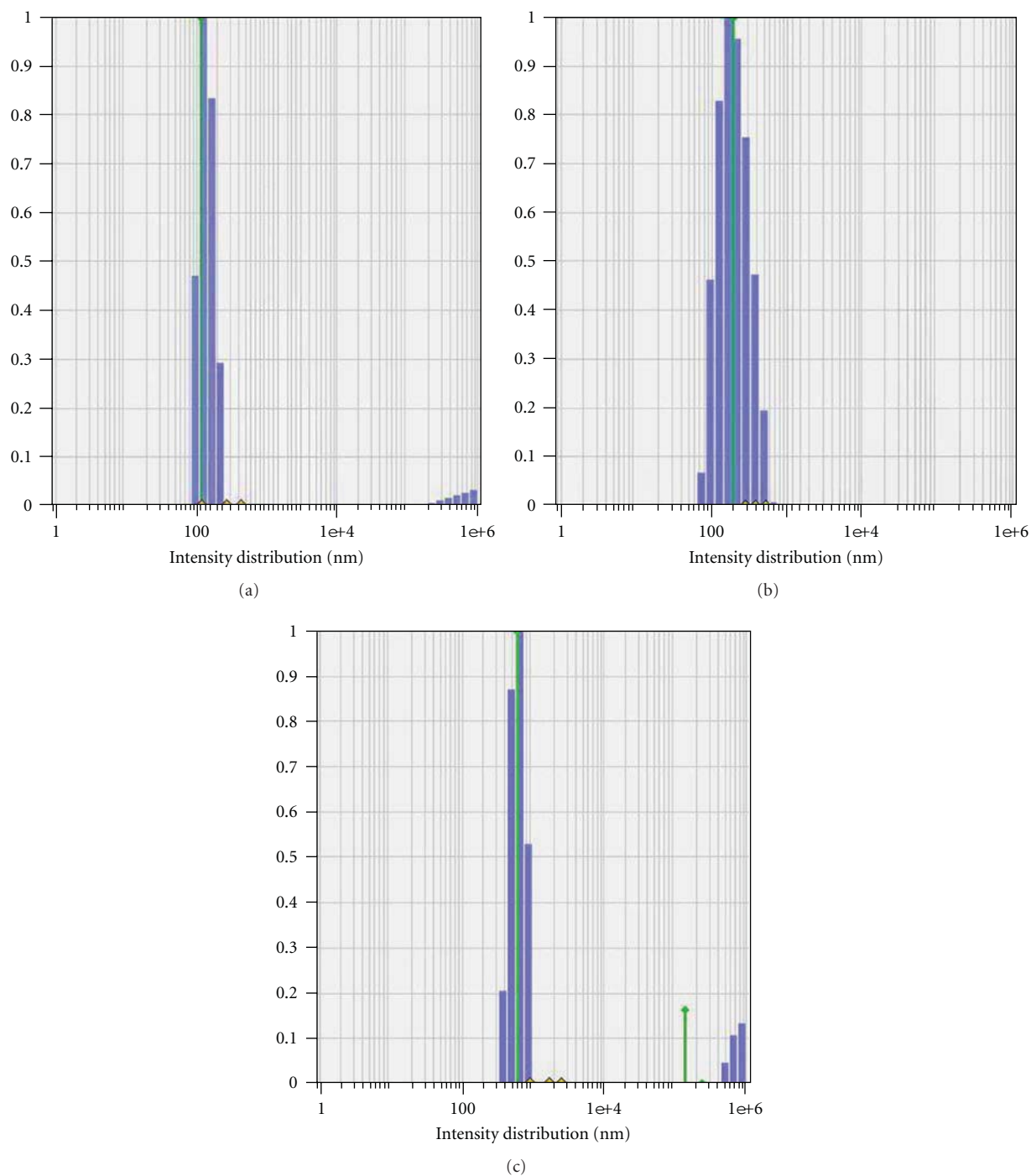
FIGURE 4: DLS measurement of the neat nanogels (a) and drug-loaded nanogels at 2.5 wt.% (b) and 4.7 wt.% (c) drug loading-level. Nanogels were sonicated and suspended in cyclohexane for carrying out the measurement.

Several studies have been reported where these nanogels were used as biodegradable carriers of anticancer agents. Studies were performed by encapsulation of doxorubicin [17] and rhodamine B isothiocyanate-dextran [18] as model drugs. We carried out encapsulation studies of Ellagic acid, a naturally occurring polyphenolic compound, for our work. As already stated, EA has lower solubility and permeability

profile. Being a medicinally important compound, its delivery in the form of solubilised nanogels may be of interest for pharmaceutically usable dosage form. A stable solution of EA was formed in methanol with PEG-400 as cosolvent. The absorbance of characteristic peak of EA at 361 nm was measured as described in methods section. At about 10 wt.% of initial drug load, 2.5 wt.% drug loading was achieved
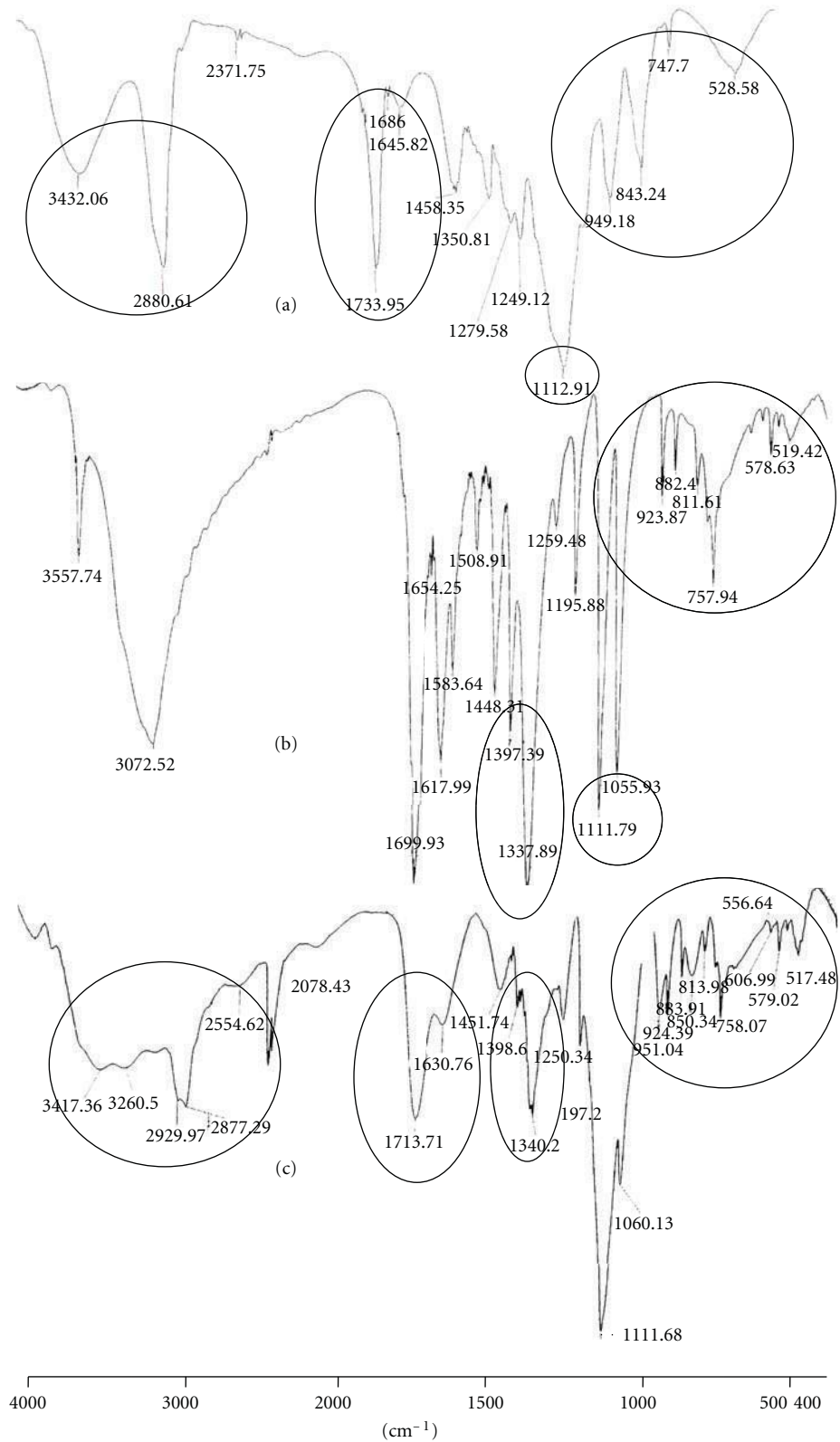
Figure 5: FTIR spectra of the nanogels (a), EA (b) and EA-loaded nanogels (c).

Table 2: Drug-loading level and encapsulation efficiency of EA into the nanogels.

EA/nanogels (wt%)	Loading level (wt%)	Loading efficiency (wt%)
10	2.5	25
20	4.7	23.5
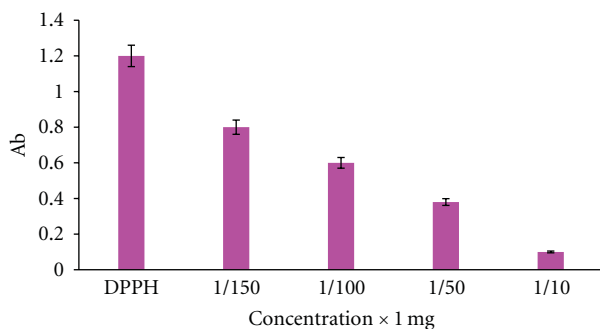
Figure 6: DPPH radical scavenging effect of the ellagic acid-loaded nanogels in terms of absorbance decay at 517 nm. Results are means ± standard error of three independent experiments.

Figure 7: EPR spectra of the DPPH radical at indicated dilutions of the 1 mg of 4.7 wt.% EA-loaded nanogels.

with an encapsulation efficiency of 25%. The drug loading levels increased to 4.7 wt.% at 20 wt.% drug load, however encapsulation efficiency decreased to 23.5 wt.% (Table 2).

Our results are similar to those reported earlier [17, 18] where the encapsulation efficiency followed the similar trend as observed in our studies. In another previous report, authors observed decrease in encapsulation efficiency trend for EA encapsulation in a different system with nanoparticle based on poly (lactide-co-glycolide) [7] using polyvinyl alcohol and chitosan as stabilizers. Moreover, in our case we did not utilize any surfactant or stabilizer for encapsulation of EA into the nanogels, hence it may be stated that our method is advantageous to earlier reported method [7] and encapsulation efficiency achieved is comparable with other cytotoxic anticancer compounds discussed above.

Loading of the drug molecules into the nanogels affects the size. EA loading was also found to be accompanied with increase in size distribution of the nanogels (Figure 4 and Table 1). The size distributions of the nanogels were 217.8 ± 105.5 and 633 ± 160.1 nm at 2.5 and 4.7 wt.% drug-loading level. This increase in the size of nanogels can be attributed to the increased amount of EA into the nanogels similar to the results reported earlier [7].

FTIR spectroscopy has been used frequently for the characterization of the prepared formulation and any kind of interaction between drug and the matrix of the carrier [12, 38, 39]. For an ideal drug carrier it becomes necessary that it should not have any chemical interaction that leads to any change in the chemical structure of drug. The FTIR spectra obtained for the nanogels, EA and EA-loaded nanogels are shown in Figure 5. The spectrum of the nanogels shows characteristic bands around 1733 and 1100 cm^{-1} which are attributed to the C=O stretch of the ester groups and C–O–C skeletal stretch of poly(ethylene glycol) backbone,
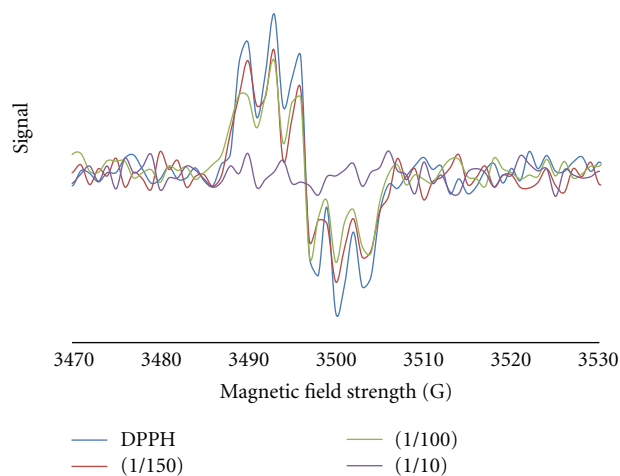
respectively, that was also observed in the spectrum of EA-loaded nanogels. A band around 1195 cm^{-1} was observed in the spectrum of EA and EA-loaded nanogels due to the C–O stretch of the lactone group. The fingerprint regions of both nanogels and EA (900 to 500 cm^{-1}) were observed in the spectrum of EA-loaded nanogels. In the IR spectrum of the EA-loaded nanogels the signal around 3400 cm^{-1} became very broad, which is due to the phenolic hydroxyl stretch of the EA. All other bands of EA (around 1397, 1337, and 1448 cm^{-1}) and nanogels (around 3400, 2880, and 1645 cm^{-1}) were observed in the spectrum of EA-loaded nanogels, particularly the presence of two characteristic peaks of EA (in the range 1300–1050 cm^{-1}) in spectrum of EA-loaded nanogels confirms the absence of any chemical interaction between gel components and EA in agreement with earlier published results [12]. Therefore, EA had been encapsulated into the nanogels and had no chemical interaction with the polymeric matrix of the nanogels.

DPPH radical scavenging activity has been used earlier for the antioxidant activity evaluation of the electrospun gallic acid-loaded poly (L-lactic acid) fiber mats [29] and in vitro antioxidant activity of a peptide isolated from Nile tilapia [40], where the antioxidant activity was evaluated in a concentration dependent manner from absorbance decay at 517 nm and decrease in EPR signal intensity as DPPH radical got scavenged. We carried out DPPH radical scavenging activity of the EA-loaded nanogels by the absorbance decay method at 517 nm (Figure 6). We also recorded EPR spectra where the height of the signal reduced when the radical got scavenged. The signal height was measured at various dilutions of 1 mg of 4.7 wt.% EA-loaded nanogels, that is, 1/10, 1/50, 1/100, 1/150. DPPH radical gives a purple colour absorbance maximum at 517 nm, but when the radical is scavenged its absorbance decays at 517 nm with decrease in the intensity of the signal in EPR spectra, which gives indirectly the radical scavenging capability of the preparation (Figure 7). EA retained its radical scavenging ability even after encapsulation into the nanogels as evident from
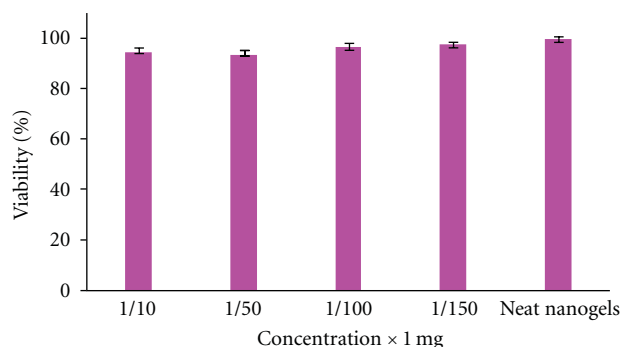
FIGURE 8: Cytotoxic effect of EA-loaded nanogels on viability of HeLa cells. Results are means ± standard error of three independent experiments.

the concentration dependent decay of absorbance at 517 nm (Figure 6) as well as increase in height of the EPR signal with dilution of the formulation (Figure 7).

For any compound or delivery carrier to be proposed as a therapeutic agent, it is very important to account for their viability levels. We performed cell viability assay of the EA-loaded nanogels using MTT assay on human cervical cancer cells (HeLa cells). MTT assay was performed at same dilutions those used in studying DPPH radical scavenging activity, that is, 1/10, 1/50, 1/100, 1/150 dilutions of the 1 mg of 4.7 wt.% of the EA-loaded nanogels with 10 mg/mL concentration of the neat nanogels as control. The cell viability data (Figure 8) showed that the EA-loaded nanogels were noncytotoxic on HeLa cells.

4. Conclusion

Nanoparticles are being consistently used for the delivery of poorly water soluble drugs. The aims for nanoparticle entrapment of drugs are enhanced delivery to or uptake by target cells and/or a reduction in the toxicity of the free drug to nontarget organs. We have been able to develop biodegradable EA-loaded nanogels. The results indicate that the method is effective for the encapsulation of EA and it still retains its radical scavenging ability as demonstrated by DPPH assay. The encapsulation of the ellagic acid was found to be accompanied with increase in the size of nanogels, and the encapsulation efficiency was quite good if we consider the poor solubility of the EA. The combination was found to be biocompatible on HeLa cells at the concentrations used for radical scavenging activity.

Conflict of Interests

The authors declared that there is no conflict of interests.

Acknowledgments

References

[1] S. U. Mertens-Talcott, S. T. Talcott, and S. S. Percival, "Low concentrations of quercetin and ellagic acid synergistically influence proliferation, cytotoxicity and apoptosis in MOLT-4 human leukemia cells," *Journal of Nutrition*, vol. 133, no. 8, pp. 2669–2674, 2003.

[2] S. Kim, Y. Liu, M. W. Gaber, J. D. Bumgardner, W. O. Haggard, and Y. Yang, "Development of chitosan-ellagic acid films as a local drug delivery system to induce apoptotic death of human melanoma cells," *Journal of Biomedical Materials Research Part B*, vol. 90, no. 1, pp. 145–155, 2009.

[3] J. N. Losso, R. R. Bansode, A. Trappey, H. A. Bawadi, and R. Truax, "In vitro anti-proliferative activities of ellagic acid," *Journal of Nutritional Biochemistry*, vol. 15, no. 11, pp. 672–678, 2004.

[4] B. A. Narayanan, O. Geoffroy, M. C. Willingham, G. G. Re, and D. W. Nixon, "p53/p21(WAF1/CIP1) expression and its possible role in G1 arrest and apoptosis in ellagic acid treated cancer cells," *Cancer Letters*, vol. 136, no. 2, pp. 215–221, 1999.

[5] A. C. Whitley, G. D. Stoner, M. V. Darby, and T. Walle, "Intestinal epithelial cell accumulation of the cancer preventive polyphenol ellagic acid-extensive binding to protein and DNA," *Biochemical Pharmacology*, vol. 66, no. 6, pp. 907–915, 2003.

[6] L. Labrecque, S. Lamy, A. Chapus et al., "Combined inhibition of PDGF and VEGF receptors by ellagic acid, a dietary-derived phenolic compound," *Carcinogenesis*, vol. 26, no. 4, pp. 821–826, 2005.

[7] I. Bala, V. Bhardwaj, S. Hariharan, J. Sitterberg, U. Bakowsky, and M. N. V. Ravi Kumar, "Design of biodegradable nanoparticles: a novel approach to encapsulating poorly soluble phytochemical ellagic acid," *Nanotechnology*, vol. 16, no. 12, pp. 2819–2822, 2005.

[8] V. Murugan, K. Mukherjee, K. Maiti, and P. K. Mukherjee, "Enhanced oral bioavailability and antioxidant profile of ellagic acid by phospholipids," *Journal of Agricultural and Food Chemistry*, vol. 57, no. 11, pp. 4559–4565, 2009.

[9] I. Bala, V. Bhardwaj, S. Hariharan, and M. N. V. R. Kumar, "Analytical methods for assay of ellagic acid and its solubility studies," *Journal of Pharmaceutical and Biomedical Analysis*, vol. 40, no. 1, pp. 206–210, 2006.

[10] R. C. Smart, M. T. Huang, R. L. Chang, J. M. Sayer, D. M. Jerina, and A. H. Conney, "Disposition of the naturally occurring antimutagenic plant phenol, ellagic acid, and its synthetic derivatives, 3-o-decylellagic acid and 3, 3'-di-o-methylellagic acid in mice," *Carcinogenesis*, vol. 7, no. 10, pp. 1663–1667, 1986.

[11] F. Lei, D. M. Xing, L. Xiang et al., "Pharmacokinetic study of ellagic acid in rat after oral administration of pomegranate leaf extract," *Journal of Chromatography B*, vol. 796, no. 1, pp. 189–194, 2003.

[12] G. Sharma, J. L. Italia, K. Sonaje, K. Tikoo, and M. N. V. Ravi Kumar, "Biodegradable in situ gelling system for subcutaneous administration of ellagic acid and ellagic acid loaded nanoparticles: evaluation of their antioxidant potential against cyclosporine induced nephrotoxicity in rats," *Journal of Controlled Release*, vol. 118, no. 1, pp. 27–37, 2007.

[13] M. Bagul, S. Kakumanu, T. Wilson, and R. Nicolosi, "In vitro evaluation of antiproliferative effects of self-assembling nanoemulsion of paclitaxel on various cancer cell lines," *Nano Biomedicine and Engineering*, vol. 2, pp. 100–108, 2010.

[14] H. Song, X. Cao, J. Ruan et al., "Application of rotatable central composite design in the preparation and optimization of poly

(lactic-co-glycolic acid) nanoparticles for controlled delivery of HSA," *Nano Biomedicine and Engineering*, vol. 3, pp. 34–41, 2011.

[15] W. H. De Jong and P. J. A. Borm, "Drug delivery and nano-particles: applications and hazards," *International Journal of Nanomedicine*, vol. 3, no. 2, pp. 133–149, 2008.

[16] J. K. Oh, C. Tang, H. Gao, N. V. Tsarevsky, and K. Matyjaszewski, "Inverse miniemulsion ATRP: a new method for synthesis and functionalization of well-defined water-soluble/cross-linked polymeric particles," *Journal of the American Chemical Society*, vol. 128, no. 16, pp. 5578–5584, 2006.

[17] J. K. Oh, D. J. Siegwart, H. I. Lee et al., "Biodegradable nanogels prepared by atom transfer radical polymerization as potential drug delivery carriers: synthesis, biodegradation, in vitro release, and bioconjugation," *Journal of the American Chemical Society*, vol. 129, no. 18, pp. 5939–5945, 2007.

[18] J. K. Oh, D. J. Siegwart, and K. Matyjaszewski, "Synthesis and biodegradation of nanogels as delivery carriers for carbohydrate drugs," *Biomacromolecules*, vol. 8, no. 11, pp. 3326–3331, 2007.

[19] X. Jiang, M. C. Lok, and W. E. Hennink, "Degradable-brushed pHEMA-pDMAEMA synthesized via ATRP and click chemistry for gene delivery," *Bioconjugate Chemistry*, vol. 18, no. 6, pp. 2077–2084, 2007.

[20] J. A. Johnson, D. R. Lewis, D. D. Díaz, M. G. Finn, J. T. Koberstein, and N. J. Turro, "Synthesis of degradable model networks via ATRP and click chemistry," *Journal of the American Chemical Society*, vol. 128, no. 20, pp. 6564–6565, 2006.

[21] K. L. Heredia, Z. P. Tolstyka, and H. D. Maynard, "Ami-nooxy end-functionalized polymers synthesized by ATRP for chemoselective conjugation to proteins," *Macromolecules*, vol. 40, no. 14, pp. 4772–4779, 2007.

[22] P. L. Golas and K. Matyjaszewski, "Click chemistry and ATRP: a beneficial union for the preparation of functional materials," *QSAR and Combinatorial Science*, vol. 26, no. 11-12, pp. 1116–1134, 2007.

[23] D. J. Siegwart, J. K. Oh, H. Gao et al., "Biotin-, pyrene-, and GRGDS-functionalized polymers and nanogels via ATRP and end group modification," *Macromolecular Chemistry and Physics*, vol. 209, no. 21, pp. 2179–2193, 2008.

[24] D. J. Siegwart, A. Srinivasan, S. A. Bencherif et al., "Cellular uptake of functional nanogels prepared by inverse miniemul-sion ATRP with encapsulated proteins, carbohydrates, and gold nanoparticles," *Biomacromolecules*, vol. 10, no. 8, pp. 2300–2309, 2009.

[25] M. M. Ali and H. D. H. Stöver, "Well-defined amphiphilic thermosensitive copolymers based on poly(ethylene glycol monomethacrylate) and methyl methacrylate prepared by atom transfer radical polymerization," *Macromolecules*, vol. 37, no. 14, pp. 5219–5227, 2004.

[26] F. Alexis, E. Pridgen, L. K. Molnar, and O. C. Farokhzad, "Factors affecting the clearance and biodistribution of polymeric nanoparticles," *Molecular Pharmaceutics*, vol. 5, no. 4, pp. 505–515, 2008.

[27] R. Gref, A. Domb, P. Quellec et al., "The controlled intrave-nous delivery of drugs using PEG-coated sterically stabilized nanospheres," *Advanced Drug Delivery Reviews*, vol. 16, no. 2-3, pp. 215–233, 1995.

[28] Z. Tyeklár, R. R. Jacobson, N. Wei, N. N. Murthy, J. Zubieta, and K. D. Karlin, "Reversible reaction of O_2 (and CO) with a copper(I) complex. X-ray structures of relevant mono-nuclear Cu(I) precursor adducts and the trans-(μ-1,2-peroxo) dicopper(II) product," *Journal of the American Chemical Society*, vol. 115, no. 7, pp. 2677–2689, 1993.

[29] P. Chuysinuan, N. Chimnoi, S. Techasakul, and P. Supaphol, "Gallic acid-loaded electrospun poly(L-lactic acid) fiber mats and their release characteristic," *Macromolecular Chemistry and Physics*, vol. 210, no. 10, pp. 814–822, 2009.

[30] F. Nanjo, K. Goto, R. Seto, M. Suzuki, M. Sakai, and Y. Hara, "Scavenging effects of tea catechins and their derivatives on 1,1- diphenyl-2-picrylhydrazyl radical," *Free Radical Biology and Medicine*, vol. 21, no. 6, pp. 895–902, 1996.

[31] M. B. Hansen, S. E. Nielsen, and K. Berg, "Re-examination and further development of a precise and rapid dye method for measuring cell growth/cell kill," *Journal of Immunological Methods*, vol. 119, no. 2, pp. 203–210, 1989.

[32] N. V. Tsarevsky and K. Matyjaszewski, "Combining atom transfer radical polymerization and disulfide/thiol redox chemistry: a route to well-defined (bio)degradable polymeric materials," *Macromolecules*, vol. 38, no. 8, pp. 3087–3092, 2005.

[33] J. K. Oh, R. Drumright, D. J. Siegwart, and K. Matyjaszewski, "The development of microgels/nanogels for drug delivery applications," *Progress in Polymer Science*, vol. 33, no. 4, pp. 448–477, 2008.

[34] J. K. Oh and K. Matyjaszewski, "Synthesis of poly(2-hydrox-yethyl methacrylate) in protic media through atom transfer radical polymerization using activators generated by electron transfer," *Journal of Polymer Science Part A*, vol. 44, no. 12, pp. 3787–3796, 2006.

[35] H. A. Aliyar, P. D. Hamilton, and N. Ravi, "Refilling of ocular lens capsule with copolymeric hydrogel containing reversible disulfide," *Biomacromolecules*, vol. 6, no. 1, pp. 204–211, 2005.

[36] S. Carelli, A. Ceriotti, A. Cabibbo, G. Fassina, M. Ruvo, and R. Sitia, "Cysteine and glutathione secretion in response to protein disulfide bond formation in the ER," *Science*, vol. 277, no. 5332, pp. 1681–1684, 1997.

[37] M. L. Hans and A. M. Lowman, "Biodegradable nanoparticles for drug delivery and targeting," *Current Opinion in Solid State and Materials Science*, vol. 6, no. 4, pp. 319–327, 2002.

[38] B. Chauhan, S. Shimpi, and A. Paradkar, "Preparation and characterization of etoricoxib solid dispersions using lipid carriers by spray drying technique," *AAPS PharmSciTech*, vol. 6, no. 3, pp. E405–E412, 2005.

[39] P. Piyakulawat, N. Praphairaksit, N. Chantarasiri, and N. Muangsin, "Preparation and evaluation of chitosan/carra-geenan beads for controlled release of sodium Diclofenac," *AAPS PharmSciTech*, vol. 8, no. 4, pp. E1–E11, 2007.

[40] D.-H. Ngo, Z.-J. Qian, B. Ryu, J. W. Park, and S.-K. Kim, "In vitro antioxidant activity of a peptide isolated from Nile tilapia (Oreochromis niloticus) scale gelatin in free radical-mediated oxidative systems," *Journal of Functional Foods*, vol. 2, no. 2, pp. 107–117, 2010.

Review Article

MRI Contrast Agent-Based Multifunctional Materials: Diagnosis and Therapy

Hyeona Yim, Seogjin Seo, and Kun Na

Department of Biotechnology, The Catholic University of Korea, 43-1 Yeokkok2-dong, Wonmi-gu, Gyeonggi-do, Bucheon-si 420-743, Republic of Korea

Correspondence should be addressed to Kun Na, kna6997@catholic.ac.kr

Various imaging technologies have become increasingly important in developing a better understanding of information on the biological and clinical phenomena associated with diseases of interest. Of these technologies, magnetic resonance imaging (MRI) is one of the most powerful for clinical diagnosis and in vivo imaging without the exposure to ionising radiation or radiotracers. Despite its many advantages, there are intrinsic limitations caused by MRI contrast agents, such as short vascular half-life circulation, which lead to unwanted side effects. In this review, we will focus on the multifunctional modification of MRI contrast agents for diagnosis and therapy.

1. Introduction

Powerful imaging tools such as fluorescence imaging (FI), magnetic resonance imaging (MRI), computed tomography (CT), positron emission tomography (PET), single-photon emission computed-tomography (SPECT), and ultrasound provide scientific and clinical information [1, 2]. The properties and characteristics of these imaging tools are summarised in Table 1. Among these technologies, MRI is one of the best noninvasive imaging modalities in both the clinical and basic research fields because of its ability to provide a wealth of spatial and temporal resolution. Moreover, it does not harm the patient because it uses strong magnetic fields and nonionising radiation in the radio frequency range, unlike CT and traditional X-rays, which both use ionising radiation. A basic understanding of MRI contrast is founded upon the nuclear magnetic resonance (NMR) phenomenon. MRI contrast is defined by the two-principle NMR processes of spin relaxation, T1 (longitudinal), and T2 (transverse) [3].

Based on MRI principles, several types of paramagnetic or superparamagnetic contrast agents have been used to enhance MRI contrast. MRI contrast agents work by shortening the T1 relaxation time of protons located nearby. The T1 shortening is due to an increase in the rate of stimulated emission from high-energy states to low-energy states. Paramagnetic metal ions used as T1 contrast agents principally accelerate T1 relaxation and produce the "bright" contrast in a T1-weighted image, whereas superparamagnetic iron oxides (SPIOs) used as T2 contrast agents primarily increase the rate of T2 relaxation and create "dark" contrast effects. Although most paramagnetic (i.e., gadolinium (Gd)-based complexes) materials are currently employed in clinical applications, they must be modified for safety and functionality due to limitations caused by their very low molecule weights, which is many unwanted side effects [1, 4–6]. Additionally, the modification of SPIO particles by conjugating targeting moieties for their multifunctional modalities is required to overcome the particles' limitations, such as their very short blood circulation time. However, their nanostructured agents are extensively used in the clinic or in research fields. This review surveys the development of nanostructured and multifunctional contrast agents for diagnosis and therapy in the MRI.

2. Nanostructured MRI Contrast Agents

The principal paramagnetic ions used as T1 contrast agents in MRI applications involve manganese (Mn), chromium

TABLE 1: Properties and characteristics of various imaging techniques.

Modality	Probe	Spatial resolution	Advantages	Limit
Magnetic resonance imaging (MRI)	Paramagnetic metals (e.g., Gd and Mn) superparamagnetic metals (e.g., iron oxide)	25–$100\,\mu m$	High resolution no radiation physiological and anatomical details	In patient with limit (metallic devices) High cost
Optical imaging	Fluorescent dyes, quantum dots	2–$5\,mm$	High sensitivity functional information no radiation	Low resolution low tissue penetration
Computed tomography (CT)	Gold, iodine	50–$200\,\mu m$	High spatial resolution. differentiate between tissues.	Requires contrast agent Radiation tissue nonspecificity
Gamma scintigraphy (PET and SPECT)	Radionuclides (F-18, In-111, Cu-64)	1-$2\,mm$	Monitoring biochemical processes	Radiation low resolution high cost

(Cr), and gadolinium (Gd). These metallic ions are relatively toxic in their free forms, but this toxicity may be reduced by chelation with ethylenediaminetetra acetic acid (EDTA), diethylenetriaminepenta acetic acid (DTPA), glucoheptonic acid, or desferrioxamine [7]. In particular, Gd chelates are currently available worldwide. Of the Gd chelate agents, gadopentetate dimeglumine (Gd-DTPA), gadoteridol, and gadodiamide (Gd-DTPA-BMA) have the greatest market share. These Gd chelate agents have been manufactured to be safe for the patient, and they follow strict FDA regulations to avoid any health complications. However, the low molecular weight Gd chelates are essentially first-pass agents, which may limit their use in other parts of the body. Most current commercial agents exhibit poor performance in several clinical applications, such as gastrointestinal tract and intravascular imaging, because of their systemic distribution despite their development [8].

These agents must be modified to target specific organs, regions of the body, or diseased tissue to gain the greatest diagnostic value from MRI. The requirements state that the agents must be designed to contain a large number of paramagnetic centres that can be selectively bound to the target tissue and that the modified agents must be of sufficiently high molecular weight to prolong vascular retention and, thus, slow tissue clearance. Over the past several years, there have been several approaches to produce structural modifications. These approaches include the conjugation of paramagnetic agents with macromolecular polymers, polymeric paramagnetic nanoparticles, and dendrimer-based metal chelates [9–11].

Kun Na developed Gd-DTPA chelate compounds by conjugation with pullulan (Gd-DTPA-pullulan, GDP) [5]. Pullulan, a natural and nonionic polysaccharide containing repeating maltotriose units condensed through α-1,6 linkage, has been reported to demonstrate a high affinity for asialoglycoprotein receptors in liver parenchymal cells, namely, hepatocytes [12]. Figure 1 Showed that GDP was able to distinguish between malignant and normal regions in delayed MRI. The signal intensities of GDP in regions of interest (ROI) were four times higher than those of Gd-DTPA-BMA. Additionally, GDP demonstrated a prolonged circulation time in the body compared to Gd-DTPA-BMA,

which resulted in enhanced discriminative contrast power of hepatocytes [5].

Cheng et al. reported that dendrimer nanoclusters (DNCs) are composed of individual Gd-labeled polyamidoamine (PAMAM) dendrimers that have been cross-linked to form larger nanoparticulate carriers. They also described how Gd-labeled DNCs could possibly target cancer tissues or cells specifically by conjugation with folic acid as a special ligand for ultrasensitive MRI detection of various cancer types of interest. As a consequence, the biodegradable dendrimer-based Gd-labeled nanoparticles exhibited longer circulation and retention times as compared to other Gd chelates and could be eliminated from the body within a reasonable period of time after performing their diagnostic function [13].

Additionally, Terreno's group reported the use of paramagnetic liposomes as contrast agents for monitoring the processes of drug delivery and release by MRI. Their formulation of liposome-loaded Gd chelates was proposed to allow the fast and full release of Gd chelates at pH 5.5 in endosomes using pH-sensitive liposomes. As a result, Gd-chelated contrast agents were released faster from pH-sensitive liposomes; this release was dependent on the reduction in pH. The image showed the highest intensity at pH 5.5 due to increased opportunity for contact with water molecules [14].

Unlike the widely used paramagnetic Gd chelates, the nanostructures of SPIOs composed of maghemite or magnetite crystals less than 20 nm in diameter contain thousands of Fe atoms and approach saturation magnetisation under a magnetic field typical. Each nanocrystal can generate signal contrast several orders of magnitude greater than a Gd chelate. Additionally, iron oxides have little known toxicity in in vivo applications. For these reasons, SPIOs have been researched extensively over the past two decades as a popular type of MRI contrast agent. However, general SPIOs have a short blood circulation half-life, especially in mice, which leads to their nonspecific uptake by cells in the blood, including macrophages. To increase the circulation and signal sensitivity of SPIOs for the in vivo imaging of molecular markers, their core must be coated with special functional moieties such as amphiphilic polymers or tumour-targeting ligands. SPIOs that circulate for longer may have an increased
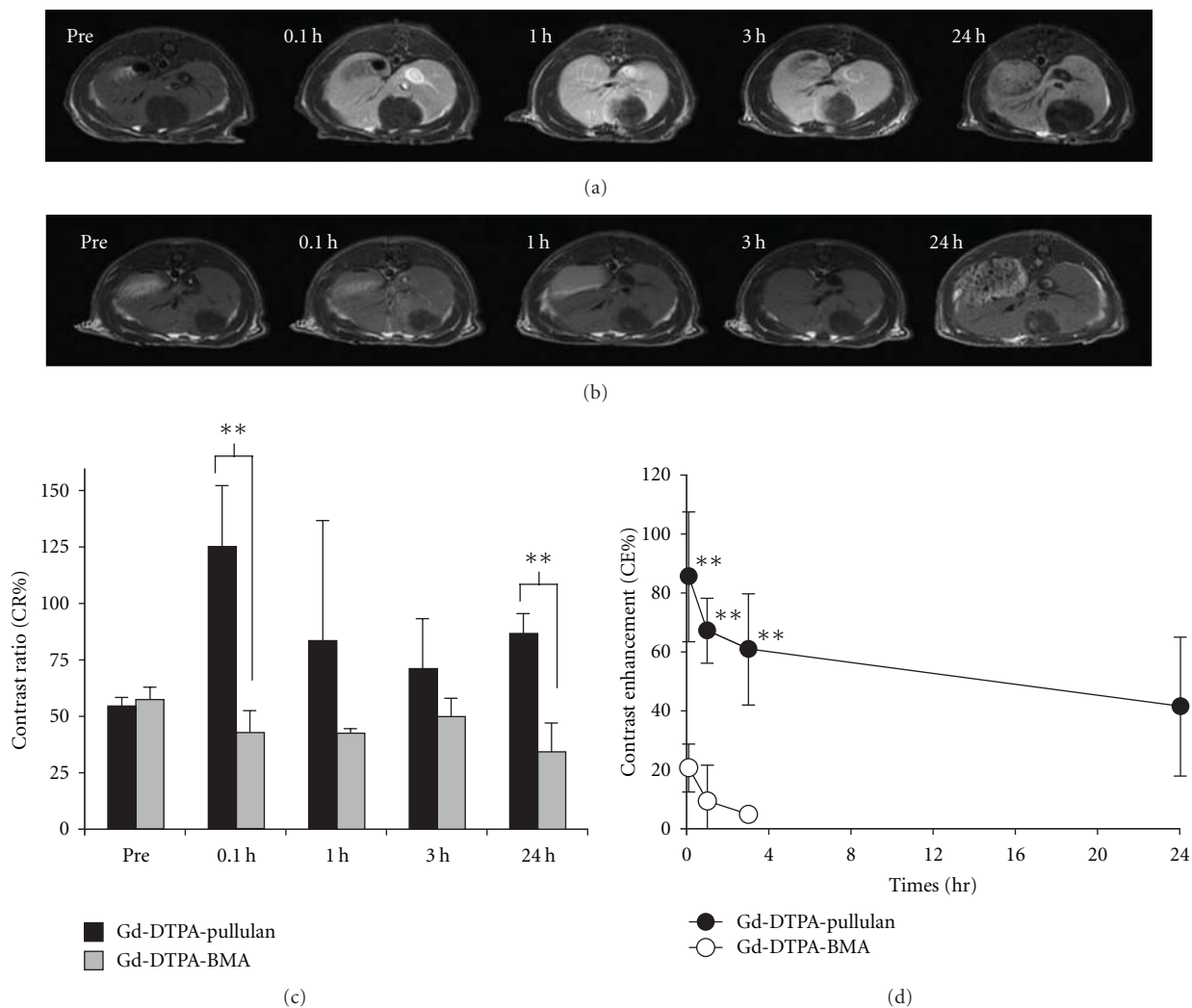
FIGURE 1: (a) and (b), time-dependent MR images of HCC rats after IV injection of Gd-DTPA-pullulan (a) and Gd-DTPA-BMA (b). (c), contrast ratio (CR) of Gd-DTPA-pullulan and Gd-DTPA-BMA; the CR is the relative contrast of hepatic lesion to normal region. (d), contrast enhancement (CE) of Gd-DTPA-pullulan and Gd-DTPA-BMA; the CE was calculated from the contrast ratio of the normal liver region between pre- and postinjection. Data are expressed as the mean ± s.d ($n = 4$), ($**P < 0.01$, $***P < 0.001$ with unpaired t-test) (see [5]).

chance of binding to the target molecules and thus produce enhanced contrast effect. However, most of the magnetic field surrounding coated SPIOs falls within the coating. Therefore, the coating molecules of SPIOs can expel water from their surface, hinder water diffusion, or immobilise nearby water molecules by forming hydrogen bonds; all these abilities may affect the nuclear relaxation of water protons. To prevent this interference, a dual solvent-exchange method has been employed to coat nanocrystals with small amphiphilic molecules, such as poloxamer and hydrophobically modified PEG [15, 16].

Tong et al. focused on a versatile coating method to generate an array of water-soluble SPIOs with different core sizes and coating thicknesses for signal enhancement. Using a dual solvent-exchange method, iron oxide cores were coated with a 1,2-distearoyl-sn-glycero-3-phosphoethanolamine-N-[methoxy (polyethylene glycol)] copolymer (DSPE-mPEG)

in which amphiphilic DSPE-mPEG on the hydrophobic surface of a nanocrystal can be induced by enhancing the polarity of solvent systems, which results in increased water solubility of SPIOs (Figure 2). The resulting DSPE-mPEG coating is stable and versatile and offers an optimal shell/core ratio. DSPE-mPEG-coated SPIO nanocrystals can increase the intensity of iron oxide under the optimal conditions by controlling the size and thickness of iron oxide [16].

Chertok et al. also reported the use of PEGylated silane-coated magnetic iron oxide nanoparticles to enhance MRI contrast in tumours. After intravenous injection, greater accumulation of colloidal stable PEGylated magnetic nanoparticles in the 40 nm size range was observed in murine tumours as compared to those in the 20 nm size range [17].

In addition to size control, surface modification by conjugation with specific ligands is of critical importance in

(a) Chloroform

(b) DMSO

(c) Water

(d)

(e)
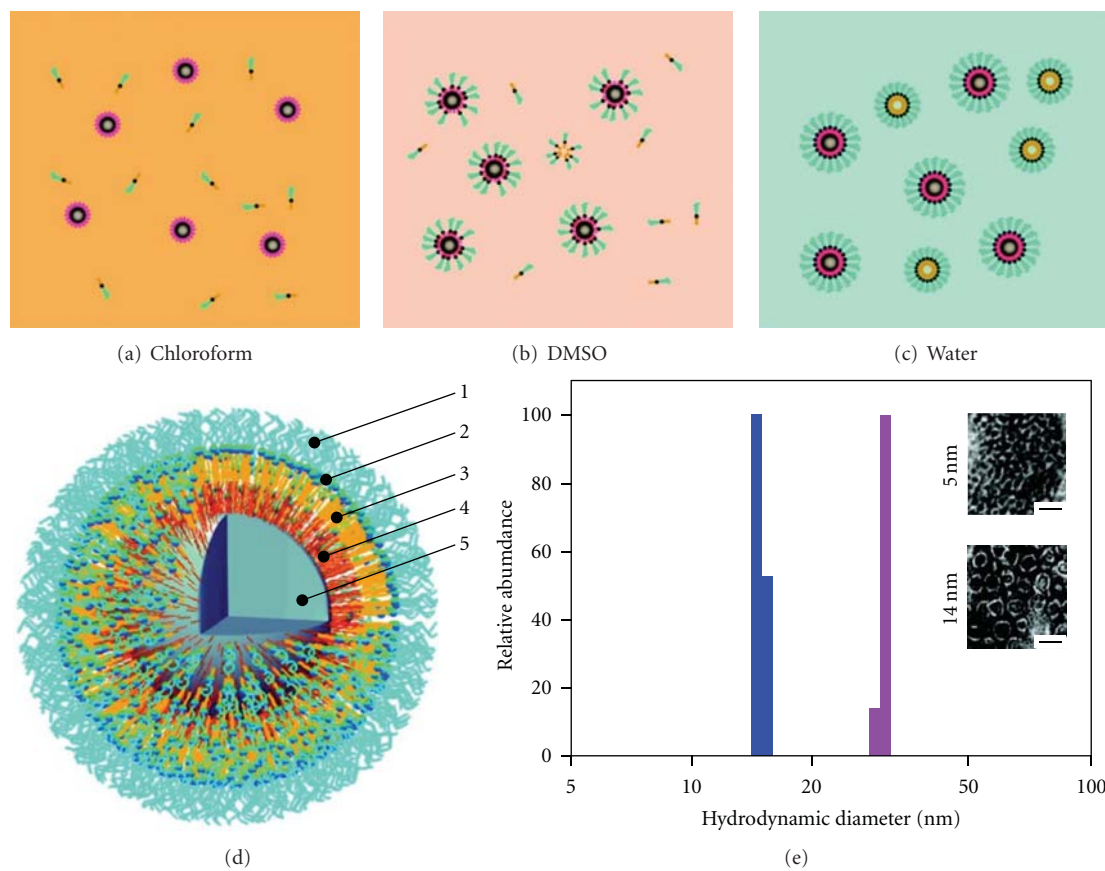
FIGURE 2: Schematic diagram of the SPIO synthesis and coating. (a) Both iron oxide cores and DSPE-PEG are dissolved in chloroform. (b) The addition of DMSO induces assembly between iron oxide cores and DSPE-PEG molecules. (c) The transition into water further strengthens the hydrophobic interaction between DSPE-PEG and oleic acid/oleylamine on the iron oxide cores. Due to its extremely low critical micelle concentration ($\sim 5\,\mu M$ in water), unoccupied DSPE-PEG exists mainly in the form of empty micelles. (d) A schematic diagram of a SPIO with a 4.8-nm iron oxide core and DSPE-mPEG1000 coating. Layers 1 through 5 represent PEG, phosphate, DSPE, oleic acid/oleylamine, and the iron oxide core, respectively. The dimensions are based on transmission electron microscopy (TEM) measurements and numerical analysis (supporting information, SII and SIII). (e) Dynamic light scattering of the SPIOs coated with DSPE-mPEG1000: blue, number-weighted size distribution of 5 nm iron oxide core coated with DSPE-mPEG1000, average size 14.8 (1.2 nm; purple, 14 nm iron oxide core coated with DSPE-mPEG1000, average size) 28.6 (0.4 nm). Shown in the inset are TEM images of coated SPIOs negatively stained with phosphotungstic acid to yield a white layer surrounding the iron oxide cores that indicate the DSPE-mPEG1000 coating layer (see [16]).

determining the pharmacokinetic profile of the iron oxide nanoparticles and the success of in vivo targeting. Among the neoplastic markers, integrin $\alpha_v \beta_3$, a cell adhesion molecule, plays a vital role in tumour angiogenesis and metastasis. Arginine-glycine-aspartic acid (RGD) peptide sequences are well known as specific probes for integrin targeting. RGD-iron oxide nanoparticle conjugates have been developed for integrin targeting. Chen's group reported the use of iron oxide nanoparticles-RGD conjugates coated with a PEGylated amphiphilic triblock copolymer composed of segments of polybutylacrylate, polyethylacrylate, polymethacrylic acid, octylamine, and a hydrophobic hydrocarbon side chain for tumour integrin targeting and MRI. A triblock copolymer was subsequently coated onto the particle surface, which resulted in a bilayer coating with multiple amine-terminated PEG chains exposed outside. Thus, a triblock copolymer renders the iron oxide-RGD nanoparticles water soluble.

Such a phase transfer is straightforward with high throughput and high yield. Clear tumour contrast was observed by MRI with RGD-triblock PEGylated iron oxide nanoparticles, indicating successful RGD-integrin governed tumour targeting and remarkably limited hepatic uptake [18]. PEGylated iron oxide-RGD conjugates showed excellent tumour integrin binding efficiency and specificity as well as limited reticuloendothelial system (RES) uptake for molecular MRI. In summary, size control and functional surface modification easily increases the intensity and efficacy of the contrast agent for diagnosis.

The gadolinium hybrid nanoparticulate MRI contrast agents also have been reported as gadolinium oxide [19], gadolinium fluoride [20], and gadolinium phosphate [21], are different from gadolinium chelate compound. Gadolinium hybrid MRI contrast agents, which were composed of a gadolinium oxide core, show a higher signal-to-noise ratio

and a better anatomic resolution in T1-weighted images due to having nanoparticulate shapes, lower r_2/r_1 values. These nanoparticles were dispersed in aqueous phase [21].

Olivier Tillement group have been offered contrast agent, which gadolinium oxide core embedded in a polysiloxane shell. This contrast agent is functionalized by organic dyes at inner phase and shielded by PEG at outer phase and is well appropriated in vivo dual modality magnetic resonance and fluorescence imaging. The hydrodynamic diameter is 8.9 nm, and core size is 4.6 nm. These hybrid gadoliniums are able to circulate in the vessels without aggregation since no uptake was observed in the liver, and the particles were naturally eliminated by renal excretion due to small size [22].

GdF_3 nanoparticles were conjugated with 2-aminoethyl phosphate group (GdF_3/LaF_3: AEP) or citrate group (GdF_3: cit) [20]. The surface of gadolinium nanoparticles has been shown positive or negative charge by outer group. Dextran-coated $GdPO_4$ nanoparticles (PGP/dextran-K01) were synthesized by a hydrothermal process in the presence of dextran [21]. The advantage of these gadolinium hybrid nanoparticulate MRI contrast agents is higher solubility, higher relaxivity than chelated gadolinium at identical gadolinium concentration [23].

3. Multimodal MRI Contrast Agent: Fluorescence, CT, and PET

Multimodal contrast agents can provide more accurate and detailed information associated with diseases than single contrast agents. MRI is able to achieve deep penetration of light into tissues and provide anatomical details and high quality 3D images of soft tissue [6, 24] but exhibits lower sensitivity than radioactive or optical methods. In contrast, FI has much higher sensitivity and potential for real-time imaging, but it has limited depth perception [25]. As a consequence, intensive attempts have been made to develop MRI-FI nanoprobes due to their prominent advantages for medical diagnosis.

Hoshino et al. reported a simple and versatile method to develop dual modality nanoprobes by incorporating paramagnetic Gd ions onto surface modified-quantum dots (QDs) with zinc oxide nanocrystals. Surface modification of QDs is essential to prevent self-aggregation and loss of luminescence in the intracellular environment or under isotonic conditions. However, these molecules are excellent candidates for organic fluorophores based on their high luminescence, stability against photobleaching, and a range of fluorescence wavelengths from blue to infrared depending on particle size [26]. The typical transmission electron microscopy (TEM) images in Figures 3(a) and 3(b) depicted the diameters of ZnO QDs and Gd-doped ZnO QDs ($x = 0.08$) as approximately 6 nm and 4 nm, respectively. Nevertheless, in the sample with a higher Gd concentration ($x = 0.3$), the particles were so small that they could not be seen clearly (Figure 3(c)). Meanwhile, selected area electron diffraction analysis presented similar patterns for ZnO QDs and Gd-doped ZnO QDs ($x = 0.08$ and 0.3), and all the diffraction rings could be indexed to wurtzite ZnO. The high resolution

TEM images shown in Figures 3(d) and 3(e) revealed lattice fringes with a spacing of approximately 0.26 nm for both ZnO QDs and Gd-doped ZnO QDs ($x = 0.08$), which was very consistent with the lattice spacing in the (0.02) planes of the ZnO wurtzite phase. This result suggests that Gd doping did not induce any significant lattice distortions of ZnO QDs. However, when x increased to 0.3, the crystallinity of the ZnO QDs became so weak that no clear lattice fringe could be observed (Figure 3(f)). These properties of Gd-doped ZnO QDs are allowed to function as effective dual modal imaging nanoprobes due to their effect on the T1 relaxation time, and they remain high viability even at a high dose of QDs [25]. Although many efforts have been made to reduce the intrinsic toxicity and maintain the long-term photostability of QDs by conjugation with paramagnetic agents or in combination with dye-doped silica and SPIOs as multimodal imaging probes, the size control problem remained an issue because their fluorescence sensitivity depends on particle size. To solve the problem, the Hyeon group reported the combination of QDs and upconverting nanoparticles (UCNPs) such as $NaYF4 : Yb3^+$, $Er3^+$ and $NaYF4 : Yb3^+$, $Tm3^+$ to yield bimodal imaging probes that can provide the high sensitivity and resolution of fluorescence imaging as well as the noninvasive and real-time monitoring abilities of MRI. As UCNPs absorb near-infrared (NIR) photons and emit visible or near-UV photons, optical imaging with these nanoparticles has several advantages over conventional fluorescence imaging: (1) the signal-to-noise ratio and detection sensitivity are improved because autofluorescence is absent; (2) in vivo imaging is facilitated by deep penetration of noninvasive NIR excitation; (3) photodamage to living organisms is very low. Unlike other nanocomposites that exhibit multimodality, UCNPs work alone and do not require the addition of any other moieties. The deep penetration depth of NIR excitation, excellent photostability, and absence of autofluorescence of UCNPs make them suitable for applications such as targeting of tumour tissues in vivo and long-term cellular and/or animal imaging [27].

The X-ray, CT imaging widely used for diagnosis, generates accurate and bright images. However, it is necessary to administer a contrast agent. These agents include iodinated molecules [28, 29] that have rapid pharmacokinetics and high viscosity, which most likely leads to allergic reaction. Many alternatives to iodinated contrast have recently been developed to overcome these intrinsic problems. Gold-encapsulated Gd chelate nanoparticles are considered alternative contrast agents for medical imaging because the properties of gold nanoparticles include a relatively longer vascular half-life than other molecular contrast agents. Taken together, gold nanoparticles combined with fluorescence imaging and MRI are probably the most frequently studied because they join the high sensitivity of the fluorescence phenomenon with the increased spatial resolution of MRI. Alric's group reported that the gold-encapsulated Gd chelates, which have a multilayered organic shell, bound to each other through disulphide bonds for both X-ray, CT and MRI. The contrast enhancement in the MRI resulted from the presence of Gd ions trapped in the organic shell, whereas

(a)

(d)

(b)

(e)

(c)

(f)
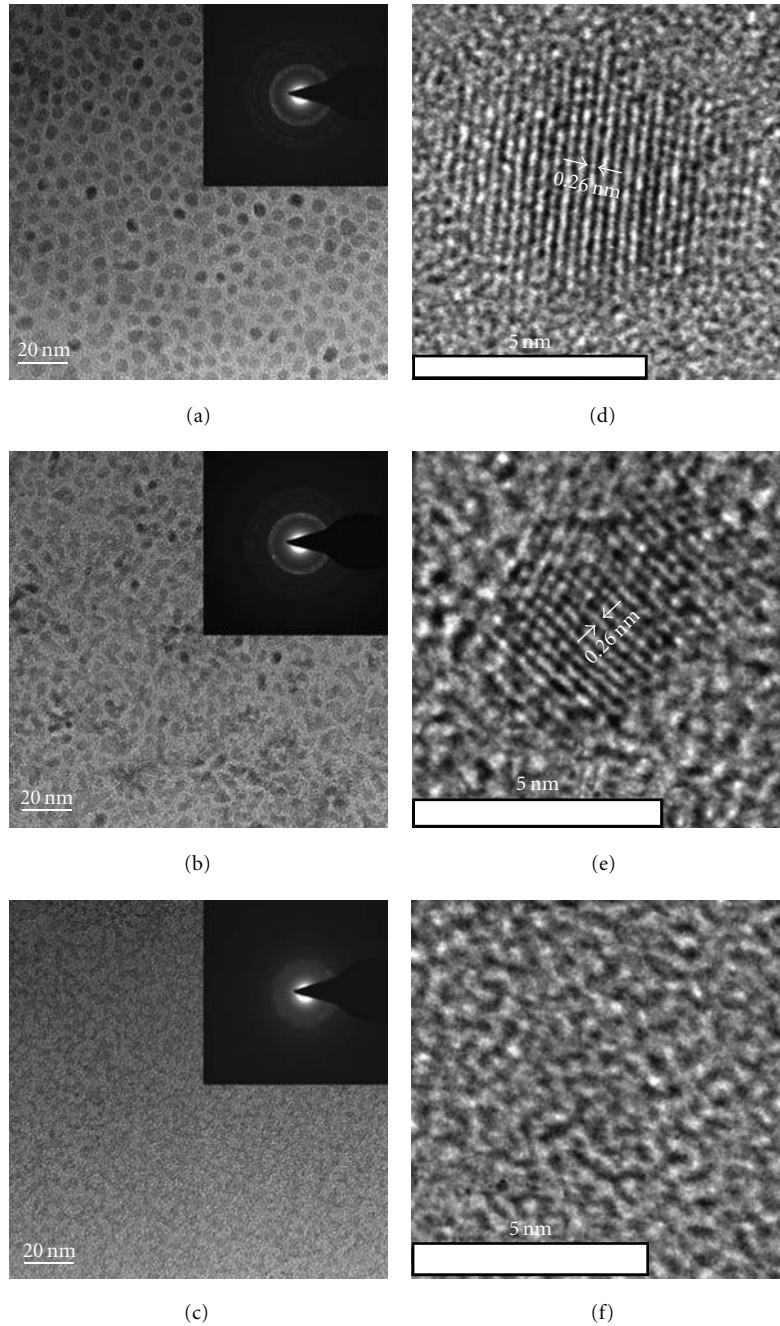
FIGURE 3: (a)–(c) TEM images of Gd-doped ZnO QDs with $x = 0$, 0.08 and 0.3. The insets show the corresponding electron diffraction patterns. (d)–(f) High-resolution TEM images of Gd-doped ZnO QDs with $x = 0$, 0.08 and 0.3 (see [48]).

the gold core provided strong X-ray absorption. The results revealed that the Gd-bound gold nanoparticles used for dual modality imaging freely circulate in the blood vessels without undesirable uptake by macrophages [30].

PET is an analytical imaging tool that uses signals emitted by compounds labelled with positron-emitting radioisotopes such as fluorine-18 as molecular probes to image and measures biochemical processes of mammalian biology in vivo. Advances in PET using established imaging tools have resulted in spatial resolution greater than 2 mm [31, 32].

However, it may still be impossible to accurately localize an area of increased activity using PET images alone due to the absence of identifiable anatomical structures, particularly in the abdomen. Although a simultaneous PET/CT scanner that precisely and simultaneously registers functional data from PET and anatomical image from CT is used to solve the limitations on a routine basis in clinical oncology, the intrinsic functional resolution restrictions of PET and PET/CT remain the same. In addition to accurate functional and anatomical localization, highly accurate image registration, which can be

provided by MRI, is required to correct PET partial volume effects and aid in PET image reconstruction. Compared with PET/CT, PET/MRI has the advantage of greatly reducing radiation exposure. Polyaspartic acid-coated iron oxide nanoparticles conjugated with cyclic RGD peptides and the macrocyclic chelating agent 1,4,7,10-tetraazacyclododecane-N,N′,N″,N‴,-tetraacetic acid (DOTA) for integrin $\alpha_v\beta_3$ recognition and positron-emitting radionuclide ^{64}Cu (half-life [$t_{1/2}$] = 12.7 h) labelling were prepared for dual PET/MRI of tumour integrin $\alpha_v\beta_3$ expression in vivo. This bifunctional imaging approach to PET/MRI may allow for earlier tumour detection with a high degree of accuracy and provide further insight into the molecular mechanisms of cancer [33].

Jeongsoo Yoo and his coworkers developed magnetism-engineered iron oxide (MEIO) with a composition of $MnFe_2O_3$ (MnMEIO), which has exceptionally high MRI contrast effects. They also prepared serum albumin (SA)-coated MnMEIO nanoparticles conjugated with ^{124}I ($t_{1/2}$ = 4.2 days, β^+ 23%) (^{124}I-SA-MnMEIO) as molecular nanoprobes for dual modality PET/MRI because the T2 relaxivity coefficient is two or three times better than that of conventional iron oxide-based SPIO probes (Figure 4). The accurate positioning of brachial lymph nodes (LN) was achieved when PET and MRI were overlaid. Two different types of LNs could be clearly identified and accurately localized in a PET/MR fusion image as a result of the highly complementary nature of the PET and MRI techniques [34].

Recently, PET/MRI/near-infrared fluorescence (NIRF) trimodality imaging contrast agents have been researched to gain precise information about diseases [35]. For example, serum albumin(SA)-coated iron oxide nanoparticles dually labelled with ^{64}Cu-DOTA and Cy5.5 were tested in a subcutaneous U87MG xenograft mouse model. With the compact SA coating, the nanoparticles demonstrated a prolonged circulation half-life, and they also showed massive accumulation in lesions, a high extravasation rate, and low uptake of the nanoparticles by macrophages at the tumour area. The MRI contrast agents combined with other techniques have been developed to increase the sensitivity around the disease region. Furthermore, with instrument development of the diagnostic hardware, advances in nanoparticle-based probes are a prerequisite for successful multimodal diagnosis.

4. Multifunctional MRI Contrast Agent: Drug Delivery and Cell Tracking

Multifunctional MRI contrast agents loaded with drugs have received considerable attention as attractive carriers for diagnosis and therapy.

The magnetic nanoparticle can serve as both a contrast agent for MRI and a drug carrier for delivery. Nanoparticles have been designed to possess specific properties, including highly accurate targeting to specific regions containing the cell types of interest [36–38]. For example, after anticancer drug-loaded SPIO nanoparticles conjugated with specific ligands are injected into an intravenous vessel, the nanoparticles can easily reach the tumour area by systemic delivery

with specific ligands and simultaneously release the anticancer drugs at the tumour sites. Additionally, the process can be monitored in real time by MRI contrast agents.

The pH-triggered system is currently one of the most extensively studied stimulus systems for cancer therapy because the increased aerobic glycolysis, or the Warburg effect, in cancer cells leads to the lower extracellular pH of cancer cells (pH 6.5 to 7.2). Based on this system, anti-HER2/neu (HER: herceptin) antibody-modified pH-sensitive drug-delivering magnetic nanoparticles (HER-DMNP) were investigated as a prototype of theragnosis for effective cancer therapy guided by molecular imaging [39]. The nanoparticles are delivered to herceptin and release the anticancer drug (i.e., doxorubicin, DOX) because of the low extracellular pH (Figure 5). Simultaneously, the magnetic nanoparticles serve as MRI contrast agents to show a vivid contrast image [40].

Additionally, the magnetic particles can be designed for hyperthermia in cancer treatment in the magnetic field and degraded into nontoxic iron ions in vivo [41–43]. Thermally cross-linked SPIO nanoparticles (TCL-SPIONs) coated with protein- or cell-resistant polymers serve as MRI contrast agents and induce the anticancer effect in the magnetic field. TCL-SPIONs reduced the side effects when compared to free DOX because of the excellent cancer targeting efficiency created by the enhanced permeability and retention (EPR) effect. The antibiofouling polymer-coated TCL-SPIONs can circulate long term in the vascular system by escaping from uptake by RES. After administering the coated TCL-SPIONs into tumour xenograft mice by intravenous injection, the tumour could be detected by T2-weighted MRI within 1 h as a result of the accumulation of nanomagnets within the tumour site. Consequently, TCL-SPIONs have been developed as multifunctional smart agents for theragnosis [42, 44, 45].

A nanostructured multifunctional smart MRI contrast agent is also suitable and effective as a drug carrier for a variety of chemotherapeutic agents [46, 47].

The visualisation of transplanted stem cells with a noninvasive technique is essential for cell implantation. MRI may be the best technique for cell tracking based on its high spatial and temporal resolution and free selection of the imaging plane. For MRI observation, stem cells must be marked by magnetic labelling to distinguish them from existing cells in the organ. Despite several trials of modifications of SPIONs via linking to peptides or monoclonal antibodies, the results lead to some potential problems, technical complexity, and poor availability in cell labelling procedures. Liu et al. reported the development of low-molecular-weight polyethylenimine (PEI)/SPIO nanocomposites with efficient cell-labelling capability. PEI-wrapped magnetic nanoparticles easily interacted with cell membranes of stem cells and were monitored with a clinical 3T MRI system [48] (Figure 6).

Gd-based contrast agents are also suitable for the monitoring and fate mapping of stem cells in a T1-weighted image. Dong-Ming Huang's group studied the use of dual functional mesoporous silica nanoparticles (MSNs) conjugated with fluorescent isothiocyanate and Gd chelates (Gd-Dye MSNs) for stem cell tracking and high contrast efficacy. Stem cells

(a)

(b)
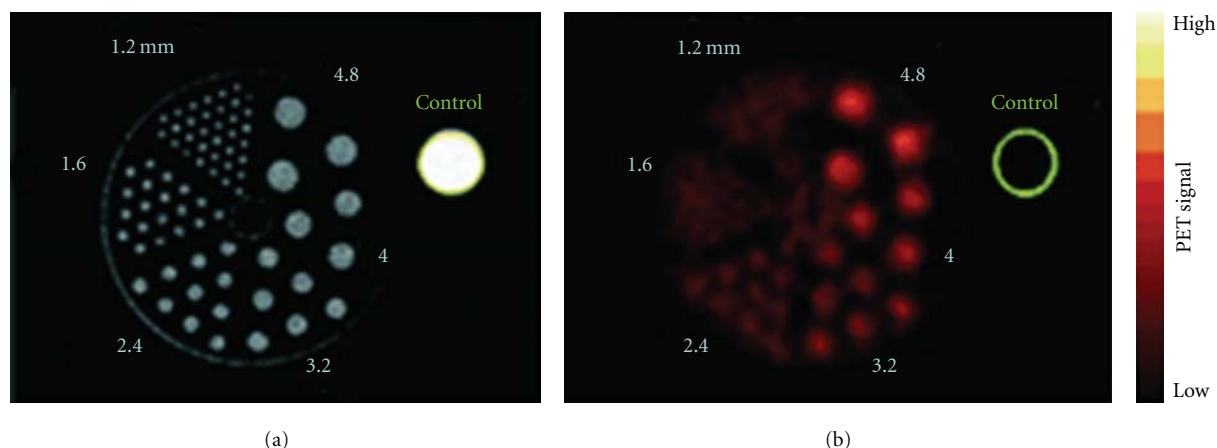
FIGURE 4: Comparison of spatial resolution of (a) MRI and (b) PET techniques with a Derenzo phantom (circle diameters of 1.2, 1.6, 2.4, 3.2, 4.0, and 4.8 mm), which contains the contrast agents MnMEIO (50 μg mL^{-1} (Mn+Fe)) and 124I (2.5 μCi mL^{-1}); yellow circle: water (control). MnMEIO: Mn-doped magnetism-engineered iron oxide (see [34]).

(a)

(b)
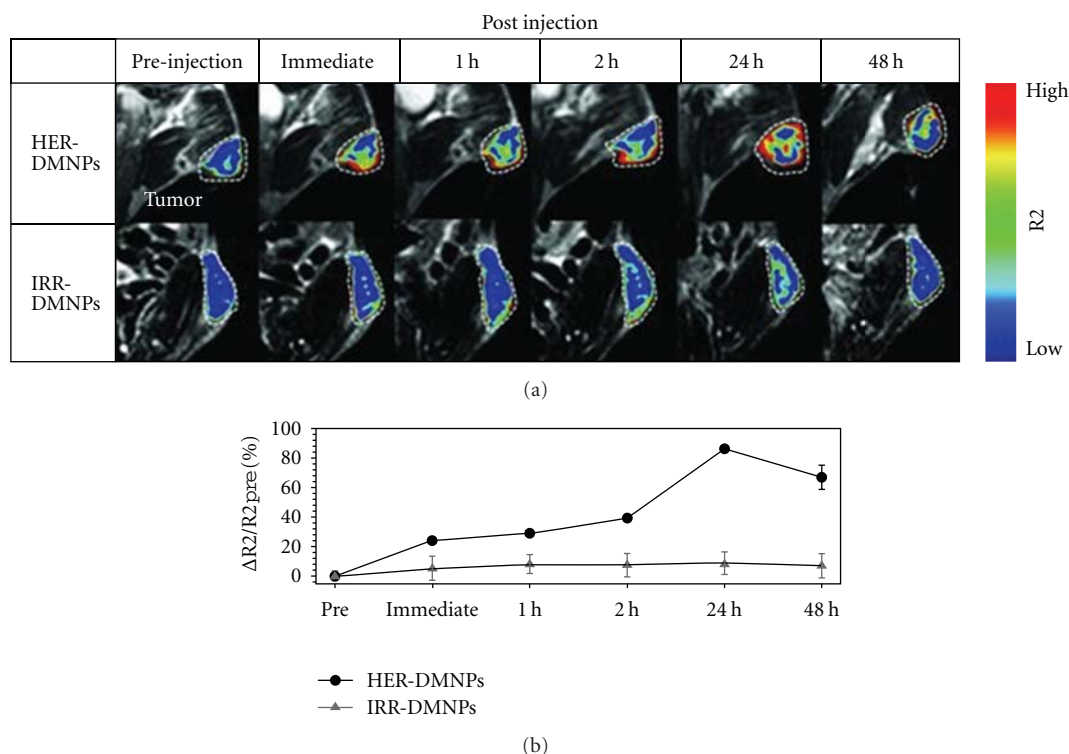
FIGURE 5: (a) Color-coded T2-weighted MR images of tumor-bearing mice after the intravenous injection of HER-DMNPs and IRR-DMNPs at various time intervals, respectively. Tumor regions are indicated with a white dashed boundary. (b) ΔR2/R2 Pre graph versus time after the injection of HER-DMNPs (black circle) and IRR-DMNPs (gray triangle) (see [40]).

labelled with Gd-Dye MSNs in an endocytosis-mediated manner were detected with a 1.5T MRI for at least 14 days. Gd-Dye MSNs did not affect cytotoxicity, growth, or differentiation of hMSCs [49].

Song et al. described Gd-enriched polyvalent DNA-gold nanoparticle conjugates (DNA-AuNPs) with the ability to efficiently penetrate cells and accumulate to a level that provides sufficient contrast enhancement for the imaging of small cell populations with microsized Gd incubation concentrations. Moreover, labelling of the conjugates with a fluorescent dye permitted multimodal imaging to confirm cellular uptake and intracellular accumulation and provide a means for histological validation. These particles exhibit a high loading efficiency of Gd, a 50-fold increase in cellular uptake compared to the commercial Gd-DOTA, and relatively high relaxivity [50].

(a)

(d)

(b)

(e)

(c)

(f)
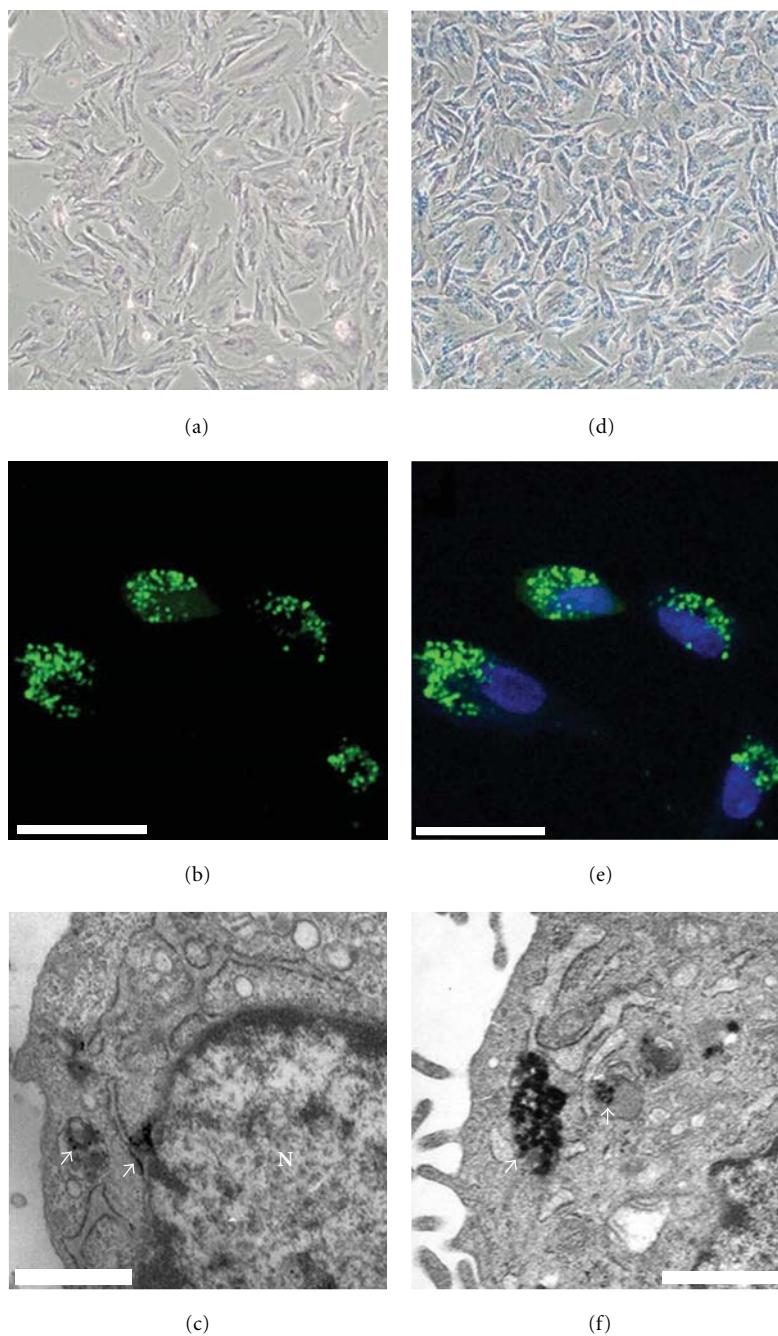
FIGURE 6: Mesenchymal stem cells (MSCs) labeled with alkyl-PEI/SPIO nanocomposites. Prussian blue staining of unlabeled MSCs (a) and SPIO-labeled MSCs (b) (7 mg Fe/mL, 24 h). The morphology of these SPIO-labelled MSCs is not changed, and blue granules were evident in the cytoplasm around the nuclei; CLSM investigation of the SPIO-labeled MSCs before (c) and after merging with nuclei (d). Electron microscopy of cells labelled with SPIO probes (arrows) (e, f). Magnification (a, b), scale bar 1/4 10 mm (c, d), scale bar 1/4 50 nm (e), scale bar 1/4 100 nm (f) (see [48]).

5. Conclusion

Functionally modified MRI contrast agents with enhanced intensity and sensitivity may improve diagnostic technique as well as therapeutic efficacy. Additionally, the use of multimodal contrast agents with other types of imaging tools can maximize their prominent advantages and compensate for their intrinsic disadvantages to provide excellent diagnostic images with anatomical and functional information.

Also, the safety of contrast agent should be considered to overcome its limit of use in clinic. In previous study, contrast agent does not cause side effects in normal patients whereas generates serious nephrogenic system fibrosis (NSF) in patient with failure kidney. NFS is emerging systemic

disordered character by widespread tissue fibrosis [5]. The body clearance ways and distribution of MRI contrast agent is one to the very important topic in use of contrast agent to reduce the side effect. For this reason, contrast agent should be designed to be able to perfectly remove from body through kidney and bile without accumulation in body and not separated into free gadolinium from chelated compounds.

The development of contrast agents has been accelerated with advance of several nanotechnologies over the past decade. Contrast agents that use new nanotechnology must continue to increase their theranostic efficiency and safety in clinical and research applications.

Acknowledgments

References

[1] J. Kim, Y. Piao, and T. Hyeon, "Multifunctional nanostructured materials for multimodal imaging, and simultaneous imaging and therapy," *Chemical Society Reviews*, vol. 38, no. 2, pp. 372–390, 2009.

[2] L. Frullano and T. J. Meade, "Multimodal MRI contrast agents," *Journal of Biological Inorganic Chemistry*, vol. 12, no. 7, pp. 939–949, 2007.

[3] G. M. Lanza, P. M. Winter, S. D. Caruthers et al., "Magnetic resonance molecular imaging with nanoparticles," *Journal of Nuclear Cardiology*, vol. 11, no. 6, pp. 733–743, 2004.

[4] M. A. Hahn, A. K. Singh, P. Sharma, S. C. Brown, and B. M. Moudgil, "Nanoparticles as contrast agents for in-vivo bioimaging: current status and future perspectives," *Analytical and Bioanalytical Chemistry*, vol. 399, no. 1, pp. 3–27, 2011.

[5] H. Yim, S.-G. Yang, Y. S. Jeon et al., "The performance of gadolinium diethylene triamine pentaacetate-pullulan hepatocyte-specific T1 contrast agent for MRI," *Biomaterials*, vol. 32, no. 22, pp. 5187–5194, 2011.

[6] C. Sun, J. S. H. Lee, and M. Zhang, "Magnetic nanoparticles in MR imaging and drug delivery," *Advanced Drug Delivery Reviews*, vol. 60, no. 11, pp. 1252–1265, 2008.

[7] D. H. Carr, J. Brown, and G. M. Bydder, "Gadolinium-DTPA as a contrast agent in MRI: initial clinical experience in 20 patients," *American Journal of Roentgenology*, vol. 143, no. 2, pp. 215–224, 1984.

[8] C. H. Reynolds, N. Annan, K. Beshah et al., "Gadolinium-loaded nanoparticles: new contrast agents for magnetic resonance imaging," *Journal of the American Chemical Society*, vol. 122, no. 37, pp. 8940–8945, 2000.

[9] X. Montet, K. Montet-Abou, F. Reynolds, R. Weissleder, and L. Josephson, "Nanoparticle imaging of integrins on tumor cells," *Neoplasia*, vol. 8, no. 3, pp. 214–222, 2006.

[10] C. J. Sunderland, M. Steiert, J. E. Talmadge, A. M. Derfus, and S. E. Barry, "Targeted nanoparticles for detecting and treating cancer," *Drug Development Research*, vol. 67, no. 1, pp. 70–93, 2006.

[11] C. Zhang, M. Jugold, E. C. Woenne et al., "Specific targeting of tumor angiogenesis by RGD-conjugated ultrasmall superparamagnetic iron oxide particles using a clinical 1.5-T magnetic resonance scanner," *Cancer Research*, vol. 67, no. 4, pp. 1555–1562, 2007.

[12] M. R. Rekha and C. P. Sharma, "Pullulan as a promising biomaterial for biomedical applications: a perspective," *Trends in Biomaterials and Artificial Organs*, vol. 20, no. 2, pp. 111–116, 2007.

[13] Z. Cheng, D. L. J. Thorek, and A. Tsourkas, "Gadolinium-conjugated dendrimer nanoclusters as a tumor-targeted T1 magnetic resonance imaging contrast agent," *Angewandte Chemie - International Edition*, vol. 49, no. 2, pp. 346–350, 2010.

[14] E. Torres, F. Mainini, R. Napolitano et al., "Improved paramagnetic liposomes for MRI visualization of pH triggered release," *Journal of Controlled Release*, vol. 154, no. 2, pp. 196–202, 2011.

[15] S. S. Yu, R. L. Scherer, R. A. Ortega et al., "Enzymatic- and temperature-sensitive controlled release of ultrasmall superparamagnetic iron oxides (USPIOs)," *Journal of Nanobiotechnology*, vol. 9, article 7, 2011.

[16] S. Tong, S. Hou, Z. Zheng, J. Zhou, and G. Bao, "Coating optimization of superparamagnetic iron oxide nanoparticles for high T2 relaxivity," *Nano Letters*, vol. 10, no. 11, pp. 4607–4613, 2010.

[17] B. Chertok, A. E. David, and V. C. Yang, "Polyethyleneimine-modified iron oxide nanoparticles for brain tumor drug delivery using magnetic targeting and intra-carotid administration," *Biomaterials*, vol. 31, no. 24, pp. 6317–6324, 2010.

[18] K. Chen, J. Xie, H. Xu et al., "Triblock copolymer coated iron oxide nanoparticle conjugate for tumor integrin targeting," *Biomaterials*, vol. 30, no. 36, pp. 6912–6919, 2009.

[19] M. A. McDonald and K. L. Watkin, "Investigations into the physicochemical properties of dextran small particulate gadolinium oxide nanoparticles," *Academic Radiology*, vol. 13, no. 4, pp. 421–427, 2006.

[20] F. Evanics, P. R. Diamente, F. C. J. M. Van Veggel, G. J. Stanisz, and R. S. Prosser, "Water-soluble GdF3 and GdF3/LaF3 nanoparticles—physical characterization and NMR relaxation properties," *Chemistry of Materials*, vol. 18, no. 10, pp. 2499–2505, 2006.

[21] H. Hifumi, S. Yamaoka, A. Tanimoto, D. Citterio, and K. Suzuki, "Gadolinium-based hybrid nanoparticles as a positive MR contrast agent," *Journal of the American Chemical Society*, vol. 128, no. 47, pp. 15090–15091, 2006.

[22] J. L. Bridot, A. C. Faure, S. Laurent et al., "Hybrid gadolinium oxide nanoparticles: multimodal contrast agents for in vivo imaging," *Journal of the American Chemical Society*, vol. 129, no. 16, pp. 5076–5084, 2007.

[23] J. L. Bridot, D. Dayde, C. Rivière et al., "Hybrid gadolinium oxide nanoparticles combining imaging and therapy," *Journal of Materials Chemistry*, vol. 19, no. 16, pp. 2328–2335, 2009.

[24] C. F. G. C. Geraldes and S. Laurent, "Classification and basic properties of contrast agents for magnetic resonance imaging," *Contrast Media and Molecular Imaging*, vol. 4, no. 1, pp. 1–23, 2009.

[25] Y. Liu, K. Ai, Q. Yuan, and L. Lu, "Fluorescence-enhanced gadolinium-doped zinc oxide quantum dots for magnetic resonance and fluorescence imaging," *Biomaterials*, vol. 32, no. 4, pp. 1185–1192, 2011.

[26] A. Hoshino, K. Fujioka, T. Oku et al., "Physicochemical properties and cellular toxicity of nanocrystal quantum dots

depend on their surface modification," *Nano Letters*, vol. 4, no. 11, pp. 2163–2169, 2004.

[27] Y. I. Park, J. H. Kim, K. T. Lee et al., "Nonblinking and nonbleaching upconverting nanoparticles as an optical imaging nanoprobe and T1 magnetic resonance imaging contrast agent," *Advanced Materials*, vol. 21, no. 44, pp. 4467–4471, 2009.

[28] J. M. Idee, I. Nachman, M. Port et al., "Iodinated contrast media: from non-specific to blood-pool agents," in *Contrast Agents II*, pp. 151–171, Springer, Berlin, Germany, 2002.

[29] W. Krause and P. Schneider, "Chemistry of X-ray contrast agents," in *Contrast Agents II*, pp. 107–150, Springer, Berlin, Germany, 2002.

[30] C. Alric, J. Taleb, G. Le Duc et al., "Gadolinium chelate coated gold nanoparticles as contrast agents for both X-ray computed tomography and magnetic resonance imaging," *Journal of the American Chemical Society*, vol. 130, no. 18, pp. 5908–5915, 2008.

[31] S. S. Gambhir, "Molecular imaging of cancer with positron emission tomography," *Nature Reviews Cancer*, vol. 2, no. 9, pp. 683–693, 2002.

[32] W. A. Weber, "Use of PET for monitoring cancer therapy and for predicting outcome," *Journal of Nuclear Medicine*, vol. 46, no. 6, pp. 983–995, 2005.

[33] H. Y. Lee, Z. Li, K. Chen et al., "PET/MRI dual-modality tumor imaging using arginine-glycine-aspartic (RGD)-conjugated radiolabeled iron oxide nanoparticles," *Journal of Nuclear Medicine*, vol. 49, no. 8, pp. 1371–1379, 2008.

[34] J. S. Choi, J. C. Park, H. Nah et al., "A hybrid nanoparticle probe for dual-modality positron emission tomography and magnetic resonance imaging," *Angewandte Chemie - International Edition*, vol. 47, no. 33, pp. 6259–6262, 2008.

[35] J. Xie, K. Chen, J. Huang et al., "PET/NIRF/MRI triple functional iron oxide nanoparticles," *Biomaterials*, vol. 31, no. 11, pp. 3016–3022, 2010.

[36] J. H. Maeng, D. H. Lee, K. H. Jung et al., "Multifunctional doxorubicin loaded superparamagnetic iron oxide nanoparticles for chemotherapy and magnetic resonance imaging in liver cancer," *Biomaterials*, vol. 31, no. 18, pp. 4995–5006, 2010.

[37] C. Sun, C. Fang, Z. Stephen et al., "Tumor-targeted drug delivery and MRI contrast enhancement by chlorotoxin-conjugated iron oxide nanoparticles," *Nanomedicine*, vol. 3, no. 4, pp. 495–505, 2008.

[38] S. Langereis, J. Keupp, J. L. J. Van Velthoven et al., "A temperature-sensitive liposomal 1H CEST and 19F contrast agent for MR image-guided drug delivery," *Journal of the American Chemical Society*, vol. 131, no. 4, pp. 1380–1381, 2009.

[39] K. Na, E. S. Lee, and Y. H. Bae, "Adriamycin loaded pullulan acetate/sulfonamide conjugate nanoparticles responding to tumor pH: pH-dependent cell interaction, internalization and cytotoxicity in vitro," *Journal of Controlled Release*, vol. 87, no. 1–3, pp. 3–13, 2003.

[40] E. K. Lim, Y. M. Huh, J. Yang, K. Lee, J. S. Suh, and S. Haam, "PH-triggered drug-releasing magnetic nanoparticles for cancer therapy guided by molecular imaging by MRI," *Advanced Materials*, vol. 23, no. 21, pp. 2436–2442, 2011.

[41] M. C. Franchini, G. Baldi, D. Bonacchi et al., "Bovine serum albumin-based magnetic nanocarrier for MRI diagnosis and hyperthermic therapy: a potential theranostic approach against cancer," *Small*, vol. 6, no. 3, pp. 366–370, 2010.

[42] J. T. Jang, H. Nah, J. H. Lee, S. H. Moon, M. G. Kim, and J. Cheon, "Critical enhancements of MRI contrast and hyperthermic effects by dopant-controlled magnetic nanoparticles,"

Angewandte Chemie - International Edition, vol. 48, no. 7, pp. 1234–1238, 2009.

[43] M. K. Yu, Y. Y. Jeong, J. Park et al., "Drug-loaded superparamagnetic iron oxide nanoparticles for combined cancer imaging and therapy in vivo," *Angewandte Chemie - International Edition*, vol. 47, no. 29, pp. 5362–5365, 2008.

[44] K. Park, S. Lee, E. Kang, K. Kim, K. Choi, and I. C. Kwon, "New generation of multifunctional nanoparticles for cancer imaging and therapy," *Advanced Functional Materials*, vol. 19, no. 10, pp. 1553–1566, 2009.

[45] C. G. Hadjipanayis, M. J. Bonder, S. Balakrishnan, X. Wang, H. Mao, and G. C. Hadjipanayis, "Metallic iron nanoparticles for MRI contrast enhancement and local hyperthermia," *Small*, vol. 4, no. 11, pp. 1925–1929, 2008.

[46] B. Chertok, B. A. Moffat, A. E. David et al., "Iron oxide nanoparticles as a drug delivery vehicle for MRI monitored magnetic targeting of brain tumors," *Biomaterials*, vol. 29, no. 4, pp. 487–496, 2008.

[47] M. Mahmoudi, A. Simchi, M. Imani, and U. O. Hafeli, "Superparamagnetic iron oxide nanoparticles with rigid cross-linked polyethylene glycol fumarate coating for application in imaging and drug delivery," *Journal of Physical Chemistry C*, vol. 113, no. 19, pp. 8124–8131, 2009.

[48] G. Liu, Z. Wang, J. Lu et al., "Low molecular weight alkyl-polycation wrapped magnetite nanoparticle clusters as MRI probes for stem cell labeling and in vivo imaging," *Biomaterials*, vol. 32, no. 2, pp. 528–537, 2011.

[49] J. K. Hsiao, C. P. Tsai, T. H. Chung et al., "Mesoporous silica nanoparticles as a delivery system of gadolinium for effective human stem cell tracking," *Small*, vol. 4, no. 9, pp. 1445–1452, 2008.

[50] Y. Song, X. Xu, K. W. MacRenaris, X. Q. Zhang, C. A. Mirkin, and T. J. Meade, "Multimodal gadolinium-enriched DNA-gold nanoparticle conjugates for cellular imaging," *Angewandte Chemie - International Edition*, vol. 48, no. 48, pp. 9143–9147, 2009.

Research Article

Development of Quantitative Structure-Property Relationship Models for Self-Emulsifying Drug Delivery System of 2-Aryl Propionic Acid NSAIDs

Chen-Wen Li,[1] Sheng-Yong Yang,[2] Rui He,[1] Wan-Jun Tao,[3] and Zong-Ning Yin[1]

[1] *Department of Pharmaceutics, West China School of Pharmacy, Sichuan University, Chengdu, Sichuan 610041, China*

[2] *State Key Laboratory of Biotherapy and Cancer Center, West China Medical School, Sichuan University, Chengdu, Sichuan 610041, China*

[3] *Department of Pharmacy, Chengdu Family Planning Guidance Institute, Chengdu, Sichuan 610041, China*

Correspondence should be addressed to Zong-Ning Yin, yzn@scu.edu.cn

We developed the quantative structure-property relationships (QSPRs) models to correlate the molecular structures of surfactant, cosurfactant, oil, and drug with the solubility of poorly water-soluble 2-aryl propionic acid nonsteroidal anti-inflammatory drugs (2-APA-NSAIDs) in self-emulsifying drug delivery systems (SEDDSs). The compositions were encoded with electronic, geometrical, topological, and quantum chemical descriptors. To obtain reliable predictions, we used multiple linear regression (MLR) and artificial neural network (ANN) methods for model development. The obtained equations were validated using a test set of 42 formulations and showed a great predictive power, and linear models were found to be better than nonlinear ones. The obtained QSPR models would greatly facilitate fast screening for the optimal formulations of SEDDS at the early stage of drug development and minimize experimental effort.

1. Introduction

Low water solubility of many drug candidates has been a big challenge to pharmaceutical industry since the oral delivery of these drugs may lead to low bioavailability high intra- and intersubject variability [1]. Several formulation approaches to improve solubility of these drugs have been investigated including cyclodextrins [2], micelles [3], nanoparticles [4], solid dispersions [5], and self-emulsifying drug delivery systems (SEDDSs). SEDDS are isotropic mixtures of an oil, surfactant, co-surfactant and drug that form O/W emulsion or microemulsion when introduced into aqueous phases under gentle agitation [6–8]. They can enhance the oral bioavailability of hydrophobic drugs, which are attractive carriers for poorly water-soluble drugs [8–11]. Dissolution in SEDDS and no precipitation in the gastrointestinal tract are some of the prerequisites for the efficient intestinal absorption of drugs [12]. The drug solubility in SEDDS is a key parameter to select optimal formulations [13].

Pharmaceutical preparation is a complicated procedure including preformulation studies, formulation screening, technology optimization, and stability studies. Among them, screening for the optimum formulation is a crucial step. Usually, the first stage is to select suitable excipients and preparation technology through preliminary experiments, and then to screen for the optimized formulation using single-factor design, orthogonal design, or uniform design. These experimental processes are expensive and time consuming. Therefore, estimating properties using theoretical modeling is an efficient way for formulation screening. Quantitative structure-property relationships (QSPRs) are the process by which chemical structure is quantitatively correlated with its physical, chemical, or biological property. It has been widely used in pharmaceutical research [14–16] including predicting the biological activity [17], absorption [18, 19], distribution [20, 21], metabolism, excretion [22], and chemical reactivity-related toxicity [23] (ADMET) properties of drugs. However, QSPR is rarely applied in the pharmaceutics
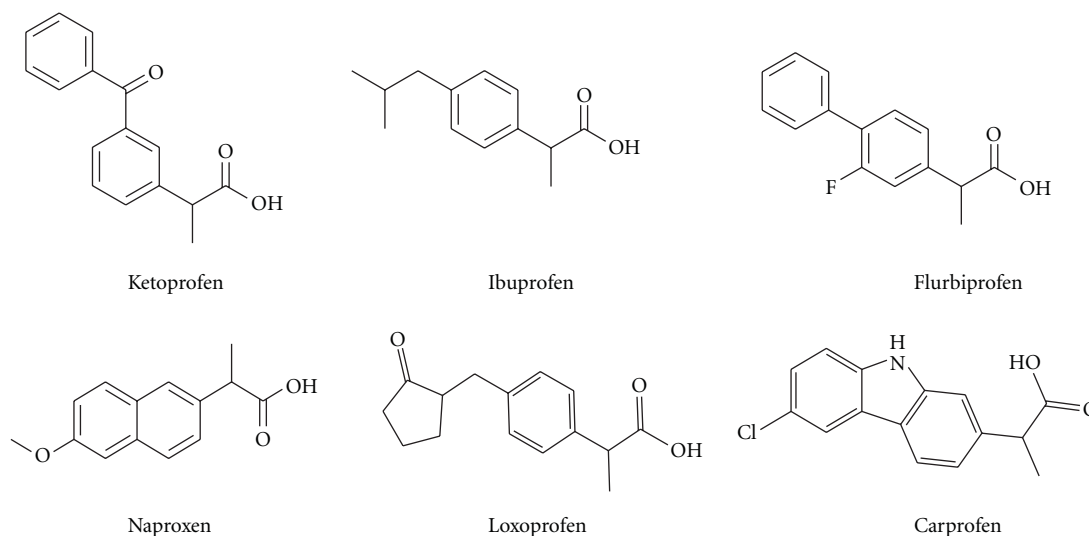
Figure 1: Molecular structures of model drugs.

Table 1: The selected SEDDS.

Formulation	Oil	Surfactant	Cosurfactant
1	Oleic acid	Tween20	Ethanol
2	IPM	Tween40	Ethylene glycol monoethyl ether
3	Ethyl oleate	Tween80	1, 2-propanol
4	Methyl laurate	Tween20	n-Butanol
5	Butyl oleate	Tween40	Isopropyl alcohol
6	Methyl oleate	Tween80	Diethylene glycol monoethyl ether
7	Butyl oleate	Tween20	Isopropyl alcohol
8	Ethyl oleate	Tween40	Ethanol

[24–26] since numerous factors might affect the preparation process. Therefore, it is a good attempt to introduce QSPR into pharmaceutics, establishing the relationship between the property of formulation and the chemical structure of compositions by mathematical methods, which will decrease the experimental time.

The aim of this study was to develop available QSPR models for predicting the drug solubility in SEDDS. We investigated a set of poorly water-soluble 2-aryl propionic acid nonsteroidal anti-inflammatory drugs (2-APA-NSAIDs). We then applied the model such obtained to understand the solubility mechanism of drug in SEDDS as well as to fast screen for the optimized formulations.

2. Materials and Methods

2.1. Materials. Ketoprofen was provided by Southwest Pharmaceuticals Co., Ltd. (Chongqing, China). Flurbiprofen and loxoprofen were purchased from Wuhan Yuancheng Technology Development Co., Ltd. (Wuhan, China). Ibuprofen was a gift from Hubei Biocause Pharmaceutical Co., Ltd. (Hubei, China). Naproxen was obtained from Chengdu Jinhua Pharmaceutical Co., Ltd. (Chengdu, China). Carprofen was purchased from Shandong Fangxing Technology Development Co., Ltd. (Shandong, China). All other agents were of analytical grade.

2.2. Data Collection

2.2.1. Preparation Self-Emulsifying Mixtures. SEDDSs consisted of surfactant, cosurfactant oil, and drug. Surfactants employed were Tween20, Tween40, and Tween80. Oil and cosurfactant selected in the present study had definite, simple structures and commonly used in pharmaceutics. Table 1 shows the composition of the formulations. The weight ratio of surfactant to cosurfactant (Km) varied as 1 : 2, 1 : 1, 2 : 1, 3 : 1, and 4 : 1. The self-emulsifying mixtures containing oil, surfactant and cosurfactant, were prepared at a specific ratio of oil to surfactant/cosurfactant mixture (Smix), 5 : 95, 10 : 90, and 15 : 85 (w/w). Each component was accurately weighed in the same screw-cap tubes and mixed by gentle stirring and vortex-mixing. Model drugs were hydrophobic 2-aryl propionic acid NSAIDs including ketoprofen, ibuprofen, flurbiprofen, naproxen, loxoprofen, and carprofen. The structures of these drugs are shown in Figure 1.

2.2.2. Solubility Studies. In the study, 0.1 g self-emulsifying mixture was diluted with distilled water to 5 ml in a sealed tube and gently mixed by a Vortex mixture (Ika, Germany). An excess amount of drugs was added to the formed microemulsions or emulsions. The blend was mixed and left to equilibrate at 37°C for 48 h in a water bath and then centrifuged at 6,000 rpm for 10 min. The supernatant was

Table 2: Values of important descriptors.

Component	Dipole	MaxQ$^-$	MaxQ$^+$	ABSQ	E_{LUMO}	E_{HOMO}	LogD	Volume	Wiener index
Ketoprofen	4.6178	−0.1264	0.7765	9.4418	0.07479	−0.33786	1.906	167.38	724
Ibuprofen	1.9316	−0.0067	0.7825	8.4045	0.13177	−0.32242	2.150	152.63	404
Flurbiprofen	3.2118	−0.0234	0.7838	8.3569	0.09569	−0.28772	1.394	155.37	530
Naproxen	0.3521	−0.7313	0.7820	8.2233	0.09868	−0.31306	3.748	155.72	626
Loxoprofen	1.7058	−0.3306	0.3272	3.6074	0.27676	−0.27805	3.003	168.75	672
Carprofen	4.7591	−1.0815	0.7836	9.0201	0.08655	−0.29753	2.233	178.7	689
Tween HS	7.0424	−0.5202	0.6213	38.9571	0.17706	−0.40723	−4.492	749.79	44308
Tween20Ls	0.0547	−0.2885	0.1508	7.0901	0.22476	−0.41273	5.389	137.54	220
Tween40Ls	0.0546	−0.2885	0.1507	9.4410	0.22384	−0.40605	7.214	183.5	560
Tween80Ls	0.2610	−0.1646	0.1666	10.3074	0.18531	−0.33536	7.682	209.91	816
Oleic acid	2.0597	−0.1638	0.7540	12.8007	0.16604	−0.33764	5.412	231.18	1313
Ethyl oleate	2.2099	−0.1640	0.7924	13.7649	0.17516	−0.33703	7.435	257.24	1720
IPM	2.2730	−0.2715	0.8086	12.7784	0.17604	−0.40761	6.432	227.4	1072
Methyl laurate	2.3148	−0.1217	0.7871	9.8417	0.17346	−0.4139	4.793	173.9	538
Methyl oleate	2.0349	−0.1218	0.7872	13.0583	0.17314	−0.33705	7.086	243.18	1506
Butyl oleate	2.2902	−0.1522	0.7658	14.935	0.17492	−0.33731	8.415	279.88	2215
Ethanol	2.1046	−0.4459	0.4001	2.4001	0.22361	−0.43772	−0.010	38.75	4
1, 2-propanol	3.1810	−0.4491	0.4246	3.9863	0.2109	−0.42825	−0.520	54.87	18
Ethylene glycol monoethyl ether	0.4875	−0.4526	0.4074	3.9245	0.21824	−0.4152	−0.141	67.91	35
n-Butanol	2.0417	−0.2890	0.3996	3.6342	0.22567	−0.43685	0.970	60.36	20
Isopropyl alcohol	2.0903	−0.4291	0.3965	3.2827	0.21465	−0.43207	0.368	49.39	9
Diethylene glycol monoethyl ether	2.0613	−0.4526	0.4079	5.4420	0.21531	−0.41581	−0.272	98.09	120

filtered through a filter membrane (0.22 μm), diluted with methanol to a suitable concentration range, and quantified by HPLC (see Section 2.2.3).

2.2.3. HPLC Analysis of the Model Drugs. The HPLC analysis was performed with a Waters pump 515 and a UV-VIS detector 2487. The column was a Diamosil C18 100 mm × 4.6 mm column (Dikama, China). The mobile phase consisted of a mixture of methanol, water, and phosphoric acid (20 : 80 : 0.1, v/v/v). The UV detector wavelengths were set at 254 nm (ketoprofen), 222 nm (ibuprofen), 247 nm (flurbiprofen), 273 nm (naproxen), 222 nm (loxoprofen), 300 nm (carprofen), respectively. The elution was carried out at a flow rate of 1.0 mL/min, and the temperature of column oven (PH-730A, Phenomen, China) was set to 30°C. Each measurement was repeated for three times.

2.3. Descriptor Generation and Variable Selection. Molecular descriptors are commonly used to represent the structural and physicochemical features of compositions, so that they can be used in a QSPR model. Thus, to establish a QSPR model, *Ab initio* quantum mechanical calculations were first performed for relevant molecular descriptors using Gaussian 03 software package (Gaussian 03, Gaussian, Inc., Pittsburgh, 2003.). Geometric optimization and quantum chemical, electrostatic parameters were calculated at RHF/6-31G* level. Quantum chemical parameters including the dipole moment (Dipole), the energy of the highest occupied molecular orbital (E_{HOMO}), and the lowest unoccupied molecular

orbital (E_{LUMO}) as well as electrostatic parameters including MaxQ$^-$, MaxQ$^+$, ABSQ, and ABSQon were obtained. In addition, Discovery Studio 1.7 package (Accelrys Inc., USA) was used to calculate parameters such as molecular volume, polar surface area, wiener index, logD, and logP. Constitutional parameters including surfactant ratio (SR), cosurfactant ratio (CoSR), and oil ratio (OR) were also calculated. Table 2 shows the values of important descriptors.

Nonionic surfactants, Tween20, Tween40, and Tween80 belong to the polyoxyethylene sorbitan family. They have similar head structures, and the difference observed in behavior is mainly due to different hydrophobic portions [27]. So each surfactant structure was cleaved into two parts: the same hydrophilic segment (HS) and a different lipophilic segment (LS); and their descriptors were calculated separately. The cleavage method was performed as in Taha et al. [26].

The role of cosurfactant in the formation of SEDDS is to increase the interfacial flexibility by extending into the surfactant interfacial monolayer and consequently creating void space among the surfactant molecules [13]. Both surfactant and cosurfactant in SEDDS are used to reduce the interfacial tension. So for simplification purpose, we combined the descriptors of surfactant and cosurfactant together. The overall descriptor was calculated as follows:

$$\text{Descriptor of Smix} = \text{Rs} \times \text{Ds} + \text{Rcos} \times \text{Dcos}, \quad (1)$$

where Rs is the ratio (w/w) of surfactant; Ds is the molecular descriptor of lipophilic segment of surfactant. Rcos is the

TABLE 3: Equations of statistical parameters.

Parameter	Equation
MSE	$\mathrm{MSE} = (1/n) \sum_{i=1}^{n} (y_{\mathrm{pred}} - y_{\mathrm{exp}})^2$
RMSEP	$\mathrm{RMSEP} = [(1/n) \sum_{i=1}^{n} (y_{\mathrm{pred}} - y_{\mathrm{exp}})^2]^{0.5}$
RSEP	$\mathrm{RSEP}\,(\%) = 100 \times [\sum_{i=1}^{n} (y_{\mathrm{pred}} - y_{\mathrm{exp}})^2 / \sum_{i=1}^{n} (y_{\mathrm{exp}})^2]^{0.5}$
MAE	$\mathrm{MAE}\,(\%) = (100/n) \times \sum_{i=1}^{n} |y_{\mathrm{pred}} - y_{\mathrm{exp}}|$

y_{pred} and y_{exp} are predicted and experimental solubility values, respectively; n is the number of samples in the data set.

ratio (w/w) of cosurfactant; Dcos is the molecular descriptor of cosurfactant.

The descriptors were selected to make a stable and interpretable model. A three-stage manual descriptor selection process was performed: (1) descriptors with too many zero values or the same values (descriptors of Tween HS) were eliminated; (2) descriptors with very small standard deviation values (<0.5%) were removed; (3) a particular descriptor was chosen to represent a group of highly correlated variables (correlation coefficients >0.80), thereby minimizing the redundancy and overlapping of the descriptors. Since the ranges of descriptor values influence the quality of the models generated, we normalized the rest descriptor values to a range of 0 to 1 [28].

2.4. QSPR Modeling. To begin the model development process, the solubility data of drugs in formula 1–6 were split into a training set (80% of the total number of formulations) and an internal validation set (20% of the total number of formulations) randomly. The solubility data of drugs in formula 7–8 were used as a predicting set. The selected descriptors in Section 2.3 were regressed against the solubility of the training set by means of multiple linear regression (MLR). The best equations were determined based on the highest squared multiple correlation coefficient (R^2), Fisher ration (F), and lowest standard error (s).

Artificial neural network (ANN) is a proper method for modeling nonlinear relationship [29]. It was also attempted to develop the better predictive models. All networks used in this study were three-layered back-propagation (BP) type. The input data included the descriptors selected in linear models, and the output neuron referred to the solubility values of drugs in SEDDS. Sigmoid transfer functions were used in all layers. The number of neurons in the hidden layer was adjusted to optimize the network, and the best model gave the highest correlation coefficient (r) and the lowest MSE. The internal validation set (18 formulations) was used to prevent the overfitting.

2.5. Statistical Analysis. To evaluate the predictive ability of QSPR models, the statistical parameters of mean square error (MSE), root mean square error of prediction (RMSEP), the RMSE, the relative standard error of prediction (RSEP), and mean absolute error (MAE) [30] were used. Table 3 shows these equations.

3. Results and Discussion

3.1. QSPR Models. Table 4 shows the solubility of 2-APA-NSAIDs in various formulations.

3.1.1. MLR. The best MLR models were given as follows:

$$
\begin{aligned}
S_{\mathrm{ketoprofen}} = {} & 1.073(\pm0.068) + 1.176(\pm0.073)\mathrm{SR} \\
& + 0.316(\pm0.031)\mathrm{OR} - 0.165(\pm0.046) \\
& \times \mathrm{O\text{-}ABSQ} - 0.511(\pm.048)\mathrm{O\text{-}E_{LUMO}} \\
& + 0.125(\pm0.085)\mathrm{S\text{-}Volume} \\
& + 0.176(\pm0.072)\mathrm{S\text{-}Dipole},
\end{aligned}
$$

$$
\begin{aligned}
S_{\mathrm{ibuprofen}} = {} & 1.346(\pm0.112) + 1.578(\pm0.120)\mathrm{SR} \\
& + 0.935(\pm0.051)\mathrm{OR} - 0.170(\pm0.076) \\
& \times \mathrm{O\text{-}ABSQ} - 0.056(\pm0.078)\mathrm{O\text{-}E_{LUMO}} \\
& + 0.242(\pm0.140)\mathrm{S\text{-}Volume} \\
& + 0.329(\pm0.118)\mathrm{S\text{-}Dipole},
\end{aligned}
$$

$$
\begin{aligned}
S_{\mathrm{flurbiprofen}} = {} & 0.685(\pm0.057) + 0.641(\pm0.061)\mathrm{SR} \\
& + 0.28(\pm0.026)\mathrm{OR} + 0.277(\pm0.039) \\
& \times \mathrm{O\text{-}ABSQ} - 0.063(\pm0.040)\mathrm{O\text{-}E_{LUMO}} \\
& + 0.364(\pm0.071)\mathrm{S\text{-}Volume} \\
& - 0.153(\pm0.060)\mathrm{S\text{-}Dipole},
\end{aligned}
$$

$$
\begin{aligned}
S_{\mathrm{naproxen}} = {} & 0.239(\pm0.017) + 0.222(\pm0.016)\mathrm{SR} \\
& + 0.030(\pm0.009)\mathrm{OR} + 0.024(\pm0.010) \\
& \times \mathrm{O\text{-}Dipole} + 0.178(\pm0.018)\mathrm{O\text{-}ABSQ} \\
& - 0.039(\pm0.016)\mathrm{O\text{-}MaxQ^-} + 0.077 \\
& \times (\pm0.032)\mathrm{S\text{-}Volume} + 0.097 \\
& \times (\pm0.032)\mathrm{S\text{-}MaxQ^-},
\end{aligned}
$$

$$
\begin{aligned}
S_{\mathrm{loxoprofen}} = {} & 1.452(\pm0.103) + 0.996(\pm0.110)\mathrm{SR} \\
& + 0.285(\pm0.047)\mathrm{OR} + 0.070(\pm0.070) \\
& \times \mathrm{O\text{-}ABSQ} - 0.222(\pm0.071)\mathrm{O\text{-}E_{LUMO}} \\
& + 0.059(\pm0.128)\mathrm{S\text{-}Volume} \\
& + 0.237(\pm0.108)\mathrm{S\text{-}Dipole},
\end{aligned}
$$

$$
\begin{aligned}
S_{\mathrm{carprofen}} = {} & 0.212(\pm0.058) + 0.999(\pm0.065)\mathrm{SR} \\
& + 0.182(\pm0.032)\mathrm{OR} + 0.268(\pm0.048) \\
& \times \mathrm{O\text{-}ABSQ} + 1.157(\pm0.069)\mathrm{S\text{-}Volume} \\
& + 0.550(\pm0.072)\mathrm{S\text{-}Dipole}.
\end{aligned}
$$

(2)

In all the equations, variable inflation factor (VIF) was less than 10, suggesting the absence of multicollinearity. As
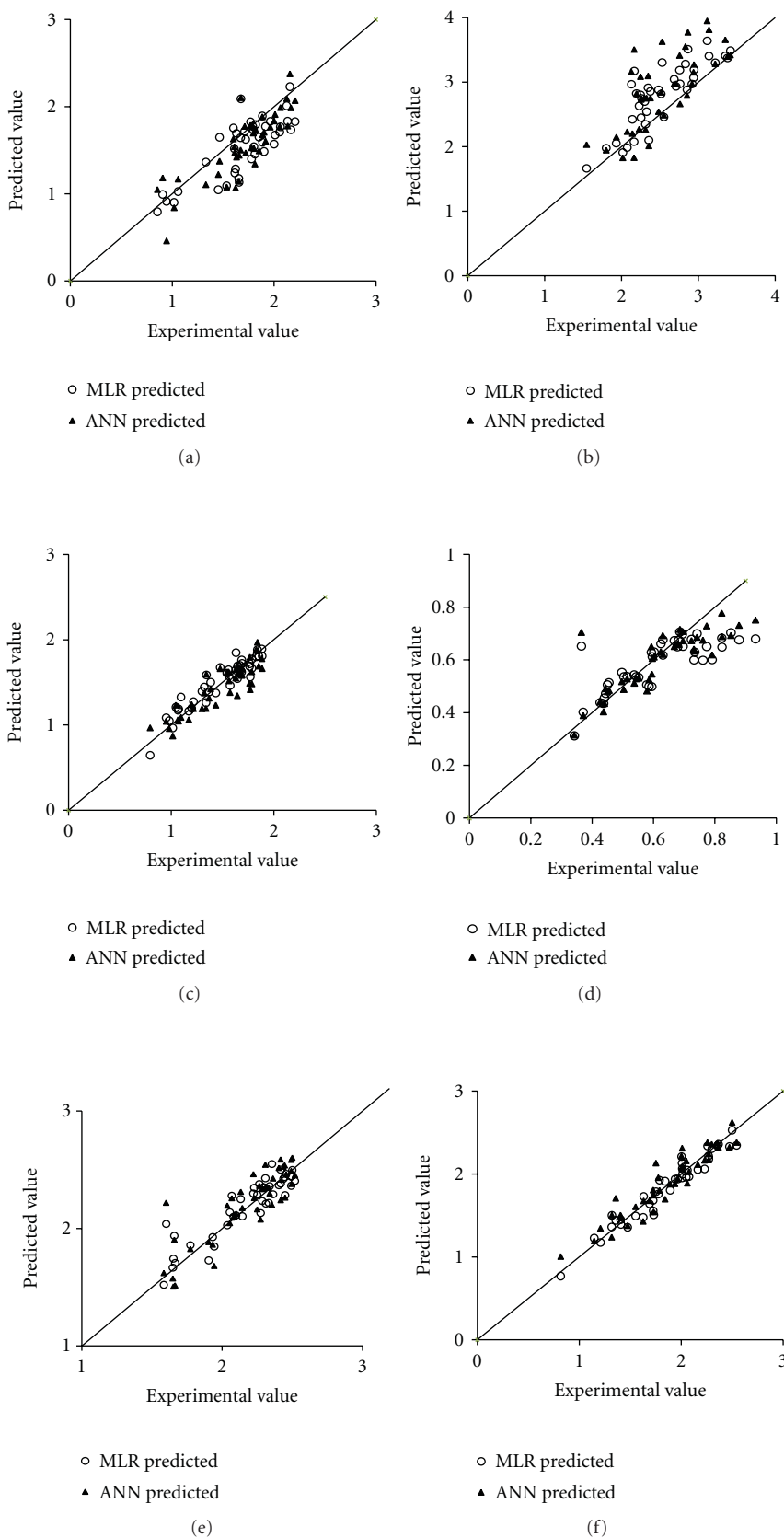
FIGURE 2: Experimental versus predicted solubility for MLR and ANN; (a) ketoprofen, (b) ibuprofen, (c) flurbiprofen, (d) naproxen, (e) loxoprofen, (f) carprofen.

TABLE 4: Solubility of drugs in SEDDS.

NO.	Formula	Km	Oil : Smix	S_{Keto} (mg·mL^{-1})	S_{Ibu} (mg·mL^{-1})	S_{Flu} (mg·mL^{-1})	S_{Nap} (mg·mL^{-1})	S_{Loxo} (mg·mL^{-1})	S_{car} (mg·mL^{-1})
1[a]	1	1 : 2	0.5 : 9.5	0.961	1.756	0.848	0.332	1.909	0.989
2[a]	1	1 : 2	1 : 9	1.207	2.075	0.948	0.350	2.002	1.014
3[a]	1	1 : 2	1.5 : 8.5	1.439	2.634	1.014	0.366	2.422	1.086
4[a]	1	1 : 1	0.5 : 9.5	1.519	2.293	1.054	0.423	2.072	1.139
5[b]	1	1 : 1	1 : 9	1.464	2.552	1.199	0.426	2.144	1.146
6[a]	1	1 : 1	1.5 : 8.5	1.864	2.958	1.315	0.420	2.431	1.321
7[a]	1	2 : 1	0.5 : 9.5	1.825	2.436	1.442	0.553	2.131	1.502
8[a]	1	2 : 1	1 : 9	1.943	2.995	1.541	0.554	2.209	1.594
9[b]	1	2 : 1	1.5 : 8.5	1.674	3.221	1.564	0.552	2.457	1.689
10[a]	1	3 : 1	0.5 : 9.5	2.033	2.678	1.535	0.592	2.177	1.633
11[a]	1	3 : 1	1 : 9	2.354	3.06	1.598	0.594	2.387	1.605
12[a]	1	3 : 1	1.5 : 8.5	2.485	3.355	1.705	0.569	2.499	1.757
13[b]	1	4 : 1	0.5 : 9.5	2.155	2.762	1.541	0.596	2.355	1.842
14[a]	1	4 : 1	1 : 9	2.438	3.112	1.647	0.618	2.497	1.871
15[a]	1	4 : 1	1.5 : 8.5	2.220	3.520	1.714	0.582	2.510	1.799
16[a]	2	1 : 2	0.5 : 9.5	0.798	1.538	0.933	0.397	1.522	0.957
17[a]	2	1 : 2	1 : 9	0.845	1.899	0.958	0.403	1.563	0.964
18[a]	2	1 : 2	1.5 : 8.5	0.856	2.164	1.042	0.390	1.475	0.956
19[b]	2	1 : 1	0.5 : 9.5	1.057	2.074	1.045	0.450	1.904	1.475
20[a]	2	1 : 1	1 : 9	1.295	2.444	1.228	0.466	1.928	1.498
21[a]	2	1 : 1	1.5 : 8.5	1.196	2.577	1.535	0.514	1.877	1.491
22[a]	2	2 : 1	0.5 : 9.5	1.438	2.608	1.465	0.609	2.165	1.777
23[a]	2	2 : 1	1 : 9	1.353	2.824	1.569	0.620	2.091	1.836
24[a]	2	2 : 1	1.5 : 8.5	1.430	3.099	1.666	0.631	2.186	1.88
25[a]	2	3 : 1	0.5 : 9.5	1.577	2.706	1.716	0.647	2.215	1.923
26[a]	2	3 : 1	1 : 9	1.665	3.066	1.740	0.646	2.082	2.103
27[b]	2	3 : 1	1.5 : 8.5	1.600	3.418	1.830	0.696	2.229	2.009
28[a]	2	4 : 1	0.5 : 9.5	1.637	2.770	1.749	0.703	2.310	2.165
29[a]	2	4 : 1	1 : 9	1.705	3.176	1.791	0.694	2.268	2.171
30[a]	2	4 : 1	1.5 : 8.5	1.640	3.816	1.959	0.715	2.358	2.113
31[a]	3	1 : 2	0.5 : 9.5	0.840	1.495	0.839	0.414	1.483	1.378
32[b]	3	1 : 2	1 : 9	1.018	2.356	1.015	0.437	1.653	1.405
33[a]	3	1 : 2	1.5 : 8.5	1.027	2.432	1.030	0.399	1.771	1.407
34[a]	3	1 : 1	0.5 : 9.5	1.217	2.243	1.202	0.587	1.930	1.903
35[a]	3	1 : 1	1 : 9	1.183	2.407	1.244	0.530	1.937	1.894
36[b]	3	1 : 1	1.5 : 8.5	1.330	2.918	1.300	0.497	2.100	1.939
37[a]	3	2 : 1	0.5 : 9.5	1.537	2.573	1.393	0.637	2.331	2.307
38[a]	3	2 : 1	1 : 9	1.739	3.148	1.638	0.627	2.396	2.404
39[b]	3	2 : 1	1.5 : 8.5	1.631	3.352	1.670	0.624	2.339	2.366
40[a]	3	3 : 1	0.5 : 9.5	1.746	3.059	1.644	0.651	2.552	2.637
41[a]	3	3 : 1	1 : 9	1.803	3.494	1.752	0.680	2.458	2.659
42[a]	3	3 : 1	1.5 : 8.5	1.755	3.674	1.826	0.705	2.344	2.46
43[a]	3	4 : 1	0.5 : 9.5	1.935	3.216	1.815	0.765	2.606	2.714
44[a]	3	4 : 1	1 : 9	1.874	3.554	1.831	0.739	2.608	2.757
45[a]	3	4 : 1	1.5 : 8.5	2.033	3.687	2.012	0.749	2.439	2.676
46[b]	4	1 : 2	0.5 : 9.5	0.944	1.545	0.794	0.342	1.585	0.818
47[a]	4	1 : 2	1 : 9	0.961	1.969	0.950	0.359	1.426	0.729
48[a]	4	1 : 2	1.5 : 8.5	0.980	2.448	0.985	0.345	1.489	0.853
49[a]	4	1 : 1	0.5 : 9.5	1.302	2.219	1.047	0.438	1.844	1.102
50[a]	4	1 : 1	1 : 9	1.316	2.754	1.134	0.476	1.722	1.262
51[a]	4	1 : 1	1.5 : 8.5	1.451	3.137	1.310	0.441	2.136	1.103
52[b]	4	2 : 1	0.5 : 9.5	1.671	2.23	1.071	0.444	2.081	1.553

TABLE 4: Continued.

NO.	Formula	Km	Oil : Smix	S_{Keto} (mg·mL^{-1})	S_{Ibu} (mg·mL^{-1})	S_{Flu} (mg·mL^{-1})	S_{Nap} (mg·mL^{-1})	S_{Loxo} (mg·mL^{-1})	S_{car} (mg·mL^{-1})
53[a]	4	2 : 1	1 : 9	1.711	2.782	1.351	0.484	2.053	1.642
54[a]	4	2 : 1	1.5 : 8.5	1.863	3.328	1.316	0.442	2.422	1.496
55[b]	4	3 : 1	0.5 : 9.5	1.962	2.483	1.095	0.455	2.133	1.725
56[a]	4	3 : 1	1 : 9	2.006	3.172	1.356	0.489	2.447	1.663
57[a]	4	3 : 1	1.5 : 8.5	2.130	3.946	1.344	0.461	2.470	1.801
58[a]	4	4 : 1	0.5 : 9.5	2.092	2.545	1.168	0.458	2.427	1.94
59[b]	4	4 : 1	1 : 9	2.124	3.380	1.385	0.503	2.519	1.892
60[a]	4	4 : 1	1.5 : 8.5	1.999	4.062	1.431	0.491	2.639	1.945
61[a]	5	1 : 2	0.5 : 9.5	0.816	1.609	0.921	0.442	1.606	0.807
62[b]	5	1 : 2	1 : 9	0.854	2.017	0.980	0.440	1.649	1.208
63[a]	5	1 : 2	1.5 : 8.5	0.876	2.101	1.002	0.423	1.701	1.273
64[a]	5	1 : 1	0.5 : 9.5	0.985	1.945	1.344	0.525	1.945	1.577
65[a]	5	1 : 1	1 : 9	1.227	2.211	1.343	0.561	2.001	1.646
66[a]	5	1 : 1	1.5 : 8.5	1.246	2.713	1.424	0.548	2.064	1.699
67[a]	5	2 : 1	0.5 : 9.5	1.398	2.662	1.544	0.689	2.134	2.134
68[b]	5	2 : 1	1 : 9	1.610	2.853	1.678	0.678	2.286	2.010
69[a]	5	2 : 1	1.5 : 8.5	1.617	3.307	1.819	0.655	2.419	2.199
70[a]	5	3 : 1	0.5 : 9.5	1.558	2.932	1.774	0.735	2.268	2.256
71[a]	5	3 : 1	1 : 9	1.747	3.260	1.698	0.693	2.355	2.416
72[b]	5	3 : 1	1.5 : 8.5	1.791	3.617	1.841	0.694	2.495	2.300
73[a]	5	4 : 1	0.5 : 9.5	1.617	2.985	1.820	0.766	2.337	2.454
74[a]	5	4 : 1	1 : 9	1.921	3.393	1.953	0.760	2.374	2.505
75[a]	5	4 : 1	1.5 : 8.5	1.812	3.685	2.055	0.752	2.503	2.429
76[a]	6	1 : 2	0.5 : 9.5	0.839	1.769	0.849	0.381	1.544	1.439
77[b]	6	1 : 2	1 : 9	0.906	2.163	0.951	0.371	1.665	1.32
78[a]	6	1 : 2	1.5 : 8.5	1.066	2.414	1.135	0.402	1.712	1.392
79[a]	6	1 : 1	0.5 : 9.5	1.237	2.203	1.242	0.485	1.794	1.759
80[a]	6	1 : 1	1 : 9	1.537	2.349	1.299	0.510	1.869	1.811
81[a]	6	1 : 1	1.5 : 8.5	1.513	2.938	1.527	0.540	1.962	1.88
82[a]	6	2 : 1	0.5 : 9.5	1.581	2.455	1.437	0.636	1.912	2.331
83[b]	6	2 : 1	1 : 9	1.711	2.686	1.559	0.631	2.069	2.258
84[a]	6	2 : 1	1.5 : 8.5	1.721	3.068	1.728	0.656	2.143	2.406
85[b]	6	3 : 1	0.5 : 9.5	1.768	2.710	1.647	0.668	2.295	2.500
86[a]	6	3 : 1	1 : 9	1.980	3.265	1.775	0.659	2.652	2.657
87[a]	6	3 : 1	1.5 : 8.5	1.949	3.709	1.924	0.686	2.595	2.421
88[a]	6	4 : 1	0.5 : 9.5	1.959	3.256	1.781	0.685	2.572	2.728
89[a]	6	4 : 1	1 : 9	1.984	3.646	1.860	0.694	2.729	2.806
90[a]	6	4 : 1	1.5 : 8.5	2.155	3.742	2.069	0.725	2.798	2.793

[a]Training set.
[b]Internal validation set.

shown in Table 5, the correlation matrix for these descriptors shows no high correlation between variables and could be used to develop QSPR models. The statistical results indicate that these equations represent good models for calculating the solubility (Table 6).

Models in (2) shows the significance of the combination of SR, OR, O-MaxQ$^-$, O-ABSQ, O-E$_{LUMO}$, S-Volume, and S-Dipole in the solubility of drugs in SEDDS. According to t-test criterion, the most important descriptor is SR. The positive coefficient suggests that high-concentration surfactant will increase the solubility. Surfactant plays an impor-

tant role in O/W microemulsion/emulsion formation: it forms a layer around emulsion droplets, which reduces the interfacial energy and provides a mechanical barrier to coalescence [31]. And the result suggests that drugs are mainly dissolved in the phase of surfactant.

The specific effect of O-MaxQ$^-$, O-ABSQ, and S-Dipole to the solubility depends on the drug type.

2.4. QSPR Modeling. ANN models were constructed with the same descriptors as in MLR models using Leavenberg-Marquardt (LM) algorithm as activity function. The proper

Table 5: Correlation matrix for selected descriptors.

	SR	OR	O-dipole	O-MaxQ$^-$	O-ABSQ	O-LUMO	S-volume	S-dipole	S-MaxQ$^-$
SR	1.000	−0.170	0.003	−0.003	0.065	0.045	0.671	−0.615	0.617
OR		1.000	0.011	0.053	−0.143	−0.025	−0.049	−0.041	0.027
O-dipole			1.000	−0.295	−0.153	0.652	−0.141	−0.214	−0.111
O-MaxQ$^-$				1.000	−0.158	−0.295	−0.020	0.521	0.439
O-ABSQ					1.000	0.159	0.345	0.111	−0.163
O-LUMO						1.000	0.472	−0.130	0.195
S-volume							1.000	−0.333	0.704
S-dipole								1.000	−0.057
S-MaxQ$^-$									1.000

Table 6: Statistical qualities of different models.

Model	n	R^2	MSE	RMSEP	RSEP (%)	MAE (%)	Model	n	R^2	MSE	RMSEP	RSEP (%)	MAE (%)
1[MLR]	72	0.948	0.0094	0.097	5.999	7.9375	**7[ANN]**	**72**	**0.989**	**0.0080**	**0.089**	**5.507**	**5.993**
2[MLR]	72	0.932	0.0254	0.159	5.539	13.402	**8[ANN]**	**72**	**0.994**	**0.0089**	**0.094**	**3.269**	**5.112**
3[MLR]	72	0.943	0.0065	0.081	5.417	6.204	**9[ANN]**	**72**	**0.994**	**0.0037**	**0.061**	**4.098**	**4.190**
4[MLR]	72	0.949	0.0008	0.028	4.942	2.292	**10[ANN]**	**72**	**0.993**	**0.0003**	**0.016**	**2.778**	**1.209**
5[MLR]	72	0.822	0.0213	0.1459	6.683	12.053	**11[ANN]**	**72**	**0.989**	**0.0046**	**0.0677**	**3.100**	**5.243**
6[MLR]	72	0.967	0.0104	0.1019	5.326	8.316	**12[ANN]**	**72**	**0.990**	**0.0089**	**0.0943**	**4.928**	**6.272**

Table 7: Experimental and predicted values of predicting set.

(a)

NO.	$S_{\text{Keto Exp.}}$	MLR	ANN	$S_{\text{Ibu Exp.}}$	MLR	ANN	$S_{\text{Flu Exp.}}$	MLR	ANN
1[a]	1.464	1.649	1.376	2.552	2.457	2.488	1.199	1.195	1.241
2[a]	1.674	2.090	2.104	3.221	3.299	3.285	1.564	1.572	1.518
3[a]	2.155	2.230	2.378	2.762	2.973	2.663	1.541	1.608	1.615
4[a]	1.057	1.026	1.169	2.074	1.983	2.233	1.045	1.209	1.233
5[a]	1.600	1.756	1.631	3.418	3.487	3.420	1.830	1.801	1.885
6[a]	1.018	0.901	0.841	2.356	2.099	2.014	1.015	0.964	0.871
7[a]	1.330	1.363	1.106	2.918	2.970	2.973	1.300	1.395	1.191
8[a]	1.631	1.693	1.422	3.352	3.407	3.655	1.670	1.699	1.615
9[a]	0.944	0.913	0.461	1.545	1.663	2.033	0.794	0.645	0.967
10[a]	1.671	1.644	1.504	2.230	2.631	2.274	1.071	1.189	1.046
11[a]	1.962	1.832	1.767	2.483	2.881	2.543	1.095	1.328	1.090
12[a]	2.124	2.011	2.093	3.380	3.373	3.396	1.385	1.501	1.425
13[a]	0.854	0.794	1.050	2.017	1.909	1.828	0.980	1.049	0.958
14[a]	1.610	1.519	1.542	2.853	2.880	2.794	1.678	1.640	1.593
15[a]	1.791	1.773	1.775	3.617	3.476	3.584	1.841	1.881	1.971
16[a]	0.906	0.994	1.183	2.163	2.075	1.830	0.951	1.084	1.043
17[a]	1.711	1.718	1.775	2.686	3.044	2.975	1.559	1.646	1.624
18[a]	1.768	1.827	1.788	2.710	2.934	2.976	1.647	1.694	1.691
19[b]	1.452	1.047	1.223	1.801	1.978	1.947	1.065	1.173	1.062
20[b]	1.657	1.132	1.443	2.314	2.346	2.265	1.217	1.273	1.193
21[b]	1.614	1.241	1.476	2.261	2.748	2.749	1.369	1.386	1.315
22[b]	1.778	1.402	1.530	2.255	2.447	2.732	1.322	1.444	1.375
23[b]	1.901	1.486	1.708	2.516	2.816	2.842	1.645	1.544	1.345
24[b]	2.000	1.571	1.837	2.757	3.185	3.413	1.630	1.644	1.552
25[b]	1.887	1.591	1.680	2.304	2.699	2.751	1.342	1.587	1.596
26[b]	2.009	1.675	1.911	2.938	3.068	3.152	1.765	1.687	1.490

(a) Continued.

NO.	$S_{Keto\ Exp.}$	MLR	ANN	$S_{Ibu\ Exp.}$	MLR	ANN	$S_{Flu\ Exp.}$	MLR	ANN
27[b]	2.165	1.735	1.988	3.140	3.404	3.810	1.786	1.773	1.625
28[b]	2.056	1.710	1.774	2.377	2.856	2.754	1.477	1.675	1.661
29[b]	2.062	1.770	1.991	2.944	3.192	3.273	1.687	1.761	1.582
30[b]	2.206	1.830	2.071	3.603	3.528	3.916	1.632	1.848	1.654
31[b]	1.534	1.092	1.080	1.933	2.053	2.149	1.171	1.162	1.062
32[b]	1.653	1.177	1.144	2.142	2.422	2.205	1.339	1.262	1.194
33[b]	1.622	1.286	1.068	2.195	2.824	2.822	1.435	1.376	1.233
34[b]	1.812	1.457	1.344	2.327	2.542	2.753	1.574	1.464	1.381
35[b]	1.802	1.541	1.521	2.347	2.911	3.096	1.770	1.564	1.415
36[b]	1.721	1.626	1.471	2.833	3.280	3.551	1.787	1.664	1.483
37[b]	1.852	1.651	1.494	2.247	2.803	3.085	1.685	1.621	1.657
38[b]	1.796	1.736	1.698	2.165	3.172	3.504	1.690	1.721	1.586
39[b]	1.820	1.796	1.733	2.865	3.508	3.771	1.877	1.808	1.662
40[b]	1.916	1.773	1.604	2.129	2.967	3.157	1.767	1.718	1.796
41[b]	2.133	1.833	1.779	2.529	3.303	3.627	1.855	1.805	1.691
42[b]	1.884	1.893	1.885	3.116	3.639	3.948	1.884	1.891	1.778

(b)

NO.	$S_{Nap\ Exp.}$	MLR	ANN	$S_{Loxo\ Exp.}$	MLR	ANN	$S_{Car\ Exp}$	MLR	ANN
1[a]	0.426	0.438	0.441	2.144	2.104	2.175	1.146	1.227	1.193
2[a]	0.552	0.534	0.531	2.457	2.465	2.462	1.689	1.641	1.680
3[a]	0.596	0.612	0.606	2.355	2.549	2.201	1.842	1.913	1.698
4[a]	0.450	0.505	0.479	1.904	1.728	1.884	1.475	1.357	1.378
5[a]	0.696	0.651	0.672	2.229	2.347	2.260	2.009	2.132	2.082
6[a]	0.437	0.435	0.403	1.653	1.742	1.505	1.405	1.449	1.505
7[a]	0.497	0.553	0.518	2.100	2.112	2.127	1.939	1.939	1.884
8[a]	0.624	0.661	0.631	2.339	2.360	2.300	2.366	2.359	2.326
9[a]	0.342	0.312	0.315	1.585	1.520	1.620	0.818	0.769	1.006
10[a]	0.444	0.473	0.491	2.081	2.100	2.099	1.553	1.495	1.606
11[a]	0.455	0.514	0.485	2.133	2.250	2.313	1.725	1.681	1.808
12[a]	0.503	0.536	0.488	2.419	2.404	2.455	1.892	1.805	1.879
13[a]	0.440	0.456	0.435	1.649	1.666	1.574	1.208	1.175	1.346
14[a]	0.678	0.650	0.661	2.286	2.233	2.339	2.010	2.065	2.313
15[a]	0.694	0.697	0.708	2.435	2.445	2.379	2.300	2.305	2.361
16[a]	0.371	0.402	0.389	1.665	1.706	1.514	1.320	1.501	1.505
17[a]	0.631	0.618	0.621	2.069	2.279	2.258	2.258	2.338	2.381
18[a]	0.668	0.673	0.651	2.295	2.352	2.336	2.500	2.529	2.624
19[b]	0.403	0.536	0.528	1.774	1.858	1.825	1.318	1.362	1.239
20[b]	0.480	0.537	0.528	1.660	1.938	1.904	1.409	1.390	1.489
21[b]	0.501	0.543	0.512	1.601	2.039	2.220	1.358	1.440	1.709
22[b]	0.544	0.628	0.650	2.054	2.138	2.046	1.632	1.730	1.677
23[b]	0.514	0.629	0.633	2.333	2.218	2.346	1.776	1.759	1.957
24[b]	0.537	0.631	0.611	2.223	2.298	2.463	1.753	1.787	2.133
25[b]	0.593	0.677	0.692	2.250	2.288	2.163	1.788	1.925	1.804
26[b]	0.734	0.678	0.673	2.405	2.368	2.516	2.008	1.954	2.063
27[b]	0.602	0.674	0.659	2.309	2.428	2.544	2.050	1.961	2.160
28[b]	0.630	0.707	0.716	2.418	2.382	2.242	2.060	2.046	1.890
29[b]	0.724	0.703	0.693	2.493	2.442	2.585	2.163	2.054	2.116
30[b]	0.682	0.700	0.686	2.417	2.501	2.588	2.230	2.061	2.167
31[b]	0.686	0.499	0.546	1.944	1.846	1.681	1.627	1.478	1.430
32[b]	0.852	0.500	0.525	1.933	1.926	1.862	1.731	1.507	1.544
33[b]	0.742	0.506	0.482	2.037	2.027	2.195	1.725	1.556	1.746

(b) Continued.

NO.	$S_{\text{Nap Exp.}}$	MLR	ANN	$S_{\text{Loxo Exp.}}$	MLR	ANN	$S_{\text{Car Exp}}$	MLR	ANN
34[b]	0.489	0.599	0.675	2.274	2.131	2.076	1.966	1.940	1.945
35[b]	0.529	0.600	0.641	2.313	2.211	2.357	2.077	1.969	2.028
36[b]	0.499	0.601	0.619	2.363	2.291	2.426	2.012	1.998	2.097
37[b]	0.595	0.651	0.729	2.449	2.283	2.263	2.271	2.182	2.172
38[b]	0.586	0.652	0.705	2.493	2.363	2.490	2.003	2.211	2.219
39[b]	0.579	0.648	0.689	2.437	2.423	2.527	2.268	2.218	2.244
40[b]	0.761	0.683	0.778	2.265	2.379	2.363	2.474	2.331	2.325
41[b]	0.732	0.680	0.751	2.446	2.438	2.539	2.356	2.339	2.375
42[b]	0.791	0.676	0.732	2.500	2.498	2.603	2.544	2.347	2.383

[a]Internal validation set.
[b]External prediction set.

TABLE 8: Statistical comparison between MLR and ANN.

Model	N	MSE	RMSEP	RSEP (%)	MAE (%)	Model	n	MSE	RMSEP	RSEP (%)	MAE (%)
1[MLR]	42	0.072	0.268	15.405	21.436	7[ANN]	**42**	**0.065**	**0.255**	**14.677**	**21.168**
2[MLR]	**42**	**0.147**	**0.384**	**14.605**	**29.965**	8[ANN]	42	0.258	0.508	19.351	38.576
3[MLR]	**42**	**0.011**	**0.106**	**7.074**	**8.506**	9[ANN]	42	0.021	0.146	9.701	11.573
4[MLR]	42	0.010	0.100	15.649	6.965	10[ANN]	**42**	**0.007**	**0.086**	**13.565**	**5.735**
5[MLR]	**42**	**0.014**	**0.119**	**5.445**	**8.487**	11[ANN]	42	0.024	0.156	7.119	11.207
6[MLR]	**42**	**0.010**	**0.100**	**5.270**	**8.039**	12[ANN]	42	0.020	0.141	7.411	11.066

number of neurons in the hidden layer was set as 10 to ensure the lowest mean square error (MSE). Table 6 shows the statistical qualities of the ANN models, compared with MLR models. R^2 of QSPR models indicate that they can explain more than 90% of the variation in the formulations, which correspond to a significant explanatory capacity.

3.2. QSPR Models for Solubility Prediction. Table 7 shows the solubility prediction for the internal and external validation sets obtained from these models. As shown in Figures 2(a)–2(f), the plots of experimental values versus predicted values obtained by the MLR and ANN modeling indicate good correlations between the experimental and predicted values and confirm the satisfied predictive ability of QSPR models.

A statistical evaluation of both MLR and ANN models is shown in Table 8. According to the comparison between the two models in this study, except for the model drugs of ketoprofen and naproxen, MLR was found to be more reliable for the solubility prediction than ANN.

Based on the models, the optimal formulations in internal validation set were as follows: oleic acid/Tween20/ethanol (Km = 4:1, 0.5:9.5) for ketoprofen; butyl oleate/Tween40/isopropyl alcohol (Km = 3:1, 1.5:8.5) for ibuprofen, flurbiprofen, and naproxen; oleic acid/Tween20/Ethanol (Km = 2:1, 1.5:8.5) for loxoprofen; methyl oleate/Tween80/diethylene glycol monoethyl ether for carprofen. The best formulations for the predicting set were as follows: butyl oleate/Tween20/isopropyl alcohol (Km = 4:1, 1.5:8.5) for ketoprofen and ibuprofen; ethyl oleate/Tween40/ethanol (Km = 4:1, 1.5:8.5) for flurbiprofen, loxoprofen, and carprofen; butyl oleate/Tween20/isopropyl alcohol (Km = 4:1, 0.5:9.5) for naproxen. All

the predicted optimum formulations were consistent with the experimental ones except for naproxen, indicating the significance of the models in formulation screening.

3.3. The Drug Effect on the Solubility. To examine the influence of drugs on the solubility, the descriptors of drugs (X) were correlated with the drug solubility in different formulations (Y). The multiple linear regression analyses gave the following equations:

$$S_{\text{Formula 1}} = 3.710(\pm 0.138) + 0.793(\pm 0.058)\text{SR}$$
$$+ 0.368(\pm 0.047)\text{OR} + 2.453(\pm 0.162)\text{D-Dipole}$$
$$- 2.457(\pm 0.074)\text{D-MaxQ}^+$$
$$- 1.245(\pm 0.071)\text{D-E}_{\text{HOMO}}$$
$$- 2.670(\pm 0.121)\text{D-Wiener}$$
$$+ 0.978(\pm 0.162)\text{D-LogD},$$
$$n = 90, \ R^2 = 0.953, \ s = 0.178,$$
$$F = 237.739, \ \text{MSE} = 0.029,$$
$$S_{\text{Formula 2}} = 2.241(\pm 0.137) + 1.002(\pm 0.058)\text{SR}$$
$$+ 0.293(\pm 0.046)\text{OR}$$
$$+ 2.994(\pm 0.160)\text{D-Dipole}$$
$$- 1.801(\pm 0.074)\text{D-MaxQ}^+$$

$$- 0.454(\pm0.070)\text{D-E}_{\text{HOMO}}$$

$$- 3.122(\pm0.120)\text{D-Wiener}$$

$$+ 1.770(\pm0.160)\text{D-LogD},$$

$$n = 90, \ R^2 = 0.948, \ s = 0.177,$$

$$F = 214.550, \ \text{MSE} = 0.028,$$

$$\text{S}_{\text{Formula 3}} = 1.693(\pm0.147) + 1.119(\pm0.062)\text{SR}$$

$$+ 0.301(\pm0.050)\text{OR} + 4.343(\pm0.172)\text{D-Dipole}$$

$$- 1.972(\pm0.079)\text{D-MaxQ}^+$$

$$- 0.379(\pm0.075)\text{D-E}_{\text{HOMO}}$$

$$- 3.864(\pm0.129)\text{D-Wiener}$$

$$+ 2.931(\pm0.172)\text{D-LogD},$$

$$n = 90, \ R^2 = 0.952, \ s = 0.190,$$

$$F = 234.809, \ \text{MSE} = 0.033,$$

$$\text{S}_{\text{Formula 4}} = 3.215(\pm0.200) + 0.942(\pm0.085)\text{SR}$$

$$+ 0.409(\pm0.068)\text{OR}$$

$$+ 2.985(\pm0.234)\text{D-Dipole}$$

$$- 2.428(\pm0.108)\text{D-MaxQ}^+$$

$$- 1.226(\pm0.102)\text{D-E}_{\text{HOMO}}$$

$$- 3.167(\pm0.176)\text{D-Wiener}$$

$$+ 1.616(\pm0.234)\text{D-LogD},$$

$$n = 90, \ R^2 = 0.914, \ s = 0.258,$$

$$F = 123.981, \ \text{MSE} = 0.061,$$

$$\text{S}_{\text{Formula 5}} = 1.925(\pm0.147) + 1.113(\pm0.062)\text{SR}$$

$$+ 0.355(\pm0.050)\text{OR}$$

$$+ 3.447(\pm0.172)\text{D-Dipole}$$

$$- 1.827(\pm0.079)\text{D-MaxQ}^+$$

$$- 0.334(\pm0.075)\text{D-E}_{\text{HOMO}}$$

$$- 3.335(\pm0.129)\text{D-Wiener}$$

$$+ 2.166(\pm0.172)\text{D-LogD},$$

$$n = 90, \ R^2 = 0.946, \ s = 0.190,$$

$$F = 204.247, \ \text{MSE} = 0.033,$$

$$\text{S}_{\text{Formula 6}} = 1.708(\pm0.151) + 1.135(\pm0.064)\text{SR}$$

$$+ 0.385(\pm0.051)\text{OR} + 4.076(\pm0.177)\text{D-Dipole}$$

$$- 1.907(\pm0.081)\text{D-MaxQ}^+$$

$$- 0.415(\pm0.077)\text{D-E}_{\text{HOMO}}$$

$$- 3.579(\pm0.133)\text{D-Wiener}$$

$$+ 2.598(\pm0.177)\text{D-LogD},$$

$$n = 90, \ R^2 = 0.948, \ s = 0.195,$$

$$F = 212.012, \ \text{MSE} = 0.035.$$

$$(3)$$

Equation (3) reveals a significant effect of the shape-related descriptor (Wiener index), charge-related descriptor (MaxQ$^+$, Dipole moment), quantum chemical parameter (E$_{\text{HOMO}}$), and logD on the solubility of 2-APA-NSAIDs in SEDDS. According to t-test criterion, the most important factors are Dipole, MaxQ$^+$, wiener index, and logD. The negative coefficient of wiener index showed that a drug with small size tended to have a good solubility in SEDDS. The positive coefficient of logD indicated that the increase of lipophilicity favors the solubility.

4. Conclusions

In the present study, we used QSPR to predict the solubility of 2-APA-NSAIDs in self-emulsifying drug delivery system by means of linear and nonlinear methods. We examined the effects of component ratio, stereoscopic effect, hydrophobic interactions, and electric effect on the solubility by MLR and ANN. In all the models, the ratio of compositions (SR, OR), charge-related descriptor, and the quantum chemical parameter (E$_{\text{HOMO}}$) appeared to be the most important factors. The obtained models in (3) indicate the significance of wiener index, charge-related descriptor, and logD of drugs on the solubility. The results of MLR and ANN methods were satisfactory, and nonlinear models were not found to be superior to linear models. Since the predicted optimum formulations were consistent with the experimental ones, the QSPR models obtained would be useful to predict the solubility of 2-APA-NSAIDs in SEDDS, screen for the optimal formulation, and reduce experimental time.

Acknowledgment

References

[1] E. Atef and A. A. Belmonte, "Formulation and in vitro and in vivo characterization of a phenytoin self-emulsifying drug delivery system (SEDDS)," *European Journal of Pharmaceutical Sciences*, vol. 35, no. 4, pp. 257–263, 2008.

[2] K. Hussein, M. Türk, and M. A. Wahl, "Drug loading into β-cyclodextrin granules using a supercritical fluid process for improved drug dissolution," *European Journal of Pharmaceutical Sciences*, vol. 33, no. 3, pp. 306–312, 2008.

[3] M. F. Francis, M. Piredda, and F. M. Winnik, "Solubilization of poorly water soluble drugs in micelles of hydrophobically modified hydroxypropylcellulose copolymers," *Journal of Controlled Release*, vol. 93, no. 1, pp. 59–68, 2003.

[4] M. Rutnakornpituk, S. Meerod, B. Boontha, and U. Wichai, "Magnetic core-bilayer shell nanoparticle: a novel vehicle for entrapmentof poorly water-soluble drugs," *Polymer*, vol. 50, no. 15, pp. 3508–3515, 2009.

[5] T. Vasconcelos, B. Sarmento, and P. Costa, "Solid dispersions as strategy to improve oral bioavailability of poor water soluble drugs," *Drug Discovery Today*, vol. 12, no. 23-24, pp. 1068–1075, 2007.

[6] C. W. Pouton, "Lipid formulations for oral administration of drugs: non-emulsifying, self-emulsifying and 'self-micro-emulsifying' drug delivery systems," *European Journal of Pharmaceutical Sciences*, vol. 11, no. S2, pp. S93–S98, 2000.

[7] P. P. Constantinides, "Lipid microemulsions for improving drug dissolution and oral absorption: physical and biopharmaceutical aspects," *Pharmaceutical Research*, vol. 12, no. 11, pp. 1561–1572, 1995.

[8] S. A. Charman, W. N. Charman, M. C. Rogge, T. D. Wilson, F. J. Dutko, and C. W. Pouton, "Self-emulsifying drug delivery systems: formulation and biopharmaceutic evaluation of an investigational lipophilic compound," *Pharmaceutical Research*, vol. 9, no. 1, pp. 87–93, 1992.

[9] D. J. Hauss, S. E. Fogal, J. V. Ficorilli et al., "Lipid-based delivery systems for improving the bioavailability and lymphatic transport of a poorly water-soluble LTB4 inhibitor," *Journal of Pharmaceutical Sciences*, vol. 87, no. 2, pp. 164–169, 1998.

[10] C. J. Porter, A. M. Kaukonen, B. J. Boyd, G. A. Edwards, and W. N. Charman, "Susceptibility to lipase-mediated digestion reduces the oral bioavailability of danazol after administration as a medium-chain lipid-based microemulsion formulation," *Pharmaceutical Research*, vol. 21, no. 8, pp. 1405–1412, 2004.

[11] T. R. Kommuru, B. Gurley, M. A. Khan, and I. K. Reddy, "Self-emulsifying drug delivery systems (SEDDS) of coenzyme Q10: formulation development and bioavailability assessment," *International Journal of Pharmaceutics*, vol. 212, no. 2, pp. 233–246, 2001.

[12] G. L. Amidon, H. Lennernas, V. P. Shah, and J. R. Crison, "A theoretical basis for a biopharmaceutic drug classification: the correlation of in vitro drug product dissolution and in vivo bioavailability," *Pharmaceutical Research*, vol. 12, no. 3, pp. 413–420, 1995.

[13] R. N. Gursoy and S. Benita, "Self-emulsifying drug delivery systems (SEDDS) for improved oral delivery of lipophilic drugs," *Biomedicine and Pharmacotherapy*, vol. 58, no. 3, pp. 173–182, 2004.

[14] I. I. Grover, I. I. Singh, and I. I. Bakshi, "Quantitative structure-property relationships in pharmaceutical research—part 1," *Pharmaceutical Science and Technology Today*, vol. 3, no. 1, pp. 28–35, 2000.

[15] I. I. Grover, I. I. Singh, and I. I. Bakshi, "Quantitative structure-property relationships in pharmaceutical research—part 2," *Pharmaceutical Science and Technology Today*, vol. 3, no. 2, pp. 50–57, 2000.

[16] Y. B. Liou, H. O. Ho, C. J. Yang, Y. K. Lin, and M. T. Sheu, "Construction of a quantitative structure-permeability relationship (QSPR) for the transdermal delivery of NSAIDs," *Journal of Controlled Release*, vol. 138, no. 3, pp. 260–267, 2009.

[17] H. Y. Xu, J. W. Zou, Q. S. Yu, Y. H. Wang, J. Y. Zhang, and H. X. Jin, "QSPR/QSAR models for prediction of the physico-chemical properties and biological activity of polybrominated diphenyl ethers," *Chemosphere*, vol. 66, no. 10, pp. 1998–2010, 2007.

[18] A. Talevi, M. Goodarzi, E. V. Ortiz et al., "Prediction of drug intestinal absorption by new linear and non-linear QSPR," *European Journal of Medicinal Chemistry*, vol. 46, no. 1, pp. 218–228, 2011.

[19] A. Guerra, N. E. Campillo, and J. A. Páez, "Neural computational prediction of oral drug absorption based on CODES 2D descriptors," *European Journal of Medicinal Chemistry*, vol. 45, no. 3, pp. 930–940, 2010.

[20] T. Ghafourian, M. Barzegar-Jalali, S. Dastmalchi, T. Khavari-Khorasani, N. Hakimiha, and A. Nokhodchi, "QSPR models for the prediction of apparent volume of distribution," *International Journal of Pharmaceutics*, vol. 319, no. 1-2, pp. 82–97, 2006.

[21] J. V. Turner, D. J. Maddalena, and D. J. Cutler, "Pharmacokinetic parameter prediction from drug structure using artificial neural networks," *International Journal of Pharmaceutics*, vol. 270, no. 1-2, pp. 209–219, 2004.

[22] D. E. Mager, "Quantitative structure-pharmacokinetic/pharmacodynamic relationships," *Advanced Drug Delivery Reviews*, vol. 58, no. 12-13, pp. 1326–1356, 2006.

[23] M. T. Saçan, M. Özkul, and S. S. Erdem, "QSPR analysis of the toxicity of aromatic compounds to the algae (*Scenedesmus obliquus*)," *Chemosphere*, vol. 68, no. 4, pp. 695–702, 2007.

[24] M. O. Taha, H. Abdel-Halim, M. Al-Ghazawi, and E. Khalil, "QSPR modeling of pseudoternary microemulsions formulated employing lecithin surfactants: application of data mining, molecular and statistical modeling," *International Journal of Pharmaceutics*, vol. 295, no. 1-2, pp. 135–155, 2005.

[25] T. Ghafourian, A. Safari, K. Adibkia, F. Parviz, and A. Nokhodchi, "A drug release study from hydroxypropylmethyl-cellulose (HPMC) matrices using QSPR modeling," *Journal of Pharmaceutical Sciences*, vol. 96, no. 12, pp. 3334–3351, 2007.

[26] M. O. Taha, M. Al-Ghazawi, H. Abu-Amara, and E. Khalil, "Development of quantitative structure-property relationship models for pseudoternary microemulsions formulated with nonionic surfactants and cosurfactants: application of data mining and molecular modeling," *European Journal of Pharmaceutical Sciences*, vol. 15, no. 5, pp. 461–478, 2002.

[27] M. Ruiz-Peña, R. Oropesa-Nuñez, T. Pons, S. R. Louro, and A. Pérez-Gramatges, "Physico-chemical studies of molecular interactions between non-ionic surfactants and bovine serum albumin," *Colloids and Surfaces B Biointerfaces*, vol. 75, no. 1, pp. 282–289, 2010.

[28] H. Zhang, Q. Y. Chen, M. L. Xiang, C. Y. Ma, Q. Huang, and S. Y. Yang, "In silico prediction of mitochondrial toxicity by using GA-CG-SVM approach," *Toxicology in Vitro*, vol. 23, no. 1, pp. 134–140, 2009.

[29] S. Agatonovic-Kustrin and R. Beresford, "Basic concepts of artificial neural network (ANN) modeling and its application in pharmaceutical research," *Journal of Pharmaceutical and Biomedical Analysis*, vol. 22, no. 5, pp. 717–727, 2000.

[30] M. Goodarzi, M. P. Freitas, and R. Jensen, "Ant colony optimization as a feature selection method in the QSAR modeling of anti-HIV-1 activities of 3-(3,5-dimethylbenzyl)uracil derivatives using MLR, PLS and SVM regressions," *Chemometrics and Intelligent Laboratory Systems*, vol. 98, no. 2, pp. 123–129, 2009.

[31] B. K. Kang, J. S. Lee, S. K. Chon et al., "Development of self-microemulsifying drug delivery systems (SMEDDS) for oral bioavailability enhancement of simvastatin in beagle dogs," *International Journal of Pharmaceutics*, vol. 274, no. 1-2, pp. 65–73, 2004.

Review Article

Nano-Oncology: Clinical Application for Cancer Therapy and Future Perspectives

Cristina Riggio, Eleonora Pagni, Vittoria Raffa, and Alfred Cuschieri

Life Science Institute, Scuola Superiore Sant'Anna, Piazza Martiri della Libertà, 33-56127 Pisa, Italy

Correspondence should be addressed to Alfred Cuschieri, a.cuschieri@sssup.it

Nano-oncology, the application of Nanomedicine to cancer diagnosis and treatment, has the potential to transform clinical oncology by enhancing the efficacy of cancer chemotherapy for a wide spectrum of invasive cancers. It achieves this by enabling novel drug delivery systems which target the tumour site with several functional molecules, including tumour-specific ligands, antibodies, cytotoxic agents, and imaging probes simultaneously thereby improving tumour response rates in addition to significant reduction of the systemic toxicity associated with current chemotherapy regimens. For this reason, nano-oncology is attracting considerable scientific interest and a growing investment by the global pharmaceutical industry. Several therapeutic nano-carriers have been approved for clinical use and others are undergoing phase II and III clinical trials. This paper describes the current approved formulations, such as liposomes and polymeric nanoparticles, and discusses the overall present status of nano-oncology as an emerging branch of nanomedicine and its future perspectives in cancer and therapy.

1. Introduction

Nanotechnology is defined as the development of small devices in a range of 1 to 100 nm. Such nano-structures/ devices can offer to the clinical practice of medicine in general, and to oncology in particular, many potentially significant and desirable applications which address unmet clinical needs [1].

These nano-structures by virtue of the quantum effects acquire at the nanoscale unique physical and chemical properties not present at their macroscale. Additionally, by virtue of molecular scale, they are able to interact with biological systems at cellular level.

The current focus of new technologies is to design and develop novel pharmaceutical formulations or drug carriers, which are both size- and site-specific aimed at targeted delivery of the active drug to the tumour site whilst evading clearance by the reticuloendothelial system (RES).

The ideal *nano-carrier* for drug delivery and cancer chemotherapy should (i) stabilize without altering the pharmacological activity of the drug, (ii) prevent premature metabolic degradation of the drug in the systemic circulation such that it arrives in a pristine state at the intended target,

(iii) release the drug at the intended site/tumour, and (iv) exhibit similar or lower toxicity than that of the free drug. Other ideal characteristics include ability for visualisation by MRI for guided chemotherapy and molecular imaging. In general, schedule-dependent regimes requiring steady state drug levels are ideal for these controlled drug delivery systems (CDDSs), for example, cytotoxic agents when a prolonged sustained drug concentration in the tumour is necessary to kill cancers cells as these enter and exit the sensitive phase of the cell cycle.

Such CDDSs overcome the problems encountered when cytotoxic agents are administrated systemically as these chemotherapeutic drugs lack specificity and thus cause significant damage to noncancerous tissues (systemic toxicity), including bone marrow suppression, hair loss (alopecia) and gut mucosal damage. Lack of specificity for cytotoxicity of these drugs is further compounded by escalating doses required in chemotherapy for solid cancers because of their rapid excretion and low therapeutic index [2]. The use of nano-carriers should improve the pharmacokinetics by prolonging the half-life of drugs in the systemic circulation. Moreover, nano-carriers can improve the aqueous solubility of poorly soluble drugs. In this respect, the majority of

Characteristic of an ideal carrier for cancer therapy:
Biocompatible and biodegradable
Facilitate cellular uptake and intracellular trafficking
Retain the drug at the target site for the desired period of time
Protect the drug from the degradation and from premature clereance
Ensure minimal drug leakage during transit to target
Decrease drug localisation in sensitive, non target tissue
Increase drug localisation in the tumour
(a) Passive targeting
(b) Active targeting

cytotoxic agents used in cancer chemotherapy are water insoluble and need to be dissolved in toxic organic solvents, such as Cremophor EL, for their intravenous systemic [3, 4]. The relevant advantages of nano-carriers as CDDS over free drugs are summarised in Table 1.

The following sections provide an overview of the arsenal of most promising nano-carriers, underlined by their current established clinical usage and evaluation in on-going clinical trials.

2. Nano-Carriers for Oncology

2.1. Liposomes. Liposomes have a long history as drug carrier systems because of their easy preparation, acceptable toxicity, and biodegradability profiles [5, 6]. Liposomes are self-assembling colloid structures composed of lipid bilayers surrounding an aqueous compartment(s) and can encapsulate a wide variety of (chemo)therapeutic drugs whether hydrophilic or hydrophobic in nature [7, 8]. Drug loading in liposomes can be achieved through (i) liposome formation in an aqueous solution saturated with soluble drug; (ii) the use of organic solvents and solvent exchange mechanisms; (iii) the use of lipophilic drugs; and (iv) pH gradient methods [9].

Because liposomes are of the order of 400 nm in size they are rapidly cleared by mononuclear phagocytic system (MPS) which requires preliminary opsonisation by the immune system. A useful method for evading opsonisation of carriers was developed at Rutgers University in the 1960s by a process called PEGylation: a biocompatible polymer, poly(ethylene glycol) (PEG; [CH2CH2O]n), is conjugated to the drug carrier [10]. The coating by PEG chains of the surface of the nanoparticles results in significantly increased blood circulation half-life. The opsonisation process is blocked or delayed by the hydrophilic protective layer around the nanoparticles which repels the absorption of opsonin proteins.

Liposomes can be classified as first generation or naked liposomes with an unmodified phospholipid surface, second generation or stealth liposomes with a layer of hydrophilic carbohydrates or polymers, usually PEG, onto the surface of the vesicles, and third generation liposomes that incorporate surface ligands to improve the therapeutic index of the
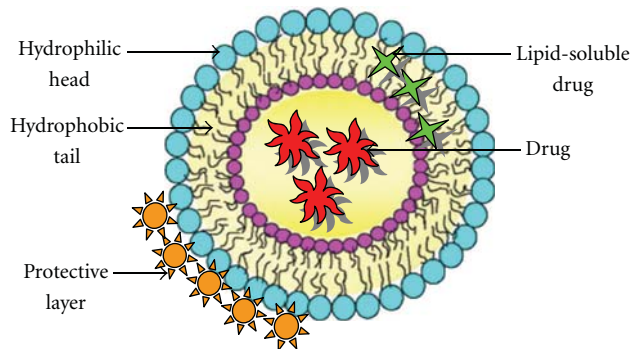
FIGURE 1: Diagram of bilayered membrane structure. The internal core entraps hydrophilic drug, while lipid soluble drugs are entrapped between the hydrophobic tails of the phospholipids. The outer surface can be functionalized with PEG and ligands for active targeting.
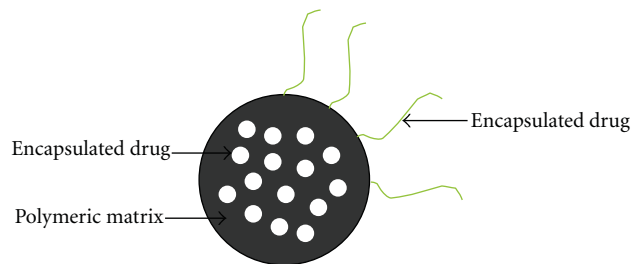
FIGURE 2: A schematic representation of polymeric particle as drug carrier: drug is entrapped in polymeric matrix and functional moieties lead to active targeting.

drug by increasing the selectivity and the specificity of the complex. Figure 1 is a schematic representation of the three classes of the liposomes.

2.2. Polymeric Nanoparticles. Delivery devices made from biodegradable polymers are an attractive option as carriers of therapeutic drugs in cancer therapy. Polymeric nanoparticles (NPs) (Figure 3), which include nanospheres and nanocapsules, are solid carriers ranging from 10 to 1000 nm in diameter made of natural or artificial polymers which are generally biodegradable and in which therapeutic drugs can be adsorbed, dissolved, entrapped, encapsulated, or covalently linked to the polymer backbone by means of a simple ester or amide bond that can be hydrolyzed *in vivo* through a change of pH (Figure 2).

Synthetic polymers, which include poly(lactic acid) (PLA) [12], poly(glycolic acid) (PGA) [13], poly(ethylene glycol) (PEG) [14], and their copolymers, have been among the most extensively researched due to their biocompatibility, biodegradability, and regulatory approval. Also natural polymers such us chitosan, alginate, and gelatine have been extensively tested [15].

When systemically administered, nanoparticles are generally more stable than liposome but are limited by poor pharmacokinetic properties that is, uptake by the RES. As with liposomes, the surface of nanoparticles can be coated with molecules, or intercalated into their structure,

Self-assembly through
Hydrophobic or
electrostatic interaction

Targeting ligand

20–100 nm

Hydrophobic domain
or polyelectrolyte

Hydrophilic domain
for example, PEG

Targeting ligand

Drug molecules

FIGURE 3: Polymeric micelle core-shell structure and drug encapsulation (reproduced from [11]).

to increase pharmacokinetics and even enable targeting for delivery and imaging purpose [16].

2.3. Micelles. Polymeric micelles are biodegradable spherical nano-carriers with a usual size range of 10–200 nm. They are formed by self-assembly of block copolymers consisting of two or more polyme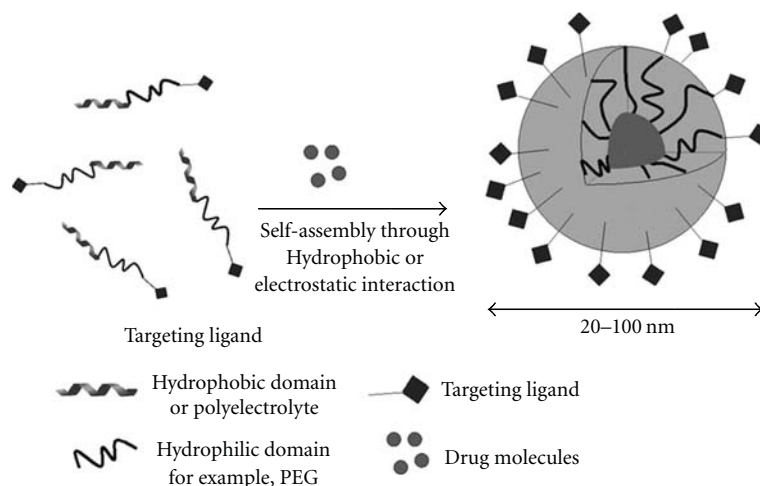r chains with different hydrophobicity. These copolymers spontaneously assemble to form a core-shell structure in an aqueous media to minimize the system's free energy (Figure 3). The hydrophobic segments form the hydrophobic inner core to minimize their exposure to environment, whereas the hydrophilic chains form the outer hydrophilic corona-like shell to stabilize the core through direct contact with water [11].

Micelles are considered ideal drug delivery vehicles because they provide a set of important advantages. The hydrophobic core can be used to carry pharmaceuticals, especially lipophilic drugs which are solubilized and physically entrapped in the inner region with high loading capacity. It must be remembered that hydrophobic drugs can only be administered intravenously after addition of solubilizing adjuvants like ethanol or Cremophor EL, which often induce toxic side effects. The incorporation of these drugs in micelles avoids the use of adjuvants. The hydrophilic shell not only provides a steric protection that increases micellar stability in blood, but also provides functional groups suitable for further micelle modification. Polymeric micelles can simultaneously codeliver two or more therapeutic agents and are capable of releasing drugs in a regulated manner. The encapsulated drugs can be released through erosion of the biodegradable polymers, diffusion of the drug through the polymer matrix, or polymer swelling followed by drug diffusion. External conditions such as change of pH and temperature can also induce drug release from micelles. Moreover, the surface modification of micelles with ligands such as antibodies, peptides, or other small molecules can be used for targeted delivery and uptake of these nano-carriers, thereby reducing their systemic toxicity and improving their specificity and efficacy [11].

Core
Branch units
Chemically active end groups
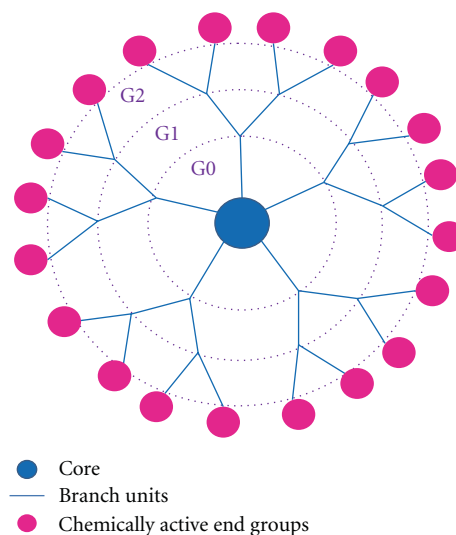
FIGURE 4: Structure of a dendrimer.

2.4. Dendrimers. Dendrimers are spherical, highly branched, and synthetic macromolecules with adjustable size and shape. They contain multiple layers with active end groups, also known as generations, that extend outwards from an initiator core called generation zero (Figure 4). The size of dendrimers is usually in the range of 1–15 nm. The branches of these polymers provide a large surface area to which chemotherapeutic drugs and targeting molecules can be attached through covalent conjugation or electrostatic adsorption. Alternatively, therapeutic agents can be loaded in the cavities of the core regions through hydrophobic interaction, hydrogen bonds, or chemical linkage [11].

The most commonly studied dendrimers belong to the family of PAMAM (polyamidoamine) dendrimers. These polymers have shown great potential for drug delivery because they are biodegradable and biocompatible and have high water solubility [17]. Recently, a G5-PAMAM dendrimer has been developed with a diameter of 5 nm and more than 100 functional amines on the surface. This nano-carrier
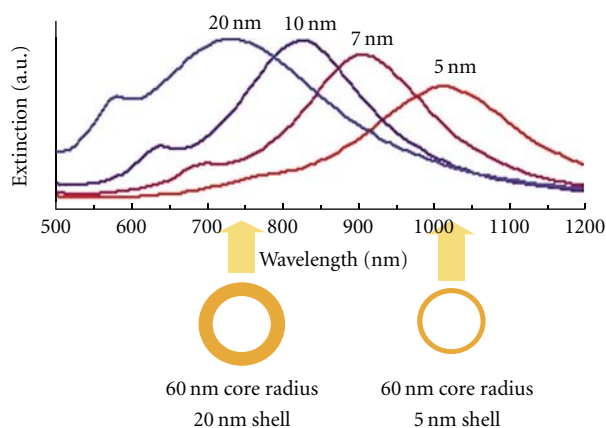
FIGURE 5: Extinction spectra of gold nano-shells depending on the core: shell diameter ratio (reproduced from [21]).

was used for the delivery of methotrexate in a preclinical study. The dendrimer surface charge was first reduced by modifying peripheral amines with acetyl groups. Then, the G5-PAMAM dendrimer was conjugated with methotrexate (as the cytotoxic agent) and with folate as the targeting molecule. A biodistribution study in mice with subcutaneous tumors showed internalization and intracellular accumulation of dendrimers in xenograft human KB tumors that over-expressed folate receptors. The *in vivo* delivery of the G5-PAMAM dendrimer conjugated with methotrexate induced a tenfold reduction in tumor size compared with that observed following systemic administration of free methotrexate at the same molar concentration [18]. This study provided the basis for further preclinical studies on dendrimers, which are now under investigation for cancer chemotherapy.

2.5. Gold Nano-Shells.
Gold nano-shells are nanospheres composed of an ultrathin layer of gold around a dielectric core, typically silica. The size of these nanoparticles ranges from 50 to 500 nm in diameter but the outer shell can be only few nanometers thick. Gold nano-shells have peculiar optical properties due to their unique interaction with light and related to a nanotechnological phenomenon known as surface plasmon resonance (SPR). In this process, the conducting surface electrons of the metal nano-shell oscillate collectively in the presence of the oscillating magnetic field of light. After absorption of radiation, the surface plasmon decays radiatively resulting in light emission or nonradiatively as heat. The SPR effect depends on nanoparticle size and shape (Figure 5), so the absorption characteristics of gold nano-shells can be tuned by adjusting the core: shell diameter thickness ratio [19, 20].

Gold nano-shells can be used for medical applications because they are resistant to corrosion, are physiologically inert and thus quite safe [19]. The primary application of gold nano-shells in cancer treatment is the photo-thermal ablation based on their absorption/heating properties (temperatures $\geq 42°C$) in tumors. With other forms of hyperthermic ablation, for example, radiofrequency probes, it is difficult to avoid thermal damage to the normal tissues surrounding the tumor. Gold nano-shells offer a solution

to this problem. Indeed, gold nano-shells targeted to tumor site can be locally heated by radiation with a near-infrared laser (wavelength in the range of 650–950 nm), allowing selective tumor ablation without any collateral damage to normal tissues [19–22]. Recent studies have demonstrated the efficacy of gold nano-shells in the destruction of mouse carcinoma tumors and in the photo-thermal ablation of human breast carcinoma tumors implanted in mice [23, 24]. These experimental studies have led to the initiation of a clinical trial using gold nano-shells as hyperthermia agents for cancer therapy in patients with oropharyngeal malignancies. However, near-infrared thermal ablation with gold nano-shells can only be effective for the treatment of superficial tumors, because near-infrared radiation is significantly attenuated by biomolecules and cannot penetrate the deeper tissues [22].

The ability of gold nano-shells to scatter light can also be used for imaging, thus allowing the detection and diagnosis of cancer. In particular, gold nano-shells have been useful as *in vivo* contrast agents [25], and when conjugated to antibodies to epidermal growth factor receptor, they have been used for the imaging of early cervical cancers [26].

2.6. Superparamagnetic Iron Oxide Nanoparticles (SPIOs).
SPIOs are nanoparticles usually composed of Fe_3O_4 (magnetite) with a size of less than 20 nm [21]. These materials show peculiar superparamagnetic properties related to nanoscale dimensions. Like ferromagnetic materials, SPIOs strongly magnetize under the influence of a magnetic field, but as with other paramagnetic materials, the removal of the field eliminates the phenomenon. The magnetic behavior of paramagnetic and superparamagnetic species is due to the presence of unpaired electrons, whose spins align with the applied magnetic field. Pools of adjacent electrons aligned in the same direction form the so-called magnetic domains. The difference between paramagnetic and superparamagnetic materials is that the latter are smaller and do not possess multiple domains, but only a single magnetic domain where all spins are mutually aligned. This produces a large magnetic moment, which can be exploited for medical applications. SPIOs have intrinsic toxicity, so they have to be suitably modified through surface coatings (e.g., dextran or PEG coatings) for biocompatibility before any medical use [19] SPIO surface can also be functionalized through the attachment of targeting ligands [21].

Like gold nano-shells, SPIOs are attracting particular interest as hyperthermia agents for cancer thermal ablation. It is known that oscillating magnetic fields (in the range of kHz–MHz) applied to SPIOs result in generation of heat because of the great relaxation loss of the single magnetic domain. Energy can be dissipated through Brownian relaxation (heat due to total particle oscillation) or Neél relaxation (heat due to the rotation of the magnetic moment in the oscillating magnetic field) [27]. After their delivery and accumulation at the tumor site, SPIOs can be remotely activated through oscillating magnetic fields for the ablation of malignant tumors situated in deep regions of the body. Magnetic fields are not absorbed by normal tissues, so that

TABLE 2: Examples of liposomes available on the market and in clinical use.

Composition	Trade name	Company	Indication	Administration
Liposomal daunorubicin	DaunoXome	Gilead Sciences	Kaposi's sarcoma	intravenous
Stealth liposomal doxorubicin	Doxil/Caelyx	Ortho Biotech, Schering-Plough	Kaposi's Sarcoma; refractory ovarian cancer; refractory breast cancer	intramuscular
Liposomal doxorubicin	Myocet	Zeneus	Metastatic breast cancer in combination with cylophosphamide	intravenous
Liposomal muramyl Tripeptide phosphatidyl Ethanolamine	MEPACT	Taked	Osteosarcoma	intravenous
Cytarabine	Depocyt	SkyePharma PLC	Lymphomatous meningitis	intrathecal
Liposomal vincristine	Onco-TCS	Inex Enzon	Non-hodgking lymphoma	intravenous

magnetic thermal ablation of tumors does not damage normal tissues [21]. Recent clinical trials have demonstrated the feasibility and good tolerability of magnetic thermotherapy for the treatment of human prostate cancer after the transperitoneal injection of iron oxide nanoparticles and the application of an alternating magnetic field [1]. However, the efficacy of magnetic thermo-ablation of tumors as monotherapy is limited and requires improvement. Thus, it seems likely that SPIOs thermotherapy will probably be used as part of a combination regimen.

The peculiar magnetic properties of SPIOs can also be useful for cancer diagnosis and detection by magnetic resonance imaging (MRI), an important medical imaging technique depending on signals from water protons of the body. By virtue of their large magnetic moment, SPIOs can enhance image contrast in MRI, thus producing distinct images and allowing the discrimination between neoplastic and healthy tissues. Several SPIOs have been in long established clinical use as contrast agents for MRI [19].

3. Nano-Carriers in Clinical Usage

3.1. Liposomes: Clinical Use. Many liposomal formulations of anticancer drugs have been approved for human use and are already available on market. The list of the cytotoxic agents marketed for clinical use by various pharmaceutical companies are shown in Table 2.

The first liposome formulations approved by the regulatory authorities were Doxil and Myocet. Both products contain the cytotoxic drug doxorubicin, a chemotherapeutic agent used widely in the treatment of breast, ovarian, bladder, and lung cancers. The two liposomal formulations, Myocet and Doxil, differ in PEG coating: Doxil is a PEG-liposome formulation designed to prolong blood circulation time. Free doxorubicin has an elimination half-life time of 0.2 h. This value is prolonged to 2.5 h and 55 h for Myocet and Doxil, respectively (Table 3) [28].

Liposomal encapsulation and consequently polymer coating can substantially affect a drug's functional properties relative to those of the unencapsulated drug. Harris et al., have reported on the advantages of Myocet over free doxorubicin in terms of cardiotoxicity by evaluating two parameters: the incidence of cardiac events and congestive

TABLE 3: Values for half-life and AUC for two liposomal formulations and free doxorubicin.

	Half-life time	AUC (Area Under Curve)
Free doxorubicin	0.2 h	4 μgh/mL
Myocet	2.5 h	45 μgh/mL
Caelyx/Doxil	55 h	900 μgh/mL

TABLE 4: Effect of Myocet on cardiotoxicity than free doxorubicin.

	Incidence of cardiac events	Congestive Heart failure
Free doxorubicin	29%	8%
Myocet	13%	2%

heart failure with significant decrease of cardiac events and congestive cardiac failure of 16% and 6%, respectively [29] (Table 4).

Myocet is currently used in the chemotherapy of breast cancer in combination with other chemotherapeutic agent (cyclophosphamide). Doxil is used to treat women with metastatic breast cancer who have an increased risk of heart damage, in patients with advanced ovarian cancer and in AIDS-related Kaposi's sarcoma.

Other liposomal systems have been approved and are currently on the market such as MEPACT, DepoCyt and Onco-TCS. MEPACT is a liposomal formulation of mifamurtide, an immune modulator proposed for clinical use in adjuvant chemotherapy of children and young adults with high grade resectable non-metastatic osteosarcoma.

DepoCyt, used in the treatment of lymphomatous meningitis, is a sustained-release liposomal formulation of the active ingredient cytarabine designed for direct administration into the cerebrospinal fluid (CSF). Onco-TCS is a non-PEGylated liposomal formulation (about 50 nm in diameter) of daunorubicin and vincristine. DaunoXome is a liposomal preparation of daunorubicin, formulated to maximize the selectivity of daunorubicin in AIDS related Kaposi's sarcoma. As with Myocet, both the pharmacokinetic parameters and incidence of side effects are decreased by DaunoXome (Tables 5 and 6).

TABLE 5: Pharmacokinetic parameters of DaunoXome compared to free daunorubicin.

	Half-life time (h)	Plasma Clereance (mL/min)
Conventional daunorubicin	0.77 + 0.3	236 + 181
DaunoXome	4.41 + 2.33	17.3 + 6.1

TABLE 6: Comparative toxicity (neuropathy and alopecia) of DaunoXomeand free daunorubicine.

	Neuropathy (%)	Alopecia (%)
Conventional daunorubicin	41	36
DaunoXome	13	8

4. Nano-Carriers in Clinical Trial

4.1. Liposomes. Drug-encapsulated liposomes dominate clinical trials designed to study the effects of these CDDS in overcoming rapid clearance from the blood by phagocytic cell of the RES and thus improving the therapeutic index.

The main liposome formulations currently in clinical trials are listed in Table 7.

Aroplatin is a novel liposomal third generation formulation of cisplatin (platinum). Its antitumour activity has been demonstrated in the treatment of colorectal cancer. SPI-77, a pegylated liposomal formulation of cisplatin developed specifically to reduce systemic toxicity and improve cisplatin delivery, is currently undergoing a phase III clinical trial [30].

A new targeting strategy consisting in "activable" nanocarrier is also being evaluated in a clinical trial. The liposomal formulation developed by Needham and Dewhirst's groups at Duke (USA) underwent further pharmaceutical development by the biopharmaceutical company Celsion, which has now reached the stage of phase III clinical trial and is marketed as Thermodox. Two main studies are currently on-going combining Thermodox with hyperthermia in patients with loco-regional breast carcinoma of the chest wall and Thermodox with radiofrequency ablation in patients with primary or metastatic liver cancer. Results of these trials have not yet been published. However, the reported results to date have indicated the need for confirmatory clinical phase III trials in patients with liver cancer patients (http://www.ClinicalTrials.gov/). These promising developments indicate the high potential of combining hyperthermia with thermosensitive liposomes for delivery of chemotherapy to solid cancers. Nano-carriers maintain the stealth function during circulation; upon arrival at the tumour site the drug release is triggered by application of external stimuli allowing a controlled and selective targeting of the cells now referred to as environmentally responsive DDS.

Another strategy adopted to increase the accumulation of liposomes in the desired tumour tissue is by attaching targeting ligands such as antibodies, peptides, and small molecules (i.e., folate, transferrin) to the liposome surface. The targeted liposome formulations involved in clinical trials are summarized in Table 8.

Two examples of liposomal formulations for targeted drug/gene delivery are MBP-426 and SGT-53, which are currently undergoing phase I and phase II of clinical trials. They utilize transferrin and an antitransferrin receptor single-chain antibody fragment as targeting moieties, respectively.

MBP-426, transferrin-conjugated liposomal oxaliplatin formulation, was developed to improve the safety and efficacy of oxaliplatin through the prolongation of drug plasma circulation time and thus bioavailability and by targeting transferrin receptor on tumour cell.

Many human tumours possess loss or mutation of wild-type p53 (wtp53). In addition to playing a crucial role in cell cycle control, the p53 gene is a critical component in two of the pathways involved in regulating tumor cell growth: cell death (apoptosis) and the regulation of angiogenesis. The loss of such critical tumour suppressor activity is believed to be responsible for p53's involvement in such a broad array of human tumors and resistance to chemo/radiotherapy. SGT-53 is a complex composed of a wild-type p53 gene (plasmid DNA) encapsulated in a liposome that is targeted to tumor cells by means of an antitransferrin receptor single-chain antibody fragment (TfRscFv) attached to the outside of the liposome.

4.2. Polymeric Nanoparticles. The majority of polymeric nanoparticles are still in preclinical phase of development but have potential for targeted drug delivery of anticancer drugs owing to the ease with which ligands can be attached (Table 9).

Albumin-bound nanoparticles of paclitaxel (Abraxane) have been successfully used to deliver paclitaxel for the treatment of metastatic breast cancer after failure of combination chemotherapy for metastatic disease or relapse within 6 months of adjuvant chemotherapy. The advantages with the use of Abraxane include (i) albumin is nontoxic and well tolerated by immune system because it is a plasma protein (molecular weight of 66 kDa); (ii) its use eliminates the need for toxic solvent (Cremophor EL polyoxyethylated castor oil) which has been shown to limit the dose of Taxol that can be administered [31]. Abraxane has also intriguing properties due to the pharmacokinetics of the albumin, especially its long half-life which is particularly attractive to the design of drug carriers for passive targeting. It has been proposed that Abraxane targets cancer tissues because of the high metabolic demand and active transport of plasma proteins for anabolic processes [31]. Albumin seems to help endothelial transcytosis of protein bound and unbound plasma constituents via the binding to a cell surface receptor (gp60). Gp60 binds to caveolin-1 with subsequent formation of transcytolic vesicles. Abraxane could be transported into tumour by secreted protein acidic rich in cysteine (SPARC) or osteonectin, which binds albumin because of a sequence homology with gp60. SPARC as caveolin-1 is often expressed in some cancers (e.g., breast, lung and prostate), which could explain why albumin is known to accumulate in some tumors and thus facilitates intratumoral accumulation of albumin-bound drugs. In a Phase III study, Abraxane resulted in higher tumour response rates, a better safety

TABLE 7: Liposomes in clinical trials.

Compound	Name	Status	Indication
Liposomal cisplatin	SPI-77	Phase III	Non-small cell lung cancer
Liposomal interleukin 2	Oncolipin	Phase I	Non-hodgking lymphoma
Liposomal annamycin	L-Annamycin	Phase I	Acute lymphocytic leukemia
Liposomal oxaliplatin	Aroplatin	Phase II	Advanced colorectal cancer
Liposomal lurtotecan	OSI-211	Phase II	Ovarian cancer
Cationic liposomal c-Raf AON	LErafAON	Phase I/II	Various
Cationic liposomal EI A pDNA	PLD-EIA	Phase I/II	Breast, Ovarian
Thermosensitive liposomal doxorubicin	Thermodox	Phase III	Breast, liver

TABLE 8: Examples of targeted liposome in clinical trials.

Compound	Therapeutic agent	Status	Targeting agent
MCC-465	Doxorubicin	Phase I	F(ab')2 fragment of human antibody GAH
MBP-426	Oxaliplatin	Phase II	Transferrin
SGT-53	Plasmid DNA with p53 gene	Phase I	Transferrin receptor antibody fragment
CALAA-01	Small interfering RNA	Phase I	Transferrin

profile and improved survival compared with conventional paclitaxel, in patients receiving second-line chemotherapy [32].

4.3. Micelles. In cancer chemotherapy, a multitude of preclinical studies on polymeric micelles has been published, which have shown that micelle-based drug delivery is advantageous over free drug delivery in laboratory animals, resulting in less adverse effects and toxicity to nontargeted areas. To-date, five products for anticancer therapy has been investigated in clinical trials, of which Genexol-PM has FDA approval for use in patients with breast cancer (Table 10).

Genexol-PM is a novel Cremophor EL-free polymeric micelle formulation of paclitaxel (Taxol) consisting of two block copolymers: poly-(ethylene glycol), which is useful as a non-immunogenic carriers, and the core-forming poly-(D,L-lactide) that allows the solubilization of the hydrophobic drug. Preclinical *in vivo* studies have shown that compared with free paclitaxel, the bio-distribution of paclitaxel administered as Genexol-PM was 2-3 times higher in various tissues, including liver, spleen, kidneys, lungs, heart, and tumor. Moreover, Genexol-PM demonstrated a 3-fold increase in the maximum tolerated dose (MTD) and a significantly increased antitumor efficacy compared to free paclitaxel [33]. In phase I studies, no acute hypersensitivity reactions occurred in patients at the MTD 390 mg/m^2 administered every 3 weeks or 120 mg/m^2 weekly [34, 35]. Phase II studies have demonstrated the safety and efficacy of Genexol-PM with high response rates in patients with metastatic breast cancer and advanced pancreatic cancer. In patients with metastatic breast cancer, however, hypersensitivity reactions were seen in the 19.5% of patients [36, 37]. Moreover, Genexol-PM plus cisplatin combination chemotherapy has shown significant antitumor activity and allowed the administration of higher doses of paclitaxel compared to the Cremophor EL-based formulation in patients with advanced non-small-cell lung cancer. Furthermore, no additional toxicity was reported, although hypersensitivity reactions were observed [38]. Clinical studies are now being conducted on Genexol-PM for the treatment of several malignancies, including a phase III and IV study in patients with recurrent breast cancer.

5. Drawbacks and Future Challenges

In this paper, we have focused on the main achievements obtained with organic and inorganic nanoparticles in cancer therapy, but we must also consider their drawbacks, current limitations, and the important challenges for the future development of nano-oncology. Additionally, aspects of higher performance, nanosafety, and regulatory issues need to be addresses in the near future.

The first requirement relates to improvement of the targeting efficacy of nano-vectors to specific cancers and their immediate microenvironment in order to concentrate delivery of the cytotoxic agents to the tumor site. Targeting methods involve the conjugation of specific recognition molecules to the surface of nano-vectors. Another requirement is the development of effective triggers for release of the cytotoxic drugs, for example, nano-carriers which release their payload of active drugs at the intended site by external energy (e.g., light and electromagnetic fields) or environmentally responsive by conditions preferentially expressed at tumor site (e.g., low pH) [38–40]. Equally important is progress in the ability of nano-carriers to escape or overcome physiological barriers such as cellular multidrug resistance, clearance by the RES, blood-brain barrier, hypersensitivity

TABLE 9: Examples of polymeric nanoparticles in clinical trials.

Compound	Name	Status	Indication
Albumin-paclitaxel	Abraxane	Approved	Metastatic breast cancer
Doxorubicin	Transdrug	Approved	Hepatocarcinoma
Paclitaxel	Nanoxel	Phase I	Advanced breast cancer
Paclitaxel	Paclimer	Phase I	Various

TABLE 10: Polymeric micelles in clinical trials.

Polymeric micelle	Block copolymer	Drug	Diameter (nm)	Indication	Clinical phase
NK012	PEG-PGlu(SN-38)	SN-38	20	Breast cancer	II
NK105	PEG-P(aspartate)	Paclitaxel	85	Advanced stomach cancer	II
SP1049C	Pluronic L61 and F127	Doxorubicin	22–27	Adenocarcinoma of esophagus, gastro esophageal junction and stomach	III
NC-6004	PEG-PGlu(cisplatin)	Cisplatin	30	Solid tumors	I/II
				Breast cancer	I
				Pancreatic cancer	V
Genexol-PM	PEG-P(D,L-lactide)	Paclitaxel	20–50	Non-small-cell lung cancer in combination with carboplatin	II
				Pancreatic cancer in combination with gemcitabine Ovarian cancer in combination with carboplatin	I/II

reactions induced by carrier, increased osmotic pressure within cancer lesions [27].

The ideal system would be attained by the design and development of "smart" multifunctional nanoparticles concurrently able to image, target, and treat tumours imaging (Figure 6). These nanoparticles would be able to carry: one or more drugs, a specific targeting moiety, an imaging agent, a cell-penetrating agent, a stimulus-sensitive element for controlled release of drugs, and a stabilizing polymer for biocompatibility [1].

Before this can be materialized, however, there is an urgent need to resolve the outstanding issues relating to safety of nanoparticles and material, which have to be engineered for biocompatibility, biodegradability, and non-toxicity to enable safe use in patients. Unfortunately, little is known about the fate of nanoparticles in human body. As the size and surface properties of nano-vectors allow them to reach locations denied to larger particles, their bio-distribution may be different from the expected and may result in accumulation in nontarget organs (such as liver, spleen and bone marrow), with possible undesired toxic effects [39].

Additionally, as with many applications in the nanofield, currently there is no internationally agreed regulation and legislation related to the development and subsequent clinical introduction of nanobased drug delivery systems [40]. Legislators have addressed the problem in the short term, by applying existing regulatory measures to nanomedical products. This is unsatisfactory and the only interim solution for nanomedicine consists of a governance-based pro-active regulatory system which, whilst not hindering research and development, governs what can and cannot be translated into clinical practice based on the best available information on the nanosafety of the product. There is a real need for more information on nanosafety as currently the published data are insufficient and at times conflicting especially on nano-particle characterization, their detection and measurement, and persistence in humans and in the environment.

Research is essential to the future progress of nano-medicine and the realization of its potential in the treatment of various life-threatening disorders and others which severely impair the quality of life, and this research should encompass all aspects of nanosafety rather than the more limited field of nanotoxicity. The European Union has recognized the importance of this by establishing the "Nanosafety Network", by commissioning various reports and inclusion of Health Technology Assessment (HTA) calls within its more recent invitation for research projects within Framework 7 Programme. The two key issues are thus (i) improved knowledge on nanosafety and improved methods of HTA which, in addition to the conventional HTA measures, include additional nano-technology-related outcome measures. In turn these measures should provide the basis for effective regulation of newer nanomedicine products for healthcare.

Aside from regulatory and safety issues the translation of nanomedical products into clinical practice will remain restricted until the current limitations such as their selectivity, efficacy in protected drug carriage and release at the intended are resolved or improved by basic biological and

Imaging agent
Drug A
Specific targeting moiety
Stimulus-sensitive agent A
Biocompatible polymer
Drug B
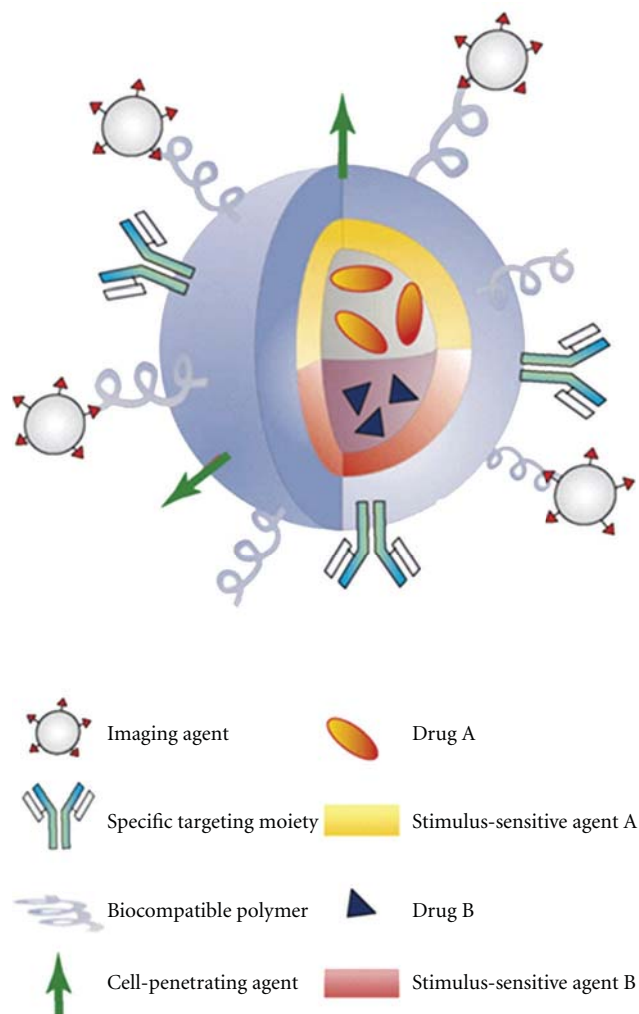Cell-penetrating agent
Stimulus-sensitive agent B

FIGURE 6: Structure of a smart multifunctional nanoparticle (reproduced from [1]).

in-vivo animal studies. Their full potential will then be realized as standard drug delivery systems for routine cancer chemotherapy. With the progress made in this field to-date, it is likely that in the not-distant future, nanoparticles-based approaches will usher a new era of personalized oncology, tailored to the phenotypical characteristics of the individual patient and his or her cancer—this is the ultimate objective for curative cancer chemotherapy and nano-oncology may be the means to provide this.

Acknowledgments

References

[1] M. Ferrari, "Cancer nanotechnology: opportunities and challenges," *Nature Reviews Cancer*, vol. 5, no. 3, pp. 161–171, 2005.

[2] C. M. Walko and H. McLeod, "Pharmacogenomic progress in individualized dosing of key drugs for cancer patients," *Nature Clinical Practice Oncology*, vol. 6, no. 3, pp. 153–162, 2009.

[3] G. S. Kwon, "Polymeric micelles for delivery of poorly water-soluble compounds," *Critical Reviews in Therapeutic Drug Carrier Systems*, vol. 20, no. 5, pp. 357–403, 2003.

[4] D. J. Bharali and S. A. Mousa, "Emerging nanomedicines for early cancer detection and improved treatment: current perspective and future promise," *Pharmacology and Therapeutics*, vol. 128, no. 2, pp. 324–335, 2010.

[5] A. Bangham, The 1st Description of Liposomes—a Citation Classic Commentary on Diffusion of Univalent Ions across the Lamellae of Swollen Phospholipids by Bangham ,A.D., Standish, M.M., and Watkins, J.C. Current Contents/Life Sciences 1989:14-14.

[6] G. Gregoriadis, "The carrier potential of liposomes in biology and medicine. II," *The New England Journal of Medicine*, vol. 295, no. 14, pp. 765–770, 1976.

[7] L. Zhang and S. Granick, "How to stabilize phospholipid liposomes (using nanoparticles)," *Nano Letters*, vol. 6, no. 4, pp. 694–698, 2006.

[8] V. P. Torchilin, "Recent advances with liposomes as pharmaceutical carriers," *Nature Reviews Drug Discovery*, vol. 4, no. 2, pp. 145–160, 2005.

[9] L. Qiu, N. Jing, and Y. Jin, "Preparation and in vitro evaluation of liposomal chloroquine diphosphate loaded by a transmembrane pH-gradient method," *International Journal of Pharmaceutics*, vol. 361, no. 1-2, pp. 56–63, 2008.

[10] A. S. Hoffman, "The origins and evolution of "controlled" drug delivery systems," *Journal of Controlled Release*, vol. 132, no. 3, pp. 153–163, 2008.

[11] C. Oerlemans, W. Bult, M. Bos, G. Storm, J. F. W. Nijsen, and W. E. Hennink, "Polymeric micelles in anticancer therapy: targeting, imaging and triggered release," *Pharmaceutical Research*, vol. 27, pp. 2569–2589, 2010.

[12] K. Hu, J. Li, Y. Shen et al., "Lactoferrin-conjugated PEG-PLA nanoparticles with improved brain delivery: in vitro and in vivo evaluations," *Journal of Controlled Release*, vol. 134, no. 1, pp. 55–61, 2009.

[13] J. Cheng, B. A. Teply, I. Sherifi et al., "Formulation of functionalized PLGA-PEG nanoparticles for in vivo targeted drug delivery," *Biomaterials*, vol. 28, no. 5, pp. 869–876, 2007.

[14] J. M. Chan, L. Zhang, K. P. Yuet et al., "PLGA-lecithin-PEG core-shell nanoparticles for controlled drug delivery," *Biomaterials*, vol. 30, no. 8, pp. 1627–1634, 2009.

[15] Z. Liu, Y. Jiao, Y. Wang, C. Zhou, and Z. Zhang, "Polysaccharides-based nanoparticles as drug delivery systems," *Advanced Drug Delivery Reviews*, vol. 60, no. 15, pp. 1650–1662, 2008.

[16] A. K. Bajpai, S. K. Shukla, S. Bhanu, and S. Kankane, "Responsive polymers in controlled drug delivery," *Progress in Polymer Science*, vol. 33, no. 11, pp. 1088–1118, 2008.

[17] D. Peer, J. M. Karp, S. Hong, O. C. Farokhzad, R. Margalit, and R. Langer, "Nanocarriers as an emerging platform for cancer therapy," *Nature Nanotechnology*, vol. 2, no. 12, pp. 751–760, 2007.

[18] J. F. Kukowska-Latallo, K. A. Candido, Z. Cao et al., "Nanoparticle targeting of anticancer drug improves therapeutic

response in animal model of human epithelial cancer," *Cancer Research*, vol. 65, no. 12, pp. 5317–5324, 2005.

[19] V. V. Mody, R. Siwale, A. Singh, and H. R. Mody, "Introduction to metallic nanoparticles," *Journal of Pharmacy and Bioallied Science*, vol. 2, pp. 282–289, 2010.

[20] P. Cherukuri, E. S. Glazer, and S. A. Curley, "Targeted hyperthermia using metal nanoparticles," *Advanced Drug Delivery Reviews*, vol. 62, no. 3, pp. 339–345, 2010.

[21] C. Loo, A. Lin, L. Hirsch et al., "Nanoshell-enabled photonics-based imaging and therapy of cancer," *Technology in Cancer Research and Treatment*, vol. 3, no. 1, pp. 33–40, 2004.

[22] A. M. Gobin, M. H. Lee, N. J. Halas, W. D. James, R. A. Drezek, and J. L. West, "Near-infrared resonant nanoshells for combined optical imaging and photothermal cancer therapy," *Nano Letters*, vol. 7, no. 7, pp. 1929–1934, 2007.

[23] L. R. Hirsch, R. J. Stafford, J. A. Bankson et al., "Nanoshell-mediated near-infrared thermal therapy of tumors under magnetic resonance guidance," *Proceedings of the National Academy of Sciences of the United States of America*, vol. 100, no. 23, pp. 13549–13554, 2003.

[24] K. Fu, J. Sun, A. W. H. Lin, H. Wang, N. J. Halas, and R. A. Drezek, "Polarized angular dependent light scattering properties of bare and PEGylated gold nanoshells," *Current Nanoscience*, vol. 3, no. 2, pp. 167–170, 2007.

[25] C. Loo, L. Hirsch, M. H. Lee et al., "Gold nanoshell bioconjugates for molecular imaging in living cells," *Optics Letters*, vol. 30, no. 9, pp. 1012–1014, 2005.

[26] L. R. Hirsch, A. M. Gobin, A. R. Lowery et al., "Metal nanoshells," *Annals of Biomedical Engineering*, vol. 34, no. 1, pp. 15–22, 2006.

[27] M. E. Davis, Z. Chen, and D. M. Shin, "Nanoparticle therapeutics: an emerging treatment modality for cancer," *Nature Reviews Drug Discovery*, vol. 7, no. 9, pp. 771–782, 2008.

[28] R. D. Hofheinz, S. U. Gnad-Vogt, U. Beyer, and A. Hochhaus, "Liposomal encapsulated anti-cancer drugs," *Anti-Cancer Drugs*, vol. 16, no. 7, pp. 691–707, 2005.

[29] L. Harris, G. Batist, R. Belt et al., "Liposome-encapsulated doxorubicin compared with conventional doxorubicin in a randomized multicenter trial as first-line therapy of metastatic breast carcinoma," *Cancer*, vol. 94, no. 1, pp. 25–36, 2002.

[30] N. Seetharamu, E. Kim, H. Hochster, F. Martin, and F. Muggia, "Phase II study of liposomal cisplatin (SPI-77) in platinum-sensitive recurrences of ovarian cancer," *Anticancer Research*, vol. 30, no. 2, pp. 541–545, 2010.

[31] W. J. Gradishar, S. Tjulandin, N. Davidson et al., "Phase III trial of nanoparticle albumin-bound paclitaxel compared with polyethylated castor oil-based paclitaxel in women with breast cancer," *Journal of Clinical Oncology*, vol. 23, no. 31, pp. 7794–7803, 2005.

[32] W. Gradishar, T. Vishalpura, M. Franklin, and T. Bramley, "Cost-effectiveness of nanoparticle albumin-bound paclitaxel versus docetaxel in the treatment of metastatic breast cancer," *Breast Cancer Research and Treatment*, vol. 94, pp. S220–S221, 2005.

[33] S. C. Kim, D. W. Kim, Y. H. Shim et al., "In vivo evaluation of polymeric micellar paclitaxel formulation: toxicity and efficacy," *Journal of Controlled Release*, vol. 72, no. 1–3, pp. 191–202, 2001.

[34] T. Y. Kim, D. W. Kim, J. Y. Chung et al., "Phase I and pharmacokinetic study of Genexol-PM, a Cremophor-free, polymeric micelle-formulated paclitaxel, in patients with advanced malignancies," *Clinical Cancer Research*, vol. 10, no. 11, pp. 3708–3716, 2004.

[35] E. Tan, S. S. Leong, W. T. Lim, C. K. Toh, and B. Chowbay, "Weekly administration of a Cremophor-free, polymeric micelle formulation of paclitaxel to Asian patients with advanced solid tumor: phase I study results," in *Proceedings of the Gastrointestinal Cancers Symposium*, 2007.

[36] K. S. Lee, H. C. Chung, S. A. Im et al., "Multicenter phase II trial of Genexol-PM, a Cremophor-free, polymeric micelle formulation of paclitaxel, in patients with metastatic breast cancer," *Breast Cancer Research and Treatment*, vol. 108, no. 2, pp. 241–250, 2008.

[37] M. W. Saif, M. Rubin, J. Figueroa, and R. O. Kerr, "Multicenter phase II trial of Genexol-PM (GPM), a novel Cremophor-free, polymeric micelle formulation of paclitaxel in patients with advanced pancreatic cancer (APC): final results," in *Proceedings of the Gastrointestinal Cancers Symposium*, 2008.

[38] D. W. Kim, S. Y. Kim, H. K. Kim et al., "Multicenter phase II trial of Genexol-PM, a novel Cremophor-free, polymeric micelle formulation of paclitaxel, with cisplatin in patients with advanced non-small-cell lung cancer," *Annals of Oncology*, vol. 18, no. 12, pp. 2009–2014, 2007.

[39] N. Sanvicens and M. P. Marco, "Multifunctional nanoparticles—properties and prospects for their use in human medicine," *Trends in Biotechnology*, vol. 26, no. 8, pp. 425–433, 2008.

[40] J. S. Murday, R. W. Siegel, J. Stein, and J. F. Wright, "Translational nanomedicine: status assessment and opportunities," *Nanomedicine: Nanotechnology, Biology, and Medicine*, vol. 5, no. 3, pp. 251–273, 2009.

Research Article

Mechanical Properties of Chitosan-Starch Composite Filled Hydroxyapatite Micro- and Nanopowders

Jafar Ai,[1] Mostafa Rezaei-Tavirani,[2] Esmaeil Biazar,[3] Saeed Heidari K,[2] and Rahim Jahandideh[3]

[1] *School of Advanced Medical Technologies, Tehran University of Medical Sciences, Tehran, Iran*
[2] *Proteomics Research Center, Faculty of Paramedical Sciences, Shahid Beheshty University of Medical Sciences, Tehran, Iran*
[3] *Department of Biomaterials Engineering, Tonekabon Branch, Islamic Azad University, Tonekabon, Iran*

Correspondence should be addressed to Esmaeil Biazar, e.biazar@tonekaboniau.ac.ir

Hydroxyapatite is a biocompatible ceramic and reinforcing material for bone implantations. In this study, Starch-chitosan hydrogel was produced using the oxidation of starch solution and subsequently cross-linked with chitosan via reductive alkylation method (weight ratio (starch/chitosan): 0.38). The hydroxyapatite micropowders and nanopowders synthesized by sol-gel method (10, 20, 30, 40 %W) were composited to hydrogels and were investigated by mechanical analysis. The results of SEM images and Zetasizer experiments for synthesized nanopowders showed an average size of 100 nm. The nanoparticles distributed as uniform in the chitosan-starch film. The tensile modulus increased for composites containing hydroxyapatite nano-(size particle: 100 nanometer) powders than composites containing micro-(size particle: 100 micrometer) powders. The swelling percentage decreased for samples containing hydroxyapatite nanopowder than the micropowders. These nanocomposites could be applied for hard-tissue engineering.

1. Introduction

Hydroxyapatite (HA; $Ca_{10}(PO_4)_6(OH)_2$) is a type of calcium phosphate that has extensive application in the healing of bones and teeth, due to its biocompatibility and similar composition to that of natural bone. Biodegradability and nontoxicity, especially mechanical properties, are important factors for scaffolds in hard-tissue engineering [1–5].

Chitosan has been proved and regarded as biodegradable noncytotoxic material which has some interesting biological activities [6–8]. Some of the recent studies, however, indicate that chitosan, with higher than 60% deacetylation degree, shows little amount of degradation and is not absorbed easily in-vivo [8]. Starch, an biodegradable biopolymer, is getting increasingly more attractive because of its renewability, biodegradability, and low cost. Starch-based polymers have recently been proposed as having great potential for applications in biomedical field as implant materials, drug delivery systems, and tissue engineering scaffolds [9, 10]. In order to use it in temporary medical applications, such as temporary hard-tissue replacement, bone fracture fixation, and bone tissue scaffold, blends of starch with different materials such as ethylene-vinyl alcohol copolymer (SEVA) and poly (caprolactone) (SPCL) have been proposed [11–13]. Over the past 30 years, synthetic hydroxyl apatite and glass/ceramics have been developed and used in the medical field [14]. It is well known that when these bioactive ceramics are implanted in the body, spontaneously bond to living bone via an apatite layer deposited on their surface and is expected to confer a bone-bonding behavior and to improve the mechanical properties of these composites [15, 16]. Starch/ethylene vinyl alcohol (SEVA-C) as scaffold showed unsuitable mechanical properties for bone engineering, but starch-based polymers are a potential alternative, especially when reinforced by bioactive bone-like [17, 18]. In most biomedical applications, membranes are in direct contact with living tissues. Therefore, besides the usual mechanical characterization carried out in the dry state, new systems should also be subjected to test routines that
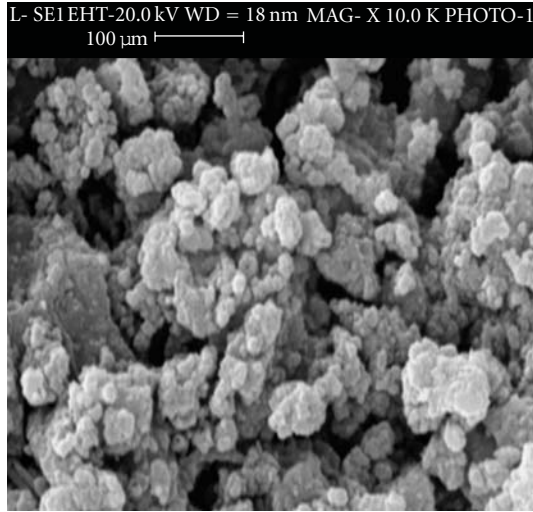
(a)
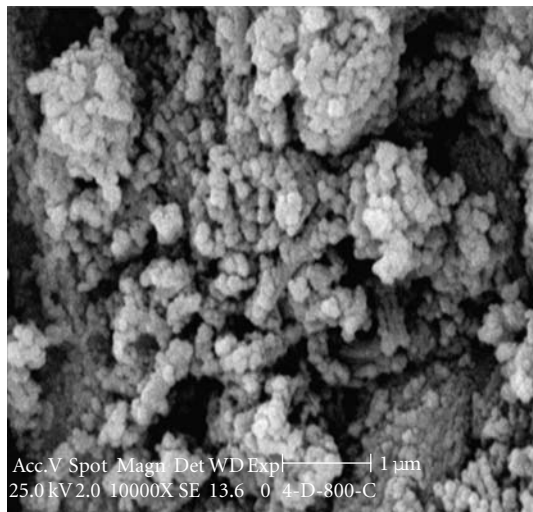
(b)

FIGURE 1: SEM micrographs of HAp nano- and micropowders (a) HAp micropowders (b) HAp nanoparticles (10000X).

FIGURE 2: Particle size distribution of HAP nanopowder in $10000°C$.

TABLE 1: Tensile modulus of starch-chitosan composites containing HAP micro and nanopowders. E1% (elasticity modulus in 1% strain).

HAP%	E1% (Gpa) composite containing HAP micropowder	E1% (Gpa) composite containing HAP nanopowder
0	1.8	1.8
10	3.4	3.8
20	4.1	4.7
30	5.1	5.5
40	5.8	6.1

allow for the evaluation of their mechanical performance in more realistic conditions [17–22]. In this study, the starch-chitosan composites containing micro- and nanopowders were synthesized and investigated by mechanical analysis.

2. Materials and Methods

2.1. Materials. Chitosan (deacetylation degree 87%), acetic acid, sodium hydroxide, sodium periodate (merk), $Ca(NO_3)_2 \cdot 4H_2O$ (Acros 99%), P_2O_5 (Acros 99%), HAP (sigma-aldrich; particle size: 60–180 micrometer), ethyl alcohol, PBS Solution, and deionized water.

2.2. Methods. The Hap nanopowder was prepared (Ca/P molar ratio: 1.67) using $Ca (NO_3)_2 \cdot 4H_2O$ and P_2O_5 by a simple sol-gel approach. A designed amount of phosphoric pentoxide was dissolved in absolute ethanol to form a 0.5 mol/L solution. A designed amount of calcium nitrate tetrahydrate was also dissolved in absolute ethanol to form a 1.67 mol/L solution. The mixture was stirred constantly for 24 h by a mechanical stirrer, allowing the reaction to complete at $800°C$. A transparent gel was obtained. The gels were individually heated at a rate of $5°C/min$ up to $1000°C$ for 6 h. The sintered powders were ball-milled at 100 rpm to get fine powders.

Commercially obtained $Ca(NO_3)_2 \cdot 4H_2O$ (0.01 mol; Acros 99%) and P_2O_5 (0.03 mol; Acros 99%) were poured into 10 mL of ethyl alcohol with the molar ratio of 10 : 3 (which is desired Ca/P ratio for hydroxyapatite). This solution transformed into a gel after stirring slowly for 1 h. The gel was then dried in an oven at $120°C$ in air for 15 h followed by subsequent heat-treating in stagnant air at $950°C$ for 12 h. HAP powders were obtained with particle sizes of 100–150 nanometers by this sol-gel method. Oxidized starch was prepared according to the procedure described by Hermanson [23]. 4.65 mL oxidized starch was mixed with 20 mL (1% w/v) of chitosan (weight ratio of 0.38). Then, the nanoparticles and microparticles in the

(a)

(b)

(c)
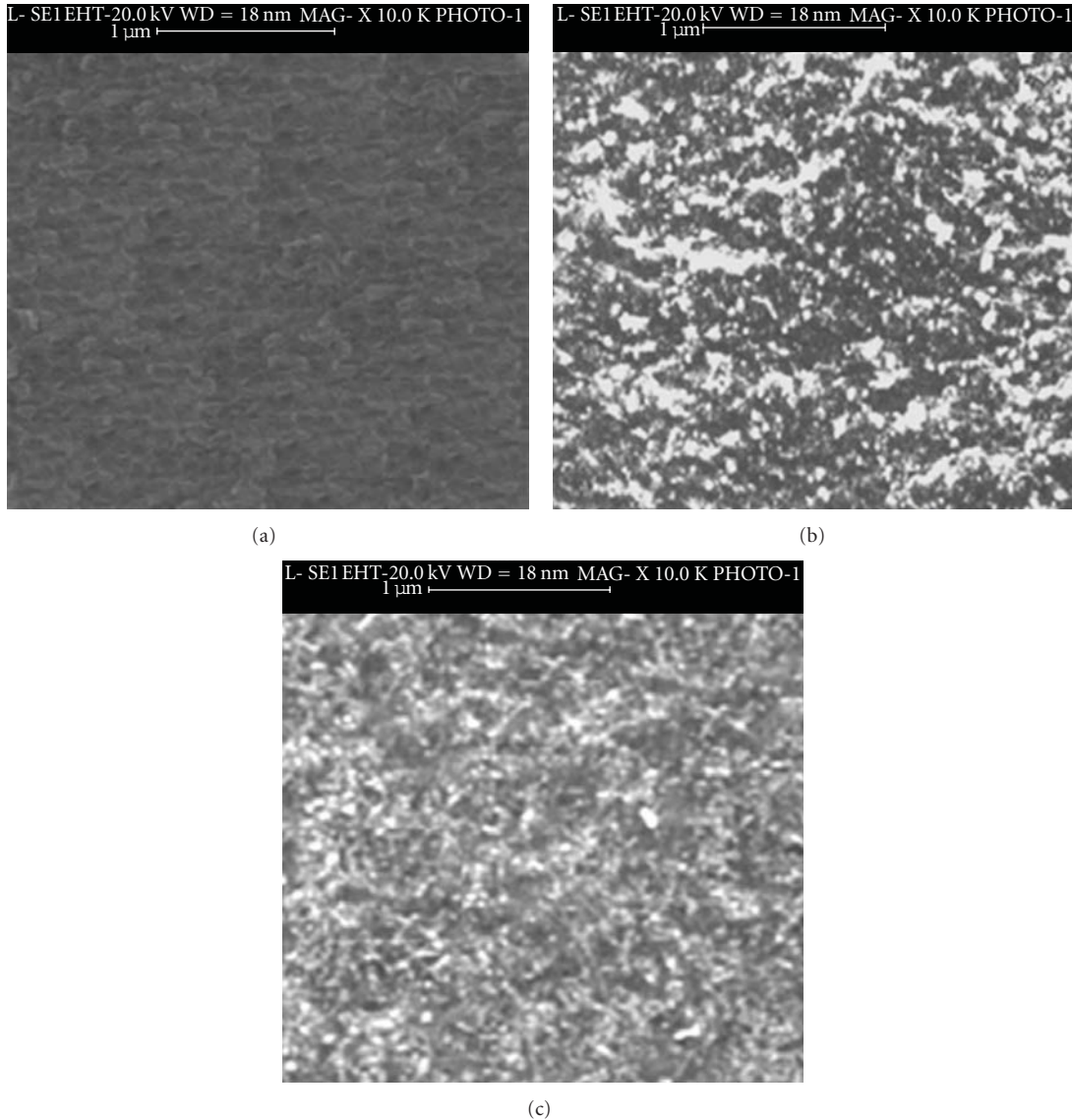
FIGURE 3: SEM micrographs of chitosan-starch/HAp nano- and microcomposite samples (a) chitosan-starch (b) chitosan-starch/HAp micro composite samples 30% (w/w), (c) chitosan-starch/HAp nanocomposite samples 30% (w/w).

different ratios were added slowly with vigorous stirring with the help of a mechanical stirrer at 3000 rpm. After addition of entire nanoparticles to the polymer solution, the resulting solution mixture was kept in a vacuum desiccator to remove the bubbles. Then, the mixture was heated in a water bath to evaporate water. The resulting slurry was poured into a glass petri dish and dried to make a film, keeping it in a vacuum oven at 60°C over night. Samples were washed several times with distilled water and then were incubated with aqueous sodium borohydride solution (0.05%) for 1 h to reduce excess noncross-linked aldehyde groups and chitosan. After washing several times with distilled water, samples were allowed to be dried on the petri dishes at room temperature. The morphological characteristics and size of the samples were studied by Zetasizer (3000 HAS; Malvern Instruments Ltd, Malvern, UK), scanning electron microscopy (SEM)

(XL30; Philips, Eindhoven, Holland), and transmission electron microscopy (TEM) (CM200FEG; Philips). The tensile test of composite (membrane strips with 5 mm in width) in dry state was carried out with Instron Universal Mechanical Tensile Machine at room temperature using a crosshead speed of 1 mm/min and 40 mm grip distance. The presented results are the mean values of five independent measurements. The swelling percentage of swollen samples was measured after reaching equilibration point (3 h) where no change in weight of samples was observed. This percentage could be calculated according to the following:

$$\%S = \frac{(Mw - Mi)}{Mi} \times 100, \tag{1}$$

where %S is the percentage of swelling, and mi and mw are the weight of the samples before immersion and after

FIGURE 4: Stress-strain curve obtained for starch-chitosan with weight ratio of 0.38.
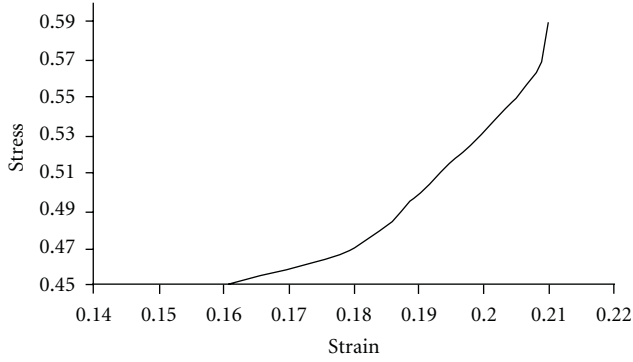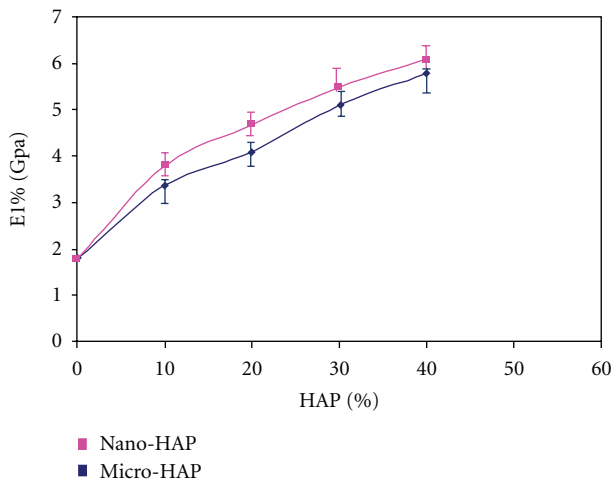

FIGURE 5: Tensile modulus of starch-chitosan composites containing HAP micro- and nanopowders. (The tensile modulus of these composites was increased gradually with increasing filler percentage. Error bars indicate the maximum and minimum values for 4–6 samples measured.)

TABLE 2: Swelling percentage of starch-chitosan composites containing HAP micropowders.

HAP%	Swelling % composite containing HAP micropowder	Swelling % composite containing HAP nanopowder
0	0.135	0.135
10	0.1	0.09
20	0.08	0.05
30	0.06	0.03
40	0.04	0.02

equilibration period in physiological buffer solution (PBS), respectively.

3. Results and Discussion

3.1. Microscopic Results. SEM images of powders with magnification 10,000X are shown in Figures 1(a) and 1(b).
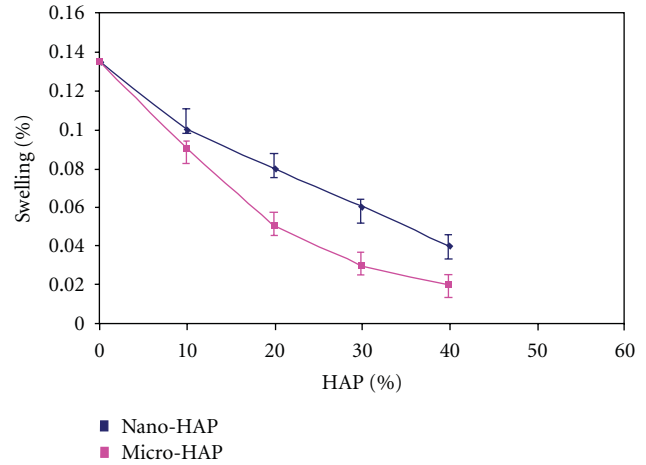
FIGURE 6: Swelling Percentage of starch-chitosan composite containing HAP micro- and nanopowders. The swelling percentage of composites with HAP micro and nanopowders was decreased gradually with increasing filler percentage, but swelling percentage of composites with HAP nanopowders is lower than composites with HAP micropowders.

Figure 1(a) shows particle sizes about 100 μm for commercial particles, and spherical particles formed in sol-gel method showed particle sizes to be about 100 nm. Considering the SEM image, it seems that the agglomerates were sufficiently dispersed in the Zetasizer testing conditions. The Zetasizer experiments for the dispersed particles in its own conditions showed particle sizes with an average size of 100 nm (Figure 2). Figure 3 shows SEM micrographs of chitosan-starch/HAp nano- and microcomposite samples (30% W). The figures indicated uniform distribution of nanoparticles in the polymer, but it is not for microparticles.

3.2. Mechanical Test. Figure 4 illustrates stress-strain curve for chitosan-starch copolymer. This figure shows that strain increases with stress increasing. Table 1 and Figure 5 show tensile modulus of composites containing HAP micro- and nanopowders. It could be observed that tensile modulus of these composites increases from 1.8 to 5.8 Gpa with the increasing HAP micropowders from 0 to 40% and from 1.8 to 6.1 Gpa with increasing of HAP nanopowders from 0 to 40%.

3.3. Swelling Test. Figure 6 and Table 2 show that swelling percentage of composites containing HAP powders decreases with increasing HAP percentage, and also values obtained from results show that swelling percentage for composites containing HAP nanopowders is less than this percentage for composites containing HAP micropowders.

4. Conclusions

In this study, starch-chitosan hydrogel were produced by oxidation of starch solution and subsequently cross-linked with chitosan via reductive alkylation (weight ratio

(starch/chitosan): 0.38) and then filled with HAP nanopowders produced by sol-gel method and micropowders (10, 20, 30, 40 %W). The SEM and Zetasizer analysis showed morphology and size average of nanoparticles. The results obtained from SEM images showed uniform distribution of nanoparticles in the chitosan-starch composite. The tensile modulus of composites containing the HAP micro- or nanopowders was increased gradually with increasing filler ratio, but strength of composite with the HAP micropowders was lower than the HAP nanopowders due to more uniform distribution of nanoparticles in the polymeric matrix. The swelling percentage of composites with the HAP micro- or nanopowders was decreased gradually with filler percentage increasing, but swelling percentage of composite with the HAP nanopowders was lower than the composite with the HAP micropowders that could be due to more uniform distribution of nanoparticles in polymeric matrix and barrier for water penetration in membrane. These composite containing nanopowders could be used for hard tissue engineering.

References

[1] B. Cengiz, Y. Gokce, N. Yildiz et al., "Synthesis and characterization of hydroxyapatite nanoparticles," *Colloids and Surfaces A*, vol. 322, no. 1–3, pp. 29–33, 2008.

[2] M. J. Larsen and S. J. Jensen, "Solubility, unit cell dimensions and crystallinity of fluoridated human dental enamel," *Archives of Oral Biology*, vol. 34, no. 12, pp. 969–973, 1989.

[3] M. J. Finkelstein and G. H. Nancollas, "Trace fluoride and its role in enamel mineralization," *Journal of Biomedical Materials Research*, vol. 14, no. 4, pp. 533–535, 1980.

[4] R. Z. Legeros, L. M. Silverstone, G. Daculsi, and L. M. Kerebel, "In vitro caries-like lesion formation in F-containing tooth enamel," *Journal of Dental Research*, vol. 62, no. 2, pp. 138–144, 1983.

[5] J. Shackelford, *Bioceramics (Advanced Ceramics)*, Prentice Hall, New Jersey, NJ, USA, 1992.

[6] B. Ratner, D. Hoffman, F. Schoen, and J. Lemons, *Biomaterials Science: An Introduction to Materials in Medicine*, Academic press, San Diego, Calif, USA, 1996.

[7] A. H. Reddi, "Morphogenesis and tissue engineering of bone and cartilage: inductive signals, stem cells, and biomimetic biomaterials," *Tissue Engineering*, vol. 6, no. 4, pp. 351–359, 2000.

[8] J. P. Fisher and A. H. Reddi, *Functional Topics in Tissue Engineering of Bone: Signals and Scaffolds*, Topics in Tissue English, Edited by N. Ashama Ki and P. Ferreti, 2003.

[9] I. S. Kim and P. N. Kumta, "Sol-gel synthesis and characterization of nanostructured hydroxyapatite powder," *Materials Science and Engineering B*, vol. 111, no. 2-3, pp. 232–236, 2004.

[10] M. F. Cerera, J. Heinamaki, K. krogars, and C. Jorgensen Anna, "Solid-state and mechanical Properties of aqueous chitosan-amylose starch films plasticized with polyls," *AAPS Pharmaceutical Science and Technology*, no. 1, article 5, 2004.

[11] A. Lazaridou and C. G. Biliaderis, "Thermophysical properties of chitosan, chitosan-starch and chitosan-pullulan films near the glass transition," *Carbohydrate Polymers*, vol. 48, no. 2, pp. 179–190, 2002.

[12] F. Mano, D. Koniarova, and R. Reis, "Thermal properties of thermoplastic starch/synthetic polymer blends with potential biomedical applicability," *Journal of Materials Science*, vol. 14, no. 2, pp. 127–135, 2003.

[13] E. T. Baran, J. F. Mano, and R. Reis, "Starch-chitosan hydrogels prepared by reductive alkylation cross-linking," *Journal of Materials Science*, vol. 15, no. 7, pp. 759–765, 2004.

[14] T. Kokubo, H. M. Kim, M. Kawashita, and T. Nakamura, "Novel ceramics for biomedical applications," *The Australian Ceramic Society*, vol. 36, pp. 37–46, 2000.

[15] R. L. Reis, S. C. Mendes, A. M. Cunha, and M. J. Bevis, "Processing and in vitro degradation of starch/EVOH thermoplastic blends," *Polymer International*, vol. 43, no. 4, pp. 347–352, 1997.

[16] R. L. Reis, A. M. Cunha, and M. J. Bevis, "Structure development and control of injection-molded hydroxylapatite-reinforced starch/EVOH composites," *Advances in Polymer Technology*, vol. 16, no. 4, pp. 263–277, 1997.

[17] S. H. Pak and C. Caze, "Acid-base interactions on interfacial adhesion and mechanical responses for glass-fiber-reinforced low-density polyethylene," *Journal of Applied Polymer Science*, vol. 65, no. 1, pp. 143–153, 1997.

[18] Z. Demjen, B. Pukanszky, and J. Nagy, "Possible coupling reactions of functional silanes and polypropylene," *Polymer*, vol. 40, no. 7, pp. 1763–1773, 1999.

[19] M. L. Gaillard, J. van der Brink, C. A. van Blitterswijk, and Z. B. Luklinska, "Applying a calcium phosphate layer on PEO/PBT copolymers affects bone formation in vivo," *Journal of Materials Science*, vol. 5, no. 6-7, pp. 424–428, 1994.

[20] J. I. Velasco, J. A. de Saja, and A. B. Martínez, "Crystallization behavior of polypropylene filled with surface-modified talc," *Journal of Applied Polymer Science*, vol. 61, no. 1, pp. 125–132, 1996.

[21] M. Tanoglu, S. H. McKnight, G. R. Palmese, and J. W. Gillespie, "Use of silane coupling agents to enhance the performance of adhesively bonded alumina to resin hybrid composites," *International Journal of Adhesion and Adhesives*, vol. 18, no. 6, pp. 431–434, 1998.

[22] W. Qiu, M. Kancheng, and H. Zeng, "Effect of macromolecular coupling agent on the property of PP/GF composites," *Journal of Applied Polymer Science*, vol. 71, no. 10, pp. 1537–1542, 1999.

[23] G. T. Hermanson, "Bioconjugate Techniques," *Academic Press, San Diego, California*, p. 116, 1996.

Research Article

Montmorillonite Clay-Based Polyurethane Nanocomposite As Local Triamcinolone Acetonide Delivery System

Flávia Carmo Horta Pinto,[1] Armando Silva-Cunha,[2] Gerson Antônio Pianetti,[2] Eliane Ayres,[3] Rodrigo Lambert Oréfice,[4] and Gisele Rodrigues Da Silva[1]

[1] *School of Pharmacy, Federal University of São João Del Rei, MG 35.501-296, Divinópolis, Brazil*
[2] *School of Pharmacy, Federal University of Minas Gerais, Belo Horizonte, MG, Brazil*
[3] *Department of Materials, Technologies and Processes, Minas Gerais State University, Belo Horizonte, MG, Brazil*
[4] *Department of Metallurgical and Materials Engineering, Federal University of Minas Gerais, Belo Horizonte, MG, Brazil*

Correspondence should be addressed to Gisele Rodrigues Da Silva, giselersilva@ufsj.edu.br

Biodegradable polyurethane was synthesized by preparing aqueous polyurethane dispersion having poly(caprolactone) and poly(ethylene glycol) as soft segments. Montmorillonite particles were delaminated within the waterborne polyurethane to produce a nanocomposite. The triamcinolone acetonide (TA), an important corticoid drug, was dispersed into the nanocomposite followed by a drying step to produce an implantable drug delivery system. Infrared (FTIR) results demonstrated that the original chemical structure of the TA was preserved after incorporation into the nanocomposite. Wide angle (WAXS) and small angle X-ray scattering (SAXS) results suggested that TA and clay do not dramatically change the morphology phase of the polymer although they can interact with each other. The presence of montmorillonite particles in the nanocomposite reduced the rate of TA release as compared to the pure polyurethane and enhanced the mechanical properties of the polymer. The overall results indicate that montmorillonite clay-based polyurethane nanocomposite could be potentially applied as local TA delivery system.

1. Introduction

Nanoparticles derived from expandable clays, such as montmorillonite, have been considered for more than 15 years as a reinforcing agent for polymers [1]. These clays have an interlayer space than can be promptly impregnated by many species including polymers [2]. Exchanging natural cations present in clay by Na$^+$ can allow water to enhance interlayer spacing up to several hundred angstroms [3]. Nonpolar cations can also be used to improve the compatibility between hydrophobic polymers and clays, but these special cations may lead to toxicity when biomedical applications are considered.

Nanocomposites composed on polyurethane and montmorillonite particles have been widely investigated [4–6]. They are usually prepared by dispersing the layered silicate particles into the polyurethane matrix. The resulting polymer-layered silicate nanocomposites frequently display advanced properties (such as mechanical properties) due to their high surface area [1, 7]. Many properties, such as mechanical [8], water vapor permeability [5], and water permeability [9, 10] can be improved by incorporating small amounts of delaminated clay to a polyurethane matrix [11]. Montmorillonite clay-based polyurethane nanocomposites have been also explored as implantable drug-delivery systems. In this case, nanocomposites were loaded with therapeutic agents and then implanted in specific organs. They would be able to control the release of a therapeutic agent to a specific target to treat or prevent different types of pathological processes [12–14]. All these studies demonstrated the potential applicability of nanocomposites composed on polyurethane and montmorillonite in different fields.

Intercalated and/or exfoliated morphologies can be obtained when clay nanoparticles are included into polymers [2]. An intercalated nanocomposite is obtained when polymer chains impregnate the clay interlayer gap to produce a

multilayered structure. The properties of this type of composite are usually similar to polymers containing micrometer particles. In the exfoliated or delaminated structure, clay layers are well dispersed within the polymer matrices, and polymer-clay interactions are dramatically enhanced [15, 16]. Exfoliation of clays within polymer is usually associated with large improvements in properties not always possible to be obtained with micrometer particles are used [17].

In the preparation of polyurethane/clay nanocomposites, modifications of montmorillonite by using organic modifiers such as alkylammonium to improve the compatibility between hydrophilic organomontmorillonite and hydrophobic polyurethanes are often employed [3, 6, 18, 19]. These organic chains having positively charged ends can be bonded to the surface of the negatively charged silicate layers resulting in an increase of the interlayer gap [20, 21]. However, these modifications can be potentially toxic when considering biomedical applications of the yielded devices. To avoid this type of potential toxicity, montmorillonite without any modification can be intercalated and/or delaminated using aqueous polyurethane dispersions to produce nanocomposites. In this type of nanocomposite processing technique, water is used to enlarge the space between silicate layers [10, 22, 23].

In this study, polyurethane based on poly(caprolactone) and poly(ethylene glycol), as soft segment, and isophorone diisocyanate and hydrazine, as hard segments, was synthesized and dispersed in water. Montmorillonite particles and triamcinolone acetonide were dispersed directly in the waterborne polyurethane. The triamcinolone acetonide-loaded polyurethane nanocomposite implants were obtained by cutting the nanocomposite films into the desired shape (squares of 5 mm of side). The structure of the implantable devices was characterized by analytical techniques to identify not only the intercalation and/or exfoliation of the montmorillonite onto the nanocomposite, but also how the drug interacted and affected its morphology. The effect of the clay particles distribution on the mechanical properties of the polyurethane was also evaluated. The analyzed structure of the implants was useful in understanding the *in vitro* drug-controlled release. Additionally, the *in vivo* release profile of the drug was evaluated through their subcutaneous implantation on the back of mice. Finally, it was revealed the applicability of the montmorillonite clay-based polyurethane nanocomposite loaded with triamcinolone acetonide as local controlled drug-delivery systems.

2. Materials and Methods

2.1. Synthesis of the Aqueous Polyurethane Dispersion (PU).

Aqueous polyurethane dispersion (PU) was prepared by a prepolymer mixing process, using a 250 mL three-neck glass flask equipped with a heating mantel, a mechanical stirrer, and a thermometer. The macrodiol components-polycaprolactone—diol (PCL 1000) (Tone Polyol 2221, $\overline{M}_n$ = 1000 g·mol^{-1}), polycaprolactone-diol (PCL 2000) (Tone Polyol 0249, $\overline{M}_n$ = 2000 g·mol^{-1}) (Dow-USA) (Sigma-Aldrich), and poly(ethylene glycol) (PEG,

TABLE 1: Composition (wt.%) of the aqueous PU dispersion*.

Reagents	Concentration (wt.%)
Isophorone diisocyanate (IPDI)	8.58
Polycaprolactone-diol 1000 (PCL1000)	4.85
Polycaprolactone-diol 2000 (PCL2000)	9.09
Polyethylene glycol 1500 (PEG 1500)	0.73
2,2-bis(hydroxymethyl) propionic acid (DMPA)	0.97
Triethylamine (TEA)	0.73
Water	74.70
Hydrazine (HZ)	1.08

*0.01% of dibutyl tin dilaurate based on the amounts of IPDI, PCL, and DMPA.

M_n = 1500 g·mol^{-1}, Sigma-Aldrich), isophorone diisocyanate (IPDI) (Bayer-Brazil) (NCO/OH ratio of 2.3) and 2,2-bis(hydroxymethyl) propionic acid (DMPA) (98.3%, Fluka) were added to the reactor in the presence of dibutyl tin dilaurate (DBDLT) (Miracema Nuodex-Brazil) and the reaction was carried out at 70°C–75°C in a nitrogen atmosphere for 4 h. The amount of free NCO groups on a percentage basis was determined by the standard dibutyl amine back titration method. After titration, the prepolymer temperature was allowed to drop to 40°C. The carboxylic acid groups were neutralized by the addition of triethylamine (TEA) (98%, Vetec-Brazil). The mixture was stirred for another 40 min to ensure that the reaction had been completed. All samples were dispersed by adding deionized water to the neutralized prepolymer which was stirred vigorously. After the dispersion, the amount of hydrazine (HZ) (solution 64%, Arch Química-Brazil) enough to react with free NCO groups was added to the reactor with a small amount of water, and stirring was continued for another 30 min. This chemical procedure was successful in producing a polyurethane dispersion with a solid content of about 25%. The composition of the polyurethane dispersion is shown in Table 1. Films were produced by casting the dispersion in a Teflon mould and allowing them to dry at room temperature for one week. Afterwards the films were placed in an oven at 60°C for 24 h [24]. A schematic representation of the chemical reactions and processing steps used to produce the polyurethane dispersion and nanocomposites is shown in Figure 1.

2.2. Incorporation of Clay Nanoparticles-Cloisite Na⁺.

The montmorillonite clay without any treatment (Cloisite Na⁺, Southern Clay Products) was dispersed in water (5 wt.%) by stirring it for 24 hours at room temperature. This procedure is useful to reduce the average particle size of the clay particles to yield clay nanoparticles dispersed in water [25]. Clay nanoparticles were incorporated into the polyurethane aqueous dispersion by mixing the polymer with the aqueous dispersion of the clay (Figure 1). The dispersions were mixed in proportions to yield a final nanocomposite containing 5 wt.% of clay in the polyurethane.
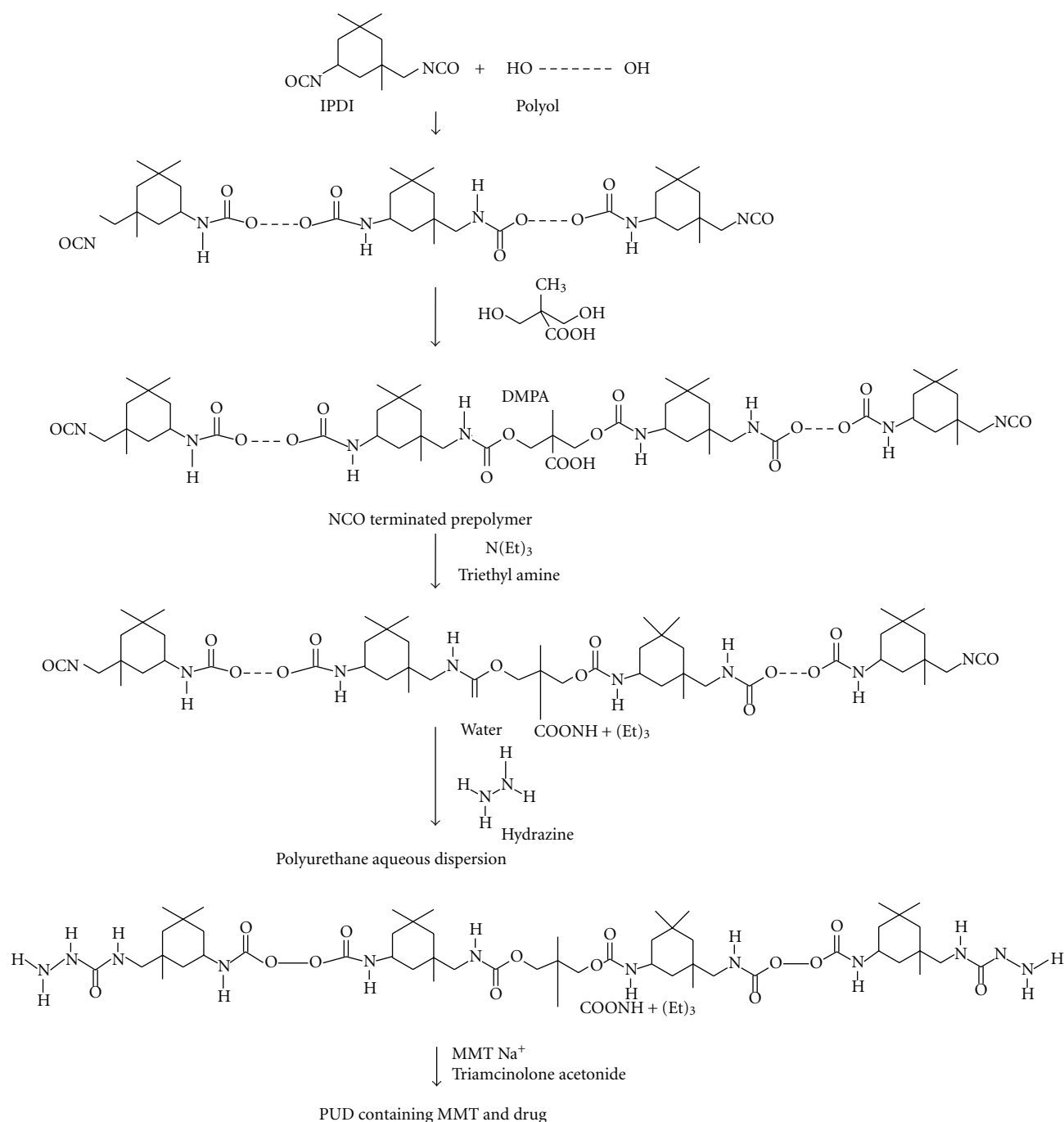
FIGURE 1: Schematic representation of the process used to prepare polyurethane containing montmorillonite (MMT-Na$^+$) and triamcinolone acetonide.

2.3. Incorporation of Triamcinolone Acetonide and Preparation of the Implants.

Triamcinolone acetonide (TA) (Sigma-Aldrich, 99.0%) was incorporated into the polymer by dispersing it in the nanocomposite prior of casting the films to yield materials having 20.5 wt% of the drug (Figure 1). The dried films were cut into squares (5 mm in side) to obtain the triamcinolone acetonide-loaded polyurethane nanocomposite implants (TA PU-NC implants) having approximately 1.27 mg each one. Triamcinolone acetonide-loaded polyurethane implants (without clay particles) (TA PU implants) were also prepared.

2.4. Characterization

2.4.1. Fourier Transform Infrared.

Infrared spectra were collected in a Fourier transform infrared spectrophotometer (FTIR; Perkin Elmer, model Spectrum 1000). Measurements

were carried out using the attenuated total reflectance (ATR) technique. Each spectrum was a result of 32 scans with a resolution of 4 cm^{-1}.

2.4.2. Small Angle X-Ray Scattering.

The measurements of synchrotron small angle X-ray scattering (SAXS) were performed using the beam line of the national synchrotron light laboratory (LNLS, Campinas, Brazil). The photon beam used in the LNLS SAXS beamline comes from one of the 12 bending magnets of the electron storage ring. The white photon beam is extracted from the ring through a high-vacuum path. After passing through a thin beryllium window, the beam is monochromatized (λ = 1.608 Å) and horizontally focused by a cylindrically bent and asymmetrically cut silicon single crystal. The focus is located at the detection plane. The X-ray scattering intensity, $I(q)$, was experimentally deter-mined as a function of the scattering vector "q" whose modulus is given by $q = (4\pi/\lambda)\sin(\theta)$, where λ is the X-ray wavelength and θ being half the scattering angle. Each SAXS pattern corresponds to a data collection time of 900 s. From the experimental scattering intensity produced by all the studied samples, the parasitic scattering intensity produced by the collimating slits was subtracted. All SAXS patterns were corrected for the nonconstant sensitivity of the PSD, for the time varying intensity of the direct synchrotron beam and for differences in sample thickness. Because of the normalization procedure, the SAXS intensity was determined for all samples in the same arbitrary units so that they can be directly compared.

2.4.3. Wide Angle X-Ray Scattering.

Wide angle X-ray scattering (WAXS) was performed by using a synchrotron light beam with a wavelength of 1.608 Å and an exposition time of 300 s. The scattering intensity was recorded by a Pilatus (100 K, 33 mm × 84 mm) detector. The sample to detector distance used was 80 mm.

2.4.4. Scanning Electron Microscopy.

Scanning electron microscopy (SEM) was performed using a JEOL microscope (model JSM-6360LV) operating at 15 kV. The TA PU implants were cryofractured and mounted on aluminium stubs using double-sided adhesive tape. Prior to microscopic examination, all the samples were sputter-coated with a gold layer under argon atmosphere using a sputter apparatus (Balzers Union SCD 040 unit, Balzers, Germany). The implants surfaces were viewed at 1000–10000x magnification, and the images were transferred to the computer by means of a digital image transference interface (DITI). The photomicrographs were adjusted using the software Adobe Photoshop 6.0 and Adobe Illustrator 9.01 (Adobe Systems Incorporated, 2000, USA).

2.4.5. Mechanical Tests.

Mechanical tensile tests were performed by following information reported in the ASTM D638. Samples were cut from sheets using a dog-bone die and tested using a 1.0 mm/min load rate and a load cell of 200 N.

2.5. In Vitro Release of TA from the PU-NC and PU Implants.

The United States Pharmacopeia [26] states in the general chapter ⟨1092⟩ the dissolution procedure: "sink conditions are defined as the volume of medium at least three times that required to form a saturated solution of drug substance. When sink conditions are present, it is more likely that dissolution results will reflect the properties of the dosage form".

The *in vitro* release of TA was carried out under sink conditions during 8 months. As the aqueous solubility of TA is 21.0 μg/mL at 28°C [27], sink conditions were achieved with at least 181 mL for the evaluated polymeric implants.

The TA PU-NC and TA PU implants were placed in different Erlenmeyers containing 181 mL of phosphate buffer solution (PBS pH = 7.4) (n = 5). These Erlenmeyers were placed inside an incubator set at 37°C and 30 rpm. At predetermined intervals, 181 mL of the PBS was sampled and the same volume of fresh PBS was added to each tube. The amount of TA released from each PU-NC and PU implants was assayed by high performance liquid chromatographic method described above, and expressed as the cumulative percentage of TA released in the medium. The average of the obtained measurements was calculated and used to plot the release profile curve.

The TA released from PU-NC and PU implants was measured by high-performance liquid chromatography (HPLC) by a Hewlett Packard HP 1100 apparatus equipped with an autosampler model HP 1100. An HP 1100 pump was set at a constant flow rate of 1.2 mL/min. A C-18 reversed-phase column (4.6 mm × 250 mm, macropore size of 5 μm) (Chromolith RP-18E, Merck KGaA Performance & Life Science Chemicals, Germany) was also used. The mobile phase was a mixture of acetonitrile (EM Science, Merck KGaA, Germany) and ultrafiltrated water obtained from Milli Q Plus, Millipore (USA) (50 : 50). An HP 1100 ultraviolet detector was used at a wavelength of 242 nm. The HPLC method was previously validated, and demonstrated to be specific, linear, precise and accurate as well as simple and reliable.

2.6. In Vivo Release of TA from the PU-NC and PU Implants.

Six-to-eight-week-old female Swiss mice from the Centro de Bioterismo of the Federal University of Minas Gerais (UFMG) were maintained in individual cages, with food and water *ad libitum*, and controlled temperature and humidity in the animal house of the School of Pharmacy of the Federal University of São João Del Rei (UFSJ). Experiments were approved by the Ethics Committee in Animal Experimentation at UFSJ.

The animals were anesthetized with a mixture of (10 mg kg^{-1}) xylazine and (100 mg kg^{-1}) ketamine hydrochloride (i.p.). Their dorsal hair was shaved and the skin wiped with 70% ethanol. TA PU-NC and TA PU implants were incorporated into the sponge discs, and they were aseptically inserted into a subcutaneous pouch that had been made with curved artery forceps through a 1cm long dorsal mid-line incision. After the implantation procedure, the animals were maintained in individual cages and provided with chow pellets and water *ad libitum*. The light/dark cycle was 12 : 12 h with lights on at 7:00 am and lights off at 7:00 pm.

Postoperatively, the animals were monitored for any signs of infection at the operative site, or upon discomfort or distress; any mice presenting such signs were immediately sacrificed.

TA PU-NC and TA PU implants were inserted into a subcutaneous pouch of the mice as described above. At 4, 7, 15, and 30 days after implantation, animals ($n = 5$ for each time) were euthanized, and the TA PU-NC and TA PU implants were carefully removed. The implant was fragmented using a scissor, and the pieces were dissolved in 50 mL of a mixture of acetonitrile and ultrafiltrated water (1:1). The content of TA remaining in the PU-NC and PU implants was measured by HPLC method previously described.

3. Results and Discussion

The incorporation of clay nanoparticles into the polymer matrix affected the mechanical properties of the polymer as initially predicted. Clay nanoparticles improved the elastic modulus of the polymer approximately two and a half times when compared to the pure polymer, as indicated in Table 2. Therefore, clay particles could be used to tune the stiffness of the PU, avoiding the necessity of changing some of the parameters of the PU synthesis, such as the ratio between soft and hard segments. The adjustment of the stiffness of the nanocomposite is an attractive characteristic for designing biomedical scaffolds and implantable solid systems [13], since stiff needle-shaped implants can be easily inserted through soft tissues without the need of a special incision. The reduction in both the strength and strain failure rates is a consequence of the interactions between the clay and polymer chains that restrict chain mobility.

Figure 2 shows the infrared spectra of pure PU (Figure 2(a)), PU-NC (containing clay) (Figure 2(b)), TA PU implants (Figure 2(c)), TA PU-NC implants (Figure 2(d)), pure TA (Figure 2(e)), and pure montmorillonite (Figure 2(f)). Characteristic infrared bands observed in pure PU include 2945–2866 cm^{-1} related to the stretching vibration of –CH$_2$ groups and 1723–1600 cm^{-1} equivalent to the stretching vibration of free and hydrogen-bonded carbonyl in the urethane, urea, and ester bonds in the poly(caprolactone) segments. The hydrogen bonded carbonyl in the urethane and urea (in the hard segment) and ester bonds in poly(caprolactone) (in the soft segment) could interact not only with the polar surface of the clay nanoparticles to yield a higher degree of hydrogen bonded species, but also with the primary amine present in the molecular structure of the polyurethane. The absorption band that resulted from stretching vibrations of bonded primary amine was observed in 3333 cm^{-1}, confirming the existence of interaction between the hydrogen of the primary amine and carbonyl in the urethane, urea, and ester groups. However, an absorption infrared band at 1531 cm^{-1} was also identified corresponding to bending vibrations of nonbonded primary amine. An absorption band around 2270 cm^{-1} was not observed in spectra, which indicated the absence of nonreactive NCO groups [28]. If this type of chemical group was present, the occurrence of side reactions which leads to the formation of allophanate

TABLE 2: Mechanical properties of PU and PU-NC films.

	Elastic modulus (MPa)	Strength (MPa)	Strain at failure (%)
PU	125	33	944
PU-NC	333	25	503

or biuret linkages would be possible [29]. The same infrared bands observed in pure PU were identified in spectra of PU-NC (Figure 2(b)), TA PU implants (Figure 2(c)) and TA PU-NC implants (Figure 2(d)).

The infrared spectra of pure clay (Figure 2(f)) revealed a weak infrared band at 3600 cm^{-1} due to the –OH band stretch in Al-OH and Si-OH, and an intense absorption band at approximately 1040 cm^{-1} due to Si-O stretching (out-of-plane) and Si-O stretching (in-plane) vibration in layered silicates [30, 31]. The infrared band corresponding to Si-O bonds is also observed in the spectra of PU-NC and TA PU-NC implants (Figures 2(b) and 2(d)), but the intensity is lower than that present in the spectra of pure clay. It is suggested that the intensity change in the Si-O stretching vibration band is related to the low concentration of clay in polyurethane, the weakening of interactions between interlayer water molecules and surface oxygen [32], and also due to the intercalation of the polyurethane and/or TA between clay lamellas.

Typical absorption bands observed in pure TA (Figure 2(e)) can be visualized in the spectra of TA PU (Figure 2(c)) and TA PU-NC implants (Figure 2(d)), such as 3392 cm^{-1} corresponding to the hydroxyl groups, between 3000–2900 cm^{-1} related to C–H stretching of sp3 and sp2 carbons, 1700–1730 cm^{-1} and 1662 cm^{-1} due to carbonyl groups of aliphatic ester and ketone. The obtained FTIR results corroborated with those previously reported [33]. The maintenance of the characteristic infrared bands of the PU, PU-NC, and TA, as well as the absence of new bands, demonstrated that there was no detectable chemical interaction between the polymer and drug during the manufacture process of the implants and indicated that the drug was successfully incorporated into the polyurethane-nanocomposite.

Figure 3 shows wide-angle x-ray scattering (WAXS) of pure PU (Figure 3(a)), PU-NC (containing clay) (Figure 3(b)), TA PU implants (Figure 3(c)), TA PU-NC implants (Figure 3(d)), and pure TA (Figure 3(e)). The WAXS curve of the pure PU (Figure 3(a)) revealed that no defined scattering peaks can be noted as a consequence of the presence of a highly amorphous structure. Crystallization of poly(caprolactone) segments is restricted, having low molar mass (<2000 g/mol) in polyurethanes, since low molar mass oligomers are confined between hard domains that do not allow them to have regular conformations that can lead to crystallization [34]. The WAXS curve recorded for PU containing clay nanoparticles (Figure 3(b)) revealed also an amorphous pattern of the nanocomposite. According to Kiersnowski et al. [35], the WAXS curve of montmorillonite reveals diffraction peaks related to the crystalline structure of this clay. By contrast, WAXS data obtained for PU-NC
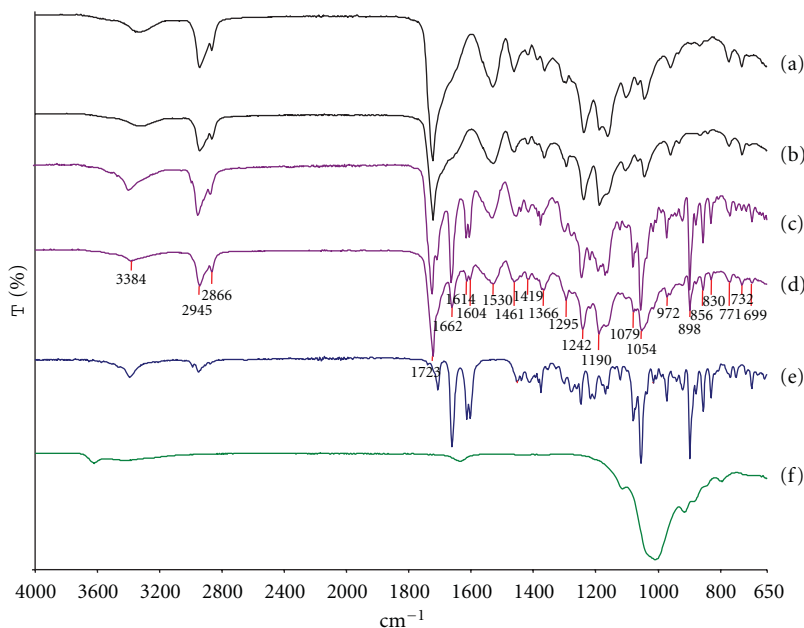
FIGURE 2: FTIR spectra of pure PU (a), PU-NC (containing clay) (b), TA PU implants (c), TA PU-NC implants (d), pure TA, (e) and pure montmorillonite (f).

did not show diffraction peaks, suggesting the disruption of the regular layered structure of the montmorillonite are due to the delamination of the clay incorporated into the polymer. The presence of poly(ethylene glycol) segments within the polyurethane macromolecular architecture was useful in promoting complete exfoliation of the clay structure, since the hydrophilic poly(ethylene glycol) possibly interacted efficiently with the polar clay surface to restrict clay nanoparticles to pack again during drying of the aqueous dispersion [36]. Typical scattering peaks observed in pure TA (Figure 3(e)) can be visualized in the WAXS curves of TA PU (Figure 3(c)) and TA PU-NC implants (Figure 3(d)), demonstrating the preserved crystalline pattern of the drug. However, the incorporation of clay nanoparticles and drug into the polyurethane led to a small shift of the diffraction peaks of TA to lower angles. This shift in q values suggested interactions between drug and clay nanoparticles due to the diffusion of the TA into the clay sheets and crystallization within the clay lamella, leading to the enlargement of the distance between crystalline planes of the drug. The interactions between silicate layers and guest molecules, such as nonionic TA, are weak interaction bonds represented by hydrogen bonding and hydrophobic interactions (Van der Walls). Complexes with montmorillonite and anionic or other nonionic drugs also exhibited bonding via absorption due to the establishment of weak interaction bonds [37]. On the other hand, McGinity and Lach [38] confirmed that basic molecules bonded strongly with montmorillonite, since clay minerals are naturally inorganic cationic exchangers and they may undergo ion exchange with basic drugs.

Small angle X-ray scattering (SAXS) has been used to characterize the morphology of nanoscaled phase-separated
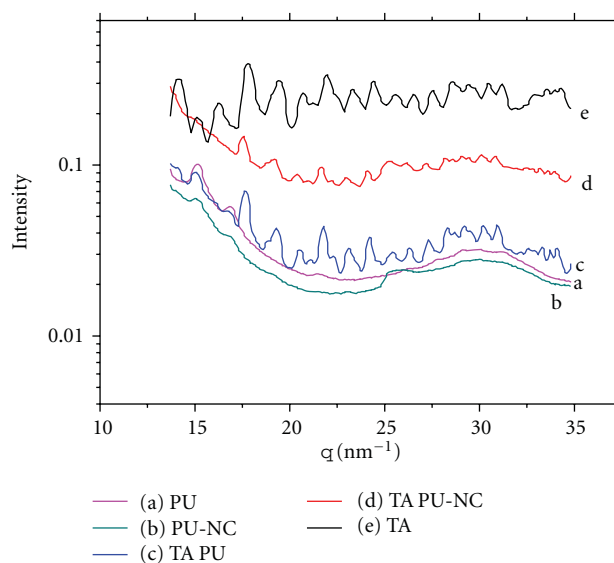
FIGURE 3: WAXS curves of pure PU (a), PU-NC (containing clay) (b), TA PU implants (c), TA PU-NC implants (d), and pure TA (e).

materials, such as polymer nanocomposites, block copolymers, and segmented polymers, since this technique records electron density fluctuations throughout the material in a nanometer range [39, 40]. SAXS provides useful data to study segmental polymers such as polyurethanes, since this type of polymer often phase separate in hard and soft domains that have enough electronic contrast to affect X-ray scattering at low angles. Nanocomposites containing clay has also

been investigated by SAXS [41, 42] to show the degree of clay delamination and nanoparticle orientation within the polymer.

Figure 4 shows SAXS data for PU-based materials that comprise nanoparticles derived from clay and TA. SAXS data in Figure 4 was reformatted using the Lorentz correction ($I_{(q)}q^2$), that is, useful to enhance the resolution of small SAXS peaks. No scattering peak can be clearly seen in SAXS curve associated with the pure PU (Figure 4(a)) even after the Lorentz correction, indicating the low electron difference between segments of the polyurethane. Considering the fact that this polyurethane is based on poly(caprolactone) and poly(ethylene glycol), as soft segments, and urethane hard segments, the hydrophilic domains were able to chemically interact by means of hydrogen bonds, producing a more homogeneous structure with possibly very small domains with no major differences in electron density. The incorporation of TA into the polymer did not lead to major changes in the scattering profile (Figure 4(c)). Therefore, the presence of TA did not alter the original structure of pure PU. Otherwise, an increase in scattering (mainly for lower values of q) was observed when clay nanoparticles were introduced into PU (Figure 4(b)) as an evidence of the presence of these nanoentities that have a higher electron density than the pure polymer. It was demonstrated previously [43] that clay nanoparticles can interact with hard segments of polyurethane through the formation of hydrogen bonds to change the course of the phase separation process. Additionally, the polar clay surface can also interact with the poly(ethylene glycol)-based soft segments of the polymer, changing the morphology of the polyurethane. The level of scattering was even more enhanced when TA was also incorporated into PU together with clay nanoparticles (Figure 4(d)). This result may indicate that interactions between the drug and clay may have created a larger number of scattering sites within the polymer. The interactions between silicate layers and TA, accommodated in their gallery spaces, might be hydrophobic interactions (Van der Walls) and hydrogen bonding, since the drug was absorbed in the clay mainly in the neutral form [37].

Scanning electron microscopy (SEM) was used for examination of the fractured surfaces of pure PU (Figure 5(a)), PU-NC (containing clay) (Figure 5(b)), TA PU implants (Figure 5(c)), and TA PU-NC implants (Figure 5(d)). The cross-sectional area of the pure PU was smooth and dense, with no evidence of pores or channels. On the other hand, the PU-NC surface was completely rough due to the homogeneous distribution of the clay nanoparticles in the polymer surface. This could be attributed to the chemical interactions between the polar clay surface and polar urethane bonds and/or poly(ethylene glycol) present in the segments of the polyurethane. The cross-sectional area of the TA PU-NC implants was also rough due to the presence of the clay nanoparticles and TA crystals not only in the PU matrix, but also on the clay sheets. Since no large clay and TA aggregates could be observed on the fractured surface of the samples, it can be suggested that the manufacture procedure of the implants
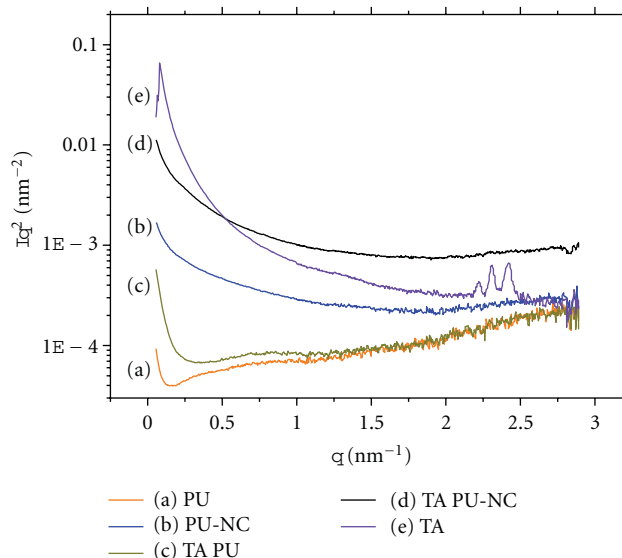
FIGURE 4: Lorentz corrected SAXS scattering data of pure PU (a), PU-NC (containing clay) (b), TA PU implants (c), TA PU-NC implants (d), and pure TA (e).

yielded a high-quality polyurethane nanocomposite loaded with small crystals of the drug.

Figure 6 shows the percentage of the cumulative TA release profile from PU implants (Figure 6(a)) and PU-NC implants (Figure 6(b)). The TA leached from the implantable devices was quantified by HPLC method. Neither any peak for a degradation product nor any alteration of the chromatographic pattern of TA was observed, indicating that the preparation technique of the PU and PU-NC implants and the conditions of the *in vitro* release of the drug did not affect the stability of the drug. TA PU and TA PU-NC implants led to a controlled release of the drug which followed a bimodal pattern: during the first 15 days, a faster dissolution and diffusion of the drug was released corresponding to a minimal burst effect. Over this period, approximately 16% and 24% of TA was released from PU-NC and PU implants, respectively, corresponding to the leaching of TA crystals deposited in the implant surfaces. In the second stage, approximately 93% and 85% of TA was released from the PU and PU-NC implants. It suggests that this phase was characterized by the diffusion of the drug and the degradation of the polymeric matrix. The presence of poly(ethylene glycol) in the soft segments of the polyurethane increased hydrophilicity and aqueous permeability in the polymer backbone, promoting hydrolytic cleavage of ester bonds of the poly(caprolactone) also present in the soft segments of the polyurethane. Furthermore, the scission of the poly(caprolactone) increased the porosity and surface area for drug diffusion [44]. In terms of the bonds present in poly(ester urethanes), the most susceptible to hydrolysis are ester bonds. However, the hydrolysis of ester bonds of urethane groups in one order of magnitude is slower relative to ester bonds of the soft segment. Therefore, the soft segment bonds hydrolyze at a greater rate than

(a)

(b)

(c)

(d)
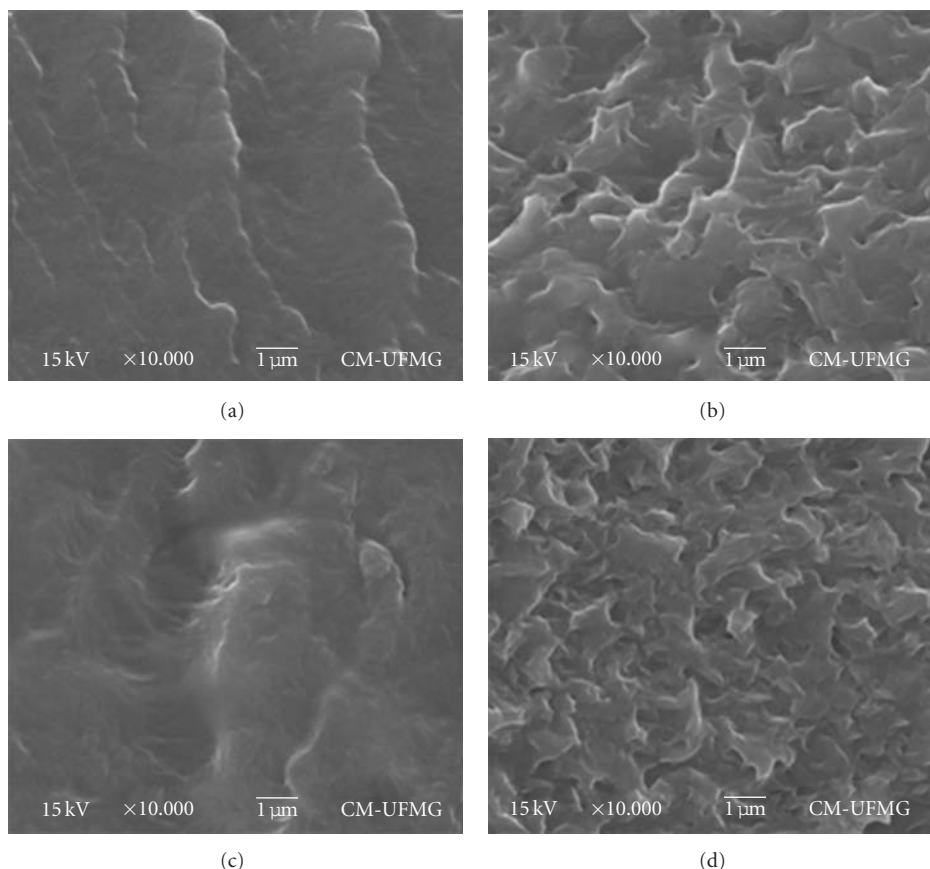
FIGURE 5: SEM images of pure PU (a), PU-NC (containing clay) (b), TA PU implants (c), and TA PU-NC implants (d).

hard segment bonds and govern the degradation rate of the poly(ester urethanes) [45].

The incorporation of montmorillonite particles into the polymeric matrix loaded with the drug reduced the rate of TA release over the time. This may be due to the establishment of different types of host-guest interactions between clay nanoparticles and TA intercalated into montmorillonite (as detected by WAXS and SAXS). Besides the interactions between them being weak interaction bonds, they contributed to a more extensive release of the drug from the PU-NC implants.

Figure 7 shows the percentage of the cumulative TA release profile from PU implants (Figure 7(a)) and PU-NC implants (Figure 7(b)). The TA-loaded PU and PU-NC implants maintained a sustained release of the drug for at least 30 days within the subcutaneous tissue of the mice. The PU and PU-NC implants showed an initial burst release of the drug over the first 7 days. Over this period, approximately 36% and 27% of TA was released from PU and PU-NC implants, indicating faster dissolution of the drug deposited on the surface of the polymeric implants. In a second stage that occurred between the 8th and the 30th days of the test, the PU and PU-NC implants released 80% and 73% of TA, respectively, providing controlled and sustained TA release within the subcutaneous tissue of the mice. During this period, the dissolution and diffusion of
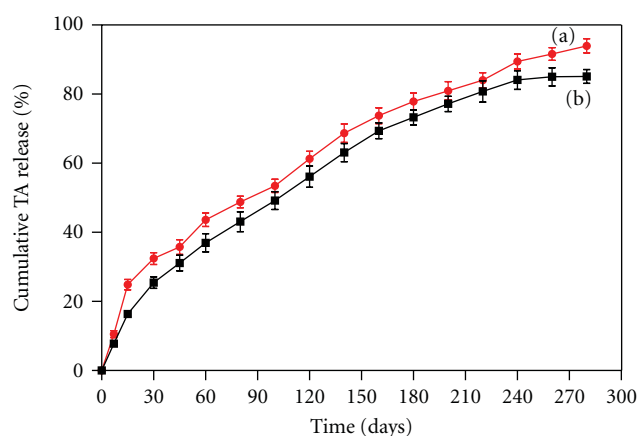
FIGURE 6: Cumulative TA release profile from PU implants (a) and PU-NC implants (b). Results represent mean ± standard deviation ($n = 5$ for each time and each sample).

the drug and the degradation of the polymeric matrix might modulate the TA release rate. It was previously described that the *in vivo* degradation of polyurethanes involves the hydrolysis of ester linkages in polyester soft segments, and the enzymatic hydrolysis by the presence of esterases, since those enzymes are able to recognize and act upon unnatural
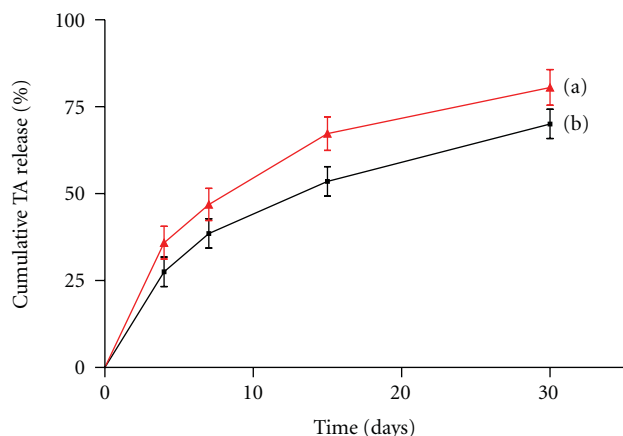
Figure 7: Cumulative TA release profile from PU (a) and PU-NC (b) subcutaneous implants in mice. Sustained release of TA was observed up to day 30 after implantation. Results represent mean ± standard deviation ($n = 5$ for each time and each sample).

substrates such as polyurethanes [46]. Additionally, the overall rate of TA released from the PU-NC implants was lower than that obtained for the PU implants. Therefore, the intercalation capability offered by the montmorillonite particles was applied to decrease the release of the TA, providing a prolonged delivery of the drug over the time in comparison with the free polymer. This can be relevant for long-term treatment of chronic inflammatory pathologies.

It was observed that approximately 31% of TA was released from PU-NC implants *in vitro* and 73% of drug was delivered by PU-NC implants *in vivo* during 30 days. The differences between the physiological environment (*in vivo* test) and the simulated physiological conditions (*in vitro* test) explain the lack of correlation between the *in vivo* and *in vitro* profile release of TA from PU-NC implants.

4. Conclusion

In the present work, the montmorillonite without any treatment could be intercalated within the polymer chains due to the use of aqueous polyurethane dispersion to produce the nanocomposite. The triamcinolone acetonide, an important corticoid, was incorporated into the nanocomposite by dispersing it in the waterborne polyurethane. Triamcinolone acetonide-loaded polyurethane nanocomposite implants were successfully designed. The incorporation of nanocomposite into the polymer chains modulated the mechanical properties of the polymer system that became more attractive not only for designing implantable solid systems but also for biomedical scaffolds. FTIR and WAXS data showed that the incorporation of the drug into the nanocomposite did not severely change the chemical and crystallographic aspects of the drug respectively. SAXS data demonstrated that the introduction of the clay nanoparticles into the polyurethane provided no major modifications of the morphology of the polymer. However, this technique provided some evidences that clay can interact with the drug. *In vitro* and *in vivo* triamcinolone acetonide release studies

showed that the drug was released slower from the nanocomposite compared to the pure polyurethane, as a result of the interaction between the montmorillonite and the drug present in the interlayer spacing of the host clay. Therefore, the incorporation of montmorillonite nanoparticles into the biodegradable polyurethane chains was useful not only to tune the mechanical properties of the polymer but also to provide controlled long-term delivery of the drug over the time. The treatment of chronic inflammatory diseases by montmorillonite clay-based polyurethane implants seems feasible.

Acknowledgments

References

[1] E. P. Giannelis, "Polymer layered silicate nanocomposites," *Advanced Materials*, vol. 8, no. 1, pp. 29–35, 1996.

[2] A. K. Barick and D. K. Tripathy, "Effect of organically modified layered silicate nanoclay on the dynamic viscoelastic properties of thermoplastic polyurethane nanocomposites," *Applied Clay Science*, vol. 52, no. 3, pp. 312–321, 2011.

[3] E. Ayres, R. L. Oréfice, and D. Sousa, "Influence of bentonite type in waterborne polyurethane nanocomposite mechanical properties," *Macromolecular Symposia*, vol. 245-246, pp. 330–336, 2006.

[4] A. Cheng, S. Wu, D. Jiang, F. Wu, and J. Shen, "Study of elastomeric polyurethane nanocomposites prepared from grafted organic-montmorillonite," *Colloid and Polymer Science*, vol. 284, no. 9, pp. 1057–1061, 2006.

[5] M. M. Rahman, H. D. Kim, and W. K. Lee, "Preparation and characterization of waterborne polyurethane/clay nanocomposite: effect on water vapor permeability," *Journal of Applied Polymer Science*, vol. 110, no. 6, pp. 3697–3705, 2008.

[6] N. Salahuddin, A. Abo-El-Enein, A. Selim, and O. Salah El-Dien, "Synthesis and characterization of polyurethane/organo-montmorillonite nanocomposites," *Applied Clay Science*, vol. 47, no. 3-4, pp. 242–248, 2010.

[7] M. Alexandre and P. Dubois, "Polymer-layered silicate nanocomposites: preparation, properties and uses of a new class of materials," *Materials Science and Engineering*, vol. 28, no. 1, pp. 1–63, 2000.

[8] Y. I. Tien and K. H. Wei, "High-tensile-property layered silicates/polyurethane nanocomposites by using reactive silicates as pseudo chain extenders," *Macromolecules*, vol. 34, no. 26, pp. 9045–9052, 2001.

[9] B. Han, A. Cheng, G. Ji, S. S. Wu, and J. Shen, "Effect of organophilic montmorillonite on polyurethane/montmorillonite nanocomposites," *Journal of Applied Polymer Science*, vol. 91, no. 4, pp. 2536–2542, 2004.

[10] G. R. Da Silva, A. Da Silva Cunha, E. Ayres, and R. L. Oréfice, "Effect of the macromolecular architecture of biodegradable polyurethanes on the controlled delivery of ocular drugs," *Journal of Materials Science: Materials in Medicine*, vol. 20, no. 2, pp. 481–487, 2009.

[11] S. Pavlidou and C. D. Papaspyrides, "A review on polymer-layered silicate nanocomposites," *Progress in Polymer Science*, vol. 33, no. 12, pp. 1119–1198, 2008.

[12] G. R. Da Silva, E. Ayres, R. L. Orefice, S. A. L. Moura, D. C. Cara, and A. Da Silva Cunha, "Controlled release of dexamethasone acetate from biodegradable and biocompatible polyurethane and polyurethane nanocomposite," *Journal of Drug Targeting*, vol. 17, no. 5, pp. 374–383, 2009.

[13] G. R. Da Silva, A. Da Silva-Cunha, F. Behar-Cohen, E. Ayres, and R. L. Oréfice, "Biodegradable polyurethane nanocomposites containing dexamethasone for ocular route," *Materials Science and Engineering C*, vol. 31, no. 2, pp. 414–422, 2011.

[14] M. Smith, Y. Omidi, and M. Gumbleton, "Primary porcine brain microvascular endothelial cells: biochemical and functional characterisation as a model for drug transport and targeting," *Journal of Drug Targeting*, vol. 15, no. 4, pp. 253–268, 2007.

[15] P. Kiliaris and C. D. Papaspyrides, "Polymer/layered silicate (clay) nanocomposites: an overview of flame retardancy," *Progress in Polymer Science*, vol. 35, no. 7, pp. 902–958, 2010.

[16] J. K. Pandey, K. Raghunatha Reddy, A. Pratheep Kumar, and R. P. Singh, "An overview on the degradability of polymer nanocomposites," *Polymer Degradation and Stability*, vol. 88, no. 2, pp. 234–250, 2005.

[17] P. C. Lebaron, Z. Wang, and T. J. Pinnavaia, "Polymer-layered silicate nanocomposites: an overview," *Applied Clay Science*, vol. 15, no. 1-2, pp. 11–29, 1999.

[18] M. Zanetti, P. Bracco, and L. Costa, "Thermal degradation behaviour of PE/clay nanocomposites," *Polymer Degradation and Stability*, vol. 85, no. 1, pp. 657–665, 2004.

[19] A. Pegoretti, A. Dorigato, M. Brugnara, and A. Penati, "Contact angle measurements as a tool to investigate the filler-matrix interactions in polyurethane-clay nanocomposites from blocked prepolymer," *European Polymer Journal*, vol. 44, no. 6, pp. 1662–1672, 2008.

[20] A. S. Zerda and A. J. Lesser, "Intercalated clay nanocomposites: morphology, mechanics, and fracture behavior," *Journal of Polymer Science Part B: Polymer Physics*, vol. 39, no. 11, pp. 1137–1146, 2001.

[21] G. M. Kim, D. H. Lee, B. Hoffmann, J. Kressler, and G. Stöppelmann, "Influence of nanofillers on the deformation process in layered silicate/polyamide-12 nanocomposites," *Polymer*, vol. 42, no. 3, pp. 1095–1100, 2001.

[22] J. M. Yeh, C. T. Yao, C. F. Hsieh et al., "Preparation, characterization and electrochemical corrosion studies on environmentally friendly waterborne polyurethane/Na+-MMT clay nanocomposite coatings," *European Polymer Journal*, vol. 44, no. 10, pp. 3046–3056, 2008.

[23] R. C. M. Dias, A. M. Góes, R. Serakides, E. Ayres, and R. L. Oréfce, "Porous biodegradable polyurethane nanocomposites: preparation, characterization, and biocompatibility tests," *Materials Research*, vol. 13, no. 2, pp. 211–218, 2010.

[24] E. Ayres, R. L. Oréfice, and M. I. Yoshida, "Phase morphology of hydrolysable polyurethanes derived from aqueous dispersions," *European Polymer Journal*, vol. 43, no. 8, pp. 3510–3521, 2007.

[25] G. Lagaly and S. Ziesmer, "Colloid chemistry of clay minerals: the coagulation of montmorillonite dispersions," *Advances in Colloid and Interface Science*, vol. 100–102, pp. 105–128, 2003.

[26] United States Pharmacopeial Convention, *The United States Pharmacopeia*, United States Pharmacopeial Convention Inc., Rockville, Md, USA, 31th edition, 2008.

[27] L. H. Block and R. N. Patel, "Solubility and dissolution of triamcinolone acetonide," *Journal of Pharmaceutical Sciences*, vol. 62, no. 4, pp. 617–621, 1973.

[28] I. H. L. Pereira, E. Ayres, P. S. Patrício et al., "Photopolymerizable and injectable polyurethanes for biomedical applications: synthesis and biocompatibility," *Acta Biomaterialia*, vol. 6, no. 8, pp. 3056–3066, 2010.

[29] V. Thomas and M. Jayabalan, "A new generation of high flex life polyurethane urea for polymer heart valve—studies on in vivo biocompatibility and biodurability," *Journal of Biomedical Materials Research—Part A*, vol. 89, no. 1, pp. 192–205, 2009.

[30] H. T. Lee and L. H. Lin, "Waterborne polyurethane/clay nanocomposites: novel effects of the clay and its interlayer ions on the morphology and physical and electrical properties," *Macromolecules*, vol. 39, no. 18, pp. 6133–6141, 2006.

[31] G. V. Joshi, B. D. Kevadiya, H. A. Patel, H. C. Bajaj, and R. V. Jasra, "Montmorillonite as a drug delivery system: intercalation and in vitro release of timolol maleate," *International Journal of Pharmaceutics*, vol. 374, no. 1-2, pp. 53–57, 2009.

[32] C. M. L. Preston, G. Amarasinghe, J. L. Hopewell, R. A. Shanks, and Z. Mathys, "Evaluation of polar ethylene copolymers as fire retardant nanocomposite matrices," *Polymer Degradation and Stability*, vol. 84, no. 3, pp. 533–544, 2004.

[33] A. A. da Silva-Junior, J. R. de Matos, T. P. Formariz et al., "Thermal behavior and stability of biodegradable spray-dried microparticles containing triamcinolone," *International Journal of Pharmaceutics*, vol. 368, no. 1-2, pp. 45–55, 2009.

[34] P. Ping, W. Wang, X. Chen, and X. Jing, "Poly(ε-caprolactone) polyurethane and its shape-memory property," *Biomacromolecules*, vol. 6, no. 2, pp. 587–592, 2005.

[35] A. Kiersnowski, M. Serwadczak, E. Kułaga et al., "Delamination of montmorillonite in serum-A new approach to obtaining clay-based biofunctional hybrid materials," *Applied Clay Science*, vol. 44, no. 3-4, pp. 225–229, 2009.

[36] G. R. da Silva, A. da Silva-Cunha, F. Behar-Cohen, E. Ayres, and R. L. Oréfice, "Biodegradation of polyurethanes and nanocomposites to non-cytotoxic degradation products," *Polymer Degradation and Stability*, vol. 95, no. 4, pp. 491–499, 2010.

[37] C. Aguzzi, P. Cerezo, C. Viseras, and C. Caramella, "Use of clays as drug delivery systems: possibilities and limitations," *Applied Clay Science*, vol. 36, no. 1–3, pp. 22–36, 2007.

[38] J. W. McGinity and J. L. Lach, "In vitro adsorption of various pharmaceuticals to montmorillonite," *Journal of Pharmaceutical Sciences*, vol. 65, no. 6, pp. 896–902, 1976.

[39] R. L. Oréfice, E. Ayres, M. M. Pereira, and H. S. Mansur, "Using the nanostructure of segmented polyurethanes as a template in the fabrication of nanocomposites," *Macromolecules*, vol. 38, no. 10, pp. 4058–4060, 2005.

[40] B. Chu and B. S. Hsiao, "Small-angle X-ray scattering of polymers," *Chemical Reviews*, vol. 101, no. 6, pp. 1727–1761, 2001.

[41] A. Bafna, G. Beaucage, F. Mirabella, and S. Mehta, "3D hierarchical orientation in polymer-clay nanocomposite films," *Polymer*, vol. 44, no. 4, pp. 1103–1115, 2003.

[42] M. Song, H. S. Xia, K. J. Yao, and D. J. Hourston, "A study on phase morphology and surface properties of polyurethane/organoclay nanocomposite," *European Polymer Journal*, vol. 41, no. 2, pp. 259–266, 2005.

[43] I. M. Pereira, S. Carvalho, M. M. Pereira, M. F. Leite, and R. L. Oréfice, "Effect of the degree of clay delamination on the phase morphology, surface chemical aspects, and properties of hydrolyzable polyurethanes for periodontal regeneration,"

Journal of Applied Polymer Science, vol. 114, no. 1, pp. 254–263, 2009.

[44] B. Li, K. V. Brown, J. C. Wenke, and S. A. Guelcher, "Sustained release of vancomycin from polyurethane scaffolds inhibits infection of bone wounds in a rat femoral segmental defect model," *Journal of Controlled Release*, vol. 145, no. 3, pp. 221–230, 2010.

[45] L. Tatai, T. G. Moore, R. Adhikari et al., "Thermoplastic biodegradable polyurethanes: the effect of chain extender structure on properties and in-vitro degradation," *Biomaterials*, vol. 28, no. 36, pp. 5407–5417, 2007.

[46] J. P. Santerre, K. Woodhouse, G. Laroche, and R. S. Labow, "Understanding the biodegradation of polyurethanes: from classical implants to tissue engineering materials," *Biomaterials*, vol. 26, no. 35, pp. 7457–7470, 2005.

Research Article

An Evaluation on Transfection Efficiency of pHRE-Egr1-EGFP in Hepatocellular Carcinoma Cells Bel-7402 Mediated by PEI-MZF-NPs

Mei Lin,[1, 2] Dongsheng Zhang,[1] Junxing Huang,[2] Jia Zhang,[1] Li Wang,[2] Ting Guo,[2] Li Xiao,[2] Jun Ye,[2] and Lixin Zhang[2]

[1] *Medical School of Southeast University, Jiangsu Province, Nanjing 210009, China*
[2] *Taizhou People's Hospital, Yangzhou University, Jiangsu Province, Taizhou 225300, China*

Correspondence should be addressed to Dongsheng Zhang, zdszds1222@163.com

To improve transfection and expression efficiency of target gene, especially under cancer anoxic microenvironment, we have developed pHRE-Egr1-EGFP/PEI-MZF-NPs nanosystem, in which pHRE-Egr1-EGFP, eukaryotic gene expression plasmid, is constructed by combining radiation promoter Egr1 with anoxia induction components (HRE), forming anoxic radiation double sensitive HRE/Egr1 promoter to activate reporter gene EGFP expression. MZF-NPs ($Mn_{0.5} Zn_{0.5} Fe_2O_4$ magnetic nanoparticles), obtained by coprecipitation method, are coated with cation poly(ethylenimine) (PEI). We transferred pHRE-Egr1-EGFP into hepatocellular carcinoma Bel-7402 cells, using PEI-MZF-NPs as the carrier and tested some relevant efficacy. The results show that PEI-MZF-NPs have good DNA-binding ability, protection ability, release ability, little toxicity, and high transfection efficiency, obviously superior to those of the liposome method and electricity perforation method. Moreover, the expression level of EGFP gene induced by anoxia and radiation was significantly higher than that of single radiation activation. It is therefore concluded that HRE/Egr1 can induce and improve target gene expression efficiency in cancer anoxic microenvironment, and that PEI-MZF-NPs can be used as a novel nonviral gene vector which offers a viable approach to the mediated radiation gene therapy of cancer.

1. Introduction

Developed recently to address the problems in gene therapy and radiation therapy, radiation-gene therapy is a promising area of study in cancer treatment. More specifically, it is a cancer therapeutic method that while doing local radiotherapy, the genes with antitumor effect are induced by the radiation to express to kill cancer cells, resulting in dual therapy of ray and gene on cancer, thus working together to their best advantage, and playing a synergistic antitumor role. Egr1, a transcription factor, regulating cell growth early after being radiated, can induce the expression of its downstream genes by ionizing radiation, attaining a spatio-temporal regulation on the target gene expression. Notable achievements in radiation-gene therapy by using radiosensitivity of Egr1 radiation promoter have been obtained [1–3]. However, this method has not overcome the common problem in gene therapy yet, that is, how to ensure a safe gene delivery into cells with high transfection efficacy. In addition, the anoxic microenvironment in solid tumor is likely to curb the induction activity of radiation promoter.

Hypoxia response element (HRE), an enhancer sensitive to hypoxia, can induce the expression of its downstream genes when combined particularly with HIF-1, hypoxia inducible factor-1. It was reported that HRE/HIF system existed in both mammalian cells and human tissue, and HIF-1α was overexpressed in 68–84% of cancers, which suggested that HRE can be used to regulate expression of target gene in tumor hypoxia environment [4–7]. Shibata et al. [8] has confirmed that 5 copies of HRE connected with a promoter can increase its downstream gene expression by 500 times in hypoxia condition.

In this study, 5HRE was inserted in the front of Egr1 promoter to construct a hypoxia-radiation dual-sensitive

promoter and then connected with EGFP, a reporter gene, to develop an eukaryotic recombinant plasmid–pHRE–Egr1–EGFP to induce and improve EGFP expression in tumor cells using hypoxia and radiation. In this system, radiation can be used as a switch to start the transcription of target gene, regulating its expression in space-time. Because of the radiation dose, range and times can be artificially controlled; the expression of the target gene is likely to occur within a certain range, at an appropriate time, even at the desirable level. Thus, the goal of controlling gene expression can be achieved to some extent, and the level of target gene expression will be improved in hypoxic microenvironment of solid tumors.

The choice of gene transfer vector is another key issue in gene therapy. As two major kinds of gene transfer vectors currently viral vector system and nonviral vector system both have their own advantages and disadvantages. Being the most efficient so far, the former is not regularly used in clinic due to small gene capacity, poor targeting specificity, self-immunogenicity, and serious biosafety risk in particular. In spite of having avoided the major security risk, the latter is greatly inferior to the former in transfection efficiency, and meaningful expression of target gene is hardly available. Currently lipofection and electroporation are the two non-viral vector transfection methods used most. But besides high cytotoxicity, liposome can be quickly cleared by serum in vivo, which greatly limits its utility, in spite of good transfection efficiency [3]. Electroporation method with high efficiency is suitable for transient expression and stable transfection, but it only applies to cells or tissue in vitro, not suitable for transfection in vivo. Moreover, a large number of cells will be killed by electric shocks [9–11].

Encouragingly, nanotechnology developed recently has offered a new means for solving the problem of gene transfer vector [12–19]. The research on the gene transfer vector based on nanoparticle has attracted wide attention— the therapy genes such as DNA or RNA wrapped in the nanoparticles or adsorbed on the surface are taken into cells and released. Compared with traditional carriers, nano-vectors used for gene transfer have a lot of advantages such as nonimmunogenicity, repeated injection, no genetic toxicity and cytotoxicity, no cell transformation or death, slow release of the genes to extend response time effectively, and maintaining effective concentration of the product, improving transfection efficiency and bioavailability of the product, and so on [20, 21]. Such vectors have become a new promising carrier system because they not only integrate advantages of the virus vectors and traditional non-viral vectors, but also avoid their defects [22–28]. Particularly, besides properties of general nanoparticles, the superparamagnetic effect of magnetic nanoparticle gene transfer vector will produce transfection with high efficiency and directional movement in an external magnetic field, which in turn helps to carry out targeted gene therapy.

But it is well known that the smaller particles, the more agglomerate, and soft agglomeration widely exist in nanoparticles (especially magnetic nanoparticles). Only modified on the surface can nanoparticles get into the cells to play a role of gene transfer vector, and dispersion of
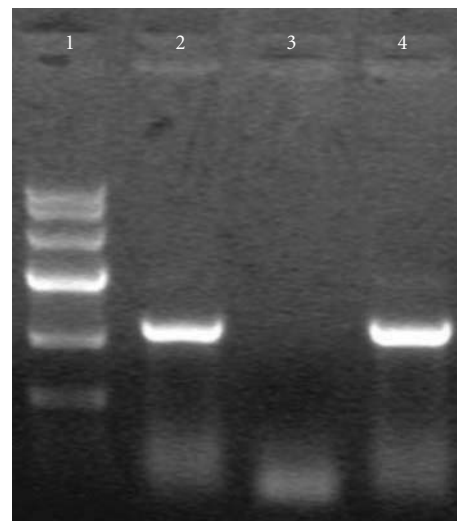
FIGURE 1: PCR gel electrophoresis of pCDNA3.1-Egr1-EGFP transfected (lane 1: Marker IV (each band in turn from top to bottom is 7 K, 5.5 K, 3.5 K, 2 K, 1 K, 500 bp); lane 2: pCDNA3.1-Egr1-EGFP; lane 4: pCDNA3.1-Egr1-EGFP).

the particles and surface functional groups have a direct impact on the further application of particles [13, 17]. As a common powder surface modification agent, PEI, whose monomer ($-CH_2-CH_2-NH_2-$) has good ability to bind DNA and adhere to cells, has electrostatic repulsion and steric hindrance effect [29–31]. In the previous study in our lab, $Mn_{0.5}Zn_{0.5}Fe_2O_4$, a thermosensitive Mn, and Zn ferrite magnetic nanoparticles, were successfully prepared chemically and modified surfacely by PEI, and good transgenic effect on cos-7 cells was obtained [32]. But whether PEI-MZF-NPs can be used for transfection of pHRE-Egr1-EGFP into cancer cells to perfect radiation-gene therapy for tumors and what the effect will be remain unknown to us.

In this project, attempts were made to develop a pHRE-Egr1-EGFP/PEI-MZF-NPs composite nanosystem, in which pHRE-Egr1-EGFP were transferred into hepatocellular carcinoma Bel-7402 cells by PEI-MZF-NPs as the carrier, and some relevant efficacy was tested. In addition, a comparative study of the level of gene expression by double induction of hypoxia and radiation and separate induction of radiation was made, which was expected to offer a viable approach to the mediated radiation gene therapy of cancer.

2. Materials and Methods

2.1. Main Reagent. Lipofectamine TM2000 purchased from Invitrogen Corporation; PEI (polyethylenimine, PEI) and dimethyl sulfoxide (DMSO) purchased from Sigma; Agarose purchased from MRI; DNaseI from Amercso; DMEM medium and fetal bovine serum from Gibco; Thiazolyl blue (MTT) from AMRESCO; PCDNA3.1-EGFP from Biotech Co.Ltd. Changsha Ying Run. Bel-7402 cells were provided by the Institute of Biochemistry and Cell Biology, Shanghai Institute of Biological Sciences, Chinese Academy of Sciences.

```
Sequence  0    1                                                                                                         0
Sequence  1   301   CAGTACATCTACGTATTAGTCATCGCTATTACCATGGTGATGCGGTTTTGGCAGTACACC   360

Sequence  0    1                                                                                                         0
Sequence  1   361   AATGGGCGTGGATAGCGGTTTGACTCACGGGGATTTCCAAGTCTCCACCCCATTGACGTC   420

Sequence  0    1                                                                                                         0
Sequence  1   421   AATGGGAGTTTGTTTTGGCACCAAAATCAACGGGACTTTCCAAAATGTCGTAACAACTGC   480

Sequence  0    1                    GACCCGGAAACGCCATATAAGGAGCAGGAAGGATCCCCCGCCGGAACAGACCTT         54
Sequence  1   481   GATCGCGACCCGGAAACGCCATATAAGGAGCAGGAAGGATCCCCCGCCGGAACAGACCTT   540

Sequence  0   55    ATTTGGGCAGCGCCTTATATGGAGTGGCCCAATATGGCCCTGCCGCTTCCGGCTCTGGGA   114
Sequence  1   541   ATTTGGGCAGCGCCTTATATGGAGTGGCCCAATATGGCCCTGCCGCTTCCGGCTCTGGGA   600

Sequence  0   115   GGAGGGGCGAGCGGGGGTTGGGGCGGGGGCAAGCTGGGAACTCCAGGCGCCTGGCCCGGG   174
Sequence  1   601   GGAGGGGCGAGCGGGGGTTGGGGCGGGGGCAAGCTGGGAACTCCAGGCGCCTGGCCCGGG   660

Sequence  0   175   AGGCCACTGCTGCTGTTCCAATACTAGGCTTTCCAGGAGCCTGAGCGCTCGCGATGCCGG   234
Sequence  1   661   AGGCCACTGCTGCTGTTCCAATACTAGGCTTTCCAGGAGCCTGAGCGCTCGCGATGCCGG   720

Sequence  0   235   AGCGGGTCGCAGGGTGGAGGTGCCCACCACTCTTGGATGGGAGGGCTTCACGTCACTCCG   294
Sequence  1   721   AGCGGGTCGCAGGGTGGAGGTGCCCACCACTCTTGGATGGGAGGGCTTCACGTCACTCCG   780

Sequence  0   295   GGTCCTCCCGGCCGGTCCTTCCAATATTAGGGCTTCCTGCTTCCCATATATGGCCATGTAC   354
Sequence  1   781   GGTCCTCCCGGCCGGTCCTTCCAATATTAGGGCTTCCTGCTTCCCATATATGGCCATGTAC   840

Sequence  0   355   GTCACGGCGGAGGCGGGCCCGTGCTGTTCCAGACCCTTGAAATAGAGGCCGATTCGGGGA   414
Sequence  1   841   GTCACGGCGGAGGCGGGCCCGTGCTGTTCCAGACCCTTGAAATAGAGGCCGATTCGGGGA   900

Sequence  0   415   GTCGCGAGAGATCCCAGCGCGCAGAACTTGG                                   445
Sequence  1   901   GTCGCGAGAGATCCCAGCGCGCAGAACTTGGGCTAGCGTTTAAACTTAAGCTTGGTACCG   960

Sequence  0   446                                                                        445
Sequence  1   961   AGCTCGGATCCACTAGTCCAGTGTGGTGGAATTCTGCAGTCGACGGTACCGCGGGCCCGG   1020

Sequence  0   446                                    445
Sequence  1  1021   GATCCACCGGTCGCCACCATGGTGAGCAAGGGCGA   1055
```
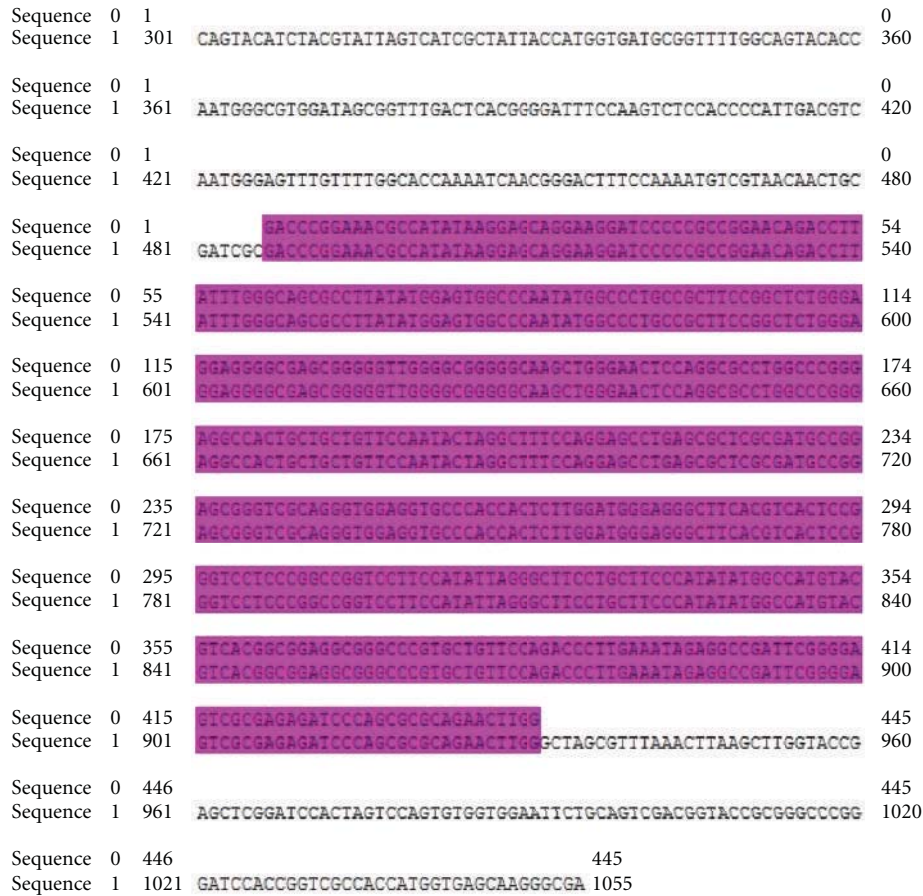
Figure 2: Sequencing and alignment of pCDNA3.1-Egr1-EGFP (sequence 0: Egr1 promoter sequences without CMVE; sequence 1: pCDNA3.1-Egr1-EGFP sequences with ab1 reverse complementary sequences; software: Dnassit 2.0).

2.2. Construction and Identification of the Eukaryotic Expression Plasmids: Egr1-HRE-EGFP

2.2.1. PCR Amplification of Egr1 Promoter Segments.
Egr1 promoter was inserted into pIRES vector. In front of the Egr1 promoter, there was a CMV fragment to enhance the expression efficiency of the promoter. The primer sequences were designed according to CMVE-Egr1p template, and CMVE-Egr1p fragments were amplified by PCR.

> Egr1-f: 5′-CCG CTCGAG CG ACGCGT GATCTT-CAATATTGGCCATTAGC-3′
>
> —MluI: CG ACGCGT;
> —XhoI: CCG CTCGAG
>
> Egr1-r: 5′-CCG CTCGAG CTA GCTAGC CCA-AGTTCTGCGCGCTGGGAT-3′
>
> —NheI: CTA GCTAGC
> —XhoI: CCG CTCGAG

Product length = 1152 bp.

2.2.2. Egr1p Were Subcloned into pCDNA3.1-EGFP.
The above CMVE-Egr1p fragments amplified were collected and subcloned into pCDNA3.1-EGFP on MluI and NheI sites. After transfection, the plasmids were purified and identified by PCR.

> Egr1-f: 5′-CCG CTCGAG CG ACGCGT GATCTT-CAATATTGGCCATTAGC-3′,
>
> Egr1-r: 5′-CCG CTCGAG CTA GCTAGC CCAAGT-TCTGCGCGCTGGGAT-3′.

Product length = 1152 bp.

According to the PCR electrophoresis results, the correct pCDNA3.1-Egr1-EGFP sequences were selected to test, EGFP-N-3 as the sequence primer.

2.2.3. To Synthesize 5HRE.
5HRE was synthesized according to [33]. In order to facilitate subsequent experiment, several restriction sites were added on the two sides of 5HRE. Synthetic products were identified by enzyme cleavage and gene sequence analysis (gene name: 5HRE; gene length: 185 bp; carrier name: pUC57; cloning site: EcoRI, HindIII).

2.2.4. Construction of pcDNA 3.1-5HRE-Egr1p-EGFP.
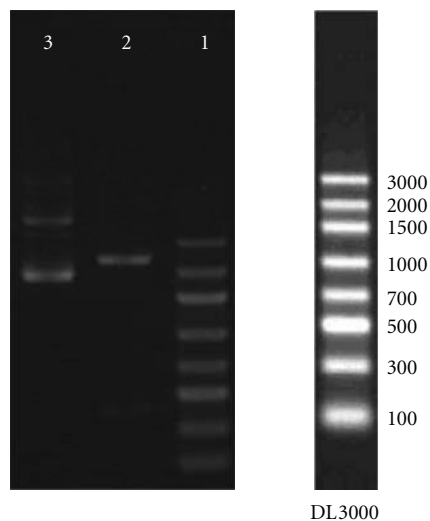PUC57-5HRE and pCDNA3.1-Egr1p-EGFP were connected

DL3000

Figure 3: pUC57-5HRE was identified by restriction enzyme digestion (Lane 1: DL3000; lane 2: pUC57-5HRE digested by NdeI and HindIII; lane 3: pUC57-5HRE).

after digestion by MluI, respectively. Then the connected products were transfected into DH5α. At last, the plasmids were isolated and purified after enlargement culturing and verified by BglII enzyme cleavage and gene sequence analysis.

2.3. MZF-NPs Preparation and Modification

2.3.1. Preparation. MZF-NPs were obtained by Chemical Coprecipitation Method, referring to [34].

2.3.2. Surface Modification [35]. Firstly, some MZF-NPs were dissolved in deionized water to prepare 4% of the magnetic fluid; supernatant was discarded after ultrasonic dispersion and high-speed centrifugation. Secondly, the precipitate was resuspended in PBS and ultrasonic dispersed. Thirdly, PEI was added slowly to the resuspender. The mixture was blended in a shaker at constant temperature for 24 h. Magnetic particles were separated from the solution by magnetic method and washed repeatedly by distilled water and methanol. After being vacuum dried, nanomagnetic particles modified surfacely by PEI were obtained (namely PEI-MZF-NPs).

2.4. Binding Assay of PEI-MZF-NPs and pHRE-Egr1-EGFP. PEI-MZF-NPs and pHRE-Egr1-EGFP were mixed together at mass ratios $0:1$, $5:1$, $10:1$, $20:1$, $40:1$, and $80:1$ (the final volume was 500 μL, and DNA concentration was constantly 0.01 μg/μL). 30 minutes later at room temperature, 10 μL of the above composite was taken, respectively, to test DNA binding ability of magnetic nanoparticles using agarose gel electrophoresis. According to the electrophoresis results, the optimal ratio of binging DNA with nano-magnetic particles could be observed.

2.5. DNase-I Digestion Experiment of PEI-MZF-NPs-DNA. PHRE-Egr1-EGFP and PEI-MZF-NPs were mixed in Tris Buffer, containing 60 mM $MgCl_2$, at $1:40$ of mass ratio. 30 minutes later at room temperature, DNase I was added to the above mixture, water bathing at 37°C. Stop solution (400 mmol/L NaCI, 100 mmol/L EDTA) was used to terminate the reaction at 10, 20, 40 min of digestion. pHRE-Egr1-EGFP was eluted from the composite by SDS, then extracted by phenol and chloroform, precipitated by absolute ethyl alcohol, and washed by 75% ethanol. The sediment was dissolved in distilled water, and the product was taken to do agarose gel electrophoresis assay to observe the ability of pHRE-Egr1-EGFP/PEI-MZF-NPs to resist nucleic acid enzymatic hydrolysis. As a control, the naked plasmids pHRE-Egr1-EGFP were done by the same approach.

2.6. DNA Release Assay for DNA-PEI-MZF-NPs. pHRE-Egr1-EGFP and PEI-MZF-NPs were mixed at $1:40$ of mass proportion to form a composite. Then the composite was stirred in a shaker at 37°C after being dissolved by TE. Respectively, at 1 h, 4 h, 8 h, 12 h, 1 d, 2 d, 3 d, 4 d, the solution was centrifuged at 15000 r/min, and then 20 μL supernate was taken to do agarose gel electrophoresis to observe DNA release ability of PEI-MZF-NPs-DNA. TE was replenished whenever some supernatant was taken, and the stir was continued.

2.7. To Evaluate Transfection Efficiency of PEI-MZF-NPs and the Gene Expression Induced by Anoxia and Radiation

2.7.1. Cell Culture. Bel-7402 cells were cultured in DMEM medium supplemented with 10% heat-inactivated calf serum, penicillin (100 units/mL), and streptomycin (0.1 g/ liter) and grew in the presence of 5% CO_2 in air at 37°C.

2.7.2. Evaluation of Transfection Efficiency and Gene Expression Induced by Anoxia and Radiation. pHRE-Egr1-EGFP were transfected into Bel-7402 cells by using PEI-MZF-NPs as carrier, and the transfection efficiency was evaluated, compared with that of lipofection transfection method and that of electroporation transfection method.

PEI-MZF-NPs transfection: (1) the plasmid DNA and PEI-MZF-NPs were diluted with serum-free culture medium, respectively, and then they were mixed together (mass ratio of PEI-MZF-NPs and DNA was $40:1$). 30 minutes later at room temperature, pHRE-Egr1-EGFP/PEI-MZF-NPs composite was obtained. (2) The Bel-7402 cells were seeded in 6-well plates (5×10^5 cells per well) and incubated in routine conditions. About 18 hours later (80% cells were confluent), the original culture medium was discarded, and the cells were washed twice by PBS and washed once by DMEM with no serum. (3) Serum-free DMEM with pHRE-Egr1-EGFP/PEI-MZF-NPs was added to the wells (Every well contained 3 μg DNA), and then the plates continued to be in the couveuse. 5 hours later, the medium with no serum was replaced by fresh DMEM medium with serum, and then the cells continued to be incubated for 48 h.

Sequence 0 1   0
Sequence 1 1   TGAAAACCTCTGACACATGCAGCTCCCGGAGACGGTCACAGCTTGTCTGTAAGCGGATGCCG 62

Sequence 0 1   0
Sequence 1 63 GGAGCAGACAAGCCCGTCAGGGCGCGTCAGCGGGTGTTGGCGGGTGTCGGGGCTGGCTTAAC 124

Sequence 0 1   0
Sequence 1 125 TATGCGGCATCAGAGCAGATTGTACTGAGAGTGCACCATATGCGGTGTGAAATACCGCACAG 186

Sequence 0 1   0
Sequence 1 187 ATGCGTAAGGAGAAAATACCGCATCAGGCGCCATTCGCCATTCAGGCTGCGCAACTGTTGGG 248

Sequence 0 1   0
Sequence 1 249 AAGGGCGATCGGTGCGGGCCTCTTCGCTATTACGCCAGCTGGCGAAAGGGGGATGTGCTGCA 310

Sequence 0 1   0
Sequence 1 311 AGGCGATTAAGTTGGGTAACGCCAGGGTTTTCCCAGTCACGACGTTGTAAAACGACGGCCAG 372

Sequence 0 1   ACGCGTGCTAGCAATTGCCACAGTGCATACGTGGGCTCCAACAGGTCCACAGTGC 55
Sequence 1 373 TGAATTCACGCGTGCTAGCAATTGCCACAGTGCATACGTGGGCTCCAACAGGTCCACAGTGC 434

Sequence 0 56 ATACGTGGGCTCCAACAGGTCCACAGTGCATACGTGGGCTCCAACAGGTCCACAGTGCATAC 117
Sequence 1 435 ATACGTGGGCTCCAACAGGTCCACAGTGCATACGTGGGCTCCAACAGGTCCACAGTGCATAC 496

Sequence 0 118 GTGGGCTCCAACAGGTCCACAGTGCATACGTGGGCTCCAACAGGTGGATCAGATCTACGCGT 179
Sequence 1 497 GTGGGCTCCAACAGGTCCACAGTGCATACGTGGGCTCCAACAGGTGGATCAGATCTACGCGT 558

Sequence 0 180 AAGCTT 185
Sequence 1 559 AAGCTTGGCGTAATCATGGTCATAGCTGTTTCCTGTGTGAA 599

FIGURE 4: Sequencing and alignment of pUC57-5HRE (sequence 0: 5HRE; sequence 1: 5HRE with ab1 reverse complementary sequences; software: Dnassit 2.0).


FIGURE 5: PCDNA3.1-5HRE-Egr1-EGFP was identified by restriction enzyme digestion (lane 1: KB Ladder; lane 2: pCDNA3.1-5HRE-Egr1p-EGFP digested by BglII; lane 3: pCDNA3.1-5HRE-Egr1p-EGFP).

Liposome method: (1) the plasmid DNA and liposome were diluted with serum-free culture medium, respectively, and then they were mixed together (mass ratio of PEI-MZF-NPs and DNA was 40 : 1). 30 minutes later at room temperature, DNA-liposome composite was obtained. (2) The Bel-7402 cells before transfection were done by the same way as PEI-MZF-NPs group. (3) Serum-free DMEM with DNA-liposome was added to the wells (every well contained 3 μg DNA, mass ratio of liposome and DNA was 5 : 3). After plates continued to be incubated for 5 hours, the medium

with no serum was replaced by fresh DMEM medium with serum, and then the cells continued to be incubated for 48 h.

Electroporation transfection: (1) the cells, digested by trypsin, were collected and centrifuged for 5 minutes (1000 g) after the trypsin reaction was terminated with culture medium with serum. (2) After the supernatant was discarded, the cells were washed twice by 1.25% E buffer (containing 1.25% DMSO in medium with no serum). (3) The cells were diluted with concentration of 5×10^6/mL by E buffer. (4) 3 μg DNA was added to every 400 mL of the cell suspension. (5) When being blended, the above mixture was transferred to electrode cup. (6) Electrode parameters were 250 v/950 uf, and the thickness of the electrode cup was 4 mm. (7) The electrode cup containing cells and DNA was placed in the electric box and received the electric shock. Then it was kept at room temperature for 10 minutes, and the cell suspension was transferred into full culture medium and then cultured in routine conditions. 24 h later, fresh full DMEM medium was used to replace the old medium to abandon dead cells, and then the cells continued to be incubated for 48 h.

The cells, transfected by the above three methods, were exposed to X-ray at 4 Gy (6 Mev) and then cultured for 24 h at 37°C in hypoxia environment (0.1% O_2, 5% CO_2 and N_2 balance gas). Fluorescent protein expressed in the cells was observed under the fluorescence microscope, and fluorescence intensity and transfection ratio were tested quantitatively by flow cytometric analysis. As a control, a group transfected by PEI-PEI-MZF-NPs and induced by radiation alone was designed, and the untransfected cells were used as a negative control.

```
Sequence 0   1                                                                                    0
Sequence 1   1    ACCGACAATTGCATGAAGAATCTGCTTAGGGTTAGGCGTTTTGCGCTGCTTCGCGATGTACG 62

Sequence 0   1         ACGCGTGCTAGCAATTGCCACAGTGCATACGTGGGCTCCAACAGGTCCACAG 52
Sequence 1   63   GGCCAGATATACGCGTGCTAGCAATTGCCACAGTGCATACGTGGGCTCCAACAGGTCCACAG 124

Sequence 0   53   TGCATACGTGGGCTCCAACAGGTCCACAGTGCATACGTGGGCTCCAACAGGTCCACAGTGCA 114
Sequence 1   125  TGCATACGTGGGCTCCAACAGGTCCACAGTGCATACGTGGGCTCCAACAGGTCCACAGTGCA 186

Sequence 0   115  TACGTGGGCTCCAACAGGTCCACAGTGCATACGTGGGCTCCAACAGGTGGATCAGATCTACG 176
Sequence 1   187  TACGTGGGCTCCAACAGGTCCACAGTGCATACGTGGGCTCCAACAGGTGGATCAGATCTACG 248

Sequence 0   177  CGT                                                               179
Sequence 1   249  CGTGATCTTCAATATTGGCCATTAGCCATATTATTCATTGGTTATATAGCATAAATCAATAT 310

Sequence 0   180                                                               179
Sequence 1   311  TGGCTATTGGCCATTGCATACGTTGTATCTATATCATAATATGTACATTTATATTGGCTCAT 372

Sequence 0   180                                                               179
Sequence 1   373  GTCCAATATGACCGCCATGTTGGCATTGATTATTGACTAGTTATTAATAGTAATCAATTACG 434

Sequence 0   180                                                               179
Sequence 1   425  GGGTCATTAGTTCATAGCCCATATATGGAGTTCCGCGTTACATAACTTACGGTAAATGGCCC 496

Sequence 0   180                                                               179
Sequence 1   497  GCCTGGCTGACCGCCCAACGACCCCCGCCCATTGACGTCAATAATGACGTATGTTCCCATAG 558

Sequence 0   180                    179
Sequence 1   559  TAACGCCAA 567
```

FIGURE 6: Sequencing and alignment of pCDNA3.1-5HRE-Egr1-EGFP (sequence 0: 5HRE, sequence 1: pCDNA3.1-5HRE-Egr1p-EGFP with ab1 reverse complementary sequences; software: Dnassit 2.0).
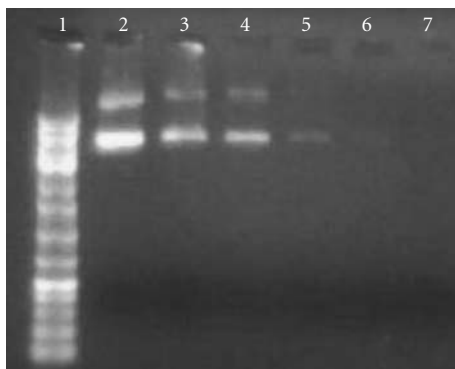
FIGURE 7: Image of agarose gel electrophoresis of pHRE-Egr1-EGFP, free and mixed with PEI-MZF-NPs at different mass ratios (PEI-MZF-NPs: pHRE-Egr1-EGFP) (lane 1: Mark; lane 2: 0 : 1; lanes 3 to 5: 1; lane 4: 10 : 1; lane 5: 20 : 1; lane 6: 40 : 1; lane 7: 80 : 1).

FIGURE 8: DNase-I resistance of pHRE-Egr1-EGFP-PEI-MZF-NPs (lane 1: Mark; lane 2: DNA-PEI-MZF-NPs with DNase-I for 10 min; lane 3: DNA-PEI-MZF-NPs with DNase-I for 20 min; lane 4: DNA-PEI-MZF-NPs with DNase-I for 30 min; lane 5: DNA -PEI-MZF-NPs with DNase-I for 40 min; lane 6: DNA -PEI-MZF-NPs with DNase-I for 60 min; lane 7: DNA without DNase-I; lane 8: DNA with DNase-I for 10 min; lane 9: DNA with DNase-I for 20 min; lane 10: DNA with DNase-I for 30 min; lane 11: DNA with DNase-I for 40 min).

2.7.3. MTT Assay for DNA-PEI-MZF-NPs Cytotoxicity. Bel-7402 cells, transfected by the above three methods, were subcultured in 96-well plates (2×10^3/well) for 72 h in air 5% CO_2 at 37°C, respectively. The same number of cells seeded without transfection were taken as the negative control. Then $20 \mu L$ (5 g/liter) of MTT was added to the cells in every well and incubated for 4 h at 37°C. The culture medium was replaced by $150 \mu L$ of DMSO and vibrated for 10 min. Then the optical density (OD) values were measured at a wavelength of 493 nm using a microplate reader (Multiskan MK3-353, USA). The cell survival ratio was counted with the following formula: survival ratio (%) = (OD of the experimental group)/(OD of the negative control group) $\times$ 100%.

2.8. Statistical Analysis. Values were expressed as mean ± SD. The data were analyzed with the SPSS 14.0 program, with $P < 0.05$ taken as the criterion for statistical significance.

3. Results and Discussion

3.1. Construction and Identification of pHRE-Egr1-EGFP Plasmid. Recombinant plasmid of pCDNA3.1-Egr1-EGFP was confirmed by PCR amplification and gene sequence analysis, which can be seen from Figure 1 with Egr1 specific banding in lane 2 and lane 4 and Figure 2 with the same sequence as that of Egr1 template.
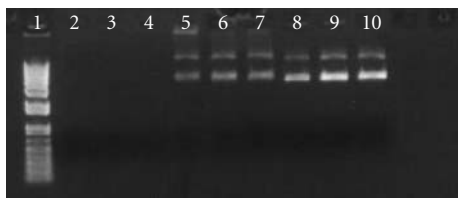
FIGURE 9: In vitro DNA release of PEI-MZF-NPs (lane 1: Mark; lane 2: 1 h; lane 3: 4 h; lane 4: 8 h; lane 5: 12 h; lane 6: 1 d; lane 7: 2 d; lane 8: 3 d; lane 9: 4 d; lane 10: 5 d).

If 5HRE fragment was successfully inserted, the fragment length between NdeI and HindII should be about 480 bp, because the length between NdeI and HindIII in empty pUC57 vector is about 290 bp. As shown in Figure 3 of restriction enzyme digestion and Figure 4 of sequencing, PUC57-5HRE was cloned correctly. Figure 5 was the restriction pattern of pCDNA3.1-5HRE-Egr1-EGFP, and Figure 6 was the HRE sequencing of pCDNA3.1-5HRE-Egr1-EGFP. Theoretically, there was only one BglII restriction site in the original pCDNA3.1-Egr1p-EGFP, if 5HRE was successfully inserted into the plasmid, another BglII restriction site would be brought in, and the fragment length between the two sites of BglII should be about 380 bp. Seen from Figure 5, 5HRE has been successfully inserted into pCDNA3.1-Egr1p-EGFP. As shown in Figure 6, DNA sequencing is quite correct. So it can be seen that the eukaryotic recombinant plasmid pCDNA3.1-HRE-Egr1p-EGFP was successfully constructed.

3.2. pHRE-Egr1-EGFP Packaging of PEI-MZF-NPs. Figure 7 represents the results of agarose gel electrophoresis of the composite with different proportion of pHRE-Egr1-EGFP and PEI-MZF-NPs. A clear DNA band could be seen in each lane with 1 : 0, 1 : 5 and 1 : 10 of DNA and PEI-MZF-NPs, and the band in the lane with 1 : 20 was significantly weakening, and there was no band to be seen in either the lane with 1 : 40 or over. These results suggested that PEI-MZF-NPs could combine all the plasmids in the system at the ratio of 1 : 40 and beyond, and 1 : 40 was the optimal proportion.

3.3. Nuclease Resistance of the Composite. When exposed to DNase I for 60 minutes, no change in strip brightness could be observed in the case of compound nanoparticles, whereas, with the digestion time extended, gradual degradation of naked DNA was apparent, and almost all was digested 40 minutes later (Figure 8). These results indicated that the DNA was stably incorporated within the nanoparticle matrix and therefore effectively protected from nuclease degradation. The reason for this protection against enzymatic digestion may be due to (1) repulsion of Mg^{2+} ions (which are necessary for the enzymatic reaction) by the amino groups, (2) a hindered access of the enzymes to the DNA that was immobilized on the nanoparticle surface, or (3) both (1) and (2) [36].

3.4. PEI-MZF-NPs Release. To be a candidate as a DNA carrier, the plasmid should be released from the particles in
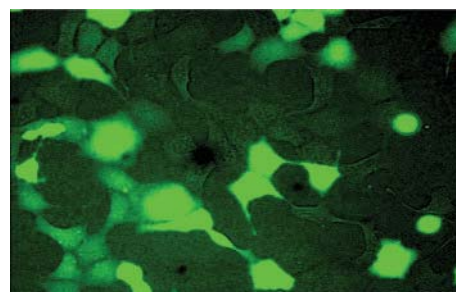
(a)
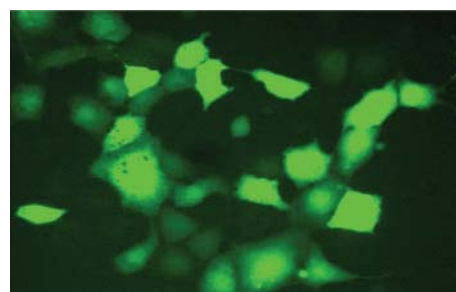
(b)
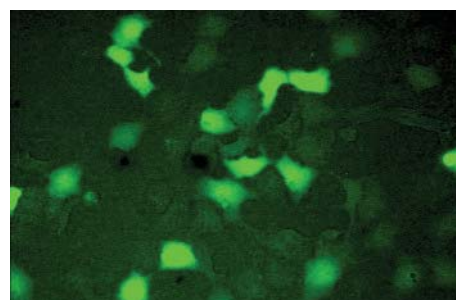
(c)
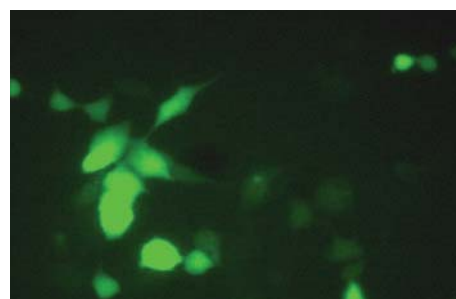
(d)

FIGURE 10: Bel-7402 cells transfected with pHRE-Egr1-EGFP delivered with PEI-MZF-NPs, electroporation, and liposome and induced by double hypoxia-radiation or radiation alone. The observed green cellular fluorescence is from the expressed EGFP, which has been confirmed by fluorescence microscopy ((a) magnetic nanoparticle group induced by hypoxia-radiation; (b) electroporation group induced by hypoxia radiation; (c), liposome group induced by radiation-hypoxia; (d) magnetic nanoparticle group induced by radiation alone).
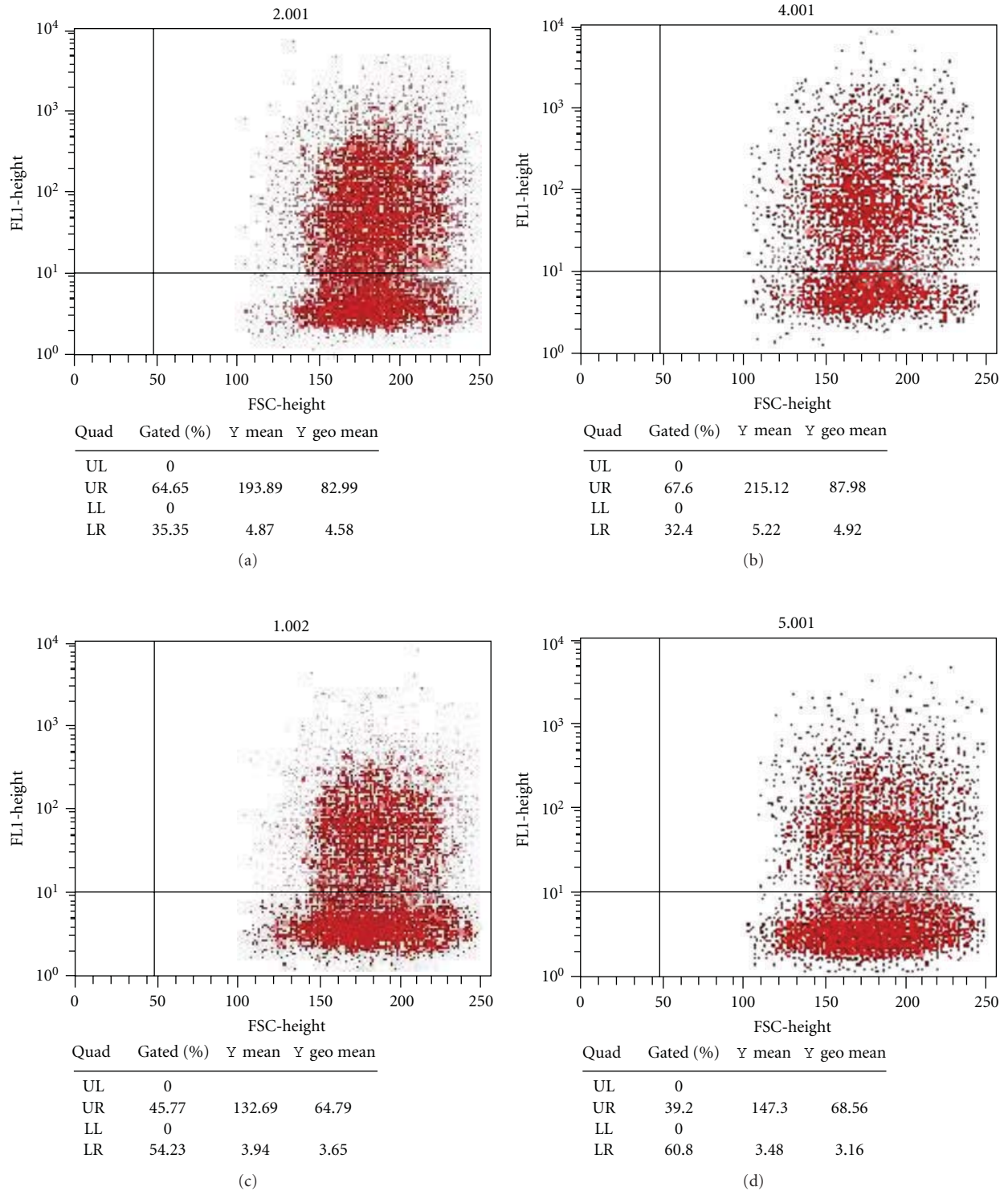
FIGURE 11: Flow cytometry showed the expression of EGFP in Bel-7402 cells with pHRE-Egr1-EGFP delivered by PEI-MZF-NPs, electroporation, and liposome and induced by double hypoxia radiation or radiation alone ((a) magnetic nanoparticle group induced by hypoxia-radiation; (b) electroporation group induced by hypoxia radiation; (c) liposome group induced by radiation hypoxia; (d) magnetic nanoparticle group induced by radiation alone).

TABLE 1: Comparison of toxicity on Bel-7402 cells transfected by means of PEI-MZF-NPs, electric perforation, and liposome over a period of 72 h ($\overline{x} \pm s$, $n = 5$).

Group	Optical density (OD)	Relative survival rate (%)
Negative control group	0.599 ± 0.012	
PEI-MZF-NPS group	$0.581 \pm 0.009^{b,c}$	97.1
Electricity perforation group	0.394 ± 0.009^{a}	65.8
Liposomes group	0.249 ± 0.073^{a}	41.5

[a] $P < 0.001$ versus negative control group; [b] $P < 0.001$ versus electricity perforation group. [c] $P < 0.001$ versus liposomes group.

order to allow its expression in cells. The release increased over the first 3 d, showing gradual increase in brightness of electrophoretic bands, reaching the maximum on the 3rd day and then leveled off (Figure 9). It was confirmed, thus, that besides good DNA-binding ability and protection from degradation, PEI-MZF-NPs have a good DNA release ability in appropriate conditions.

3.5. Carrying Efficiency and Cytotoxicity In Vitro. Under fluorescence microscope, green fluorescence in the three transfected groups was visible, and the cells with green fluorescence in electroporation group were more and brighter than those in the other two groups, and the PEI-MZF-NPs group came next, the liposome group the worst, and no green fluorescence in the untransfected group (Figure 10).

Tested by flow cytometry (Figure 11), transfection ratio and mean fluorescence intensity of magnetic nanoparticle group were 64.65% and 193.89, respectively, slightly lower than 67.60% and 215.12 of electroporation group, but obviously higher than 45.77% and 132.69 of liposome group. Moreover, in the magnetic nanoparticle groups, transfection ratio and fluorescence intensity induced by radiation and hypoxia both were significantly higher than 48.94% and 169.15 induced by radiation alone, which was consistent with the results observed by fluorescence microscope.

MTT assay is commonly used as a cell proliferation assay. Bel 7402 cells transfected with pHRE-Egr1-EGFP by PEI-MZF-NPs, liposome, electroporation, respectively, were incubated over a period of 5 d, and the cell viability was determined as described above by MTT. As shown in Table 1, optical density (OD) of the negative control was close to that of PEI-MZF-NPs group ($P > 0.05$), without statistically significant differences, but significantly higher than that of electroporation group ($P < 0.001$) and liposome group ($P < 0.001$), with statistically significant differences. The relative survival rate (97.1%) of cells in the group transfected by PEI-MZF-NPs was significantly higher than that in electroporation group (65.8%) and liposome group (41.5%), with electroporation group lower and liposome group lowest, indicating that transfection by electroporation and lipofection method equally has much toxicity on Bel-7402 cells, whereas almost no toxicity was detected by means of PEI-MZF-NPs.

4. Conclusions

In this study, we developed pHRE-Egr1-EGFP/PEI-MZF-NPs composite nano-system in which pHRE-Egr1-EGFP, eukaryotic gene expression plasmid, was constructed by combining radiation promoter Egr1 with HRE, forming anoxia radiation double sensitive promoter of HRE/Egr1 to activate reporter gene EGFP expression. MZF-NPs, obtained by coprecipitation method, were coated with PEI. The in vitro experimental results demonstrated that PEI-MZF-NPs have good DNA-binding ability, protection ability, release ability, little toxicity, and high transfection efficiency on Bel-7402 cells, obviously superior to those of the liposome and electricity perforation. Moreover, the expression level of EGFP gene induced by anoxia and radiation was significantly higher than that of single radiation activation. It is therefore concluded that HRE/Egr1 can induce and improve target gene expression efficiency in cancer anoxic microenvironment, and that PEI-MZF-NPs can be used as a novel non-viral gene vector which offers a viable approach to the mediated radiation-gene therapy of cancer.

References

[1] M. Hingorani, C. L. White, A. Merron et al., "Inhibition of repair of radiation-induced DNA damage enhances gene expression from replication-defective adenoviral vectors," *Cancer Research*, vol. 68, no. 23, pp. 9771–9778, 2008.

[2] H. Tsurushima, X. Yuan, L. E. Dillehay, and K. W. Leong, "Radiation-inducible caspase-8 gene therapy for malignant brain tumors," *International Journal of Radiation Oncology Biology Physics*, vol. 71, no. 2, pp. 517–525, 2008.

[3] X. J. Xu, L. H. Ding, L. X. Wang et al., "Construction of human Egr-1 promoter and its response to ionizing radiation in tumor cells," *Xi Bao yu Fen zi Mian yi Xue za Zhi*, vol. 25, no. 11, pp. 973–975, 2009.

[4] G. L. Semenza, "Targeting HIF-1 for cancer therapy," *Nature Reviews Cancer*, vol. 3, no. 10, pp. 721–732, 2003.

[5] G. Bartholomeusz, P. Cherukuri, J. Kingston et al., "In vivo therapeutic silencing of hypoxia-inducible factor 1 alpha (HIF-1α) using single-walled carbon nanotubes noncovalently coated with siRNA," *Nano Research*, vol. 2, no. 4, pp. 279–291, 2009.

[6] A. Rapisarda, M. Hollingshead, B. Uranchimeg et al., "Increased antitumor activity of bevacizumab in combination with hypoxia inducible factor-1 inhibition," *Molecular Cancer Therapeutics*, vol. 8, no. 7, pp. 1867–1877, 2009.

[7] L. Marignol, R. Foley, T. D. Southgate, M. Coffey, D. Hollywood, and M. Lawler, "Hypoxia response element-driven cytosine deaminase/5-fluorocytosine gene therapy system: a highly effective approach to overcome the dynamics of tumour hypoxia and enhance the radiosensitivity of prostate cancer

cells in vitro," *Journal of Gene Medicine*, vol. 11, no. 2, pp. 169–179, 2009.

[8] T. Shibata, A. J. Giaccia, and J. M. Brown, "Development of a hypoxia-responsive vector for tumor-specific gene therapy," *Gene Therapy*, vol. 7, no. 6, pp. 493–498, 2000.

[9] B. Kealy, A. Liew, J. M. McMahon et al., "Comparison of viral and nonviral vectors for gene transfer to human endothelial progenitor cells," *Tissue Engineering—Part C*, vol. 15, no. 2, pp. 223–231, 2009.

[10] H. Akita and H. Harashima, "Nonviral gene delivery," *Contributions to Nephrology*, vol. 159, pp. 13–29, 2008.

[11] Y. Kaneda and Y. Tabata, "Non-viral vectors for cancer therapy," *Cancer Science*, vol. 97, no. 5, pp. 348–354, 2006.

[12] E. Cohen-Sela, M. Chorny, D. Gutman et al., "Characterization of monocytes-targeted nanocarriers biodistribution in leukocytes in ex-vivo and in-vivo models," *Nano Biomedicine and Engineering*, vol. 2, no. 2, pp. 91–99, 2010.

[13] B. Pan, D. Cui, Y. Sheng et al., "Dendrimer-modified magnetic nanoparticles enhance efficiency of gene delivery system," *Cancer Research*, vol. 67, no. 17, pp. 8156–8163, 2007.

[14] C. Liu, "Research and development of nanopharmaceuticals in China," *Nano Biomedicine and Engineering*, vol. 1, no. 1, pp. 1–12, 2009.

[15] E. Anton, K. Swetha, W. Thomas et al., "Dextran-based nanocarriers as efficient media delivery vehicles to cell production bioreactors," *Nano Biomedicine and Engineering*, vol. 2, no. 2, pp. 126–132, 2010.

[16] D. Cui, Y. Han, Z. Li et al., "Fluorescent magnetic nanoprobes for in vivo targeted imaging and hyperthermia therapy of prostate cancer," *Nano Biomedicine and Engineering*, vol. 1, no. 1, pp. 61–74, 2009.

[17] S. Chen, Y. Ji, Q. Lian et al., "Gold nanorods coated with multilayer polyelectrolyte as intracellular delivery vector of antisense oligonucleotides," *Nano Biomedicine and Engineering*, vol. 2, no. 1, pp. 15–23, 2010.

[18] P. Huang, Z. Li, and J. Lin, "Photosensitizer-conjugated magnetic nanoparticles for in vivo simultaneous magnetofluorescent imaging and targeting therapy," *Biomaterials*, vol. 32, pp. 3447–3458, 2011.

[19] G. Gao, P. Huang, Y. Zhang, K. Wang, W. Qin, and D. Cui, "Gram scale synthesis of superparamagnetic Fe_3O_4 nanoparticles and fluid via a facile solvothermal route," vol. 13, no. 6, pp. 1782–1785, 2011.

[20] J. Panyam and V. Labhasetwar, "Biodegradable nanoparticles for drug and gene delivery to cells and tissue," *Advanced Drug Delivery Reviews*, vol. 55, no. 3, pp. 329–347, 2003.

[21] G. Bhakta, S. Mitra, A. Maitra et al., "DNA encapsulated magnesium and manganous phosphate nanoparticles: potential non-viral vectors for gene delivery," *Biomaterials*, vol. 26, no. 14, pp. 2157–2163, 2005.

[22] S. Liang, Y. Wang, J. Yu, C. Zhang, J. Xia, and D. Yin, "Surface modified superparamagnetic iron oxide nanoparticles: as a new carrier for bio-magnetically targeted therapy," *Journal of Materials Science*, vol. 18, no. 12, pp. 2297–2302, 2007.

[23] S. Mansouri, P. Lavigne, K. Corsi, M. Benderdour, E. Beaumont, and J. C. Fernandes, "Chitosan-DNA nanoparticles as non-viral vectors in gene therapy: strategies to improve transfection efficacy," *European Journal of Pharmaceutics and Biopharmaceutics*, vol. 57, no. 1, pp. 1–8, 2004.

[24] V. Vijayanathan, T. Thomas, and T. J. Thomas, "DNA nanoparticles and development of DNA delivery vehicles for gene therapy," *Biochemistry*, vol. 41, no. 48, pp. 14085–14094, 2002.

[25] J. M. Wang, B. L. Xiao, J. W. Zheng, H. B. Chen, and S. Q. Zou, "Effect of targeted magnetic nanoparticles containing 5-FU on expression of bcl-2, bax and caspase 3 in nude mice with transplanted human liver cancer," *World Journal of Gastroenterology*, vol. 13, no. 23, pp. 3171–3175, 2007.

[26] X. Wang, B. Yu, Y. Wu, R. J. Lee, and L. J. Lee, "Efficient downregulation of CDK4 by novel lipid nanoparticle-mediated siRNA delivery," *Anticancer Research*, vol. 31, no. 5, pp. 1619–1626, 2011.

[27] Y. Liu, T. Wang, F. He et al., "An efficient calcium phosphate nanoparticle-based nonviral vector for gene delivery," *International Journal of Nanomedicine*, vol. 6, pp. 721–727, 2011.

[28] M. B. Jesus, C. V. Ferreira, E. Paula et al., "Design of solid lipid nanoparticles for gene delivery into prostate cancer," *Journal of Controlled Release*, vol. 148, no. 1, pp. e89–e90, 2010.

[29] D. Wang, Y. Lin, L. X. Gu et al., "Study on Properties of nano-sized antimony doped tin oxide suspension," *China Powder Science and Technology*, vol. 1, pp. 10–13, 2004.

[30] F. Gao, B. F. Pan, W. M. Zheng, L. M. Ao, and H. C. Gu, "Study of streptavidin coated onto PAMAM dendrimer modified magnetite nanoparticles," *Journal of Magnetism and Magnetic Materials*, vol. 293, no. 1, pp. 48–54, 2005.

[31] R. Goyal, R. Bansal, S. Tyagi, Y. Shukla, P. Kumar, and K. C. Gupta, "1,4-Butanediol diglycidyl ether (BDE)-crosslinked PEI-g-imidazole nanoparticles as nucleic acid-carriers in vitro and in vivo," *Molecular BioSystems*, vol. 7, no. 6, pp. 2055–2065, 2011.

[32] Q. S. Tang, D. S. Zhang, X. M. Cong, M. L. Wan, and L. Q. Jin, "Using thermal energy produced by irradiation of Mn-Zn ferrite magnetic nanoparticles (MZF-NPs) for heat-inducible gene expression," *Biomaterials*, vol. 29, no. 17, pp. 2673–2679, 2008.

[33] A. Q. Zheng, X. R. Song, J. M. Yu et al., "Construction of a chimeric promoter HRE/CarG and its regulation of hypoxia and radition on liver cancer cell," *Chinese Journal of Cancer Biotherapy*, vol. 12, no. 1, pp. 69–71, 2005.

[34] X. Cong, D. Zhang, Q. Tang, N. Gu, S. Zhao, and J. Zhang, "Biocompatibility of $Mn_{0.5}Zn_{0.5}Fe_2O_4$ nanoparticles used in tumor hyperthermia," *Journal of Southeast University (National Science Education)*, vol. 3, pp. 23–27, 2007.

[35] Q. S. Tang, D. S. Zhang, and N. Gu, "Synthesis and in vitro study of PEI-coated MneZn ferrite e a novel gene vector," *Journal of Functional Materials*, vol. 38, Article ID 1268e72, 2007.

[36] O. Bayguinov, B. Hagen, and K. M. Sanders, "Substance P modulates localized calcium transients and membrane current responses in murine colonic myocytes," *British Journal of Pharmacology*, vol. 138, no. 7, pp. 1233–1243, 2003.

Review Article

Bacterial Magnetosome: A Novel Biogenetic Magnetic Targeted Drug Carrier with Potential Multifunctions

Jianbo Sun,[1] Ying Li,[2] Xing-Jie Liang,[3, 4] and Paul C. Wang[5]

[1] *Department of Microbiology and Immunology, College of Physicians and Surgeons, Columbia University, New York, NY 10032, USA*
[2] *State Key Laboratories for Agro-biotechnology and College of Biological Sciences, China Agricultural University, Beijing 100193, China*
[3] *Laboratory of Nanomedicine and Nanosafety, Division of Nanomedicine and Nanobiology, National Center for Nanoscience and Technology, Beijing 100190, China*
[4] *CAS Key Laboratory for Biomedical Effects of Nanomaterials and Nanosafety, Chinese Academy of Sciences, Beijing 100190, China*
[5] *Laboratory of Molecular Imaging, Department of Radiology, Howard University, Washington, DC 20060, USA*

Correspondence should be addressed to Xing-Jie Liang, liangxj@nanoctr.cn and Paul C. Wang, pwang@howard.edu

Bacterial magnetosomes (BMs) synthesized by magnetotactic bacteria have recently drawn great interest due to their unique features. BMs are used experimentally as carriers for antibodies, enzymes, ligands, nucleic acids, and chemotherapeutic drugs. In addition to the common attractive properties of magnetic carriers, BMs also show superiority as targeting nanoscale drug carriers, which is hardly matched by artificial magnetic particles. We are presenting the potential applications of BMs as drug carriers by introducing the drug-loading methods and strategies and the recent research progress of BMs which has contributed to the application of BMs as drug carriers.

1. Introduction

Nanoscale drug carriers for targeted drug delivery have great potential [1–4] to resolve the issues associated with regular drug administration such as nonspecific biodistribution of pharmaceuticals; the lack of drug specific affinity and the necessity of a large dosage to achieve high local concentration; the crossing of biological barriers such as organs, cells, and intracellular biolayers; and nonspecific toxicity and other adverse side effects (immunity, neural systems, etc.) due to high drug doses [5, 6].

Pharmaceutical carriers include soluble polymers, microstructures, cell ghosts, lipoproteins, liposomes, dendrimers, micelles and so on [2–6], which can all be designed for drug delivery vehicles. Such vehicles include (a) direct application of carriers with drug into the affected zone; (b) passive drug accumulation in the tissues with leaky vasculature; (c) physiological targeting based on abnormal pH and/or temperature in the pathological zone; (d) magnetic targeting under the use of an external magnetic field; (e) intelligentized targeting using specific molecules such as ligands or antibodies, which can recognize the targeted area and increase the affinity to it.

Magnetic-targeted drug carriers are prepared using Fe_3O_4 or Fe_2O_3 as a core and coated with biocompatible polymers for drug delivery [7–9] due to their attractive advantages for medical applications which are (a) paramagnetism for magnetic resonance imaging (MRI); (b) position altering with magnetic field; (c) hyperthermia with an external alternating magnetic field; (d) controllable size; (e) surface modification with diverse bioactive molecules; (f) nonsignificant safety concerns. This technology has evolved rapidly since the 1970s [10], although its application has been hampered by problems such as low drug loading, propensity of congregating, poor dispersion, and difficult control of microspheric shape or size [9]. Bacterial magnetosomes (BMs) [11] synthesized by magnetotactic bacteria have recently drawn great interest [12–15] as alternatives for targeting drug carriers due to their unique features such as paramagnetism, nanoscale, narrow-size distribution, and being bounded to the membrane [16–20].

2. Characterization of BMs

Magnetosomes are found in all magnetotactic bacteria and consisted of magnetic iron mineral particles and present species-specific characteristics. Magnetosomes from the same species have the same unique composition and uniform morphology with narrow-size distribution. In various magnetotactic bacteria, magnetosomes have shapes in cubo-octahedral, elongated hexagonal prismatic, and bullet-shaped morphologies (Figure 1) [16, 21–23]. Magnetosomes in most magnetotactic bacteria strains consist of magnetite, Fe_3O_4. The Raman Spectrum of BMs from *M. gryphiswaldense* shows resemblance to Fe_3O_4. The FTIR spectrum of BMs also shows the presence of Fe_3O_4 [24]. Typical particle sizes are 35–120 nm, however, in some locations, crystals larger than 200 nm are found. Magnetosomes, in several magnetotactic bacteria from sulfuric environments, consist of the iron-sulfide mineral greigite, Fe_3S_4, which is ferrimagnetically ordered [16, 25].

2.1. Characterization of Magnetosome Membrane. All magnetosomes examined to date have a lipid bilayer admixed with special proteins, which is termed magnetosome membrane. The magnetosome membrane of *M. magnetotacticum* MS-1 contains neutral lipids and free fatty acids; as well as glycolipids, sulfolipids, and phospholipids (in a weight ratio of 1 : 4 : 6). The phospholipids include phosphatidylserine and phosphatidylethanolamino. There are numerous proteins detected in the magnetosome membrane which were not found in other cell membranes or soluble fractions [18]. The fatty acid and proteomic analysis of the magnetosome membrane of *M. magneticum* AMB-1 showed a striking similarity between the cytoplasmic and magnetosome membrane profiles [19, 26]. The results showed that palmitoleic acid and oleic acid account for 90% of the total fatty acids and phospholipids compose 58% of the total lipid; with phosphatidyl ethanolamino accounting for 50% of the total phospholipids. 78 identified magnetosome membrane proteins were also found to be common in the cytoplasmic membrane, several of which are related to magnetosome biosynthesis.

The magnetosome membrane of *M. gryphiswaldense* is composed of phospholipids and fatty acids, which is similar to that from outer and cytoplasmic membranes but with different proportions [20]. There are at least 18 proteins that make up the magnetosome subproteome, and most of these proteins are unique for *M. gryphiswaldense*. The FTIR spectrum of BMs has shown these membrane lipids and the amino groups [24].

Analysis of magnetosome membrane proteins in different *Desulfovibrio magneticus* strains RS-1, AMB-1, and MSR-1 indicated three magnetosome-specific proteins MamA (Mms24), MamK, and MamM. The collagen-like protein and alleged iron-binding proteins are considered to play key roles in magnetite crystal formation and are identified as specific proteins in strain RS-1. The newly identified magnetosome membrane proteins might contribute to the formation of the unique irregular, bullet-shaped crystals in the strain [27].

The presence of polarizable primary amino groups in the magnetosome membrane offers an explanation of the elevation of external pH increasing the surface negativity of magnetosome membrane. The zeta potential of BMs from *M. gryphiswaldense* in pH 7.4 buffer is -24.4 ± 4.0 mV. The zeta potential for the BMs of M. magneticum AMB-1 changes from -2.5 to -25.0 mV when the pH value changes from 4.0 to 7.0 [24, 28]. The biodistribution of nanosize drug carriers following intravenous administration depends heavily on particle size and surface properties such as surface charge and hydrophobicity [29, 30]. The mononuclear phagocytic system (MPS), or reticuloendothelial system (RES), mainly consists of macrophages in the liver and spleen. The RES has the ability to remove unprotected nanoparticles from the bloodstream within seconds after intravenous administration. In general nanoscale size of BMs (35–120 nm) and the negative zeta potential of BMs are good to reduce liver clearance. It has been shown that after the injection of BMs through sublingual vena; BMs were accumulated in the liver of SD rats [24].

2.2. Magnetic Properties of BMs. The analysis of the magnetic properties of magnetosomes focused on the magnetic microstructure, hysteresis, and relaxation time. Researches by various groups showed that magnetosomes from *M. Magnetotacticum* MS-1, M. magneticum AMB-1, M. gryphiswaldense, the marine vibrioid strain MV-1, and the coccoid strain MC-1 were all single-magnetic-domain particles [11, 16, 21, 31–36]. The magnetization directions of small super paramagnetic crystals were constrained by magnetic interactions with larger crystals in the magnetosome chain having predominant saturation magnetization [32]. Shape anisotropy was found to dominate magnetocrystalline anisotropy in elongated crystals, grain elongation, and separation for chains of identical magnetite grains. The inclusion of magnetic interactions was found to decrease the blocking volume, thereby increasing the range of stable single magnetic domain, a scale not attainable for chemically synthesized nanoparticles [37].

Holograms showed a coercive field of 300 Oe for *M. magnetotacticum* [38] and coercive field of 300–450 Oe for the MV-1 chain [32]. The exact value of coercive fieldfor any given magnetosome chain is sensitive to the particle size, separation, and chain length, as well as magnetocrystalline anisotropy [31]. For aqueous suspensions of magnetosomes extracted from *M. gryphiswaldense*, the coercivity at room temperature is 0.7 kA/m, while coercivity increases to 2.6 kA/m or 6.5 kA/m Bby suspending magnetosomes in aqueous solution of gelatin, with subsequent particle immobilization by gelation, coercivity increases to 2.6 kA/m or 6.5 kA/m [39, 40]. Compared to 20 A/m of the commercially available ferrofluid Resovist, this extremely high value confirms the high anisotropy-related Néel relaxation time. The magnetic losses, converted into heat in hyperthermia, were determined calorimetrically to be 960 W/g at 10 kA/m and 410 kHz. This value is exceptionally large and may even exceed those of compared metallic magnetic particles such as cobalt particles, which are hardly matched by artificial magnetic particles [39, 41].

(a)

(b)

(c)

(d)
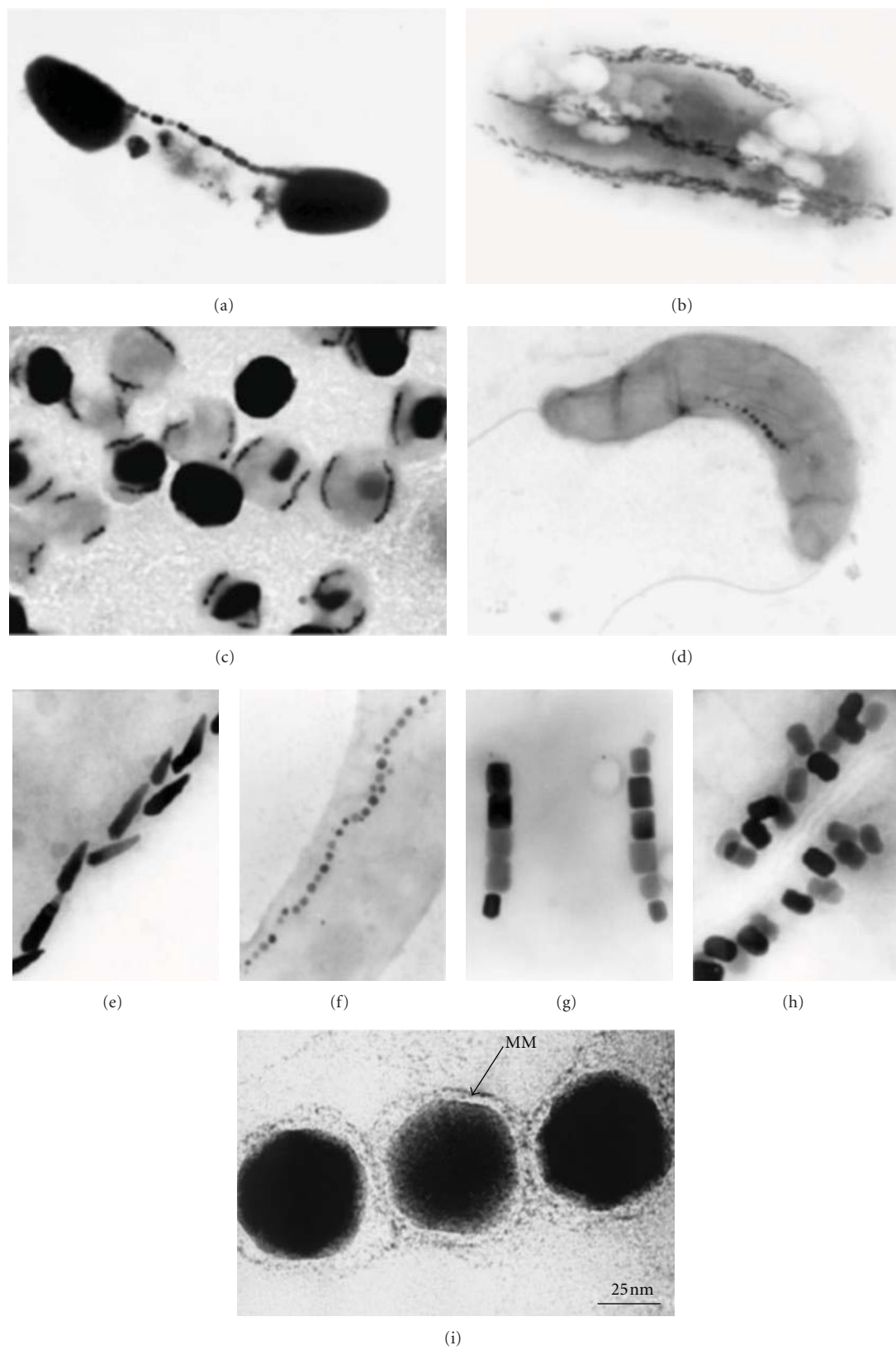
(e)

(f)

(g)

(h)

MM

25 nm

(i)

FIGURE 1: Magnetotactic bacteria with magnetosomes (a–d) and its membrane (i). Various morphologies of magnetosomes (e–h) [22, 23].

Alphandéry et al. [42] examined mechanisms of heat production by whole intact cells and extracted chains and individual magnetosomes of the magnetotactic bacterium *M. magneticum* strain AMB-1- when exposed to an oscillating magnetic field of frequency 108 kHz and field amplitudes of 23 and 88 mT. In this study, magnetosomes did not contain magnetite as the magnetite oxidized to maghemite. Intact bacterial cells that contain chains of magnetosomes, heat is generated through hysteresis losses yielding specific absorption rates of 115 ± 12 W/gFe at 23 mT and 864 ± 9 W/gFe at 88 mT. When the chains of magnetosomes are extracted from the bacterial cells and exposed to the same magnetic field, there is an additional contribution to the heat-producing mechanism due to the rotation of the magnetosomes. This contribution results in higher observed specific absorption rates of 864 ± 13 W/gFe at 23 mT and 1242 ± 24 W/gFe at 88 mT. Individual magnetosomes whose membranes had been removed produced specific absorption rate values of 529 ± 14 W/gFe at 23 mT and 950 ± 18 W/gFe at 88 mT.

Magnetotactic bacteria embedded with magnetosomes affect the T2-relaxation more greatly than T1-relaxation rate in MRI system [35] and can be used as a negative contrast agent for MRI. The physicochemical and magnetorelaxometric characterizations of bacterial magnetosomes and iron oxide nanoparticles were investigated. The longitudinal and transverse relaxivities of the magnetosomes were studied with a 1.5 T MRI system to be R1 = 7.688 mmol-1s-1 and R2 = 147.67 mmol-1s-1, respectively [39]. Magnetosomes in agarose gel were analyzed [43] using a 3.0 T MRI-scanner and showed T2 relaxivity of 1175 mM-1s-1, which was larger than synthetic magnetic nanoparticles with 551 mM-1s-1 and Resovists with 230 mM-1s-1. Both bacterial magnetosomes and synthetic magnetites can be used as a negative contrast agents and show slight T1 effects and strong T2 effects on MRI images. The signal attenuation of bacterial magnetite samples is more prominent than that of synthetic magnetite samples at the same concentration because bacterial magnetosomes have larger mean aggregate size, better dispersion, and stronger ferromagnetism compared to synthetic magnetites.

2.3. Biocompatibility of BMs.

BMs have been predicted to be highly biocompatible because they are formed by bacterial cells rather than artificially synthesized. BMs also pose potential risks as they are nanosized particles isolated from bacterial cells and their membrane contains various nonhuman proteins [18–20, 26]. Chemical toxicity of BMs from iron ions is negligible [44, 45] due to the insolubility of Fe_3O_4. Therefore, the toxicity of BMs may be primarily due to (a) their nanoscale size, which leads to embolism, blockage, and deposition in the body and (b) impurities, particularly proteins, nucleic acids, and polysaccharides associated with BMs extracted from bacterial cells, resulting in immunotoxicity.

Sun et al. have studied the biocompatibility of BMs and have shown the body tissue distribution and host tissue elimination following administration of BMs into the vascular system [24] and in vitro cytotoxicity for mouse fibroblasts [46]. BMs displayed targeted distribution in SD rat liver, suggesting that BMs may be less likely to congregate than other nanoparticles; that is, BMs may avoid incurring organ congestion or infarction in vivo since they can be transferred from the sublingual vein to the liver. Purified and sterilized magnetosomes were found to be nontoxic to mouse fibroblasts in vitro. The injection of 1 mg BMs did not increase body temperature of rabbits during the pyrogen test, which showed antigens or pyrogens free with BMs administration [47].

The biocompatibility of purified magnetosomes was also evaluated comprehensively by Sun et al. It was found that magnetosomes showed slight acute toxicity, immune toxicity, and cytotoxicity [47]. The LD50 of BMs was 62.7 mg/kg when injected into the sublingual vein of SD rats. Further studies, with injection of 40 mg/kg BMs, showed no significant difference between BM-treated and nontreated control rats in terms of routine blood exam results, liver and kidney function tests, organ coefficients of major organs, or Stimulation Index of lymph cells with ConA and/or LPS antigens. The histological examination of major organs from these 40 mg/kg BM-treated rats showed no obvious pathological changes, except increased number of vacuoles in livers and thicker interlobular septa in lungs. BMs showed little cytotoxic effect on H22, HL60, or EMT-6 cells. Incubation with 9 μg/mL BMs neither inhibited nor stimulated the growth of all three cells and had no effect on DNA content, cell size, or cell membrane integrity. Kim et al. reported that magnetosomes without surface modification were incorporated into endothelial progenitor cells in vitro, and cells containing BMs showed high viability [48].

3. Superiority of BMs as Targeted Nanoscale Drug Carriers

Bacterial magnetosomes also show superiority as targeting nanoscale drug carriers, which is hardly matched by artificial magnetic particles. Using magnetosomes of M. gryphiswaldense as an example, BMs show superiority as follows: (a) very narrow size distribution (25–55 nm) and uniform morphology, which is biogenetically controllable and reproducible; (b) an inorganic component of Fe_3O_4 with high purity [49]; (c) stable single-magnetic-domain particles, which show paramagnetism with extremely high coercivity values, exceptionally larger magnetic losses converted into heat in hyperthermia, and more obvious T2 signal attenuation in MRI than that of synthetic magnetite samples; (d) negatively charged surface and better dispersion due to polarized primary amino groups in the magnetosome bilayer lipid membrane; (e) easy functionalization with diverse bioactive molecules because of the abundance of primary amino groups in the surface of magnetosomes; (f) potentially slow drug release from magnetosomes in vivo due to the digestible magnetosome membrane; (g) a well-established large-scale production method of magnetosomes with high purity [50, 51]; (h) high biocompatibility.

4. Drug-Loading Strategies with BMs

BMs are able to be modified very easily with diverse bioactive molecules due to the abundance of primary amino groups on the surface of magnetosome membrane and chimeric proteins displayed specifically on the surfaces of genetically engineered isolated magnetosomes [52]. There are two major drug-loading strategies: directly loading drugs to BMs with dual function linkers, and indirectly loading drugs to BMs with linkers after modification of BMs and/or drugs.

4.1. Direct Drug-Loading onto BMs with Dual Functional Linkers. There are many chemotherapeutic drugs which contain one or more amino groups per drug molecule. Doxorubicin, epirubicin, daunorubicin, idarubicin, and pirarubicin contain one amino group per molecule, while mitomycin, bleomycin, and peplomycin contain multi-amino groups per molecule. BMs can be linked to these drugs by the homobifunctional crosslinking agents such as aliphatic binary aldehyde, diisocyanates, diisothiocyanates, di(succinimido) aliphatic esters, and their derivatives (Table 1) [53]. Drugs with carboxyls or phosphate groups also can be linked to the amino groups of BMs by using 1-Ethyl-3-[3-dimethyllam-inopropyl] carbodiimide (EDC).

4.2. Indirect Drug-Loading onto BMs After Modification of BMs and/or Drugs. Drugs without amino or carboxyl groups cannot be directly linked to BMs through the previously mentioned methods. There are three ways to load such drugs to BMs: attaching an amino or carboxyl group to the drugs by modification of the drugs, modifying the BMs without changing the drug molecules, and modifying both the drug molecules and BMs so that they can be linked with bifunctional reagents.

Drugs with sulphydryl or disulfide bond can be linked to BMs with modified SPDP (N-Succinimidyl 3-[2-pyridyldithio] propionate) and then reduced with DTT (Dithiothreitol). For example, antibodies can be linked to BMs by this method [54, 55]. It is simple to switch amino groups into sulfydryls in the BMs or drugs when Traults reagent 2-iminothiolane reacts with primary amino groups [53]. This reaction provides more choices for drug loading onto BMs. Drugs with primary amino groups can also be loaded onto BMs with this indirect method. For other drugs without amino group, sulphydryl or disulfide bond, drug loading onto BMs can be achieved by introducing one of these residues in the drugs and then using the strategies mentioned above.

Another unique method to load drugs onto BMs is by linking BMs with macromolecules, which are loaded with numerous small drug molecules [56]. Such macromolecules include poly-Glu, poly-Lys, poly-Asp, polyethylene glycol, and dextran. Poly-L-glutamic acid (PLGA) is a polymer of amino acids which contains multicarboxyl groups and only one single amino group. The single amino group of PLGA can be masked with a thiol group first and form PLGA-3-[2-pyridyldithio] propionyl (PLGA-PDP). PLGA-PDP, with the help of EDC, can react with small drug molecules carrying amino groups such as doxorubicin (DOX) and form PDP-PLGA-(DOX)n. This compound then reacts with the BMs modified with SPDP and DTT, and the PLGA-(DOX)n can be loaded onto BMs. The process is summarized in Figure 2.

There are also drug loading methods without additional chemical reactions. For example, BMs have a negatively charged surface can be modified with cationic silane such as N(trimethoxysilylpropyl) isothiouronium chloride, 3-Aminopropyltriethoxysilane, and 3-[2-(2-aminoethyl)-ethylamino]-propyltrimethoxysilane. The modified BMs show a cationic surface and can absorb nucleic acid drug [57, 58]. Protein A can be expressed in the membrane of BMs with genetic engineering can conjugate antibody drugs directly [52, 59].

5. Drug-Loading Types with BMs

There are four major groups of drugs that are able to be loaded onto BMs: protein drugs, nuclei acid drugs, radioactive isotopes, and chemotherapeutic drugs.

5.1. Protein Drugs. Protein drugs come in all shapes and sizes: recombinant human proteins such as insulin, growth hormone, and erythropoietin; monoclonal antibodies such as Remicade, Rituxan, and Erbitux; viral or bacterial proteins used as vaccines to elicit a specific immune response [60]. These protein drugs on the market fail to deliver in one or more target areas because they are digested or disrupted very readily during the process of crossing biological barriers such as organs, cells, and intracellular compartments. Therapeutic anticancer antibodies suffer from poor curative effects against solid tumors. Solid tumors are usually bounded with a pyknotic basement membrane and show lymphatic backflow obstacles, which impede the transfer of antibodies into solid tumors. This drawback can be overcome if the antibodies are loaded onto BMs and maintained in the solid tumors with magnets.

Methods for loading proteins onto BMs were developed by the research group led by T. Matsunaga. In 1987, Matsunaga et al. successfully immobilized glucose oxidase and uricase on BMs. The activity of glucose oxidase immobilized on BMs was 40 times than that of immobilized artificial magnetites or Zn-ferrite particles. Both glucose oxidase and uricase coupled with BMs retained their activities when they were reused five times [61]. The same research group also immobilized FITC conjugated anti-IgG antibodies on BMs, which were modified with glutaraldehyde or SPDP for the detection of allergen [19, 54, 55]. In 2001, the group loaded Hemoglobin A1c (HbA1c) onto modified BMs, which were coupled with m-aminophenylboronic acid (mAPB) by using homobifunctional crosslinker, Bis-(succcimidyl)suberate (BS3) (Figure 3) [62].

Recombinant BMs with Protein A expressed on their surface were constructed using magA. MagA is a key gene in the BMs biosynthesis of magnetotactic bacteria. Homogenous chemiluminescence enzyme immunoassay using antibody bound Protein A-BMs complexes was developed for detection of human IgG (Figure 4) [52, 59].

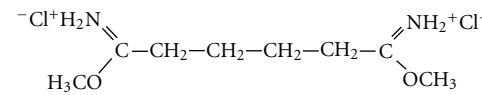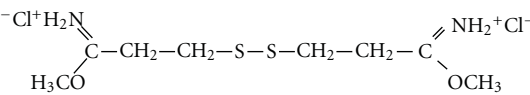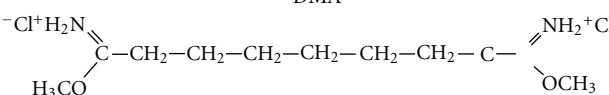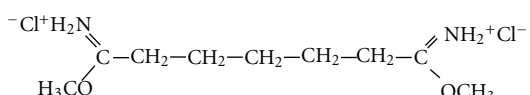TABLE 1: Homobifunctional cross linkers that can react with amino group [53].
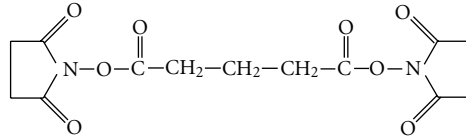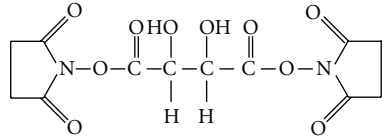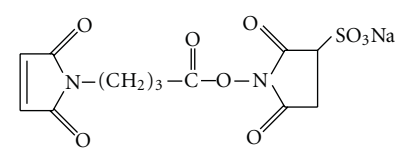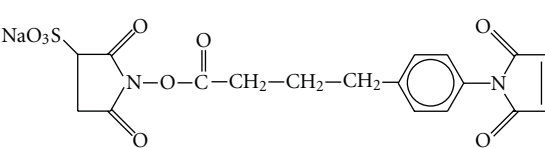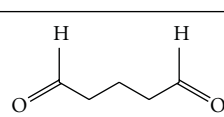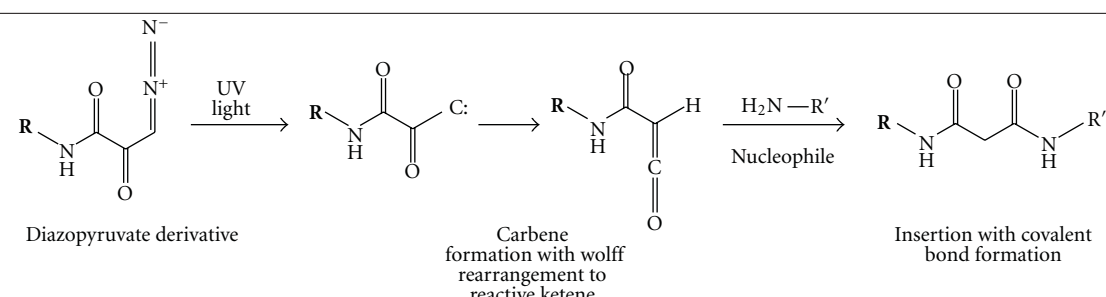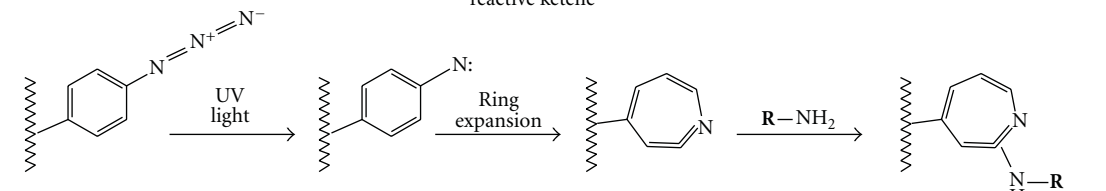
Linker reagents

TABLE 1: Continued.

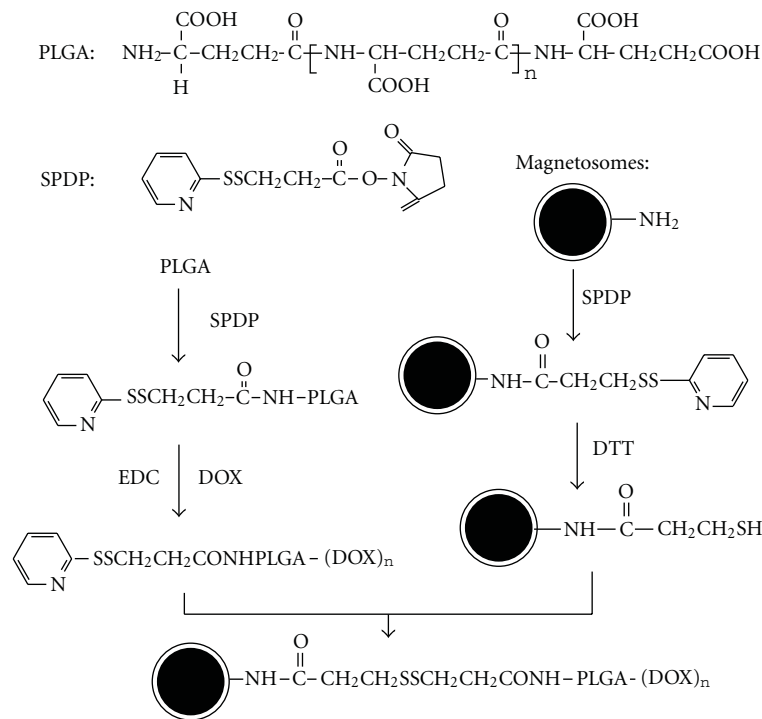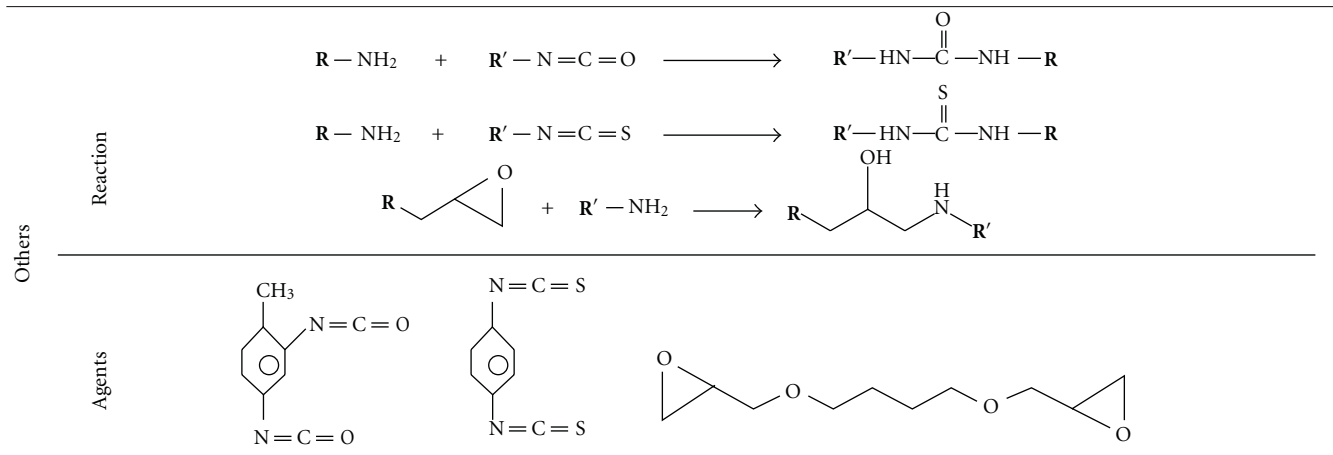|		
Photoreactive crosslinkers	Agents	 Based
Carbodiimides	Reaction	
	Agents	 EDC
Halides	Reaction	
	Agents	 DFDNB DFDNPS
Bis-diazonium derivatives	Reaction	
	Agents	

TABLE 1: Continued.

FIGURE 2: Schematic diagram of using PLGA as a bridge to link DOX with BMs.

Yoshino et al. established a method for displaying functional proteins on BMPs [63–65]. A novel promoter, termed msp3 promoter, was identified for the strong expression of BMs' membrane-specific protein using M. magneticum AMB-1 genome and proteome databases. The msp3 promoter showed 400 times higher activity than the magA promoter previously used. Efficient protein display on BMs was performed using the newly identified promoter sequences. This developed display system will facilitate the assembly of various functional proteins onto BMs.

5.2. Nucleic Acid Drugs. Nucleic acids, DNA, and RNA are endogenous materials which encode genetic information responsible for the biological process and also for dreadful

diseases as well. The nucleic acids act as drugs through different mechanisms such as binding with the synthesized proteins and hybridizing to a messenger RNA, that leads to translation altering or inducing degradation of target RNA. Through this process, the nucleic acids act as drugs for gene expression and regulation. BMs were reported for DNA and RNA extraction and gene delivery and detection [57, 58, 67–71].

BMs have a negatively charged surface and a membrane that contains 25% phosphatidylethanolamino and can absorb much lower nucleic acids (less than 0.5 ug DNA per 100 ug BMs) directly. Matsunaga's group modified BMs with cationic silanes such as N(trimethoxysilylpropyl) isothiouronium chloride, 3-Aminopropyltriethoxysi-
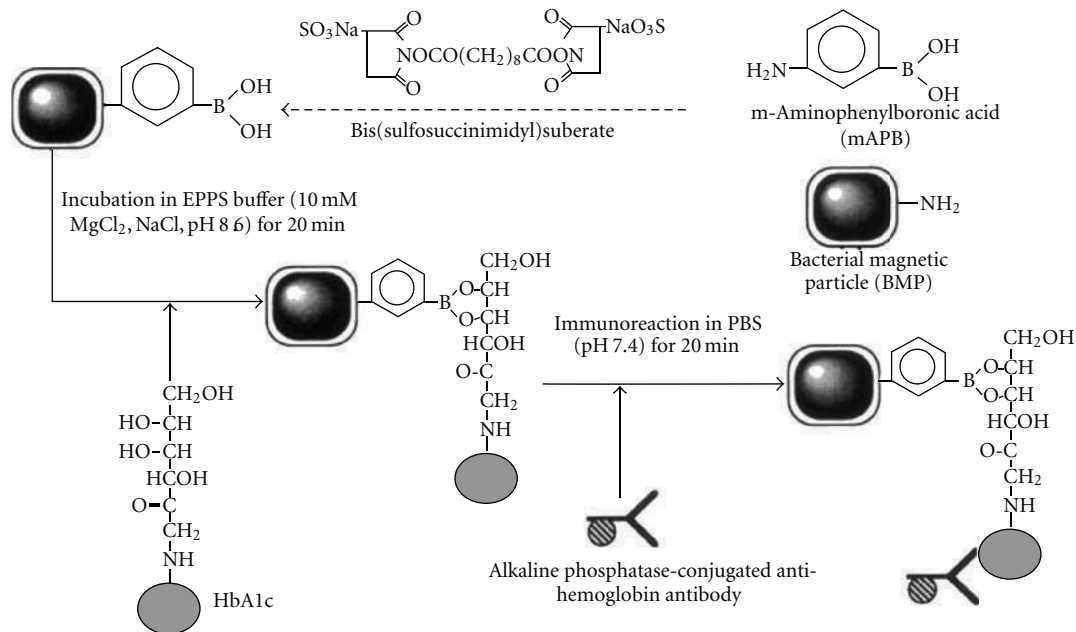
FIGURE 3: Schematic diagram of the boronate affinity immunoassay using mAPB-BMPs and alkaline phosphatase-conjugated anti-Ho antibody (ALP-antibody) [62].
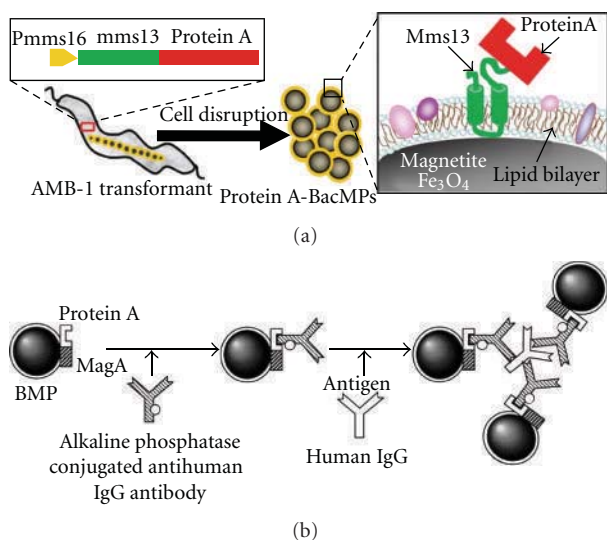

(a)

(b)

FIGURE 4: Schematic diagram of production of Protein A-BMs (A) and the homogenous chemiluminescence enzyme immunoassay using Protein A-BMs complexes [52, 65].

lane, and 3-[2-(2-aminoethyl)-ethylamino]-propyltrimethoxysilane. The DNA binding efficiency of the modified BMs increased with the number of amino groups presented on the silane compounds and was 14-fold higher than that of untreated BMs [57]. They also developed a better method of direct formation of a cascading hyperbranched polyamidoamino dendrimer onto the surface of amino silane modified BMs (Figure 5) [58]. Characterization of the synthesis revealed linear doubling of the surface

amino charge from generations one through five starting with an amino silane initiator. The dendrimer modified BMs have been used to carry out magnetic separation of DNA. Binding and release efficiencies increased with the number of generations of dendrimer. The binding and release efficiencies of bacterial magnetite modified with six-generation dendrimer (1.7×106 aminos/BM) were 7 and 11 times, compared with bacterial magnetites modified with only amino silane.

The Matsunaga group also immobilized biotin-labeled oligonucleotide probes onto BMs, which were modified with Sulfo-NHS-LC-LC-biotin and streptavidin [68–71]. A semiautomated system for the large-scale detection of single nucleotide polymorphisms (SNPs) has been developed with these probes-BMs particles [71]. Matsunaga et al. developed this method which binds nucleic acid fragments or protein to BMs modified with dual functional reagents after several reaction steps [71]. Biotin groups were attached to the magnetosome membrane either by incorpration of [1,2-dipalmitoyl-sn-glycero-3-phosphoethanolamino-N-(biotinyl)(sodiumsalt)] (biotin-DPPE) or by the covalent modification of the proteins within the magnetosome membrane using sulfo-N-hydroxy-succinimide ester sodium salt (NHS-biotin). Magnetosomes modified with surface-bound biotin groups were used to bind streptavidin (STV), and the resulting STV-functionalized BMs were functionalized with biotinylated DNA oligomers and/or antibodies.

5.3. Radioactive Isotopes. Radiotherapy can be used to treat diseases, especially cancer, using radiation to weaken or destroy particular targeted cells. Different types of radiation sources such as X-rays, γ-rays, particle beams, protons or neutrons are used to destroy the cancer cells within
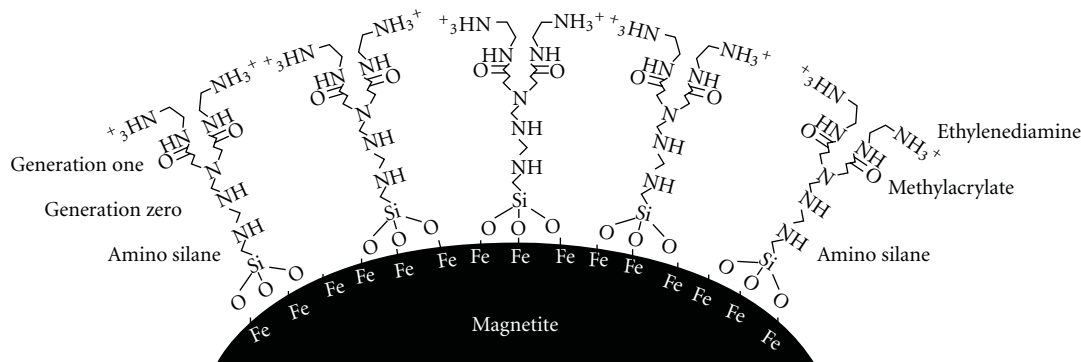
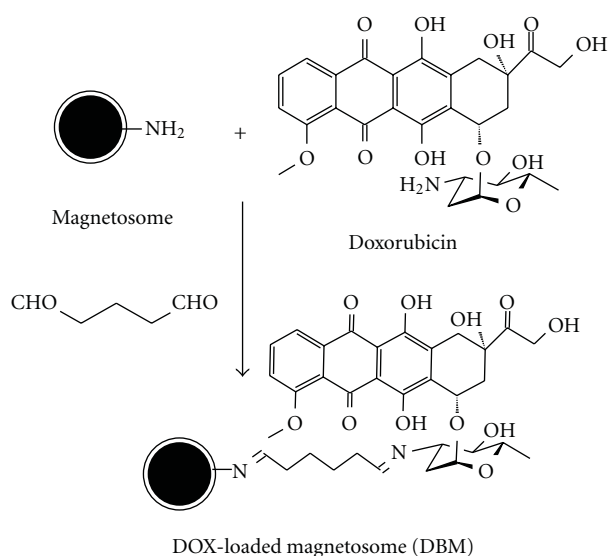FIGURE 5: Structure of amino silane modified bacterial magnetite dendrimer [58].

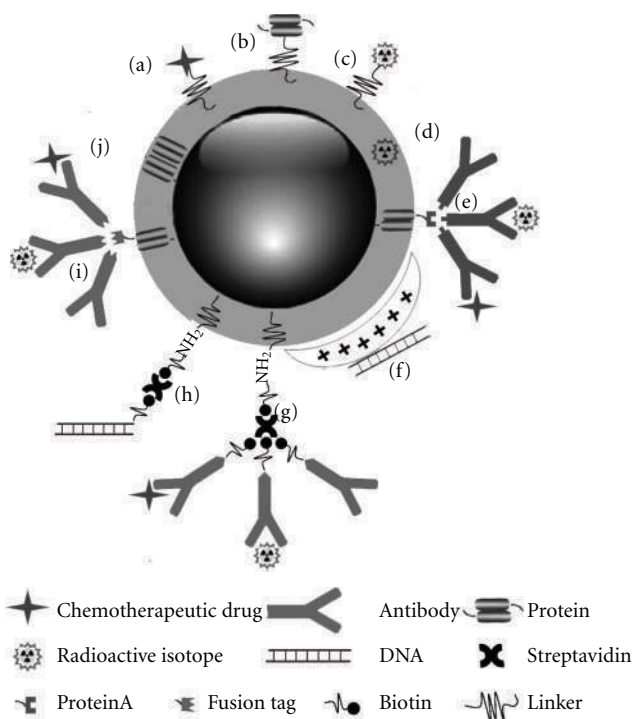FIGURE 6: Schematic diagram for preparing DBMs with glutaraldehyde [66].

FIGURE 7: Schematic diagram of multifunctional BMs. Chemotherapeutic drug (a), protein drug (b), and radioactive isotope (c) could be loaded onto BMs by cross linkers or chelators. Radioactive isotopes could be incorporated in the membrane of BMs during the formation of BMs (d). Antibodies modified with or without radioactive isotopes or chemotherapeutic drugs could be loaded onto BMs by immunoconjugating the genetic engineering expressed Protein A (e) or fusion protein tag (i) or by streptavidin-mediated conjugation with the biotin-streptavidin-biotin (g). DNA drugs could be absorbed onto BMs modified with cationic silanes (f) or linked to BMs with biotin-streptavidin-biotin (h). Specific protein drug could be expressed in BMs membrane by genetic fusion to BMs membrane protein (j).

the body [72, 73]. The most commonly used radioactive isotope in clinic is technetium-99, and accounts for 80% of nuclear medicine procedures. In the US alone, over 18 million nuclear medicine procedures are recorded each year. Radioactive isotopes such as 99mTc, 131I, 123I, and 111In can be linked to BMs with suitable chelates, radioactive-labeled molecules such as nucleic acids and proteins, and by including the radioactive isotopes in culture medium during BMs' formation. BMs labeled with radioactive isotopes show advantages in internal radiation or brachytherapy of solid tumors due to their targeted delivery.

5.4. Chemotherapeutic Drugs. The era of cancer chemotherapy began in the 1940s with the use of nitrogen mustards and folic acid antagonist drugs, and cancer drug development has been used widely since then [74, 75]. Modern chemotherapy avails itself, further to the cytotoxic drugs, of further agents that are differentiation inductors, radiosensitising agents, biological response modifiers, and/or agents capable of inducing hypoxia in the neoplastic clone

cells. The majority of chemotherapeutic drugs can be divided into alkylating agents, antimetabolites, anthracyclines, plant alkaloids, topoisomerase inhibitors, and other antitumour agents [76]. All of these drugs affect cell division or DNA

synthesis and function in some way. The activities of the most chemotherapeutic drugs suffer from the inability to accumulate selectively at the site of action. Drug targeting may attenuate adverse effects.

BMs' membrane contains an abundance of primary amino groups which can be modified and/or linked with chemotherapeutic drugs by various strategies mentioned above. Sun et al. provided an effective method of loading doxorubicin (DOX) onto BMs with glutaradehyde (Figure 6) and explored the clinical potential of magnetosomes as drug carriers in target therapy of cancers [13, 66]. Cancer suppressant effects in response to DOX-loaded BMs (DBMs) was evaluated. The DBMs prepared were cytotoxic to H22, HL60, and EMT-6 cells with inhibition of cell proliferation, suppression in c-myc expression, and diminishment of cell size and DNA content, which is consistent with free DOX. The in vivo antitumor effects were evaluated in BABL/c mice bearing tumors formed with H22 cells. In H22 cell-bearing mice, DBMs, DOX, and BMs displayed tumor suppression rates of 86.8%, 78.6%, and 4.3%, respectively. The mortality rates following administration of DBMs, DOX, and BMs were 20%, 80%, and 0%, respectively. Pathological examination of hearts and tumors revealed that both DBMs and DOX effectively inhibited tumor growth, but DBMs displayed a much lower cardiac toxicity compared with DOX.

6. Prospective

Magnetosomes are shown to be excellent magnetic nanocarriers for antibodies, enzymes, ligands, nucleic acids, and chemotherapeutic drugs. It was reported that functionalized magnetosomes could be used for DNA/RNA recovery, ELISA, cell sorting, target therapy of cancers, gene delivery, and as a contrast agent in MRI and cellular markers for gene expression. Although most of these studies are still at the proof-of-concept stage, and each study showed only one type of potential application of magnetosomes, these findings indicated that it will be very easy to develop multifunctional magnetosomes for clinical application. For instance, magnetosomes premodified with anticancer drugs can be linked with radioactive isotope-labeled antibodies and can recognize carcinoembryonic antigens. The multifunctional magnetosomes can simultaneously be used as molecular probes for tumor detection with MRI and as targeting drug carriers for tumor chemotherapy and radioimmunotherapy combined with magnetic hyperthermia (Figure 7). There are great potentials for the preclinical and clinical applications of the BMs.

Acknowledgments

References

[1] P. Couvreur, B. Kante, and L. Grislain, "Toxicity of polyalkyl-cyanoacrylate nanoparticles. II: doxorubicin-loaded nanoparticles," *Journal of Pharmaceutical Sciences*, vol. 71, no. 7, pp. 790–792, 1982.

[2] G. A. Hughes, "Nanostructure-mediated drug delivery," *Nanomedicine*, vol. 1, no. 1, pp. 22–30, 2005.

[3] M. Yokoyama, "Drug targeting with nano-sized carrier systems," *Journal of Artificial Organs*, vol. 8, no. 2, pp. 77–84, 2005.

[4] A. Singh, G. Garg, and P. K. Sharma, "Nanospheres: a novel approach for targeted drug delivery system," *International Journal of Pharmaceutical Sciences Review and Research*, vol. 5, no. 3, pp. 84–88, 2010.

[5] V. P. Torchilin, "Drug targeting," *European Journal of Pharmaceutical Sciences*, vol. 11, no. 2, pp. S81–S91, 2000.

[6] G. A. Silva, "Nanotechnology approaches for drug and small molecule delivery across the blood brain barrier," *Surgical Neurology*, vol. 67, no. 2, pp. 113–116, 2007.

[7] Q. A. Pankhurst, J. Connolly, S. K. Jones, and J. Dobson, "Applications of magnetic nanoparticles in biomedicine," *Journal of Physics D*, vol. 36, no. 13, pp. R167–R181, 2003.

[8] J. Dobson, "Magnetic nanoparticles for drug delivery," *Drug Development Research*, vol. 67, no. 1, pp. 55–60, 2006.

[9] J. Akhtar, R. Chaturvedi, J. Sharma et al., "Magnetized carrier as novel drug delivery system," *International Journal of Drug Delivery Technology*, vol. 1, no. 1, pp. 28–35, 2009.

[10] K. J. Widder, A. E. Senyei, and D. G. Scarpelli, "Magnetic microspheres: a model system for site specific drug delivery in vivo," *Proceedings of the Society for Experimental Biology and Medicine*, vol. 158, no. 2, pp. 141–146, 1978.

[11] D. L. Balkwill, D. Maratea, and R. P. Blakemore, "Ultrastructure of a magnetotactic spirillum," *Journal of Bacteriology*, vol. 141, no. 3, pp. 1399–1408, 1980.

[12] M. Hopkin, "Magnet-making bacteria could target tumours," *Naturenews*, 2004.

[13] J. B. Sun, J. H. Duan, S. L. Dai et al., "In vitro and in vivo antitumor effects of doxorubicin loaded with bacterial magnetosomes (DBMs) on H22 cells: the magnetic bio-nanoparticles as drug carriers," *Cancer Letters*, vol. 258, no. 1, pp. 109–117, 2007.

[14] V. K. Varadan, L. Chen, and J. Xie, "Magnetosomes and their biomedical applications," in *Nanomedicine*, pp. 175–213, John Wiley & Sons, Chichester, UK, 2008.

[15] J. Xie, K. Chen, and X. Chen, "Production, modification and bio-applications of magnetic nanoparticles gestated by magnetotactic bacteria," *Nano Research*, vol. 2, no. 4, pp. 261–278, 2009.

[16] D. A. Bazylinski, A. J. Garratt-Reed, and R. B. Frankel, "Electron microscopic studies of magnetosomes in magnetotactic bacteria," *Microscopy Research and Technique*, vol. 27, no. 5, pp. 389–401, 1994.

[17] A. Hoell, A. Wiedenmann, U. Heyen, and D. Schüler, "Nanostructure and field-induced arrangement of magnetosomes studied by SANSPOL," *Physica B*, vol. 350, no. 1–3, pp. E309–E313, 2004.

[18] Y. A. Gorby, T. J. Beveridge, and R. P. Blakemore, "Characterization of the bacterial magnetosome membrane," *Journal of Bacteriology*, vol. 170, no. 2, pp. 834–841, 1988.

[19] N. Nakamura, K. Hashimoto, and T. Matsunaga, "Immunoassay method for the determination of immunoglobulin G using bacterial magnetic particles," *Analytical Chemistry*, vol. 63, no. 3, pp. 268–272, 1991.

[20] K. Grünberg, E. C. Müller, A. Otto et al., "Biochemical and proteomic analysis of the magnetosome membrane in magnetospirillum gryphiswaldense," *Applied and Environmental Microbiology*, vol. 70, no. 2, pp. 1040–1050, 2004.

[21] U. Lins, F. Freitas, C. N. Keim, and M. Farina, "Electron spectroscopic imaging of magnetotactic bacteria: magnetosome morphology and diversity," *Microscopy and Microanalysis*, vol. 6, no. 5, pp. 463–470, 2000.

[22] D. Schüler and R. B. Frankel, "Bacterial magnetosomes: microbiology, biomineralization and biotechnological applications," *Applied Microbiology and Biotechnology*, vol. 52, no. 4, pp. 464–473, 1999.

[23] D. Schüler, "The biomineralization of magnetosomes in Magnetospirillum gryphiswaldense," *International Microbiology*, vol. 5, no. 4, pp. 209–214, 2002.

[24] J. B. Sun, Z. L. Wang, J. H. Duan et al., "Targeted distribution of bacterial magnetosomes isolated from magnetospirillum gryphiswaldense MSR-1 in healthy sprague-dawley rats," *Journal of Nanoscience and Nanotechnology*, vol. 9, no. 3, pp. 1881–1885, 2009.

[25] M. Pósfai, P. R. Buseck, D. A. Bazylinski, and R. B. Frankel, "Reaction sequence of iron sulfide minerals in bacteria and their use as biomarkers," *Science*, vol. 280, no. 5365, pp. 880–883, 1998.

[26] M. Tanaka, Y. Okamura, A. Arakaki, T. Tanaka, H. Takeyama, and T. Matsunaga, "Origin of magnetosome membrane: proteomic analysis of magnetosome membrane and comparison with cytoplasmic membrane," *Proteomics*, vol. 6, no. 19, pp. 5234–5247, 2006.

[27] T. Matsunaga, M. Nemoto, A. Arakaki, and M. Tanaka, "Proteomic analysis of irregular, bullet-shaped magnetosomes in the sulphate-reducing magnetotactic bacterium Desulfovibrio magneticus RS-1," *Proteomics*, vol. 9, no. 12, pp. 3341–3352, 2009.

[28] T. Tanaka and T. Matsunaga, "Fully automated chemiluminescence immunoassay of insulin using antibody—Protein A—bacterial magnetic particle complexes," *Analytical Chemistry*, vol. 72, no. 15, pp. 3518–3522, 2000.

[29] A. Vonarbourg, C. Passirani, P. Saulnier, and J. P. Benoit, "Parameters influencing the stealthiness of colloidal drug delivery systems," *Biomaterials*, vol. 27, no. 24, pp. 4356–4373, 2006.

[30] L. Juillerat-Jeanneret and F. Schmitt, "Chemical modification of therapeutic drugs or drug vector systems to achieve targeted therapy: looking for the grail," *Medicinal Research Reviews*, vol. 27, no. 4, pp. 574–590, 2007.

[31] B. M. Moskowitz, R. B. Frankel, P. J. Flanders, R. P. Blakemore, and B. B. Schwartz, "Magnetic properties of magnetotactic bacteria," *Journal of Magnetism and Magnetic Materials*, vol. 73, no. 3, pp. 273–288, 1988.

[32] R. E. Dunin-Borkowski, M. R. McCartney, R. B. Frankel, D. A. Bazylinski, M. Pósfai, and P. R. Buseck, "Magnetic microstructure of magnetotactic bacteria by electron holography," *Science*, vol. 282, no. 5395, pp. 1868–1870, 1998.

[33] M. Timko, A. Džarová, P. Kopčanský et al., "Magnetic properties of magnetite formed by biomineralization and chemical synthesis," *Acta Physica Polonica A*, vol. 113, no. 1, pp. 573–576, 2008.

[34] R. Hergt, R. Hiergeist, M. Zeisberger et al., "Magnetic properties of bacterial magnetosomes as potential diagnostic

[35] O. Felfoul, M. Mohammadi, and S. Martel, "Magnetic resonance imaging of Fe3O4 nanoparticles embedded in living magnetotactic bacteria for potential use as carriers for in Vivo applications," in *Proceedings of the 29th Annual International Conference of IEEE-EMBS, Engineering in Medicine and Biology Society (EMBC '07)*, pp. 1463–1466, August 2007.

[36] F. C. Meldrum, S. Mann, B. R. Heywood, R. B. Frankel, and D. A. Bazylinski, "Electron microscopy study of magnetosomes in two cultured vibrioid magnetotactic bacteria," *Proceedings of the Royal Society B*, vol. 251, no. 1332, pp. 237–242, 1993.

[37] A. R. Muxworthy and W. Williams, "Critical superparamagnetic/single-domain grain sizes in interacting magnetite particles: implications for magnetosome crystals," *Journal of the Royal Society Interface*, vol. 6, no. 41, pp. 1207–1212, 2009.

[38] I. Penninga, H. de Waard, B. M. Moskowitz, D. A. Bazylinski, and R. B. Frankel, "Remanence measurements on individual magnetotactic bacteria using a pulsed magnetic field," *Journal of Magnetism and Magnetic Materials*, vol. 149, no. 3, pp. 279–286, 1995.

[39] C. U. Herborn, N. Papanikolaou, R. Reszka, K. Grünberg, D. Schüler, and J. F. Debatin, "Magnetosomes as biological model for iron binding: relaxivity determination with MRI," *Fortschr Röntgenstr*, vol. 175, no. 6, pp. 830–834, 2003.

[40] D. Eberbeck, V. Janke, S. Hartwig et al., "Blocking of magnetic moments of magnetosomes measured by magnetorelaxometry and direct observation by magnetic force microscopy," *Journal of Magnetism and Magnetic Materials*, vol. 289, pp. 70–73, 2005.

[41] R. Hergt, S. Dutz, R. Müller, and M. Zeisberger, "Magnetic particle hyperthermia: nanoparticle magnetism and materials development for cancer therapy," *Journal of Physics Condensed Matter*, vol. 18, no. 38, article S26, pp. S2919–S2934, 2006.

[42] E. Alphandéry, S. Faure, L. Raison, E. Duguet, P. A. Howse, and D. A. Bazylinski, "Heat production by bacterial magnetosomes exposed to an oscillating magnetic field," *The Journal of Physical Chemistry C*, vol. 115, no. 1, pp. 18–22, 2011.

[43] L. L. Hu, F. Zhang, Z. Wang et al., "Comparison of the 1H NMR relaxation enhancement produced by bacterial magnetosomes and synthetic iron oxide nanoparticles for potential use as MR molecular probes," *IEEE Transactions on Applied Superconductivity*, vol. 20, no. 3, pp. 822–825, 2010.

[44] U. O. Häfeli and G. J. Pauer, "In vitro and in vivo toxicity of magnetic microspheres," *Journal of Magnetism and Magnetic Materials*, vol. 194, no. 1, pp. 76–82, 1999.

[45] V. Wagner, A. Dullaart, A. K. Bock, and A. Zweck, "The emerging nanomedicine landscape," *Nature Biotechnology*, vol. 24, no. 10, pp. 1211–1217, 2006.

[46] L. Xiang, J. Wei, S. Jianbo, W. Guili, G. Feng, and L. Ying, "Purified and sterilized magnetosomes from Magnetospirillum gryphiswaldense MSR-1 were not toxic to mouse fibroblasts in vitro," *Letters in Applied Microbiology*, vol. 45, no. 1, pp. 75–81, 2007.

[47] J. Sun, T. Tang, J. Duan et al., "Biocompatibility of bacterial magnetosomes: acute toxicity, immunotoxicity and cytotoxicity," *Nanotoxicology*, vol. 4, no. 3, pp. 271–283, 2010.

[48] J. A. Kim, H. J. Lee, H. J. Kang, and T. H. Park, "The targeting of endothelial progenitor cells to a specific location within a microfluidic channel using magnetic nanoparticles," *Biomedical Microdevices*, vol. 11, no. 1, pp. 287–296, 2009.

[49] A. Fischer, M. Schmitz, B. Aichmayer, P. Fratzl, and D. Faivre, "Structural purity of magnetite nanoparticles in magnetotactic

bacteria," *Journal of the Royal Society Interface*, vol. 8, no. 60, pp. 1011–1018, 2011.

[50] J. B. Sun, F. Zhao, T. Tang et al., "High-yield growth and magnetosome formation by *Magnetospirillum gryphiswaldense* MSR-1 in an oxygen-controlled fermentor supplied solely with air," *Applied Microbiology and Biotechnology*, vol. 79, no. 3, pp. 389–397, 2008.

[51] Y. Liu, G. R. Li, F. F. Guo, W. Jiang, Y. Li, and L. J. Li, "Large-scale production of magnetosomes by chemostat culture of *Magnetospirillum gryphiswaldense* at high cell density," *Microbial Cell Factories*, vol. 9, article 99, 2010.

[52] T. Matsunaga, R. Sato, S. Kamiya, T. Tanaka, and H. Takeyama, "Chemiluminescence enzyme immunoassay using ProteinA-bacterial magnetite complex," *Journal of Magnetism and Magnetic Materials*, vol. 194, no. 1, pp. 126–131, 1999.

[53] G. Hermanson, *Bioconjugate Techniques*, Academic Press, New York, NY, USA, 2nd edition, 2008.

[54] N. Nakamura, J. G. Burgess, K. Yagiuda, S. Kudo, T. Sakaguchi, and T. Matsunaga, "Detection and removal of Escherichia coli using fluorescein isothiocyanate conjugated monoclonal antibody immobilized on bacterial magnetic particles," *Analytical Chemistry*, vol. 65, no. 15, pp. 2036–2039, 1993.

[55] N. Nakamura and T. Matsunaga, "Highly sensitive detection of allergen using bacterial magnetic particles," *Analytica Chimica Acta*, vol. 281, no. 3, pp. 585–589, 1993.

[56] Y. Kato, N. Umemoto, Y. Kayama et al., "A novel method of conjugation of daunomycin with antibody with a poly-L-glutamic acid derivative as intermediate drug carrier. An anti-α-fetoprotein antibody-daunomycin conjugate," *Journal of Medicinal Chemistry*, vol. 27, no. 12, pp. 1602–1607, 1984.

[57] B. Yoza, M. Matsumoto, and T. Matsunaga, "DNA extraction using modified bacterial magnetic particles in the presence of amino silane compound," *Journal of Biotechnology*, vol. 94, no. 3, pp. 217–224, 2002.

[58] B. Yoza, A. Arakaki, and T. Matsunaga, "DNA extraction using bacterial magnetic particles modified with hyperbranched polyamidoamine dendrimer," *Journal of Biotechnology*, vol. 101, no. 3, pp. 219–228, 2003.

[59] T. Matsunaga, A. Arakaki, and M. Takahoko, "Preparation of luciferase-bacterial magnetic particle complex by artificial integration of MagA-luciferase fusion protein into the bacterial magnetic particle membrane," *Biotechnology and Bioengineering*, vol. 77, no. 6, pp. 614–618, 2002.

[60] I. M. Tomlinson, "Next-generation protein drugs," *Nature Biotechnology*, vol. 22, no. 5, pp. 521–522, 2004.

[61] T. Matsunaga and S. Kamiya, "Use of magnetic particles isolated from magnetotactic bacteria for enzyme immobilization," *Applied Microbiology and Biotechnology*, vol. 26, no. 4, pp. 328–332, 1987.

[62] T. Tanaka and T. Matsunaga, "Detection of HbA1c by boronate affinity immunoassay using bacterial magnetic particles," *Biosensors and Bioelectronics*, vol. 16, no. 9–12, pp. 1089–1094, 2001.

[63] T. Yoshino and T. Matsunaga, "Development of efficient expression system for protein display on bacterial magnetic particles," *Biochemical and Biophysical Research Communications*, vol. 338, no. 4, pp. 1678–1681, 2005.

[64] T. Yoshino, F. Kato, H. Takeyama, M. Nakai, Y. Yakabe, and T. Matsunaga, "Development of a novel method for screening of estrogenic compounds using nano-sized bacterial magnetic particles displaying estrogen receptor," *Analytica Chimica Acta*, vol. 532, no. 2, pp. 105–111, 2005.

[65] T. Yoshino, H. Hirabe, M. Takahashi, M. Kuhara, H. Takeyama, and T. Matsunaga, "Magnetic cell separation using nano-sized bacterial magnetic particles with reconstructed magnetosome membrane," *Biotechnology and Bioengineering*, vol. 101, no. 3, pp. 470–477, 2008.

[66] J. B. Sun, J. H. Duan, S. L. Dai et al., "Preparation and antitumor efficiency evaluation of doxorubicin-loaded bacterial magnetosomes: magnetic nanoparticles as drug carriers isolated from Magnetospirillum gryphiswaldense," *Biotechnology and Bioengineering*, vol. 101, no. 6, pp. 1313–1320, 2008.

[67] H. Takeyama, A. Yamazawa, C. Nakamura, and T. Matsunaga, "Application of bacterial magnetic particles as novel DNA carriers for ballistic transformation of a marine cyanobacterium," *Biotechnology Techniques*, vol. 9, no. 5, pp. 355–360, 1995.

[68] H. Ota, H. Takeyama, H. Nakayama, T. Katoh, and T. Matsunaga, "SNP detection in transforming growth factor-β1 gene using bacterial magnetic particles," *Biosensors and Bioelectronics*, vol. 18, no. 5-6, pp. 683–687, 2003.

[69] K. Maruyama, H. Takeyame, E. Nemoto, T. Tanaka, K. Yoda, and T. Matsunaga, "Single nucleotide polymorphism detection in aldehyde dehydrogenase 2 (ALDH2) gene using bacterial magnetic particles based on dissociation curve analysis," *Biotechnology and Bioengineering*, vol. 87, no. 6, pp. 687–694, 2004.

[70] B. Ceyhan, P. Alhorn, C. Lang, D. Schüler, and C. M. Niemeyer, "Semisynthetic biogenic magnetosome nanoparticles for the detection of proteins and nucleic acids," *Small*, vol. 2, no. 11, pp. 1251–1255, 2006.

[71] T. Matsunaga, K. Maruyama, H. Takeyama, and T. Katoh, "High-throughput SNP detection using nano-scale engineered biomagnetite," *Biosensors and Bioelectronics*, vol. 22, no. 9-10, pp. 2315–2321, 2007.

[72] C. A. Boswell and M. W. Brechbiel, "Development of radioimmunotherapeutic and diagnostic antibodies: an inside-out view," *Nuclear Medicine and Biology*, vol. 34, no. 7, pp. 757–778, 2007.

[73] A. V. S. Anil Kumar, P. G. Kumar, and S. Shankar, "Role of nuclear medicine in evaluation and management of joint diseases," *Indian Journal of Rheumatology*, vol. 4, no. 2, pp. 61–68, 2009.

[74] J. Hirsch, "An anniversary for cancer chemotherapy," *Journal of the American Medical Association*, vol. 296, no. 12, pp. 1518–1520, 2006.

[75] M. J. Camp, J. W. Gilmore, M. M. Gullatte et al., "Antineoplastic agents," in *Clinical Guide to Antineoplastic Therapy: A Chemotherapy Handbook*, M. M. Gullatte, Ed., pp. 81–356, Oncology Nursing Society, Pittsburgh, Pa, USA, 2nd edition, 2007.

[76] B. R. Minev, *Cancer Management in Man: Chemotherapy, Biological Therapy, Hyperthermia and Supporting Measures*, vol. 13, Springer, Dordrecht, The Netherlands, 1st edition, 2011.

Review Article

Biosynthesis of Nanoparticles by Microorganisms and Their Applications

Xiangqian Li,[1,2] Huizhong Xu,[3] Zhe-Sheng Chen,[2] and Guofang Chen[4]

[1] *School of Life Science and Chemical Engineering, Huaiyin Institute of Technology, Huai'an, Jiangsu 223003, China*
[2] *Department of Pharmaceutical Sciences, College of Pharmacy and Allied Health Professions, Queens, NY 11439, USA*
[3] *Department of Physics, St. John's College of Liberal Arts and Science, St. John's University, Queens, NY 11439, USA*
[4] *Department of Chemistry, St. John's College of Liberal Arts and Science, St. John's University, Queens, NY 11439, USA*

Correspondence should be addressed to Xiangqian Li, lixq2002@126.com and Guofang Chen, cheng@stjohns.edu

The development of eco-friendly technologies in material synthesis is of considerable importance to expand their biological applications. Nowadays, a variety of inorganic nanoparticles with well-defined chemical composition, size, and morphology have been synthesized by using different microorganisms, and their applications in many cutting-edge technological areas have been explored. This paper highlights the recent developments of the biosynthesis of inorganic nanoparticles including metallic nanoparticles, oxide nanoparticles, sulfide nanoparticles, and other typical nanoparticles. Different formation mechanisms of these nanoparticles will be discussed as well. The conditions to control the size/shape and stability of particles are summarized. The applications of these biosynthesized nanoparticles in a wide spectrum of potential areas are presented including targeted drug delivery, cancer treatment, gene therapy and DNA analysis, antibacterial agents, biosensors, enhancing reaction rates, separation science, and magnetic resonance imaging (MRI). The current limitations and future prospects for the synthesis of inorganic nanoparticles by microorganisms are discussed.

1. Introduction

Nanoparticles—particles having one or more dimensions of the order of 100 nm or less—have attracted great attention due to their unusual and fascinating properties, and applications advantageous over their bulk counterparts [1, 2]. There are a large number of physical, chemical, biological, and hybrid methods available to synthesize different types of nanoparticles [3–6]. Although physical and chemical methods are more popular in the synthesis of nanoparticles, the use of toxic chemicals greatly limits their biomedical applications, in particular in clinical fields. Therefore, development of reliable, nontoxic, and eco-friendly methods for synthesis of nanoparticles is of utmost importance to expand their biomedical applications. One of the options to achieve this goal is to use microorganisms to synthesize nanoparticles.

Nanoparticles produced by a biogenic enzymatic process are far superior, in several ways, to those particles produced by chemical methods. Despite that the latter methods are able to produce large quantities of nanoparticles with a defined size and shape in a relatively short time, they are complicated, outdated, costly, and inefficient and produce hazardous toxic wastes that are harmful, not only to the environment but also to human health. With an enzymatic process, the use of expensive chemicals is eliminated, and the more acceptable "green" route is not as energy intensive as the chemical method and is also environment friendly. The "biogenic" approach is further supported by the fact that the majority of the bacteria inhabit ambient conditions of varying temperature, pH, and pressure. The particles generated by these processes have higher catalytic reactivity, greater specific surface area, and an improved contact between the enzyme and metal salt in question due to the bacterial carrier matrix [7, 8].

Nanoparticles are biosynthesized when the microorganisms grab target ions from their environment and then turn the metal ions into the element metal through enzymes

generated by the cell activities. It can be classified into intracellular and extracellular synthesis according to the location where nanoparticles are formed [8, 9]. The intracellular method consists of transporting ions into the microbial cell to form nanoparticles in the presence of enzymes. The extracellular synthesis of nanoparticles involves trapping the metal ions on the surface of the cells and reducing ions in the presence of enzymes [10]. The biosynthesized nanoparticles have been used in a variety of applications including drug carriers for targeted delivery, cancer treatment, gene therapy and DNA analysis, antibacterial agents, biosensors, enhancing reaction rates, separation science, and magnetic resonance imaging (MRI).

This paper provides a brief overview of the current research activities that center on the biological synthesis of metallic nanoparticles, oxide nanoparticles, sulfide nanoparticles, and other types of nanoparticles. This is followed by discussions of the particle biosynthesis mechanisms and the conditions to control the size/shape and monodispersity of particles. Next, current applications of biosynthesized nanoparticles in the nanomedicine and biological fields are presented. The paper concludes with discussions on the current limitations and prospects of nanoparticle synthesis by microorganisms.

2. Biological Synthesis of Nanoparticles by Microorganisms

Biological entities and inorganic materials have been in constant touch with each other ever since inception of life on the earth. Due to this regular interaction, life could sustain on this planet with a well-organized deposit of minerals. Recently scientists become more and more interested in the interaction between inorganic molecules and biological species. Studies have found that many microorganisms can produce inorganic nanoparticles through either intracellular or extracellular routes. This section describes the production of various nanoparticles via biological methods following the categories of metallic nanoparticles including gold, silver, alloy and other metal nanoparticles, oxide nanoparticles consisting of magnetic and nonmagnetic oxide nanoparticles, sulfide nanoparticles, and other miscellaneous nanoparticles.

2.1. Metallic Nanoparticles. Some typical metal nanoparticles produced by microorganisms are summarized in Table 1.

2.1.1. Gold Nanoparticles. Gold nanoparticles (AuNPs) have a rich history in chemistry, dating back to ancient Roman times where they were used to stain glasses for decorative purposes. AuNPs were already used for curing various diseases centuries ago. The modern era of AuNPs synthesis began over 150 years ago with the work of Michael Faraday, who was possibly the first to observe that colloidal gold solutions have properties that differ from bulk gold [11]. Biosynthesis of nanoparticles as an emerging bionanotechnology (the intersection of nanotechnology and biotechnology) has received considerable attention due to a growing need to develop environment-friendly technologies

in materials synthesis. Sastry and coworkers have reported the extracellular synthesis of gold nanoparticles by fungus *Fusarium oxysporum* and actinomycete *Thermomonospora* sp., respectively [12, 13]. They reported the intracellular synthesis of gold nanoparticles by fungus *Verticillium* sp. as well [14]. Southam and Beveridge have demonstrated that gold particles of nanoscale dimensions may readily be precipitated within bacterial cells by incubation of the cells with Au^{3+} ions [15]. Monodisperse gold nanoparticles have been synthesized by using alkalotolerant *Rhodococcus* sp. under extreme biological conditions like alkaline and slightly elevated temperature conditions [16]. Lengke et al. claimed the synthesis of gold nanostructures in different shapes (spherical, cubic, and octahedral) by filamentous cyanobacteria from Au(I)-thiosulfate and Au(III)-chloride complexes and analyzed their formation mechanisms [17, 18]. Nair and Pradeep reported the growth of nanocrystals and nanoalloys using *Lactobacillus* [19]. Some other typical gold nanoparticles produced by microorganisms are summarized in Table 1 [20–27].

2.1.2. Silver Nanoparticles. Silver nanoparticles, like their bulk counterpart, show effective antimicrobial activity against Gram-positive and Gram-negative bacteria, including highly multiresistant strains such as methicillin-resistant *Staphylococcus aureus* [28]. The secrets discovered from nature have led to the development of biomimetic approaches to the growth of advanced nanomaterials. Recently, scientists have made efforts to make use of microorganisms as possible eco-friendly nanofactories for the synthesis of silver nanoparticles. Various microbes are known to reduce the Ag^+ ions to form silver nanoparticles, most of which are found to be spherical particles [29–31]. Klaus and coworkers have shown that the bacterium *Pseudomonas stutzeri* AG259, isolated from a silver mine, when placed in a concentrated aqueous solution of silver nitrate, played a major role in the reduction of the Ag^+ ions and the formation of silver nanoparticles (AgNPs) of well-defined size and distinct topography within the periplasmic space of the bacteria [32]. AgNPs were synthesized in the form of a film or produced in solution or accumulated on the surface of its cell when fungi, *Verticillium*, *Fusarium oxysporum*, or *Aspergillus flavus,* were employed [33–36]. Some other silver nanoparticles produced by microorganisms are listed in Table 1 [37–45].

2.1.3. Alloy Nanoparticles. Alloy nanoparticles are of great interest due to their applications in catalysis, electronics, as optical materials, and coatings [46, 47]. Senapati et al. reported the synthesis of bimetallic Au-Ag alloy by *F. oxysporum* and argued that the secreted cofactor NADH plays an important role in determining the composition of Au-Ag alloy nanoparticles [46]. Zheng et al. studied Au-Ag alloy nanoparticles biosynthesized by yeast cells [47]. Fluorescence microscopic and transmission electron microscopic characterizations indicated that the Au-Ag alloy nanoparticles were mainly synthesized via an extracellular approach and generally existed in the form of irregular polyg-

onal nanoparticles. Electrochemical investigations revealed that the vanillin sensor based on Au-Ag alloy nanoparticles modified glassy carbon electrode was able to enhance the electrochemical response of vanillin for at least five times. Sawle et al. demonstrated the synthesis of core-shell Au-Ag alloy nanoparticles from fungal strains *Fusarium semitectum* and showed that the nanoparticle suspensions are quite stable for many weeks [48].

2.1.4. Other Metallic Nanoparticles.

Heavy metals are known to be toxic to microorganism life. In nature, microbial resistance to most toxic heavy metals is due to their chemical detoxification as well as due to energy-dependent ion efflux from the cell by membrane proteins that function either as ATPase or as chemiosmotic cation or proton anti-transporters. Alteration in solubility also plays a role in microbial resistance [3]. Konishi and coworkers reported that platinum nanoparticles were achieved using the metal ion-reducing bacterium *Shewanella algae* [49]. Resting cells of *S. algae* were able to reduce aqueous $PtCl_6^{2-}$ ions into elemental platinum at room temperature and neutral pH within 60 min when lactate was provided as the electron donor. Platinum nanoparticles of about 5 nm were located in the periplasm. Sinha and Khare demonstrated that mercury nanoparticles can be synthesized by *Enterobacter* sp. cells [50]. The culture conditions (pH 8.0 and lower concentration of mercury) promote the synthesis of uniform-sized 2–5 nm, spherical, and monodispersed intracellular mercury nanoparticles. *Pyrobaculum islandicum*, an anaerobic hyper-thermophilic microorganism, was reported to reduce many heavy metals including U(VI), Tc(VII), Cr(VI), Co(III), and Mn(IV) with hydrogen as the electron donor [51]. The palladium nanoparticles could be synthesized by the sulfate-reducing bacterium, *Desulfovibrio desulfuricans*, and metal ion-reducing bacterium, *S. oneidensis* [52–54]. Some other nanoparticles produced by microorganisms are also listed in Table 1 [55, 56].

2.2. Oxide Nanoparticles.

Oxide nanoparticle is an important type of compound nanoparticle synthesized by microbes. In this section, we reviewed the biosynthesized oxide nanoparticles from the two aspects: magnetic oxide nanoparticles and nonmagnetic oxide nanoparticles. Most of the examples of the magnetotactic bacteria used for the production of magnetic oxide nanoparticles and biological systems for the formation of nonmagnetic oxide nanoparticles have been summarized in Table 2.

2.2.1. Magnetic Nanoparticles.

Magnetic nanoparticles are recently developed new materials, due to their unique microconfiguration and properties like super paramagnetic and high coercive force, and their prospect for broad applications in biological separation and biomedicine fields. Magnetic nanoparticles like Fe_3O_4 (magnetite) and Fe_2O_3 (maghemite) are known to be biocompatible. They have been actively investigated for targeted cancer treatment

(magnetic hyperthermia), stem cell sorting and manipulation, guided drug delivery, gene therapy, DNA analysis, and magnetic resonance imaging (MRI) [57].

Magnetotactic bacteria synthesize intracellular magnetic particles comprising iron oxide, iron sulfides, or both [58, 59]. In order to distinguish these particles from artificially synthesized magnetic particles (AMPs), they are referred to as bacterial magnetic particles (BacMPs) [60]. BacMPs, which are aligned in chains within the bacterium, are postulated to function as biological compass needles that enable the bacterium to migrate along oxygen gradients in aquatic environments, under the influence of the Earth's geomagnetic field [61]. BacMPs can easily disperse in aqueous solutions because they are enveloped by organic membranes that mainly consist of phospholipids and proteins. Furthermore, an individual BacMP contains a single magnetic domain or magnetite that yields superior magnetic properties [62].

Since the first report of magnetotactic bacteria in 1975 [61], various morphological types including cocci, spirilla, vibrios, ovoid bacteria, rod-shaped bacteria, and multicellular bacteria possessing unique characteristics have been identified and observed to inhabit various aquatic environments [62, 63]. Magnetotactic cocci, for example, have shown high diversity and distribution and have been frequently identified at the surface of aquatic sediments. The discovery of this bacterial type, including the only cultured magnetotactic coccus strain MC-1, suggested that they are microaerophilic. In the case of the vibrio bacterium, three facultative anaerobic marine vibrios—strains MV-1, MV-2, and MV-4—have been isolated from estuarine salt marshes. These bacteria have been classified as members of α-Proteobacteria, possibly belonging to the Rhodospirillaceae family, and observed to synthesize BacMPs of a truncated hexa-octahedron shape and grow chemoorganoheterotrophically as well as chemolithoautotrophically. The members of the family Magnetospirillaceae, on the other hand, can be found in fresh water sediments. With the use of growth medium and magnetic isolation techniques established, a considerable number of the magnetotactic bacteria isolated to date have been found to be members of this family. The *Magnetospirillum magnetotacticum* strain MS-1 was the first member of the family to be isolated [63], while the *Magnetospirillum gryphiswaldense* strain MSR-1 is also well studied with regard to both its physiological and genetic characteristics. *Magnetospirillum magneticum* AMB-1 isolated by Arakaki et al. was facultative anaerobic magnetotactic spirilla [60].

A number of new magnetotactic bacteria have been found in various aquatic environments since 2000. Some of the newly identified magnetotactic bacteria have been summarized in Table 2. Uncultured magnetotactic bacteria have been observed in numerous habitats [78]. Most known cultured magnetotactic bacteria are mesophilic and tend not to grow much above 30°C. Uncultured magnetotactic bacteria were mostly at 30°C and below. There are only a few reports describing thermophilic magnetotactic bacteria. Lefèvre et al. reported that one of magnetotactic bacteria called HSMV-1 was found in samples from springs whose

TABLE 1: Metal nanoparticles synthesized by microorganisms.

Microorganisms	Products	Culturing temperature (°C)	Size (nm)	Shape	Location	References
Sargassum wightii	Au	Not available	8–12	planar	Extracellular	[20]
Rhodococcus sp.	Au	37	5–15	spherical	Intracellular	[16]
Shewanella oneidensis	Au	30	12 ± 5	spherical	Extracellular	[21]
Plectonemaboryanum	Au	25–100	<10–25	cubic	Intracellular	[17]
Plectonema boryanum UTEX 485	Au	25	10 nm–6 μm	octahedral	Extracellular	[18]
Candida utilis	Au	37	Not available	Not available	Intracellular	[22]
V. luteoalbum	Au	37	Not available	Not available	Intracellular	[22]
Escherichia coli	Au	37	20–30	Triangles, hexagons	Extracellular	[23]
Yarrowia lipolytica	Au	30	15	Triangles	Extracellular	[24]
Pseudomonas aeruginosa	Au	37	15–30	Not available	Extracellular	[25]
Rhodopseudomonas capsulate	Au	30	10–20	Spherical	Extracellular	[26]
Shewanella algae	Au	25	10–20	Not available	Intracellular	[27]
Brevibacterium casei	Au, Ag	37	10–50	Spherical	Intracellular	[37]
Trichoderma viride	Ag	27	5–40	Spherical	Extracellular	[31]
Phaenerochaete chrysosporium	Ag	37	50–200	Pyramidal	Extracellular	[39]
Bacillus licheniformis	Ag	37	50	Not available	Extracellular	[40]
Escherichia coli	Ag	37	50	Not available	Extracellular	[41]
Corynebacterium glutamicum	Ag	30	5–50	Irregular	Extracellular	[42]
Trichoderma viride	Ag	10–40	2–4	Not available	Extracellular	[43]
Ureibacillus thermosphaericus	Au	60–80	50–70	Not available	Extracellular	[44]
Bacillus cereus	Ag	37	4-5	Spherical	Intracellular	[45]
Aspergillus flavus	Ag	25	8.92 ± 1.61	Spherical	Extracellular	[34]
Aspergillus fumigatus	Ag	25	5–25	Spherical	Extracellular	[35]
Verticillium sp.	Ag	25	25 ± 8	Spherical	Extracellular	[36]
Fusarium oxysporum	Ag	25	5–50	Spherical	Extracellular	[36]
Neurospora crassa	Au, Au/Ag	28	32, 20–50	Spherical	Intracellular, extracellular	[38]
Shewanella algae	Pt	25	5	Not available	Intracellular	[49]
Enterobacter sp	Hg	30	2–5	Spherical	Intracellular	[50]
Shewanella sp	Se	30	181 ± 40	Spherical	Extracellular	[55]
Escherichia coli	CdTe	37	2.0–3.2	Spherical	Extracellular	[56]
yeast	Au/Ag	30	9–25	Irregular polygonal	Extracellular	[47]
Fusarium oxysporum	Au-Ag alloy	25	8–14	Spherical	Extracellular	[46]
Pyrobaculum islandicum	U(VI), Tc(VII), Cr(VI), Co(III), Mn(IV)	100	N/A	Spherical	Extracellular	[51]
Desulfovibrio desulfuricans	Pd	25	50	Spherical	Extracellular	[52]

temperatures ranged from 32 to 63°C [71]. TEM images of unstained cell of HSMV-1 showed a single polar flagellum and a single chain of bullet-shaped magnetosomes. The average number of magnetosome crystals per cell is 12 ± 6 with an average size of 113 ± 34 nm by 40 ± 5 nm. The results from the paper clearly showed that some magnetotactic bacteria can be considered at least moderately thermophilic. They extended the upper temperature limit

Table 2: Oxide nanoparticles synthesized by microorganisms.

Microorganisms	Products	Culturing temperature (°C)	Size (nm)	Shape	Location	References
Shewanella oneidensis	Fe_3O_4	28	40–50	Rectangular, rhombic, hexagonal	Extracellular	[64]
QH-2	Fe_3O_4	22–26	$81 \pm 23 \times 58 \pm 20$	Rectangular	Intracellular	[65]
Recombinant AMB-1	Fe_3O_4	28	20	Cubo-octahedral	Intracellular	[66]
Yeast cells	Fe_3O_4	36	Not available	Wormhole-like	Extracellular	[67]
Yeast cells	$FePO_4$	36	Not available	Nanopowders	Extracellular	[68]
WM-1	Fe_3O_4	28	$54 \pm 12.3 \times 43 \pm 10.9$	Cuboidal	Intracellular	[69]
Shewanella oneidensis MR-1	Fe_2O_3	25	30–43	Pseudohexagonal/irregular or rhombohedral	Intracellular	[70]
HSMV-1	Fe_3O_4	63	$113 \pm 34 \times 40 \pm 5$	Bullet-shaped	Intracellular	[71]
Saccharomyces cerevisiae	Sb_2O_3	25–60	2–10	Spherical	Intracellular	[72]
Lactobacillus sp.	$BaTiO_3$	25	20–80	Tetragonal	Extracellular	[73]
Lactobacillus sp.	TiO_2	25	8–35	Spherical	Extracellular	[74]
Fusarium oxysporum	TiO_2	300	6–13	Spherical	Extracellular	[75]
Fusarium oxysporum	$BaTiO_3$	25	4-5	Spherical	Extracellular	[76]
Fusarium oxysporum	ZrO_2	25	3–11	Spherical	Extracellular	[77]

for environments where magnetotactic bacteria exist and likely grow (~63°C) and where magnetosome magnetite is deposited [71]. Zhou et al. reported that magnetic Fe_3O_4 materials with mesoporous structure were synthesized by coprecipitation method using yeast cells as a template [67, 68]. Some other magnetic oxide nanoparticles are listed in Table 2 [64–66, 69, 70].

2.2.2. Nonmagnetic Oxide Nanoparticles. Beside magnetic oxide nanoparticles, other oxide nanoparticles have also been studied including TiO_2, Sb_2O_3, SiO_2, $BaTiO_3$, and ZrO_2 nanoparticles [72–77, 96]. Jha and co-workers found a green low-cost and reproducible *Saccharomyces cerevisiae* mediated biosynthesis of Sb_2O_3 nanoparticles [72]. The synthesis was performed akin to room temperature. Analysis indicated that Sb_2O_3 nanoparticles unit was a spherical aggregate having a size of 2–10 nm [72]. Bansal et al. used *F. oxysporum* (Fungus) to produce SiO_2 and TiO_2 nanoparticles from aqueous anionic complexes SiF_6^{2-} and TiF_6^{2-}, respectively [75]. They also prepared tetragonal $BaTiO_3$ and quasi-spherical ZrO_2 nanoparticles from *F. oxysporum* with a size range of 4-5 nm and 3–11 nm, respectively [76, 77].

2.3. Sulfide Nanoparticles. In addition to oxide nanoparticles, sulfide nanoparticles have also attracted great attention in both fundamental research and technical applications as quantum-dot fluorescent biomarkers and cell labeling agents because of their interesting and novel electronic and optical properties [97]. CdS nanocrystal is one typical type of

sulfide nanoparticle and has been synthesized by microorganisms. Cunningham and Lundie found that *Clostridium thermoaceticum* could precipitate CdS on the cell surface as well as in the medium from $CdCl_2$ in the presence of cysteine hydrochloride in the growth medium where cysteine most probably acts as the source of sulfide [98]. *Klebsiella pneumoniae* exposed to Cd^{2+} ions in the growth medium were found to form 20–200 nm CdS on the cell surface [99]. Intracellular CdS nanocrystals, composed of a wurtzite crystal phase, are formed when *Escherichia coli* is incubated with $CdCl_2$ and Na_2SO_4 [83]. Nanocrystal formation varies dramatically depending on the growth phase of the cells and increases about 20-fold in *E. coli* grown in the stationary phase compared to that grown in the late logarithmic phase. Dameron et al. have used *S. pombe* and *C. glabrata* (yeasts) to produce intracellular CdS nanoparticles with cadmium salt solution [85]. ZnS and PbS nanoparticles were successfully synthesized by biological systems. *Rhodobacter sphaeroides* and *Desulfobacteraceae* have been used to obtain ZnS nanoparticles intracellularly with 8 nm and 2–5 nm in average diameter, respectively [86, 87]. PbS nanoparticles were also synthesized by using *Rhodobacter sphaeroides*, whose diameters were controlled by the culture time [88]. Ahmad et al. have found Eukaryotic organisms such as fungi to be a good candidate for the synthesis of metal sulfide nanoparticles extracellularly [89]. Some stable metal sulfide nanoparticles, such as CdS, ZnS, PbS, and MoS_2, can be produced extracellularly by the fungus *F. oxysporum* when exposed to aqueous solution of metal sulfate. The quantum dots were formed by the reaction of Cd^{2+} ions with sulfide

ions which were produced by the enzymatic reduction of sulfate ions to sulfide ions.

Another kind of sulfide nanoparticle was magnetic Fe_3S_4 or FeS nanoparticle. Bazylinski et al. reported the formation of Fe_3S_4 by uncultured magnetotactic bacteria [59]. They examined a sediment sample that contained approximately 1×10^5 magnetotactic bacteria per cm^3, and approximately 10^5 cells were obtained after purification by the racetrack method. Magnetosomes in the uncultured cells exhibited elongated rectangular shape. The average magnetosome number per cell was approximately 40, and they were mainly located as a large cluster within the cell. Aligned magnetosomes forming a chainlike structure were also observed beside the large cluster. Sulfate-reducing bacteria were capable of producing magnetic FeS nanoparticles [90]. Some other sulfide nanoparticles produced by microorganisms are summarized in Table 3 [79–84].

2.4. Other Nanoparticles. In biological systems, a large variety of organisms form organic/inorganic composites with ordered structures by the use of biopolymers such as protein and microbe cells. In addition to nanoparticles mentioned above, $PbCO_3$, $CdCO_3$, $SrCO_3$, PHB, $Zn_3(PO_4)_2$, and CdSe nanoparticles were reported to be synthesized by microbes (Table 4) [91–95]. $SrCO_3$ crystals were obtained when challenging fungi were incubated with aqueous Sr^{2+} ions [92]. The authors believed that secretion of proteins during growth of the fungus *Fusarium oxysporum* is responsible for modulating the morphology of strontianite crystals and directing their hierarchical assembly into higher-order superstructures. Zinc phosphate nanopowders were synthesized with yeasts as biotemplates [93]. Yan et al. demonstrated the synthesis of $Zn_3(PO_4)_2$ powders with butterfly-like microstructure with a size range of 10–80 nm in width and 80–200 nm in length [94]. Kumar et al. showed that highly luminescent CdSe quantum dots can be synthesized by *F. oxysporum* at room temperature [95].

2.5. Mechanisms of Nanoparticle Formation by Microorganisms. Different microorganisms have different mechanisms of forming nanoparticles. However, nanoparticles are usually formed following this way: metal ions are first trapped on the surface or inside of the microbial cells. The trapped metal ions are then reduced to nanoparticles in the presence of enzymes. In general, microorganisms impact the mineral formation in two distinct ways. They can modify the composition of the solution so that it becomes supersaturated or more supersaturated than it previously was with respect to a specific phase. A second means by which microorganisms can impact mineral formation is through the production of organic polymers, which can impact nucleation by favoring (or inhibiting) the stabilization of the very first mineral seeds [100]. This section reviewed the possible formation mechanisms for some typical nanoparticles: gold and silver nanoparticles, heavy metallic nanoparticles, magnetic nanoparticles, and sulfide nanoparticles.

The exact mechanism for the intracellular formation of gold and silver nanoparticles by *Verticillium* sp. or algal

biomass was not fully understood. But the fact that nanoparticles were formed on the surface of the mycelia and not in the solution supports the following hypothesis: the gold or silver ions were first trapped on the surface of the fungal cells via electrostatic interaction between the ions and negatively charged cell wall from the carboxylate groups in the enzymes. Next, the enzymes reduced the metal ions to form gold or silver nuclei, which subsequently grow through further reduction and accumulation [42]. Kalishwaralal and co-workers speculated that the nitrate reductase enzyme is involved in the synthesis of silver nanoparticles in *B. licheniformis* [101]. This enzyme is induced by nitrate ions and reduces silver ions to metallic silver. The possible mechanism that may involve the reduction of silver ions is the electron shuttle enzymatic metal reduction process. NADH and NADH-dependent nitrate reductase enzymes are important factors in the biosynthesis of metal nanoparticles. *B. licheniformis* is known to secrete the cofactor NADH and NADH-dependent enzymes, especially nitrate reductase, which might be responsible for the bioreduction of Ag^+ to Ag^0 and the subsequent formation of silver nanoparticles [25].

The formation of heavy metallic nanoparticles can be attributed to the metallophilic microorganism's developed genetic and proteomic responses to toxic environments [102]. Heavy metal ions, for example, Hg^{2+}, Cd^{2+}, Ag^+, Co^{2+}, CrO_4^{2+}, Cu^{2+}, Ni^{2+}, Pb^{2+}, and Zn^{2+}, cause toxic effects to the survival of microorganisms. To counter these effects, microorganisms have developed genetic and proteomic responses to strictly regulate metal homeostasis [103]. Microorganisms harbor numerous metal resistance gene clusters enabling cell detoxification via a number of mechanisms such as complexation, efflux, or reductive precipitation. Hence metallophilic bacteria thrive in environments containing high concentrations of mobile heavy metal ions, such as mine waste rock piles, efflux streams of metal processing plants, and naturally mineralized zones [104].

The molecular mechanism of BacMP biomineralization is hypothesized to be a multistep process [60]. The first step involves the invagination of the cytoplasmic membrane, and the vesicle formed serves as the precursor of the BacMP membrane. The mechanism of envelope formation, however, still remains unclear. It is most probable that the mechanisms of vesicle formation for magnetotactic bacteria are similar to most eukaryotes and that a specific GTPase mediates the priming of the invagination. The formed vesicles were then assembled into a linear chain along with cytoskeletal filaments. The second step of BacMP biomineralization involves the accumulation of ferrous ions into the vesicles by the transmembrane iron transporters. External iron is internalized by transport proteins and siderophores. The internal iron is controlled strictly by an oxidation-reduction system. In the final step, tightly bound BacMP proteins trigger magnetite crystal nucleation and/or regulate morphology. Various proteins associated with the BacMP membrane could play functional roles involved in magnetite generation. These include the accumulation of supersaturating iron concentrations, maintenance of reductive conditions and the

TABLE 3: Sulfide nanoparticles synthesized by microorganisms.

Microorganisms	Products	Culturing temperature (°C)	Size (nm)	Shape	Location	References
Multicellular Prokaryotes	Fe_3S_4	25	Not available	Not available	Intracellular	[78]
Uncultured Magnetotactic Bacterium	Probably polyphosphate	Not available	Not available	Rectangular	Extracellular	[79]
Rhodopseudomonas palustris	CdS	30	8	Cubic	Intracellular	[80]
Coriolus versicolor	CdS	25	100–200	Spherical	Extracellular	[81]
Lactobacillus	CdS	25–60	4.9 ± 0.2	Spherical	Intracellular	[82]
Yeast	CdS	25–60	3.6 ± 0.2	Spherical	Intracellular	[82]
E. coli	CdS	25	2–5	Wurtzite crystal	Intracellular	[83]
Schizosaccharomyces pombe	CdS	Not available	1–1.5	Hexagonal lattice	Intracellular	[84]
Schizosaccharomyces pombe and *Candida glabrata*	CdS	Not available	2	Hexagonal lattice	Intracellular	[85]
Rhodobacter sphaeroides	CdS	Not available	8	Hexagonal lattice	Intracellular	[86]
Desulfobacteraceae	CdS	Not available	2–5	Hexagonal lattice	Intracellular	[87]
Rhodobacter sphaeroides	ZnS	Not available	10.5 ± 0.15	Spherical	Extracellular	[88]
Fusarium oxysporum	CdS	Not available	5–20	Spherical	Extracellular	[89]
Sulfate-reducing bacteria	FeS	Not available	2	Spherical	Extracellular	[90]

TABLE 4: Other miscellaneous nanoparticles synthesized by microorganisms.

Microorganisms	Products	Culturing temperature (°C)	Size (nm)	Shape	Location	References
Fusarium oxysporum	$PbCO_3$, $CdCO_3$	27	120–200	Spherical	Extracellular	[91]
Fusarium oxysporum	$SrCO_3$	27	10–50	Needlelike	Extracellular	[92]
Brevibacterium casei	PHB	37	100–125	Not available	Intracellular	[93]
Yeasts	$Zn_3(PO_4)_2$	25	$10–80 \times 80–200$	Rectangular	Extracellular	[94]
Fusarium oxysporum	CdSe	10	9–15	Spherical	Extracellular	[95]

oxidation of iron to induce mineralization, or the partial reduction and dehydration of ferrihydrite to magnetite [60].

Another possible mechanism for the synthesis of magnetites using *Shewanella oneidensis*, which consists of both passive and active mechanisms, was recently suggested by Perez-Gonzalez and coworkers [64]. First, active production of Fe^{2+} occurs when bacteria utilize ferrihydrite as a terminal electron acceptor, and the pH value surrounding the cells rises probably due to the bacterial metabolism of amino acids. Then, through a passive mechanism, the localized concentration of Fe^{2+} and Fe^{3+} at the net negatively charged cell wall, cell structures, and/or cell debris induces a local rise of supersaturation of the system with respect to magnetite, causing the magnetite phase to precipitate.

Sanghi and Verma proposed that the formation of CdS NPs is through disulfide (cystine) bridges and may be attributed to cleavage of S–H bond and formation of a new bond, that is, –S–Cd bond of Cd-thiolate (Cd–S–CH_2COOH) complex on the nanoparticle surface [81]. The –COOH groups from the cadmium-thiolate complexes do not react with the –NH_2 groups of protein but interact with hydrogen bond. Therefore, the capped CdS nanoparticles are bonded to –NH_2 groups by hydrogen bond [105]. One of

the oxygen atoms of the carboxylic group (–COOH) formed the coordinate bond between the oxygen atom and Cd^{2+} ions [106], thus competing with the thiol group to assemble onto the surfaces of the CdS nanoparticles.

2.6. Control of Size and Morphology of Nanoparticles. It is well known that the electronic and optical properties of nanoparticles are heavily dependent on their size and shape. Thus, there has been tremendous interest in controlling the size, shape, and surrounding media of nanoparticles. Particular emphasis has recently been placed on the control of shape, because in many cases it allows properties to be fine-tuned with a great versatility that gives the particles a unique nature. Despite that the physical and chemical methods are able to produce large quantities of nanoparticles with a defined size and shape in a relatively short time, these methods are complicated and have certain drawbacks such as producing hazardous toxic wastes that are harmful, not only to the environment but also to human health. Microbes, which are regarded as potent eco-friendly green nanofactories, have the potential to control the size and shape of biological nanoparticles.

Gericke and Pinches found that the intracellular synthesis of gold nanoparticles of various morphologies and sizes could be obtained in two fungal cultures [22], *V. luteoalbum* and another named Isolate 6–3. The rate of particle formation and the particle size could, to an extent, be manipulated by controlling parameters such as pH, temperature, gold concentration, and exposure time to $AuCl_4^-$. Various particle morphologies including spherical, triangular, hexagonal, and other shapes were present, as revealed by scanning electron microscopy. Large variations in particle size were observed and particle size varied from a few nanometers to approximately 100 nm in diameter. Their results also suggested that the spherical particles tended to be smaller than the hexagonal- and triangular-shaped particles. The bacterial cultures screened during the study tended to synthesize small, relatively uniform-sized gold nanoparticles intracellularly. The particles were observed mainly in the cytoplasm of the cells, and the majority of the particles were spherical in shape.

Gurunathan et al. studied optimum reaction conditions for maximum synthesis of AgNPs and reduction in particle size [41]. To find the optimum conditions, different medium and medium of varying concentrations of $AgNO_3$, reaction temperatures and pH values were used in the synthesis of AgNPs. The medium contributing to the maximum synthesis was found to be a nitrate medium at a concentration of 5 mM $AgNO_3$, a reaction temperature of 60°C, and a pH value of 10.0. Under these optimum conditions, only 30 min was required to obtain over 95% conversion using the culture supernatant of *E. coli*. This is comparable to or faster than the synthesis rate of similar particles obtained using chemical methods. The average particle size could be tuned from 10–90 nm by varying the $AgNO_3$ concentration, reaction temperature, and pH.

On the synthesis of Pt nanoparticles, Riddin and co-workers found that in the absence of the spatial restrictions of the cell wall, the cell-soluble extract (CSE) was able to reduce Pt(IV) to form nanoparticles, which are stabilized in solution by bound proteins and exhibit both geometric and irregular morphologies [107]. It appeared that high initial Pt(IV) concentrations resulted in particles that were more regular and geometric in nature. At high initial Pt(IV) concentrations, more hydrochloride was generated (pH ≤ 4) within the system, resulting in the precipitation of the nanoparticle-protein bioconjugates and the subsequent decrease of the number of soluble particles present in the colloid. Furthermore, they demonstrated that protein-stabilized biogenic Pt(0) nanoparticles with a great variation in size and shape can be synthesized in the absence of the cellular restrictions.

Magnetotactic bacteria produce iron oxide magnetic particles with uniform sizes and morphologies. Magnetites formed by magnetotactic bacteria take various shapes such as cuboids, bullet-shaped, rhombic, and rectangular. Various crystal morphologies and compositions have been observed that are species or strain dependent, indicating the presence of a high degree of biological control [66].

Arakaki et al. found that Mms6 is a dominant protein that tightly associates with the surface of bacterial magnetites in *Magnetospirillum magneticum* AMB-1 [108]. The protein was showed to mediate the formation of uniform magnetite crystals of cubo-octahedral morphology. Magnetite formation was investigated using synthetic peptides mimicking the Mms6 protein. Particles synthesized in the presence of short peptides harboring the C-terminal acidic region of Mms6 exhibited a spherical morphology with circularities of 0.70–0.90, similar to those of bacterial magnetites and particles formed in the presence of the Mms6 protein. In contrast, a rectangular morphology with circularities of 0.60–0.85 was obtained when other peptides were used in synthesis [108].

The same group introduced another method for the highly regulated synthesis of magnetite crystals at reduced temperatures in aqueous solution using recombinant magnetotactic bacterial protein Mms6. Crystallographic analysis of the magnetite crystals indicates that Mms6 mediates the formation of magnetite particles with a specific crystal shape and narrow size distribution similar to those observed in magnetic bacteria. Mms6 aggregates in aqueous solution, has a strong affinity for iron ions, and contains a sequence motif similar to several biomineralization scaffold proteins in other organisms. The crystals exhibit similar sizes (20 nm) and morphologies (cubo-octahedral), as opposed to crystals formed in the absence of Mms6. This suggests that Mms6 has a strong effect in regulating the size and shape of nanoparticles during the synthesis process [66].

The control of particle size has also been demonstrated for other nanoparticles. For example, Yan et al. found that the inducing of yeasts is an effective way to obtain zinc phosphate powders with narrow size distribution in diameter [94]. Their method utilized the function of the yeasts in the reaction system to inhibit the excess agglomeration of $Zn_3(PO_4)_2$ crystals to effectively control the particle size and size distribution.

3. Applications of Nanoparticles

Nanomedicine is a burgeoning field of research with tremendous prospects for the improvement of the diagnosis and treatment of human diseases [109]. Dispersed nanoparticles are usually employed in nanobiomedicine as fluorescent biological labels [110, 111], drug and gene delivery agents [112, 113], and in applications such as biodetection of pathogens [114], tissue engineering [115, 116], tumor destruction via heating (hyperthermia) [117], MRI contrast enhancement [118], and phagokinetic studies [119].

A plethora of reviews and research papers studying the applications of nanoparticle in biomedicine have been published [120–129]. While the field of biosynthesized nanoparticles is relatively new, researchers have already started exploring their use in applications such as targeted drug delivery, cancer treatment, gene therapy and DNA analysis, antibacterial agents, biosensors, enhancing reaction rates, separation science, and MRI. Here, we provide some examples to illustrate these applications.

3.1. Drug Delivery. Delivering the drugs precisely and safely to their target sites at the right time to have a controlled release and achieve the maximum therapeutic effect is a key issue in the design and development of novel drug delivery systems. Targeted nanocarriers must navigate through blood-tissue barriers to reach target cells. They must enter target cells to contact cytoplasmic targets via specific endocytotic and transcytotic transport mechanisms across cellular barriers [109].

Because of their small size, nanoparticle drug carriers can bypass the blood-brain barrier and the tight epithelial junctions of the skin that normally impede delivery of drugs to the desired target site. Secondly, as a result of their high surface area to volume ratio, nanocarriers show improved pharmacokinetics and biodistribution of therapeutic agents and thus minimize toxicity by their preferential accumulation at the target site [123]. They improve the solubility of hydrophobic compounds and render them suitable for parenteral administration. Furthermore, they increase the stability of a variety of therapeutic agents like peptides and oligonucleotides [120].

Magnetic nanoparticles like Fe_3O_4 (magnetite) and Fe_2O_3 (maghemite) are known to be biocompatible. They have been actively investigated for targeted cancer treatment (magnetic hyperthermia), stem cell sorting and manipulation, guided drug delivery, gene therapy and DNA analysis, and MRI [57]. Xiang L. et al. evaluated the toxicity of magnetosomes from *Magnetospirillum gryphiswaldense* to mouse fibroblasts *in vitro* and found that the purified and sterilized magnetosomes were not toxic to mouse fibroblasts *in vitro* [129]. Meng et al. recently studied the influence of native bacterial magnetic particles on mouse immune response [130]. In their experiment, ovalbumin was used as an antigen, mixed with complete Freund's adjuvant, BacMps, and phosphate buffer solution, to immunize BALB/C mouse. After 14 days, the titers of the antiovalbumin (IgG) and subtype (IgG1, IgG2), the proliferation ability of T lymphocyte, and the expression of IL-2, IL4, IL-10, and IFN-gamma

were detected. The results showed that native BMPs do not have significant influence on mouse immune response and magnetosomes have the potential to be used as novel drug or gene carriers for tumor therapy. In another study, Sun et al. loaded doxorubicin (DOX) onto bacterial magnetosomes (BMs) through covalent attachment and evaluated the ability of these particles to inhibit tumor growth [131]. In this study performed on H22 tumor-bearing mice, these DOX-loaded BMs showed a comparable tumor suppression rate to DOX alone (86.8% versus 78.6%), but with much lower cardiac toxicity. Although, in this preliminary study, the particles were administrated subcutaneously into the solid tumor, the potential exists to magnetically manipulate these drug-loaded BMs, making them accumulate and execute therapeutic effects only at the disease sites.

Regarding the biocompatibility and pharmacokinetics of BMs, Sun et al. studied the distribution of BMs in dejecta, urine, serum, and main organs when BMs were injected into the sublingual vena of Sprague-Dawley (SD) rats [132]. They obtained BMs of high purity and narrow size-distribution using an effective method for purification and sterilization of BMs. Their results showed that BMs were only found in livers and there was no obvious evidence to indicate the existence of BMs in the dejecta and urine within 72 h following the intravenous administration [132].

Magnetotactic bacteria (MTB) MC-1 with magnetosomes was also used as drug delivery agent. Felfoul et al. applied magnetotaxis to change the direction of each MTB embedded with combination of nanoparticles magnetite and the flagella to steer in small-diameter blood vessels [133]. However, in order to guide these MTBs towards a target, it is essential to be able to image these living bacteria *in vivo* using an existing medical imaging modality. It was shown that the magnetosomes embedded in each MTB can be used to track the displacement of these bacteria using an MRI system, since these magnetosomes disturb the local magnetic field affecting T_1 and T_2 relaxation times during MRI. Magnetic resonance, T_1-weighted and T_2-weighted images, as well as T_2 relaxivity of MTB are studied in order to validate the possibility of monitoring MTB drug delivery operations using a clinical MR scanner. It was found that MTB affect the T_2 relaxation rate much more than the T_1 relaxation rate and it can be thought as a negative contrast agent. As the signal decay in the T_2-weighted images was found to change proportionally to the bacterial concentration, a detection limit of 2.2×10^7 cells/mL for bacterial concentration was achieved using a T_2-weighted image.

Xie et al. reported their efforts to utilize MTB-NPs for gene delivery, in which they managed to use PEI-associated MTB-NPs to deliver β-galactosidase plasmids, at both *in vitro* and *in vivo* levels [134]. They concluded in their work that such MTB-PEI-NP systems are more efficient and less toxic compared with PEI alone.

Gold and its compounds have long been used as medicinal agents throughout the history of civilization with its earliest record dating back to 5000 years ago in Egypt [135–139]. In addition to a high surface-to-volume ratio, AuNPs have unique size- and shape-dependent optical and electronic properties. The surfaces of AuNPs can also be

readily modified with ligands containing functional groups such as thiols, phosphines, and amines, which exhibit affinity for gold surfaces [139]. Gold nanoparticles have emerged as a promising scaffold for drug and gene delivery that provide a useful complement to more traditional delivery vehicles. The combination of low inherent toxicity, high surface area, stability, and function tunability provides them with unique attributes that should enable new delivery strategies. Biomedical applications of chemically synthesized AuNPs were studied before [138, 139], but to our best knowledge there are no reports on the use of biosynthesized AuNPs for drug delivery.

Silver nanoparticles have been widely used as a novel therapeutic agent extending its use as antibacterial, antifungal, antiviral and antiinflammatory agent. Kalishwaralal et al. found silver nanoparticles, produced by *Bacillus licheniformis*, have the potential of anti-angiogenic [140]. Bovine retinal endothelial cells (BRECs) were treated with different concentrations of silver nanoparticles for 24 h in the presence and absence of vascular endothelial growth factor (VEGF), where 500 nM (IC_{50}) silver nanoparticle solution was able to block the proliferation and migration of BRECs. The cells showed a clear enhancement in caspase-3 activity and formation of DNA ladders, evidence of induction of apoptosis. The results showed that silver nanoparticles inhibit cell survival via PI3K/Akt-dependent pathway in BRECs [140].

It is anticipated that nanoparticle-mediated targeted delivery of drugs might significantly reduce the dosage of anticancer drugs with better specificity, enhanced efficacy, and low toxicities. We believe that in the next few years we will see growing number of applications of nanotechnology-based therapeutics and diagnostics in clinics. In addition, individualized medicine is another important area where nanotechnology can play a pivotal role. Due to cancer heterogeneity and development of drug resistance, any particular targeted therapy may not be effective for every population of patients. Moreover, magnetic nanoparticles can be used for hyperthermia cancer treatment. Hyperthermia cancer treatment involves administering magnetic nanoparticles into the body, specifically at cancer tissue sites. Local heating at specific sites is enabled by means of an external magnetic field [141].

3.2. Antibacterial Agent. With the prevalence and increase of microorganisms resistant to multiple antibiotics, silver-based antiseptics have been emphasized in recent years. Silver nanoparticles were biosynthesized using fungus *Trichoderma viride* [31]. It was observed that the aqueous silver (Ag^+) ions, when exposed to a filtrate of *T. viride*, were reduced in solution, thereby leading to the formation of extremely stable AgNPs with the size of 5–40 nm. The nanoparticles were also evaluated for their increased antimicrobial activities with various antibiotics against Gram-positive and Gram-negative bacteria. The antibacterial activities of ampicillin, kanamycin, erythromycin, and chloramphenicol were increased in the presence of AgNPs against test strains. The highest enhancing effect was observed for ampicillin against test strains. The result showed that the combination

of antibiotics with AgNPs has better antimicrobial effects and provided helpful insight into the development of new antimicrobial agents. Durán and coworkers showed that extracellularly produced silver nanoparticles using *Fusarium oxysporum* can be incorporated into textile fabrics to prevent or minimize infection with pathogenic bacteria such as *Staphylococcus aureus* [142].

3.3. Biosensor. Nanoparticles possess interesting electronic and optical properties and can be used in biosensor applications. Spherical selenium nanoparticles formed by the *Bacillus subtilis* with diameters ranging from 50 to 400 nm were reported [143]. These spherical monoclinic Se nanoparticles can be transformed into highly anisotropic, one-dimensional (1D) trigonal structure after one day at room temperature since their synthesis. Furthermore, Se nanomaterial crystals with high surface-to-volume ratio, good adhesive ability, and biocompatibility were employed as enhancing and settled materials for building HRP (horseradish peroxidase) biosensor. These sensors exhibited good electrocatalytic activity towards the reduction of H_2O_2 due to the good adhesive ability and biocompatibility of Se nanomaterials. These H_2O_2 biosensors had high sensitivity and affinity for H_2O_2 with a detection limit of 8×10^{-8} M. Their results also showed that different crystals of Se nanomaterials had no significant difference in electrochemical application. Thus, the Se nanomaterials-modified electrode will probably be promising for a wide range of applications related to the detection of H_2O_2 in food, pharmaceutical, clinical, industrial and environmental analyses. Zheng et al. reported that Au-Ag alloy nanoparticles biosynthesized by yeast cells were applied to fabricate a sensitive electrochemical vanillin sensor [47]. Electrochemical investigations revealed that the vanillin sensor based on Au-Ag alloy nanoparticles-modified glassy carbon electrode was able to enhance the electrochemical response of vanillin for at least five times. Under optimal working conditions, the oxidation peak current of vanillin at the sensor linearly increased with its concentration in the range of 0.2–50 μM with a low detection limit of 40 nM. This vanillin sensor was successfully applied to the determination of vanillin from vanilla bean and vanilla tea sample, suggesting that it may have practical applications in vanillin monitoring systems. In another study, AuNP-based glucose oxidase (GO_x) biosensors were developed based on observations that AuNPs can increase the enzyme activity of GO_x [144]. The linear response range of the glucose biosensor is 20 μM to 0.80 mM glucose with a detection limit of 17 μM ($S/N = 3$). This type of biosensor was successfully applied to determine the glucose content in commercial glucose injections.

3.4. Reaction Rate Enhancement Agent. Nanoparticles have been widely used to improve various reactions as reductants and/or catalysts due to their large surface areas and specific characteristics [145]. Magnetic nanoparticles have been used to improve the microbiological reaction rates. In fact, magnetic nanoparticles were utilized not only for their catalytic function but also for their good ability to disperse. Shan et al. made use of the coated microbial cells of

Pseudomonas delafieldii with magnetic Fe_3O_4 nanoparticles to fulfill desulfurization of dibenzothiophene [146]. The high surface energies of nanoparticles resulted in their strong adsorption on the cells. The application of an external magnetic field ensured that the cells were well diffused in the solution even without mixing and enhanced the possibility to collect cells for reuse. The results showed that the desulfurization efficiencies of *P. delafieldii* were not reduced and the cells could be reused several times.

3.5. Magnetic Separation and Detection. Magnetic particles conjugated with biological molecules, which are attractive materials for building assay systems, have been proposed for use as a biological label. Competitive chemiluminescence enzyme immunoassays using antibodies immobilized onto BacMPs were developed for the rapid and sensitive detection of small molecules, such as environmental pollutants, hormone, and toxic detergents [147, 148]. Xenoestrogens, such as alkylphenol ethoxylates, bisphenol A (BPA), and linear alkylbenzene sulonates (LAS), were detectable using monoclonal antibodies immobilized onto BacMPs, based on the competitive reaction of xenoestrogens. The entire procedure was completed in 15 min, while typical plate methods could take more than 2.5 hours. This method provided a wider detection range and lower detection limit than ELISA, in which the same antibodies were used for comparison.

Surface modification of magnetic nanoparticles is an exciting area of research with various potential applications. The BacMP surface can be modified with aminosilane compounds in order to develop magnetic nanoparticle systems for DNA extraction. The use of magnetic particles as a solid-phase adsorbent is well suited for DNA extraction techniques because they can be easily manipulated through simple application of a magnet.

4. Future Prospects

There have been tremendous developments in the field of microorganism-produced nanoparticles and their applications over the last decade. However, much work is needed to improve the synthesis efficiency and the control of particle size and morphology. It is known that the synthesis of nanoparticles using microorganisms is a quite slow process (several hours and even a few days) compared to physical and chemical approaches. Reduction of synthesis time will make this biosynthesis route much more attractive. Particle size and monodispersity are two important issues in the evaluation of nanoparticle synthesis. Therefore, effective control of the particle size and monodispersity must be extensively investigated. Several studies have shown that the nanoparticles formed by microorganisms may be decomposed after a certain period of time. Thus, the stability of nanoparticles produced by biological methods deserves further study and should be enhanced [149–151]. Since the control of particle shape in chemical and physical synthesis of nanoparticles is still an ongoing area of research, biological processes with the ability to strictly control particle morphology would therefore offer considerable advantage. By varying

parameters like microorganism type, growth stage (phase) of microbial cells, growth medium, synthesis conditions, pH, substrate concentrations, source compound of target nanoparticle, temperature, reaction time, and addition of nontarget ions, it might be possible to obtain sufficient control of particle size and monodispersity. Biosynthesis methods are advantageous also because nanoparticles are sometimes coated with a lipid layer that confers physiological solubility and stability, which is critical for biomedical applications and is the bottleneck of other synthetic methods. Research is currently carried out manipulating cells at the genomic and proteomic levels. With a better understanding of the synthesis mechanism on a cellular and molecular level, including isolation and identification of the compounds responsible for the reduction of nanoparticles, it is expected that short reaction time and high synthesis efficiency can be obtained.

5. Summary

Nanomedicine is a burgeoning field of research with tremendous prospects for the improvement of the diagnosis and treatment of human diseases. The biosynthesis of nanoparticles by microbes is thought to be clean, nontoxic, and environmentally acceptable "green chemistry" procedures. The use of microorganisms including bacteria, yeast, fungi, and actinomycetes can be classified into intracellular and extracellular synthesis according to the location where nanoparticles are formed. The rate of intracellular particle formation and therefore the size of the nanoparticles could, to an extent, be manipulated by controlling parameters such as pH, temperature, substrate concentration, and exposure time to substrate. Research is currently carried out manipulating microorganisms at the genomic and proteomic levels. With the recent progress and the ongoing efforts in improving particle synthesis efficiency and exploring their biomedical applications, it is hopeful that the implementation of these approaches on a large scale and their commercial applications in medicine and health care will take place in the coming years.

Abbreviations

TEM:	Transmission Electron Microscope
BacMPs:	Bacterial magnetic particles
AgNPs:	Silver nanoparticles
AuNPs:	Gold nanoparticles
CSE:	Cell-soluble extract
GTPase:	Guanosine triphosphatase
CdS NPs:	CdS nanoparticles
mAbs:	Antibodies
MRI:	Magnetic resonance imaging
PHB:	Polyhydroxybutyrate
BRECs:	Bovine retinal endothelial cells
HRP:	Horseradish peroxidise
BMs:	Bacterial magnetosomes
MTB:	Magnetotactic bacteria.

Acknowledgments

References

[1] M. C. Daniel and D. Astruc, "Gold nanoparticles: assembly, supramolecular chemistry, quantum-size-related properties, and applications toward biology, catalysis, and nanotechnology," *Chemical Reviews*, vol. 104, no. 1, pp. 293–346, 2004.

[2] H. Kato, "In vitro assays: tracking nanoparticles inside cells," *Nature Nanotechnology*, vol. 6, no. 3, pp. 139–140, 2011.

[3] J. Liu, S. Z. Qiao, Q. H. Hu, and G. Q. Lu, "Magnetic nanocomposites with mesoporous structures: synthesis and applications," *Small*, vol. 7, no. 4, pp. 425–443, 2011.

[4] N. A. Luechinger, R. N. Grass, E. K. Athanassiou, and W. J. Stark, "Bottom-up fabrication of metal/metal nanocomposites from nanoparticles of immiscible metals," *Chemistry of Materials*, vol. 22, no. 1, pp. 155–160, 2010.

[5] D. K. Tiwari, J. Behari, and P. Sen, "Time and dose-dependent antimicrobial potential of Ag nanoparticles synthesized by top-down approach," *Current Science*, vol. 95, no. 5, pp. 647–655, 2008.

[6] P. Mohanpuria, N. K. Rana, and S. K. Yadav, "Biosynthesis of nanoparticles: technological concepts and future applications," *Journal of Nanoparticle Research*, vol. 10, no. 3, pp. 507–517, 2008.

[7] R. Bhattacharya and P. Mukherjee, "Biological properties of "naked" metal nanoparticles," *Advanced Drug Delivery Reviews*, vol. 60, no. 11, pp. 1289–1306, 2008.

[8] K. Simkiss and K. M. Wilbur, *Biomineralization*, Academic, New York, NY, USA, 1989.

[9] S. Mann, *Biomineralization: Principles and Concepts in Bioinorganic Materials Chemistry*, Oxford University Press, Oxford, UK, 2001.

[10] X. Zhang, S. Yan, R. D. Tyagi, and R. Y. Surampalli, "Synthesis of nanoparticles by microorganisms and their application in enhancing microbiological reaction rates," *Chemosphere*, vol. 82, no. 4, pp. 489–494, 2011.

[11] M. A. Hayat, *Colloidal Gold: Principles, Methods, and Applications*, Academic Press, San Diego, Calif, USA, 1989.

[12] P. Mukherjee, S. Senapati, D. Mandal et al., "Extracellular synthesis of gold nanoparticles by the fungus *Fusarium oxysporum*," *ChemBioChem*, vol. 3, no. 5, pp. 461–463, 2002.

[13] A. Ahmad, S. Senapati, M. I. Khan, R. Kumar, and M. Sastry, "Extracellular biosynthesis of monodisperse gold nanoparticles by a novel extremophilic actinomycete, thermomonospora sp," *Langmuir*, vol. 19, no. 8, pp. 3550–3553, 2003.

[14] P. Mukherjee, A. Ahmad, D. Mandal et al., "Bioreduction of AuCl4− ions by the fungus, Verticillium sp. and surface trapping of the gold nanoparticles formed," *Angewandte Chemie—International Edition*, vol. 40, no. 19, pp. 3585–3588, 2001.

[15] G. Southam and T. J. Beveridge, "The occurrence of sulfur and phosphorus within bacterially derived crystalline and pseudocrystalline octahedral gold formed *in vitro*," *Geochimica et Cosmochimica Acta*, vol. 60, no. 22, pp. 4369–4376, 1996.

[16] A. Ahmad, S. Senapati, M. I. Khan et al., "Intracellular synthesis of gold nanoparticles by a novel alkalotolerant actinomycete, Rhodococcus species," *Nanotechnology*, vol. 14, no. 7, pp. 824–828, 2003.

[17] M. F. Lengke, M. E. Fleet, and G. Southam, "Morphology of gold nanoparticles synthesized by *filamentous cyanobacteria* from gold(I)-Thiosulfate and gold(III)-chloride complexes," *Langmuir*, vol. 22, no. 6, pp. 2780–2787, 2006.

[18] M. F. Lengke, B. Ravel, M. E. Fleet, G. Wanger, R. A. Gordon, and G. Southam, "Mechanisms of gold bioaccumulation by *filamentous cyanobacteria* from gold(III)-chloride complex," *Environmental Science & Technology*, vol. 40, no. 20, pp. 6304–6309, 2006.

[19] B. Nair and T. Pradeep, "Coalescence of nanoclusters and formation of submicron crystallites assisted by *lactobacillus strains*," *Crystal Growth & Design*, vol. 2, no. 4, pp. 293–298, 2002.

[20] G. Singaravelu, J. S. Arockiamary, V. G. Kumar, and K. Govindaraju, "A novel extracellular synthesis of monodisperse gold nanoparticles using marine alga, *Sargassum wightii* Greville," *Colloids and Surfaces B*, vol. 57, no. 1, pp. 97–101, 2007.

[21] A. K. Suresh, D. A. Pelletier, W. Wang et al., "Biofabrication of discrete spherical gold nanoparticles using the metal-reducing bacterium *Shewanella oneidensis*," *Acta Biomaterialia*, vol. 7, no. 5, pp. 2148–2152, 2011.

[22] M. Gericke and A. Pinches, "Biological synthesis of metal nanoparticles," *Hydrometallurgy*, vol. 83, no. 1–4, pp. 132–140, 2006.

[23] L. Du, H. Jiang, X. Liu, and E. Wang, "Biosynthesis of gold nanoparticles assisted by *Escherichia coli DH5α* and its application on direct electrochemistry of hemoglobin," *Electrochemistry Communications*, vol. 9, no. 5, pp. 1165–1170, 2007.

[24] M. Agnihotri, S. Joshi, A. R. Kumar, S. Zinjarde, and S. Kulkarni, "Biosynthesis of gold nanoparticles by the tropical marine yeast *Yarrowia lipolytica* NCIM 3589," *Materials Letters*, vol. 63, no. 15, pp. 1231–1234, 2009.

[25] M. I. Husseiny, M. A. El-Aziz, Y. Badr, and M. A. Mahmoud, "Biosynthesis of gold nanoparticles using *Pseudomonas aeruginosa*," *Spectrochimica Acta Part A*, vol. 67, no. 3-4, pp. 1003–1006, 2007.

[26] S. He, Z. Guo, Y. Zhang, S. Zhang, J. Wang, and N. Gu, "Biosynthesis of gold nanoparticles using the bacteria *Rhodopseudomonas capsulata*," *Materials Letters*, vol. 61, no. 18, pp. 3984–3987, 2007.

[27] Y. Konishi, T. Tsukiyama, T. Tachimi, N. Saitoh, T. Nomura, and S. Nagamine, "Microbial deposition of gold nanoparticles by the metal-reducing bacterium *Shewanella algae*," *Electrochimica Acta*, vol. 53, no. 1, pp. 186–192, 2007.

[28] A. Panáček, L. Kvítek, R. Prucek et al., "Silver colloid nanoparticles: synthesis, characterization, and their antibacterial activity," *The Journal of Physical Chemistry B*, vol. 110, no. 33, pp. 16248–16253, 2006.

[29] P. Mukherjee, A. Ahmad, D. Mandal et al., "Fungus-mediated synthesis of silver nanoparticles and their immobilization in the mycelial matrix: a novel biological approach to nanoparticle synthesis," *Nano Letters*, vol. 1, no. 10, pp. 515–519, 2001.

[30] A. Ahmad, P. Mukherjee, S. Senapati et al., "Extracellular biosynthesis of silver nanoparticles using the fungus *Fusarium oxysporum*," *Colloids and Surfaces B*, vol. 28, no. 4, pp. 313–318, 2003.

[31] A. M. Fayaz, K. Balaji, M. Girilal, R. Yadav, P. T. Kalaichelvan, and R. Venketesan, "Biogenic synthesis of silver nanoparticles and their synergistic effect with antibiotics: a study against gram-positive and gram-negative bacteria," *Nanomedicine:*

Nanotechnology, Biology, and Medicine, vol. 6, no. 1, pp. e103–e109, 2010.

[32] T. Klaus, R. Joerger, E. Olsson, and C. -G. Granqvist, "Silver-based crystalline nanoparticles, microbially fabricated," *Proceedings of the National Academy of Sciences of the United States of America*, vol. 96, no. 24, pp. 13611–13614, 1999.

[33] N. Jain, A. Bhargava, S. Majumdar, J. C. Tarafdar, and J. Panwar, "Extracellular biosynthesis and characterization of silver nanoparticles using *Aspergillus flavus* NJP08: a mechanism perspective," *Nanoscale*, vol. 3, no. 2, pp. 635–641, 2011.

[34] N. Vigneshwaran, N. M. Ashtaputre, P. V. Varadarajan, R. P. Nachane, K. M. Paralikar, and R. H. Balasubramanya, "Biological synthesis of silver nanoparticles using the fungus *Aspergillus flavus*," *Materials Letters*, vol. 61, no. 6, pp. 1413–1418, 2007.

[35] K. C. Bhainsa and S. F. D'Souza, "Extracellular biosynthesis of silver nanoparticles using the fungus *Aspergillus fumigatus*," *Colloids and Surfaces B*, vol. 47, no. 2, pp. 160–164, 2006.

[36] S. Senapati, D. Mandal, A. Ahmad et al., "Fungus mediated synthesis of silver nanoparticles: a novel biological approach," *Indian Journal of Physics A*, vol. 78A, no. 1, pp. 101–105, 2004.

[37] K. Kalishwaralal, V. Deepak, S. Ram Kumar Pandian et al., "Biosynthesis of silver and gold nanoparticles using *Brevibacterium casei*," *Colloids and Surfaces B*, vol. 77, no. 2, pp. 257–262, 2010.

[38] E. Castro-Longoria, A. R. Vilchis-Nestor, and M. Avalos-Borja, "Biosynthesis of silver, gold and bimetallic nanoparticles using the filamentous fungus *Neurospora crassa*," *Colloids and Surfaces B*, vol. 83, no. 1, pp. 42–48, 2011.

[39] N. Vigneshwaran, A. A. Kathe, P. V. Varadarajan, R. P. Nachane, and R. H. Balasubramanya, "Biomimetics of silver nanoparticles by white rot fungus, *Phaenerochaete chrysosporium*," *Colloids and Surfaces B*, vol. 53, no. 1, pp. 55–59, 2006.

[40] K. Kalimuthu, R. Suresh Babu, D. Venkataraman, M. Bilal, and S. Gurunathan, "Biosynthesis of silver nanocrystals by *Bacillus licheniformis*," *Colloids and Surfaces B*, vol. 65, no. 1, pp. 150–153, 2008.

[41] S. Gurunathan, K. Kalishwaralal, R. Vaidyanathan et al., "Biosynthesis, purification and characterization of silver nanoparticles using *Escherichia coli*," *Colloids and Surfaces B*, vol. 74, no. 1, pp. 328–335, 2009.

[42] K. Sneha, M. Sathishkumar, J. Mao, I. S. Kwak, and Y. S. Yun, "*Corynebacterium glutamicum*-mediated crystallization of silver ions through sorption and reduction processes," *Chemical Engineering Journal*, vol. 162, no. 3, pp. 989–996, 2010.

[43] A. Mohammed Fayaz, K. Balaji, P. T. Kalaichelvan, and R. Venkatesan, "Fungal based synthesis of silver nanoparticles—an effect of temperature on the size of particles," *Colloids and Surfaces B*, vol. 74, no. 1, pp. 123–126, 2009.

[44] M. M. Juibari, S. Abbasalizadeh, G. S. Jouzani, and M. Noruzi, "Intensified biosynthesis of silver nanoparticles using a native extremophilic Ureibacillus thermosphaericus strain," *Materials Letters*, vol. 65, no. 6, pp. 1014–1017, 2011.

[45] M. M. G. Babu and P. Gunasekaran, "Production and structural characterization of crystalline silver nanoparticles from *Bacillus cereus* isolate," *Colloids and Surfaces B*, vol. 74, no. 1, pp. 191–195, 2009.

[46] S. Senapati, A. Ahmad, M. I. Khan, M. Sastry, and R. Kumar, "Extracellular biosynthesis of bimetallic Au-Ag alloy nanoparticles," *Small*, vol. 1, no. 5, pp. 517–520, 2005.

[47] D. Zheng, C. Hu, T. Gan, X. Dang, and S. Hu, "Preparation and application of a novel vanillin sensor based on

[48] B. D. Sawle, B. Salimath, R. Deshpande, M. D. Bedre, B. K. Prabhakar, and A. Venkataraman, "Biosynthesis and stabilization of Au and Au-Ag alloy nanoparticles by fungus, Fusarium semitectum," *Science and Technology of Advanced Materials*, vol. 9, no. 3, Article ID 035012, pp. 1–6, 2008.

[49] Y. Konishi, K. Ohno, N. Saitoh et al., "Bioreductive deposition of platinum nanoparticles on the bacterium *Shewanella algae*," *Journal of Biotechnology*, vol. 128, no. 3, pp. 648–653, 2007.

[50] A. Sinha and S. K. Khare, "Mercury bioaccumulation and simultaneous nanoparticle synthesis by *Enterobacter sp.* cells," *Bioresource Technology*, vol. 102, pp. 4281–4284, 2011.

[51] K. Kashefi and D. R. Lovley, "Reduction of Fe(III), Mn(IV), and toxic metals at 100∘C by *Pyrobaculum islandicum*," *Applied and Environmental Microbiology*, vol. 66, no. 3, pp. 1050–1056, 2000.

[52] J. R. Lloyd, P. Yong, and L. E. Macaskie, "Enzymatic recovery of elemental palladium by using sulfate-reducing bacteria," *Applied and Environmental Microbiology*, vol. 64, no. 11, pp. 4607–4609, 1998.

[53] P. Yong, N. A. Rowson, J. P. G. Farr, I. R. Harris, and L. E. Macaskie, "Bioreduction and biocrystallization of palladium by *Desulfovibrio desulfuricans* NCIMB 8307," *Biotechnology and Bioengineering*, vol. 80, no. 4, pp. 369–379, 2002.

[54] W. De Windt, P. Aelterman, and W. Verstraete, "Bioreductive deposition of palladium (0) nanoparticles on *Shewanella oneidensis* with catalytic activity towards reductive dechlorination of polychlorinated biphenyls," *Environmental Microbiology*, vol. 7, no. 3, pp. 314–325, 2005.

[55] J. H. Lee, J. Han, H. Choi, and H. G. Hur, "Effects of temperature and dissolved oxygen on Se(IV) removal and Se(0) precipitation by Shewanella sp. HN-41," *Chemosphere*, vol. 68, no. 10, pp. 1898–1905, 2007.

[56] H. Bao, Z. Lu, X. Cui et al., "Extracellular microbial synthesis of biocompatible CdTe quantum dots," *Acta Biomaterialia*, vol. 6, no. 9, pp. 3534–3541, 2010.

[57] T. X. Fan, S. K. Chow, and D. Zhang, "Biomorphic mineralization: from biology to materials," *Progress in Materials Science*, vol. 54, no. 5, pp. 542–659, 2009.

[58] D. A. Bazylinski, A. J. Garratt-Reed, and R. B. Frankel, "Electron microscopic studies of magnetosomes in magnetotactic bacteria," *Microscopy Research and Technique*, vol. 27, no. 5, pp. 389–401, 1994.

[59] D. A. Bazylinski, R. B. Frankel, B. R. Heywood et al., "Controlled biomineralization of magnetite (Fe_3O_4) and greigite (Fe3S4) in a magnetotactic bacterium," *Applied and Environmental Microbiology*, vol. 61, no. 9, pp. 3232–3239, 1995.

[60] A. Arakaki, H. Nakazawa, M. Nemoto, T. Mori, and T. Matsunaga, "Formation of magnetite by bacteria and its application," *Journal of the Royal Society Interface*, vol. 5, no. 26, pp. 977–999, 2008.

[61] R. Blakemore, "Magnetotactic bacteria," *Science*, vol. 190, no. 4212, pp. 377–379, 1975.

[62] R. H. Thornhill, J. G. Burgess, and T. Matsunaga, "PCR for direct detection of indigenous uncultured magnetic cocci in sediment and phylogenetic analysis of amplified 16S ribosomal DNA," *Applied and Environmental Microbiology*, vol. 61, no. 2, pp. 495–500, 1995.

[63] S. Spring and K. H. Schleifer, "Diversity of magnetotactic bacteria," *Systematic and Applied Microbiology*, vol. 18, no. 2, pp. 147–153, 1995.

[64] T. Perez-Gonzalez, C. Jimenez-Lopez, A. L. Neal et al., "Magnetite biomineralization induced by *Shewanella oneidensis*," *Geochimica et Cosmochimica Acta*, vol. 74, no. 3, pp. 967–979, 2010.

[65] K. Zhu, H. Pan, J. Li et al., "Isolation and characterization of a marine magnetotactic spirillum axenic culture QH-2 from an intertidal zone of the China Sea," *Research in Microbiology*, vol. 161, no. 4, pp. 276–283, 2010.

[66] Y. Amemiya, A. Arakaki, S. S. Staniland, T. Tanaka, and T. Matsunaga, "Controlled formation of magnetite crystal by partial oxidation of ferrous hydroxide in the presence of recombinant magnetotactic bacterial protein Mms6," *Biomaterials*, vol. 28, no. 35, pp. 5381–5389, 2007.

[67] W. Zhou, W. He, S. Zhong et al., "Biosynthesis and magnetic properties of mesoporous Fe$_3$O$_4$ composites," *Journal of Magnetism and Magnetic Materials*, vol. 321, no. 8, pp. 1025–1028, 2009.

[68] W. Zhou, W. He, X. Zhang et al., "Biosynthesis of iron phosphate nanopowders," *Powder Technology*, vol. 194, no. 1-2, pp. 106–108, 2009.

[69] W. Li, L. Yu, P. Zhou, and M. Zhu, "A Magnetospirillum strain WM-1 from a freshwater sediment with intracellular magnetosomes," *World Journal of Microbiology and Biotechnology*, vol. 23, no. 10, pp. 1489–1492, 2007.

[70] S. Bose, M. F. Hochella, Y. A. Gorby et al., "Bioreduction of hematite nanoparticles by the dissimilatory iron reducing bacterium *Shewanella oneidensis* MR-1," *Geochimica et Cosmochimica Acta*, vol. 73, no. 4, pp. 962–976, 2009.

[71] C. T. Lefèvre, F. Abreu, M. L. Schmidt et al., "Moderately thermophilic magnetotactic bacteria from hot springs in Nevada," *Applied and Environmental Microbiology*, vol. 76, no. 11, pp. 3740–3743, 2010.

[72] A. K. Jha, K. Prasad, and K. Prasad, "A green low-cost biosynthesis of Sb$_2$O$_3$ nanoparticles," *Biochemical Engineering Journal*, vol. 43, no. 3, pp. 303–306, 2009.

[73] A. K. Jha and K. Prasad, "Ferroelectric BaTiO$_3$ nanoparticles: biosynthesis and characterization," *Colloids and Surfaces B*, vol. 75, no. 1, pp. 330–334, 2010.

[74] A. K. Jha, K. Prasad, and A. R. Kulkarni, "Synthesis of TiO$_2$ nanoparticles using microorganisms," *Colloids and Surfaces B*, vol. 71, no. 2, pp. 226–229, 2009.

[75] V. Bansal, D. Rautaray, A. Bharde et al., "Fungus-mediated biosynthesis of silica and titania particles," *Journal of Materials Chemistry*, vol. 15, no. 26, pp. 2583–2589, 2005.

[76] V. Bansal, P. Poddar, A. Ahmad, and M. Sastry, "Room-temperature biosynthesis of ferroelectric barium titanate nanoparticles," *Journal of the American Chemical Society*, vol. 128, no. 36, pp. 11958–11963, 2006.

[77] V. Bansal, D. Rautaray, A. Ahmad, and M. Sastry, "Biosynthesis of zirconia nanoparticles using the fungus *Fusarium oxysporum*," *Journal of Materials Chemistry*, vol. 14, no. 22, pp. 3303–3305, 2004.

[78] C. T. Lefèvre, F. Abreu, U. Lins, and D. A. Bazylinski, "Nonmagnetotactic multicellular prokaryotes from low-saline, nonmarine aquatic environments and their unusual negative phototactic behavior," *Applied and Environmental Microbiology*, vol. 76, no. 10, pp. 3220–3227, 2010.

[79] A. Arakaki, M. Shibusawa, M. Hosokawa, and T. Matsunaga, "Preparation of genomic DNA from a single species of uncultured magnetotactic bacterium by multiple-displacement amplification," *Applied and Environmental Microbiology*, vol. 76, no. 5, pp. 1480–1485, 2010.

[80] H. J. Bai, Z. M. Zhang, Y. Guo, and G. E. Yang, "Biosynthesis of cadmium sulfide nanoparticles by photosynthetic bacteria *Rhodopseudomonas palustris*," *Colloids and Surfaces B*, vol. 70, no. 1, pp. 142–146, 2009.

[81] R. Sanghi and P. Verma, "A facile green extracellular biosynthesis of CdS nanoparticles by immobilized fungus," *Chemical Engineering Journal*, vol. 155, no. 3, pp. 886–891, 2009.

[82] K. Prasad and A. K. Jha, "Biosynthesis of CdS nanoparticles: an improved green and rapid procedure," *Journal of Colloid and Interface Science*, vol. 342, no. 1, pp. 68–72, 2010.

[83] R. Y. Sweeney, C. Mao, X. Gao et al., "Bacterial biosynthesis of cadmium sulfide nanocrystals," *Chemistry & Biology*, vol. 11, no. 11, pp. 1553–1559, 2004.

[84] M. Kowshik, N. Deshmuke, W. Vogal et al., "Microbial synthesis of semiconductor CdS nanoparticles, their characterization, and their use in the fabrication of an ideal diode," *Biotechnology and Bioengineering*, vol. 78, no. 5, pp. 583–588, 2002.

[85] C. T. Dameron, R. N. Reese, R. K. Mehra et al., "Biosynthesis of cadmium sulphide quantum semiconductor crystallites," *Nature*, vol. 338, no. 6216, pp. 596–597, 1989.

[86] H. J. Bai, Z. M. Zhang, and J. Gong, "Biological synthesis of semiconductor zinc sulfide nanoparticles by immobilized *Rhodobacter sphaeroides*," *Biotechnology Letters*, vol. 28, no. 14, pp. 1135–1139, 2006.

[87] M. Labrenz, G. K. Druschel, T. Thomsen-Ebert et al., "Formation of sphalerite (ZnS) deposits in natural biofilms of sulfate-reducing bacteria," *Science*, vol. 290, no. 5497, pp. 1744–1747, 2000.

[88] H. J. Bai and Z. M. Zhang, "Microbial synthesis of semiconductor lead sulfide nanoparticles using immobilized Rhodobacter sphaeroides," *Materials Letters*, vol. 63, no. 9-10, pp. 764–766, 2009.

[89] A. Ahmad, P. Mukherjee, D. Mandal et al., "Enzyme mediated extracellular synthesis of CdS nanoparticles by the fungus, *Fusarium oxysporum*," *Journal of the American Chemical Society*, vol. 124, no. 41, pp. 12108–12109, 2002.

[90] J. H. P. Watson, D. C. Ellwood, A. K. Soper, and J. Charnock, "Nanosized strongly-magnetic bacterially-produced iron sulfide materials," *Journal of Magnetism and Magnetic Materials*, vol. 203, no. 1–3, pp. 69–72, 1999.

[91] A. Sanyal, D. Rautaray, V. Bansal, A. Ahmad, and M. Sastry, "Heavy-metal remediation by a fungus as a means of production of lead and cadmium carbonate crystals," *Langmuir*, vol. 21, no. 16, pp. 7220–7224, 2005.

[92] D. Rautaray, A. Sanyal, S. D. Adyanthaya, A. Ahmad, and M. Sastry, "Biological synthesis of strontium carbonate crystals using the fungus *Fusarium oxysporum*," *Langmuir*, vol. 20, no. 16, pp. 6827–6833, 2004.

[93] S. R. K. Pandian, V. Deepak, K. Kalishwaralal, J. Muniyandi, N. Rameshkumar, and S. Gurunathan, "Synthesis of PHB nanoparticles from optimized medium utilizing dairy industrial waste using *Brevibacterium casei* SRKP2: a green chemistry approach," *Colloids and Surfaces B*, vol. 74, no. 1, pp. 266–273, 2009.

[94] S. Yan, W. He, C. Sun et al., "The biomimetic synthesis of zinc phosphate nanoparticles," *Dyes and Pigments*, vol. 80, no. 2, pp. 254–258, 2009.

[95] S. A. Kumar, A. A. Ansary, A. Abroad, and M. I. Khan, "Extracellular biosynthesis of CdSe quantum dots by the fungus, *Fusarium oxysporum*," *Journal of Biomedical Nanotechnology*, vol. 3, no. 2, pp. 190–194, 2007.

[96] K. B. Narayanan and N. Sakthivel, "Biological synthesis of metal nanoparticles by microbes," *Advances in Colloid and Interface Science*, vol. 156, no. 1-2, pp. 1–13, 2010.

[97] H. Yang, S. Santra, and P. H. Holloway, "Syntheses and applications of Mn-doped II-VI semiconductor nanocrystals," *Journal of Nanoscience and Nanotechnology*, vol. 5, no. 9, pp. 1364–1375, 2005.

[98] D. P. Cunningham and L. L. Lundie Jr., "Precipitation of cadmium by *Clostridium thermoaceticum*," *Applied and Environmental Microbiology*, vol. 59, no. 1, pp. 7–14, 1993.

[99] J. D. Holmes, D. J. Richardson, S. Saed, R. Evans-Gowing, D. A. Russell, and J. R. Sodeau, "Cadmium-specific formation of metal sulfide "Q-particles" by *Klebsiella pneumoniae*," *Microbiology*, vol. 143, no. 8, pp. 2521–2530, 1997.

[100] K. Benzerara, J. Miot, G. Morin, G. Ona-Nguema, F. Skouri-Panet, and C. Férard, "Significance, mechanisms and environmental implications of microbial biomineralization," *Comptes Rendus Geoscience*, vol. 343, no. 2-3, pp. 160–167, 2010.

[101] K. Kalishwaralal, V. Deepak, S. Ramkumarpandian, H. Nellaiah, and G. Sangiliyandi, "Extracellular biosynthesis of silver nanoparticles by the culture supernatant of *Bacillus licheniformis*," *Materials Letters*, vol. 62, no. 29, pp. 4411–4413, 2008.

[102] F. Reith, M. F. Lengke, D. Falconer, D. Craw, and G. Southam, "The geomicrobiology of gold," *The ISME Journal*, vol. 1, no. 7, pp. 567–584, 2007.

[103] D. H. Nies, "Microbial heavy-metal resistance," *Applied Microbiology and Biotechnology*, vol. 51, no. 6, pp. 730–750, 1999.

[104] M. Mergeay, S. Monchy, T. Vallaeys et al., "*Ralstonia metallidurans*, a bacterium specifically adapted to toxic metals: towards a catalogue of metal-responsive genes," *FEMS Microbiology Reviews*, vol. 27, no. 2-3, pp. 385–410, 2003.

[105] H. Tang, M. Yan, H. Zhang, M. Xia, and D. Yang, "Preparation and characterization of water-soluble CdS nanocrystals by surface modification of ethylene diamine," *Materials Letters*, vol. 59, no. 8-9, pp. 1024–1027, 2005.

[106] T. Løver, W. Henderson, G. A. Bowmaker, J. M. Seakins, and R. P. Cooney, "Functionalization and capping of a cds nanocluster: a study of ligand exchange by electrospray mass spectrometry," *Chemistry of Materials*, vol. 9, no. 8, pp. 1878–1886, 1997.

[107] T. Riddin, M. Gericke, and C. G. Whiteley, "Biological synthesis of platinum nanoparticles: effect of initial metal concentration," *Enzyme and Microbial Technology*, vol. 46, no. 6, pp. 501–505, 2010.

[108] A. Arakaki, F. Masuda, Y. Amemiya, T. Tanaka, and T. Matsunaga, "Control of the morphology and size of magnetite particles with peptides mimicking the Mms6 protein from magnetotactic bacteria," *Journal of Colloid and Interface Science*, vol. 343, no. 1, pp. 65–70, 2010.

[109] B. Fadeel and A. E. Garcia-Bennett, "Better safe than sorry: understanding the toxicological properties of inorganic nanoparticles manufactured for biomedical applications," *Advanced Drug Delivery Reviews*, vol. 62, no. 3, pp. 362–374, 2010.

[110] W. C. W. Chan and S. Nie, "Quantum dot bioconjugates for ultrasensitive nonisotopic detection," *Science*, vol. 281, no. 5385, pp. 2016–2018, 1998.

[111] F. Tian, A. Prina-Mello, G. Estrada et al., "A novel assay for the quantification of internalized nanoparticles in macrophages," *Nanotoxicology*, vol. 2, no. 4, pp. 232–242, 2008.

[112] D. Cui, F. Tian, S. R. Coyer et al., "Effects of antisense-myc-conjugated single-walled carbon nanotubes on HL-60 cells," *Journal of Nanoscience and Nanotechnology*, vol. 7, no. 4-5, pp. 1639–1646, 2007.

[113] D. Pantarotto, C. D. Partidos, J. Hoebeke et al., "Immunization with peptide-functionalized carbon nanotubes enhances virus-specific neutralizing antibody responses," *Chemistry and Biology*, vol. 10, no. 10, pp. 961–966, 2003.

[114] R. L. Edelstein, C. R. Tamanaha, P. E. Sheehan et al., "The BARC biosensor applied to the detection of biological warfare agents," *Biosensors and Bioelectronics*, vol. 14, no. 10-11, pp. 805–813, 2000.

[115] A. De la Isla, W. Brostow, B. Bujard et al., "Nanohybrid scratch resistant coatings for teeth and bone viscoelasticity manifested in tribology," *Materials Research Innovations*, vol. 7, no. 2, pp. 110–114, 2003.

[116] J. Ma, H. Wong, L. B. Kong, and K. W. Peng, "Biomimetic processing of nanocrystallite bioactive apatite coating on titanium," *Nanotechnology*, vol. 14, no. 6, pp. 619–623, 2003.

[117] M. Shinkai, M. Yanase, M. Suzuki et al., "Intracellular hyperthermia for cancer using magnetite cationic liposomes," *Journal of Magnetism and Magnetic Materials*, vol. 194, no. 1, pp. 176–184, 1999.

[118] R. Weissleder, G. Elizondo, J. Wittenberg, C. A. Rabito, H. H. Bengele, and L. Josephson, "Ultrasmall superparamagnetic iron oxide: characterization of a new class of contrast agents for MR imaging," *Radiology*, vol. 175, no. 2, pp. 489–493, 1990.

[119] W. J. Parak, R. Boudreau, M. Le Gros et al., "Cell motility and metastatic potential studies based on quantum dot imaging of phagokinetic tracks," *Advanced Materials*, vol. 14, no. 12, pp. 882–885, 2002.

[120] D. F. Emerich and C. G. Thanos, "The pinpoint promise of nanoparticle-based drug delivery and molecular diagnosis," *Biomolecular Engineering*, vol. 23, no. 4, pp. 171–184, 2006.

[121] F. K. Alanazi, A. A. Radwan, and I. A. Alsarra, "Biopharmaceutical applications of nanogold," *Saudi Pharmaceutical Journal*, vol. 18, no. 4, pp. 179–193, 2010.

[122] E. Rodríguez-Carmona and A. Villaverde, "Nanostructured bacterial materials for innovative medicines," *Trends in Microbiology*, vol. 18, no. 9, pp. 423–430, 2010.

[123] R. Vaidyanathan, K. Kalishwaralal, S. Gopalram, and S. Gurunathan, "Nanosilver—the burgeoning therapeutic molecule and its green synthesis," *Biotechnology Advances*, vol. 27, no. 6, pp. 924–937, 2009.

[124] M. Mahmoudi, S. Sant, B. Wang, S. Laurent, and T. Sen, "Superparamagnetic iron oxide nanoparticles (SPIONs): development, surface modification and applications in chemotherapy," *Advanced Drug Delivery Reviews*, vol. 63, pp. 24–46, 2010.

[125] A. M. G. C. Dias, A. Hussain, A. S. Marcos, and A. C. A. Roque, "A biotechnological perspective on the application of iron oxide magnetic colloids modified with polysaccharides," *Biotechnology Advances*, vol. 29, no. 1, pp. 142–155, 2011.

[126] Z. Shen, Y. Li, K. Kohama, B. Oneill, and J. Bi, "Improved drug targeting of cancer cells by utilizing actively targetable folic acid-conjugated albumin nanospheres," *Pharmacological Research*, vol. 63, no. 1, pp. 51–58, 2011.

[127] M. J. Piao, K. A. Kang, I. K. Lee et al., "Silver nanoparticles induce oxidative cell damage in human liver cells through inhibition of reduced glutathione and induction of mitochondria-involved apoptosis," *Toxicology Letters*, vol. 201, no. 1, pp. 92–100, 2011.

[128] K. V. Chakravarthy, A. C. Bonoiu, W. G. Davis et al., "Gold nanorod delivery of an ssRNA immune activator inhibits pandemic H1N1 influenza viral replication," *Proceedings of*

the National Academy of Sciences of the United States of America, vol. 107, no. 22, pp. 10172–10177, 2010.

[129] L. Xiang, J. Wei, S. Jianbo, W. Guili, G. Feng, and L. Ying, "Purified and sterilized magnetosomes from Magnetospirillum gryphiswaldense MSR-1 were not toxic to mouse fibroblasts in vitro," *Letters in Applied Microbiology*, vol. 45, no. 1, pp. 75–81, 2007.

[130] C. Meng, J. Tian, Y. Li, and S. Zheng, "Influence of native bacterial magnetic particles on mouse immune response," *Wei Sheng Wu Xue Bao*, vol. 50, no. 6, pp. 817–821, 2010.

[131] J. B. Sun, J. H. Duan, S. L. Dai et al., "*In vitro* and *in vivo* antitumor effects of doxorubicin loaded with bacterial magnetosomes (DBMs) on H22 cells: the magnetic bio-nanoparticles as drug carriers," *Cancer Letters*, vol. 258, no. 1, pp. 109–117, 2007.

[132] J. B. Sun, Z. L. Wang, J. H. Duan et al., "Targeted distribution of bacterial magnetosomes isolated from magnetospirillum gryphiswaldense MSR-1 in healthy sprague-dawley rats," *Journal of Nanoscience and Nanotechnology*, vol. 9, no. 3, pp. 1881–1885, 2009.

[133] O. Felfoul, M. Mohammadi, and S. Martel, "Magnetic resonance imaging of Fe_3O_4 nanoparticles embedded in living magnetotactic bacteria for potential use as carriers for in vivo applications," in *Proceedings of the 29th Annual International Conference of the IEEE Engineering in Medicine and Biology Society (EMBS '07)*, pp. 1463–1466, 2007.

[134] J. Xie, K. Chen, and X. Chen, "Production, modification and bio-applications of magnetic nanoparticles gestated by magnetotactic bacteria," *Nano Research*, vol. 2, no. 4, pp. 261–278, 2009.

[135] P. Mukherjee, R. Bhattacharya, C. R. Patra et al., *Nanogold in Cancer Therapy and Diagnosis*, vol. 7, chapter 3, Wiley-VCH, Weinheim, Germany, 2007.

[136] S. Mahdihassan, "Alchemy, Chinese versus Greek, an etymological approach: a rejoinder," *American Journal of Chinese Medicine*, vol. 16, no. 1-2, pp. 83–86, 1988.

[137] G. J. Higby, "Gold in medicine: a review of its use in the West before 1900," *Gold bulletin*, vol. 15, no. 4, pp. 130–140, 1982.

[138] C. R. Patra, R. Bhattacharya, D. Mukhopadhyay, and P. Mukherjee, "Fabrication of gold nanoparticles for targeted therapy in pancreatic cancer," *Advanced Drug Delivery Reviews*, vol. 62, no. 3, pp. 346–361, 2010.

[139] D. A. Giljohann, D. S. Seferos, W. L. Daniel, M. D. Massich, P. C. Patel, and C. A. Mirkin, "Gold nanoparticles for biology and medicine," *Angewandte Chemie International Edition*, vol. 49, no. 19, pp. 3280–3294, 2010.

[140] K. Kalishwaralal, E. Banumathi, S. R. K. Pandian et al., "Silver nanoparticles inhibit VEGF induced cell proliferation and migration in bovine retinal endothelial cells," *Colloids and Surfaces B*, vol. 73, no. 1, pp. 51–57, 2009.

[141] B. Chertok, B. A. Moffat, A. E. David et al., "Iron oxide nanoparticles as a drug delivery vehicle for MRI monitored magnetic targeting of brain tumors," *Biomaterials*, vol. 29, no. 4, pp. 487–496, 2008.

[142] N. Durán, P. D. Marcato, G. I. H. De Souza, O. L. Alves, and E. Esposito, "Antibacterial effect of silver nanoparticles produced by fungal process on textile fabrics and their effluent treatment," *Journal of Biomedical Nanotechnology*, vol. 3, no. 2, pp. 203–208, 2007.

[143] T. Wang, L. Yang, B. Zhang, and J. Liu, "Extracellular biosynthesis and transformation of selenium nanoparticles and application in H_2O_2 biosensor," *Colloids and Surfaces B*, vol. 80, no. 1, pp. 94–102, 2010.

[144] B. Zheng, L. Qian, H. Yuan et al., "Preparation of gold nanoparticles on eggshell membrane and their biosensing application," *Talanta*, vol. 82, no. 1, pp. 177–183, 2010.

[145] H. Hildebrand, K. Mackenzie, and F.-D. Kopinke, "Novel nano-catalysts for waste water treatment," *Global NEST Journal*, vol. 10, pp. 47–53, 2008.

[146] G. Shan, J. Xing, H. Zhang, and H. Liu, "Biodesulfurization of dibenzothiophene by microbial cells coated with magnetite nanoparticles," *Applied and Environmental Microbiology*, vol. 71, no. 8, pp. 4497–4502, 2005.

[147] T. Matsunaga, F. Ueki, K. Obata et al., "Fully automated immunoassay system of endocrine disrupting chemicals using monoclonal antibodies chemically conjugated to bacterial magnetic particles," *Analytica Chimica Acta*, vol. 475, no. 1-2, pp. 75–83, 2003.

[148] T. Tanaka, H. Takeda, F. Ueki et al., "Rapid and sensitive detection of 17β-estradiol in environmental water using automated immunoassay system with bacterial magnetic particles," *Journal of Biotechnology*, vol. 108, no. 2, pp. 153–159, 2004.

[149] L. Xiang, W. Bin, J. Huali et al., "Bacterial magnetic particles (BMPs)-PEI as a novel and efficient non-viral gene delivery system," *Journal of Gene Medicine*, vol. 9, no. 8, pp. 679–690, 2007.

[150] R. Hergt, R. Hiergeist, M. Zeisberger et al., "Magnetic properties of bacterial magnetosomes as potential diagnostic and therapeutic tools," *Journal of Magnetism and Magnetic Materials*, vol. 293, no. 1, pp. 80–86, 2005.

[151] R. Hergt and S. Dutz, "Magnetic particle hyperthermia-biophysical limitations of a visionary tumour therapy," *Journal of Magnetism and Magnetic Materials*, vol. 311, no. 1, pp. 187–192, 2007.

Research Article

Enhancement of Oral Bioavailability of Puerarin by Polybutylcyanoacrylate Nanoparticles

Lixia Zhao,[1,2] Anchang Liu,[1,2] Min Sun,[1,3] Jinsong Gu,[4] Haigang Wang,[2] Shuang Wang,[1] Jing Zhang,[1] Chenyu Guo,[1] Rui Duan,[1] and Guangxi Zhai[1]

[1] *School of Pharmaceutical Sciences, Shandong University, Jinan 250012, China*
[2] *Department of Pharmacy, Qilu Hospital of Shandong University, Jinan 250012, China*
[3] *Deparment of Pharmacy, Central Hospital of Zibo, Zibo 255036, China*
[4] *Department of Biotechnology, College of Life Science and Technology, University of Jinan, Jinan 250022, China*

Correspondence should be addressed to Guangxi Zhai, professorgxzhai@yahoo.cn

The interest using novel drug delivery systems to improve oral bioavailability of drug with poor solubility is increasing. In this study, a new oral delivery system, polybutylcyanoacrylate nanoparticles (PBCNs), was introduced to improve the oral bioavailability of puerarin (PUE). PUE-loaded PBCN was successfully prepared by anionic polymerization method. Characterization of PUE-loaded PBCN was evaluated with morphology, size, zeta potential, and in vitro release study. The PBCN loading PUE exhibited a spherical shape under transmission electron microscopy with an average size of 159.4 nm, and the zeta potential was -15.0 mV. The in vitro release of PUE-loaded PBCN showed an initial burst release followed by a sustained release. Physicochemical state of PUE in PBCN was investigated by differential scanning colorimetry, X-ray diffraction, and Fourier transform infrared spectroscopy. The results indicated that PUE in PBCN was in a noncrystalline state. The oral pharmacokinetic study in rats showed that the relative bioavailability of PUE-encapsulated PBCN to the crude PUE was more than 550%. It can be concluded that PBCN as an oral drug carrier can significantly improve the oral bioavailability of PUE.

1. Introduction

The bioavailability is an important parameter showing the degree and rate of drug molecules entering blood circulation, indicating the effectiveness and safety of an extravascular administration formulation. It can be influenced by drug formulations, food, and physiological factors. However, up to 50% of orally administered drugs present formulation problems related to poor solubility (0.011 M) [1]. In recent years, many specific pharmaceutical approaches such as micro- and nanotechnology have been developed to improve the bioavailability [2]. As one promising delivery system with improved bioavailability, polybutylcyanoacrylate nanoparticles (PBCNs) have attracted considerable attention [3]. It is a type of solid colloidal particles ranging in size from 10 nm to 1000 nm made of biodegradable polymers [4, 5] which could significantly enhance the oral absorption of some drugs such as thymopentin [6]. The PBCNs that served as the oral

carriers can prevent the destruction of drugs (e.g., peptide drugs) by the acid and enzymes in gastrointestinal tract [7, 8], improve the drug absorption through Peyer's patches (PP), the immunization-related tissue in small intestine of human and animals which accounts for about 25% of the intestinal mucosa, and other intestinal lymphoid tissue into the blood circulation [9], and prolong the residence time in vivo because of the small particles and bioadhesive property [6].

Puerarin (PUE, Figure 1) is the naturally occurring isoflavone C-glycoside extracted from the roots of *Pueraria lobata* (Willd.), *Ohwi, and P. thomsonni Benth*, which is widely used in China for the treatment of cerebrovascular and cardiovascular disease. Although PUE has definite therapeutic effectiveness, its clinical application is limited by its poor solubility, short elimination half-life, and poor oral bioavailability. The commercial available preparation for PUE is its injection which has poor patient compliance
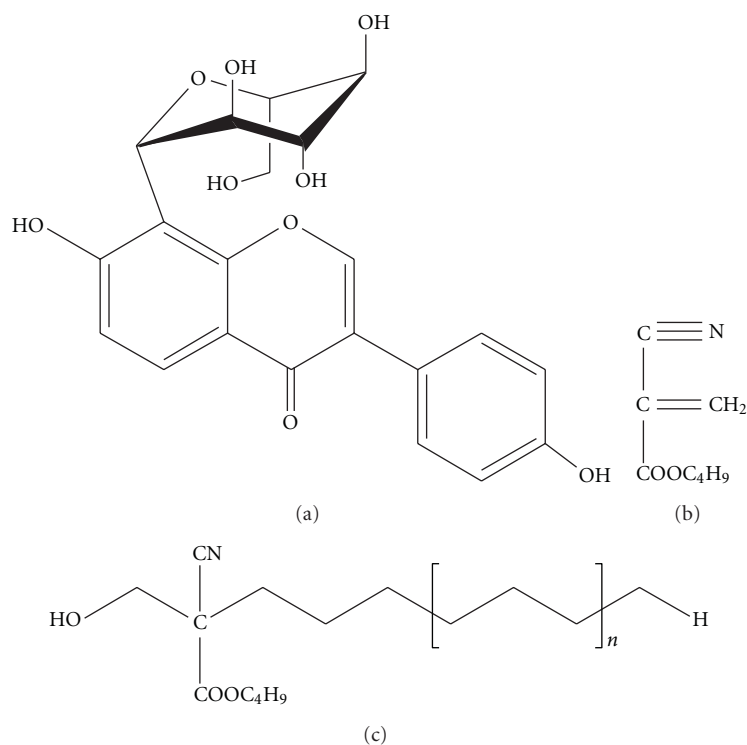
Figure 1: Chemical structure of puerarin (a), BCA (b) and PBCA (c).

because of the high frequency of injecting administration [10]. The oral preparation containing *Pueraria lobata* extraction is Yufengningxin tablet which needs to be orally given five tables each time and three times each day. Therefore, the development of a suitable oral preparation is a research focus of PUE. In the past few years, several pharmaceutical techniques were adopted to improve the oral absorption of puerarin, such as microemulsion [10–12] and solid lipid nanoparticles [13]. However, up to date no study on PBCN for enhancing the oral bioavailability of PUE has been reported.

In this study, PUE-loaded PBCN (PUE-PBCN) was prepared by anionic polymerization method in order to improve the oral bioavailability of PUE and was characterized with morphology, size, zeta potential, and in vitro release study. Physicochemical state of PUE in PBCN was investigated by differential scanning colorimetry (DSC), X-ray diffraction (XRD), and Fourier transform infrared (FTIR) spectroscopy. Additionally, the pharmacokinetics of PUE-loaded PBCN was studied in rats.

2. Materials and Methods

2.1. Materials. PUE was purchased from Nanjing Zelang Medical Technology Co., Ltd. (Nanjing, China). Dextran 70 (D-(+) glucose) and poloxamer 188 (F68) were provided by the Shanghai Treechem Biotech Co., Ltd. (Shanghai, China). N-Butylcyanoacrylate (BCA) was a gift sample from Beijing Suncon Medical Adhesive Co., Ltd. (Beijing, China). All other reagents used in the study were of analytical regent grade.

2.2. Preparation of PBCN. Based on the previous reports with some modifications [14–16], PUE-PBCN was prepared using open anionic polymerization of n-butyl-2-cyanoacrylate (BCA) monomer in acidic medium (0.01 M HCl), containing 0.5% (w/v) of dextran 70 and 0.5% (w/v) of poloxamer 188 as stabilizer and emulsifier. The monomer BCA was injected drop by drop into the stirred medium including PUE (the weight ratio of drug to polymer was 1 : 2). Polymerization was conducted for 4 hours under magnetic agitation at 400 rpm and room temperature. Subsequently, sodium hydroxide solution (1 M) was used to adjust the pH of resulting suspension to 6.8 ± 0.1. The above mixture was stirred for an additional 1 h at the same conditions, and the reaction was gradually completed. The PUE-PBCN suspension was obtained after the above system was filtered through 0.8 μm filter membrane.

2.3. Characterization of PBCN

2.3.1. Morphology. PUE-loaded PBCN was observed under a transmission electron microscope (TEM, JEM-1200EX, JEOL, Tokyo, Japan) using the negative-staining method. One drop of diluted PUE-PBCN was added to a copper grid to form a thin liquid film, and then the film was negatively stained by adding 2% (w/v) phosphotungstic acid (PTA, pH 7.0). Extra droplet was instantly removed with filter paper, and then the grid was dried at room temperature as a TEM sample. The film was examined under TEM and photographed.

2.3.2. Particle Size and Zeta Potential. The particle size of PUE-PBCN was analyzed using a particle sizer (Zetasizer 3000 HAS, Malvern Instruments Ltd., Malvern, Worcestershire, UK) with photon correlation spectroscopy (PCS) at a fixed angle of 90° at a temperature of 25°C. It was conducted with He-Ne laser of 3 mW at a wavelength of 633 nm, and the particle size analysis data were evaluated using the volume distribution.

Zeta potential of PUE-PBCN was determined using TV microscopic electrophoresis system (DXD-II, Optics Co., Ltd., Jiangsu, China) at room temperature.

2.3.3. Encapsulation Efficiency (EE) and Drug Loading (DL). The measurement for encapsulation efficiency and drug loading of PUE-PBCN was carried out with centrifugation ultrafiltration method according to the previous reports [17, 18]. The free PUE was separated from PUE-PBCN by centrifugal filter tubes (Amicon Ultra-4, Millipore, Ireland) with a molecular cut off of 10 kDa. Briefly, 2 mL of PUE-loaded nanoparticle suspension was added into centrifugal filter tube and centrifuged at 4000 rpm for 20 min at room temperature using a centrifuge (Biofuge primo R. Heraeus, Hanau, Germany). The initial total amount of PUE in the suspension system and the amount of free drug in the filtrate were measured using UV at the wavelength of 251 nm. The encapsulation efficiency and drug loading in the PBCN were calculated as, respectively follows:

$$EE\% = \frac{W_{\text{total drug}} - W_{\text{free drug}}}{W_{\text{total drug}}} \times 100\%, \quad (1)$$

$$DL\% = \frac{W_{\text{total drug}} - W_{\text{free drug}}}{W_{\text{polymer}}} \times 100\%, \quad (2)$$

where "$W_{\text{free drug}}$" is the amount of PUE unloaded in PBCA nanoparticles, "$W_{\text{total drug}}$" is the initial total amount of PUE in the suspension system, and "W_{polymer}" is the weight of butyl-cyanoacrylate monomer.

2.3.4. DSC and XRD Analysis. The physical state of the drug entrapped in the PBCN was characterized using a differential scanning calorimeter (CDR-4P, Shanghai Tianping Instrument Ltd., Shanghai, China) and an X-ray diffractometer (D/max r-B, Rigaku Co., Tokyo, Japan). Prior to analysis, PUE-PBCN and blank PBCN used for DSC and XRD were obtained by freeze-drying without any freeze-dried protectants.

For DSC measurement, about 10 mg of samples (PUE, PUE-PBCN, or blank PBCN) were sealed in the aluminum pan and heated at a scanning rate of 10°C/min from 30 to 400°C under dry nitrogen atmosphere at a flow rate of 0.2 mL/min.

X-ray diffraction patterns were determined for PUE-PBCN, blank PBCN, and cure PUE with a Cu line as the source of radiation. A radiation at 40 kV voltage and 40 mA current was used, and diffractograms were performed with a scanning rate of 2°/min over a 2θ range of from 6° to 40°.

2.3.5. Fourier Transform Infrared (FTIR) Spectroscopy. FTIR analysis was performed to provide further information on the drug-polymer relationship using an FTIR spectrometer (Thermo Electron Scientific Instruments Corp.). FTIR spectra of PUE or BCA monomer or PUE-PBCN (with or without drug) were recorded in KBr pellets or KBr cell on an FTIR spectrometer with resolution of 2 cm^{-1}. A total of 64 scans were used and data were recorded over the range 4000–400 cm^{-1}.

2.3.6. In Vitro Release Study. The in vitro release of PUE from the nanoparticles was studied by dialysis against phosphate buffer solutions (PBS) with 12–14 kDa molecular cutoff bag pH 7.4 [19]. PUE-PBCN suspension or PUE propylene glycol solution (containing 3 mg/mL of PUE) was placed into dialysis bags, respectively. Then the bags were suspended in flasks containing 150 mL of PBS as dissolution medium at 37°C in shaking water bath at 100 rpm. 1 mL of dissolution medium was withdrawn at regular time intervals, and the same volume was added with fresh release medium. The concentrations of PUE in dissolution medium were measured using UV spectrophotometer at 251 nm. All experiments were performed in triplicates.

2.4. Pharmacokinetics Study. The study on the pharmacokinetics of PUE-PBCN was performed in male Wistar rats (200 ± 20 g) supplied by the Medical Animal Test Center of Shandong University [20]. All animal experiments complied with the requirements of the National Act on the use of experimental animals (China). The animals were divided randomly into 2 groups ($n = 5$), housed in an environmentally controlled breeding room (temperature 25 ± 2 °C, humidity 60 ± 5%, 12 h dark/light cycle) for 7 days and fasted overnight before experiment with free access to water. Group 1 was orally administrated PUE suspension (30 mg/kg, PUE dispersed in 0.5% sodium carboxymethylcellulose (CMC-Na) solution), and Group 2 was given PUE-PBCN at the same dose of 30 mg/kg through the same route. 0.3 mL of blood was withdrawn from the subclavian vein at 0 min, 5 min, 10 min, 20 min, 40 min, 1 h, 2 h, 4 h, 6 h, 8 h, 12 h, and 24 h. The samples were placed into heparinized tubes and isolated immediately by centrifugation at 4000 rpm for 10 min. The plasma obtained was stored at −20°C before analysis.

2.5. Liquid Chromatography Tandem Mass Spectrometry (LC-MS) Analysis. Extraction of PUE from plasma was conducted as follows: 25 μL of internal standard solution (genistein, 1 μg/mL) and 75 μL of methanol were added to 25 μL of plasma and the resulting mixture was vortexed for 1 min and then centrifuged at 11,000 rpm for 5 min to obtain a clean supernatant. An aliquot (20 μL) of supernatant was injected into the LC-MS for analysis [21].

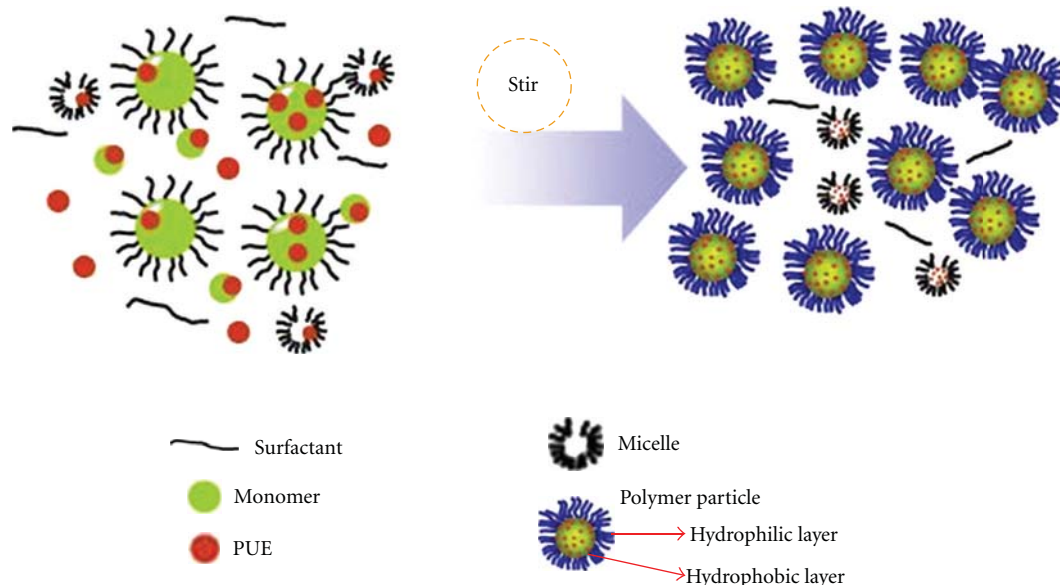PUE in plasma was determined by LC-MS analysis using an Agilent 1200 system equipped with an autosampler,

Figure 2: The fabrication of PUE loaded PBCN.

a vacuum degasser unit, and a binary pump. The HPLC system was coupled to an Agilent G6410B triple-quadrupole mass spectrometer (Agilent Technologies, USA), equipped with electrospray ionization (ESI) run by Agilent Mass Hunter Workstation B.01.03.

Mass spectrometric analysis was performed in multiple reaction monitoring (MRM) mode by monitoring ion transitions at m/z $415.1 \to 295.1$ for PUE and $269.1 \to 133.0$ for genistein (IS), with spray gas pressure of 350 Pa, protective air of nitrogen gas at a flow rate of 10 L/min, dwell time of 200 ms, capillary voltage of 4000 V, fragment electric voltage of 150 V for PUE and 135 V for genistein, and collision energy of 20 eV for PUE and 25 eV for genistein. Chromatographic peaks of analyte and IS were identified on the basis of retention time and MRM response.

Chromatographic separation was performed using a ProntoSIL C18 column (150 mm $\times$ 3 mm, 3 μm, Bischoff, Germany). The mobile phase consisted of a mixture of 10 mM ammonium acetate in water containing 0.1% formic acid and methanol (20 : 80, v/v). The separation was performed under isocratic conditions with a constant flow rate of 0.6 mL/min. The analytical method was validated according to "Guidance for Industry-Bioanalytical Method Validation" [22]. Pharmacokinetic parameters were evaluated using Pharmacokinetic program DAS 2.0 (supplied by Chinese Pharmacological Society).

2.6. Statistical Analysis. The statistical analysis of the data was carried out using Student's t-test with $P < 0.05$ as the minimal level of significance.

3. Results and Discussion

3.1. Fabrication of PUE-PBCN. PUE-PBCN was prepared by anionic polymerization based on the reported method

[3]. Based on the reported mechanism of polymerization [3, 23], the PUE-PBCN may fabricate as follows (Figure 2). Firstly, the surfactant such as F68 dissolved in acidic media above the critical micelle concentration (CMC) and the monomer-swollen micelles were formed as micelles took up BCA monomer. Secondly, the anionic radicals present in the media entered the swollen structures to initiate the polymerization, resulting in the formation of the primary particles. The newly formed polymer particles continued to grow in size by absorbing monomer molecules until the monomer completely disappeared. These primary particles were stabilized by the surfactant (F68) and stabilizer (Dextran 70), which prevented the aggregation of formed particles by steric repulsion. Concurrently, PUE, a high hydrophobic drug, might be gradually dispersed in the hydrophobic part of the swollen micelles and further incorporated in polymer nanoparticles by emulsion during the polymerization. The mean encapsulation efficiency and drug loading of PUE-PBCN suspension were 48.75% and 15.02%, respectively.

3.2. Characterization of PUE-PBCN. As shown in Figure 3, PUE-PBCN was spherical in shape with a smooth surface under TEM, which was in consistent with the reported result of PBCN loading curcuminoids [3].

It can be seen from Figure 4 that more than 85% of PUE-PBCN was between 100 nm to 300 nm, indicating that the size range of PBCN was narrow. The mean diameter was 159.4 nm with polydispersity index (PDI) of 0.139.

In the present study, the mean zeta potential of PUE-PBCN was -15.00 mV, which was similar to the report of Rivastigmine-loaded PBCN [5].

3.3. DSC and XRD Analysis. DSC, characterizing the thermal behavior of polymer and drug correlated to their melting and recrystallization, was used to investigate the physicochemical
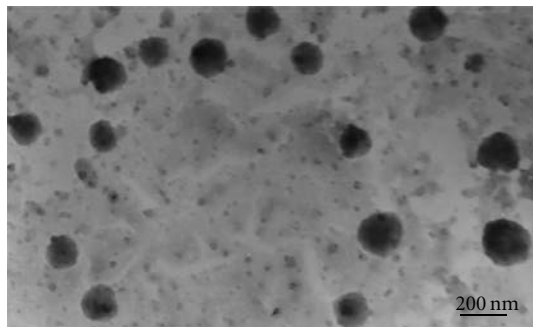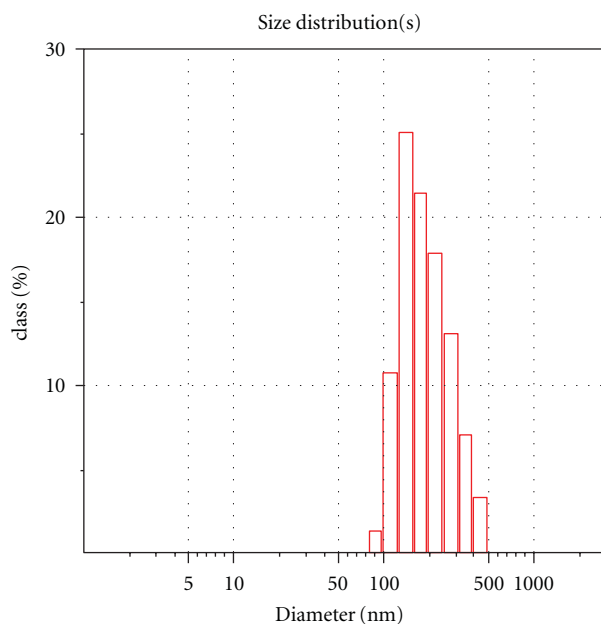
FIGURE 3: TEM photograph of PUE-PBCN.

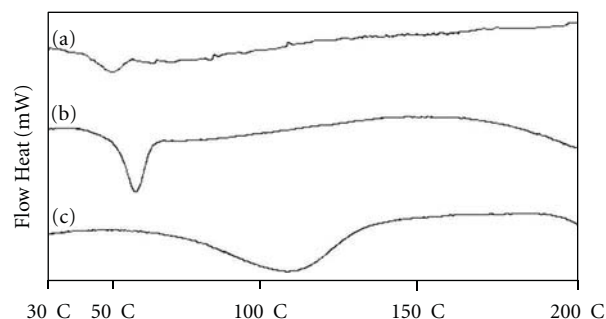FIGURE 4: The size distribution of the PUE-PBCN.

FIGURE 5: DSC thermograms of PUE-PBCN (a), blank PBCN (b) and pure PUE (c).
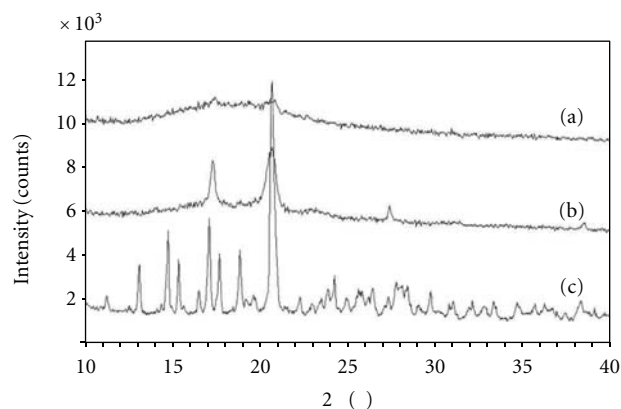
FIGURE 6: XRD diffractograms of PUE-PBCN (a), blank PBCN (b) and pure PUE (c).

state of PUE in the formulation [24]. The DSC thermograms of pure PUE, blank PBCN, and PUE-PBCN were shown in Figure 5. The wide endothermic peak at 112.2°C present in the thermogram of the crude PUE was not visible in that of PUE-PBCN, implying that PUE in PBCN was not in crystalline state but in an amorphous form. Blank PBCN showed an endothermic peak about 55°C, while the peak disappeared in the thermogram of PUE-PBCN, which might be due to drug interfering in the heat flow [25].

XRD analysis was employed to study the potential changes of the crystalline state of PUE in PBCN. The XRD patterns for PUE-PBCN, blank PBCN, and pure PUE were shown in Figure 6. Compared with the diffractograms for blank PBCN and pure PUE, almost all diffraction peaks disappeared in that of PUE-PBCN, indicating that PUE was in an amorphous form.

3.4. FTIR Analysis. FTIR analysis was proposed to evaluate possible interactions between drug and polymer carrier. Figure 7 showed the infrared spectra of BCA monomer (a),

blank PBCN (b), PUE-PBCN (c), and pure PUE (d). The peak at about $2200\,cm^{-1}$ in spectra of BCA is characteristic of C≡N (stretching mode of the polymer). The C≡N peak was also present in the spectra of blank PBCN and PUE-PBCN, indicating that C≡N did not participate in the polymerization. Broader bands at about $3400\,cm^{-1}$ were observed in the spectra of blank PBCN, PUE-PBCN, and pure PUE, which were corresponding to hydroxyl radicals. Compared to the spectrum of BCA monomer, these bands in spectra of PBCN may be a result of polymerization, which can be inferred from the chemical structures of BCA and PBCA (Figures 1(b) and 1(c)) [25]. Moreover, the fingerprint region at $1600\,cm^{-1}$ and $650\,cm^{-1}$ assigned to the absorption peak of benzene did not change or shift and only got weak in the spectrum of PUE-PBCN, which could be a strong evidence showing no new chemical bond produced. All results indicated that PUE did not participate in the polymerization reaction and was only encapsulated in PBCN by possible intermolecular forces such as hydrogen bond. Similar results were obtained in the previous report [26].

3.5. In Vitro Release Study. The in vitro release of PUE from PBCN was conformed in phosphate buffer at pH 7.4 with dynamic dialysis method. The results of drug release from PUE solution or PBCN suspension at pH 7.4 were shown in Figure 8. The PUE release from solution was found to
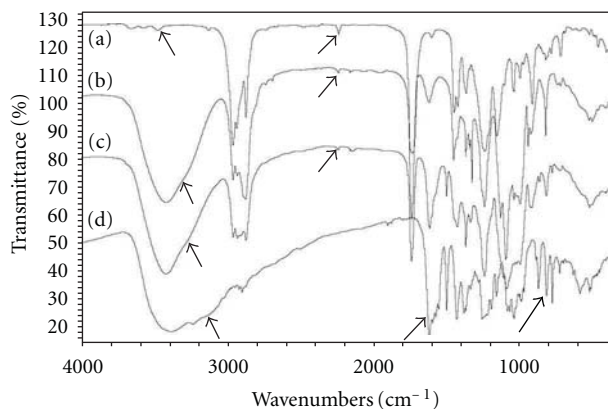
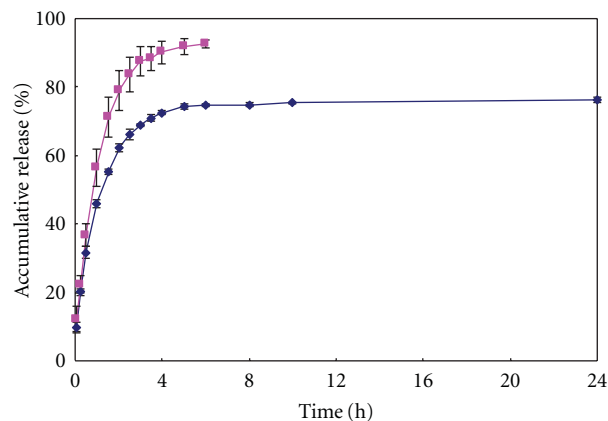FIGURE 7: FTIR spectra of BCA (a), blank PBCN (b), PUE-PBCN (c) and pure PUE (d).

FIGURE 8: In vitro release profiles of PUE from PBCN in PBS at pH = 7.4.

FIGURE 9: Concentration-time curves of PUE suspension and PUE-PBCN in rats.

be much faster, nearly 100% in 5 h. In contrast, the release profile of PUE from PBCN demonstrated two phases: an initial burst release followed by a sustained release, only about 75% over the period of 24 h. This could be attributed to the fact that PUE loaded on or near the surface of PBCN was released first, and subsequently the drug embedded in the nanoparticles was released, which might release slowly by diffusion from the matrix or along with the degradation of polymer [27]. The result was in agreement with the previous reports that drug-loaded PBCN provided a controlled release pattern [28].

3.6. Pharmacokinetics Study. The mean concentrations of PUE in the plasma after oral administration of a single dose in rats were measured using a highly sensitive and specific LC/MS/MS method. The retention time of puerarin and genistein was 1.4 min and 1.8 min, respectively. The mean recovery of PUE was more than 93.0%, and the precision for interday and intraday was less than 15%. Besides, PUE in analyzed samples was stable for 24 h at room temperature, 30 days at $-20°C$ and three freeze-thaw cycles.

The calibration curve was linear over the concentration range of 2–10000 ng/mL for PUE, and the regression equation was $A = 8.01 \times 10^{-5}C + 2.35 \times 10^{-4}$ with the mean correlation coefficient (r) of 0.9996.

The data for pharmacokinetics in rats were analyzed with DAS 2.0, and pharmacokinetic parameters were shown in Table 1. The pharmacokinetic behaviors of PUE suspension and PUE-PBCN were described using noncompartment model. As shown in Table 1, the area under the concentration-time curve (AUC) of PUE-PBCN was 6.765 ± 2.374 mg/L∗h, which was 5.56-fold greater than that of PUE suspension administration (1.216 ± 0.158 mg/L∗h, $P < 0.01$). The mean residence time (MRT) of PUE-PBCN (6.299 ± 0.925 h) and half-life $T_{1/2}$ (3.937 ± 0.972) were 1.63 times those of CUR suspension (3.864 ± 0.832 h for MRT, 2.409 ± 0.791 h for $T_{1/2}$), while the plasma clearance (4.936 ± 1.810 L/h·kg) of CUR-PBCN was much lower relative to that of the control suspension (25.04 ± 3.489 L/h·kg). These results might be related to the small size of nanoparticles and coating of F68 on the surface to keep the nanoparticles contacting closely and long with the gastrointestinal (GI) tract [29]. The mean plasma concentration-time profiles for PUE and PUE-PBCN were presented in Figure 9. At all time points, the PUE concentrations in plasma were significantly higher for rats treated with PUE-PBCN than those treated with PUE suspension. Twenty-four hours after oral administration of PUE-PBCN, the PUE concentration in plasma was still more than 0.025 mg/L, while it was undetectable after 12 h for PUE suspension. Double peaks in the profile of PUE-PBCN may be contributed to, on the one hand, the possible enterohepatic recirculation; on the other hand, the absorption time lag after the first absorption existing due to the more time for PUE was needed to be released from PBCN and absorbed [30]. The similar phenomenon has been in agreement with the pharmacokinetic study of oral administration of PUE load SLNs [13]. These results indicated that PUE entrapped into PBCN led to the increased absorption of PUE by oral administration.

TABLE 1: Main pharmacokinetic parameters of PUE suspension and PUE-PCBN in rats.

Parameters	Unit	Value (mean ± SD)	
		PUE suspension	PUE-PCBN
$AUC_{(0-\infty)}$	mg/L·h	1.216 ± 0.158	6.765 ± 2.374**
$MRT_{(0-\infty)}$	h	3.864 ± 0.832	6.299 ± 0.925**
$T_{1/2}$	h	2.409 ± 0.791	3.937 ± 0.972*
V_z	L/kg	85.41 ± 21.63	28.33 ± 13.95**
CL	L/h·kg	25.04 ± 3.489	4.936 ± 1.810**
C_{max}	mg/L	0.363 ± 0.045	0.897 ± 0.135**

** Comparing to PUE suspension group, $P < 0.001$; * Comparing to PUE suspension group, $P < 0.05$.

The relative bioavailability (F_{rel}) was calculated as

$$F_{rel} = \frac{AUC_{PUE-PBCN}}{AUC_{PUE}} \times 100\%. \tag{3}$$

The result indicated that PBCN could significantly enhance the oral bioavailability of PU (more than 5.5-fold that of PUE suspension). The enhanced bioavailability by the PBCN formulation might be a cowork of direct uptake of nanoparticles through the GI tract, increased permeability by surfactants, and decreased degradation and clearance for PUE. The particles in nanorange could be directly uptaken by the mucus and microfold cells (M cells) of the Peyer's patches and the lymphatics through the GI tract [31, 32]. In addition, PUE could be protected by incorporation into PBCN during the absorption process [33]. The high affinity of PBCN to M cells in the GI tract and increased permeability by surfactants could result in long MRT and $T_{1/2}$, thus leading to the enhanced bioavailability [34, 35]. The results support that PBCN is a promising delivery system for improving oral bioavailability of PUE.

4. Conclusions

In the present study, PUE-PBCN was successfully prepared to improve the bioavailability. The drug-loaded PBCN was sphere-like shape with a mean diameter of 159.4 nm and the zeta potential was -15.00 mV. It could be concluded from DSC, FTIR, and X-ray analysis that PUE loaded in nanoparticles was in an amorphous form. The pharmacokinetic data showed that the PBCN could improve the oral bioavailability of PUE by 5.5-fold. It can be concluded that PBCN can improve the oral absorption of PUE.

Acknowledgments

References

[1] A. Dolenc, J. Kristl, S. Baumgartner, and O. Planinšek, "Advantages of celecoxib nanosuspension formulation and transformation into tablets," *International Journal of Pharmaceutics*, vol. 376, no. 1-2, pp. 204–212, 2009.

[2] M. Kakran, N. G. Sahoo, L. Li et al., "Fabrication of drug nanoparticles by evaporative precipitation of nanosuspension," *International Journal of Pharmaceutics*, vol. 383, no. 1-2, pp. 285–292, 2010.

[3] R. Mulik, K. Mahadik, and A. Paradkar, "Development of curcuminoids loaded poly(butyl) cyanoacrylate nanoparticles: physicochemical characterization and stability study," *European Journal of Pharmaceutical Sciences*, vol. 37, no. 3-4, pp. 395–404, 2009.

[4] C. Vauthier and K. Bouchemal, "Methods for the preparation and manufacture of polymeric nanoparticles," *Pharmaceutical Research*, vol. 26, no. 5, pp. 1025–1058, 2009.

[5] S. A. Joshi, S. S. Chavhan, and K. K. Sawant, "Rivastigmine-loaded PLGA and PBCA nanoparticles: preparation, optimization, characterization, in vitro and pharmacodynamic studies," *European Journal of Pharmaceutics and Biopharmaceutics*, vol. 76, no. 2, pp. 189–199, 2010.

[6] W. He, X. Jiang, and Z. R. Zhang, "Preparation and evaluation of poly-butylcyanoacrylate nanoparticles for oral delivery of thymopentin," *Journal of Pharmaceutical Sciences*, vol. 97, no. 6, pp. 2250–2259, 2008.

[7] G. Fontana, G. Pitarresi, V. Tomarchio, B. Carlisi, and P. L. San Biagio, "Preparation, characterization and in vitro antimicrobial activity of ampicillin-loaded polyethylcyanoacrylate nanoparticles," *Biomaterials*, vol. 19, no. 11-12, pp. 1009–1017, 1998.

[8] C. Damgé, C. P. Reis, and P. Maincent, "Nanoparticle strategies for the oral delivery of insulin," *Expert Opinion on Drug Delivery*, vol. 5, no. 1, pp. 45–68, 2008.

[9] M. P. Desai, V. Labhasetwar, G. L. Amidon, and R. J. Levy, "Gastrointestinal uptake of biodegradable microparticles: effect of particle size," *Pharmaceutical Research*, vol. 13, no. 12, pp. 1838–1845, 1996.

[10] A. Yu, H. Wang, J. Wang et al., "Formulation optimization and bioavailability after oral and nasal administration in rabbits of puerarin-loaded microemulsion," *Journal of Pharmaceutical Sciences*, vol. 100, no. 3, pp. 933–941, 2011.

[11] D. Q. Quan, G. X. Xu, and X. G. Wu, "Studies on preparation and absolute bioavailability of a self-emulsifying system containing puerarin," *Chemical and Pharmaceutical Bulletin*, vol. 55, no. 5, pp. 800–803, 2007.

[12] H. Wu, A. Zhou, C. Lu, and L. Wang, "Examination of lymphatic transport of puerarin in unconscious lymph duct-cannulated rats after administration in microemulsion drug

delivery systems," *European Journal of Pharmaceutical Sciences*, vol. 42, no. 4, pp. 348–353, 2011.

[13] C.-F. Luo, M. Yuan, M.-S. Chen et al., "Pharmacokinetics, tissue distribution and relative bioavailability of puerarin solid lipid nanoparticles following oral administration," *International Journal of Pharmaceutics*, vol. 410, no. 1-2, pp. 138–144, 2011.

[14] N. Behan, C. Birkinshaw, and N. Clarke, "Poly n-butyl cyanoacrylate nanoparticles: a mechanistic study of polymerisation and particle formation," *Biomaterials*, vol. 22, no. 11, pp. 1335–1344, 2001.

[15] C. Vauthier, C. Dubernet, E. Fattal, H. Pinto-Alphandary, and P. Couvreur, "Poly(alkylcyanoacrylates) as biodegradable materials for biomedical applications," *Advanced Drug Delivery Reviews*, vol. 55, no. 4, pp. 519–548, 2003.

[16] L. Cai, G. Niu, Z. Hu, W. Jin, J. Wang, and L. Sun, "Polybutylcyanoacrylate magnetic nanoparticles as carriers of adriamycin," *Journal of Drug Targeting*, vol. 17, no. 3, pp. 200–206, 2009.

[17] L. J. Jia, D. R. Zhang, Z. Y. Li et al., "Preparation and characterization of silybin-loaded nanostructured lipid carriers," *Drug Delivery*, vol. 17, no. 1, pp. 11–18, 2009.

[18] Q. Lv, A. Yu, Y. Xi et al., "Development and evaluation of penciclovir-loaded solid lipid nanoparticles for topical delivery," *International Journal of Pharmaceutics*, vol. 372, no. 1-2, pp. 191–198, 2009.

[19] A. Bayat, B. Larijani, S. Ahmadian, H. E. Junginger, and M. Rafiee-Tehrani, "Preparation and characterization of insulin nanoparticles using chitosan and its quaternized derivatives," *Nanomedicine*, vol. 4, no. 2, pp. 115–120, 2008.

[20] C. F. Luo, M. Yuan, M. S. Chen, S. M. Liu, and H. Ji, "Metabolites of puerarin identified by liquid chromatography tandem mass spectrometry: similar metabolic profiles in liver and intestine of rats," *Journal of Chromatography B*, vol. 878, no. 3-4, pp. 363–370, 2010.

[21] Y. Z. Gu, W. Zhou, and G. X. Zhai, "Preparation of puerarin liposome and its oral absorption in rat," *Journal of Chinese Medicinal Materials*, vol. 30, no. 8, pp. 970–973, 2007.

[22] US Food and Drug Administration, "Guidance for Industry: Bioanalytical Method Validation," 2001, http://www.fda.gov/downloads/Drugs/GuidanceComplianceRegulatoryInformation/Guidances/UCM070107.pdf.

[23] R. S. R. Murthy and L. H. Reddy, "Poly (alkyl cyanocrylate) nanoparticles for delivery of anti-cancer drugs," in *Nanotechnology*, M. M. Amiji, Ed., pp. 251–288, CRC Press, Boca Raton, Fla, USA, 2007.

[24] B. Sarmento, D. Ferreira, F. Veiga, and A. Ribeiro, "Characterization of insulin-loaded alginate nanoparticles produced by ionotropic pre-gelation through DSC and FTIR studies," *Carbohydrate Polymers*, vol. 66, no. 1, pp. 1–7, 2006.

[25] M. Sun, Y. Gao, C. Guo et al., "Enhancement of transport of curcumin to brain in mice by poly(n-butylcyanoacrylate) nanoparticle," *Journal of Nanoparticle Research*, vol. 12, no. 8, pp. 3111–3122, 2010.

[26] M. Simeonova, G. Ivanova, V. Enchev et al., "Physicochemical characterization and in vitro behavior of daunorubicin-loaded poly(butylcyanoacrylate) nanoparticles," *Acta Biomaterialia*, vol. 5, no. 6, pp. 2109–2121, 2009.

[27] F. Ren, R. Chen, Y. Wang, Y. Sun, Y. Jiang, and G. Li, "Paclitaxel-loaded poly(n-butylcyanoacrylate) nanoparticle delivery system to overcome multidrug resistance in ovarian cancer," *Pharmaceutical Research*, vol. 28, no. 4, pp. 897–906, 2011.

[28] L. H. Reddy and R. R. Murthy, "Influence of polymerization technique and experimental variables on the particle properties and release kinetics of methotrexate from poly(butylcyanoacrylate) nanoparticles," *Acta Pharmaceutica*, vol. 54, no. 2, pp. 103–118, 2004.

[29] J. Liu, J. Zhu, Z. Du, and B. Qin, "Preparation and pharmacokinetic evaluation of Tashinone IIA solid lipid nanoparticles," *Drug Development and Industrial Pharmacy*, vol. 31, no. 6, pp. 551–556, 2005.

[30] Y. Li, W. S. Pan, S. L. Chen, H. X. Xu, D. J. Yang, and A. S. C. Chan, "Pharmacokinetic, tissue distribution, and excretion of puerarin and puerarin-phospholipid complex in rats," *Drug Development and Industrial Pharmacy*, vol. 32, no. 4, pp. 413–422, 2006.

[31] A. E. Gulyaev, S. E. Gelperina, I. N. Skidan, A. S. Antropov, G. Y. Kivman, and J. Kreuter, "Significant transport of doxorubicin into the brain with polysorbate 80- coated nanoparticles," *Pharmaceutical Research*, vol. 16, no. 10, pp. 1564–1569, 1999.

[32] N. Hussain, V. Jaitley, and A. T. Florence, "Recent advances in the understanding of uptake of microparticulates across the gastrointestinal lymphatics," *Advanced Drug Delivery Reviews*, vol. 50, no. 1-2, pp. 107–142, 2001.

[33] A. Dembri, M. J. Montisci, J. C. Gantier, H. Chacun, and G. Ponchel, "Targeting of 3′-azido 3′-deoxythymidine (AZT)-loaded poly(isohexylcyanoacrylate) nanospheres to the gastrointestinal mucosa and associated lymphoid tissues," *Pharmaceutical Research*, vol. 18, no. 4, pp. 467–473, 2001.

[34] D. Duchêne and G. Ponchel, "Bioadhesion of solid oral dosage forms, why and how?" *European Journal of Pharmaceutics and Biopharmaceutics*, vol. 44, no. 1, pp. 15–23, 1997.

[35] N. Venkatesan, K. Uchino, K. Amagase, Y. Ito, N. Shibata, and K. Takada, "Gastro-intestinal patch system for the delivery of erythropoietin," *Journal of Controlled Release*, vol. 111, no. 1-2, pp. 19–26, 2006.

Research Article

Preparation of Rhodamine B Fluorescent Poly(methacrylic acid) Coated Gelatin Nanoparticles

Zhenhai Gan,[1] Jianhui Ju,[1] Ting Zhang,[2] and Daocheng Wu[1]

[1] *Key Laboratory of Biomedical Information Engineering of Education Ministry, School of Life Science and Technology, Xi'an Jiaotong University, Xi'an 710049, China*
[2] *Scientific Research Center, The Second Affiliated Hospital, School of Medicine, Xi'an Jiaotong University, Xi'an 710004, China*

Correspondence should be addressed to Daocheng Wu, wudaocheng@mail.xjtu.edu.cn

Poly(methacrylic acid) (PMAA)-coated gelatin nanoparticles encapsulated with fluorescent dye rhodamine B were prepared by the coacervation method with the aim to retard the release of rhodamine B from the gelatin matrix. With sodium sulfate as coacervation reagent for gelatin, a kind of biopolymer with excellent biocompatibility, the formed gelatin nanoparticles were cross-linked by formaldehyde followed by the polymerization of methacrylic acid coating. The fluorescent poly(methacrylic acid) coated gelatin (FPMAAG) nanoparticles had a uniform spherical shape and a size distribution of 60 ± 5 nm. Infrared spectral analysis confirmed the formation of PMAA coating on the gelatin nanoparticles. Based on UV-Vis spectra, the loading efficiency of rhodamine B for the FPMAAG nanoparticles was 0.26 μg per mg nanoparticles. The encapsulated rhodamine B could sustain for two weeks. Favorable fluorescence property and fluorescence imaging of cells confirmed that the FPMAAG nanoparticles have promising biochemical, bioanalytical, and biomedical applications.

1. Introduction

Recently, various kinds of functional nanoparticles have been developed and widely used in material and biomedical fields such as quantum dots (QDs) [1], colloidal gold nanoparticles [2], and magnetite (Fe_3O_4) nanoparticles [3] owing to their unique characteristics of large specific surface area, homogeneous size, higher sensitivity, and better function [4, 5]. Among them, fluorescent dye-doped nanoparticles have attracted special attention for several reasons. Firstly, they can provide high intensity of the fluorescent signal for the measurement. The traditional label method could have only one or a few fluorophores to signal one bimolecular recognition event. Fortunately, the dye-doped nanoparticles might contain hundreds to thousands of dye molecules, therefore, an intense fluorescence signal that is up to 30,000 fold better than that of a single organic fluorophore [6–8]. This extreme brightness makes them especially suitable for ultrasensitive bioanalysis and negates the need for additional reagents or signal amplification steps [9]. Secondly, the dye-doped fluorophore could have favorable photostability due

to the exclusion of oxygen by matrix encapsulation. Other advantages are the good potential for surface modification with various biomolecules, and easy manufacturing process [6]. These advantages indicated that dye molecules encapsulated in the nanoparticles had high stability and retained their optical activity, thus providing a viable route for various applications with unique properties, such as biochemical and bio-analytical applications [10–13].

However, the biocompatibility of currently available fluorescent nanoparticles is not acceptable, thus limiting their applications *in vivo* [12]. One approach to develop fluorescent nanoparticles with excellent biocompatibility and easy combination with biomacromolecules are to load fluorescent dye into a suitable natural biopolymer carrier [4]. The natural biopolymer gelatin has the characteristics of excellent biocompatibility, nontoxic biodegradation *in vivo*, and readily excreted products. It also has the highly effective drug encapsulation and can be fabricated into various forms of carriers for controlled drug delivery [14]. Nevertheless, because gelatin nanoparticles consist of cross-linkage of peptide side chains, small pores or gaps exist
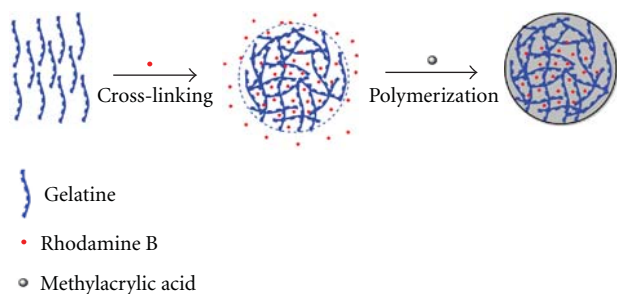
FIGURE 1: Schematic illustration of preparation for the FPMAAG nanoparticles. Rhodamine B was mixed with gelatin to form gelatin nanoparticles by coacervation and cross-liking. Methylacrylic acid was also mixed before the cross-liking. Next, the temperature of this system was raised to initiate the polymerization. The PMAA combined into the gelatin matrix and formed a coating on the surface of gelatin nanoparticles.

on the nanoparticles surface, which leads to the leakage of encapsulated materials and instability especially for water-soluble dyes or drugs [12, 13]. These limited the application for the fluorescent gelatin nanoparticles.

To overcome this problem, we design a new method for fabricating rhodamine B encapsulated fluorescent poly(methacrylic acid) coated gelatin (FPMAAG) nanoparticles. The strategy of the preparation is to mix the methacrylic acid into the gelatin solution first. After the gelatin nanoparticles were formed through the coacervation method using sodium sulfate as the coacervation reagent and are cross-linked by formaldehyde, the methacrylic acid polymerized slowly under a mild condition by the initiator. This process can lead to the formation of a coating on the surface of the gelatin nanoparticles, as illustrated in Figure 1, which will then block the small pores or gaps. The obtained FPMAAG nanoparticles show a uniform spherical shape, retardant dye releasing, and excellent absorption and fluorescence properties. The fluorescence intensity showed linearity about three orders of magnitude. The FPMAAG nanoparticles were also tested for cell imaging which showed stronger intensity for cell fluorescence imaging and prolonged dye preservation time.

2. Experimental Section

2.1. Chemicals and Materials.
Gelatin (Type B, 238–282 Bloom, isoelectric point 4.0–5.7) was purchased from Amresco Inc. (Solon, Ohio, USA). Tween-20 was obtained from Sigma-Aldrich Corporation (St. Louis, Mo. USA). Methacrylic acid was purchased from Tianjin Kermel Chemical Reagents Development Center (Tianjin, China). 2,2′-Azobis 2-methylpropionamide dihydrochloride (AIBA) was purchased from Qingdao Runxing Photoelectric Material Co. Ltd. (Qingdao, China). Rhodamine B was obtained from Sanland Chemical (Los Angeles, USA). Pancreatic cancer cell line PC-2 was purchased from Lab Animal Center, Fourth Military Medical University of China (Xi'an, China). Sodium sulfate, sodium hydroxide, isopropanol, and formaldehyde (37%) were analytical grade and used as purchased. A 14 KD dialyzer was purchased from Sino-American Biotechnology

Company. All the chemicals and solvents were used without further purification. Double-distilled water was used in entire process.

2.2. Preparation of FPMAAG Nanoparticles.
The preparation method for FPMAAG nanoparticles involved the process of coacervation with sodium sulfate, followed by phase separation using isopropanol, cross-linking by formaldehyde, and initiated polymerization by AIBA. Briefly, FPMAAG nanoparticles were obtained as follows: 10 mL distilled water containing 5 mg rhodamine B, 500 mg sodium hydroxide, and 250 mg gelatin was under continuous stirring for 10 min (300 rpm) at 50°C with a dropwise addition of 500 μL methacrylic acid. After 100 μL of Tween-20 were added as surfactant and the solution was stirred for 5 min, 20% w/w sodium sulfate solution was added dropwise to the mixture until a small amount of precipitation formed, which could be observed as the solution changed from clean to opaque. This was followed by the addition of 400 μL isopropanol for phase separation, which could lead the solution translucent. Next, 4.0 mL formaldehyde was introduced to the mixture as a cross-linking reagent. After stirring for 30 min, 50 mg AIBA was added as an initiator, and the temperature of the system was raised to 60°C. The mixture was maintained at this temperature for 6 hours with continuous stirring to produce rhodamine B encapsulated FPMAAG nanoparticles. The dark-red final product was dialyzed with double-distilled water for 3 days to remove the free rhodamine B and other unreacted reagents. The obtained FPMAAG nanoparticles were filtered through a 200 nm filtration membrane under vacuum and stored at 4°C prior to use.

2.3. Morphology Analysis and Spectra Properties.
The morphology of FPMAAG nanoparticles was evaluated through transmission electron microscopy (TEM, JEM-2100F, JOEL, Japan) observations. Size distribution of the FPMAAG nanoparticles was determined using dynamic light scattering (DLS, Malvern Zetasizer Nano ZS90, Malvern instruments Ltd., UK).

Functional groups on the surface of the FPMAAG nanoparticles were evaluated by a Fourier transform infrared spectrometer (FTIR, IR presitge-21, Japan). In a typical procedure, 5 mL of dialyzed FPMAAG nanoparticles solution was lyophilized to powder. These powder were mixed with IR-grade KBr (0.1 g), pressed into tablet form, and then the spectrum recorded. Pure gelatin and MAA were also measured for comparison.

Fluorescent spectra were measured by FluoroMax-4 (Horiba Jobin Yvon, NJ, USA) with excitation and emission slits both set to 2 nm. UV-Vis absorption spectra were measured by T-6 UV-Vis spectrophotometers (Purkinje general, Beijing, China) using double-distilled water as blank. The loading efficiency of rhodamine B was the amount of encapsulated rhodamine B in the FPMAAG nanoparticles, which was determined by UV-Vis and fluorescence measurements using a series of standard rhodamine B solutions as calibration.

The retardant release of the FPMAAG nanoparticles was assessed by dynamic dialysis method as reported [14]. Briefly,

the newly prepared FPMAAG nanoparticles mixture solution containing 5.0 mg rhodamine B was placed into a dialysis bag and placed in 1000 mL of double-distilled water with magnetic stirring at 200 rpm and 25°C. At predetermined time intervals, 1.5 mL of release medium was withdrawn, and the rhodamine B content was determined by UV-Vis absorption spectra at wavelength of 555 nm. The gelatin nanoparticles without PMAA coating and the PMAA system without the addition of gelatin were also measured for comparisons.

To examine the quantitative potential of the FPMAAG nanoparticles, serial dilution of FPMAAG solutions was prepared with various concentrations of encapsulated rhodamine B which covered three orders of magnitude, from $4.0 \, \text{ng} \cdot \text{mL}^{-1}$ to $4.0 \, \mu\text{g} \cdot \text{mL}^{-1}$. Fluorescent spectra measurements of these solutions was carried out under the same condition as mentioned above. The peak fluorescence intensities were plotted against the concentration of encapsulated rhodamine B to show as a calibration curve. Linear range and linearity of the calibration curve were discussed.

2.4. Fluorescence Imaging of Cells. Pancreatic cancer cell line PC-2 were incubated in 100 mL growth buffer as adherent cells according to the manufacturer's instructions and at 37°C in an atmosphere containing $50 \, \text{mL} \cdot \text{L}^{-1}$ CO_2 and $950 \, \text{mL} \cdot \text{L}^{-1}$ with a relative humidity until labeling. Then the cells were incubated for 15 min at room temperature, washed 3 times with cold PBS ($137 \, \text{mmol} \cdot \text{L}^{-1}$ NaCl, $2.7 \, \text{mmol} \cdot \text{L}^{-1}$ KCl, $10 \, \text{mmol} \cdot \text{L}^{-1}$ Na_2HPO_4, $1.8 \, \text{mmol} \cdot \text{L}^{-1}$ KH_2PO_4, pH 7.4), and incubated with the FPMAAG nanoparticles ($10.0 \, \text{mg} \cdot \text{mL}^{-1}$ in 5.0 mL buffer solution) for 45 min at room temperature. To demonstrate the cells label results of FPMAAG nanoparticles, fluorescence images of the cells were observed by fluorescence microscope (Olympus CX41, Japan) excited by 520 nm laser (Olympus U-RFLT50, Japan) at room temperature. The direct incubation of rhodamine B and cells were carried out as controls.

3. Results and Discussions

3.1. Preparation and Morphology of FPMAAG Nanoparticles. In the preparation process, methacrylic acid was chosen because it could form a polymeric layer to retard the release of encapsulated drug in a hydrogel drug delivery system [15]. Vishal Gupta et al. reported that by adding a PMAA system to the gelatin polymers, the formation of a Gelatin-PMAA interpenetrating polymer hydrogel system could retard the drug release at an acidic pH [16]. In our study, the FPMAAG nanoparticles were prepared by coacervation and phase separation method, the PMAA could form a protection layer at the surface of gelatin nanoparticles. The preparation was carried out at an alkaline pH, which was required by the cross-linking reaction of gelatin nanoparticles using formaldehyde as the cross-linking reagent. Consequently, after dialysis to remove the free rhodamine B and other unreacted reagents, and using under physiological conditions, the surrounding solution of the FPMAAG nanoparticles was changed to a neutral pH which could retard the release of encapsulated rhodamine B from the nanoparticles. The other advantage

of adding methacrylic acid to the gelatin mixture was the increased solubility of gelatin at the preparation step, which can reduce preparation time and results in a narrow range of size distribution of the FPMAAG nanoparticles.

For the preparation of Gelatin-PMAA nanoparticles, a higher reaction temperature was used in this study compared to the previous research of our group [17]. Jahanshahi et al. discussed that at low temperature, gelatin nanoparticles are not easy to form because gelatin is in a highly viscous gel formation at that condition. At a temperature above 50°C, the gelatin chain could uncoil sufficiently to be in a better condition for nanoparticles formation [18]. Meanwhile, a higher temperature could reduce the time for the cross-linking of gelatin to form nanoparticles and for the polymerization of the PMAA coating layer. On the other hand, if the reaction temperature is too high, the organic dye encapsulated in the nanoparticles could be decomposed due to some side reactions. Given all these concerns, the reaction temperature in the present study was thus set to 50°C at the mixture step and raised to 60°C for the polymerization. Under this condition, the polymerization could be initiated by the AIBA, and the formation of PMAA will be completed in 6 hours.

In the preparation process of FPMAAG nanoparticles, formaldehyde was used as a cross-linking reagent rather than glutaraldehyde which was usually used in reported papers [17, 19], because glutaraldehyde could form a dark-yellow solution with amino acid when the temperature was above 50°C. This colored solution could interfere with the absorption and fluorescence measurement of FPMAAG nanoparticles. Formaldehyde is known to react with several peptide side chain groups, especially lysine residues along the gelatin chain in order to form a methylene bridge or a cross-linkage [20]. With this cross-linking reaction, the final FPMAAG nanoparticle product could remain transparent, which could avoid the effect of the yellow-colored byproduct of glutaraldehyde on the absorption and fluorescence characteristics of the encapsulated rhodamine B. The optimized pH range for the cross-linking of formaldehyde is 8-9. Thus, the acidity of the reaction should be carefully adjusted in the mixing step with enough sodium hydroxide to neutralize the added methacrylic acid.

The morphology and size distribution of the FPMAAG nanoparticles was examined by TEM (Figure 2) and size analyzer (Figure 3). The FPMAAG nanoparticles were spherically shaped with a diameter of approximately 60 ± 5 nm, which was consistent with the results from the previous study of our group (46 nm) [17]. The increased size could attribute to the formation of PMAA coating layer. From Figure 2, the dark core of gelatin nanoparticles with gray shell of PMAA coating were also observed. From literature searching, the available reported preparation methods for gelatin hydrogels were in the formation of a piece of sheet with a thickness in the scale of millimeters [16], or a nanosphere with a diameter around the micrometers scale [21]. For the preparation of gelatin particles in nanometer scales, Gupta et al. prepared a series of gelatin nanoparticles measuring 37 nm by the reverse micelle method [22]. Another commonly used method was the addition of acetone to the gelatin aqueous
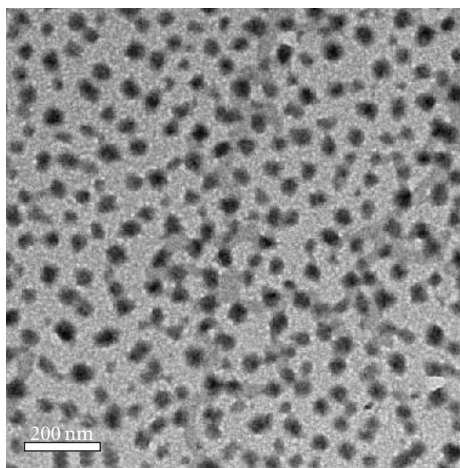
FIGURE 2: TEM image of PMAA coated gelatin nanoparticles.

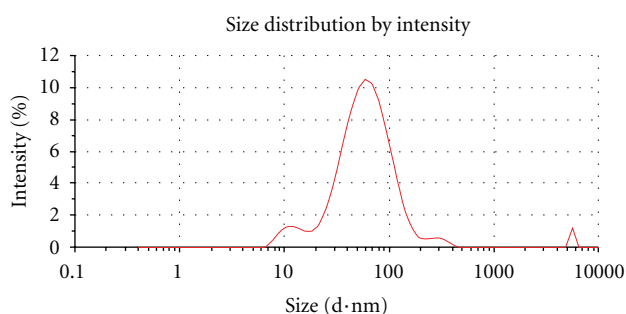Size distribution by intensity

FIGURE 3: Size distribution of FPMAAG nanoparticles.

solution to form the precipitation of gelatin nanoparticles with a diameter of about 50 nm [18, 21]. In our coacervation method, the diameters of the gelatin nanoparticles were controlled around 60 nm by the gelatin concentration and the amount of added inorganic coacervation reagent. With higher gelatin concentration and more sodium sulfate added, the diameter of the nanoparticles will increase. On the other hand, if a lower stirring velocity was used, it would cause the increase of nanoparticles diameter. Meanwhile, a higher temperature or longer reaction time for the cross-linking would also increase the nanoparticles diameter. With many attempts, the optical conditions for the preparation of FPMAAG nanoparticles were determined as mentioned in the experimental section. In addition, there was no hydrophobic solvent used to avoid the washing step concerning the biochemical applications.

3.2. IR Spectra of FPMAAG Nanoparticles. Figure 4 shows the IR spectra of the FPMAAG nanoparticles powder prepared by lyophilizing the dialyzed PMAAG nanoparticles blank solution which had not encapsulated any rhodamine B. To make a clear comparison, the IR spectra of gelatin and methacrylic acid were also presented in the same figure. The transparencies of the three spectra were normalized and separated for the convenience of comparison, so the Y-axis was set in arbitrary unit (a.u.). From the IR spectra, the moderate stretching vibration of the N–H bond can be observed

around $3300 \, \mathrm{nm^{-1}}$ which revealed the existence of amide in the gelatin compared to the IR spectra of gelatin [23]. The strong absorption at $2900 \, \mathrm{nm^{-1}}$ is due to the stretching vibration of the C-H bond in the PMAA coating of the FPMAAG nanoparticles. Strong absorption at $1650 \, \mathrm{nm^{-1}}$ is the evidence that carbonyl group exists in the FPMAAG nanoparticles, which were derived from the carboxyl group of methacrylic acid. From the attribution of IR peaks of FPMAAG nanoparticles between 1000 and $1500 \, \mathrm{nm^{-1}}$ to the IR spectra of either gelatin or methacrylic acid, a conclusion regarding the formation of PMAA combining into gelatin matrix could be drawn.

3.3. Absorption Spectra of FPMAAG Nanoparticles. UV-Vis absorption and fluorescence emission spectra of the FPMAAG nanoparticles solution are shown in Figure 5. The fluorescence spectrum was normalized to the same level of absorption spectrum in the same figure for a clear comparison. The absorption and normalized fluorescence emission spectra of rhodamine B aqueous solution ($0.8 \, \mu\mathrm{g \cdot mL^{-1}}$) are also shown in the same figure. The absorption and emission peak of encapsulated rhodamine B was found to have no significant change compared to the rhodamine B dissolved in water with an absorption peak at 555 nm and an emission peak at 575 nm, which were mirror images of each other. This result meant that the formed FPMAAG nanoparticles are transparent and have no effect on the optical behavior of the encapsulated organic dye.

From the absorbance of UV-Vis spectra, the total amount of encapsulated rhodamine B in the FPMAAG nanoparticles could be calculated as $82 \pm 5 \, \mu\mathrm{g}$ after three days of dialysis. It was assumed that the molar extinction coefficient (ε) of encapsulated rhodamine B had no change compared with the rhodamine B dissolved in distilled water. Thus, a series of rhodamine B aqueous solution with different concentrations were used as calibration. On the other hand, a certain volume of FPMAAG nanoparticles solution was lyophilized, and the powder was weighed. The total mass of the FPMAAG nanoparticles was 310 mg. Thus, the rhodamine B loading efficiency of the FPMAAG nanoparticles was $0.26 \, \mu\mathrm{g}$ per mg nanoparticles.

3.4. Fluorescence Spectra of FPMAAG Nanoparticles. Based on the fluorescence intensity of fluorescent emission in Figure 5, we also calculated that the amount of encapsulated rhodamine B in the FPMAAG nanoparticles was $65 \pm 5 \, \mu\mathrm{g}$ after three days of dialysis. This was consistent with the amount calculated by UV-Vis absorption measurement. The pH effect on the fluorescence intensity of FPMAAG nanoparticles was carried out by dilute same amounts of FPMAAG nanoparticles solution to the same volume with different PBS buffer (pH = 6.0, 7.0, 8.0, and 9.0, resp.). The fluorescence intensities of these serial solutions had no significant differences (data not shown). The same amount of FPMAAG nanoparticles were also diluted with different KCl solution (concentration of KCl were 0.01, 0.02, 0.05, 0.1, and 0.2 M, resp.) to verify the effect of ionic strength to the fluorescence intensity. The fluorescence intensities kept at the same level with various ionic strengths (data not shown).
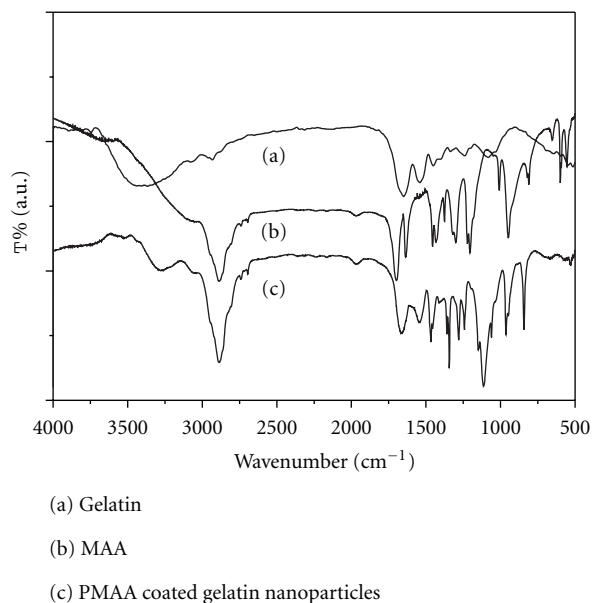
(a) Gelatin

(b) MAA

(c) PMAA coated gelatin nanoparticles

FIGURE 4: IR spectra of gelatin (a), methacrylic acid (b), and PMAA coated gelatin nanoparticles (c). The transparences of the three spectra were normalized and separated for the convenience of comparison.

These results revealed that the encapsulated rhodamine B in the FPMAAG nanoparticles still had strong emission intensity and high fluorescent yield, which means that the nanoparticles were transparent for the encapsulated dye to perform its optical behavior. Meanwhile, the nanoparticles could provide a suitable environment for the dye molecules to be concentrated at a certain location with high emission efficiency. The protection and concentration of rhodamine B provided by the nanoparticles could result in enhanced emission intensity with lower dye concentration compared to the rhodamine B solution, which could be used for higher sensitive fluorescence tracing in the future.

3.5. Fluorescence Calibration Curve Fitting. To evaluate the possibility for quantitative bioanalytical applications, linear relationships between concentrations of FPMAAG nanoparticles and fluorescence emission intensity were examined. From the fluorescence intensities of series diluted FPMAAG nanoparticles solutions, a linear curve fitting was obtained as shown in Figure 6. The linear relationships between fluorescence intensity and concentration of encapsulated rhodamine B in FPMAAG nanoparticles were confirmed ranging from $4.0 \, \text{ng·mL}^{-1}$ to $0.4 \, \mu\text{g·mL}^{-1}$ with the linear regression equations: $I_F = 1.29 \times 10^7 C + 5.68 \times 10^4$ and correlation coefficient $R^2 = 0.9990$, where I_F and C referred to fluorescence intensity and concentration of rhodamine B encapsulated in FPMAAG nanoparticles, respectively. The fluorescence intensities obtained at the concentration from 0.8–$4.0 \, \mu\text{g·mL}^{-1}$ were not in the linear relationship because the fluorescence emissions were too strong which were out of the signal response range of the fluorescence spectrometer. By these attempts, the wide linear range that covers three orders of magnitude could be confirmed. The rhodamine
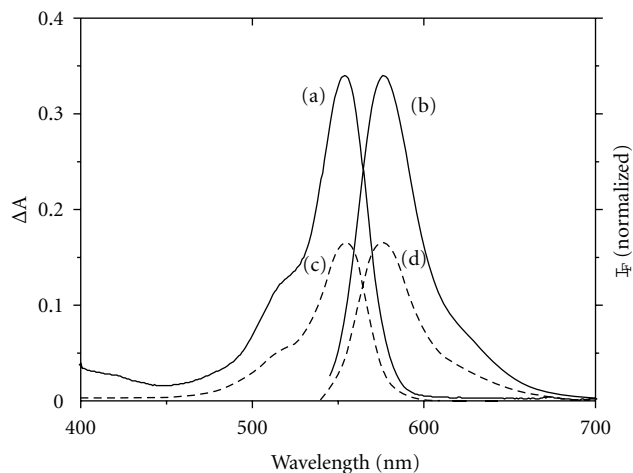

FIGURE 5: Absorption (a) and fluorescence (b) spectra of FPMAAG nanoparticles compared with absorption (c) and fluorescence (d) spectra of rhodamine B aqueous solution ($0.8 \, \mu\text{g·mL}^{-1}$). The intensity of fluorescence spectra were normalized to make a clear comparison.

B-doped silica nanoparticles for the quantitative determination of aflatoxin B_1 using competitive-type fluorescence immunoassay by Tang et al. have been reported recently [9]. The linear response range was only one order of magnitude (0.5–$7 \, \text{ng·mL}^{-1}$ for aflatoxin B_1). Another research using rhodamine B adsorbed golden nanoparticles for the quantitative detection of mercury had a linear correlation the range of 15–$250 \, \text{nM}$ [24]. By the comparison of our FPMAAG nanoparticles system with the reported dye-doped nanoparticles, a more accurate and sensitive fluorescence bioanalytical method could be established in the future.

3.6. Retardant Release of Rhodamine B. To study the retardant release of the FPMAAG nanoparticles, the dynamic dialysis was carried out for the measurement of release of encapsulated rhodamine B. The results were shown in Figure 7. After the beginning of the dynamic dialysis, the rhodamine B contents in the release medium were increased dramatically within 30 hours for all three solutions. After that, the release of rhodamine B in FPMAAG nanoparticles was slowed and saturated after 60 hours with a release percentage of 60%. As comparison, the release profile of PMAA solution in the absence of gelatin showed a free release of rhodamine B, which indicated that only the polymerization of MAA could not hold rhodamine B. The sample of gelatin nanopartilces without PMAA coating showed a faster release of encapsulated rhodamine B with a release percentage around 80% after 60 hours dialysis. The fast release at the beginning of dynamic dialysis experiment for FPMAAG nanoparticles could be due to the release of the free rhodamine B in the mixture. After 40 hours dialysis, the increased rhodamine B content in the release medium was contributed to the release of encapsulated rhodamine B, which showed a retardant release property compared to the gelatin nanoparticles without PMAA coating.
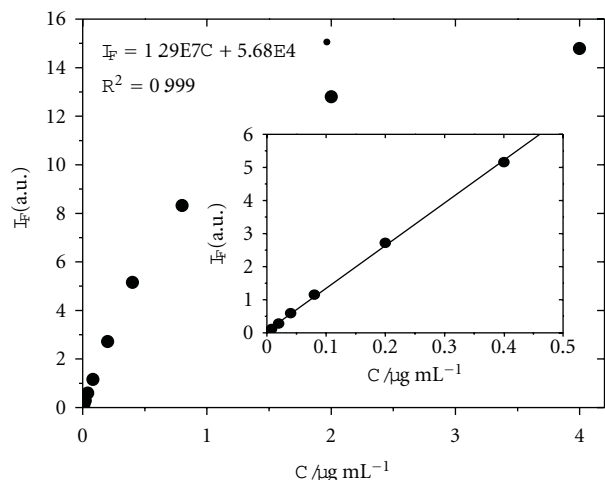
FIGURE 6: Calibration curve of FPMAAG nanoparticles solution. The concentration of encapsulated rhodamine B ranged from $4.0\ \mathrm{ng\cdot mL^{-1}}$ to $4.0\ \mu\mathrm{g\cdot mL^{-1}}$. Insert was the linear curve fitting from $4.0\ \mathrm{ng\cdot mL^{-1}}$ to $0.4\ \mu\mathrm{g\cdot mL^{-1}}$.
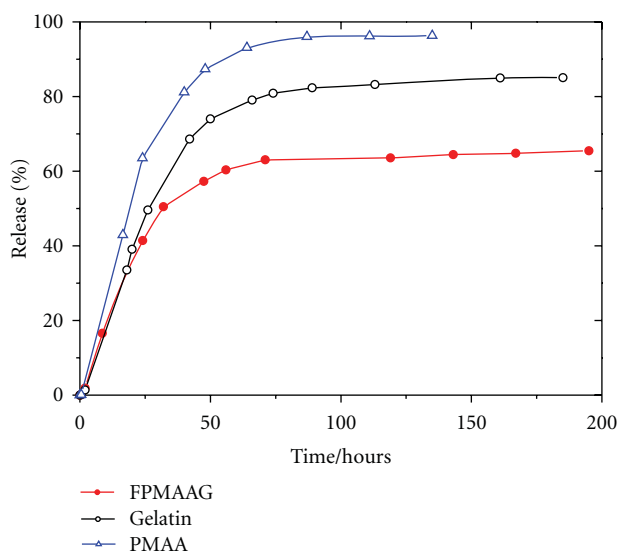

FIGURE 7: Dynamic dialysis release curve of FPMAAG nanoparticles (solid circle), gelatin nanoparticles without PMAA coating (opened circle), and PMAA system in the absence of gelatin (opened triangle). Double-distilled water was used as dialysis medium.

We continued the dialysis after the saturated rhodamine B content was reached. The pink color of the PFMAAG nanoparticles solution did not vanish until after two weeks had passed. As comparison, the pink the rhodamine B encapsulated gelatin nanoparticles without PMAA coating disappeared within 3 days. It was reported that the release of encapsulated medicine in gelatin nanoparticles would be completed in 100 hours [14, 22, 25–28], while our FPMAAG nanoparticles could be maintained at a certain concentration after six days of dialysis. The retardant dye release property indicates that PMAA, which combined into the gelatin matrix and formed a coating layer on the
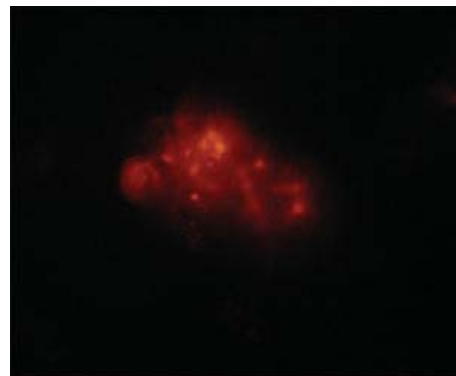
FIGURE 8: Fluorescence imaging of pancreatic cancer cell line PC-2 incubated with FPMAAG nanoparticles. Excitation wavelength was set at 520 nm.

gelatin nanoparticles, had a protective effect because it can block the pores on the surface of gelatin nanoparticles and thus delay the release of encapsulated rhodamine B. One of the reasons for the retardance could be the methyl groups of the methacrylic acid, which could form a branch structure after polymerization to block the release of rhodamine B encapsulated in the gelatin nanoparticles. Another reason could be the combination of PMAA into gelatin matrix that results in a transfer barrier between the interfaces to retard the release of rhodamine B. Obtaining a more detailed mechanism and investigating the controlled release of FPMAAG nanoparticles will be our next goal. The elongated release time of the FPMAAG nanoparticles could be used for biochemical and bioanalytical applications in the future.

3.7. Fluorescence Imaging of Cells. The fluorescence imaging of pancreatic cancer cell line PC-2 was shown in **Figure 8**. After 45 min of incubation, the fluorescence imaging of pancreatic cancer cells were observed. It suggested that FPMAAG nanoparticles could penetrate the membrane of cell and be endocytosed easily. This property of FPMAAG nanoparticles was resulted from the small size of the nanoparticles. It was also derived from the excellent biocompatibility of gelatin and PMAA, which made the nanoparticles could not be rejected by the cells.

From the fluorescence imaging, the FPMAAG nanoparticles could be observed with strong red emission, which were the aggregation of nanoparticles. The FPMAAG nanoparticles didn't distribute uniformly in the cell that could be attributed to the different affinity of the organelle to the FPMAAG nanoparticles. Additionally, the strong emission under the fluorescence microscope could sustain for 15 hours compared with 3 hours for the direct incubation of rhodamine B and cells. The easy endocytosis and sustained retention time suggested that FPMAAG nanoparticles were an excellent candidate for cell imaging and targeting [29–32]. After cross-liking with ligand, the FPMAAG could be used as promising a targeting and therapy label for specific receptor in cells in our future research.

4. Conclusions

In summary, rhodamine B encapsulated PMAA coated gelatin nanoparticles were prepared using an improved coacervation and phase separation method with formaldehyde as a cross-linking reagent at 60°C. The polymerization of methacrylic acid was initiated after the cross-linking. IR spectra confirmed that poly(methacrylic acid) combining into gelatin matrix which could block the pores of gelatin nanoparticles. From TEM image, the diameter of FPMAAG nanoparticles was measured. The coating of PMAA layer on the surface of gelatin nanoparticles was also confirmed. The UV-Vis and fluorescence measurements showed that the encapsulated rhodamine B could have excellent spectral properties. The FPMAAG nanoparticles were stable and the encapsulated rhodamine B was released at a slower rate compared with the rates of gelatin nanoparticles without PMAA coating. The linear relationships between fluorescence intensity and nanoparticles concentration were over three orders of magnitude. In the fluorescence imaging of pancreatic cancer cell line PC-2, the FPMAAG nanoparticles also showed excellent biocompatibility and sustained retention time. The results indicate a high fluorescent yield of the FPMAAG nanoparticles thus; it could provide a promising functional nanoparticles material for biochemical and bioanalytical applications.

Acknowledgment

References

[1] I. L. Medintz, H. T. Uyeda, E. R. Goldman, and H. Mattoussi, "Quantum dot bioconjugates for imaging, labelling and sensing," *Nature Materials*, vol. 4, no. 6, pp. 435–446, 2005.

[2] M. C. Daniel and D. Astruc, "Gold nanoparticles: assembly, supramolecular chemistry, quantum-size-related properties, and applications toward biology, catalysis, and nanotechnology," *Chemical Reviews*, vol. 104, no. 1, pp. 293–346, 2004.

[3] Y. W. Jun, J. W. Seo, and J. Cheon, "Nanoscaling laws of magnetic nanoparticles and their applicabilities in biomedical sciences," *Accounts of Chemical Research*, vol. 41, no. 2, pp. 179–189, 2008.

[4] S. Sushmitha, K. Joydip, and C. K. Subhas, "Biopolymeric nanoparticles," *Science and Technology of Advanced Materials*, vol. 11, no. 1, article 014104, 2010.

[5] J. Kim, Y. Piao, and T. Hyeon, "Multifunctional nanostructured materials for multimodal imaging, and simultaneous imaging and therapy," *Chemical Society Reviews*, vol. 38, no. 2, pp. 372–390, 2009.

[6] L. Wang, K. Wang, S. Santra et al., "Watching silica nanoparticles glow in the biological world," *Analytical Chemistry*, vol. 78, no. 3, pp. 646–654, 2006.

[7] W. Lian, S. A. Litherland, H. Badrane et al., "Ultrasensitive detection of biomolecules with fluorescent dye-doped nanoparticles," *Analytical Biochemistry*, vol. 334, no. 1, pp. 135–144, 2004.

[8] M. Nakamura, M. Shono, and K. Ishimura, "Synthesis, characterization, and biological applications of multifluorescent silica nanoparticles," *Analytical Chemistry*, vol. 79, no. 17, pp. 6507–6514, 2007.

[9] D. Tang, Y. Yu, R. Niessner, M. Miró, and D. Knopp, "Magnetic bead-based fluorescence immunoassay for aflatoxin B1 in food using biofunctionalized rhodamine B-doped silica nanoparticles," *Analyst*, vol. 135, no. 10, pp. 2661–2667, 2010.

[10] W. Yang, C. G. Zhang, H. Y. Qu, H. H. Yang, and J. G. Xu, "Novel fluorescent silica nanoparticle probe for ultrasensitive immunoassays," *Analytica Chimica Acta*, vol. 503, no. 2, pp. 163–169, 2004.

[11] Z. Tian, W. Wu, and A. D. Q. Li, "Photoswitchable fluorescent nanoparticles: preparation, properties and applications," *ChemPhysChem*, vol. 10, no. 15, pp. 2577–2591, 2009.

[12] F. Wang, W. B. Tan, Y. Zhang, X. Fan, and M. Wang, "Luminescent nanomaterials for biological labelling," *Nanotechnology*, vol. 17, no. 1, pp. R1–R13, 2006.

[13] A. Burns, H. Ow, and U. Wiesner, "Fluorescent core-shell silica nanoparticles: towards "lab on a particle" architectures for nanobiotechnology," *Chemical Society Reviews*, vol. 35, no. 11, pp. 1028–1042, 2006.

[14] G. K. Saraogi, P. Gupta, U. D. Gupta, N. K. Jain, and G. P. Agrawal, "Gelatin nanocarriers as potential vectors for effective management of tuberculosis," *International Journal of Pharmaceutics*, vol. 385, no. 1-2, pp. 143–149, 2010.

[15] N. Zhang and W. Knoll, "Thermally responsive hydrogel films studied by surface plasmon diffraction," *Analytical Chemistry*, vol. 81, no. 7, pp. 2611–2617, 2009.

[16] N. Vishal Gupta, C. S. Satish, and H. G. Shivakumar, "Preparation and characterization of gelatin-poly(methacrylic acid) interpenetrating polymeric network hydrogels as a pH-sensitive delivery system for glipizide," *Indian Journal of Pharmaceutical Sciences*, vol. 69, no. 1, pp. 64–68, 2007.

[17] D. Wu and M. Wan, "A novel fluoride anion modified gelatin nanogel system for ultrasound-triggered drug release," *Journal of Pharmacy & Pharmaceutical Sciences*, vol. 11, no. 4, pp. 32–45, 2008.

[18] M. Jahanshahi, M. H. Sanati, S. Hajizadeh, and Z. Babaei, "Gelatin nanoparticle fabrication and optimization of the particle size," *Physica Status Solidi A*, vol. 205, no. 12, pp. 2898–2902, 2008.

[19] Z. Lu, T. K. Yeh, M. Tsai, J. L. S. Au, and M. G. Wientjes, "Paclitaxel-loaded gelatin nanoparticles for intravesical bladder cancer therapy," *Clinical Cancer Research*, vol. 10, no. 22, pp. 7677–7684, 2004.

[20] M. Madaghiele, A. Piccinno, A. Saponaro, A. Maffezzoli, and A. Sannino, "Collagen- and gelatine-based films sealing vascular prostheses: evaluation of the degree of crosslinking for optimal blood impermeability," *Journal of Materials Science: Materials in Medicine*, vol. 20, no. 10, pp. 1979–1989, 2009.

[21] C. J. Coester, K. Langer, H. Von Briesen, and J. Kreuter, "Gelatin nanoparticles by two step desolvation—a new preparation method, surface modifications and cell uptake," *Journal of Microencapsulation*, vol. 17, no. 2, pp. 187–193, 2000.

[22] A. K. Gupta, M. Gupta, S. J. Yarwood, and A. S. G. Curtis, "Effect of cellular uptake of gelatin nanoparticles on adhesion, morphology and cytoskeleton organisation of human fibroblasts," *Journal of Controlled Release*, vol. 95, no. 2, pp. 197–207, 2004.

[23] Z. Dong, Q. Wang, and Y. Du, "Alginate/gelatin blend films and their properties for drug controlled release," *Journal of Membrane Science*, vol. 280, no. 1-2, pp. 37–44, 2006.

[24] C. C. Huang and H. T. Chang, "Selective gold-nanoparticle-based "turn-on" fluorescent sensors for detection of mercury(II) in aqueous solution," *Analytical Chemistry*, vol. 78, no. 24, pp. 8332–8338, 2006.

[25] G. Kaul and M. Amiji, "Long-circulating poly(ethylene glycol)-modified gelatin nanoparticles for intracellular delivery," *Pharmaceutical Research*, vol. 19, no. 7, pp. 1061–1067, 2002.

[26] T. G. Shutava, S. S. Balkundi, P. Vangala et al., "Layer-by-layer-coated gelatin nanoparticles as a vehicle for delivery of natural polyphenols," *ACS Nano*, vol. 3, no. 7, pp. 1877–1885, 2009.

[27] M. A. Vandelli, M. Romagnoli, A. Monti et al., "Microwave-treated gelatin microspheres as drug delivery system," *Journal of Controlled Release*, vol. 96, no. 1, pp. 67–84, 2004.

[28] J. Wang, Y. Tabata, and K. Morimoto, "Aminated gelatin microspheres as a nasal delivery system for peptide drugs: evaluation of in vitro release and in vivo insulin absorption in rats," *Journal of Controlled Release*, vol. 113, no. 1, pp. 31–37, 2006.

[29] C. Chotimarkorn, R. Nagasaka, H. Ushio, T. Ohshima, and S. Matsunaga, "Development of novel fluorescent probe 3-perylene diphenylphosphine for determination of lipid hydroperoxide with fluorescent image analysis," *Biochemical and Biophysical Research Communications*, vol. 338, no. 2, pp. 1222–1228, 2005.

[30] D. Varghai, K. Azizuddin, Y. Ahmad, N. L. Oleinick, and D. Dean, "Fluorescence of Pc 4 in U87 cells following photodynamic therapy," in *Photonic Therapeutics and Diagnostics III*, vol. 6424, article 64242A of *Proceedings of SPIE*, San Jose, Calif, USA, January 2007.

[31] E. Q. Song, G. P. Wang, H. Y. Xie et al., "Visual recognition and efficient isolation of apoptotic cells with fluorescent-magnetic-biotargeting multifunctional nanospheres," *Clinical Chemistry*, vol. 53, no. 12, pp. 2177–2185, 2007.

[32] M. Goutayer, S. Dufort, V. Josserand et al., "Tumor targeting of functionalized lipid nanoparticles: assessment by in vivo fluorescence imaging," *European Journal of Pharmaceutics and Biopharmaceutics*, vol. 75, no. 2, pp. 137–147, 2010.

Review Article

Nanoparticles Escaping RES and Endosome: Challenges for siRNA Delivery for Cancer Therapy

Shutao Guo and Leaf Huang

Division of Molecular Pharmaceutics, School of Pharmacy, University of North Carolina, Chapel Hill, NC 27599, USA

Correspondence should be addressed to Leaf Huang, leafh@email.unc.edu

Small interfering RNAs (siRNAs) technology has emerged as a promising potential treatment for viral, genetic diseases and cancers. Despite the powerful therapeutic potential of siRNA, there are challenges for developing efficient and specific delivery systems for systemic administration. There are extracellular and intracellular barriers for nanoparticle-mediated delivery. First, nanoparticles are rapidly cleared from the circulation by the reticuloendothelial system (RES). Second, following their cellular uptake, nanoparticles are trapped in endosomes/lysosomes, where siRNA would be degraded by enzymes. In this review, we describe strategies for grafting a polyethylene glycol (PEG) brush to the nanoparticles for evading RES, such that they may effectively accumulate in the tumor by the enhanced permeability and retention (EPR) effect. PEG has to shed from the nanoparticles to allow close interaction with the tumor cells. Current strategies for facilitating endosome escape, such as ion pair formation, "proton sponge effect", destabilizing endosome membrane, and hydrophobic modification of the vector, are discussed.

1. Introduction

RNA interference was firstly discovered by Fire et al. in 1998 [1], and this technology has emerged as a powerful tool for analyzing gene function and inhibiting gene expression in cell culture and in animal models. Small interfering RNA (siRNA), resulting from the cleavage of longer double stranded RNA precursors by endonuclease dicer, could enter the RNA-induced silencing complex, where the complementary mRNA is degraded and as a result the expression of the corresponding protein is reduced [2, 3]. However, systemic delivery of naked siRNA is limited by rapid blood clearance, RNA degradation, and poor cellular penetration due to the large molecular weight and negative charge of siRNA.

The success in the application of siRNA for cancer therapy is highly dependent on the development of vectors which are nontoxic and can selectively and efficiently deliver siRNA into the specific tissue in vivo [4, 5]. Gene therapy vectors can be generally divided into two categories: viral vectors and nonviral vectors. Viral vectors are highly efficient, but the drawbacks of high cost, safety concerns and immunity significantly limit their application. To over the limitations of viral vectors, nonviral vectors have been widely developed as alter-

natives. The majority of nonviral vectors are based on synthetic polymers and lipids. To date, these synthetic vectors are still relatively less efficient than viral vectors. It is a result of many barriers, extracellular as well as intracellular, encountered between the site of administration and the nucleus or cytoplasm of the target cells for DNA or siRNA delivery [5–8]. Extracellular barriers include condensing nucleic acid into stable complexes which would not be deassembled in the solution and blood, maintaining stability and circulation of nanoparticles in the blood stream, penetrating the tissue, and specific binding to the target cells of interest. Following internalization, gene delivery vectors are challenged by intracellular barriers, including endosome entrapment and nucleic acid unpacking from vectors. Among these barriers, escaping the reticuloendothelial system (RES) uptake and endosome will be focused in this review.

2. Strategies for Nanoparticles Escaping RES Uptake

The applications of siRNA in vitro and in vivo are hampered by their high molecular weight, negative charge, low stability,

and rapid blood clearance [9–11]. Approaches to overcome these drawbacks have relied on nonviral siRNA carriers based on cationic polymers or lipids. Cationic vectors suffer from fast blood clearance by the RES. Nanoparticle size and surface charge are the two major properties strongly influencing the clearance [12, 13]. Nanoparticle with the size of 100–200 nm would readily accumulate and retain in the tumor interstitium because of the enhanced permeability and retention (EPR) effect [14–17], which is further facilitated by the lack of a draining lymphatic system in tumor tissues. The success of stealth nanoparticles for tumor therapy is highly dependent on reduced RES uptake and prolonged circulation time in the blood.

To prolong the circulation time, coating by polyethylene glycol (PEG), or PEGylation, is the most effective method to reduce protein adsorption in vivo and thereby helps to avoid the RES system [18–22]. Although there are successful attempts to develop alternative polymers to PEG, such as poloxamer [23, 24], polyvinyl alcohol [25, 26], poly(amino acid)s [27], and polysaccharide [28–31], PEG is still the most widely used material. PEG-lipid (such as PEG-DSPE) is usually inserted into liposomes to form a hydrated layer on the liposome surface. There are two kinds of conformation for PEG covering the surface of nanoparticles. For PEG-DSPE-stabilized liposomes, PEG is ready to take mushroom conformation at low degree of PEGylation and will shift to brush conformation as the content of PEG-DSPE is increased to certain levels. The brush mode is the ideal configuration for protecting nanoparticles from serum absorption. However, due to the detergent-like property of PEG-lipid, it is difficult to form stable liposomes with high content of PEG-lipid. To tackle this problem, Li and Huang [32, 33] developed PEGylated liposome-polycation-DNA (LPD) nanoparticles by inserting PEG-DSPE after formation of LPD nanoparticles. Negative and nanosized cores were formed by condensing DNA with protamine, which then bind cationic lipids to form DNA/protamine-encapsulated liposomes. The DNA/protamine cores played an important role to stabilize liposomes by electrostatic interaction. Therefore, LPD nanoparticles were still stable, even if 10.6% (by molar) of PEG-lipid was incorporated into the LPD nanoparticles [32, 33]. Stealth LPD nanoparticles were characterized by lower liver uptake through evasion of RES uptake and efficient delivery of siRNA to tumors [34, 35]. After 4 hours of i.v. injection, RES uptake of LPD nanoparticles was as low as 5–15% of the injected dose, and 30% of the dose accumulated in the tumor. It was hypothesized that the brushed PEG shed overtime, resulting in reducing the PEG content in the nanoparticles and further blood clearance [33, 36–38]. Pharmacokinetics (PK) data showing a rapid distribution phase and not much prolonged circulation time of the injected particles is consistent with the hypothesis. PEG shedding, which is not well understood and requires further study, is important for endosome escape and cargo discharge after the nanoparticle enters into the cell by endocytosis. This aspect will be discussed in Section 3.

To overcome the PEG dilemma, several strategies are designed. The first strategy is to modify the nanoparticles with tumor-specific ligand to enhance intracellular uptake.

Among the ligands, iron-saturated transferrin (Tf) has been widely investigated to target tumor cells overexpressing Tf-receptors [39–43]. Ogris et al. [40] demonstrated that Tf-bearing PEG-polyethyleneimine (PEI) could selectively deliver plasmid into tumor, leading to 100-fold higher gene expression in tumor cells than that of other tissues. Bartlett et al. [10] prepared siRNA-containing, Tf-targeted nanoparticles. Although Tf could not enhance the accumulation of nanoparticles in the tumor in mice, it facilitated cell uptake of nanoparticles, thereby improved gene knockdown efficiency. Very recently, they performed the first gene inhibition experiment by administration of Tf-targeted, siRNA-containing cyclodextrin containing polycation (CDP) nanoparticles in humans [42] and showed that siRNA successfully silenced the target gene in both mRNA and protein levels. In addition, several other ligands, such as RGD [44, 45], CNGRC [46], anisamide [35, 45, 47], and folate [48, 49], have also been applied to target specific tumor delivery in vivo.

Ligand-mediated nanoparticles are usually internalized into tumor cells by receptor-mediated endocytosis and finally taken up into endosomal/lysosomal vesicles. Therefore, the second strategy is to incorporate sheddable PEG to facilitate drug escape from endosomal/lysosomal vesicles. Exploiting the microenvironment of tumor and acidic nature of endosome, PEG-lipids and polyplexes with pH-sensitive degradable spacers are used to prepare PEG sheddable liposomes and cationic polymer vectors. Usually, pH-sensitive degradable bonds are orthoester [50, 51], hydrazone [52, 53], vinyl ethers [54], or acetals [55], and this has been reviewed elsewhere [56]. Enzyme cleavable PEG has also been developed [57, 58]. In addition to use sheddable PEG, we will discuss other methods to facilitate disruption of the endosomal membrane in the next section.

In addition to the PEG dilemma, another problem of PEGylation, that is, accelerated blood clearance (ABC), has been reported [59]. Although PEGylation could significantly prolong the circulation time of nanoparticles in the blood, repeated i.v. injections of the PEGylated nanoparticles resulted in the lost of the long-circulating characteristics [59–61]. The mechanism of ABC developed by Ishida et al. is that first injected dose of PEGylated liposomes activates the splenic synthesis of anti-PEG IgM, resulting in the opsonization of the second dose of PEGylated liposomes and uptake by the liver Kupffer cells [62–64].

To overcome the ABC problem, alternative hydrophilic polymers (such as poly(N-vinyl-2-pyrrolidone) (PVP) and poly(hydroxyethyl-l-asparagine) (PHEA)) [65, 66] and cleavable PEG-lipid derivatives [67] are used. PVP-coated nanoparticles showed improved blood circulation and no ABC phenomenon [65]. For in vivo siRNA delivery, Kiwada group [68] demonstrated that conventional PEG-coated siRNA-lipoplex (PSCL) also caused anti-PEG IgM production, which is lower than that of PEG-coated naked cationic liposomes (PCL). A similar PEGylated lipid nanocarrier termed PEGylated wrapsome (PEG-WS) was further developed for siRNA delivery [69, 70]. Anti-PEG IgM production of the new PEG-WS formulation is less than that of PSCL and significantly dependant on the sequence of siRNA [70]. It shows that anti-PEG IgM production induced by potent immune

stimulatory siRNA is much higher, and 2′-O-methyl (2′-OMe) uridine modification can significantly reduce anti-PEG IgM production by inhibiting cytokine induction.

3. Strategies for Promoting Nanoparticles Escape from Endosome

Having solved the problems with RES uptake, another challenge for siRNA delivery is to have the cargo escape from endosomes to reach cytoplasm. Here several strategies designed to enhance endosomal escape are described (Table 1).

3.1. Ion-Pair Formation. The mechanism whereby cationic lipids destabilize endosome membrane to facilitate the endosomal escape of nucleic acid such as plasmid DNA or siRNA is originally proposed by Xu and Szoka [105]. Cationic lipids form ion pairs with anionic lipids within endosome membrane to destabilize the endosome membrane. Because the cross-sectional area of the combined headgroup in ion pair is less than that of the sum of individual headgroup areas in isolation, a "cylindrical" shape of individual charged lipids is transformed to a "cone" shape of ion pair which further promote the formation of the inverted hexagonal (H_{II}) phase as proposed by Cullis et al. [128, 129].

The exposure of the positive charge in liposomes to endosomal membranes is a prerequisite for electrostatic interaction between cationic lipids and anionic lipids. PEGylation of liposomes for systemic drug delivery therefore inhibits the formation of ion pairs. As mentioned in Section 2, the shedding character of LPD nanoparticles is helpful to overcome the PEG dilemma [32–35]. After PEG comes off the LPD nanoparticles, cationic lipids are exposed to anionic lipids. In this novel formulation, the brushed but sheddable PEG not only grants LPD nanoparticles evasion of the RES for the initial period of time such that LPD nanoparticles can penetrate into the tumor by EPR effect but also facilitates the endosomal escape of the cargo siRNA. Due to successful RES evasion and endosomal escape, LPD nanoparticle is a very promising carrier for systemic delivery of siRNA.

Obata et al. [108] synthesized zwitterionic lipids with amino acid-modified head group. The fusogenic potential of these liposomes with endosome-mimicking anionic membrane is pH-responsive, and it increases as pH decreases. The zeta potential of these liposomes in physiological conditions is negative and switches to positive as pH declines, which means that these lipoplexes may have prolonged circulation time in the blood. The properties of these liposomes provided great promise for drug delivery in vivo but no such report has been seen yet.

Heyes et al. [130] synthesized 1,2-dilinoleyloxy-3-dimethylaminopropane (DLinDMA) lipid with two double bonds per alkyl chain, which has strong fusogenicity and high gene transfection efficiency. Recently, Semple et al. [131] developed DLinDMA derivatives by optimizing the headgroup and linker moiety to formulate stable nucleic acid-lipid particles (SNALPs). They introduced an acid degradable ketalized linker. SNALP formulation containing DLin-KC2-DMA lipid presented excellent in vivo silencing activity in liver in rodents and nonhuman primates. This novel for-mulation could evade RES uptake and circulate in the blood for longer time due to its low pKa under neutral pH, because the amine head groups remain unprotonated and the zeta potential of nanoparticles was nearly neural or negative at pH 7.4. After the nanoparticles were internalized into intracellular endosomes, the amine groups became protonated to form cationic lipids, which was necessary to escape endosome by ion-pair mechanism. As known, it is difficult for liposome formulations to avoid drug leakage in the blood on one hand and achieve rapid drug release in target tissues on the other [132–137]. In this novel SNALP formulation, the hydrolysis of ketal bond might increase the content of neutral lipid in liposomes, which likely triggers siRNA release due to reorganization of the lipid domains [138, 139] and is key for its excellent performance at in vivo siRNA delivery. Therefore, this formulation may be advantageous to release cargo efficiently from both endosome and liposomes.

3.2. "Proton Sponge Effect". Successful escape of siRNA carriers from endosome and release of the payload into cytoplasm is necessary to improve the efficiency of gene silencing. Due to the acid nature of endosomal/lysosomal vesicles, pH-buffering agents are widely exploited to promote cargo release. Under acidic condition, various macromolecules with low pKa amine group have been shown to exhibit "proton sponge effect", such as PEI and its derivates [74, 94, 140, 141]. When the complexes formed by these compounds and nucleic acid are internalized into the cell, these compounds are capable of buffering the endosomal vesicle, leading to endosomal swelling and lysis, thus releasing the nucleic acids into the cytoplasm.

Charge-reversal copolymers could shift their charge nature between positive and negative in a pH-dependent fashion [76–79, 142]. Charge conversion can occur in acidic intracellular organelles such as endosome or lysosome (pH = 5∼6), and then these copolymers facilitate the endosomal escape of nucleic acids by enhancing the capacity of "proton sponge". Pittella et al. [79] synthesized a hybrid nanocarrier system composed of calcium phosphate (CaP), a block copolymer PEG, and a charge-conversional polymer (CCP) to deliver siRNA. Confocal laser scanning microscopic observation confirmed that CCP was helpful for endosomal escape of siRNA with the nanoparticles. This hybrid nanocarrier system achieved significant knockdown of vascular endothelial growth factor (VEGF) in PanC-1 cells with low cytotoxicity. Guo et al. prepared charge-reversal functionalized gold nanoparticles (CRFGNs) with *cis*-aconitic anhydride-functionalized poly(allylamine) (PAH-Cit) [75]. The charge reversion of PAH-Cit was confirmed by polyacrylamide gel electrophoresis and confocal laser scanning microscopy. In vitro quantification of lamin A/C protein expression by western blot indicated that the knockdown efficiency of siRNA delivered by CRFGN was dose-dependent in Hela cell line. At 10:1 Au : siRNA ratio, siRNA delivered by CRFGN achieved the highest (80.0%) knockdown efficiency, which is better than Lipofectamine 2000 which inhibited about 66.0%. CRFGN achieved similar results in DNA transfection experiments.

TABLE 1: Examples of endosomal escape compounds for systemic siRNA delivery.

Category	Compounds	Mechanism of endosomal escape	Compatible with RES evasion	References
Polymers				
	Polyethylenimine PEI	Proton sponge effect	Unlikely	[71–73]
	Poly(amidoamine)s (PAAs)	Proton sponge effect	Unknown	[74]
	Charge-reversal copolymers	Proton sponge effect	Unknown	[75–79]
	Poly(propylacrylic acid) (PPAA) and its derivatives	Destabilizing membrane	Unknown	[80–87]
	Amphiphilic cationic copolymers	Hydrophobic interaction and Proton sponge effect	Likely	[88–99]
	pH-sensitive degradable polymers	Increasing endosomal osmotic pressure	Unknown	[100–103]
Lipids				
	Cationic lipids	Forming ion pairs with anionic phospholipids within the endosomal membrane	Yes	[104–107]
	Zwitterionic lipids	Forming ion pairs with anionic phospholipids within the endosomal membrane	Likely	[108]
Lipid coated nanoparticles				
	Lipid coated calcium phosphate (LCP)	Forming ion pairs and increasing endosomal osmotic pressure	Yes	[109]
	Liposome-polycation-DNA (LPD)	Forming ion pairs and Proton sponge effect	Yes	[32, 34, 35, 110, 111]
Inorganic nanoparticles				
	Layered double hydroxide (LDH)	Increasing endosomal osmotic pressure	Unknown	[112]
	Calcium phosphate (CaP)	Increasing endosomal osmotic pressure	Unlikely	[113–116]
	Carbonate apatite (CAp)	Increasing endosomal osmotic pressure	Unlikely	[117]
	Magnesium and manganous phosphate nanoparticles	Increasing endosomal osmotic pressure	Unlikely	[118, 119]
	Calcium carbonate	Increasing endosomal osmotic pressure	Unlikely	[120]
Peptides				
	KALA	Destabilizing membrane	Unknown	[121, 122]
	GALA	Destabilizing membrane	Unknown	[123–126]
	Hemagglutinin protein	Destabilizing membrane	Unknown	[127]

In fact, layered double hydroxide (LDH) [112], calcium phosphate [116, 124], and some other inorganic nanoparticles [118] also belong to materials which are able to deplete protons in acid environment. Because these nanoparticles could be degraded in acidic buffer, they are also able to release cargo from endosomal vesicles. For example, siRNA-loaded LDH nanoparticles [112] were dissolved due to the low pH in the endosome, which facilitated cargo escape from endosomes into the cytoplasm and significant downregulation of protein expression in HEK293T cells. Carbonate apatite nanoparticles [117] were developed to facilitate siRNA escape from the endosomes. It was remarkable that carbonate apatite nanoparticles could efficiently silence reporter genes at a low dose and were more efficient than Lipofectamine. Calcium phosphate has been widely used in biomaterials due to excellent biocompatibility. In vitro gene transfection efficiency of calcium phosphate nanoparticles with hydroxyapatite phase structure was found to be higher than that of the commercial transfecting reagent Polyfect [116]. Nevertheless, these particles are not stable and readily form large aggregates; therefore their in vivo applications are limited. To synthesize stable siRNA-loaded calcium phosphate, Kataoka et al. [113–115] utilized PEG-polycarboxylate block copolymer (such as PEG-b-poly(aspartic acid) and PEG-b-poly(methacrylic acid)) to achieve stable and size-controlled CaP nanoparticles, which showed good stability in serum and significant gene knockdown in vitro. Incorporation of PEG-SS-siRNA instead of PEG-polycarboxylate for stabilization achieved high PEG density in CaP nanoparticles, which could be potentially useful for the systemic delivery of siRNA. The PEG-stabilized CaP nanoparticles were observed to escape from endosome/lysosome exhibited RNAi efficacy for in vitro gene silencing. To improve the endosomal escape of CaP nanoparticles, a diblock copolymer composed of PEG and a charge-reversal polymer was incorporated [79] and resulting hybrid nanoparticles showed significant VEGF knockdown in PanC-1 cells because of the rapid endosomal escape. However, there is no in vivo study of PEG-stabilized CaP nanoparticles for siRNA delivery.

Recently, Li et al. [109] prepared siRNA-encapsulated calcium phosphate by reverse water-in-oil microemulsion technique and then coated calcium phosphate nanoparticles with lipid to obtain a novel siRNA formulation of lipid-coated calcium phosphate (LCP) nanoparticle for siRNA systemic delivery. As mentioned before, calcium phosphate is acid-sensitive, and its degradation in endosome/lysosome increases osmotic pressure of endosome, leading to release of siRNA into the cytoplasm. In addition, lipid component is well known to be helpful for nanoparticles uptake and cargo release from endosome. Antiluciferse (luc) siRNA-loaded LCP nanoparticles showed significant gene silencing of luciferase both in vitro and in vivo with negligible immunotoxicity. The in vivo results suggested that LCP nanoparticles offer significant promise for siRNA delivery in clinical trails.

3.3. Membrane-Destabilizing Macromolecules.
To date, there is no kind of synthetic vector which has comparable efficiency as viral vectors. Hemagglutinin protein, which is pH-sensitive and membrane-destabilizing, helps viral vectors to disrupt the endosome efficiently and enter the cytoplasm [127]. The escape mechanism of hemagglutinin and other fusion proteins is that they shift from an ionized and hydrophilic conformation to a hydrophobic and membrane-active conformation as the environment changes from neutral to acidic, resulting in destabilization of the endosomal membrane and its leakage subsequently. Therefore, incorporation of membrane-destabilizing peptides is another effective strategy to utilize the low pH environment of endosomes/lysosomes.

To mimic the function of viral hemagglutinin protein, many peptides [123, 143–145] and polymers [80, 146–149] with similar properties were synthesized to enhance gene and siRNA delivery. Among the synthetic peptides, the GALA peptide (WEAALAEALAEALAEHLAEALAEALEALAA) [123] was the most studied. Harashima group has developed a kind of multifunctional envelope type nanodevice (MEND) combining PEGylation, targeting ligand, and GALA. It was demonstrated that GALA facilitated endosomal release of siRNA, resulting in efficient knockdown [124–126]. In an in vivo gene silencing study, different MENDs with antiluciferase siRNA were directly injected into tumors of T1080-luc-tumor-bearing mice, and compared to unmodified MEND, GALA-modified MEND exhibited greater gene silencing in tumor tissues. On the other hand, poly(propylacrylic acid) (PPAA) was the most efficient and most studied membrane-destabilizing synthetic polymers, and its membrane-destabilizing capacity could be enhanced by copolymerization with hydrophobic monomers [80–84]. PPAA was demonstrated to enhance the transfection efficiency of cationic lipid/pDNA complexes both in vitro and in vivo [81, 85]. PPAA is negatively charged at physiological condition and therefore cannot condense siRNA directly. Stayton et al. synthesized a kind of diblock polymer composed of poly(2-(dimethylamino)ethyl methacrylate) (PDMAEMA) to condense siRNA and a second endosomal-releasing block composed of DMAEMA and propylacrylic acid (PAA) in roughly equimolar ratios, together with butyl methacylate (BMA). These carriers became sharply lytic at endosomal pH range. In HeLa cells, a copolymer with the most hydrophobic second block (highest BMA content) exhibited the best knockdown effect [86]. When the length of endosomolytic block and its hydrophobic content were increased, this type of copolymer could self-assemble into spherical micelle. The cationic micelle presented much higher knockdown efficiency at low siRNA dose as compared to nonmicelle formulations. These results also indicated that hydrophobic property should contribute significantly to enhancing siRNA knockdown efficiency [87]. Similarly, Lin et al. [150] synthesized a comb-like polymers constructed by a copolymer of pH-sensitive EAA monomers and hydrophobic BMA or hexyl methacrylate (HMA) as the backbone and a second copolymer of hydrophobic HMA and cationic trimethylaminoethylmethacrylate (TMAEMA) at a 50/50 molar feed ratio as grafts. The grafts were linked to the backbone by the acid-labile hydrazone bond. These comb-like polymers could deliver anti-GAPDH siRNA molecules and successfully silenced GAPDH expression at both the mRNA and protein levels in MCF-7 cells.

3.4. Hydrophobic Modifications of Cationic Polymers.

For gene delivery, it has been widely reported that hydrophobic modification of cationic polymers could improve the interaction between vectors, resulting in more efficient escape by lysis of the endosomes and therefore higher gene transfection efficiency [151–155]. Recently, hydrophobic-modified or amphiphilic cationic copolymers are also used as vectors to deliver siRNA [89–91, 94–98, 156]. Kim et al. [88, 89] synthesized water soluble lipopolymer (WSLP) by conjugating cholesterol with short PEI (1.8 kDa) or oligoarginine. WSLP/siRNA complexes showed successful VEGF knockdown in vitro and significant repression of tumor growth in vivo via intratumoral injection. Similarly, branched PEI (25 kDa) derivatives, such as PEI modified by oleic acid and stearic acid [90], tyrosine [92] or PEI grafted with hydrophobic poly(γ-benzyl L-glutamate) segment [93], and low molecular weight PEI (800 Da) modified by Michael addition with alkyl acrylates [91], could condense siRNA into more stable nanoparticles and present better siRNA silencing effect than PEI and were comparable to some of the commercially available transfection agents. These branched PEI derivatives also have low cytotoxicity.

Mao et al. [96, 97] reported self-assembled nanoparticles of monomethoxy poly(ethylene glycol)-block-poly(caprolactone)-block poly(2-aminoethyl ethylene phosphate) (PPEEA) (mPEG-b-PCL-b-PPEEA). Micellar nanoparticles have several advantages over hydrophilic cationic copolymers. For example, micellar nanoparticles could load nucleic acids and hydrophobic anticancer drugs simultaneously. Anticeramidase siRNA-loaded nanoparticles showed significant gene knockdown activities toward the endogenous acid ceramidase gene in vitro and significant inhibition of tumor growth in a BT474 xenograft murine model via tail vein injection. Evaluation of immunotoxicity indicated that this delivery system did not induce immune response. Xiong et al. [95] synthesized a type of biodegradable amphiphilic poly(ethylene oxide)-block-polycaprolactone (PEO-b-PCL) with grafted polyamines for siRNA delivery. These polyamine-grafted PEO-b-PCL micelles could efficiently deliver MDR-1-targeted siRNA to silence P-gp expression in vitro and showed effective endosomal escape after cellular uptake.

Additionally, amphiphilic copolymers have been explored in an effort to deliver nucleic acids and hydrophobic drug paclitaxel into cancer cells [98, 99]. Zhu et al. [98] synthesized PDMAEMA-PCL-PDMAEMA triblock copolymers by RAFT polymerization method. Polymeric micelles/anti-GFP siRNA complexes showed more efficient knockdown than PDMAEMA (20 kDa) and PEI (25 kDa) in MDA-MB-435-GFP cells, and codelivery of VEGF siRNA and paclitaxel with polymeric micelles/siRNA complexes achieved synergistic effects in inhibiting tumor cell growth in vitro.

3.5. pH-Sensitive Degradable Vectors.

In addition to the ability to escape from endosomes, the ideal siRNA delivery vectors should be able to release siRNA into the cytoplasm. Among the pH-sensitive bonds, acetal bond has been widely used to construct intelligent macromolecules or lipid vectors for drug delivery [100–103, 131, 157], due to its fast degradation in endosomal environment. Materials containing acetal bonds are supposed to be degraded in endosomes which precedes the release of their cargo. Hydrolysis of acetal bond will consume hydrogen, which also helps cargo escape from endosome by increasing endosomal osmotic pressure.

Shim and Kwon [101, 157, 158] developed acid-degradable ketalized branched PEI and linear PEI. These derived PEIs showed significant gene transfection efficiency and siRNA knockdown effect when compositions of the polymers were optimized. Some of them could selectively release siRNA from the endosome into cytoplasm with reduced cytotoxicity. To achieve efficient dissociate of carrier with nucleic acids, they synthesized PEG-conjugated acid-degradable poly(ketalized serine) [100] and degradable polyspermine by Michael addition [103].

4. Conclusions

To date, lipid and polymeric nanoparticles have already been widely used for siRNA delivery. For nanoparticles to efficiently deliver siRNA into target tissue and silence target genes, they must overcome two major hurdles: RES uptake and endosome entrapment. Long-circulation property is the prerequisite for nanoparticles to carry most of the siRNA cargo into the target site of interest. Circulation half-life in the blood can be improved by PEGylation or coating a neural and anionic shell. Facilitating endosomal escape is another important strategy in improving drug bioavailability. Incorporation of sheddable-PEG into nanoparticles can help solve the PEG dilemma and promote nanoparticles to escape from endosomes. Tested strategies exploiting ion pair formation, "proton sponge effect", or adding endosome destabilizing agents are effective in improving endosome escape. However, most of these endosome escape mechanisms are not compatible with RES evasion such that only local administration of the dosage form can be attempted. Some newly developed nanoparticles (LPD and LCP), which are able to escape from the endosome, deassemble, and release siRNA simultaneously, certainly represent a class of improved vectors for siRNA delivery in vivo.

Abbreviations

siRNA: Small interfering RNA
RES: Reticuloendothelial system
PEG: Polyethylene glycol
EPR: Enhanced permeability and retention
LPD: Liposome-polycation-DNA
PK: Pharmacokinetics
PAA: Poly(amidoamine)
PEI: Polyethyleneimine
PPAA: Poly(propylacrylic acid)
LCP: Lipid coated calcium phosphate (LCP)
LDH: Layered double hydroxide
CaP: Calcium phosphate
Cap: Carbonate apatite

SNALP:	Stable nucleic acid-lipid particles
DLinDMA:	1,2-dilinoleyloxy-3-dimethylaminopropane
CCP:	Charge-conversional polymer
VEGF:	Vascular endothelial growth factor
PAH-Cit:	*cis*-aconitic anhydride-functionalized poly(allylamine)
MEND:	Multifunctional envelope type nanodevice
PDMAEMA:	poly(2-(dimethylamino)ethyl methacrylate)
BMA:	Butyl methacylate
HMA:	hexyl methacrylate
TMAEMA:	Trimethylaminoethyl-methacrylate
WSLP:	Water soluble lipopolymer
mPEG-b-PCL-b-PPEEA:	monomethoxy poly(ethylene glycol)-block-poly(caprolactone)-block poly(2-aminoethyl ethylene phosphate)
PEO-b-PCL:	poly(ethylene oxide)-block-polycaprolactone.

Acknowledgments

References

[1] A. Fire, S. Xu, M. K. Montgomery, S. A. Kostas, S. E. Driver, and C. C. Mello, "Potent and specific genetic interference by double-stranded RNA in caenorhabditis elegans," *Nature*, vol. 391, no. 6669, pp. 806–811, 1998.

[2] H. Zhang, F. A. Kolb, L. Jaskiewicz, E. Westhof, and W. Filipowicz, "Single processing center models for human Dicer and bacterial RNase III," *Cell*, vol. 118, no. 1, pp. 57–68, 2004.

[3] C. Matranga, Y. Tomari, C. Shin, D. P. Bartel, and P. D. Zamore, "Passenger-strand cleavage facilitates assembly of siRNA into Ago2-containing RNAi enzyme complexes," *Cell*, vol. 123, no. 4, pp. 607–620, 2005.

[4] M. Nishikawa and L. Huang, "Nonviral vectors in the new millennium: delivery barriers in gene transfer," *Human Gene Therapy*, vol. 12, no. 8, pp. 861–870, 2001.

[5] D. W. Pack, A. S. Hoffman, S. Pun, and P. S. Stayton, "Design and development of polymers for gene delivery," *Nature Reviews Drug Discovery*, vol. 4, no. 7, pp. 581–593, 2005.

[6] K. A. Whitehead, R. Langer, and D. G. Anderson, "Knocking down barriers: advances in siRNA delivery," *Nature Reviews Drug Discovery*, vol. 8, no. 2, pp. 129–138, 2009.

[7] Y. Wang, Z. Li, Y. Han, L. H. Liang, and A. Ji, "Nanoparticle-based delivery system for application of siRNA in vivo," *Current Drug Metabolism*, vol. 11, no. 2, pp. 182–196, 2010.

[8] C. M. Wiethoff and C. R. Middaugh, "Barriers to nonviral gene delivery," *Journal of Pharmaceutical Sciences*, vol. 92, no. 2, pp. 203–217, 2003.

[9] J. Soutschek, A. Akinc, B. Bramlage et al., "Therapeutic silencing of an endogenous gene by systemic administration of modified siRNAs," *Nature*, vol. 432, no. 7014, pp. 173–178, 2004.

[10] D. W. Bartlett, H. Su, I. J. Hildebrandt, W. A. Weber, and M. E. Davis, "Impact of tumor-specific targeting on the biodistribution and efficacy of siRNA nanoparticles measured by multimodality in vivo imaging," *Proceedings of the National Academy of Sciences of the United States of America*, vol. 104, no. 39, pp. 15549–15554, 2007.

[11] F. Sams-Dodd, "Target-based drug discovery: is something wrong?" *Drug Discovery Today*, vol. 10, no. 2, pp. 139–147, 2005.

[12] S. K. Hobbs, W. L. Monsky, F. Yuan et al., "Regulation of transport pathways in tumor vessels: role of tumor type and microenvironment," *Proceedings of the National Academy of Sciences of the United States of America*, vol. 95, no. 8, pp. 4607–4612, 1998.

[13] T. L. Andresen, S. S. Jensen, and K. Jørgensen, "Advanced strategies in liposomal cancer therapy: problems and prospects of active and tumor specific drug release," *Progress in Lipid Research*, vol. 44, no. 1, pp. 68–97, 2005.

[14] Y. Matsumura and H. Maeda, "A new concept for macromolecular therapeutics in cancer chemotherapy: mechanism of tumoritropic accumulation of proteins and the antitumor agent smancs," *Cancer Research*, vol. 46, no. 12, pp. 6387–6392, 1986.

[15] H. Maeda, L. W. Seymour, and Y. Miyamoto, "Conjugates of anticancer agents and polymers: advantages of macromolecular therapeutics in vivo," *Bioconjugate Chemistry*, vol. 3, no. 5, pp. 351–362, 1992.

[16] H. Maeda, J. Wu, T. Sawa, Y. Matsumura, and K. Hori, "Tumor vascular permeability and the EPR effect in macromolecular therapeutics: a review," *Journal of Controlled Release*, vol. 65, no. 1-2, pp. 271–284, 2000.

[17] K. Maruyama, "Intracellular targeting delivery of liposomal drugs to solid tumors based on EPR effects," *Advanced Drug Delivery Reviews*, vol. 63, no. 3, pp. 161–169, 2011.

[18] A. L. Klibanov, K. Maruyama, V. P. Torchilin, and L. Huang, "Amphipathic polyethyleneglycols effectively prolong the circulation time of liposomes," *FEBS Letters*, vol. 268, no. 1, pp. 235–237, 1990.

[19] T. M. Allen and A. Chonn, "Large unilamellar liposomes with low uptake into the reticuloendothelial system," *FEBS Letters*, vol. 223, no. 1, pp. 42–46, 1987.

[20] T. M. Allen, C. Hansen, and J. Rutledge, "Liposomes with prolonged circulation times: factors affecting uptake by reticuloendothelial and other tissues," *Biochimica et Biophysica Acta*, vol. 981, no. 1, pp. 27–35, 1989.

[21] T. M. Allen, C. Hansen, F. Martin, C. Redemann, and A. F. Yau-Young, "Liposomes containing synthetic lipid derivatives of poly(ethylene glycol) show prolonged circulation half-lives in vivo," *Biochimica et Biophysica Acta*, vol. 1066, no. 1, pp. 29–36, 1991.

[22] A. L. Klibanov, K. Maruyama, A. M. Beckerleg, V. P. Torchilin, and L. Huang, "Activity of amphipathic poly(ethylene glycol) 5000 to prolong the circulation time of liposomes depends on the liposome size and is unfavorable for immunoliposome binding to target," *Biochimica et Biophysica Acta*, vol. 1062, no. 2, pp. 142–148, 1991.

[23] R. H. Müller, S. Maaßen, H. Weyhers, and W. Mehnert, "Phagocytic uptake and cytotoxicity of solid lipid nanoparticles (SLN) sterically stabilized with poloxamine 908 and poloxamer 407," *Journal of Drug Targeting*, vol. 4, no. 3, pp. 161–170, 1996.

[24] M. Morille, T. Montier, P. Legras et al., "Long-circulating DNA lipid nanocapsules as new vector for passive tumor targeting," *Biomaterials*, vol. 31, no. 2, pp. 321–329, 2010.

[25] H. Takeuchi, H. Kojima, H. Yamamoto, and Y. Kawashima, "Polymer coating of liposomes with a modified polyvinyl alcohol and their systemic circulation and RES uptake in rats," *Journal of Controlled Release*, vol. 68, no. 2, pp. 195–205, 2000.

[26] H. Takeuchi, H. Kojima, T. Toyoda, H. Yamamoto, T. Hino, and Y. Kawashima, "Prolonged circulation time of doxorubicin-loaded liposomes coated with a modified polyvinyl alcohol after intravenous injection in rats," *European Journal of Pharmaceutics and Biopharmaceutics*, vol. 48, no. 2, pp. 123–129, 1999.

[27] J. M. Metselaar, P. Bruin, L. W. T. de Boer et al., "A novel family of L-amino acid-based biodegradable polymer-lipid conjugates for the development of long-circulating liposomes with effective drug-targeting capacity," *Bioconjugate Chemistry*, vol. 14, no. 6, pp. 1156–1164, 2003.

[28] V. Sihorkar and S. P. Vyas, "Potential of polysaccharide anchored liposomes in drug delivery, targeting and immunization," *Journal of Pharmacy and Pharmaceutical Sciences*, vol. 4, no. 2, pp. 138–158, 2001.

[29] D. Peer, J. E. Park, Y. Morishita, C. V. Carman, and M. Shimaoka, "Systemic leukocyte-directed siRNA delivery revealing cyclin D1 as an anti-inflammatory target," *Science*, vol. 319, no. 5863, pp. 627–630, 2008.

[30] Z. S. Haidar, R. C. Hamdy, and M. Tabrizian, "Protein release kinetics for core-shell hybrid nanoparticles based on the layer-by-layer assembly of alginate and chitosan on liposomes," *Biomaterials*, vol. 29, no. 9, pp. 1207–1215, 2008.

[31] M. Mobed and T. M. S. Chang, "Comparison of polymerically stabilized PEG-grafted liposomes and physically adsorbed carboxymethylchitin and carboxymethyl/glycol-chitin liposomes for biological applications," *Biomaterials*, vol. 19, no. 13, pp. 1167–1177, 1998.

[32] S. D. Li and L. Huang, "Nanoparticles evading the reticuloendothelial system: role of the supported bilayer," *Biochimica et Biophysica Acta*, vol. 1788, no. 10, pp. 2259–2266, 2009.

[33] S. D. Li and L. Huang, "Stealth nanoparticles: high density but sheddable PEG is a key for tumor targeting," *Journal of Controlled Release*, vol. 145, no. 3, pp. 178–181, 2010.

[34] S. D. Li and L. Huang, "Pharmacokinetics and biodistribution of nanoparticles," *Molecular Pharmaceutics*, vol. 5, no. 4, pp. 496–504, 2008.

[35] S. D. Li, S. Chono, and L. Huang, "Efficient oncogene silencing and metastasis inhibition via systemic delivery of siRNA," *Molecular Therapy*, vol. 16, no. 5, pp. 942–946, 2008.

[36] J. W. Holland, C. Hui, P. R. Cullis, and T. D. Madden, "Poly(ethylene glycol)-lipid conjugates regulate the calcium-induced fusion of liposomes composed of phosphatidylethanolamine and phosphatidylserine," *Biochemistry*, vol. 35, no. 8, pp. 2618–2624, 1996.

[37] J. J. Wheeler, L. Palmer, M. Ossanlou et al., "Stabilized plasmid-lipid particles: construction and characterization," *Gene Therapy*, vol. 6, no. 2, pp. 271–281, 1999.

[38] M. A. Monck, A. Mori, D. Lee et al., "Stabilized plasmid-lipid particles: pharmacokinetics and plasmid delivery to distal tumors following intravenous injection," *Journal of Drug Targeting*, vol. 7, no. 6, pp. 439–452, 2000.

[39] O. Ishida, K. Maruyama, H. Tanahashi et al., "Liposomes bearing polyethyleneglycol-coupled transferrin with intracellular targeting property to the solid tumors in vivo," *Pharmaceutical Research*, vol. 18, no. 7, pp. 1042–1048, 2001.

[40] M. Ogris, G. Walker, T. Blessing, R. Kircheis, M. Wolschek, and E. Wagner, "Tumor-targeted gene therapy: strategies for the preparation of ligand-polyethylene glycol-polyethylenimine/DNA complexes," *Journal of Controlled Release*, vol. 91, no. 1-2, pp. 173–181, 2003.

[41] M. E. Davis, "The first targeted delivery of siRNA in humans via a self-assembling, cyclodextrin polymer-based nanoparticle: from concept to clinic," *Molecular Pharmaceutics*, vol. 6, no. 3, pp. 659–668, 2009.

[42] M. E. Davis, J. E. Zuckerman, C. H. J. Choi et al., "Evidence of RNAi in humans from systemically administered siRNA via targeted nanoparticles," *Nature*, vol. 464, no. 7291, pp. 1067–1070, 2010.

[43] N. C. Bellocq, S. H. Pun, G. S. Jensen, and M. E. Davis, "Transferrin-containing, cyclodextrin polymer-based particles for tumor-targeted gene delivery," *Bioconjugate Chemistry*, vol. 14, no. 6, pp. 1122–1132, 2003.

[44] R. M. Schiffelers, A. Ansari, J. Xu et al., "Cancer siRNA therapy by tumor selective delivery with ligand-targeted sterically stabilized nanoparticle," *Nucleic Acids Research*, vol. 32, no. 19, p. e149, 2004.

[45] H. D. Han, L. S. Mangala, J. W. Lee et al., "Targeted gene silencing using RGD-labeled chitosan nanoparticles," *Clinical Cancer Research*, vol. 16, no. 15, pp. 3910–3922, 2010.

[46] S. Moffatt, S. Wiehle, and R. J. Cristiano, "A multifunctional PEI-based cationic polyplex for enhanced systemic p53-mediated gene therapy," *Gene Therapy*, vol. 13, no. 21, pp. 1512–1523, 2006.

[47] S. Chono, S. D. Li, C. C. Conwell, and L. Huang, "An efficient and low immunostimulatory nanoparticle formulation for systemic siRNA delivery to the tumor," *Journal of Controlled Release*, vol. 131, no. 1, pp. 64–69, 2008.

[48] S. H. Kim, J. H. Jeong, K. C. Cho, S. W. Kim, and T. G. Park, "Target-specific gene silencing by siRNA plasmid DNA complexed with folate-modified poly(ethylenimine)," *Journal of Controlled Release*, vol. 104, no. 1, pp. 223–232, 2005.

[49] S. Guo, Y. Huang, W. Zhang et al., "Ternary complexes of amphiphilic polycaprolactone-graft-poly (N,N-dimethylaminoethyl methacrylate), DNA and polyglutamic acid-graft-poly(ethylene glycol) for gene delivery," *Biomaterials*, vol. 32, no. 18, pp. 4283–4292, 2011.

[50] W. Li, Z. Huang, J. A. MacKay, S. Grube, and F. C. Szoka, "Low-pH-sensitive poly(ethylene glycol) (PEG)-stabilized plasmid nanolipoparticles: effects of PEG chain length, lipid composition and assembly conditions on gene delivery," *Journal of Gene Medicine*, vol. 7, no. 1, pp. 67–79, 2005.

[51] C. Masson, M. Garinot, N. Mignet et al., "pH-Sensitive PEG lipids containing orthoester linkers: new potential tools for nonviral gene delivery," *Journal of Controlled Release*, vol. 99, no. 3, pp. 423–434, 2004.

[52] G. F. Walker, C. Fella, J. Pelisek et al., "Toward synthetic viruses: endosomal pH-Triggered deshielding of targeted polyplexes greatly enhances gene transfer in vitro and in vivo," *Molecular Therapy*, vol. 11, no. 3, pp. 418–425, 2005.

[53] R. M. Sawant, J. P. Hurley, S. Salmaso et al., ""SMART" drug delivery systems: double-targeted pH-responsive pharmaceutical nanocarriers," *Bioconjugate Chemistry*, vol. 17, no. 4, pp. 943–949, 2006.

[54] J. Shin, P. Shum, and D. H. Thompson, "Acid-triggered release via dePEGylation of DOPE liposomes containing

acid-labile vinyl ether PEG-lipids," *Journal of Controlled Release*, vol. 91, no. 1-2, pp. 187–200, 2003.

[55] N. Murthy, J. Campbell, N. Fausto, A. S. Hoffman, and P. S. Stayton, "Design and synthesis of pH-responsive polymeric carriers that target uptake and enhance the intracellular delivery of oligonucleotides," *Journal of Controlled Release*, vol. 89, no. 3, pp. 365–374, 2003.

[56] B. Romberg, W. E. Hennink, and G. Storm, "Sheddable coatings for long-circulating nanoparticles," *Pharmaceutical Research*, vol. 25, no. 1, pp. 55–71, 2008.

[57] H. Hatakeyama, H. Akita, K. Kogure et al., "Development of a novel systemic gene delivery system for cancer therapy with a tumor-specific cleavable PEG-lipid," *Gene Therapy*, vol. 14, no. 1, pp. 68–77, 2007.

[58] L. M. Coussens, B. Fingleton, and L. M. Matrisian, "Matrix metalloproteinase inhibitors and cancer: trials and tribulations," *Science*, vol. 295, no. 5564, pp. 2387–2392, 2002.

[59] E. T. M. Dams, P. Laverman, W. J. G. Oyen et al., "Accelerated blood clearance and altered biodistribution of repeated injections of sterically stabilized liposomes," *Journal of Pharmacology and Experimental Therapeutics*, vol. 292, no. 3, pp. 1071–1079, 2000.

[60] T. Ishida and H. Kiwada, "Accelerated blood clearance (ABC) phenomenon upon repeated injection of PEGylated liposomes," *International Journal of Pharmaceutics*, vol. 354, no. 1-2, pp. 56–62, 2008.

[61] T. Ishida, R. Maeda, M. Ichihara, K. Irimura, and H. Kiwada, "Accelerated clearance of PEGylated liposomes in rats after repeated injections," *Journal of Controlled Release*, vol. 88, no. 1, pp. 35–42, 2003.

[62] T. Ishida, M. Ichihara, X. Wang, and H. Kiwada, "Spleen plays an important role in the induction of accelerated blood clearance of PEGylated liposomes," *Journal of Controlled Release*, vol. 115, no. 3, pp. 243–250, 2006.

[63] T. Ishida, M. Ichihara, X. Wang et al., "Injection of PEGylated liposomes in rats elicits PEG-specific IgM, which is responsible for rapid elimination of a second dose of PEGylated liposomes," *Journal of Controlled Release*, vol. 112, no. 1, pp. 15–25, 2006.

[64] X. Wang, T. Ishida, and H. Kiwada, "Anti-PEG IgM elicited by injection of liposomes is involved in the enhanced blood clearance of a subsequent dose of PEGylated liposomes," *Journal of Controlled Release*, vol. 119, no. 2, pp. 236–244, 2007.

[65] T. Ishihara, T. Maeda, H. Sakamoto et al., "Evasion of the accelerated blood clearance phenomenon by coating of nanoparticles with various hydrophilic polymers," *Biomacromolecules*, vol. 11, no. 10, pp. 2700–2706, 2010.

[66] B. Romberg, C. Oussoren, C. J. Snel, M. G. Carstens, W. E. Hennink, and G. Storm, "Pharmacokinetics of poly(hydroxyethyl-l-asparagine)-coated liposomes is superior over that of PEG-coated liposomes at low lipid dose and upon repeated administration," *Biochimica et Biophysica Acta*, vol. 1768, no. 3, pp. 737–743, 2007.

[67] H. Xu, K. Q. Wang, Y. H. Deng, and D. W. Chen, "Effects of cleavable PEG-cholesterol derivatives on the accelerated blood clearance of PEGylated liposomes," *Biomaterials*, vol. 31, no. 17, pp. 4757–4763, 2010.

[68] T. Tagami, K. Nakamura, T. Shimizu, T. Ishida, and H. Kiwada, "Effect of siRNA in PEG-coated siRNA-lipoplex on anti-PEG IgM production," *Journal of Controlled Release*, vol. 137, no. 3, pp. 234–240, 2009.

[69] N. Yagi, I. Manabe, T. Tottori et al., "A nanoparticle system specifically designed to deliver short interfering RNA inhibits tumor growth in vivo," *Cancer Research*, vol. 69, no. 16, pp. 6531–6538, 2009.

[70] T. Tagami, Y. Uehara, N. Moriyoshi, T. Ishida, and H. Kiwada, "Anti-PEG IgM production by siRNA encapsulated in a PEGylated lipid nanocarrier is dependent on the sequence of the siRNA," *Journal of Controlled Release*, vol. 151, no. 2, pp. 149–154, 2011.

[71] O. Boussif, F. LezoualC'H, M. A. Zanta et al., "A versatile vector for gene and oligonucleotide transfer into cells in culture and in vivo: polyethylenimine," *Proceedings of the National Academy of Sciences of the United States of America*, vol. 92, no. 16, pp. 7297–7301, 1995.

[72] D. Fischer, T. Bieber, Y. Li, H. P. Elsässer, and T. Kissel, "A novel non-viral vector for DNA delivery based on low molecular weight, branched polyethylenimine: effect of molecular weight on transfection efficiency and cytotoxicity," *Pharmaceutical Research*, vol. 16, no. 8, pp. 1273–1279, 1999.

[73] B. Urban-Klein, S. Werth, S. Abuharbeid, F. Czubayko, and A. Aigner, "RNAi-mediated gene-targeting through systemic application of polyethylenimine (PEI)-complexed siRNA in vivo," *Gene Therapy*, vol. 12, no. 5, pp. 461–466, 2005.

[74] C. Lin, C. J. Blaauboer, M. M. Timoneda et al., "Bioreducible poly(amido amine)s with oligoamine side chains: synthesis, characterization, and structural effects on gene delivery," *Journal of Controlled Release*, vol. 126, no. 2, pp. 166–174, 2008.

[75] S. Guo, Y. Huang, Q. Jiang et al., "Enhanced gene delivery and siRNA silencing by gold nanoparticles coated with charge-reversal polyelectrolyte," *ACS Nano*, vol. 4, no. 9, pp. 5505–5511, 2010.

[76] D. B. Rozema, K. Ekena, D. L. Lewis, A. G. Loomis, and J. A. Wolff, "Endosomolysis by masking of a membrane-active agent (EMMA) for cytoplasmic release of macromolecules," *Bioconjugate Chemistry*, vol. 14, no. 1, pp. 51–57, 2003.

[77] P. Xu, E. A. van Kirk, Y. H. Zhan, W. J. Murdoch, M. Radosz, and Y. Q. Shen, "Targeted charge-reversal nanoparticles for nuclear drug delivery," *Angewandte Chemie*, vol. 46, no. 26, pp. 4999–5002, 2007.

[78] Y. Lee, K. Miyata, M. Oba et al., "Charge-conversion ternary polyplex with endosome disruption moiety: a technique for efficient and safe gene delivery," *Angewandte Chemie*, vol. 47, no. 28, pp. 5163–5166, 2008.

[79] F. Pittella, M. Zhang, Y. Lee et al., "Enhanced endosomal escape of siRNA-incorporating hybrid nanoparticles from calcium phosphate and PEG-block charge-conversional polymer for efficient gene knockdown with negligible cytotoxicity," *Biomaterials*, vol. 32, no. 11, pp. 3106–3114, 2011.

[80] C. Kusonwiriyawong, P. van de Wetering, J. A. Hubbell, H. P. Merkle, and E. Walter, "Evaluation of pH-dependent membrane-disruptive properties of poly(acrylic acid) derived polymers," *European Journal of Pharmaceutics and Biopharmaceutics*, vol. 56, no. 2, pp. 237–246, 2003.

[81] T. R. Kyriakides, C. Y. Cheung, N. Murthy, P. Bornstein, P. S. Stayton, and A. S. Hoffman, "pH-sensitive polymers that enhance intracellular drug delivery in vivo," *Journal of Controlled Release*, vol. 78, no. 1–3, pp. 295–303, 2002.

[82] J. L. Thomas and D. A. Tirrell, "Polyelectrolyte-sensitized phospholipid vesicles," *Accounts of Chemical Research*, vol. 25, no. 8, pp. 336–342, 1992.

[83] N. Murthy, J. R. Robichaud, D. A. Tirrell, P. S. Stayton, and A. S. Hoffman, "The design and synthesis of polymers for eukaryotic membrane disruption," *Journal of Controlled Release*, vol. 61, no. 1-2, pp. 137–143, 1999.

[84] R. A. Jones, C. Y. Cheung, F. E. Black et al., "Poly(2-alkylacrylic acid) polymers deliver molecules to the cytosol by

pH-sensitive disruption of endosomal vesicles," *Biochemical Journal*, vol. 372, no. 1, pp. 65–75, 2003.

[85] C. Y. Cheung, N. Murthy, P. S. Stayton, and A. S. Hoffman, "A pH-sensitive polymer that enhances cationic lipid-mediated gene transfer," *Bioconjugate Chemistry*, vol. 12, no. 6, pp. 906–910, 2001.

[86] A. J. Convertine, D. S. W. Benoit, C. L. Duvall, A. S. Hoffman, and P. S. Stayton, "Development of a novel endosomolytic diblock copolymer for siRNA delivery," *Journal of Controlled Release*, vol. 133, no. 3, pp. 221–229, 2009.

[87] A. J. Convertine, C. Diab, M. Prieve et al., "pH-responsive polymeric micelle carriers for siRNA drugs," *Biomacromolecules*, vol. 11, no. 11, pp. 2904–2911, 2010.

[88] W. J. Kim, L. V. Christensen, S. Jo et al., "Cholesteryl oligoarginine delivering vascular endothelial growth factor siRNA effectively inhibits tumor growth in colon adenocarcinoma," *Molecular Therapy*, vol. 14, no. 3, pp. 343–350, 2006.

[89] W. J. Kim, C. W. Chang, M. Lee, and S. W. Kim, "Efficient siRNA delivery using water soluble lipopolymer for anti-angiogenic gene therapy," *Journal of Controlled Release*, vol. 118, no. 3, pp. 357–363, 2007.

[90] A. Alshamsan, A. Haddadi, V. Incani, J. Samuel, A. Lavasanifar, and H. Uludağ, "Formulation and delivery of siRNA by oleic acid and stearic acid modified polyethylenimine," *Molecular Pharmaceutics*, vol. 6, no. 1, pp. 121–133, 2009.

[91] A. Philipp, X. Zhao, P. Tarcha, E. Wagner, and A. Zintchenko, "Hydrophobically modified oligoethylenimines as highly efficient transfection agents for siRNA delivery," *Bioconjugate Chemistry*, vol. 20, no. 11, pp. 2055–2061, 2009.

[92] G. Creusat and G. Zuber, "Self-assembling polyethylenimine derivatives mediate efficient siRNA delivery in mammalian cells," *ChemBioChem*, vol. 9, no. 17, pp. 2787–2789, 2008.

[93] J. Chen, H. Tian, Z. Guo et al., "A highly efficient siRNA carrier of PBLG modified hyperbranched PEI," *Macromolecular Bioscience*, vol. 9, no. 12, pp. 1247–1253, 2009.

[94] H. J. Kim, A. Ishii, K. Miyata et al., "Introduction of stearoyl moieties into a biocompatible cationic polyaspartamide derivative, PAsp(DET), with endosomal escaping function for enhanced siRNA-mediated gene knockdown," *Journal of Controlled Release*, vol. 145, no. 2, pp. 141–148, 2010.

[95] X. B. Xiong, H. Uludağ, and A. Lavasanifar, "Biodegradable amphiphilic poly(ethylene oxide)-block-polyesters with grafted polyamines as supramolecular nanocarriers for efficient siRNA delivery," *Biomaterials*, vol. 30, no. 2, pp. 242–253, 2009.

[96] C. Q. Mao, J. Z. Du, T. M. Sun et al., "A biodegradable amphiphilic and cationic triblock copolymer for the delivery of siRNA targeting the acid ceramidase gene for cancer therapy," *Biomaterials*, vol. 32, no. 11, pp. 3124–3133, 2011.

[97] T. M. Sun, J. Z. Du, L. F. Yan, H. Q. Mao, and J. Wang, "Self-assembled biodegradable micellar nanoparticles of amphiphilic and cationic block copolymer for siRNA delivery," *Biomaterials*, vol. 29, no. 32, pp. 4348–4355, 2008.

[98] C. Zhu, S. Jung, S. Luo et al., "Co-delivery of siRNA and paclitaxel into cancer cells by biodegradable cationic micelles based on PDMAEMA-PCL-PDMAEMA triblock copolymers," *Biomaterials*, vol. 31, no. 8, pp. 2408–2416, 2010.

[99] Y. Wang, S. Gao, W. H. Ye, H. S. Yoon, and Y. Y. Yang, "Co-delivery of drugs and DNA from cationic core-shell nanoparticles self-assembled from a biodegradable copolymer," *Nature Materials*, vol. 5, no. 10, pp. 791–796, 2006.

[100] M. S. Shim and Y. J. Kwon, "Acid-transforming polypeptide micelles for targeted nonviral gene delivery," *Biomaterials*, vol. 31, no. 12, pp. 3404–3413, 2010.

[101] M. S. Shim and Y. J. Kwon, "Controlled delivery of plasmid DNA and siRNA to intracellular targets using ketalized polyethylenimine," *Biomacromolecules*, vol. 9, no. 2, pp. 444–455, 2008.

[102] M. S. Shim, C. S. Kim, Y. C. Ahn, Z. Chen, and Y. J. Kwon, "Combined multimodal optical imaging and targeted gene silencing using stimuli-transforming nanotheragnostics," *Journal of the American Chemical Society*, vol. 132, no. 24, pp. 8316–8324, 2010.

[103] M. S. Shim and Y. J. Kwon, "Dual mode polyspermine with tunable degradability for plasmid DNA and siRNA delivery," *Biomaterials*, vol. 32, no. 16, pp. 4009–4020, 2011.

[104] Y. C. Tseng, S. Mozumdar, and L. Huang, "Lipid-based systemic delivery of siRNA," *Advanced Drug Delivery Reviews*, vol. 61, no. 9, pp. 721–731, 2009.

[105] Y. Xu and F. C. Szoka, "Mechanism of DNA release from cationic liposome/DNA complexes used in cell transfection," *Biochemistry*, vol. 35, no. 18, pp. 5616–5623, 1996.

[106] A. Schroeder, C. G. Levins, C. Cortez, R. Langer, and D. G. Anderson, "Lipid-based nanotherapeutics for siRNA delivery," *Journal of Internal Medicine*, vol. 267, no. 1, pp. 9–21, 2010.

[107] S. Y. Wu and N. A. J. McMillan, "Lipidic systems for in vivo siRNA delivery," *AAPS Journal*, vol. 11, no. 4, pp. 639–652, 2009.

[108] Y. Obata, S. Tajima, and S. Takeoka, "Evaluation of pH-responsive liposomes containing amino acid-based zwitterionic lipids for improving intracellular drug delivery in vitro and in vivo," *Journal of Controlled Release*, vol. 142, no. 2, pp. 267–276, 2010.

[109] J. Li, Y. C. Chen, Y. C. Tseng, S. Mozumdar, and L. Huang, "Biodegradable calcium phosphate nanoparticle with lipid coating for systemic siRNA delivery," *Journal of Controlled Release*, vol. 142, no. 3, pp. 416–421, 2010.

[110] Y. Chen, S. R. Bathula, J. Li, and L. Huang, "Multifunctional nanoparticles delivering small interfering RNA and doxorubicin overcome drug resistance in cancer," *Journal of Biological Chemistry*, vol. 285, no. 29, pp. 22639–22650, 2010.

[111] Y. Chen, J. J. Wu, and L. Huang, "Nanoparticles targeted with NGR motif deliver c-myc siRNA and doxorubicin for anticancer therapy," *Molecular Therapy*, vol. 18, no. 4, pp. 828–834, 2010.

[112] K. Ladewig, M. Niebert, Z. P. Xu, P. P. Gray, and G. Q. M. Lu, "Efficient siRNA delivery to mammalian cells using layered double hydroxide nanoparticles," *Biomaterials*, vol. 31, no. 7, pp. 1821–1829, 2010.

[113] M. Zhang, A. Lshii, N. Nishiyama et al., "PEGylated calcium phosphate nanocomposites as smart environment-sensitive carriers for siRNA delivery," *Advanced Materials*, vol. 21, no. 34, pp. 3520–3525, 2009.

[114] Y. Kakizawa, S. Furukawa, and K. Kataoka, "Block copolymer-coated calcium phosphate nanoparticles sensing intracellular environment for oligodeoxynucleotide and siRNA delivery," *Journal of Controlled Release*, vol. 97, no. 2, pp. 345–356, 2004.

[115] Y. Kakizawa, S. Furukawa, A. Ishii, and K. Kataoka, "Organic-inorganic hybrid-nanocarrier of siRNA constructing through the self-assembly of calcium phosphate and PEG-based block aniomer," *Journal of Controlled Release*, vol. 111, no. 3, pp. 368–370, 2006.

[116] S. Bisht, G. Bhakta, S. Mitra, and A. Maitra, "pDNA load-ed calcium phosphate nanoparticles: highly efficient non-viral vector for gene delivery," *International Journal of Pharmaceutics*, vol. 288, no. 1, pp. 157–168, 2005.

[117] S. Hossain, A. Stanislaus, M. J. Chua et al., "Carbonate apatite-facilitated intracellularly delivered siRNA for efficient knockdown of functional genes," *Journal of Controlled Release*, vol. 147, no. 1, pp. 101–108, 2010.

[118] G. Bhakta, S. Mitra, and A. Maitra, "DNA encapsulated magnesium and manganous phosphate nanoparticles: potential non-viral vectors for gene delivery," *Biomaterials*, vol. 26, no. 14, pp. 2157–2163, 2005.

[119] G. Bhakta, A. Shrivastava, and A. Maitra, "Magnesium phosphate nanoparticles can be efficiently used in vitro and in vivo as non-viral vectors for targeted gene delivery," *Journal of Biomedical Nanotechnology*, vol. 5, no. 1, pp. 106–114, 2009.

[120] X. W. He, T. Liu, Y. X. Chen et al., "Calcium carbonate nanoparticle delivering vascular endothelial growth factor-C siRNA effectively inhibits lymphangiogenesis and growth of gastric cancer in vivo," *Cancer Gene Therapy*, vol. 15, no. 3, pp. 193–202, 2008.

[121] T. B. Wyman, F. Nicol, O. Zelphati, P. V. Scaria, C. Plank, and F. C. Szoka, "Design, synthesis, and characterization of a cationic peptide that binds to nucleic acids and permeabilizes bilayers," *Biochemistry*, vol. 36, no. 10, pp. 3008–3017, 1997.

[122] H. Lee, J. H. Jeong, and T. G. Park, "A new gene delivery formulation of polyethylenimine/DNA complexes coated with PEG conjugated fusogenic peptide," *Journal of Controlled Release*, vol. 76, no. 1-2, pp. 183–192, 2001.

[123] W. Li, F. Nicol, and F. C. Szoka, "GALA: a designed synthetic pH-responsive amphipathic peptide with applications in drug and gene delivery," *Advanced Drug Delivery Reviews*, vol. 56, no. 7, pp. 967–985, 2004.

[124] H. Hatakeyama, H. Akita, and H. Harashima, "A multifunctional envelope type nano device (MEND) for gene delivery to tumours based on the EPR effect: a strategy for overcoming the PEG dilemma," *Advanced Drug Delivery Reviews*, vol. 63, no. 3, pp. 152–160, 2011.

[125] H. Hatakeyama, E. Ito, H. Akita et al., "A pH-sensitive fusogenic peptide facilitates endosomal escape and greatly enhances the gene silencing of siRNA-containing nanoparticles in vitro and in vivo," *Journal of Controlled Release*, vol. 139, no. 2, pp. 127–132, 2009.

[126] Y. Sakurai, H. Hatakeyama, H. Akita et al., "Efficient short interference rna delivery to tumor cells using a combination of octaarginine, gala and tumor-specific, cleavable polyethylene glycol system," *Biological and Pharmaceutical Bulletin*, vol. 32, no. 5, pp. 928–932, 2009.

[127] N. Ferrer-Miralles, E. Vázquez, and A. Villaverde, "Membrane-active peptides for non-viral gene therapy: making the safest easier," *Trends in Biotechnology*, vol. 26, no. 5, pp. 267–275, 2008.

[128] P. R. Cullis, M. J. Hope, and C. P. S. Tilcock, "Lipid polymorphism and the roles of lipids in membranes," *Chemistry and Physics of Lipids*, vol. 40, no. 2–4, pp. 127–144, 1986.

[129] I. M. Hafez, N. Maurer, and P. R. Cullis, "On the mechanism whereby cationic lipids promote intracellular delivery of polynucleic acids," *Gene Therapy*, vol. 8, no. 15, pp. 1188–1196, 2001.

[130] J. Heyes, L. Palmer, K. Bremner, and I. MacLachlan, "Cationic lipid saturation influences intracellular delivery of encapsulated nucleic acids," *Journal of Controlled Release*, vol. 107, no. 2, pp. 276–287, 2005.

[131] S. C. Semple, A. Akinc, J. Chen et al., "Rational design of cationic lipids for siRNA delivery," *Nature Biotechnology*, vol. 28, no. 2, pp. 172–176, 2010.

[132] H. J. Lim, D. Masin, N. L. Mcintosh, T. D. Madden, and M. B. Bally, "Role of drug release and liposome-mediated drug delivery in governing the therapeutic activity of liposomal mitoxantrone used to treat human A431 and LS180 solid tumors," *Journal of Pharmacology and Experimental Therapeutics*, vol. 292, no. 1, pp. 337–345, 2000.

[133] L. D. Mayer, L. C. L. Tai, D. S. C. Ko et al., "Influence of vesicle size, lipid composition, and drug-to-lipid ratio on the biological activity of liposomal doxorubicin in mice," *Cancer Research*, vol. 49, no. 21, pp. 5922–5930, 1989.

[134] N. L. Boman, L. D. Mayer, and P. R. Cullis, "Optimization of the retention properties of vincristine in liposomal systems," *Biochimica et Biophysica Acta*, vol. 1152, no. 2, pp. 253–258, 1993.

[135] A. Gabizon, M. Chemla, D. Tzemach, A. T. Horowitz, and D. Goren, "Liposome longevity and stability in circulation: effects on the in vivo delivery to tumors and therapeutic efficacy of encapsulated anthracyclines," *Journal of Drug Targeting*, vol. 3, no. 5, pp. 391–398, 1996.

[136] C. Boyer and J. A. Zasadzinski, "Multiple lipid compartments slow vesicle contents release in lipases and serum," *ACS Nano*, vol. 1, no. 3, pp. 176–182, 2007.

[137] L. D. Mayer, R. Nayar, R. L. Thies, N. L. Boman, P. R. Cullis, and M. B. Bally, "Identification of vesicle properties that enhance the antitumour activity of liposomal vincristine against murine L1210 leukemia," *Cancer Chemotherapy and Pharmacology*, vol. 33, no. 1, pp. 17–24, 1993.

[138] B. Chandra, R. Subramaniam, S. Mallik, and D. K. Srivastava, "Formulation of photocleavable liposomes and the mechanism of their content release," *Organic and Biomolecular Chemistry*, vol. 4, no. 9, pp. 1730–1740, 2006.

[139] A. I. Elegbede, J. Banerjee, A. J. Hanson et al., "Mechanistic studies of the triggered release of liposomal contents by matrix metalloproteinase-9," *Journal of the American Chemical Society*, vol. 130, no. 32, pp. 10633–10642, 2008.

[140] K. Miyata, M. Oba, M. Nakanishi et al., "Polyplexes from poly(aspartamide) bearing 1,2-diaminoethane side chains induce pH-selective, endosomal membrane destabilization with amplified transfection and negligible cytotoxicity," *Journal of the American Chemical Society*, vol. 130, no. 48, pp. 16287–16294, 2008.

[141] H. C. Kang, H. J. Kang, and Y. H. Bae, "A reducible polycationic gene vector derived from thiolated low molecular weight branched polyethyleneimine linked by 2-iminothiolane," *Biomaterials*, vol. 32, no. 4, pp. 1193–1203, 2011.

[142] X. H. Liu, J. T. Zhang, and D. M. Lynn, "Polyelectrolyte multilayers fabricated from 'charge-shifting' anionic polymers: a new approach to controlled film disruption and the release of cationic agents from surfaces," *Soft Matter*, vol. 4, no. 8, pp. 1688–1695, 2008.

[143] E. Fattal, S. Nir, R. A. Parente, and F. C. Szoka, "Pore-forming peptides induce rapid phospholipid flip-flop in membranes," *Biochemistry*, vol. 33, no. 21, pp. 6721–6731, 1994.

[144] A. M. Funhoff, C. F. van Nostrum, M. C. Lok, J. A. W. Kruijtzer, D. J. A. Crommelin, and W. E. Hennink, "Cationic polymethacrylates with covalently linked membrane destabilizing peptides as gene delivery vectors," *Journal of Controlled Release*, vol. 101, no. 1–3, pp. 233–246, 2005.

[145] N. K. Subbarao, R. A. Parente, F. C. Szoka Jr., L. Nadasdi, and K. Pongracz, "PH-dependent bilayer destabilization by an amphipathic peptide," *Biochemistry*, vol. 26, no. 11, pp. 2964–2972, 1987.

[146] M. A. Yessine and J. C. Leroux, "Membrane-destabilizing polyanions: interaction with lipid bilayers and endosomal escape of biomacromolecules," *Advanced Drug Delivery Reviews*, vol. 56, no. 7, pp. 999–1021, 2004.

[147] M. E. H. El-Sayed, A. S. Hoffman, and P. S. Stayton, "Smart polymeric carriers for enhanced intracellular delivery of therapeutic macromolecules," *Expert Opinion on Biological Therapy*, vol. 5, no. 1, pp. 23–32, 2005.

[148] D. B. Rozema, K. Ekena, D. L. Lewis, A. G. Loomis, and J. A. Wolff, "Endosomolysis by masking of a membrane-active agent (EMMA) for cytoplasmic release of macromolecules," *Bioconjugate Chemistry*, vol. 14, no. 1, pp. 51–57, 2003.

[149] M. A. Yessine, M. H. Dufresne, C. Meier, H. U. Petereit, and J. C. Leroux, "Proton-actuated membrane-destabilizing polyion complex micelles," *Bioconjugate Chemistry*, vol. 18, no. 3, pp. 1010–1014, 2007.

[150] Y. L. Lin, G. Jiang, L. K. Birrell, and M. E. H. El-Sayed, "Degradable, pH-sensitive, membrane-destabilizing, comb-like polymers for intracellular delivery of nucleic acids," *Biomaterials*, vol. 31, no. 27, pp. 7150–7166, 2010.

[151] T. Takahashi, K. Kono, T. Itoh, N. Emi, and T. Takagishi, "Synthesis of novel cationic lipids having polyamidoamine dendrons and their transfection activity," *Bioconjugate Chemistry*, vol. 14, no. 4, pp. 764–773, 2003.

[152] Z. Yang, G. Sahay, S. Sriadibhatla, and A. V. Kabanov, "Amphiphilic block copolymers enhance cellular uptake and nuclear entry of polyplex-delivered DNA," *Bioconjugate Chemistry*, vol. 19, no. 10, pp. 1987–1994, 2008.

[153] Z. Liu, Z. Zhang, C. Zhou, and Y. Jiao, "Hydrophobic modifications of cationic polymers for gene delivery," *Progress in Polymer Science*, vol. 35, no. 9, pp. 1144–1162, 2010.

[154] S. Guo, Y. Huang, T. Wei et al., "Amphiphilic and biodegradable methoxy polyethylene glycol-block-(polycaprolactone-graft-poly(2-(dimethylamino)ethyl methacrylate)) as an effective gene carrier," *Biomaterials*, vol. 32, no. 3, pp. 879–889, 2011.

[155] A. Dehshahri, R. K. Oskuee, W. T. Shier, A. Hatefi, and M. Ramezani, "Gene transfer efficiency of high primary amine content, hydrophobic, alkyl-oligoamine derivatives of polyethylenimine," *Biomaterials*, vol. 30, no. 25, pp. 4187–4194, 2009.

[156] S. Katayama, H. Hirose, K. Takayama, I. Nakase, and S. Futaki, "Acylation of octaarginine: implication to the use of intracellular delivery vectors," *Journal of Controlled Release*, vol. 149, no. 1, pp. 29–35, 2011.

[157] M. S. Shim and Y. J. Kwon, "Acid-responsive linear polyethylenimine for efficient, specific, and biocompatible siRNA delivery," *Bioconjugate Chemistry*, vol. 20, no. 3, pp. 488–499, 2009.

[158] M. S. Shim and Y. J. Kwon, "Controlled cytoplasmic and nuclear localization of plasmid DNA and siRNA by differentially tailored polyethylenimine," *Journal of Controlled Release*, vol. 133, no. 3, pp. 206–213, 2009.

Research Article

Characterization of Multiwalled Carbon Nanotubes Dispersing in Water and Association with Biological Effects

Xuelian Cheng,[1] Jun Zhong,[2] Jie Meng,[1] Man Yang,[1] Fumin Jia,[1] Zhen Xu,[1] Hua Kong,[1] and Haiyan Xu[1]

[1] *Institute of Basic Medical Sciences, Chinese Academy of Medical Sciences and Peking Union Medical College, Beijing 100005, China*
[2] *Institute of Functional Nano & Soft Materials, Soochow University, Jiangsu 215123, China*

Correspondence should be addressed to Haiyan Xu, xuhy@pumc.edu.cn

Biomedical application potentials of carbon nanotubes-based materials have been investigated intensively in recent years; however, characterization and metrology are still facing great technical challenges when the materials are intended to be used as carriers for therapeutics in aqueous solutions. Systematic characterization on the dispersing carbon nanotubes is urgently required and therefore of significance. In this paper multiwalled carbon nanotubes (MWCNTs) with different average lengths or with different oxidation degrees were dispersed in water and characterized systematically by applying UV spectroscopy, SEM, DLS, TGA, XPS, and FTIR. In particular, the characteristic absorption of the carbon nanotubes was analyzed using resolution-fitting technique to establish relations of wavelength and absorption intensity to the size distribution and surface chemistry. Results indicated that the absorption spectra of MWCNTs could reflect the variation of surface chemistry and length distribution of carbon nanotubes dispersed in water by combining with the other measurements. A vascular endothelium cell line was taken as a model to figure out association between physicochemical features and cytotoxicity of the carbon nanotubes. It was showed that the multiwalled carbon nanotubes with different oxidation degrees and similar length distribution exhibited different interaction files to the cells proliferation in a manner of time dependence and concentration dependence.

1. Introduction

Carbon nanotubes have shown their promising potentials in biomedical fields including novel delivery systems for drugs or DNAs/RNAs in recent years, which have been reviewed in detail in some publications [1–6]. Meanwhile, biological safety and risks along with the application of carbon nanotubes-based materials have been seriously concerned, as related research publications are increasing constantly and the experimental data from different research groups are often different and even conflicted each other [7–12]. For example, Takagi et al. reported an incidence of mesothelioma in p53-deficient mice injected intraperitoneally with 3 mg per mouse of multiwalled carbon nanotubes [8]. On the contrary, Muller et al. reported that, several months after the injection of nanotubes, the inflammatory reaction was almost absent and limited by a fibrotic encapsulation; hence, multiwalled carbon nanotubes (MWCNTs) with or without structural defects did not induce mesothelioma in this bioassay displaying the absence of carcinogenicity of nanotubes [9]. Accumulating evidence implied that one of the important reasons that cause these conflicts is the lack of standard metrology for carbon nanotubes due to the lack of comprehensive characterization, which makes it difficult to compare data from different laboratories worldwide. Besides making comparison, the great efforts to apply carbon nanotubes into biomedical fields are requiring comprehensive characterization urgently.

For molecular drugs, their physicochemical properties such as molecular weight, chemical composition, purity, solubility, and stability are usually necessary to analyze. The instrumentation to ascertain these properties have been well established, and the techniques are standardized. Techniques

such as nuclear magnetic resonance (NMR), mass spectrometry, ultraviolet-visible (UV-Vis) spectroscopy, infrared spectroscopy (IR), and gas chromatography (GC) can well meet the demands to analyze such molecules. However, for carbon nanotubes dispersing in water, there are big technical challenges in metrology as well as in characterization.

As it is well known, carbon nanotubes are one representative nanomaterial with heterostructure. The molecular weight of the carbon nanotubes is hard to determine due to their complicated surface chemistry induced by different modification processes and broad length distribution. Besides, they are usually required to disperse in water when being considered to be applied as carriers for therapeutic or detective molecules, while characterizations for carbon nanotubes dispersing in the aqueous solutions is facing more difficulties because most of the existing measurement technologies are just applicable to solid nanomaterials.

It has been noticed that the physicochemical features are likely to affect biological effects of the carbon nanotubes. For instance, some investigations have indicated that size distribution and surface chemistry of carbon nanotubes affected their interactions to the cells. Sato et al. reported that the degree of inflammatory response in subcutaneous tissue in rats induced by the MWCNTs of about $220\,\mu m$ in length was slight in comparison with that around those induced by the MWCNTs of about $825\,\mu m$ in length [13]; Li et al. modified MWCNTs with phosphatidylcholine (PC), polyethylene glycol (PEG), and PC-terminated polyethylene glycol (PEG-PC), and the modified MWCNT induced only low acute toxicity in reference to the original MWCNT [14]. Nevertheless, lots of experimental data are hard to be compared because in many cases only a broad size range or an average length value was given in the literature, and most of them were the description for the carbon nanotubes in the solid phase. These strongly suggest that comprehensive characterization for carbon nanotubes dispersing in the aqueous solution and the association with biological effects still requires extensive investigation.

This work aimed to make systematic and detailed characterization of as-received or oxidized multiwalled carbon nanotubes (MWCNTs) dispersing in water by applying UV-vis-NIR spectroscopy, scanning electron microscope (SEM), dynamic light scattering (DLS), thermogravimetry analysis (TGA), X-ray photoelectron spectroscopy (XPS), and Fourier transform infrared spectroscopy (FTIR). In particular, a resolution-fitting technique was applied with the UV-vis-NIR spectra of the carbon nanotubes to establish relations of wavelength and absorption intensity to the size distribution and surface chemistry. Additionally, a vascular endothelium cell line was taken as a model to figure out association between physicochemical features and cytotoxicity of the carbon nanotubes.

2. Materials and Methods

2.1. Materials. Three kinds of as-received multiwalled carbon nanotubes (MWCNTs) were purchased from Chengdu Organic Chemicals Co. Ltd. the diameter for the samples

is $20{\sim}30\,nm$, and average length of the samples is given by the manufacturer as $0.5{\sim}2\,\mu m$ (s-MWCNTs), $30\,\mu m$ (m-MWCNTs), and $50\,\mu m$ (l-MWCNTs). The samples purity is >95%, amorphous carbon <3%, and ash (catalyst residue) <1.5%.

2.2. Oxidation of l-MWCNTs. In this work, only as-received MWCNTs were treated to obtain oxidized l-MWCNTs with different oxidation degrees. The treatment procedure included a combination of concentrated acids oxidation and sonication as described in previous literature [15]. In brief, the as-received l-MWCNTs were mixed in concentrated H_2SO_4/HNO_3 ($3:1$ by volume) for $12\,h$, followed by a probe sonication at $750\,W$ for different times of 0, 30, 60, and 100 seconds to make different oxidation degrees; the resulting products are oxidized l-MWCNTs and named l-MWCNTs-O_1, l-MWCNTs-O_2, l-MWCNTs-O_3, and l-MWCNTs-O_4, respectively. The above oxidized products were rinsed, filtrated using millipore membrane (pore size: $2\,\mu m$) thoroughly with distilled water ($18.2\,\Omega$) till the pH value of the running water reached to that of original, and then dried completely in a vacuum oven at $50°C$.

2.3. UV Spectroscopy Analysis and Peak Resolution and Fitting

2.3.1. Preparation of Colloid Solutions of Carbon Nanotubes. The as-received l-MWCNTs, m-MWCNTs, and l-MWCNTs and the oxidized l-MWCNTs samples were dispersed in distilled water or in complete culture medium (that includes DMEM and 10% FCS) by aid of probe sonication at $360\,W$ for 60 seconds, followed by a centrifugation of $1540\,g/min$ for 20 minutes to remove undispersed substance from the aqueous phase. The solutions were subjected to UV-Vis-NIR spectroscopy (Lambda 950, Perkin-Elmer). The absorption spectra of the samples were resolved into 3 subpeaks and fitted to envelop using software of Igor pro 6.1.

2.3.2. Measurement of Colloids Stability of Carbon Nanotubes. To measure the colloid stability of carbon nanotubes in the water at static condition, the solution samples obtained in Section 2.3.1 were placed in vertically standing tubes and stored at room temperature for 2, 8, 17, 24, and 31 days. At each time point, a $50\,\mu L$ of the stock solutions of very upper part was taken and subjected to UV-Vis-NIR spectroscopy (Lambda 950, Perkin-Elmer). The optical density (O.D.) of the solutions was measured. For measurements in dynamic condition, the solutions obtained in Section 2.3.1 and stored post 8 days were centrifuged in $4310\,g/min$, $6740\,g/min$, and $11390\,g/min$, respectively. The O.D. of the supernatants was measured.

2.4. Scanning Electron Microscopy (SEM). Solutions obtained in Section 2.3.1 were dropped on a silicon substrate and dried at room temperature for scanning electron microscopy (SEM, Hitachi S-5200) observation. Length distribution for the four oxidized MWCNTs was obtained by counting more than 300 nanotubes randomly taken in ten SEM images.

2.5. Dynamic Light Scattering Measurement. Solutions obtained in Section 2.3.1 were subjected to dynamic light scattering spectroscopy (ZEN 3690; Malvern Instruments Ltd, Malvern, UK) at a fixed scattering angle of 90 at 25°C. Zeta potential and relative hydrodynamic diameter distribution of the MWCNTs solutions (water or the culture medium) were measured.

2.6. Thermogravimetric Analysis. Samples of as-received and oxidized MWCNTs were weighted and mounted to thermogravimetric analysis (TG209C, NETZSCH). The measurement temperature ranged from 25°C to 800°C, and heating rate is 20°C/min.

2.7. Surface Chemistry Analysis

2.7.1. FT-IR Analysis. Samples of MWCNTs were analyzed by Fourier transform infrared spectroscopy (FT-IR, Nicolet NEXUS 670). Spectra were recorded with a resolution of $2\,cm^{-1}$ over the wave number range $4000 \sim 400\,cm^{-1}$.

2.7.2. XPS Analysis. X-ray photoelectron spectroscopy (XPS) measurements were performed on a Japan JEOL Scientific JPS-9010TR XPS system with Al K Alpha radiation as the exciting source, where the binding energies were calibrated by referencing the C1s peak to reduce the sample charge effect.

2.8. MTS Assay to Examine Endothelium Cells Viability. Endothelial cell line (EA.hy926) was purchased from the Cell Bank of Shanghai Institutes of Biological Sciences, Chinese Academy of Sciences (Shanghai, China), which was maintained in DMEM media supplemented with 10% fetal calf serum, 4 mM L-glutamine, 1 mM sodium pyruvate, 4500 mg/L glucose, 1500 mg/L sodium bicarbonate, and 0.1% penicillin G and streptomycin (Invitrogen) at 37°C with 5% CO_2. Endothelial cells were detached from the culture flask using 0.125 M trypsin-EDTA when they became $70 \sim 80\%$ confluent. Then the cells were seeded on 96-well plate at a density of 4×10^3 cells/well and cultivated in an incubator overnight. The culture medium was replaced with $200\,\mu L$ of culture medium containing l-MWCNTs-O_1, l-MWCNTs-O_2, l-MWCNTs-O_3, or l-MWCNTs-O_4 with concentrations of 0.01, 0.05 and 0.25 mg/mL . The viable cells number was determined at 48 h and 72 h using MTS assay (CellTiter 96 @ A Queous Non-Radioactive Cell Proliferation Assay, Promega) according to the manufacturer's instruction. The intact culture medium was taken as control.

The viability of the cells was calculated using the following equation:

$$\text{Viability (\%)} = \left[\frac{\text{(average cell number of sample wells)}}{\text{(average cell number of control wells)}} \right] \times 100\%. \tag{1}$$

The data were expressed as average ± standard deviation ($\bar{x} \pm$ SD) unless otherwise stated. Data were analyzed using a Student's two-tailed test, assuming equal variance with SAS 8.2 software.

3. Results and Discussion

3.1. SEM Observation of As-Received MWCNTs and Oxidized MWCNTs. Length distribution for carbon nanotubes dispersing in water is one very crucial parameter because, to a large extent, it determines biological effects of carbon nanotubes in water. Detailed information of length distribution is necessary and helpful to deeply understand biological effects induced by carbon nanotubes.

SEM is widely used to characterize morphology as well as individual size of carbon nanotubes materials [16–20]. As seen in the SEM images shown in Figure 1, the length distribution for as-received s-, m-, and l-MWCNTs which are easy to distinguish is obviously different. In addition, it could be noticed that the tube surface of as-received s- or m-MWCNTs seemed not as clear as the surface of as-received l-MWCNTs. These indicated other forms of carbon substance on the tubes surface.

Figure 2 presented SEM images of l-MWCNTs treated with different oxidation degrees as an example of oxidation effect on the length of carbon nanotubes. It was clearly seen that, after oxidation treatment, the typical tube-like structures were remained while the length of as-received l-MWCNTs became obviously shorter in reference to that of original. By statistically counting from randomly selected SEM images, the length distribution of the four oxidized l-MWCNTs was very close, the four samples seemed to have similar size distributions ranging from 500 nm to $2\,\mu m$, and the average length is 940, 967, 967, and 974 nm for l-MWCNTs-O_1, l-MWCNTs-O_2, l-MWCNTs-O_3, and l-MWCNTs-O_4, respectively (inserted plots in the SEM images).

3.2. DLS Analysis of the Size Distribution of Oxidized MWCNTs. Dynamic light spectroscopy (DLS) is one measurement that may provide information of nanomaterials size distribution. Although DLS measurement is suitable to determine the diameter of particles with sphere shape, it can still provide hydrodynamic diameter for nanotubes [21, 22]; the data could be used to evaluate variation of length distribution for carbon nanotubes. The measurement of DLS and Zeta potential was conducted with the four kinds of oxidized l-MWCNTs dispersing in water or in the culture medium.

Zeta potential measurement showed that the four oxidized l-MWCNTs had very similar Zeta potential values around −42 mV when dispersing in water (Figure 3(a)), which is much lower than that of as-received l-MWCNTs of −28 mV. It is indicative that the oxidation treatment increased hydrophilicity and dispersion stability of l-MWCNTs in water. When dispersing in the culture medium, Zeta potential of the four kinds of oxidized l-MWCNTs was around −16 mV (Figure 3(c)), which is very similar to that
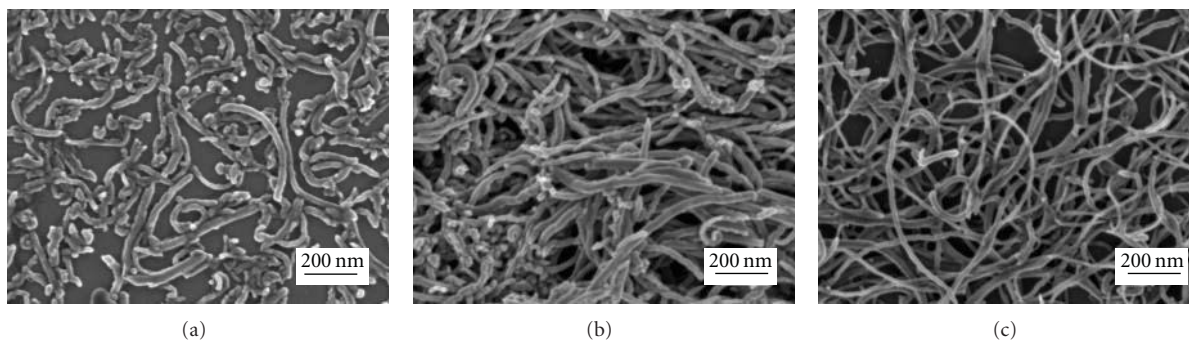
(a)

(b)

(c)

FIGURE 1: SEM images of three kinds of as-received MWCNTs with different average length: (a) $0.5 \sim 2\,\mu$m, (b) $30\,\mu$m, and (c) $50\,\mu$m.
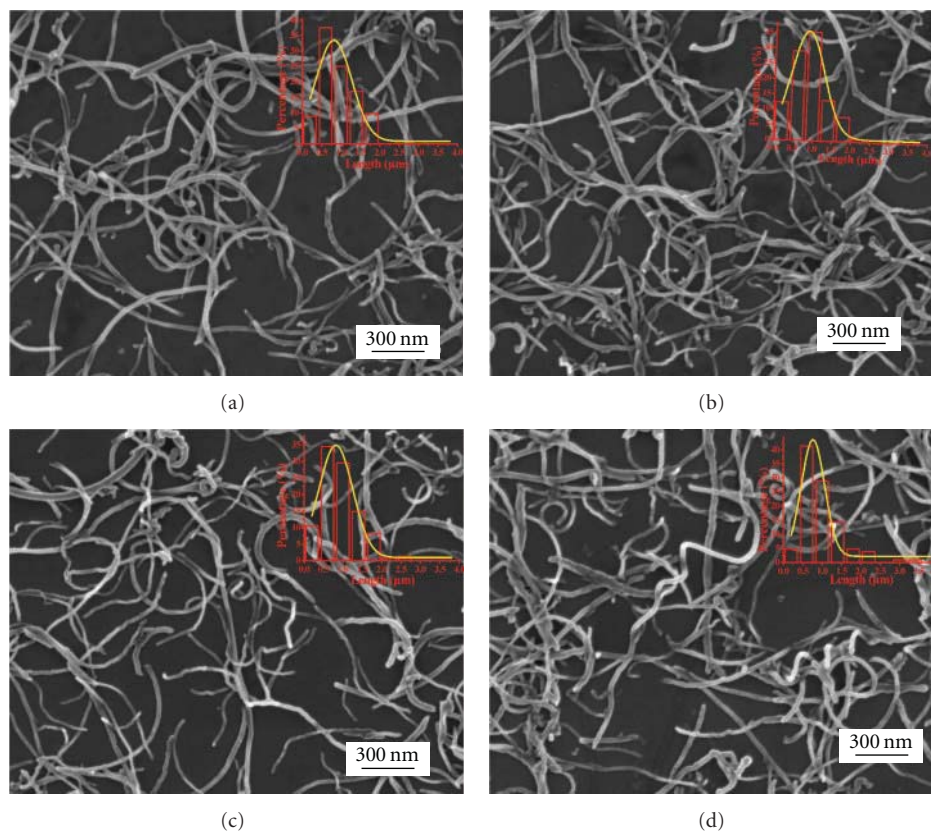

(a)

(b)

(c)

(d)

FIGURE 2: SEM images for oxidized l-MWCNTs: (a) l-MWCNT-O_1, (b) l-MWCNT-O_2, (c) l-MWCNT-O_3, and (d) l-MWCNT-O_4.

of culture medium (-17 mV as determined). This indicated that the four kinds of MWCNTs absorbed serum protein molecules onto their surface. And, with the oxidation degree increased, Zeta potential value exhibited a decreasing tendency, which implied that l-MWCNTs with higher oxidation degree had less negative surface charges than those with lower oxidation degree. A possible explanation is that Zeta potential of serum protein could be affected by oxidized l-MWCNTs with a higher oxidation degree.

For those dispersing in water, it could be noticed that the size distribution of the four kinds of oxidized l-MWCNTs became more narrow compared with as-received

l-MWCNTs. Among the four oxidized l-MWCNTs, l-MWCNTs-O_4 had the most narrow size distribution (Figure 3(b)), which is consistent with the observations from SEM. These results implied that oxidation treatment with long-time sonication would benefit size homogeneity of carbon nanotubes. The four kinds of oxidized l-MWCNTs dispersing in the culture medium showed a tendency of size distribution similar to those dispersing in water (Figure 3(d)). Comparing the results given in Figures 3(a) and 3(c), the average hydrodynamic size for the four kinds of MWCNTs dispersing in the medium was larger than that dispersing in water, which provided further evidence of

(a)

(b)

(c)

(d)
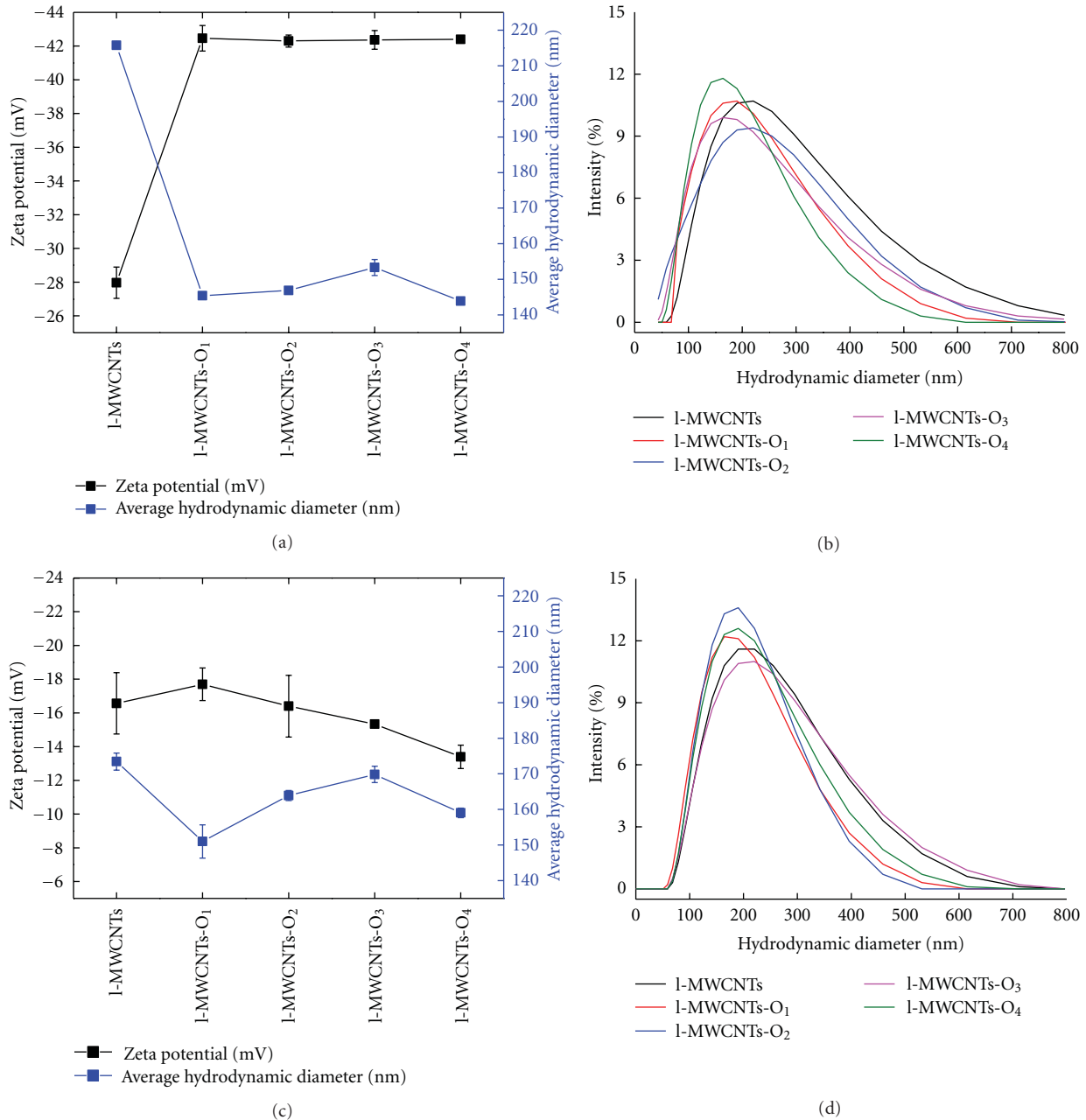
FIGURE 3: DLS analysis of as-received l-MWCNTs and the four oxidized l-MWCNTs dispersing in water, in which, (a) and (c) give average hydrodynamic diameters and Zeta potentials of as-received l-MWCNTs and the four kinds of oxidized l-MWCNTs dispersing in water and in the culture medium; (b) and (d) present DLS spectra of the four kinds of oxidized l-MWCNTs dispersing in water and in the culture medium, respectively.

serum protein adsorption. Taken in all, the average hydrodynamic diameter of the four oxidized l-MWCNTs decreased significantly in reference with as-received l-MWCNTs no matter dispersing in water or in the culture medium, and the four oxidized samples exhibited average size in a closed level.

3.3. Surface Chemistry of Oxidized MWCNTs (XPS and FTIR). Water dispersion of carbon nanotube-based materials largely depends on their surface chemistry. Usually treatment of

concentrated acids combining with sonication makes carbon nanotubes oxidized, which introduces a variety of oxygen-containing groups to the surface of carbon nanotubes such as O–C=O, C=O, and C–O along with cutting carbon nanotubes short.

As shown in XPS spectra of oxidized l-MWCNTs (Figure 4(a)), the characteristic binding energy of 284.4 eV, 285.4 eV, 286.9 eV, 288.6 eV, and 290.8 eV was attributed to C–C, C–O, C=O, O–C=O and π-π^*, respectively. It is

(a)

(b)

(c)
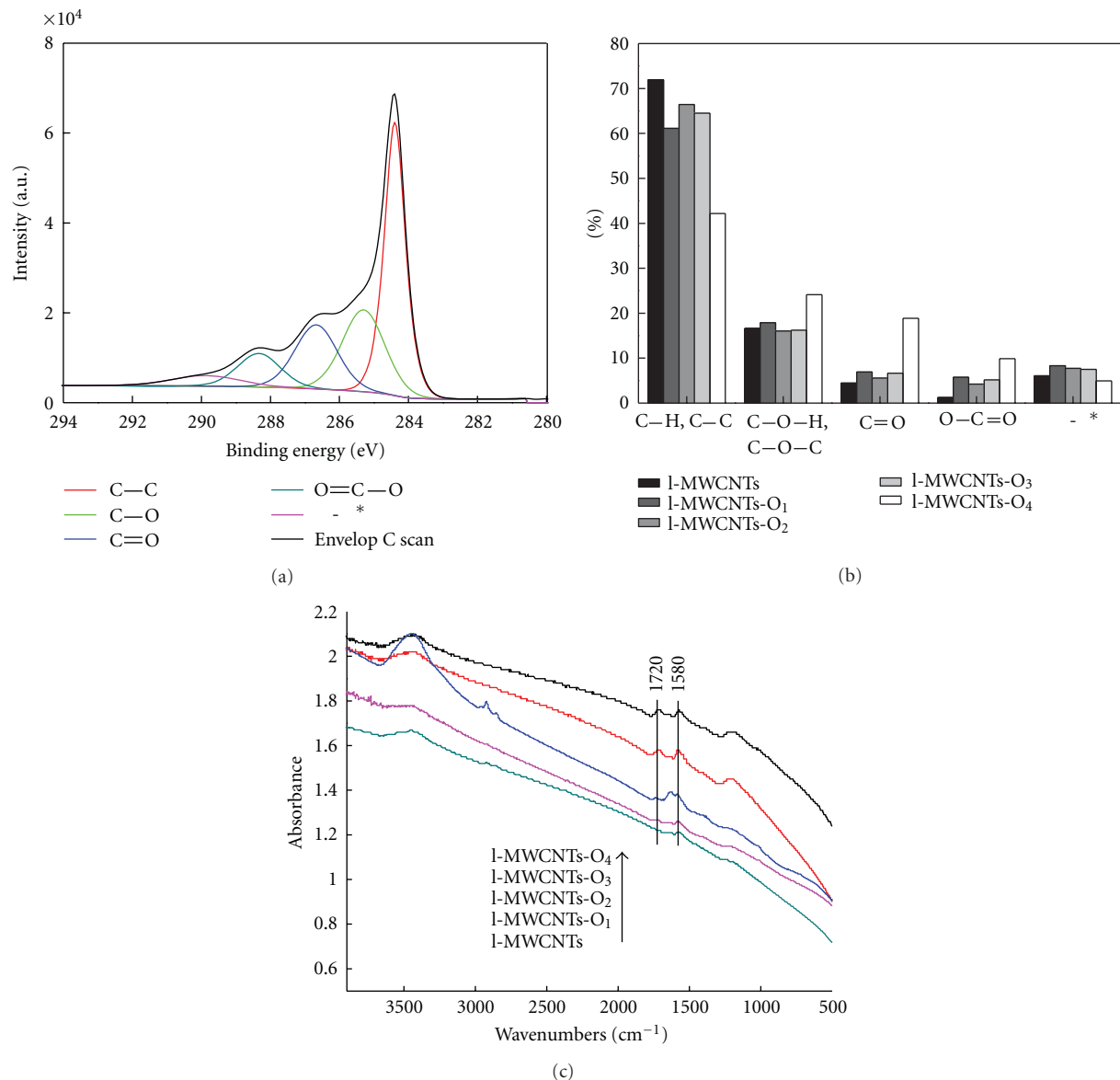
FIGURE 4: Surface chemistry of oxidized MWCNTs dispersed in the aqueous solution. (a) XPS spectra of l-MWCNT-O_4. (b) Relative amount of various oxygen species. (c) FTIR of l-MWCNTs with different oxidation degrees.

important to note that, with the sonication time increased, the amount of oxygen-containing groups increased correspondingly in particular, the order of increasing rate for the different oxygen-containing groups is; O–C=O > C=O > C–O (Figure 4(b)). FTIR spectroscopy provided further evidence of O–C=O group that existed on the surface, and the characteristic absorption peak of $1720 \, cm^{-1}$ became stronger as sonication time increased (Figure 4(c)). The above results evidenced that longer sonication time increased the oxidation degree of carbon nanotubes, resulting in more oxygen-containing groups on the surface of l-MWCNTs.

3.4. TGA Analysis of As-Received MWCNTs and Oxidized l-MWCNTs.
TGA can be used to analyze the quality of carbon

nanotubes [23] as well as to track the effects of purification process and monitor how changes in manufacturing conditions affect the percentage of carbon nanotubes within the sample [24]. Figure 5 showed TGA and DTG spectra of the three kinds of as-received MWCNTs and the four oxidized l-MWCNTs. The primary oxidation temperature for each material is defined as the temperature at the highest peak for the material on the derivative weight curve and can represent the thermal stability of the material. For the as-received MWCNTs, the oxidation temperatures were $651°C$ for l-MWCNTs, $620°C$ for m-MWCNTs, and $610°C$ for s-MWCNTs (Figure 5(a)), among which as-received l-MWCNTs exhibited the highest oxidation temperature. As given by the manufacturer, the oxygen content for the different as-received MWCNTs is 4%, 5%, and 6% for s-, m-,
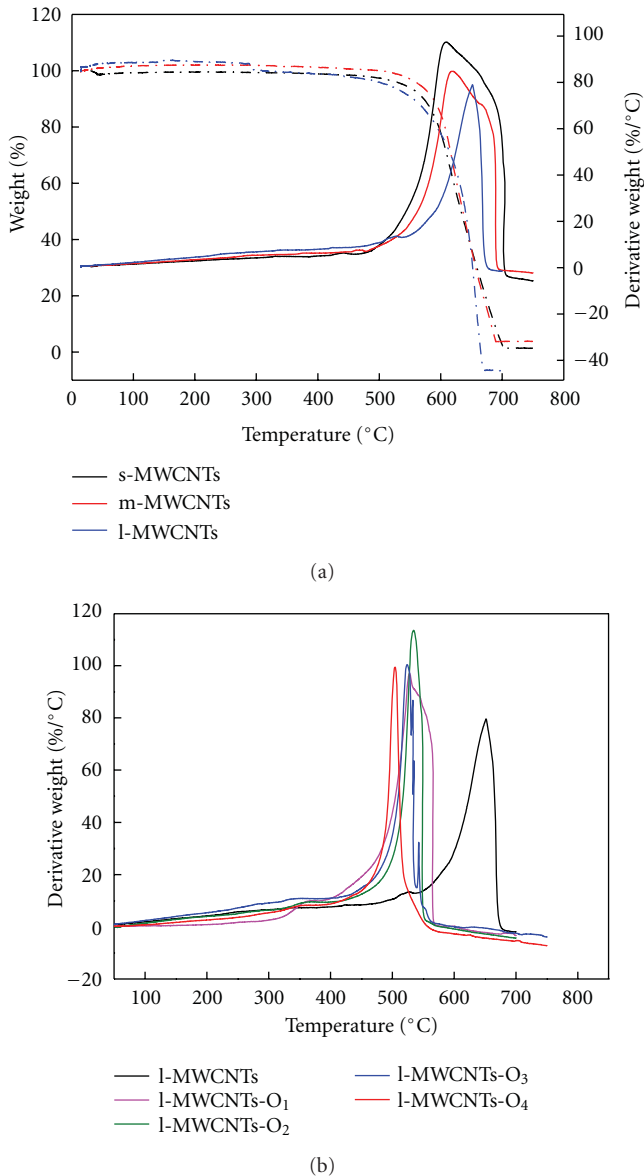
FIGURE 5: TGA and DTG spectra of as-received s-, m-, l-MWCNTs (a), and oxidized l-MWCNT (b).

and l-MWCNTs, respectively. It was indicated that the surface oxidation degree for the three of as-received MWCNTs was s- >m- >l-MWCTs because lowly oxidized carbon nanotubes are more resistant to decomposition than highly oxidized ones. These are in consistence with the data given by the manufacturer. In addition, s-MWCNTs and m-MWCNTs exhibited a fairly broad decomposition peak with multiple shoulders, which should be likely indicative of multiple types of carbons decomposing. This was consistent with the SEM observations (Figure 1).

Figure 5(b) showed result of TGA tests for the oxidized l-MWCNTs that have similar length distributions. The oxidation temperature of oxidized MWCNTs was 527.83°C, 534.62°C, 524.31°C, and 504.4°C to l-MWCNT-O_1, l-

MWCNT-O_2, l-MWCNT-O_3, and l-MWCNT-O_4, respectively. From the temperature data, first, it could be seen that oxidation temperature of the different oxidized l-MWCNTs with aid of sonication was decreased with the increasing oxidation time. It has been reported in the literature that the shift to lower temperature is consistent as the oxygen content increases [23]. Hence, it is inferred that longer sonication time resulted in higher oxidation degree. The results also showed that oxidation temperature of l-MMCNTs-O_1 was lower and the peak was broader compared to the other three kinds of oxidized l-MWCNTs, from 410°C to 566°C, indicating that treatment with the concentrated acids only would result in an unhomogeneous oxidization of carbon nanotubes. We would suggest that the part of lowly oxidized nanotubes in l-MMCNTs-O_1 made its decomposition temperature increase. Beside the variation of oxidation temperature, the oxidation peaks for the four oxidized l-MWCNTs were much narrower than the one for as-received l-MWCNTs, which indicated a sample of higher purity.

3.5. Characteristic Absorption of MWCNTs and Relation to the Size Distribution and Surface Chemistry. MWCNTs showed characteristic absorption spectra in 240~265 nm. Figures 6(a) and 6(b) presented representative UV spectra of as-received MWCNTs with different average length and the oxidized l-MWCNTs with different oxidation degrees, respectively, exhibiting the characteristic absorption. It could be seen that the spectra containing multiple peaks, which were resolved into three peaks as shown in Figure 6(c), among them peak 2, was a major one both in intensity and in area. For the three as-received MWCNTs samples, the wavelength of peak 2 shifted towards red obviously from 259 nm to 262 nm with the average length of MWCNTs increasing from 2 μm to 50 μm, while the intensity of peak 2 varied from 0.29 to 0.33 (Figure 6(d)). For the four oxidized l-MWCNTs, with the percentage of surface oxygen content increased, the intensity of peak 2 increased correspondingly, from 0.38 to 0.57 (Figure 6(e)), while the wavelength of peak 2 exhibited a slight red shift, from 263 nm to 264 nm. Together in all, it could be found that the intensity of peak 2 reflected the variation of oxidation degree of the MWCNTs, and the wavelength of peak 2 reflected the majority length of MWCNTs dispersing in water. And, from the resolved spectra, one can identify and compare MWCNTs samples from different sources.

3.6. Colloid Stability of Oxidized MWCNTs. The characteristic absorption of MWCNTs can be used to examine colloid stability of MWCNTs. L-MWCNTs-O_4 was taken as an example in this work; and dits colloid stability was monitored using the absorption spectra. Figure 7 presented the absorption peak of l-MWCNTs-O_4 dispersing in water within storage periods. When the absorption spectra were resolved into three peaks, the absorption intensity decreased with time under static condition. The dramatic variation occurred within 17 days, and then the variation extent
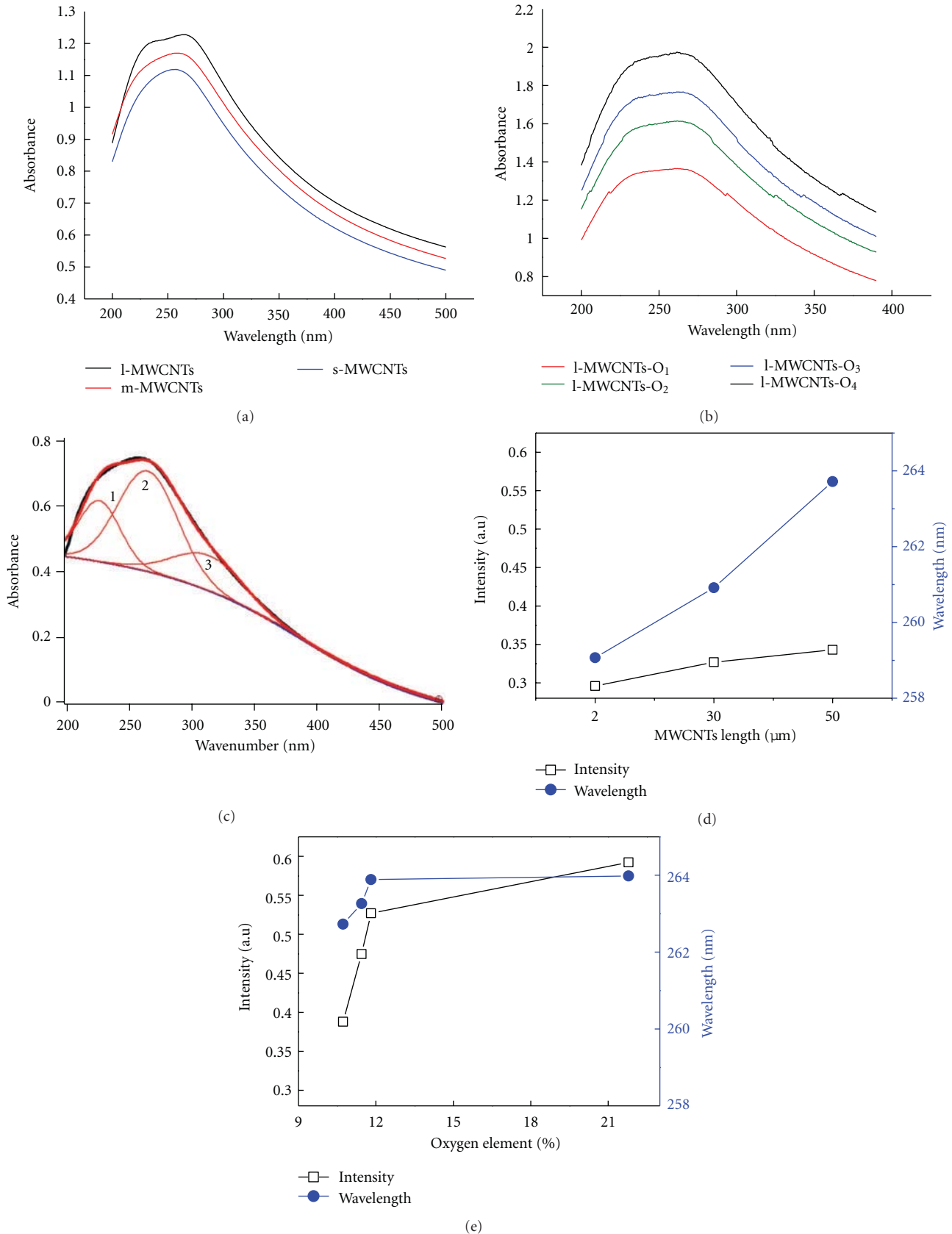
FIGURE 6: UV spectroscopy of MWCNTs, in which (a) is UV spectra of as-received MWCNTs with different average lengths, (b) is UV spectra of the four kinds of oxidized l-MWCNTs, (c) presents representative spectra of MWCNTs containing three resolved peaks, and (d) and (e) display the relation of intensity and wavelength of peak 2 with as-received MWCNTs and oxidized MWCNTs, respectively.
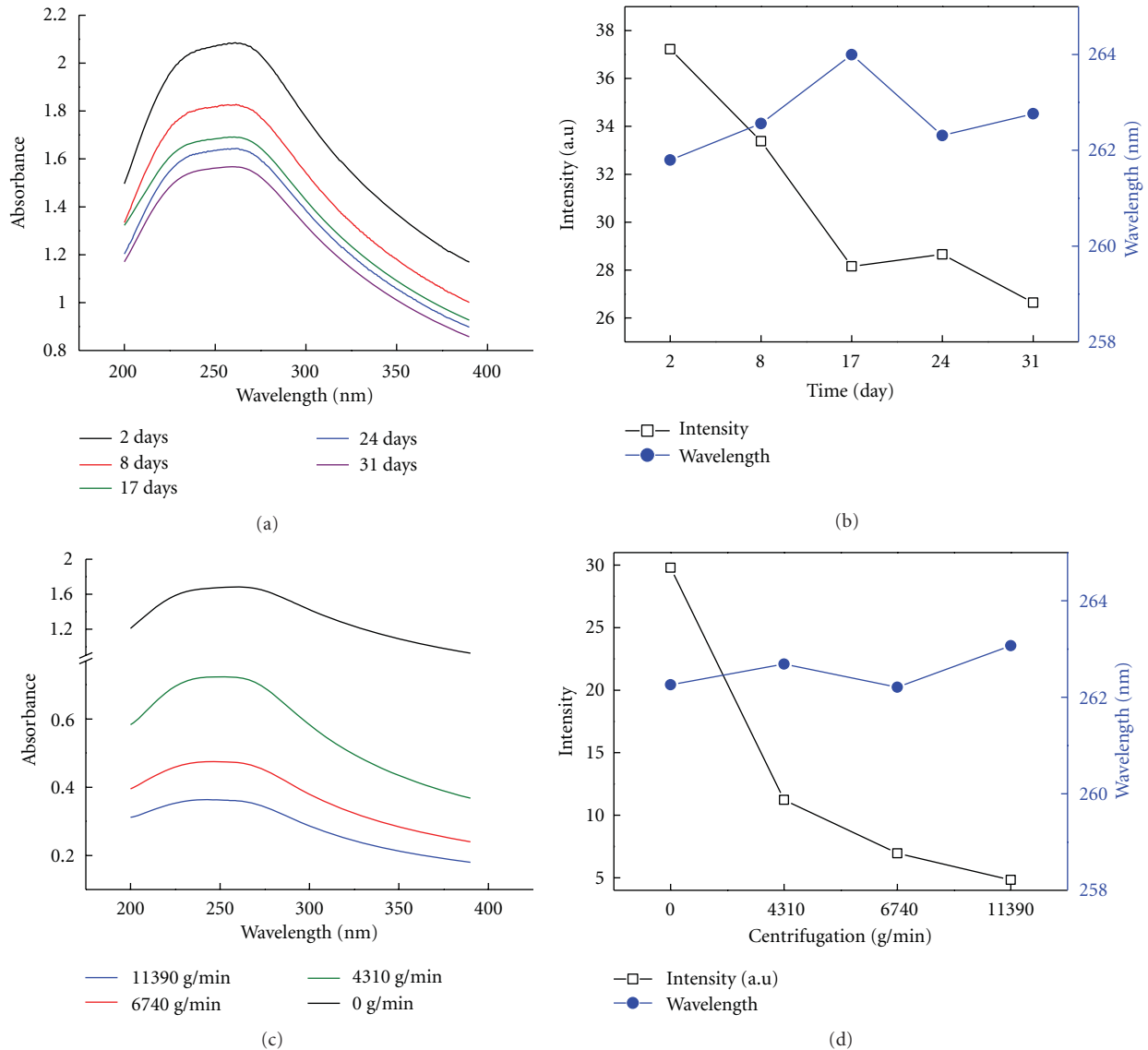
(a)

(b)

(c)

(d)

FIGURE 7: Absorption spectra of l-MWCNTs-O$_4$ under static (a) and centrifugation condition (c); peak 2 wavelength and intensity under static (b) and centrifugation condition (d).

became smaller. Peak 2 also exhibited a slight red shift from 261.7 to 262.3 except the one on day 17, which was 263.9 nm (Figures 7(a) and 7(b)). The wavelength on day 17 could be attributed to the dispersion status of l-MWCNTs-O$_4$ in water, the carbon nanotubes dispersing in water were gradually forming agglomerate, which made absorption wavelength red shifted, and then the agglomerate was gradually aggregated and left from water phase within 17 days; the absorption wavelength of the solution then shifted towards back. This is consistent with the variation of absorption intensity.

When centrifugation was applied to the solutions of l-MWCNTs-O$_4$ stored for different time, the wavelength and intensity of peak 2 decreased significantly, while the peak wavelength changed little (Figures 7(c) and 7(d)).

This implied that the length distribution of the carbon nanotubes staying in the water phase after centrifugation was similar, which can be explained by that some highly dispersing carbon nanotubes would come to a relative stability by centrifugation. And it is also suggested that proper centrifugation may speedup the process of obtaining a relative stable colloid solution of MWCNTs.

3.7. Influence of Oxidized l-MWCNTs on Endothelial Proliferation.
The proliferation of endothelial incubated with different oxidized l-MWCNTs was showed in Figure 8. At the low concentration of 0.01 mg/mL, it could be seen that the different oxidized l-MWCNTs resulted in slight reduction of cell viability than that of control after 48 h

(a)

(b)

(c)

(d)

(e)

(f)

(g)

(h)

(i)
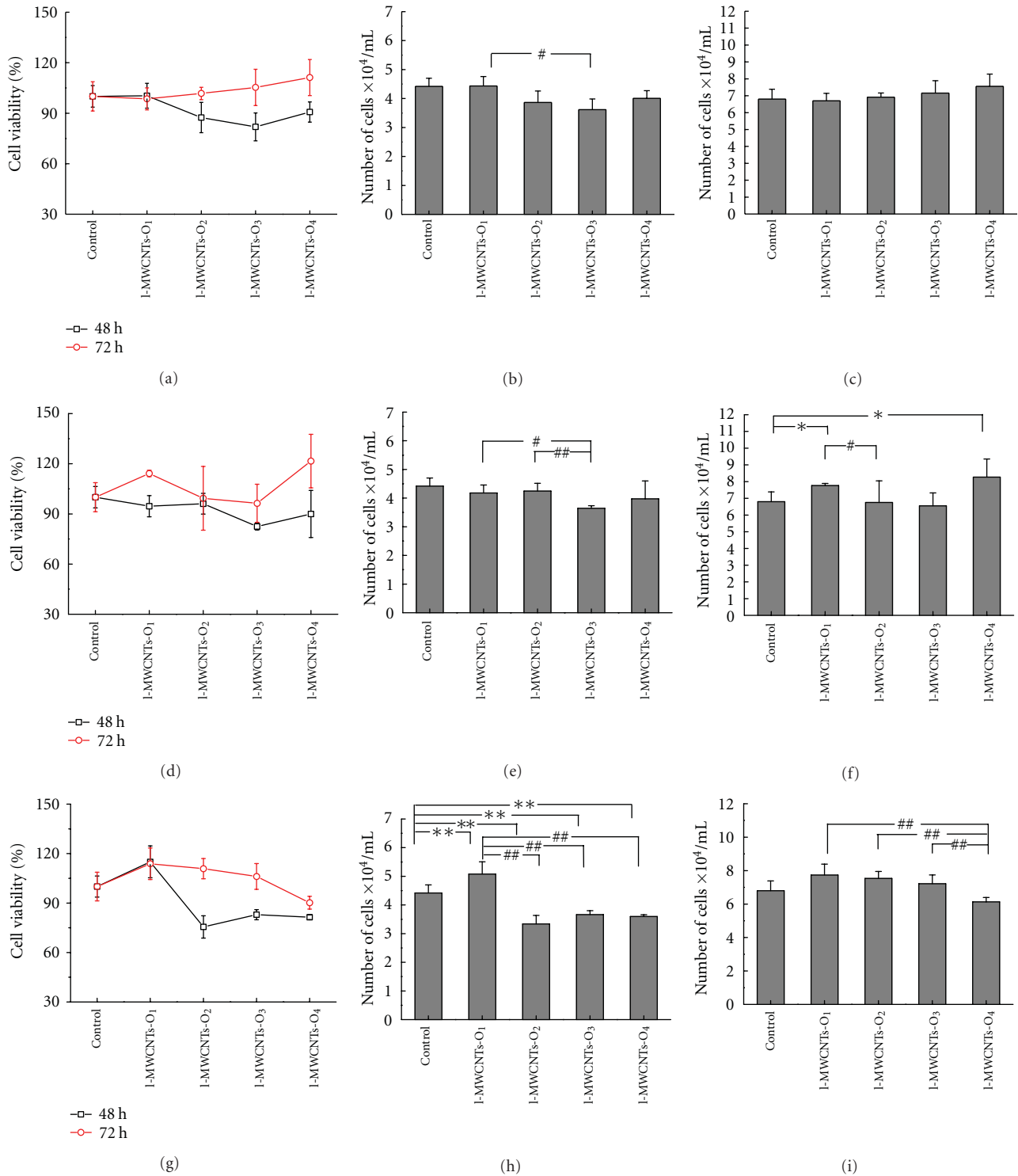
FIGURE 8: Cell proliferation of the endothelium cells cultivated different concentrations of oxidized l-MWCNTs. (a)–(c) 0.01 mg/mL; (d)–(f) 0.05 mg/mL; (g)–(i) 0.25 mg/mL. The cultivation time for (b), (e), and (h) is 48 h and for (c), (f), and (i) is 72 h.

of cultivation; however, there was no significant difference between the different oxidized MWCNTs and control. Significant difference appeared in l-MWCNT-O_3 and l-MWCNT-O_1. After 72 h of cultivation, the cell viability

of each group became normal (Figures 8(a)–8(c)). At the middle concentration of 0.05 mg/mL, there was a similar tendency to that at 0.01 mg/ml after 48 h of cultivation. Significant difference appeared between l-MWCNT-O_1 and

l-MWCNT-O_3, and l-MWCNT-O_2 and l-MWCNT-O_3 at 48 h of cultivation. As the time was increased to 72 h, cell viability also showed a recovery to normal, and l-MWCNTs-O_1 and l-MWCNTs-O_4 exhibited stimulation to the cells proliferation (Figures 8(d)–8(f)). Significant difference of proliferation inhibition existed between l-MWCNT-O_1 and l-MWCNT-O_3. At the high concentration of 0.25 mg/mL (Figures 8(g)–8(i)), profile for the cells cultivated with the four oxidized l-MWCNTs for 48 h was obviously different from those cultivated at the low or middle concentration; the four different oxidized l-MWCNTs displayed significant inhibition to the cells proliferation in reference to control. Treatment of 0.25 mg/mL l-MWCNTs-O_2 resulted in a 32% decrease in cell metabolism which is the highest in the current research. After 72 h, cells viability was little different from that of control. It was noticed that there was significant difference between l-MWCNT-O_1 and the other three kinds of oxidized MWCNTs at 48 h, while significant difference existed between l-MWCNT-O_4 and the other three kinds of oxidized MWCNTs at 72 h. Taking the above results together, the oxidized l-MWCNTs with different oxidation degree induced different inhibitory effects on the cells proliferation though the variation extents in the groups were not so many. This implied that using the above combined characterization solution might be able to probe the linkage between cells proliferation and different MWCNTs with slight difference. It is suggested that the four oxidized l-MWCNTs induced different inhibitory effects on the endothelial proliferation; the extent is related to the oxidation degree as well as to the concentration.

In summary, we would suggest that absorption spectroscopy in combination with SEM, DLS, TGA, XPS, and FTIR can provide more characteristic information of length distribution, surface chemistry, and colloid stability and dispersion status for identifying and comparing the dispersion status of multiwalled carbon nanotubes in water. And the obtained detailed information is helpful to compare the biological effects of carbon nanotubes from different sources.

References

[1] S. Beg, M. Rizwan, A. M. Sheikh, M. S. Hasnain, K. Anwer, and K. Kohli, "Advancement in carbon nanotubes: basics, biomedical applications and toxicity," *Journal of Pharmacy and Pharmacology*, vol. 63, no. 2, pp. 141–163, 2011.

[2] I. Posadas, F. J. Guerra, and V. Ceña, "Nonviral vectors for the delivery of small interfering RNAs to the CNS," *Nanomedicine*, vol. 5, no. 8, pp. 1219–1236, 2010.

[3] B. Kateb, M. Van Handel, L. Zhang, M. J. Bronikowski, H. Manohara, and B. Badie, "Internalization of MWCNTs by microglia: possible application in immunotherapy of brain tumors," *NeuroImage*, vol. 37, supplement 1, pp. S9–S17, 2007.

[4] C. Klumpp, K. Kostarelos, M. Prato, and A. Bianco, "Functionalized carbon nanotubes as emerging nanovectors for the delivery of therapeutics," *Biochimica et Biophysica Acta*, vol. 1758, no. 3, pp. 404–412, 2006.

[5] N. G. Sahoo, H. Bao, Y. Pan et al., "Functionalized carbon nanomaterials as nanocarriers for loading and delivery of a poorly water-soluble anticancer drug: a comparative study," *Chemical Communications*, vol. 47, no. 18, pp. 5235–5237, 2011.

[6] S. Ilbasmiş-Tamer, Ş. Yilmaz, E. Banoğlu, and I. T. Değim, "Carbon nanotubes to deliver drug molecules," *Journal of Biomedical Nanotechnology*, vol. 6, no. 1, pp. 20–27, 2010.

[7] N. Kobayashi, M. Naya, M. Ema et al., "Biological response and morphological assessment of individually dispersed multi-wall carbon nanotubes in the lung after intratracheal instillation in rats," *Toxicology*, vol. 276, no. 3, pp. 143–153, 2010.

[8] A. Takagi, A. Hirose, T. Nishimura et al., "Induction of mesothelioma in p53+/- mouse by intraperitoneal application of multi-wall carbon nanotube," *Journal of Toxicological Sciences*, vol. 33, no. 1, pp. 105–116, 2008.

[9] J. Muller, M. Delos, N. Panin, V. Rabolli, F. Huaux, and D. Lison, "Absence of carcinogenic response to multiwall carbon nanotubes in a 2-year bioassay in the peritoneal cavity of the rat," *Toxicological Sciences*, vol. 110, no. 2, pp. 442–448, 2009.

[10] Y. Bai, Y. Zhang, J. Zhang et al., "Repeated administrations of carbon nanotubes in male mice cause reversible testis damage without affecting fertility," *Nature Nanotechnology*, vol. 5, no. 9, pp. 683–689, 2010.

[11] K. Wako, Y. Kotani, A. Hirose, T. Doi, and S. Hamada, "Effects of preparation methods for multi-wall carbon nanotube (MWCNT) suspensions on MWCNT induced rat pulmonary toxicity," *Journal of Toxicological Sciences*, vol. 35, no. 4, pp. 437–446, 2010.

[12] D. Crouzier, S. Follot, E. Gentilhomme et al., "Carbon nanotubes induce inflammation but decrease the production of reactive oxygen species in lung," *Toxicology*, vol. 272, no. 1–3, pp. 39–45, 2010.

[13] Y. Sato, A. Yokoyama, K. I. Shibata et al., "Influence of length on cytotoxicity of multi-walled carbon nanotubes against human acute monocytic leukemia cell line THP-1 in vitro and subcutaneous tissue of rats in vivo," *Molecular BioSystems*, vol. 1, no. 2, pp. 176–182, 2005.

[14] H. Li, T. Zhang, G. Liang, Y. Zhang, and X. Wang, "In vivo evaluation of acute toxicity of water-soluble carbon nanotubes," *Toxicological and Environ-mental Chemistry*, vol. 93, no. 3, pp. 603–615, 2011.

[15] J. Meng, J. Duan, H. Kong et al., "Carbon nanotubes conjugated to tumor lysate protein enhance the efficacy of an antitumor immunotherapy," *Small*, vol. 4, no. 9, pp. 1364–1370, 2008.

[16] C. Yang, J. Mamouni, Y. Tang, and L. Yang, "Antimicrobial activity of single-walled carbon nanotubes: length effect," *Langmuir*, vol. 26, no. 20, pp. 16013–16019, 2010.

[17] W. Ma, L. Song, R. Yang et al., "Directly synthesized strong, highly conducting, transparent single-walled carbon nanotube films," *Nano Letters*, vol. 7, no. 8, pp. 2307–2311, 2007.

[18] L. Song, L. Ci, L. Lv et al., "Direct synthesis of a macroscale single-walled carbon nanotube non-woven material," *Advanced Materials*, vol. 16, no. 17, pp. 1529–1534, 2004.

[19] A. Schierz and H. Zänker, "Aqueous suspensions of carbon nanotubes: surface oxidation, colloidal stability and uranium sorption," *Environmental Pollution*, vol. 157, no. 4, pp. 1088–1094, 2009.

[20] Y. Wang, Z. Iqbal, and S. Mitra, "Rapidly functionalized, water-dispersed carbon nanotubes at high concentration," *Journal of the American Chemical Society*, vol. 128, no. 1, pp. 95–99, 2006.

[21] Y. K. Moon, J. Lee, J. K. Lee, T. K. Kim, and S. H. Kim, "Synthesis of length-controlled aerosol carbon nanotubes and their dispersion stability in aqueous solution," *Langmuir*, vol. 25, no. 3, pp. 1739–1743, 2009.

[22] B. Smith, K. Wepasnick, K. E. Schrote et al., "Colloidal properties of aqueous suspensions of acid-treated, multi-walled carbon nanotubes," *Environmental Science and Technology*, vol. 43, no. 3, pp. 819–825, 2009.

[23] E. Mansfield, A. Kar, and S. A. Hooker, "Applications of TGA in quality control of SWCNTs," *Analytical and Bioanalytical Chemistry*, vol. 396, no. 3, pp. 1071–1077, 2010.

[24] A. C. Dillon, T. Gennett, K. M. Jones, J. L. Alleman, P. A. Parilla, and M. J. Heben, "Simple and complete purification of single-walled carbon nanotube materials," *Advanced Materials*, vol. 11, no. 16, pp. 1354–1358, 1999.

Research Article

Efficient *In Vitro* TRAIL-Gene Delivery in Drug-Resistant A2780/DDP Ovarian Cancer Cell Line via Magnetofection

Fang Li,[1, 2] Sumei Niu,[1] Jing Sun,[1] Huaishi Zhu,[3] Qiujie Ba,[1] Yi Guo,[1] and Donglu Shi[2, 4]

[1] *Shanghai First Maternity and Infant Hospital, Tongji University School of Medicine, Shanghai 200040, China*
[2] *The Institute for Advanced Materials and Nanobiomedicine, Tongji University, Shanghai 200092, China*
[3] *Department of Radiology, Huangpu District Central Hospital, Shanghai 200002, China*
[4] *School of Electronic and Computing Systems 493 Rhodes Hall, University of Cincinnati, Cincinnati, OH 45221-0012, USA*

Correspondence should be addressed to Fang Li, 09lifang@tongji.edu.cn

Tumor necrosis factor-related apoptosis-inducing ligand (TRAIL) presents great promise as an anticancer agent for human cancer therapy. In this study, a magnetofection agent (polyMAG-l000) was evaluated for *in vitro* delivery of TRAIL gene towards drug-resistant A2780/DDP ovarian cancer cells. Transfection experiments showed that polyMAG-l000 was able to transfect A2780/DDP cells *in vitro*, leading to a higher level of TRAIL gene expression in the presence of a static magnetic field as compared to other transfection agent, such as Lipofectamine 2000. TRAIL gene expression in the A2780/DDP cells was also confirmed by Western blot analysis. Moreover, the TRAIL gene expression exhibited remarkable decrease in the cell viability, as determined by MTT assay. Importantly, PolyMAG-l000-mediated TRAIL gene transfection in the presence of anticancer drug cisplatin (CDDP) induced much higher percentages of apoptotic A2780/DDP cells, compared to TRAIL gene transfection or CDDP treatment alone. A further study by Western blot analysis indicated that cytochrome *c* release and caspase-9 cleavage pathway were associated with the initiation of the apoptosis in A2780/DDP cells. The results of this study indicate that polyMAG-l000 can be used as an efficient agent for TRAIL gene transfection in ovarian cancer cells.

1. Introduction

Ovarian carcinoma is the fifth most common gynaecological cancer. Due to the lack of effective methods for early diagnosis of ovarian cancer, it is often detected in an advanced stage. As such, the patients usually have to undergo surgery for removal of the tumor and receive chemotherapy using anticancer drugs, such as cisplatin and doxorubicin. In many cases, chemotherapy has to be discontinued due to intrinsic or developed drug resistance of the ovarian cancer cells. To address this critical issue, chemotherapy in combination with biological therapy has been studied in the past decade. The combined approach was proven to be more efficacious than chemotherapy or biological therapy alone. For instance, the combined cisplatin treatment with trastuzumab, a monoclonal antibody capable of interfering with the HER2/neu receptor, may enhance growth suppression of a few types of breast cancer cells [1]. In particular, some recent studies

indicated that a combined use of anticancer drugs with TNF-related apoptosis-inducing ligand (TRAIL) protein had a synergistic effect on the apoptotic activity in ovarian cancer cells [2].

TRAIL is a promising anticancer protein which is capable of inducing specific apoptosis in a broad range of cancer cells but not in normal cells [2–5]. However, the clinical use of TRAIL protein is seriously impeded due to its instability *in vivo* and potential resistance of cancer cells to the TRAIL. For enhanced tumor growth inhibition, a high dose of the protein has to be administrated *in vivo*. As an alternative approach, recombinant virus-mediated TRAIL-gene therapy has been investigated recently. This is attributed to the viruses being potent to transfer genes into the somatic cells, yielding high levels of gene expression. Griffith et al. constructed a TRAIL-encoded adenovirus and found that the virus may lead to TRAIL expression in ovarian cancer cell lines (e.g., A2780 and SKOV-3) and to their death mediated

by a caspase-activated apoptosis [3]. These results indicate that TRAIL gene therapy is promising for ovarian cancer therapy. However, there remains serious safety concerns on recombinant viruses as gene vectors for TRAIL-gene transfection.

Nonviral carriers such as cationic polymers for gene transfection have received much attention in the past decades, as they do not present major safety issues compared to other viral vectors. The safety issues of these viral vectors cannot be easily addressed including immunogenicity, toxicity, mutagenicity, and oncogenicity [6–8]. Cationic polymers can condense DNA into nanosized polymer/DNA complexes (polyplexes) via an electrostatic interaction for targeted cells nucleus deliveries. Moreover, the polymers can effectively protect DNA from nuclease degradation in the cells, thereby inducing appreciable transfection efficiency. A variety of cationic polymers, such as poly-l-lysine [9], polyethyleneimine (PEI) [10], polyamidoamine dendrimer [11], and poly(2-dimethylamino)ethyl-methacrylate [12], were studied as gene carriers for nonviral gene delivery. However, these current systems generally induced either low transfection efficiency or high cytotoxicity *in vitro* and *in vivo* [13–15]. It was shown that in the presence of a static magnetic field, polycation-modified magnetic nanoparticles enabled more efficient gene transfection as compared to conventional polymer-based gene delivery systems [16–21]. As a result of externally applied magnetic field, the magnetic nanoparticles/gene complexes can be effectively internalized in the cellular membrane. Therefore, cationic magnetic nanoparticles have been widely employed as new gene delivery systems for magnetofection *in vitro* and *in vivo* [22].

In this study, a commercial magnetofection agent, a cationic magnetic iron oxide (polyMag-1000), was evaluated for TRAIL gene delivery *in vitro* against drug-resistant A2780/DDP ovarian cancer cells, in terms of TRAIL gene transfection efficiency, cell viability, TRAIL gene transfection combined with cisplatin treatment and associated apoptotic mechanism.

2. Materials and Methods

2.1. Magnetic Iron Oxide Nanoparticles and Plasmids. Superparamagnetic iron oxide nanoparticles coated with PEI (polyMAG-1000) were ordered from Chemicell (Germany). Human TRAIL cDNA, kindly donated by Dr. H Yagita (Juntendo University School of Medicine, Japan), was subcloned into the *Eco*RI and BamH I site of the eukaryotic expression vector, pEGFP-N1 plasmid, (Clonetech), yielding the new plasmid pCMV-TRAIL-EGFP. A liposome transfection agent (Lipofectamine 2000) was purchased from Invitrogen (USA).

2.2. Cell Culture. Drug-resistant A2780/DDP cell line was provided by the American Type Culture Collection (ATCC, Manassas, Va, USA). The cells were maintained in DMEM medium supplemented with 10% fetal calf serum (GIBCO Life Technologies, Burlington, ON, Canada).

2.3. Zeta-Potential Measurements and Agarose Gel Retardation. The surface charges of polyMag-1000/plasmid com-

plexes were measured at 25°C using a nanosizer NS90 (Malvern Instruments Ltd., Malvern, UK).

PolyMag-1000/DNA complexes were prepared at varying ratios from 1/8 to 5/1 (w/v). After addition of $2\,\mu L$ of 6× loading buffer (Fermentas), the mixture was applied onto a 1% agarose gel containing $0.5\,\mu g/mL$ ethidium bromide. After development of the gel, siRNA was visualized with a UV lamp using a Tanon Gel system (Tanon Gel Image System, Thermo Scientific).

2.4. In Vitro Gene Transfection. A2780/DDP cells (1×10^5) were seeded into 6-well plates and incubated at 37°C in 5% CO_2 for 24 h before transfection. PolyMAG-1000 to DNA ratio is expressed as volume (v) to weight (w) of DNA, and written as v/w. The dose of plasmid DNA used was $3\,\mu g$ per well. These PolyMAG-1000/DNA complexes were added to 6-well plates after incubation for 30 min at room temperature. A MagnetoFACTOR plate (130 mT) was then placed under each of the 6-well plates for 15 min. After 6 h incubation with serum-free DMEM at 37°C in 5% CO_2, the medium was replaced with fresh DMEM containing 10% FBS and incubated for another 72 h. The polyMAG-1000 without TRAIL gene was served as a negative control. Liposome-mediated TRAIL gene transfection was served as a positive control and performed according to the manufacturer's instructions.

2.5. Flow Cytometry Assay. The Annexin V apoptosis detection kit was used to measure the percentage of apoptotic cells following the manufacturer's protocol (Pharmingen, BD Biosciences, San Diego, USA). Briefly, the TRAIL-gene transfection A2780/DDP cells were washed with PBS and resuspended in $100\,\mu L$ of binding buffer, and then incubated with $5\,\mu L$ of FITC-conjugated annexin V for 15 min at room temperature in the dark, followed by the addition of $400\,\mu L$ of binding buffer. Cells were sorted by a FACScan cytometer using CELLQuest software (version 3.3; BD Biosciences, Mountain View, Calif, USA).

2.6. MTT Assay. Cell metabolic activity, determined by MTT assay, was studied as a function of cell incubation time from 1 day to 4 days. At different time intervals (day 1 to day 4), MTT solution ($20\,\mu L$, 5 mg/mL) was added to each well and incubated with the cells for 4 h. The medium was then removed and DMSO ($150\,\mu L$) was added to each well. The absorbance was measured at 570 nm using a plate reader (Thermo scientific). The percentage of relative cell viability was determined relative to control cells (untreated A2780/DDP cells), and taken as 100% cell viability. All cytotoxicity experiments were performed for eight times.

2.7. Western Blot. Proteins were developed by SDS-poly acrylamide gel and then transferred onto cellulose membranes (Millipore, Bedford, Mass, USA). The membranes were first incubated with primary antibodies (anti-TRAIL 1 : 1000) and then incubated with horseradish peroxidase-labeled secondary antibodies. Peroxidase activity was visualized with the enhanced chemiluminescence kit (Amersham Biosciences) according to the manufacturer's instructions.
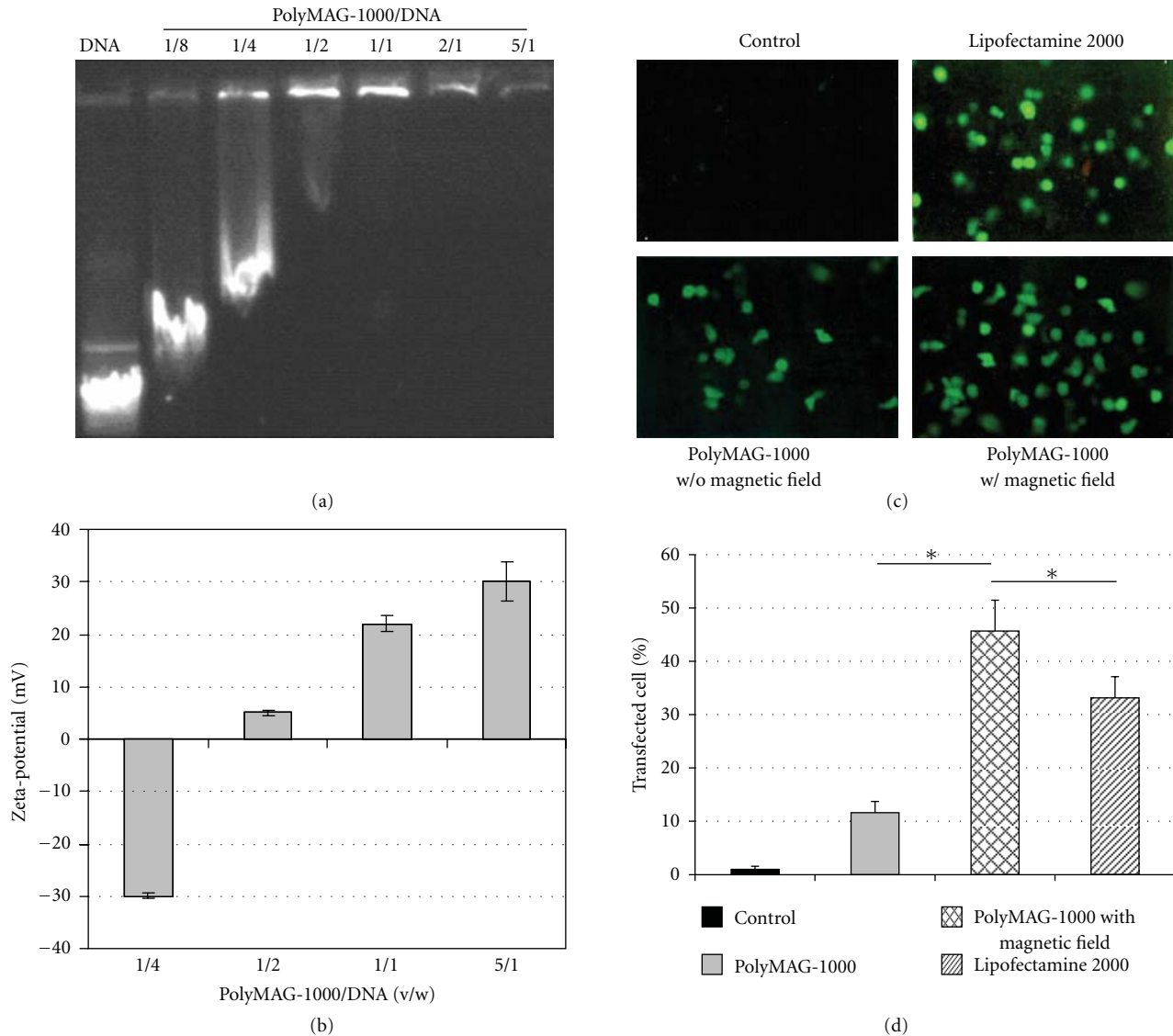
(a)

(c)

(b)

(d)

FIGURE 1: (a) Gel retardation and (b) Zeta-potential analysis on the complexation of polyMAG-1000/plasmid at varying v/w ratios; (c) Effect of a static magnetic field on gene transfection of pCMV-TRAIL-GFP plasmid towards A2780/DDP cells. The A2780/DDP cells were transfected with polyMAG-1000/plasmid, at the v/w ratio of 1/1, in the absence (w/o) or presence (w/) of a static magnetic field. As a control, the A2780/DDP cells were also transfected with lipofectamine 2000. (d) Transfection efficiency was determined by flow cytometry analysis ($*P < 0.05$). Results are shown as means and SD values of three independent experiments.

Relative band intensity of Western blot was quantified with Adobe Photoshop CS2, 9.0 edition.

2.8. Statistical Analysis. To determine significant differences in the parameters between the sample groups, a paired (for the same sample populations with different treatments) or an unpaired (for different sample population), Student's t-test was utilized.

3. Results

3.1. PolyMAG-1000 Mediation of Efficient TRAIL Gene Transfection In Vitro. In this study, PolyMAG-1000, polyethylenimine-modified magnetic nanoparticles, is used as a trans-

fection agent for TRAIL plasmid transfection. It was shown that PolyMAG-1000 is capable of efficiently binding DNA into positively charged complexes [17]. To proof this, gel retardation experiment and zeta-potential analysis were performed. As revealed in Figure 1(a), full DNA retardation was detected at and above the PolyMAG-1000/DNA ratio of 1/1 (v/w). Moreover, the complexes, prepared at the ratio of 1/1, displayed a positive surface charge of about +21 mV (Figure 1(b)). These results thus imply the formation of PolyMAG-1000/DNA complexes.

Magnetofection of polyMAG-1000 against A2780/DDP ovarian cancer cells was studied *in vitro* using pEGFP-N1-TRAIL plasmid, which was encoded with EGFP as a reporter

(a)

(b)
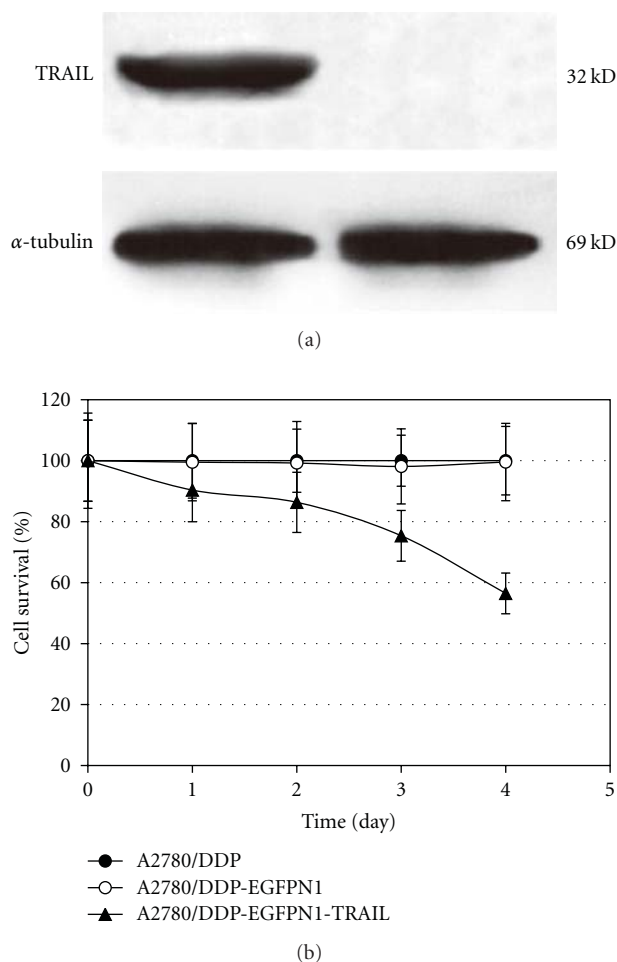
Figure 2: (a) Western blot analysis showing TRAIL gene expression after TRAIL gene transfection via magnetofection in A2780/DDP cells; (b) The effect of TRAIL gene expression on the cell survival rate of A2780/DDP cells ($n = 3$). The cell survival of transfected cells was determined by MTT assay as a functional of transfection time.

gene, at a polyMag-1000/plasmid ratio of 1/1. The gene expression was easily visualized under a fluorescent microscope after 72 h transfection. The percentages of transfected cells were quantified using FACS. As shown in Figure 1(c), polyMAG-l000 is able to efficiently transfect A2780/DDP cells, with transfection efficiency significantly higher in the presence of a static magnetic field than that without the magnetic field (Figure 1(d), 45.67 ± 5.78% versus 11.60 ± 2.12%, $P < 0.05$). As can be seen in this figure, the efficiency is also higher than that with another transfection agent, Lipofectamine 2000, as a positive control (33.14 ± 3.97%, $P < 0.05$).

3.2. TRAIL Expression in A2780 Ovarian Cancer Cells. To further confirm the expression of the TRAIL gene in the A2780/DDP cells after polyMAG-1000 mediated magnetofection, Western blot analysis was performed, and the results are shown in Figure 2(a). A strong immunoreactive protein is observed with a size of 32 kDa. This size is consistent

with that of TRAIL in a transmembrane form, indicating successful gene expression of TRAIL in the cells [3, 5, 19].

3.3. Human TRAIL Inhibition of A2780/DDP Cells Proliferation In Vitro. Figure 2(b) shows metabolic activities of transfected A2780/DDP cells as a function of transfection time, determined by MTT assay. After 72 h transfection with TRAIL gene, a significant decrease in the metabolic activity is observed for the A2780/DDP transfection by polyMAG-1000/TRAIL compared with A2780/DDP cells by EGFP-N1 plasmid without encoding TRAIL, or untreated A2780/DDP cells as a blank control. These data indicate that TRAIL gene expression in A2780/DDP cell *in vitro* has an inhibitory effect on their survival activity.

3.4. TRAIL Enhances the Sensitivity of A2780 Cells to CDDP. To evaluate the effect of anticancer drug CDDP on apoptosis in TRAIL-transfected A2780/DDP cells, polyMAG-1000-induced TRAIL transfection was carried out in the presence of CDDP ($20 \mu M$). The percentage of apoptotic cells was quantified using an annexin V-FITC staining assay, which can report the loss of phosphatidylserine asymmetry of the plasma membrane at an early stage of apoptosis. It is found that TRAIL gene transfection in the presence of CDDP exhibits statistically higher percentages of apoptotic cells, as compared to TRAIL gene transfection or CDDP treatment alone (Figure 3(b), 45.69 ± 9.21% versus 16.35 ± 3.24% or 24.18 ± 5.87%, resp., $P < 0.05$,).

3.5. Cytochrome c Release and Cleaved Caspase-9 Activation Involving TRAIL Transfected A2780/DDP Cells. Cytochrome c release and caspase-9 activation have been described as the terminal operation in cell apoptosis [23–25]. To understand cytochrome c release and cleaved caspase-9 activation involved in the apoptotic A2780/DDP cells, subcellular cytochrome c release and the activation of caspase-9 were studied by Western blot analysis (Figure 4(a)). The activation of caspase-9 was confirmed by detecting the generation of 37 kDa proteolytic fragment of caspase-9. It is shown that as compared to untreated A2780 cells, cytochrome c level increases for both TRAIL transfected and CDDP-treated A2780/DDP cells. Moreover, the combined TRAIL transfection and CDDP treatment induces upregulation of both cytochrome c and caspase-9 activation in A2780/DDP cells (Figure 4(b)).

4. Discussion

The key challenge for efficient nonviral gene delivery is to design potent carriers capable of overcoming multiple intracellular barriers, such as plasmid internalization, endosomes, cytoplasm trafficking, nuclear translocation, as well as the retention of plasmid in the nucleus [26–32]. PolyMAG-l000 has shown great promise for TRAIL plasmid transfection since it is capable of binding plasmid into positively charged complexes (Figures 1(a) and 1(b)), and also promoting efficient cellular internalization of polyplexes in the presence of a static magnetic field [17, 18]. This may explain the
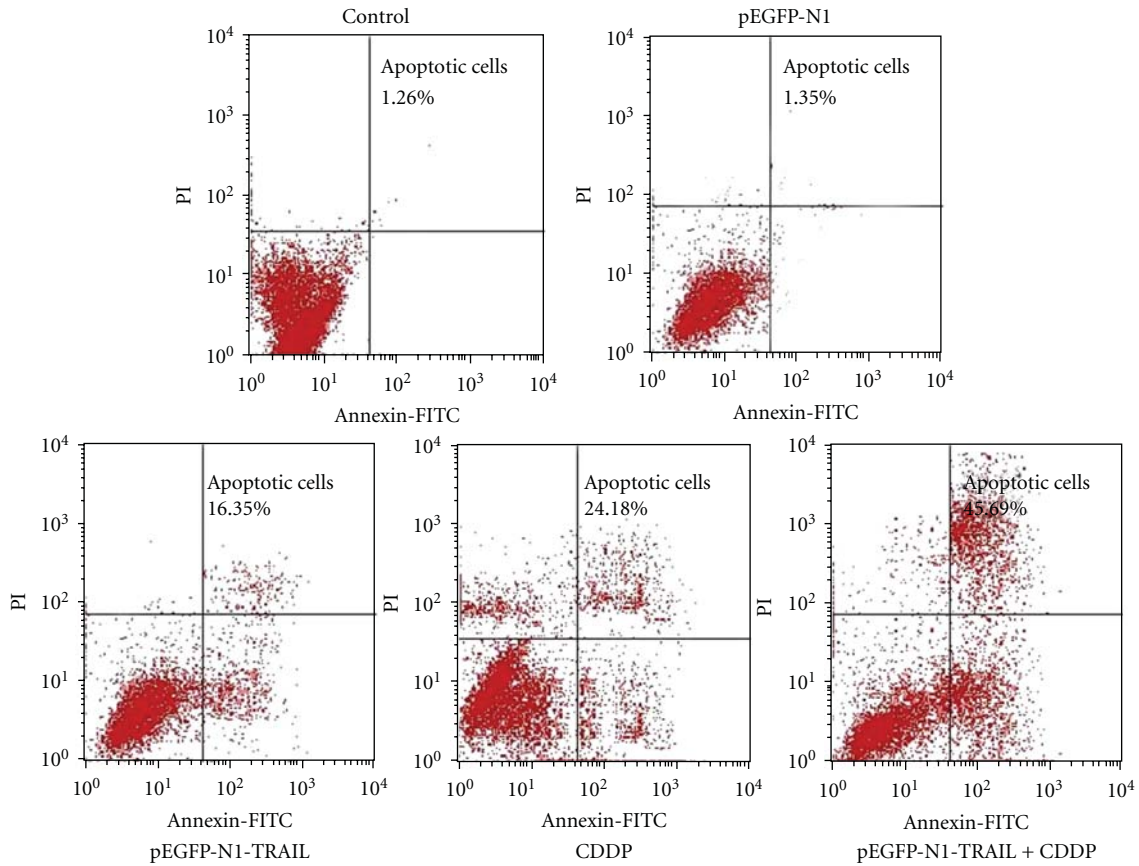
(a)
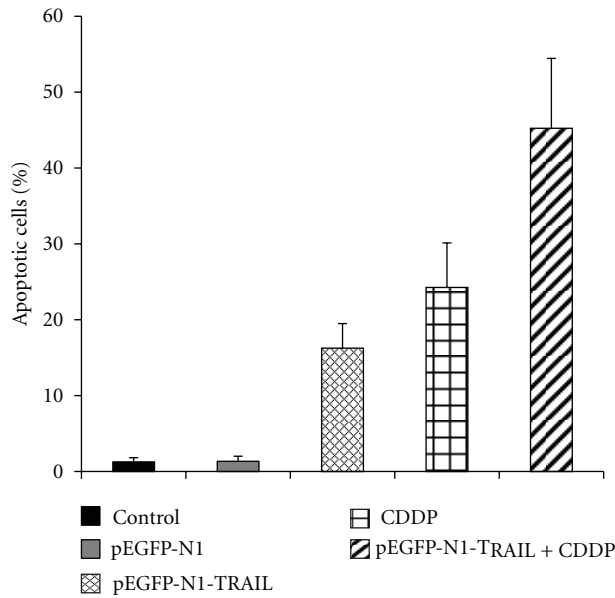
(b)

Figure 3: Treatment with CDDP induces apoptosis in TRAIL transfected drug-resistant A2780/DDP cells. (a) Histograph analysis of typical flow cytometry data to determine the percentages of apoptotic A2780/DDP cells after CDDP treatment, TRAIL gene transfection, or the combined, using Annexin V-FITC/PI staining assay. (b) Quantification data of the percentages of apoptotic A2780/DDP cells. The means and errors results were calculated from three independent experiments.
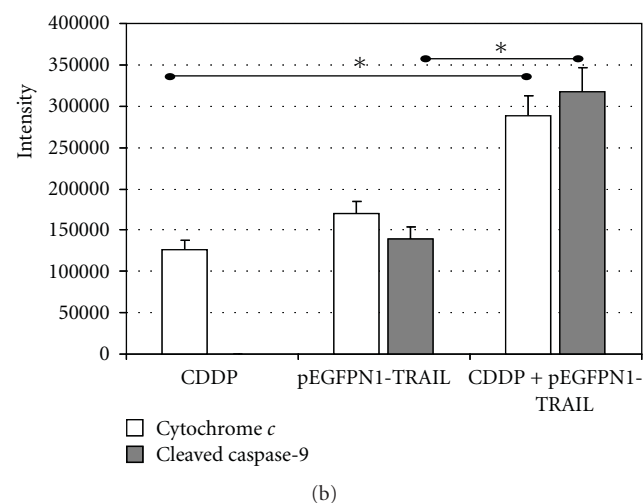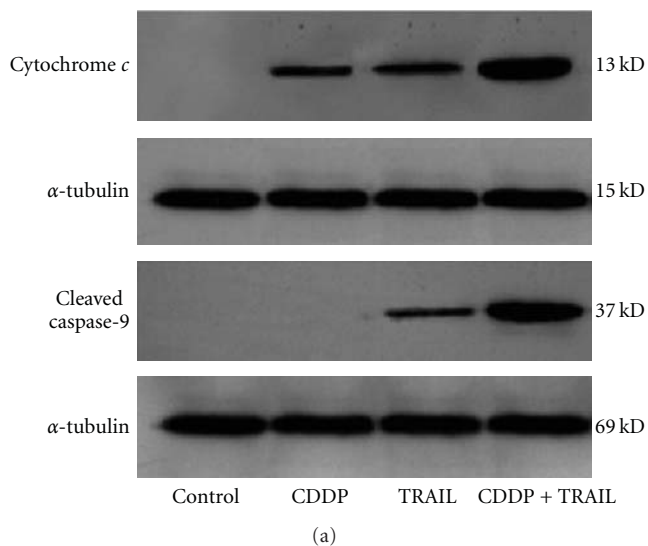
(a)

(b)

FIGURE 4: Combination of CDDP treatment and TRAIL transfection enhances cytochrome *c* release and cleaved caspase 9 in A2780/DDP cells. (a) Western blot analysis showing the cytochrome *c* expression and cleaved caspase 9 in A2780/DDP after CDDP treatment (20μM), TRAIL gene transfection, or the combined TRAIL transfection and CDDP treatment. An anti-α-tubulin was used as a reference control. (b) Quantified absolute intensity of the bands in the Western blot analysis ($P < 0.05$).

fact that more efficient TRAIL-plasmid expression mediated by polyMAG-1000 magnetofection was observed in the presence of a static magnetic field and that the transfection efficiency is higher than that of Lipfectamine 2000, as a positive control (Figures 1(c) and 1(d)). PolyMAG-l000 has been previously used for plasmid magnetofection in various cell lines such as MCF-7 and stem cells [33]. However, to our knowledge, this is the first paper on TRAIL plasmid magnetofection in ovarian cancer cells.

TRAIL protein can lead to specific apoptosis in a broad range of cancer cells, such as melanomas, gliomas, and prostatic carcinomas rather than the normal cells [3]. Thus, TRAIL is expected as a potential therapeutic agent for

ovarian cancer treatment. In this study, the TRAIL gene is found to induce apoptosis in drug-resistant A2780/DDP cells (Figure 3), which thus contributes to the decrease in the cell viability of the cells after 3-day transfection (Figure 2). Moreover, the TRAIL expression enhanced the sensitivity of the A2780/DDP cells to the anticancer drug CDDP. A higher percentage of apoptotic A2780/DDP cell was found when the cells were cotreated by both TRAIL transfection and cisplatin. The results thus imply that TRAIL gene therapy in combination with CDDP treatment is an efficient approach for the treatment of drug-resistant ovarian cancer. Further study will be focused on the combined use of the TRAIL magnetofection and CDDP treatment in the xenograft A2780/DDP tumor in a nude mouse model.

Two viable approaches of caspase activation have been identified [25, 34]. The activation of initiator caspase-8 or caspase-10 is triggered by the ligation of death receptors, such as Fas, TNFR1, or Death Receptor 3. The second one pathway is essentially controlled by mitochondria. In most cases, the apoptotic cascade is initiated by loss of integrity of the outer mitochondrial membrane accompanied by release of cytochrome *c*. Cytochrome c, released from mitochondria induces a conformational change in the apoptotic protease activating factor (Apaf-I). This mechanism results in the cleavage and activation of caspase-9 and the subsequent activation of a caspase cascade is responsible for the cell death [34]. In this study, enhanced cytochrome *c* and cleaved caspase-9 product are achieved in the A2780/DDP cells by combining the TRAIL transfection and CDDP.

5. Conclusions

We have demonstrated that PolyMag1000 is potent to transfection of drug-resistant A2780/DDP cells *in vitro*. TRAIL gene expression induces growth inhibition of A2780/DDP cell via activating cell apoptosis. PolyMag1000-mediated TRAIL transfection in combination with cisplatin treatment may lead to augmented apoptosis in A2780/DDP cells *in vitro*. These results indicate that PolyMag1000 is an efficient nonviral TRAIL-gene carrier for ovarian cancer therapy.

Acknowledgments

References

[1] J. Baselga, L. Norton, J. Albanell, Y. M. Kim, and J. Mendelsohn, "Recombinant humanized anti-HER2 antibody (herceptin(TM)) enhances the antitumor activity of paclitaxel and doxorubicin against HER2/neu overexpressing human breast cancer xenografts," *Cancer Research*, vol. 58, no. 13, pp. 2825–2831, 1998.

[2] A. Ashkenazi, R. C. Pai, S. Fong et al., "Safety and antitumor activity of recombinant soluble Apo2 ligand," *Journal of Clinical Investigation*, vol. 104, no. 2, pp. 155–162, 1999.

[3] W. Roth, S. Isenmann, U. Naumann et al., "Locoregional Apo2L/TRAIL eradicates intracranial human malignant glioma xenografts in athymic mice in the absence of neurotoxicity," *Biochemical and Biophysical Research Communications*, vol. 265, no. 2, pp. 479–483, 1999.

[4] J. Rieger, U. Naumann, T. Glaser, A. Ashkenazi, and M. Weller, "APO2 ligand: a novel lethal weapon against malignant glioma?" *FEBS Letters*, vol. 427, no. 1, pp. 124–128, 1998.

[5] J. E. Kendrick, J. M. Estes, J. M. Straughn, R. D. Alvarez, and D. J. Buchsbaum, "Tumor necrosis factor-related apoptosis-inducing ligand (TRAIL) and its therapeutic potential in breast and gynecologic cancers," *Gynecologic Oncology*, vol. 106, no. 3, pp. 614–621, 2007.

[6] T. Merdan, J. Kopeček, and T. Kissel, "Prospects for cationic polymers in gene and oligonucleotide therapy against cancer," *Advanced Drug Delivery Reviews*, vol. 54, no. 5, pp. 715–758, 2002.

[7] S. C. De Smedt, J. Demeester, and W. E. Hennink, "Cationic polymer based gene delivery systems," *Pharmaceutical Research*, vol. 17, no. 2, pp. 113–126, 2000.

[8] S. O. Han, R. I. Mahato, Y. K. Sung, and S. W. Kim, "Development of biomaterials for gene therapy," *Molecular Therapy*, vol. 2, no. 4, pp. 302–317, 2000.

[9] A. Gonsho, K. Irie, H. Susaki, H. Iwasawa, S. Okuno, and T. Sugawara, "Tissue-targeting ability of saccharide-poly(L-lysine) conjugates," *Biological and Pharmaceutical Bulletin*, vol. 17, no. 2, pp. 275–282, 1994.

[10] O. Boussif, F. Lezoualc'h, M. A. Zanta et al., "A versatile vector for gene and oligonucleotide transfer into cells in culture and in vivo: polyethylenimine," *Proceedings of the National Academy of Sciences of the United States of America*, vol. 92, no. 16, pp. 7297–7301, 1995.

[11] M. X. Tang, C. T. Redemann, and F. C. Szoka Jr., "In vitro gene delivery by degraded polyamidoamine dendrimers," *Bioconjugate Chemistry*, vol. 7, no. 6, pp. 703–714, 1996.

[12] P. V. D. Wetering, J. Y. Cherng, H. Talsma, D. J. A. Crommelin, and W. E. Hennink, "2-(dimethylamino)ethyl methacrylate based (co)polymers as gene transfer agents," *Journal of Controlled Release*, vol. 53, no. 1–3, pp. 145–153, 1998.

[13] G. A. Brazeau, S. Attia, S. Poxon, and J. A. Hughes, "In vitro myotoxicity of selected cationic macromolecules used in non-viral gene delivery," *Pharmaceutical Research*, vol. 15, no. 5, pp. 680–684, 1998.

[14] P. R. Dash, M. L. Read, L. B. Barrett, M. A. Wolfert, and L. W. Seymour, "Factors affecting blood clearance and in vivo distribution of polyelectrolyte complexes for gene delivery," *Gene Therapy*, vol. 6, no. 4, pp. 643–650, 1999.

[15] H. Bordelon, A. S. Biris, C. M. Sabliov, and W. Todd Monroe, "Characterization of plasmid DNA location within chitosan/PLGA/pDNA nanoparticle complexes designed for gene delivery," *Journal of Nanomaterials*, vol. 2011, Article ID 952060, 2011.

[16] S. Huth, J. Lausier, S. W. Gersting et al., "Insights into the mechanism of magnetofection using PEI-based magnetofectins for gene transfer," *Journal of Gene Medicine*, vol. 6, no. 8, pp. 923–936, 2004.

[17] S. W. Gersting, U. Schillinger, J. Lausier et al., "Gene delivery to respiratory epithelial cells by magnetofection," *Journal of Gene Medicine*, vol. 6, no. 8, pp. 913–922, 2004.

[18] F. Scherer, M. Anton, U. Schillinger et al., "Magnetofection: enhancing and targeting gene delivery by magnetic force in vitro and in vivo," *Gene Therapy*, vol. 9, no. 2, pp. 102–109, 2002.

[19] M. H. Kim, T. R. Billiar, and D. W. Seol, "The secretable form of trimeric TRAIL, a potent inducer of apoptosis," *Biochemical and Biophysical Research Communications*, vol. 321, no. 4, pp. 930–935, 2004.

[20] S. Huth, J. Lausier, S. W. Gersting et al., "Insights into the mechanism of magnetofection using PEI-based magnetofectins for gene transfer," *Journal of Gene Medicine*, vol. 6, no. 8, pp. 923–936, 2004.

[21] B. Pan, D. Cui, Y. Sheng et al., "Dendrimer-modified magnetic nanoparticles enhance efficiency of gene delivery system," *Cancer Research*, vol. 67, no. 17, pp. 8156–8163, 2007.

[22] A. Basarkar and J. Singh, "Nanoparticulate systems for polynucleotide delivery," *International Journal of Nanomedicine*, vol. 2, no. 3, pp. 353–360, 2007.

[23] A. Mansouri, L. D. Ridgway, A. L. Korapati et al., "Sustained activation of JNK/p38 MAPK pathways in response to cisplatin leads to Fas ligand induction and cell death in ovarian carcinoma cells," *The Journal of Biological Chemistry*, vol. 278, no. 21, pp. 19245–19256, 2003.

[24] C. Tournier, P. Hess, D. D. Yang et al., "Requirement of JNK for stress-induced activation of the cytochrome c- mediated death pathway," *Science*, vol. 288, no. 5467, pp. 870–874, 2000.

[25] D. R. Green, "Apoptic pathways: the roads to ruin," *Cell*, vol. 94, no. 6, pp. 695–698, 1998.

[26] C. Liu, "Research and development of nanopharmaceuticals in China," *Nano Biomedicine and Engineering*, vol. 1, p. 1, 2009.

[27] C. Bao, H. Yang, P. Sheng et al., "Cloning, expression, monoclonal antibody preparation of human gene NBEAL1 and its application in targeted imaging of mouse glioma," *Nano Biomedicine and Engineering*, vol. 1, p. 50, 2009.

[28] D. Cui, Y. Han, Z. Li et al., "Fluorescent magnetic nanoprobes for in vivo targeted imaging and hyperthermia therapy of prostate cancer," *Nano Biomedicine and Engineering*, vol. 1, p. 61, 2009.

[29] S. Chen, Y. Ji, Q. Lian et al., "Gold nanorods coated with multilayer polyelectrolyte as intracellular delivery vector of antisense oligonucleotides," *Nano Biomedicine and Engineering*, vol. 2, no. 1, p. 15, 2010.

[30] D. Cui, Q. Li, P. Huang et al., "Real time PCR based on fluorescent quenching of mercaptoacetic acid-modified CdTe quantum dots for ultrasensitive specific detection of nucleic acids," *Nano Biomedicine and Engineering*, vol. 2, p. 45, 2010.

[31] P. Huang, Z. Li, J. Lin et al., "Photosensitizer-conjugated magnetic nanoparticles for in vivo simultaneous magnetofluorescent imaging and targeting therapy," *Biomaterials*, vol. 32, no. 13, pp. 3447–3458, 2011.

[32] G. Gao, P. Huang, Y. Zhang, K. Wang, W. Qin, and D. Cui, "Gram scale synthesis of superparamagnetic Fe_3O_4 nanoparticles and fluid via a facile solvothermal route," *CrystEngComm*, vol. 13, no. 6, pp. 1782–1785, 2011.

[33] C. H. Lee, E. Y. Kim, K. Jeon et al., "Simple, efficient, and reproducible gene transfection of mouse embryonic stem cells by magnetofection," *Stem Cells and Development*, vol. 17, no. 1, pp. 133–141, 2008.

[34] N. A. Thornberry and Y. Lazebnik, "Caspases: enemies within," *Science*, vol. 281, no. 5381, pp. 1312–1316, 1998.

Review Article

Application of Quantum Dots in Biological Imaging

Shan Jin, Yanxi Hu, Zhanjun Gu, Lei Liu, and Hai-Chen Wu

Key Laboratory for Biomedical Effects of Nanomaterials and Nanosafety, Institute of High Energy Physics, Chinese Academy of Sciences, Beijing 100049, China

Correspondence should be addressed to Lei Liu, leiliu@ihep.ac.cn

Received 15 May 2011; Accepted 2 June 2011

Academic Editor: Xing J. Liang

Quantum dots (QDs) are a group of semiconducting nanomaterials with unique optical and electronic properties. They have distinct advantages over traditional fluorescent organic dyes in chemical and biological studies in terms of tunable emission spectra, signal brightness, photostability, and so forth. Currently, the major type of QDs is the heavy metal-containing II-IV, IV-VI, or III-V QDs. Silicon QDs and conjugated polymer dots have also been developed in order to lower the potential toxicity of the fluorescent probes for biological applications. Aqueous solubility is the common problem for all types of QDs when they are employed in the biological researches, such as *in vitro* and *in vivo* imaging. To circumvent this problem, ligand exchange and polymer coating are proven to be effective, besides synthesizing QDs in aqueous solutions directly. However, toxicity is another big concern especially for *in vivo* studies. Ligand protection and core/shell structure can partly solve this problem. With the rapid development of QDs research, new elements and new morphologies have been introduced to this area to fabricate more safe and efficient QDs for biological applications.

1. Introduction

Semiconductor nanocrystals, or so-called quantum dots (QDs), show unique optical and electronic properties, including size-tunable light emission, simultaneous excitation of multiple fluorescence colors, high signal brightness, long-term photostability, and multiplex capabilities [1–4]. Such QDs have significant advantages in chemical and biological researches in contrast to traditional fluorescent organic dyes and green fluorescent proteins on account of their photobleaching, low signal intensity, and spectral overlapping [5–7]. These properties of QDs have attracted great interest in biology and medicine in recent years. At present QDs are considered to be potential candidates as luminescent probes and labels in biological applications, ranging from molecular histopathology, disease diagnosis, to biological imaging [8–10]. Numerous studies have reported the use of QDs for *in vitro* or *in vivo* imaging of sentinel lymph nodes [11–17], tumor-specific receptors [18–20], malignant tumor detectors [21], and tumor immune responses [22].

However, the major concerns about potential toxicity of II-IV QDs (such as CdTe and CdSe) have cast doubts on their practical use in biology and medicine. Indeed, several studies have reported that size, charge, coating ligands, and oxidative, photolytic, and mechanical stability, each can contribute to the cytotoxicity of cadmium-containing QDs. Another critical factor that determines the cytotoxicity of QDs is the leakage of heavy metal ions from the core caused by photolysis and oxidation [23–25]. The long-term effects of these ions enrichment and durations within the body raise concerns about the biocompatibility and safety of QDs [24, 26]. On the other hand, the rapid clearance of QDs from the circulation by the reticuloendothelial system (RES) or entrapment of QDs in the spleen and liver [27, 28] can result in the degradation of the imaging quality of the objective and the enhancement of background noise.

One promising solution to these problems, including QDs sequestered in the liver/spleen and long-term retention in the body, is to evade the recognition and uptake by the reticuloendothelial system thus extending the circulation time of the particles in the body. In addition, for biological studies, QDs should be aqueous soluble in order to adapt the biological environment. Therefore, when QDs are employed in biological imaging, many factors should be considered and
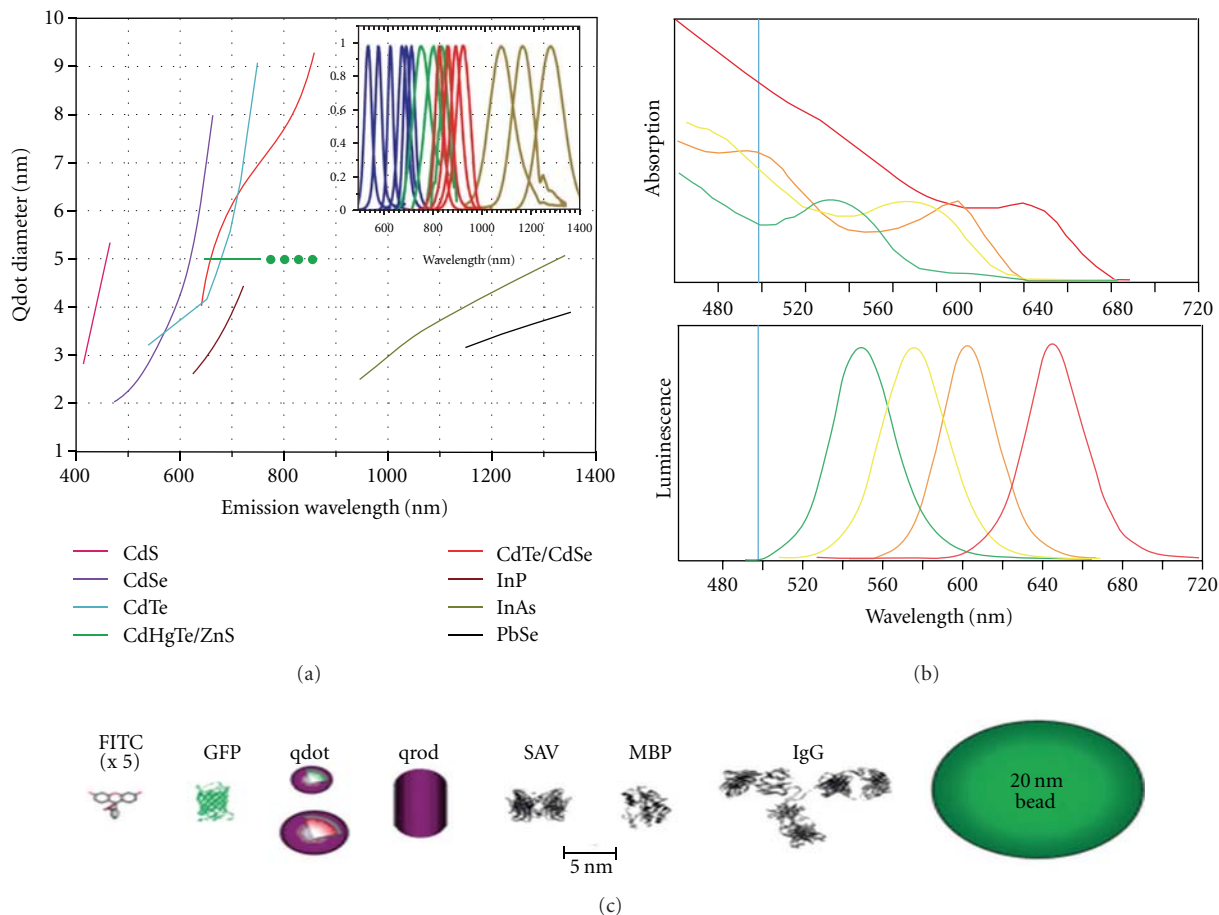
(a)

(b)

(c)

FIGURE 1: Emission maxima and sizes of quantum dots of different composition (with permission from [3]).

the system should be properly designed in order to meet a set of requirements [29–31].

In this report, we first briefly review different types of QDs that have been fabricated so far and their synthesis methods, including surface functionalization. Next, we focus on their applications in biological imaging. Finally, the new trends of QDs imaging are discussed.

2. Types and Characteristics of QDs

Traditionally, the typical QDs consist of a II-IV, IV-VI, or III-V semiconductor core (e.g., CdTe, CdSe, PbSe, GaAs, GaN, InP, and InAs; Figure 1) [3, 32, 33], which is surrounded by a covering of wide bandgap semiconductor shell such as ZnS in order to minimize the surface deficiency and enhance the quantum yield [5, 34]. The unique optical and electronic properties of QDs, including narrow light emission, wideband excitation, and photostability, provide them with significant advantages in the applications of multiplexed molecular targets detection [21] and as optical bioimaging probes [8–10]. One major drawback which severely hinders the application of II-IV, IV-VI, or III-V QDs for *in vivo* biological research is the concern about the toxicity associated with the cadmium, lead, or arsenic containing QDs. The

toxic heavy metal ions can be easily leaked out into biological systems if the surfaces are not properly covered by the shells or protected by ligands.

The limitation of heavy metal-containing QDs stimulates extensive research interests in exploring alternative strategies for the design of fluorescent nanocrystals with high biocompatibility. In this case, the practical strategy is to develop highly fluorescent nanoparticles based on nontoxic elements or explore luminescent π-conjugated polymer dots.

Silicon nanoparticle is another type of QDs which possess unique properties when their sizes are reduced to below 10 nm. Similar to their predecessors, silicon QDs also have many advantages over traditional fluorescent organic dyes [35], including resistance to photobleaching and wide emission range from visible to infrared region with relatively high quantum yields. Moreover, owing to silicon's nontoxic and environment-friendly nature, Si QDs are used as fluorescent probes for bioimaging [35]. It has been reported that for *in vivo* applications, Si QDs mainly degrade to silicic acid which can be excreted through urine [36], and for *in vitro* use, Si QDs are considered 10-times safer than Cd-containing quantum dots (Figures 2 and 3) [37]. However, the challenges present in employing Si QDs in bioimaging arise from their water solubility and biocompatibility. Usually, Si QDs

are produced in nonpolar solvents with hydrophobic ligands (such as styrene and octene) on their surface in order to protect the Si cores. Therefore, it is a common problem that Si QDs show poor solubility and unstable photoluminescence (PL) in aqueous solutions [38–40]. PL degradation can occur gradually after modified Si QDs are transferred from organic solvents to aqueous solutions. Thus, fabricating good water-disperse Si QDs with stable optical characters is vital to their applications in bioimaging studies. Recently, Tilley and Yamamoto reported that water-soluble Si QDs covered by allylamine [41, 42] and poly(acrylic acid), respectively, had been successfully obtained and showed good performance in fixed-cell labeling [40].

The semiconducting properties of conjugate polymers derive from their π-electron delocalization along the polymer chain. Mobile charges are allowed to move between π and π^* orbitals. Highly bright fluorescence can be stable under one-photon or two-photon excitation. Polymers with such structures are promising in the fields of LED and biosensors [43, 44]. Burroughes and coworkers first reported the luminescent conjugated polymers in 1990 [45]. Later on, Friend and So successfully applied π-conjugated polymers to light-emitting devices [46, 47]. Recently, related works focused on fluorescent polymer encapsulation and functionalization to yield conjugated polymer dots (CP dots) for bioimaging and probes (Figure 4) [48, 49]. Compared with other fluorescent probes, CP dots are convenient for fluorescence microscopy and laser excitation because of their absorption ranging from 350 to 550 nm. Also, fluorescence quantum yields can be slightly variable around 40%. Moreover, CP dots can exhibit higher brightness than any other nanoparticles of the same size under certain conditions [50].

3. Synthesis Methods of QDs

3.1. Organometallic Method.
Organometallic chemistry provides an efficient pathway to produce monodisperse QDs in nonpolar organic solvents, such as CdSe nanocrystals covered by tri-n-octylphosphine oxide (TOPO) ligand. In a typical preparation, Me_2Cd and Bis(trimethylsilyl)selenium ($(TMS)_2Se$) can be used as organometallic precursors. Monodisperse CdSe with uniform surface derivatization and regularity in core structure can be obtained based on the pyrolysis of organometallic reagents by injection into a hot coordinating solvent between 250°C to 300°C [51]. The adsorption of ligands results in slow growth and annealing of the cores in the coordinating solvents. QDs with different sizes can be successfully obtained at different temperatures. The advantage of this method is obvious because this method can produce a variety of QDs with high quantum yields and the size distribution can be easily controlled by altering temperature or reaction time. Organometallic method is currently considered as the most important means to synthesize QDs.

3.2. QDs Synthesized in Aqueous Solution.
Since Rajh and coworkers first reported the synthesis of thiol-capped CdTe QDs in aqueous solution, a great deal of efforts have focused on synthesizing water-dispersed QDs directly [52].
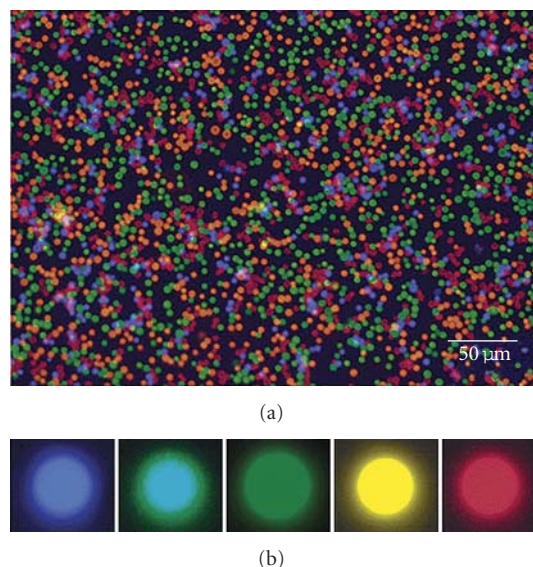

(a)

(b)

Figure 2: Fluorescence images of mesoporous silica beads (5-μm diameter, 32 nm pore size) doped with QDs emitting light at 488 (blue), 520 (green), 550 (yellow), 580 (orange), or 610 nm (red; with permission from [37]).

In this process, ionic perchlorates such as $Cd(ClO)_4 \cdot 6H_2O$ and Al_2Te_3 are used as the precursors. In the presence of ligands such as 3-mercaptopropionic acid (3-MPA), glutathione (GSH), or other hydrosulfyl-containing materials, CdTe QDs can be successfully obtained in aqueous medium. The advantage of this method lies in its environment-friendly synthesis procedure and relatively low cost. QDs produced by this method can be directly applied in biological researches without ligand exchange procedure. However, compared with the QDs produced by organometallic method, thiol-capped QDs show low quantum yields, and broad full width of half-maximum (FWHM), which can be attributed to its wide size distribution and poor stability in aqueous solution.

3.3. Hydrothermal Method/Microwave-Assisted Method.
In order to reduce QDs surface defects generated during the growth process, these two methods are put forward to synthesize QDs with narrow size distribution and high quantum yields. According to hydrothermal method, all reaction regents are loaded in hermetic container and then heated to supercritical temperature; high pressure produced by the temperature can efficiently reduce reaction time and surface defects of QDs [53]. Moreover, because high reaction temperature can separate the processes of nucleus formation and crystal growth, this method has clear advantages over traditional aqueous synthesis, affording narrow size distribution QDs.

Microwave-assisted irradiation is another attractive method for QDs synthesis. This method was first introduced by Kotov group [54] and followed by Qian and coworkers to demonstrate a fast and simple synthesis of CdTe and CdSe-CdS QDs by microwave-assisted irradiation in 2006 [55]. Microwave irradiation can be considered as heating source
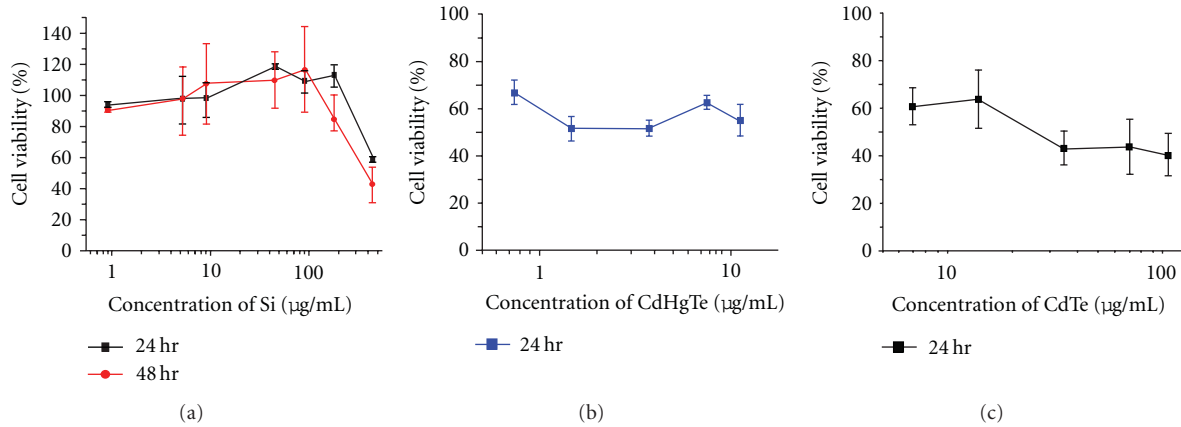
(a)

(b)

(c)

FIGURE 3: Cytotoxicity of (a) Si, (b) CdTe, and (c) HgCdTe quantum dots toward Panc-1 cells. Error bars represent standard deviation ($N = 3$). Note that the concentration range is much higher in (a) than in (b) and (c) (with permission from [38]).
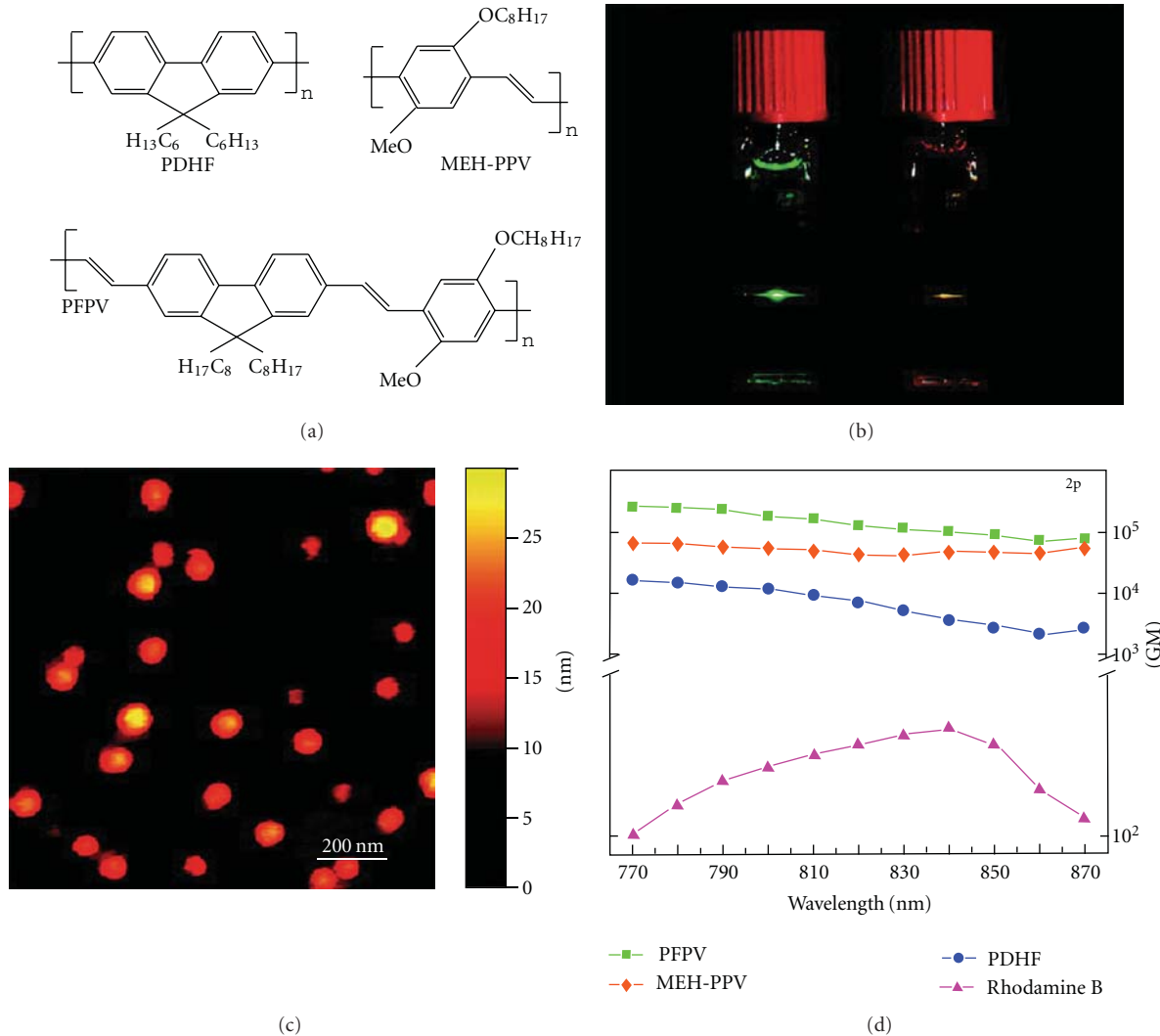

(a)

(b)

(c)

(d)

FIGURE 4: (a) Chemical structures of the conjugated polymers. (b) Photograph of the fluorescence from aqueous CP dot dispersions under two-photon excitation of an 800 nm mode-locked Ti : sapphire laser. (c) A typical AFM images of the PFPV dots on a silicon substrate. (d) Semilog plot of two-photon action cross-sections ($\sigma_{2p}\varphi$) versus the excitation wavelength for CP dots and rhodamine B (reference compound; with permission from [49]).
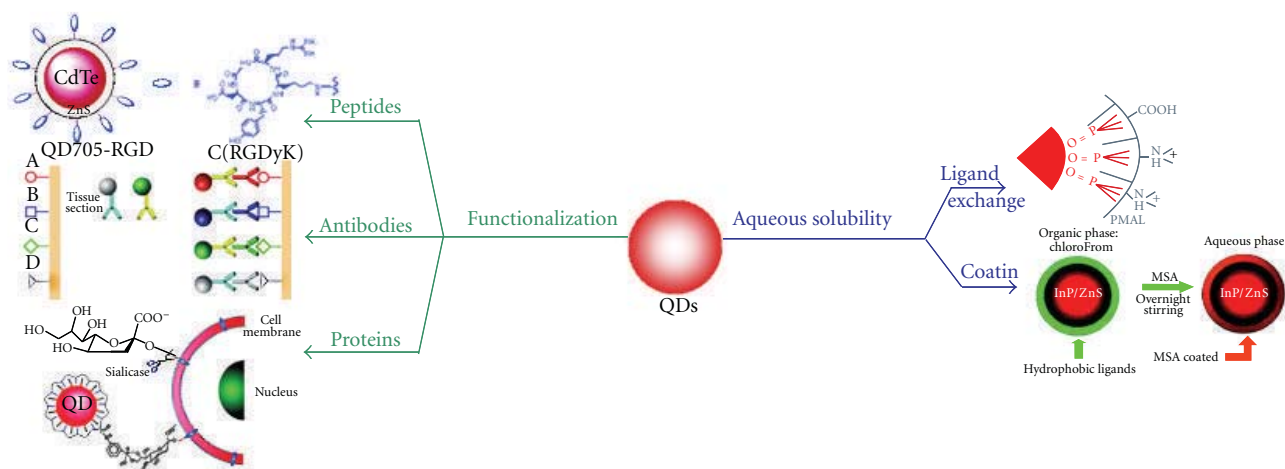
SCHEME 1: Strategies to deal with QDs aqueous solubility problems and fabricate functionalized QDs for biological applications.

to optimize synthesis conditions, and in this system, water is an excellent solvent for its $\tan \delta$ is equal to 0.127. The whole solution can be quickly heated to above 100°C to yield homogeneous QDs and the quantum yields can reach as high as 17%.

4. Toxicity, Solubilization, and Functionalization of Quantum Dots

In order to apply QDs to biological studies, safety, and biocompatibility are the issues that must be concerned. Toxicological studies have suggested that certain potential adverse human health effects may be resulted from their exposure to some novel nanomaterials, such as gold nanoparticles and QDs, but the fundamental cause-effect relationships are relatively obscure [23]. Thus, it is necessary to figure out the interaction of QDs with biological systems and their potentially harmful side effects in cells. Several studies reveal that the toxicity of QDs depends on many factors which can summarized as inherent physicochemical properties and environmental conditions [23, 24, 26]. Not all QDs are alike, each type of QDs should be characterized individually as to its potential toxicity. QD sizes, charges, concentrations, outer coatings materials and functional groups, oxidation, and mechanical stability all have been implicated as contributing factors to QD toxicity [24]. Derfus et al. studied the cytotoxicity of CdSe QDs and pointed that without coating, the cytotoxicity of CdSe cores correlated with the liberation of free Cd^{2+} ions due to deterioration of QDs lattice. And *in vivo*, the liver is the primary site of acute injury caused by cadmium ions even though the concentration of Cd^{2+} is reduced to 100–400 μM [23]. In order to eliminate QD toxicity resulted from heavy metal ions releasing, surface coating and core/shell structure are considered to be efficient solutions to this problem. Many new types of QDs such as core/shell (CdSe/ZnS) and core/shell/shell (CdSe/ZnS/TEOS) QDs with high luminescence are developed [34, 35]. Some researchers also found that the quantum size effect which resulted from the minute size of nanomaterials could lead

to cytotoxicity. Since nanoparticles within certain diameters (this value may be different according to biological environment) are of similar size to certain cellular components and proteins, they may bypass natural mechanical barriers, thus leading to adverse tissue reactions [26].

The application of QDs in biological imaging also requires QDs with good water solubility. Several strategies have been developed to circumvent this problem, which are summarized as follows.

The first one is to synthesize QDs in aqueous solution directly, which has been depicted in this review (*vide supra*). The second is to obtain QDs in organic solvents, and then transfer them to aqueous solutions (Scheme 1). Nie and Weiss groups pioneered the preparation of water-dispersed QDs by ligand exchange method (Figure 4) [5, 56]. In addition, polymer and lipid coating is another efficient way to render QDs with good water solubility [57, 58].

To improve *in vitro* and *in vivo* imaging quality and detection sensitivity in biological fields, multiplex capabilities QDs have been developed. Recent efforts mainly focus on the functionalization of QDs to accommodate the demands of imaging sensitivity and specificity [59]. Nie reported multicolor QD-antibody conjugates for the rapid detection of rare Hodgkin's and Reed-Sternberg (HRS) cells from infiltrating immune cells such as T and B lymphocytes [60]; Shi combined Fe_3O_4 with amine-terminated QDs to yield fluorescent superparamagnetic QDs for *in vivo* and *in vitro* imaging (Figure 5) [61].

5. QDs in Biological Imaging

In order to apply QDs in biological imaging, recent studies have focused on developing near-IR luminescent QDs which exhibit an emission wavelength ranging from 700 to 900 nm. Light within this range has its maximum depth of penetration in tissue and the interference of tissue autofluorescence (emission between 400 nm and 600 nm) is minimal [62, 63]. In addition, for the purpose of gathering more information during specific cellular processes in real time, QDs must be
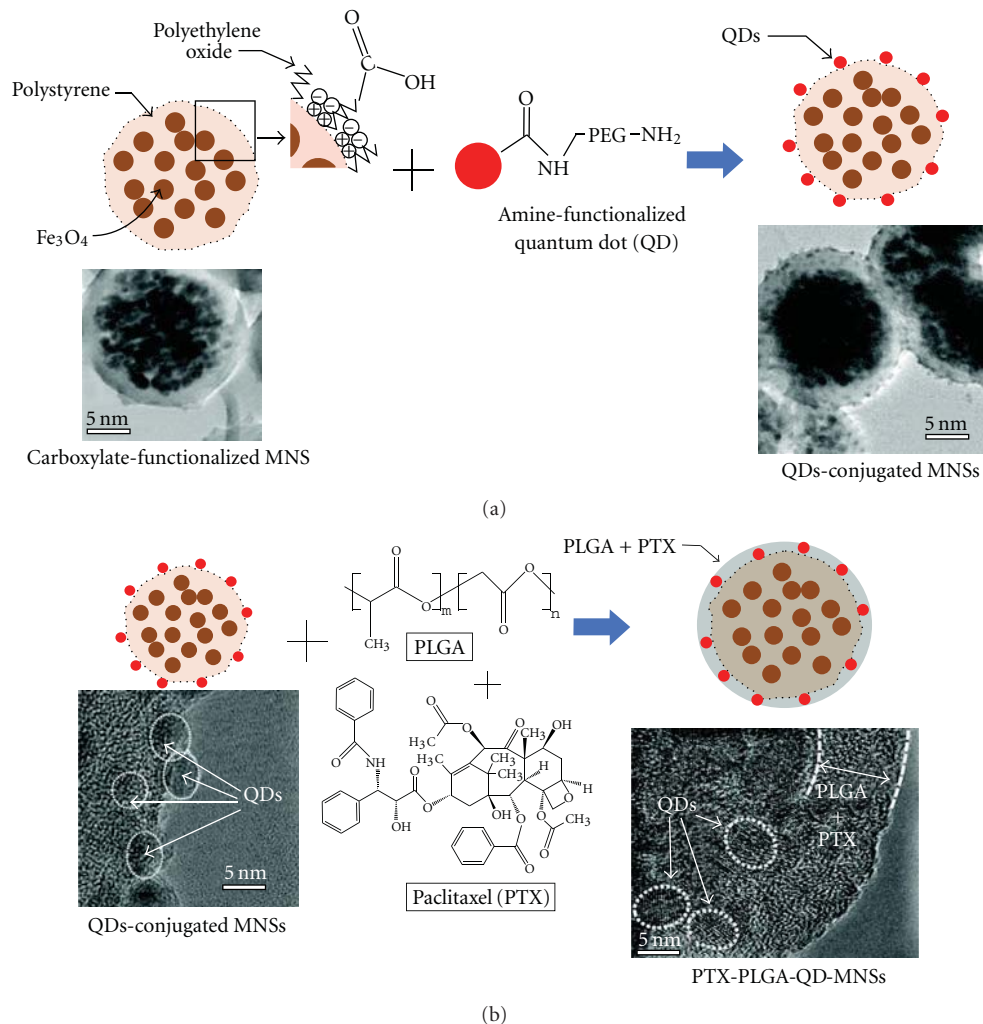
(a)

(b)

Figure 5: Schematic diagrams illustrating surface functionalization of magnetic nanospheres (MNSs): (a) conjugation of amine-functionalized quantum dots (QDs) to the surface of carboxylate-functionalized MNSs using conventional NHS/EDC coupling method; (b) PTX loading using a thin PLGA coat on the surface of QD-MNSs (with permission from [61]).

conjugated with molecules which have the capabilities of recognizing the target. These surface modifications can also help prevent aggregation, reduce the nonspecific binding, and are critical to achieving specific target imaging in biological studies. Further functionalization of QDs can be achieved by the modification of protecting ligands [64–66], introducing targeting groups such as apolipoproteins and peptides (Scheme 1) [64]. In this part, we mainly introduce the recent development of conjugated QDs for *in vitro* and *in vivo* imaging; some new QDs related to bioimaging are also included.

5.1. In Vitro Imaging. Early studies of *in vitro* imaging used QDs to label cells. For instance, PbS and PbSe capped with carboxylic groups had been obtained in aqueous solution by ligands exchange to label cells [67]; CdTe capped with 3-mercaptopropionic acid (3-MPA) was used as imaging tool to label Salmonella typhimurium cells [68]. Jaiswal et al. reported labelling HeLa cells with acid-capped CdSe/ZnS QDs [69]. It is found that the cells can store QDs in vesicles

through endocytosis after washing away the excess QDs. Further, they also demonstrated the potential application of QDs in cell tracking by using avidin-conjugated QDs to label cells.

With the development of biomarkers in cell biology, the tracking of some specific cells (such as cancer cells) becomes possible. Gac et al. have successfully detected apoptotic cells by conjugating QDs with biotinylated Annexin V, which enables the functionalized QDs to bind to phosphatidylserine (PS) moieties present on the membrane of apoptotic cells but not on healthy or necrotic cells (Figure 6) [70]. The detection and imaging of apoptotic cells makes it possible to monitor specific photostable apoptosis. Wolcott reported silica-coated CdTe QDs decorated with functionalized groups not only for labelling proteins, but also for preventing toxic Cd^{2+} leaking from the core [71]. Nie developed cell-penetrating QDs coated with polyethylene glycol (PEG) grafted polyethylenimine (PEI), which were capable of penetrating cell membranes and disrupting endosomal organelles in cells [72]. Recently, in the demand of using biocompatible
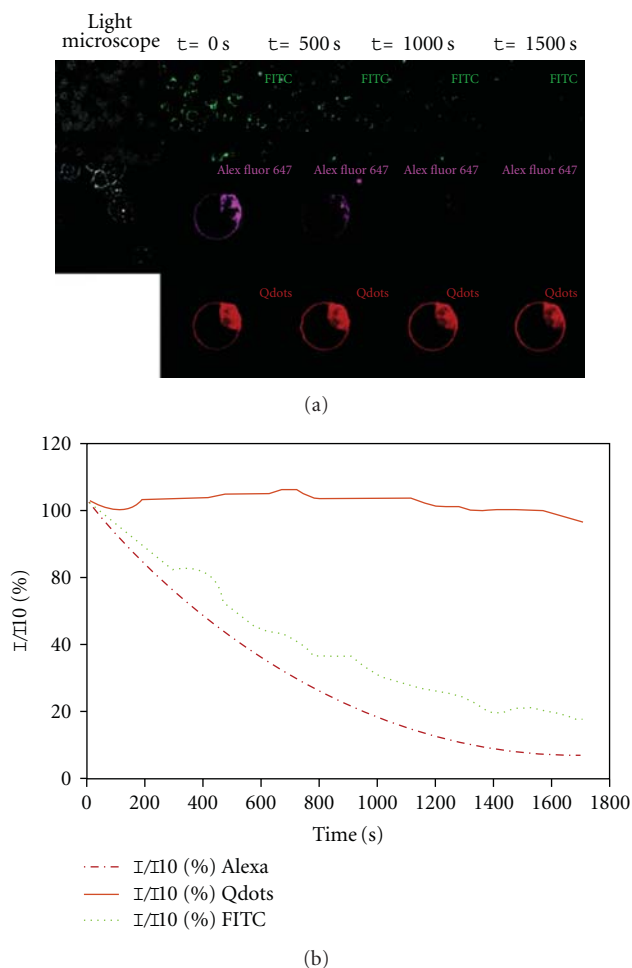
(a)

(b)

Figure 6: Comparison of the staining efficiency of Annexin V-functionalized Qdots (staining achieved in one step using 2 nM of Qdots and 4 nM of biotinylated Annexin V, red), FITC-Annexin V (0.5% v/v, green) and Alexa Fluor 647-Annexin V (0.5% v/v, pink). (a) Light microscope pictures and pictures taken at $t = 0, 500, 1000, 1500$ s. (b) Intensity variation as a function of time for the three staining agents conjugated to Annexin V, FITC, Alexa Fluor 647 and Qdots. Intensity values expressed as relative values I/I_0, where I_0 is the intensity measured at the first irradiation of the sample (with permission from [70]).

and nontoxic QDs as nanoprobes, rare earth (RE) elements are used to fabricate a new type of QDs, such as Gd-doped ZnO QDs. RE-doped QDs have distinct advantages over heavy metal-containing QDs, not only because of avoiding the increase of particle size by polymer or silica coating in synthesis procedure, but also providing a simple, green synthesis method. Liu et al. reported the development of Gd-doped ZnO QDs with enhanced yellow fluorescence, and these QDs can be used as nanoprobes for quick cell detection with very low toxicity [73]. Other progresses include CdSe/ZnS with PEG coating and CdSe/ZnS-peptide conjugation for cytosol localization and nucleus targeting [74–77], CdS passivated by DNA to yield nontoxic QDs as new biological imaging agent [78], CdSe/L-cysteine QDs designed to label serum albumin (BSA) and cells [79], polymer QDs
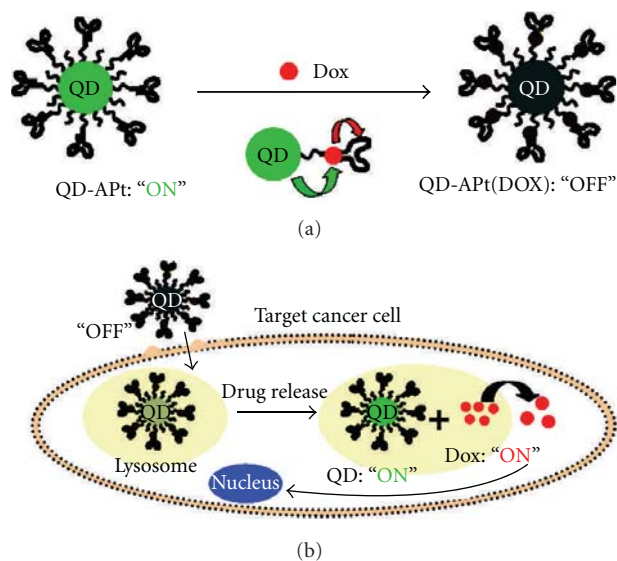

(a)

(b)

Figure 7: (a) Schematic illustration of QD-Apt(Dox) Bi-FRET system. (b) Schematic illustration of specific uptake of QD-Apt(Dox) conjugates into target cancer cell through PSMA mediate endocytosis. The release of Dox from the QD-Apt(Dox) conjugates induces the recovery of fluorescence from both QD and Dox ("ON" state), thereby sensing the intracellular delivery of Dox and enabling the synchronous fluorescent localization and killing of cancer cells (with permission from [85]).

(PS-PEG-COOH) with conjugation to biomolecules, such as streptavidin and immunoglobulin G (IgG) to label cell surface receptors and subcellular structures in fixed cells [21, 80], and other non-Cd-containing QDs such as Ge-QDs and near-IR InAs for imaging of specific cellular proteins [81, 82]. In order to broaden QDs applications, MRI detectable QDs were demanded. Many studies have set out to explore paramagnetic QDs. Sun reported a new kind of magnetic fluorescent multifunctional nanocomposite which contained silica-coated Fe_3O_4 and TGA-capped CdTe QDs. This nanocomposite was successfully employed for HeLa cell labelling and imaging, as well as in magnetic separation [83]. Mulder et al. have successfully modified CdSe/ZnS with paramagnetic coating and arginine-glycine-aspartic acid (RGD) conjugation in order to combine the functions of specific protein binding and contrast agent for molecular imaging [84].

The challenges encountered in cancer therapy stimulate comprehensive studies. Many efforts focus on the tracking and diagnosis of cancer cells. Cao et al. used near-IR QDs with an emission wavelength of 800 nm (QD800) to label squamous cell carcinoma cell line U14 (U14/QD800). The fluorescent images of U14 cells can be clearly obtained after 6 h by cell endocytosis [62]. In 2007, Bagalkot et al. reported a more complex QDs-aptamer- (Apt-) doxorubicin (Dox) conjugate system [QD-Apt(Dox)] to endow QDs with the capability of targeting, imaging, therapy, and sensing the prostate cancer cells that express the prostate-specific membrane antigen (PSMA) protein (Figure 7) [85]. Other types of QDs that have been applied in pancreatic cancer cells
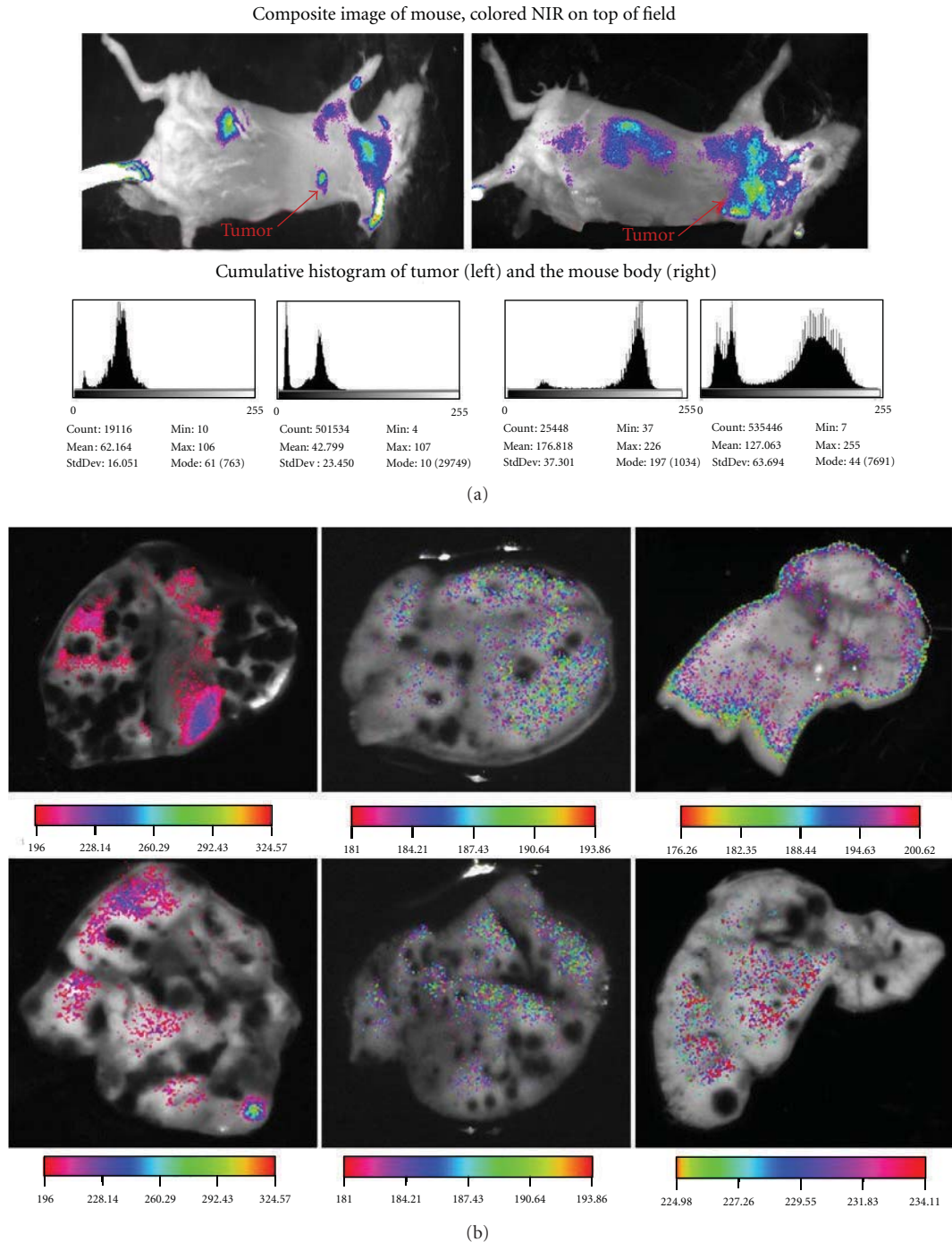
Composite image of mouse, colored NIR on top of field

Cumulative histogram of tumor (left) and the mouse body (right)

Count: 19116	Min: 10	Count: 501534	Min: 4
Mean: 62.164	Max: 106	Mean: 42.799	Max: 107
StdDev: 16.051	Mode: 61 (763)	StdDev : 23.450	Mode: 10 (29749)

Count: 25448	Min: 37	Count: 535446	Min: 7
Mean: 176.818	Max: 226	Mean: 127.063	Max: 255
StdDev: 37.301	Mode: 197 (1034)	StdDev: 63.694	Mode: 44 (7691)

(a)

(b)

FIGURE 8: Targeting of lung melanoma tumor by injecting 2C5 QD-Mic in two mice. (a) Composite images (white field image superimposed with the fluorescence intensity), and cumulative histograms for the tumor region and the whole body of two mice; (b) composite *ex vivo* images (white field image superimposed with the fluorescence intensity) of lungs from mice bearing metastatic B16F-10 lung melanoma tumor (with permission from [94]).

imaging include CdSe/CdS/ZnS using transferrin and anti-Claudin-4 as targeting ligands, InP QDs conjugated with cancer antibodies, and water-soluble Si-QDs micelles encapsulated with polymer chains [86–88]. Another important role played by QDs in biological application is transfection. Many studies reported fluorescence imaging and nucleus targeting of living cells by transfection and RNA delivery. Biju identified an insect neuropeptide, also-called allatostatin, which can transfects living NIH 3T3 and A431 human epidermoid carcinoma cells and transports quantum dots (QDs) inside the cytoplasm and even the nucleus of the cells [89]. This method showed the conjugation of QDs with

allatostatin could achieve high transection efficiency, which was promising for DNA gene delivery and cell labelling. Also, with specific conjugation with allatostatin, the QDs had another potential application in cancer, called photodynamic therapy [90].

5.2. In Vivo Imaging. In addition to their usage as nanoprobes and labels for *in vitro* imaging, QDs have also been widely used as *in vivo* imaging agents (Figure 8) [91–94]. Cancer-specific antibody, coupled to near-IR QDs with polymer coatings is the most popular QDs agent for tumor-targeted imaging. Progress in this field has been reviewed in one literature [94, 95].

However, the depth of targets makes the QDs *in vivo* imaging very challenging. This special application of QDs requires them with low toxicity, high contrast, high sensitivity, and photostability. Dubertret et al. fabricated one type of CdSe/ZnS QDs which were encapsulated individually in phospholipid block-copolymer micelles. After further modification by DNA, this multifunctionalized DNA-QD-micelles can be developed to obtain Xenopus embryo fluorescent images in PBS. Moreover, after injection into embryos, the QD micelles showed high stability and nontoxicity ($<5 \times 10^9$ nanocrystals per cell) [96]. Another study reported by Michalet showed that CdSe/ZnS QDs can exhibit high contrast and imaging depth in two-photon excitation confocal microscopy by visualizing blood vessels in live mice [3, 97]. They confirmed that coatings such as PEG on the surfaces of QDs could further reduce their toxicity and accumulation in liver. Some studies also pointed out that the increase of the length of PEG coating polymer on the surface of QDs was able to slow down their extraction toward the liver, so coating polymer on the surfaces was another factor worthy of considering when QDs are employed for *in vivo* imaging [98]. Other reports that used low-toxicity QDs include the development of non-Cd-containing QDs such as CuInS$_2$/ZnS core/shell nanocrystals for *in vivo* imaging [95]. In addition, sensitivity is another important factor that must be considered in QDs-related *in vivo* imaging. One study used nude mice for *in vivo* imaging after near-IR QD800-labeled BcaCD885 cells (BcaCD885/QD800) being implanted [99]. Fluorescence signals of QDs accumulated in the tumor could be detected after 16 days of incubation at certain concentrations. It suggested that, compared with CT and MRI, QD800-based imaging could efficiently increase the sensitivity of early diagnosis of cancer cells.

With the development of QDs in recent years, many studies tried to explore the potential of QDs in wider fields. Kobayashi reported fluorescence lymphangiography by injecting five QDs with different emission spectra [100]. Through simultaneous injection of five QDs into different sites in the middle of phalanges, the upper extremity, the ears, and the chin, different parts of the mouse body can be identified by certain fluorescence color. This is the first demonstration of simultaneous imaging of trafficking lymph nodes with QDs having different emission spectra. As biological fluorescent markers, no matter *in vitro* or *in vivo*, much attention has been concentrated on developing spherical QDs conjugations, but there are few reports on how other morphologies of QDs will interact with the biological systems. Yong et al. reported CdSe/CdS/ZnS quantum rods (QRs) coated with PEGylated phospholipids and RGD peptide for tumor targeting [101]. This conjugation was demonstrated to be a bright, photostable, and biocompatible luminescent probe for the early diagnosis of cancer and was believed to offer new opportunities for imaging early tumor growth.

6. Prospects

Owing to the initial success of QDs-biomolecule conjugates employed for *in vitro* and *in vivo* imaging, it is conceivable that future researches will continue to focus on the development of QDs conjugations for cell labelling and cancer diagnoses. However, for bioapplications, biocompatibility of QDs remains the major challenge which must be carefully dealt with. Many studies have showed the short-term stability and long-term breakdown of Cd-containing QDs in *in vivo* imaging, which raise concerns about their chronic toxicity. Some studies showed that even robust coatings on the surfaces of QDs cannot prevent their releasing of Cd^{2+} ions. The emerging picture of Cd-containing QDs toxicity not only suggests that QDs are required to improve safety before their wide biological applications as fluorescent nanoprobes, but also a variety of noncadmium alternatives are in urgent demand. At present, many efforts have focused on exploring new types of fluorescent nanomaterials such as upconversion materials NaYF$_4$ and NaGaF$_4$. In addition, with the development of new techniques and detection methods, QDs are shown to have applications in wider fields. Zhang et al. successfully introduced Kelvin force microscopy (KFM) as a method to examine the binding of QDs with DNA *in vitro* and *in vivo* [102]; Huang et al. demonstrated a QDs sensor for quantitative visualization of surface charges on single living cell [103]. We believe that with the development of new QDs with low toxicity and multiplex functionalities, QDs will find more versatile applications in biological fields other than bioimaging.

References

[1] P. Alivisatos, "The use of nanocrystals in biological detection," *Nature Biotechnology*, vol. 22, no. 1, pp. 47–52, 2004.

[2] X. H. Gao, L. L. Yang, J. A. Petros, F. F. Marshall, J. W. Simons, and S. M. Nie, "In vivo molecular and cellular imaging with quantum dots," *Current Opinion in Biotechnology*, vol. 16, no. 1, pp. 63–72, 2005.

[3] X. Michalet, F. F. Pinaud, L. A. Bentolila et al., "Quantum dots for live cells, in vivo imaging, and diagnostics," *Science*, vol. 307, no. 5709, pp. 538–544, 2005.

[4] A. M. Smith, H. W. Duan, A. M. Mohs, and S. M. Nie, "Bioconjugated quantum dots for in vivo molecular and

cellular imaging," *Advanced Drug Delivery Reviews*, vol. 60, no. 11, pp. 1226–1240, 2008.

[5] W. C. W. Chan and S. M. Nie, "Quantum dot bioconjugates for ultrasensitive nonisotopic detection," *Science*, vol. 281, no. 5385, pp. 2016–2018, 1998.

[6] B. Dubertret, P. Skourides, D. J. Norris, V. Noireaux, A. H. Brivanlou, and A. Libchaber, "In vivo imaging of quantum dots encapsulated in phospholipid micelles," *Science*, vol. 298, no. 5599, pp. 1759–1762, 2002.

[7] A. Konkar, S. Y. Lu, A. Madhukar, S. M. Hughes, and A. P. Alivisatos, "Semiconductor nanocrystal quantum dots on single crystal semiconductor substrates: high resolution transmission electron microscopy," *Nano Letters*, vol. 5, no. 5, pp. 969–973, 2005.

[8] Y. Xing, Q. Chaudry, C. Shen et al., "Bioconjugated quantum dots for multiplexed and quantitative immunohistochemistry," *Nature Protocols*, vol. 2, no. 5, pp. 1152–1165, 2007.

[9] M. V. Yezhelyev, A. Al-Hajj, C. Morris et al., "In situ molecular profiling of breast cancer biomarkers with multicolor quantum dots," *Advanced Materials*, vol. 19, no. 20, pp. 3146–3151, 2007.

[10] A. M. Smith, S. Dave, S. M. Nie, L. True, and X. Gao, "Multicolor quantum dots for molecular diagnostics of cancer," *Expert Review of Molecular Diagnostics*, vol. 6, no. 2, pp. 231–244, 2006.

[11] A. Robe, E. Pic, H. P. Lassalle, L. Bezdetnaya, F. Guillemin, and F. Marchal, "Quantum dots in axillary lymph node mapping: biodistribution study in healthy mice," *BMC Cancer*, vol. 8, no. 1, pp. 111–119, 2008.

[12] M. Takeda, H. Tada, H. Higuchi et al., "In vivo single molecular imaging and sentinel node navigation by nanotechnology for molecular targeting drug-delivery systems and tailor-made medicine," *Breast Cancer*, vol. 15, no. 2, pp. 145–152, 2008.

[13] S. Kim, Y. T. Lim, E. G. Soltesz et al., "Near-infrared fluorescent type II quantum dots for sentinel lymph node mapping," *Nature Biotechnology*, vol. 22, no. 1, pp. 93–97, 2004.

[14] E. G. Soltesz, S. Kim, R. G. Laurence et al., "Intraoperative sentinel lymph node mapping of the lung using near-infrared fluorescent quantum dots," *Annals of Thoracic Surgery*, vol. 79, no. 1, pp. 269–277, 2005.

[15] E. G. Soltesz, S. Kim, S. W. Kim et al., "Sentinel lymph node mapping of the gastrointestinal tract by using invisible light," *Annals of Surgical Oncology*, vol. 13, no. 3, pp. 386–396, 2006.

[16] C. P. Parungo, S. Ohnishi, S. W. Kim et al., "Intraoperative identification of esophageal sentinel lymph nodes with near-infrared fluorescence imaging," *Journal of Thoracic and Cardiovascular Surgery*, vol. 129, no. 4, pp. 844–850, 2005.

[17] B. Ballou, L. A. Ernst, S. Andreko et al., "Sentinel lymph node imaging using quantum dots in mouse tumor models," *Bioconjugate Chemistry*, vol. 18, no. 2, pp. 389–396, 2007.

[18] P. Diagaradjane, J. M. Orenstein-Cardona, N. E. Colon-Casasnovas et al., "Imaging epidermal growth factor receptor expression in vivo: pharmacokinetic and biodistribution characterization of a bioconjugated quantum dot nanoprobe," *Clinical Cancer Research*, vol. 14, no. 3, pp. 731–741, 2008.

[19] X. H. Gao, Y. Y. Cui, R. M. Levenson, L. W. K. Chung, and S. M. Nie, "In vivo cancer targeting and imaging with semiconductor quantum dots," *Nature Biotechnology*, vol. 22, no. 8, pp. 969–976, 2004.

[20] D. S. Lidke, P. Nagy, R. Heintzmann et al., "Quantum dot ligands provide new insights into erbB/HER receptor-mediated signal transduction," *Nature Biotechnology*, vol. 22, no. 2, pp. 198–203, 2004.

[21] L. F. Qi and X. H. Gao, "Quantum dot—amphipol nanocomplex for intracellular delivery and real-time imaging of siRNA," *ACS Nano*, vol. 2, no. 7, pp. 1403–1410, 2008.

[22] D. Sen, T. J. Deerinck, M. H. Ellisman, I. Parker, and M. D. Cahalan, "Quantum dots for tracking dendritic cells and priming an immune response in vitro and in vivo," *PLoS One*, vol. 3, no. 9, Article ID e3290, 2008.

[23] A. M. Derfus, W. C. W. Chan, and S. N. Bhatia, "Probing the cytotoxicity of semiconductor quantum dots," *Nano Letters*, vol. 4, no. 1, pp. 11–18, 2004.

[24] R. Hardman, "Toxicological review of quantum dots: toxicity depends on physicochemical and environmental factors," *Environmental Health Perspectives*, vol. 114, no. 2, pp. 165–172, 2006.

[25] G. N. Guo, W. Liu, J. G. Liang, H. B. Xu, Z. K. He, and X. L. Yang, "Preparation and characterization of novel CdSe quantum dots modified with poly (D, L-lactide) nanoparticles," *Materials Letters*, vol. 60, no. 21-22, pp. 2565–2568, 2006.

[26] Y. Pan, S. Neuss, A. Leifert et al., "Size-dependent cytotoxicity of gold nanoparticles," *Small*, vol. 3, no. 11, pp. 1941–1949, 2007.

[27] M. L. Schipper, Z. Cheng, S. W. Lee et al., "MicroPET-based biodistribution of quantum dots in living mice," *Journal of Nuclear Medicine*, vol. 48, no. 9, pp. 1511–1518, 2007.

[28] P. Diagaradjane, A. Deorukhkar, J. G. Gelovani, D. M. Maru, and S. Krishnan, "Gadolinium chloride augments tumor-specific imaging of targeted quantum dots in vivo," *ACS Nano*, vol. 4, no. 7, pp. 4131–4141, 2010.

[29] M. Q. Chu, X. Song, D. Cheng, S. P. Liu, and J. Zhu, "Preparation of quantum dot-coated magnetic polystyrene nanospheres for cancer cell labelling and separation," *Nanotechnology*, vol. 17, no. 13, pp. 3268–3273, 2006.

[30] F. Corsi, C. de Palma, M. Colombo et al., "Towards ideal magnetofluorescent nanoparticles for bimodal detection of breast-cancer cells," *Small*, vol. 5, no. 22, pp. 2555–2564, 2009.

[31] A. Quarta, R. D. Corato, L. Manna, A. Ragusa, and T. Pellegrino, "Fluorescent-magnetic hybrid nanostructures: preparation, properties, and applications in biology," *IEEE Transactions on Nanobioscience*, vol. 6, no. 4, pp. 298–308, 2007.

[32] P. N. Prasad, *Biophotonics*, Wiley-Interscience, Hoboken, NJ, USA, 2003.

[33] H. Wittcoff, B. G. Reuben, and J. S. Plotkin, *Industrial organic chemicals*, Wiley-Interscience, Hoboken, NJ, USA, 2004.

[34] B. O. Dabbousi, J. Rodriguez-Viejo, F. V. Mikulec et al., "(CdSe)ZnS core-shell quantum dots: synthesis and characterization of a size series of highly luminescent nanocrystallites," *Journal of Physical Chemistry B*, vol. 101, no. 46, pp. 9463–9475, 1997.

[35] S. T. Selvan, "Silica-coated quantum dots and magnetic nanoparticles for bioimaging applications," *Biointerphases*, vol. 5, no. 3, pp. FA110–FA115, 2010.

[36] J. H. Park, L. Gu, G. Von Maltzahn, E. Ruoslahti, S. N. Bhatia, and M. J. Sailor, "Biodegradable luminescent porous silicon nanoparticles for in vivo applications," *Nature Materials*, vol. 8, no. 4, pp. 331–336, 2009.

[37] X. H. Gao and S. M. Nie, "Doping mesoporous materials with multicolor quantum dots," *Journal of Physical Chemistry B*, vol. 107, no. 42, pp. 11575–11578, 2003.

[38] F. Erogbogbo, K. T. Yong, I. Roy et al., "In vivo targeted cancer imaging, sentinel lymph node mapping and multi-channel imaging with biocompatible silicon nanocrystals," *Nano Letters*, vol. 5, no. 1, pp. 413–423, 2011.

[39] W. J. Parak, D. Gerion, D. Zanchet et al., "Conjugation of DNA to silanized colloidal semiconductor nanocrystalline quantum dots," *Chemistry of Materials*, vol. 14, no. 5, pp. 2113–2119, 2002.

[40] S. Sato and M. T. Swihart, "Propionic-acid-terminated silicon nanoparticles: synthesis and optical characterization," *Chemistry of Materials*, vol. 18, no. 17, pp. 4083–4088, 2006.

[41] R. D. Tilley and K. Yamamoto, "The microemulsion synthesis of hydrophobic and hydrophilic silicon nanocrystals," *Advanced Materials*, vol. 18, no. 15, pp. 2053–2056, 2006.

[42] J. H. Warner, A. Hoshino, K. Yamamoto, and R. D. Tilley, "Water-soluble photoluminescent silicon quantum dots," *Angewandte Chemie International Edition*, vol. 44, no. 29, pp. 4550–4554, 2005.

[43] L. H. Chen, D. W. McBranch, H. L. Wang, R. Helgeson, F. Wudl, and D. G. Whitten, "Highly sensitive biological and chemical sensors based on reversible fluorescence quenching in a conjugated polymer," *Proceedings of the National Academy of Sciences*, vol. 96, no. 22, pp. 12287–12292, 1999.

[44] C. H. Fan, S. Wang, J. W. Hong, G. C. Bazan, K. W. Plaxco, and A. J. Heeger, "Beyond superquenching: hyper-efficient energy transfer from conjugated polymers to gold nanoparticles," *Proceedings of the National Academy of Sciences*, vol. 100, no. 11, pp. 6297–6301, 2003.

[45] J. H. Burroughes, D. D. C. Bradley, A. R. Brown et al., "Light-emitting diodes based on conjugated polymers," *Nature*, vol. 347, no. 6293, pp. 539–541, 1990.

[46] R. H. Friend, R. W. Gymer, A. B. Holmes et al., "Electroluminescence in conjugated polymers," *Nature*, vol. 397, no. 6715, pp. 121–128, 1999.

[47] F. So, B. Krummacher, M. K. Mathai, D. Poplavskyy, S. A. Choulis, and V. E. Choong, "Recent progress in solution processable organic light emitting devices," *Journal of Applied Physics*, vol. 102, no. 9, Article ID 091101, 2007.

[48] C. F. Wu, C. Szymanski, and J. McNeill, "Preparation and encapsulation of highly fluorescent conjugated polymer nanoparticles," *Langmuir*, vol. 22, no. 7, pp. 2956–2960, 2006.

[49] C. F. Wu, C. Szymanski, Z. Cain, and J. McNeill, "Conjugated polymer dots for multiphoton fluorescence imaging," *Journal of the American Chemical Society*, vol. 129, no. 43, pp. 12904–12905, 2007.

[50] C. F. Wu, B. Bull, C. Szymanski, K. Christensen, and J. McNeill, "Multicolor conjugated polymer dots for biological fluorescence imaging," *ACS Nano*, vol. 2, no. 11, pp. 2415–2423, 2008.

[51] C. B. Murray, D. J. Norris, and M. G. Bawendi, "Synthesis and characterization of nearly monodisperse CdE (E=S, Se, Te) semiconductor nanocrystallites," *Journal of the American Chemical Society*, vol. 115, no. 19, pp. 8706–8715, 1993.

[52] T. Rajh, O. I. Micic, and A. J. Nozik, "Synthesis and characterization of surface-modified colloidal CdTe quantum dots," *Journal of Physical Chemistry*, vol. 97, no. 46, pp. 11999–12003, 1993.

[53] C. Ding, Y. Li, and Y. Qu, "Synthesizing quantum dot with uniform grain diameter distribution in water phase comprises preparing molding board agent and cadmium sulfydryl composite precursor, producing water solution of sodium borohydride, and synthesizing quantum dot," East China Normal University, 2010.

[54] M. A. Correa-Duarte, M. Giersig, N. A. Kotov, and L. M. Liz-Marzan, "Control of packing order of self-assembled monolayers of magnetite nanoparticles with and without SiO$_2$ coating by microwave irradiation," *Langmuir*, vol. 14, no. 22, pp. 6430–6435, 1998.

[55] H. F. Qian, X. Qiu, L. Li, and J. C. Ren, "Microwave-assisted aqueous synthesis: a rapid approach to prepare highly luminescent ZnSe(S) alloyed quantum dots," *Journal of Physical Chemistry B*, vol. 110, no. 18, pp. 9034–9040, 2006.

[56] F. Pinaud, D. King, H. P. Moore, and S. Weiss, "Bioactivation and cell targeting of semiconductor CdSe/ZnS nanocrystals with phytochelatin-related peptides," *Journal of the American Chemical Society*, vol. 126, no. 19, pp. 6115–6123, 2004.

[57] T. Pellegrino, L. Manna, S. Kudera et al., "Hydrophobic nanocrystals coated with an amphiphilic polymer shell: a general route to water soluble nanocrystals," *Nano Letters*, vol. 4, no. 4, pp. 703–707, 2004.

[58] C. A. J. Lin, R. A. Sperling, J. K. Li et al., "Design of an amphiphilic polymer for nanoparticle coating and functionalization," *Small*, vol. 4, no. 3, pp. 334–341, 2008.

[59] J. H. Phan, R. A. Moffitt, T. H. Stokes et al., "Convergence of biomarkers, bioinformatics and nanotechnology for individualized cancer treatment," *Trends in Biotechnology*, vol. 27, no. 6, pp. 350–358, 2009.

[60] J. Liu, S. K. Lau, V. A. Varma, B. A. Kairdolf, and S. M. Nie, "Multiplexed detection and characterization of rare tumor cells in Hodgkin's lymphoma with multicolor quantum dots," *Analytical Chemistry*, vol. 82, no. 14, pp. 6237–6243, 2010.

[61] H. S. Cho, Z. Y. Dong, G. M. Pauletti et al., "Fluorescent, superparamagnetic nanospheres for drug storage, targeting, and imaging: a multifunctional nanocarrier system for cancer diagnosis and treatment," *ACS Nano*, vol. 4, no. 9, pp. 5398–5404, 2010.

[62] Y. A. Cao, K. Yang, Z. G. Li, C. Zhao, C. M. Shi, and J. Yang, "Near-infrared quantum-dot-based non-invasive in vivo imaging of squamous cell carcinoma U14," *Nanotechnology*, vol. 21, no. 47, Article ID 475104, 2010.

[63] W. Jiang, A. Singhal, J. N. Zheng, C. Wang, and W. C. W. Chan, "Optimizing the synthesis of red- to near-IR-emitting CdS-capped CdTe$_x$Se$_{1-x}$ alloyed quantum dots for biomedical imaging," *Chemistry of Materials*, vol. 18, no. 20, pp. 4845–4854, 2006.

[64] W. J. M. Mulder, R. Koole, R. J. Brandwijk et al., "Quantum dots with a paramagnetic coating as a bimodal molecular imaging probe," *Nano Letters*, vol. 6, no. 1, pp. 1–6, 2006.

[65] W. J. M. Mulder, G. J. Strijkers, G. A. F. V. Tilborg, D. P. Cormode, Z. A. Fayad, and K. Nicolay, "Nanoparticulate assemblies of amphiphiles and diagnostically active materials for multimodality imaging," *Accounts of Chemical Research*, vol. 42, no. 7, pp. 904–914, 2009.

[66] J. H. Bang, W. H. Suh, and K. S. Suslick, "Quantum dots from chemical aerosol flow synthesis: preparation, characterization, and cellular imaging," *Chemistry of Materials*, vol. 20, no. 12, pp. 4033–4038, 2008.

[67] B. R. Hyun, H. Y. Chen, D. A. Rey, F. W. Wise, and C. A. Batt, "Near-infrared fluorescence imaging with water-soluble lead salt quantum dots," *Journal of Physical Chemistry B*, vol. 111, no. 20, pp. 5726–5730, 2007.

[68] H. Li, W. Y. Shih, and W. H. Shih, "Synthesis and characterization of aqueous carboxyl-capped CdS quantum dots

for bioapplications," *Industrial and Engineering Chemistry Research*, vol. 46, no. 7, pp. 2013–2019, 2007.

[69] J. K. Jaiswal, H. Mattoussi, J. M. Mauro, and S. M. Simon, "Long-term multiple color imaging of live cells using quantum dot bioconjugates," *Nature Biotechnology*, vol. 21, no. 1, pp. 47–51, 2002.

[70] S. L. Gac, I. Vermes, and A. V. D. Berg, "Quantum dots based probes conjugated to annexin V for photostable apoptosis detection and imaging," *Nano Letters*, vol. 6, no. 9, pp. 1863–1869, 2006.

[71] A. Wolcott, D. Gerion, M. Visconte et al., "Silica-coated CdTe quantum dots functionalized with thiols for bioconjugation to IgG proteins," *Journal of Physical Chemistry B*, vol. 110, no. 11, pp. 5779–5789, 2006.

[72] H. W. Duan and S. M. Nie, "Cell-penetrating quantum dots based on multivalent and endosome-disrupting surface coatings," *Journal of the American Chemical Society*, vol. 129, no. 11, pp. 3333–3336, 2007.

[73] A. Liu, S. Peng, J. C. Soo, M. Kuang, P. Chen, and H. Duan, "Quantum dots with phenylboronic acid tags for specific labeling of sialic acids on living cells," *Analytical Chemistry*, vol. 83, no. 3, pp. 1124–1130, 2011.

[74] F. Q. Chen and D. Gerion, "Fluorescent CdSe/ZnS nanocrystal-peptide conjugates for long-term, nontoxic imaging and nuclear targeting in living cells," *Nano Letters*, vol. 4, no. 10, pp. 1827–1832, 2004.

[75] I. Yildiz, B. McCaughan, S. F. Cruickshank, J. F. Callan, and F. M. Raymo, "Biocompatible CdSe-ZnS Core-shell quantum dots coated with hydrophilic polythiols," *Langmuir*, vol. 25, no. 12, pp. 7090–7096, 2009.

[76] G. Ruan, A. Agrawal, A. I. Marcus, and S. M. Nie, "Imaging and tracking of Tat peptide-conjugated quantum dots in living cells: new insights into nanoparticle uptake, intracellular transport, and vesicle shedding," *Journal of the American Chemical Society*, vol. 129, no. 47, pp. 14759–14766, 2007.

[77] R. Wilson, D. G. Spiller, A. Beckett, I. A. Prior, and V. Sée, "Highly stable dextran-coated quantum dots for biomolecular detection and cellular imaging," *Chemistry of Materials*, vol. 22, no. 23, pp. 6361–6369, 2010.

[78] N. Ma, J. Yang, K. M. Stewart, and S. O. Kelley, "DNA-passivated CdS nanocrystals: luminescence, bioimaging, and toxicity profiles," *Langmuir*, vol. 23, no. 26, pp. 12783–12787, 2007.

[79] P. Liu, Q. S. Wang, and X. Li, "Studies on CdSe/L-cysteine quantum dots synthesized in aqueous solution for biological labeling," *Journal of Physical Chemistry C*, vol. 113, no. 18, pp. 7670–7676, 2009.

[80] C. F. Wu, T. Schneider, M. Zeigler et al., "Bioconjugation of ultrabright semiconducting polymer dots for specific cellular targeting," *Journal of the American Chemical Society*, vol. 132, no. 43, pp. 15410–15417, 2010.

[81] P. M. Allen, W. H. Liu, V. P. Chauhan et al., "InAs(ZnCdS) auantum dots optimized for biological imaging in the near-infrared," *Journal of the American Chemical Society*, vol. 132, no. 2, pp. 470–471, 2010.

[82] S. Prabakar, A. Shiohara, S. Hanada, K. Fujioka, K. Yamamoto, and R. D. Tilley, "Size controlled synthesis of germanium nanocrystals by hydride reducing agents and their biological applications," *Chemistry of Materials*, vol. 22, no. 2, pp. 482–486, 2010.

[83] P. Sun, H. Y. Zhang, C. Liu et al., "Preparation and characterization of Fe_3O_4/CdTe magnetic/fluorescent nanocomposites and their applications in immuno-labeling and fluorescent

[84] W. J. M. Mulder, R. Koole, R. J. Brandwijk et al., "Quantum dots with a paramagnetic coating as a bimodal molecular imaging probe," *Nano Letters*, vol. 6, no. 1, pp. 1–6, 2006.

[85] V. Bagalkot, L. F. Zhang, E. Levy-Nissenbaum et al., "Quantum dot-aptamer conjugates for synchronous cancer imaging, therapy, and sensing of drug delivery based on Bi-fluorescence resonance energy transfer," *Nano Letters*, vol. 7, no. 10, pp. 3065–3070, 2007.

[86] J. Qian, K. T. Yong, I. Roy et al., "Imaging pancreatic cancer using surface-functionalized quantum dots," *Journal of Physical Chemistry B*, vol. 111, no. 25, pp. 6969–6972, 2007.

[87] F. Erogbogbo, K. T. Yong, I. Roy, G. X. Xu, P. N. Prasad, and M. T. Swihart, "Biocompatible luminescent silicon quantum dots for imaging of cancer cells," *ACS Nano*, vol. 2, no. 5, pp. 873–878, 2008.

[88] K. T. Yong, H. Ding, I. Roy et al., "Imaging pancreatic cancer using bioconjugated inp quantum dots," *ACS Nano*, vol. 3, no. 3, pp. 502–510, 2009.

[89] C. Walther, K. Meyer, R. Rennert, and I. Neundorf, "Quantum dot—carrier peptide conjugates suitable for imaging and delivery applications," *Bioconjugate Chemistry*, vol. 19, no. 12, pp. 2346–2356, 2008.

[90] V. Biju, D. Muraleedharan, K. I. Nakayama et al., "Quantum dot-insect neuropeptide conjugates for fluorescence imaging, transfection, and nucleus targeting of living cells," *Langmuir*, vol. 23, no. 20, pp. 10254–10261, 2007.

[91] K. C. Weng, C. O. Noble, B. Papahadjopoulos-Sternberg et al., "Targeted tumor cell internalization and imaging of multifunctional quantum dot-conjugated immunoliposomes in vitro and in vivo," *Nano Letters*, vol. 8, no. 9, pp. 2851–2857, 2008.

[92] R. R. Smith, Z. Cheng, A. De, A. L. Koh, R. Sinclair, and S. S. Gambhir, "Real-time intravital imaging of RGD-quantum dot binding to luminal endothelium in mouse tumor neovasculature," *Nano Letters*, vol. 8, no. 9, pp. 2599–2606, 2008.

[93] H. S. Choi, W. H. Liu, F. B. Liu et al., "Design considerations for tumour-targeted nanoparticles," *Nature Nanotechnology*, vol. 5, no. 1, pp. 42–47, 2010.

[94] A. Papagiannaros, J. Upponi, W. Hartner, D. Mongayt, T. Levchenko, and V. Torchilin, "Quantum dot loaded immunomicelles for tumor imaging," *BMC Medical Imaging*, vol. 10, no. 1, article 22, 2010.

[95] L. Li, T. J. Daou, I. Texier, T. T. K. Chi, N. Q. Liem, and P. Reiss, "Highly luminescent cuins 2/ZnS core-shell nanocrystals: cadmium-free quantum dots for in vivo imaging," *Chemistry of Materials*, vol. 21, no. 12, pp. 2422–2429, 2009.

[96] B. Dubertret, P. Skourides, D. J. Norris, V. Noireaux, A. H. Brivanlou, and A. Libchaber, "In vivo imaging of quantum dots encapsulated in phospholipid micelles," *Science*, vol. 298, no. 5599, pp. 1759–1762, 2002.

[97] B. Ballou, B. C. Lagerholm, L. A. Ernst, M. P. Bruchez, and A. S. Waggoner, "Noninvasive Imaging of quantum dots in mice," *Bioconjugate Chemistry*, vol. 15, no. 1, pp. 79–86, 2004.

[98] T. J. Daou, L. Li, P. Reiss, V. Josserand, and I. Texier, "Effect of poly(ethylene glycol) length on the in vivo behavior of coated quantum dots," *Langmuir*, vol. 25, no. 5, pp. 3040–3044, 2009.

[99] K. Yang, Y. A. Cao, C. Shi et al., "Quantum dot-based visual in vivo imaging for oral squamous cell carcinoma in mice," *Oral Oncology*, vol. 46, no. 12, pp. 864–868, 2010.

[100] E. Cassette, T. Pons, C. Bouet et al., "Synthesis and characterization of near-infrared Cu-In-Se/ZnS core/shell quantum dots for in vivo imaging," *Chemistry of Materials*, vol. 22, no. 22, pp. 6117–6124, 2010.

[101] K. T. Yong, R. Hu, I. Roy et al., "Tumor targeting and imaging in live animals with functionalized semiconductor quantum rods," *ACS Applied Materials & Interfaces*, vol. 1, no. 3, pp. 710–719, 2009.

[102] W. Zhang, Y. Yao, and Y. S. Chen, "Imaging and quantifying the morphology and nanoelectrical properties of quantum dot nanoparticles interacting with DNA," *Journal of Physical Chemistry C*, vol. 115, no. 3, pp. 599–606, 2011.

[103] Y. X. Huang, X. J. Zheng, L. L. Kang et al., "Quantum dots as a sensor for quantitative visualization of surface charges on single living cells with nano-scale resolution," *Biosensors and Bioelectronics*, vol. 26, no. 5, pp. 2114–2118, 2011.

Research Article

Optimization of the Preparation Process for an Oral Phytantriol-Based Amphotericin B Cubosomes

Zhiwen Yang,[1, 2] Xinsheng Peng,[1, 3] Yinhe Tan,[1] Meiwan Chen,[1] Xingqi Zhu,[4] Min Feng,[1] Yuehong Xu,[1] and Chuanbin Wu[1, 5]

[1] *School of Pharmaceutical Sciences, Sun Yat-Sen University, Guangzhou 51006, China*

[2] *Department of Pharmaceutical Sciences, Gannan Medical College, Ganzhou, China*

[3] *GuangDong Medical College, Dongguan, China*

[4] *Anton-Paar, Shanghai, China*

[5] *GuangDong Research Center for Drug Delivery Systems, Guangzhou, China*

Correspondence should be addressed to Chuanbin Wu, cbwu2000@yahoo.com

In order to develop an oral formation of Amphotericin B (AmB) using phytantriol- (PYT-) based cubosomes with desirable properties, homogenization conditions were firstly investigated to determine their effects on the morphological and dimensional characteristics of cubosomes. Under the optimized homogenization conditions of 1200 bar for 9 cycles, cubosomes with reproducible, narrow particle size distribution and a mean particle size of 256.9 nm ± 4.9 nm were obtained. The structure of the dispersed cubosomes was revealed by SAXS (small-angle X-ray scattering) and Cryo-TEM (cryogenic transmission electron microscopy) as a bicontinuous cubic liquid crystalline phase with Pn3m geometry. To overcome the poor drug solubility and increase the drug-loading rate, a solubilization method was firstly used to develop cubosomes containing AmB. The encapsulation efficiency determined by HPLC assay was 87.8% ± 3.4%, and UV spectroscopy and stability studies in simulated gastric fluids further confirmed that AmB was successfully encapsulated in cubosomes.

1. Introduction

Amphotericin B has been widely used in clinics and is still regarded as the golden standard and a life-saving drug in the treatment of severe fungal infections for cancer, organ, or bone marrow transplant patients. Especially important, as one of the oldest antimicrobial antibiotics, AmB has not induced resistance in the clinical treatment. However, clinical applications of AmB are particularly limited because of its parenteral administration and potential organ toxicity, such as nephrotoxicity, central nervous system, and liver damage [1].

An effective and safe oral formulation of AmB will surely have significant applications in the treatment of disseminated fungal infections, because it will eliminate acute toxicity (fever and chilling) associated with intravenous (i.v.) delivery, reduce renal toxicity, shorten or avoid hospitalization, and increase patient satisfaction. Unfortunately,

due to its low solubility and poor membrane permeability, oral administration of AmB was reported to result in a poor bioavailability [2–5]. With the disappointed legacy of clinical trial failure and the physicochemical properties that precluded dissolution, it has been commonly believed that a formulation of AmB for oral administration is not a viable therapeutic strategy.

In recent years, advances in drug-delivery technologies and in-depth understanding of alternative delivery routes have inspired scientists to reassess AmB for oral administration. As a result, a substantial progress towards oral formulations of AmB has been achieved, such as AmB nanosuspension, lipid-based cochleates, and lipid nanospheres [6–8]. More encouragingly, the oral AmB cochleate formulation is currently under development by Biodelivery Sciences, Inc. (BDSI) and a recent press release regarding the favorable outcome of phase I trial was released in February 2009, and

the company emphasized that further plans of clinical trials were underway.

Because of their multilayer structures consisting of continuous lipid bilayers which are similar to those of cochleates, cubosomes are considered as novel lipid-based delivery vehicles that have potential for delivery of AmB. Cubosomes are nanoparticles, more accurately nanostructured liquid-crystalline particles [9, 10], in a liquid crystalline phase with cubic crystallographic symmetry formed by self-assembly of amphiphilic or surfactant-like molecules. This unique liquid crystalline structure of cubosomes could provide protection for entrapped drug from degradation in the gastrointestinal tract [11–13]. Indeed, the dispersed cubosomes have been highly recommended as carriers for active molecules due to their low viscosity, large interfacial areas, and the presence of both hydrophilic and hydrophobic regions. Furthermore, because of their great biocompatibility and bioadhesivity, cubosomes are suitable for oral administration [13–17]. For example, oral administration of cubosomes loaded with insulin resulted in a sustained reduce of blood glucose levels in rats [14].

Initially, the common method using high-energy dispersion of bulk cubic phase was applied to prepare phytantriol-based cubosomes containing AmB [18, 19]. However, this method had two major obstacles which made it very difficult to produce dispersed cubosomes with desirable properties, such as uniform particle size distribution and valuable drug-loading rate. Firstly, in the previously published studies which prepared cubosomes by homogenizing a certain amount of larger particles at 600 bar [20–22], it was emphasized that the fraction of larger particles in the obtained cubosomes should be taken into account for dispersion characterization as well as in vitro and in vivo studies performed on cubosomes. However, by now, no experiment had been conducted to show how to control the size distribution of dispersed cubosomes via using high-energy dispersion method. It was not clear whether the cubic liquid-crystalline structure of cubosomes was still maintained or disrupted under the high energy homogenization. Secondly, due to its amphiphilic properties, AmB is poorly soluble in water, oil, and many organic solvents. With a low solubility of AmB in PYT (less than 1 mg/g), it seems impossible to develop phytantriol-based cubosomes containing AmB with a valuable drug-loading rate.

In order to overcome these obstacles, different homogenization conditions were investigated in this study to determine the optimal conditions to produce phytantriol-based cubosomes with uniform particle size and distribution. Also, water-soluble AmB deoxycholate was selected to enhance the solubility of AmB in dispersed cubosomes. More specifically, the aim of this work was to optimize the preparation method for phytantriol-based cubosomes containing AmB with desirable properties.

2. Materials and Methods

2.1. Materials.
Amphotericin B was obtained from North China Pharmaceutical Group Corporation (Shenyang, China). Phytantriol was purchased from DSM (Basel, Switzerland). Poloxamer 407 ($PEO_{98}POP_{67}PEO_{98}$) was a gift from BASF (Ludwigshafen, Germany). Deoxycholate Sodium was purchased from Amresco (USA). Glass capillaries for SAXS experiments were obtained from Anton Paar (Graz, Austria). All the chemicals were used as received without further purification. Milli-Q grade water purified through a Millipore system (ELGA LabWater, Sartorius, UK) was used throughout this study.

2.2. Preparation of Phytantriol-Based Cubosomes

2.2.1. Production of Blank Cubosomes.
Proper amount of phytantriol, Poloxamer 407 and water were weighed for preparation of bulk cubic phases. Phytantriol and P407 at a ratio of 9 : 1 (w/w) were melted at 60°C in a hot water bath till homogenous. Then, 2 mL of deionized water were added gradually and vortex mixed for 1 min to achieve a homogenous state. The samples were equilibrated at room temperature for 48 hrs, and then, optically isotropic cubic-phase gels were formed. Subsequent fragmentation in 20 mL of water was performed by intermittent probe sonication (JYD-650, Shanghai, China) for 10 min using a pulse mode (9 sec pulses interrupted by 18 sec breaks) at 400 W energy input. The resulting milky coarse dispersions were homogenized using a high-pressure homogenizer (Avestin Em-C3, Ottawa, Canada) at certain high pressures and cycles to obtain an opalescent dispersion of the cubosomes. The final dispersions of cubic-phase gel were stored at room temperature for later studies.

2.2.2. Production of Cubosomes Containing AmB.
In the case of preparing phytantriol-based cubosomes containing AmB, AmB deoxycholate (equivalent to 60 mg of AmB) was firstly dissolved in 2 mL of deionized water. Phytantriol and P407 at a ratio of 9 : 1 (w/w) were melted at 60°C in a hot water bath till homogenous. Then, the AmB deoxycholate solution was added in gradually and vortex mixed for 1 min to achieve a homogenous state. The remaining process followed the same steps described above for preparation of blank cubosomes.

2.3. Characterization of Cubosomes

2.3.1. Particle Size Measurements.
The cubosomal particle size was determined by photon correlation spectroscopy using a Zetasizer Nano ZS90 (Malvern Instruments, Malvern, UK) at 25°C, which is based on the principles of Brownian motion. Samples were diluted in particle-free purified water to a scattering intensity of approximately 150–300 kcps and the dispersant viscosity was set to 0.8872 cP at 25°C. The mean z-average diameter and polydispersity indices (PDI) were obtained by cumulate analysis using the MALVERN software.

2.3.2. Cryogenic Transmission Electron Microscopy (Cryo-TEM).
For cryo-TEM examination, 4 μL of cubosome sample were applied on a carbon-coated holey film grid and then gently blotted with filter paper for about 3 seconds to obtain a thin liquid film on the grid. Immediately after blotting, the grid was plunged into precooled liquid ethane for flash

freeze. Then the cryo-grid was held in a Gatan 626 Cryo-Holder (Gatan, USA) and the sample was transferred into a cryo-transmission electron microscope (cryo-TEM; JOEL JEM-2010, Tokyo, Japan) at $-172°C$. Samples were observed under minimal dose condition and the images were recorded digitally by a CCD camera (Gatan 832) at the defocus of 3–5.464 μm.

2.3.3. Small-Angle X-Ray Scattering (SAXS).
Small-angle X-ray scattering (SAXS) measurements were carried out on a high-flux SAXS instrument (SAXSess, Anton Paar, Graz, Austria) operating in line collimation and equipped with an imaging plate (IP) as a detector. The IP with a pixel size of $42.3 \times 42.3 \mu m^2$ extended into a wide-angle range (the q range covered by the IP was up to $28\,nm^{-1}$, $q = (4\pi \sin \theta)/\lambda$, where λ is the wavelength of 0.1542 nm and 2θ is the scattering angle). The liquid samples were carefully loaded into a quartz capillary with a diameter of 1 mm. The gel samples were wrapped by aluminum foil and then fastened onto the sample holder. The exposure time was 60 min for the liquid samples and 20 min for the gels.

2.4. Confirmation of Cubosomes Containing AmB

2.4.1. Encapsulation Efficiency.
With the aim to quantify AmB content encapsulated in cubosomes after production, 0.5 mL of cubosomes containing AmB was added into the reservoir of centricon (YM-100, Amicon, Millipore, Bedfore, Mass, USA) [23]. After centrifuging the cubosome dispersion at 15,000 rpm for 30 min, the filtrate which contained free AmB was removed. In the process of centrifuge, free AmB (water soluble AmB deoxycholate) was removed from cubosomal formulation, because the bottom of the reservoir of centricon has the certain size of holes. Then, the filtered dispersion was diluted with methanol and analyzed for entrapped AmB content using high performance liquid chromatography (HPLC).

2.4.2. UV Spectroscopic Examination.
The spectra of AmB in different samples, which included AmB deoxycholate, cubosomes containing AmB, and a mixture of AmB deoxycholate and blank cubosomes all at the AmB concentration of 2 mg/mL, were investigates by a UV-vis spectrometer [24] at the wavelength of 250 nm to 500 nm. The ratio of the absorbance of the first peak (I) to the last peak (IV) was used to monitor the aggregation state of AmB.

2.4.3. Stability Studies in Simulated Gastric Fluids (SGFs).
AmB deoxycholate, cubosomes containing AmB, and a mixture of AmB deoxycholate and blank cubosomes all at the AmB concentration of 2 mg/mL were placed in SGF at the dilution rate of 1 : 10 (v/v) at 25°C. After 120 min of incubation, the samples were characterized by optical microscopy (Nikon Diaphot, Nikon, Tokyo, Japan). The samples were, respectively, placed on a microscopy glass over the objective of the microscope and stood for equilibration. After 40 to 60 seconds when the small particles slowed down the visible movement, photomicrographs were taken.

TABLE 1: Results of particle size measurement on three batches of blank cubosome dispersions prepared under different homogenization conditions.

Cubosome dispersion	Mean particle size (nm)	PDI
Ultrasound only	291.70 ± 37.40	0.250 ± 0.030
600 bar for 3 cycles	290.00 ± 25.00	0.210 ± 0.024
600 bar for 6 cycles	277.33 ± 4.16	0.191 ± 0.027
600 bar for 9 cycles	275.33 ± 18.82	0.189 ± 0.009
1200 bar for 3 cycles	259.66 ± 19.30	0.162 ± 0.010
1200 bar for 6 cycles	259.67 ± 12.42	0.149 ± 0.027
1200 bar for 9 cycles	241.00 ± 12.42	0.107 ± 0.027
1800 bar for 9 cycles	248.67 ± 4.93	0.103 ± 0.016

3. Results

3.1. Optimizing the Preparation Process for PYT-Based Cubosomes Containing AmB

3.1.1. Effects of Homogenization Conditions on Particle Size of Cubosomes.
Previously, it was reported that the produced cubosomes always contained a certain amount of large particles [20–22]. In order to obtain PYT-based cubosomes with fewer or no large irregular particles, this study investigated the influence of experimental parameters, specifically the homogenization pressures and the number of homogenization cycles, on the morphological and dimensional characteristics of the produced cubosomes.

Cubosomes were produced with phytantriol/Poloxamer 407 ratio of 9 : 1 w/w in water and dispersed phase/dispersing phase ratio of 5 : 95. The mean diameter of different cubosome dispersions was in an approximate range of 241–291 nm with the polydispersity indices (PDI) value of 0.25 for sonicated cubosomes and below 0.21 for homogenized cubosomes. After homogenization at 600 bar for 9 cycles, the particle size of cubosomes was reduced from micrometer to nanometer ranges. As shown in Figure 1, a few particles larger than 1 μm were still found in cubosome dispersion which was homogenized at 1200 bar for 6 cycles. With increasing the homogenization cycles to 9 at 1200 bar, cubosomes with reproducible particle size and size distribution were obtained. Further increasing the homogenization pressure to 1800 bar for 9 cycles did not show significant effect on reducing particle size and narrowing size distribution.

Simultaneously, the influence of homogenization conditions on the particle size of PYT-based cubosomes containing AmB were also investigated, and similar results as those for blank cubosomes were obtained (data not shown). Based on the results of particle size measurements, it can be recommended that phytantriol-based cubosomes with nanometer-sized particles, reproducible and narrow particle size distribution could be produced under the optimized homogenization conditions of 1200 bar and 9 cycles (Table 1).

3.1.2. Effect of AmB Content on Encapsulation Efficiency.
The encapsulation efficiency of phytantriol-based cubosomes containing AmB was evaluated by adding different amount
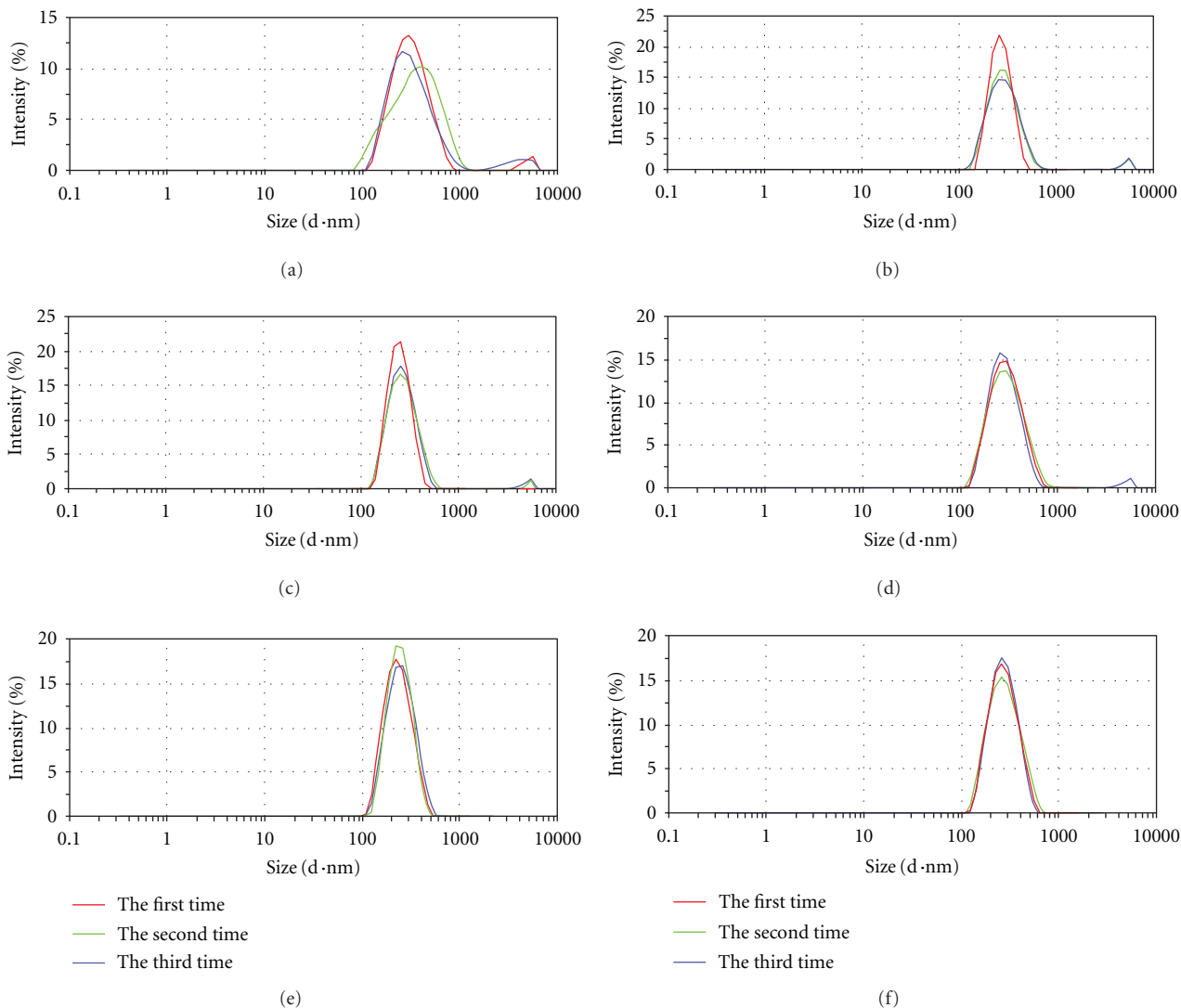
FIGURE 1: Particle size distribution of cubosome dispersion measured for three times via Zetasizer Nano ZS90. Homogenization conditions: (a) ultrasound only; (b) 600 bar for 3 cycles; (c) 600 bar for 9 cycles; (d) 1200 bar for 6 cycles; (e) 1200 bar for 9 cycles; (f) 1800 bar for 9 cycles.

of AmB (30 mg, 45 mg, and 60 mg) to the dispersed phase during preparation. The results in Table 2 showed that AmB encapsulation efficiency was 88.5% ± 0.6%, 91.8% ± 1.5%, and 87.8% ± 3.4%, respectively, and no significant effect of added AmB content on encapsulation efficiency was found. Therefore, based on the maximum solubility of AmB (60 mg of AmB dissolved in 2 mL of deionized water), PYT-based cubosomes containing 60 mg AmB with the highest drug-loading rate of 3.0% were chosen for the following studies.

3.1.3. Effect of AmB Content on Particle Size of Cubosomes.
The influence of AmB content added to the dispersed phase during preparation on the particle size of PYT-based cubosome dispersions was investigated by applying homogenization at 1200 bar for 9 cycles. The results in Table 3 indicated that there was no significant difference in

TABLE 2: Effect of AmB content on encapsulation efficiency ($n = 3$).

Amount of AmB (mg) added to cubosomes	Encapsulation efficiency (%)	Actual drug-loading rate (%)
30	88.5 ± 0.6	1.5
45	91.8 ± 1.5	2.2
60	87.8 ± 3.4	3.0

particle size of cubosome dispersions with increasing the content of AmB from 30 mg to 60 mg.

3.2. Characterization of Cubosomal Structure

3.2.1. SAXS.
The cubic phase can be fragmented into stable submicron sized particles, also known as cubosomes, which

TABLE 3: Effect of AmB content on particle size of cubosome dispersions ($n = 3$).

Amount of AmB (mg) added to cubosomes	Mean particle size (nm)	PDI
30	266.0 ± 3.2	0.12 ± 0.02
45	259.7 ± 1.9	0.09 ± 0.02
60	256.9 ± 4.9	0.10 ± 0.04

retain the internal structure of the original liquid crystalline. Cubosome formation and structure were primarily characterized by cryo-TEM in combination with SAXS to confirm the internal nanostructure of the particles. The homogenized dispersions were analyzed by X-ray diffraction and cryo-TEM, and the results indicated that the cubic structure was remained in cubosomes. Although the dispersion homogenized at 1800 bar for 9 cycles presented the same characteristics as dispersion homogenized at 1200 bar for 9 cycles, the greater shear forces applied might break down the cubic structural particles into nonequilibrium vesicular structures which later would typically fuse into unstable colloidal larger particles. Therefore, the dispersions homogenized at 1200 bar for 9 cycles were subjected to the later studies as drug carrier for oral administration.

Figure 2(d) showed the SAXS profiles of the bulk cubic phase with melts of phytantriol and Poloxamer 407 at a ratio of 9 : 1. Diffraction peaks were observed up to the sixth order at ratios of $2^{1/2} : 3^{1/2} : 4^{1/2} : 6^{1/2} : 8^{1/2} : 9^{1/2}$, which were indicated as the Miller indices, $h\,k\,l$ = 110, 111, 200, 211, 220, and 221 correspondingly. The observation fits the characteristic peaks of Pn3m crystallographic space group (Q224) which contains a diamond cube phase, and it is also in agreement with the previously published phase behavior of phytantriol [25].

Figure 2(a) showed the SAXS profiles obtained from the phytantriol-based cubosome dispersion homogenized at 1200 bar for 9 cycles. Comparing with the SAXS profiles of bulk cubic phase in Figure 2(d), five similar reflections following the relationship of $2^{1/2}$, $3^{1/2}$, $4^{1/2}$, $6^{1/2}$, and $8^{1/2}$, which were indexed as $h\,k\,l$ = 110, 111, 200, 211, and 220 peaks of a primitive cubic lattice of the Pn3m space group, were observed for cubosome dispersion. Meantime, the same peak positions for these five reflections were detected for cubosome dispersion homogenized at 1800 bar for 9 cycles as illustrated in Figure 2(b). This confirmed that the internal nanostructure of these two cubosome dispersions was Pn3m space group; in other words, the particles kept the bicontinuous cubic nature after homogenization. However, the weak peaks of 200, 211, and 220 might be attributed to the homogenization destroy.

Furthermore, Figure 2(c) showed the SAXS profiles obtained from the phytantriol-based cubosomes containing 60 mg of AmB homogenized at 1200 bar for 9 cycles. In this case, only three reflections following the relationship of $2^{1/2}$, $3^{1/2}$, and $4^{1/2}$, which were indexed as $h\,k\,l$ = 110, 111, and 200 peaks of a primitive cubic lattice of the Pn3m space group, were observed. The disappearing of other weak peaks is more likely due to the fact that some drug molecules attached to the surface of cubosomes and thus interfered with the diffraction peaks, rather than destroying the cubic liquid-crystalline structure by adding the drug. The direct evidence came from cryo-TEM below, in which the cubosomal characterization was obvious in PYT-based cubosomes containing AmB. Thus, based on the SAXS results, the internal structure of phytantriol-based cubosomes containing 60 mg AmB was the Pn3m crystallographic space group (Q224).

3.2.2. Cryo-TEM. In order to further investigate the cubic structure of the blank phytantriol-based cubosome dispersions and cubosomes containing AmB homogenized at 1200 bar for 9 cycles, the formulations were examined by cryo-TEM. Figure 3(a) showed the image of blank cubosomes which contained highly ordered cubic inner structure with a mean particle size of about 250 nm close to that observed by laser diffraction. Figure 3(b) showed the image of cubosomes containing AmB with typical cubosomal characterization and a mean particle size of about 250 nm similar to that of blank cubosomes. The typical crystal structure obtained via lowering the brightness of cryo-TEM was observed to confirm the cubic liquid-crystalline structure of AmB-loaded cubosomes, as seen in the upper right corner of Figure 3(b).

3.3. Characterization of Phytantriol-Based Cubosomes Containing AmB

3.3.1. Encapsulation Efficiency. As mentioned before, the encapsulation efficiency of phytantriol-based cubosomes containing AmB was measured by removing any free AmB through filtration and only detecting the entrapped AmB. The results in Table 2 demonstrated that as much as 90% AmB was successfully encapsulated in phytantriol-based cubosomes.

3.3.2. UV Spectroscopy. The UV spectrum of AmB depends on its aggregation state. Generally, in aqueous solution, AmB is aggregated, and its absorption spectrum presents a major broad band at 328 nm. In this study, the absorption spectra of AmB in four samples, including AmB deoxycholate, cubosomes containing AmB, and a mixture of AmB deoxycholate and blank cubosomes which all contained 2 mg/mL of AmB as well as blank cubosomes, were compared to demonstrate the successful encapsulation of AmB in cubosomes. As shown in Figure 4, the major absorption band was observed in both free AmB solution and physical mixture of AmB and cubosomes. The spectroscopy of cubosomes containing AmB showed the absorption peak at different position with much lower intensity, which suggested that AmB was actually encapsulated in phytantriol-based cubosomes rather than simply mixed with blank cubosomes.

3.3.3. Stability Studies in Simulated Gastric Fluids. Stability studies were performed on AmB deoxycholate, cubosomes containing AmB, and a mixture of AmB deoxycholate and blank cubosomes which all contained 2 mg/mL of AmB. After incubation for 120 min, some changes were optically shown in Figure 5. AmB aggregation was found in
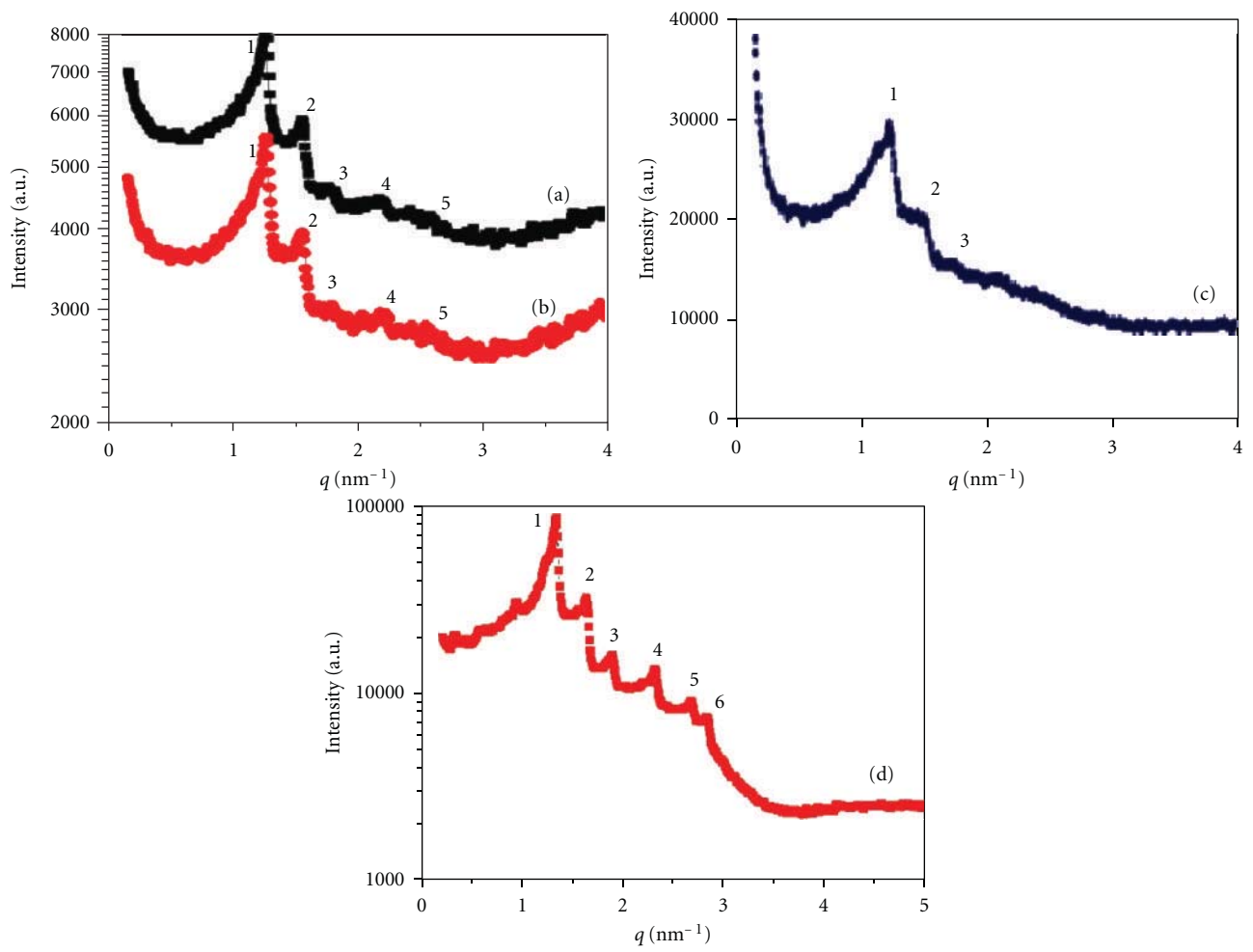
FIGURE 2: SAXS profiles of the cubic liquid-crystalline structure: (a) phytantriol-based cubosome dispersions homogenized at 1200 bar for 9 cycles; (b) at 1800 bar for 9 cycles; (c) phytantriol-based cubosomes containing AmB homogenized at 1200 bar for 9 cycles; (d) the bulk cubic phase with melts of phytantriol and Poloxamer 407 at a ratio of 9 : 1.
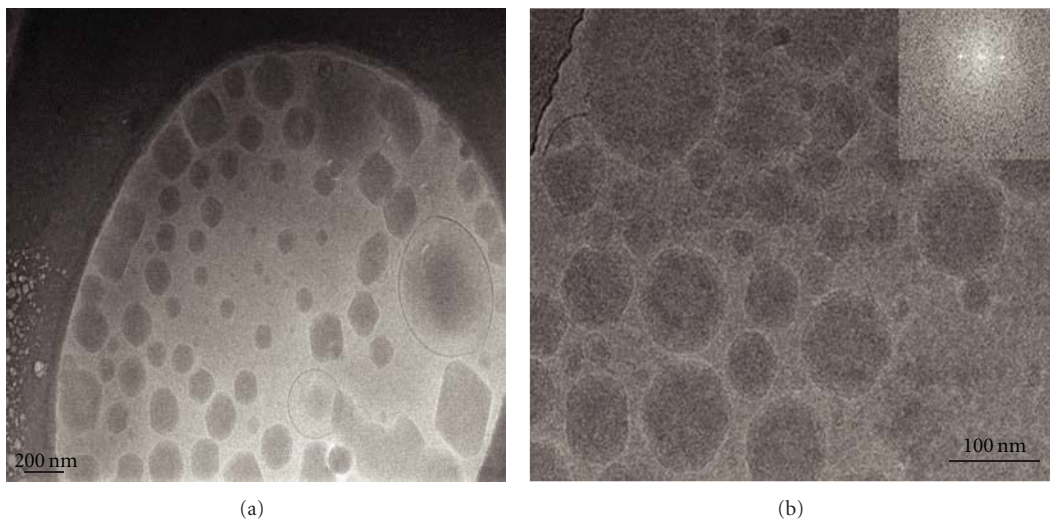

(a)

(b)

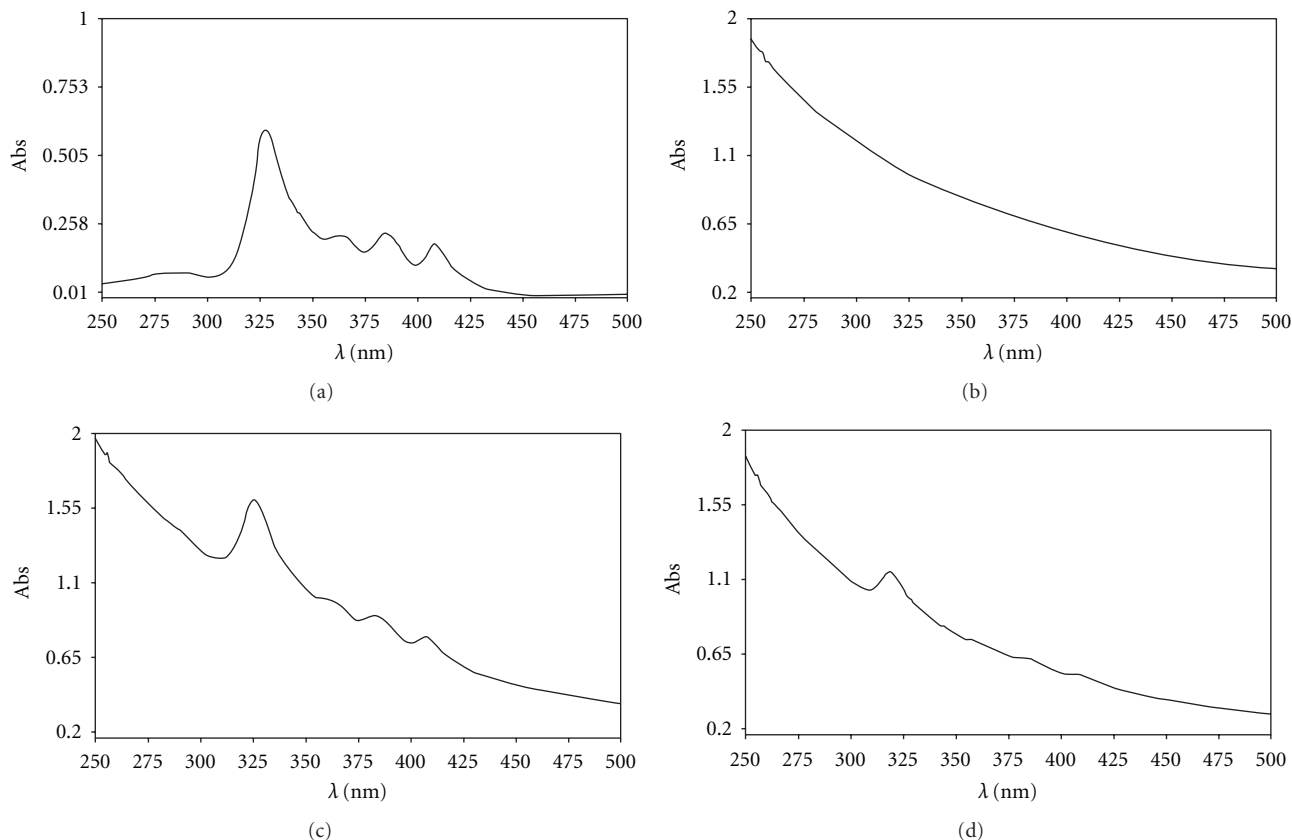FIGURE 3: Cryo-TEM micrographs of blank phytantriol-based cubosomes (a) and cubosomes containing AmB (b).

FIGURE 4: UV spectra of AmB. (a) AmB deoxycholate, (b) blank cubosomes, (c) mixture of AmB deoxycholate and blank cubosomes, and (d) cubosomes containing AmB.

both AmB solution and mixture of AmB and cubosomes (Figures 5(a) and 5(b)), while dispersed AmB was clearly observed in cubosomes containing AmB (Figure 5(c)). The different states of AmB observed in cubosomes containing AmB and the mixture of AmB and blank cubosomes demonstrated that AmB was successfully encapsulated in PYT-based cubosomes rather than simply mixed with the cubosomes. Optical observation used to evaluate the cubosomes stability is that AmB aggregation was easy happened to become a large aggregation size, which could not be determined by photon correlation spectroscopy (PCS).

4. Discussion

The advantages of cubosomes as oral delivery system may lie in the following aspects. Firstly, the lyotropic property of cubosomes with hydrophilic surface makes the contact with the endothelial cell membrane more easily and overcomes the "unstirred water layer" barrier [26–28]. Secondly, either the cubic nanoparticles or the encapsulated drug molecules can enhance the penetration across the endothelial cell membrane, which will increase the uptake efficiency of orally administrated drug [29]. Currently, in the majority of reported studies on dispersed liquid crystalline systems, glyceryl monoolein (GMO) was used for preparation [17] as it could form a bicontinuous cubic phase in excess

water. However, GMO-based cubosomes consisted of lipid composition have the same digestion process in the gastrointestinal tract as micelles, liposomes, and niosomes because the ester-based structure may be rapidly cleaved by pancreatic lipase, and the ester hydrolysis is likely to induce chemical instability and disruption of the liquid crystalline structure during the digestion. To avoid this shortcoming, one alternative resolution is PYT-based cubosomes, because phytantriol does not possess a susceptible ester bond in its molecular structure, and it is likely the cubic phase structure can be retained under the digestive conditions. Therefore, phytantriol-based cubosomes were firstly investigated as drug-delivery system in the present study.

First of all, the optimal formulation process for phytantriol-based cubosomes containing AmB was determined in order to produce cubosomes with desirable particle size and distribution and good drug-loading rate as oral drug delivery carriers. Cubosomal size is an important parameter, which could influence drug release, intestinal uptake, and thus the overall bioavailability of the formulation [30, 31]. The particles in a size of 100 nm generally present a significantly higher uptake by the intestinal tissues in terms of total mass and quantity compared to the larger particles. This is because of a particle size-dependent exclusion phenomena in which smaller particles are more likely to be internalized inside the cells and tissues [31, 32]. Unfortunately, PYT-based
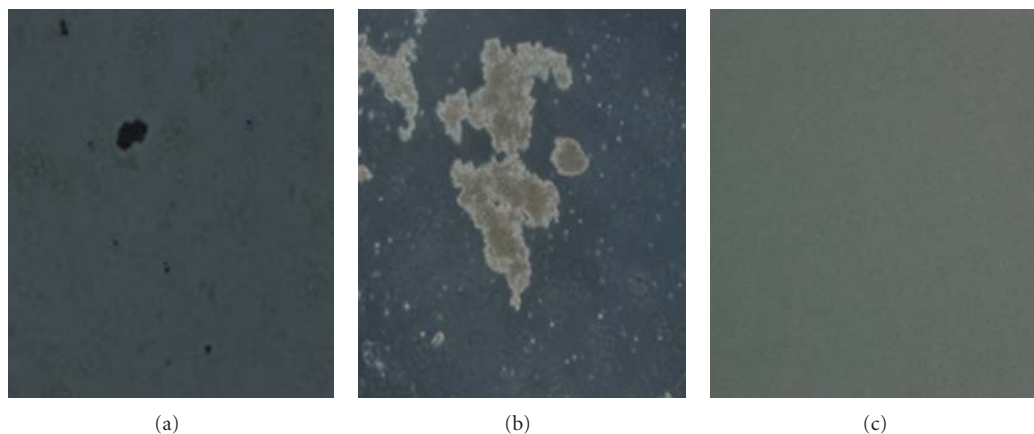
<div align="center">(a)   (b)   (c)</div>

FIGURE 5: Optical microscopy of samples in SGF (×200). (a) AmB deoxycholate, (b) mixture of AmB deoxycholate and blank cubosomes, and (c) cubosomes containing AmB.

cubosomes with a mean particle size of 250 nm and uniform size distributions were only obtained in this study.

To date, the poor solubility of AmB in oil is still a challenge, and no effective solutions have been found to enhance the solubility. Recently, a self-emulsifying drug-delivery system (SEDDS) using lipidic excipient Peceol was reported to improve the oral absorption of AmB [33]. However, solubilization of AmB in SEDDS formulations was limited at 100–500 μg/mL, which led to an unacceptable amount of lipid to be administered. With AmB solubility in PYT less than 1 mg/g, it seems also impracticable to develop phytantriol-based cubosomes containing AmB due to the low drug-loading rate. To increase drug content, several ways have been tested. Firstly, the concentration of PYT was raised to 10% wt/wt, but the higher concentration of dispersed phase led to formation of larger particles and a number of aggregates. Secondly, it was reported previously the use of surfactants as solubilizer was able to increase the solubility of AmB. Surfactants, such as F-68, tween-80, sodium dodecylsulfate and sodium deoxycholate, were used in the present study to enhance AmB solubility. But AmB was still not incorporated in cubosomal dispersions. Finally, an efficient method was found to improve the AmB solubility by gradually adding 2 mL of AmB deoxycholate solution (maximally 60 mg AmB was dissolved in 2 mL of water) into homogeneous melt of Phytantriol and P407. With this method, phytantriol-based cubosomes containing AmB with drug loading rate up to 3% were successfully produced.

As reported previously, without the aid of an emulsifier, PYT itself did not form a stable emulsion in water [22]. The surfactant is not merely absorbed at the particle surface; actually, the surfactant is more likely anchored at the apolar region or at the surface of PYT-based bilayers [22]. If AmB deoxycholate was melted together with Phytantriol and P407 at 60°C, deoxycholate might rapidly interact with PYT and destroy the micellar structure of AmB deoxycholate and accordingly lower the solubilization of AmB then formed AmB crystals precipitation. By selecting the proper surfactant and controlling the adding time of AmB deoxycholate, the addition of water soluble AmB deoxycholate into the melt of

phytantriol and P407 could keep a enough little drug-particle size for the drug-delivery system subjected to a high-pressure process leading to the complete dissolution of AmB in the cubosomes.

Theoretically, the AmB could spontaneously diffuse from the aqueous phase into the PYT layer according to its partitioning coefficient. But the possible problem lies in the dissolution of AmB, because poorly soluble drugs show simultaneously a very low-dissolution velocity. Based on this fact, localization of the AmB in the PYT layer appeared feasible to achieve when accelerating the dissolution velocity of AmB. As shown in Noyes-Whitney equation, the higher the streaming velocity of the dissolution medium across the crystal surface is, the larger is the dissolution velocity. Previous research had indicated that the stirring velocities and related streaming velocity of the fluid are enough for some little AmB crystals dissolved in lipid material when homogenizer was employed [34]. This is a reasonable principle for AmB deoxycholate encapsulated in cubosomes using high pressure homogenization rather than AmB crystals simply added into cubosomes.

In this study, the results of photon correlation spectroscopy, X-ray diffraction, and cryo-TEM illustrated the cubic nanoparticle structure in the cubosome formulation; however, it was not clarified whether the formulation was a simple mixture of AmB deoxycholate and blank cubosomes or AmB was encapsulated in cubosomes. Therefore, evaluation of encapsulation efficiency, UV spectroscopy measurement, and stability studies in simulated gastric fluids were conducted to confirm the incorporation of drug in cubosomal dispersions. At first, the encapsulated drug content was accurately determined after removing the free drug from the carrying system via ultrafiltration method. The detected encapsulation efficiency of 87.8% indicated that majority of the drug was indeed encapsulated in cubosomes. Additionally, the comparison of UV spectroscopy demonstrated that when the drug was incorporated in formulation, its absorption peak position and intensity were dramatically influenced. Moreover, the optical microscopy showed the aggregation of AmB in simulated gastric fluids

during stability study, but the aggregation was replaced by dispersed state of AmB in cubosomes containing AmB, which also indicated the drug was incorporated in cubosomes. Overall, the characterization results demonstrated the successful preparation of phytantriol-based cubosomes containing AmB with desirable particle size distribution and valuable drug loading rate. It is necessary to further investigate the cubosomes containing AmB in vivo and in vitro.

5. Conclusion

Phytantriol-based cubosomes containing Amphotericin B as a formulation for oral delivery of AmB, was successfully developed through homogenizing the bulk cubic phase gel into a cubic dispersion. Cubosomes with nanometer-sized particles and reproducible, narrow particle size distribution were optimally obtained under homogenization at 1200 bar for 9 cycles. The structure of the dispersed formulation was confirmed by SAXS and cryo-TEM as a bicontinuous cubic liquid crystalline phase with Pn3m geometry. Encapsulation efficiency, UV spectroscopy, stability studies in simulated gastric fluids further confirmed the incorporation of AmB in cubosomal dispersions. The cubosomes will be utilized in subsequent studies to determine the oral adsorption of cubosomes as a means to control loading and release of AmB.

References

[1] L. Ostrosky-Zeichner, K. A. Marr, J. H. Rex, and S. H. Cohen, "Amphotericin B: time for a new "gold standard"," *Clinical Infectious Diseases*, vol. 37, no. 3, pp. 415–425, 2003.

[2] J. S. Dangi, S. P. Vyas, and V. K. Dixit, "Effect of various lipid-bile salt mixed micelles on the intestinal absorption of amphotericin-B in rat," *Drug Development and Industrial Pharmacy*, vol. 24, no. 7, pp. 631–635, 1998.

[3] M. L. Littman, P. L. Horowitz, and J. G. Swadey, "Coccidioidomycosis and its treatment with amphotericin B," *The American Journal of Medicine*, vol. 24, no. 4, pp. 568–592, 1958.

[4] H. M. Kravetz, V. T. Andriole, M. A. Huber, and J. P. Utz, "Oral administration of solubilized amphotericin B," *The New England Journal of Medicine*, vol. 265, pp. 183–184, 1961.

[5] D. B. Louria, "Some aspects of the absorption, distribution, and excretion of amphotericin B in man," *Antibiotic Medicine & Clinical Therapy*, vol. 5, no. 5, pp. 295–301, 1958.

[6] O. Kayser, C. Olbrich, V. Yardley, A. F. Kiderlen, and S. L. Croft, "Formulation of amphotericin B as nanosuspension for oral administration," *International Journal of Pharmaceutics*, vol. 254, no. 1, pp. 73–75, 2003.

[7] G. Delmas, S. Park, Z. W. Chen et al., "Efficacy of orally delivered cochleates containing amphotericin B in a murine model of aspergillosis," *Antimicrobial Agents and Chemotherapy*, vol. 46, no. 8, pp. 2704–2707, 2002.

[8] B. Amarji, Ajazuddin, D. Raghuwanshi, S. P. Vyas, and P. Kanaujia, "Lipid nano spheres (LNSs) for enhanced oral bioavailability of amphotericin B: development and characterization," *Journal of Biomedical Nanotechnology*, vol. 3, no. 3, pp. 264–269, 2007.

[9] M. L. Lynch, A. Ofori-Boateng, A. Hippe, K. Kochvar, and P. T. Spicer, "Enhanced loading of water-soluble actives into bicontinuous cubic phase liquid crystals using cationic surfactants," *Journal of Colloid and Interface Science*, vol. 260, no. 2, pp. 404–413, 2003.

[10] X. Peng, X. Wen, X. Pan, R. Wang, B. Chen, and C. Wu, "Design and in vitro evaluation of capsaicin transdermal controlled release cubic phase gels," *The American Association of Pharmaceutical Scientists Tech*, vol. 11, no. 3, pp. 1405–1410, 2010.

[11] C. M. Chang and R. Bodmeier, "Swelling of and drug release from monoglyceride-based drug delivery systems," *Journal of Pharmaceutical Sciences*, vol. 86, no. 6, pp. 747–752, 1997.

[12] C. M. Chang and R. Bodmeier, "Effect of dissolution media and additives on the drug release from cubic phase delivery systems," *Journal of Controlled Release*, vol. 46, no. 3, pp. 215–222, 1997.

[13] B. Siekmann, H. Bunjes, M. H. J. Koch, and K. Westesen, "Preparation and structural investigations of colloidal dispersions prepared from cubic monoglyceride-water phases," *International Journal of Pharmaceutics*, vol. 244, no. 1-2, pp. 33–43, 2002.

[14] H. Chung, J. Kim, J. Y. Um, I. C. Kwon, and S. Y. Jeong, "Self-assembled "nanocubicle" as a carrier for peroral insulin delivery," *Diabetologia*, vol. 45, no. 3, pp. 448–451, 2002.

[15] J. Bender, M. B. Ericson, N. Merclin et al., "Lipid cubic phases for improved topical drug delivery in photodynamic therapy," *Journal of Controlled Release*, vol. 106, no. 3, pp. 350–360, 2005.

[16] L. B. Lopes, J. L. C. Lopes, D. C. R. Oliveira et al., "Liquid crystalline phases of monoolein and water for topical delivery of cyclosporin A: characterization and study of in vitro and in vivo delivery," *European Journal of Pharmaceutics and Biopharmaceutics*, vol. 63, no. 2, pp. 146–155, 2006.

[17] B. J. Boyd, D. V. Whittaker, S. M. Khoo, and G. Davey, "Lyotropic liquid crystalline phases formed from glycerate surfactants as sustained release drug delivery systems," *International Journal of Pharmaceutics*, vol. 309, no. 1-2, pp. 218–226, 2006.

[18] Y. D. Dong, I. Larson, T. Hanley, and B. J. Boyd, "Bulk and dispersed aqueous phase behavior of phytantriol: effect of vitamin E acetate and F127 polymer on liquid crystal nanostructure," *Langmuir*, vol. 22, no. 23, pp. 9512–9518, 2006.

[19] Y. D. Dong, A. W. Dong, I. Larson et al., "Impurities in commercial phytantriol significantly alter its lyotropic liquid-crystalline phase behavior," *Langmuir*, vol. 24, no. 13, pp. 6998–7003, 2008.

[20] E. Esposito, N. Eblovi, S. Rasi et al., "Lipid-based supramolecular systems for topical application: a preformulatory study.," *The American Association of Pharmaceutical Scientists*, vol. 5, no. 4 article E30, 2003.

[21] E. Esposito, R. Cortesi, M. Drechsler et al., "Cubosome dispersions as delivery systems for percutaneous administration of indomethacin," *Pharmaceutical Research*, vol. 22, no. 12, pp. 2163–2173, 2005.

[22] B. Siekmann, H. Bunjes, M. H. J. Koch, and K. Westesen, "Preparation and structural investigations of colloidal dispersions prepared from cubic monoglyceride-water phases,"

International Journal of Pharmaceutics, vol. 244, no. 1-2, pp. 33–43, 2002.

[23] H. Chung, J. Kim, J. Y. Um, I. C. Kwon, and S. Y. Jeong, "Self-assembled "nanocubicle" as a carrier for peroral insulin delivery," *Diabetologia*, vol. 45, no. 3, pp. 448–451, 2002.

[24] M. L. Adams and G. S. Kwon, "Relative aggregation state and hemolytic activity of amphotericin B encapsulated by poly(ethylene oxide)-block-poly(N-hexyl-L-aspartamide)-acyl conjugate micelles: effects of acyl chain length," *Journal of Controlled Release*, vol. 87, no. 1–3, pp. 23–32, 2003.

[25] F. Muller, A. Salonen, and O. Glatter, "Phase behavior of Phytantriol/water bicontinuous cubic Pn3m cubosomes stabilized by Laponite disc-like particles," *Journal of Colloid and Interface Science*, vol. 342, no. 2, pp. 392–398, 2010.

[26] T. Korjamo, A. T. Heikkinen, and J. Mönkkönen, "Analysis of unstirred water layer in in vitro permeability experiments," *Journal of Pharmaceutical Sciences*, vol. 98, no. 12, pp. 4469–4479, 2009.

[27] A. S. Sallam, E. Khalil, H. Ibrahim, and I. Freij, "Formulation of an oral dosage form utilizing the properties of cubic liquid crystalline phases of glyceryl monooleate," *European Journal of Pharmaceutics and Biopharmaceutics*, vol. 53, no. 3, pp. 343–352, 2002.

[28] J. Y. Um, H. Chung, K. S. Kim, I. C. Kwon, and S. Y. Jeong, "In vitro cellular interaction and absorption of dispersed cubic particles," *International Journal of Pharmaceutics*, vol. 253, no. 1-2, pp. 71–80, 2003.

[29] K. Katneni, S. A. Charman, and C. J. H. Porter, "An evaluation of the relative roles of the unstirred water layer and receptor sink in limiting the in-vitro intestinal permeability of drug compounds of varying lipophilicity," *Journal of Pharmacy and Pharmacology*, vol. 60, no. 10, pp. 1311–1319, 2008.

[30] G. Mittal, D. K. Sahana, V. Bhardwaj, and M. N. V. Ravi Kumar, "Estradiol loaded PLGA nanoparticles for oral administration: effect of polymer molecular weight and copolymer composition on release behavior in vitro and in vivo," *Journal of Controlled Release*, vol. 119, no. 1, pp. 77–85, 2007.

[31] M. P. Desai, V. Labhasetwar, G. L. Amidon, and R. J. Levy, "Gastrointestinal uptake of biodegradable microparticles: effect of particle size," *Pharmaceutical Research*, vol. 13, no. 12, pp. 1838–1845, 1996.

[32] M. P. Desai, V. Labhasetwar, E. Walter, R. J. Levy, and G. L. Amidon, "The mechanism of uptake of biodegradable microparticles in Caco-2 cells is size dependent," *Pharmaceutical Research*, vol. 14, no. 11, pp. 1568–1573, 1997.

[33] E. K. Wasan, K. Bartlett, P. Gershkovich et al., "Development and characterization of oral lipid-based Amphotericin B formulations with enhanced drug solubility, stability and antifungal activity in rats infected with Aspergillus fumigatus or Candida albicans," *International Journal of Pharmaceutics*, vol. 372, no. 1-2, pp. 76–84, 2009.

[34] R. H. Müller, S. Schmidt, I. Buttle, A. Akkar, J. Schmitt, and S. Brömer, "SolEmuls-novel technology for the formulation of i.v. emulsions with poorly soluble drugs," *International Journal of Pharmaceutics*, vol. 269, no. 2, pp. 293–302, 2004.

Research Article

Biodistribution of ^{60}Co–Co/Graphitic-Shell Nanocrystals *In Vivo*

Li Zhan,[1] Qi Wei,[1] Geng Yanxia,[1] Xu Junzheng,[1] and Wu Wangsuo[1, 2]

[1] *Radiochemistry Laboratory, School of Nuclera Science and Technology, Lanzhou University, Lanzhou 73000, China*
[2] *State Key Laboratory of Applied Organic Chemistry, Lanzhou University, Lanzhou 730000, China*

Correspondence should be addressed to Wu Wangsuo, wuws@lzu.edu.cn

The magnetic nano-materials, Co/graphitic carbon- (GC-) shell nanocrystals, were made *via* chemicalvapour deposition (CVD) method, and their biodistribution and excretion in mice were studied by using postintravenously (i.v.) injecting with ^{60}Co–Co/GC nanocrystals. The results showed that about 5% of Co was embedded into graphitic carbon to form multilayer Co/GC nanocrystals and the size of the particle was ∼20 nm, the thickness of the nanocrystal cover layer was ∼4 nm, and the core size of Co was ∼14 nm. Most of the nanocrystals were accumulated in lung, liver, and spleen after 6, 12, 18, and 24 h after *i.v.* with ^{60}Co–Co/GC nanocrystals. The nanoparticles were cleared rapidly from blood and closed to lower level in 10 min after injection. The ^{60}Co–Co/GC nanocrystals were eliminated slowly from body in 24 h after injection, ∼6.09% of ^{60}Co–Co/GC nanocrystals were excreted by urine, ∼1.85% by feces in 24 h, and the total excretion was less than 10%.

1. Introduction

Nanocrystals with advanced magnetics or optical properties has attracted increasing research interests in the past due to their potential biomedical applications such as bioseparation, biosensing, magnetic imaging, drug delivery, and magnetic fluid hyperthermia [1, 2]. Among various magnetic nanocrystals, cobalt is a class of ferromagnetic material with high magnetic moment density and is magnetically soft [3–6], but it has yet been explored owing to the problems of easy oxidation and potential toxicity. Previously, FeCo nanocrystals with multilayered graphitic carbon and pyrolytic carbon or inert metals have been obtained [6–8], and this nanomaterials seemed to be the best structure because of its high stability, low toxicity, and easy function alization up to now. Meanwhile, the single-shelled, discrete, chemically functionalized, and water-soluble forms, FeCo/GC nanocrystals, have been also developed for biological and medicinal applications in a recent work [9]. Therefore, researchers must investigate and improve further biocompatibility and biosafety before application *in vivo*, and then, it is important and necessary to study behavior and fate of pristine metals/GC nanocrystals *in vivo*. In order to detect simply and quantify accurately content of nanocrystals in various tissues, so radioactive isotopes were introduced into metals/GC nanocrystals, and which can be used as drug carrier and intermediate in radiation medicine fields. Thereby, as a new drug carrier with advanced magnetic and radioactive, it would be selectively localized to the target-site of tumor and focus by external magnetic field, and then, the drug and gamma ray would be delivered to cell and kill cancer cells or germ in future.

We developed a ^{60}Co–Co/GC nanocrystal with advanced magnetism and radioactivity, and the biodistribution and excretion of unfunctionalized ^{60}Co–Co/GC nanocrystals were investigated to research the behavior and fate *in vivo*, which will be important for researchers to devise and develop further functionalized, biosafe, and biocompatibly magnetic nanocrystals in clinical and radiation medicine.

2. Method and Materials

2.1. Synthesis of Co/GC Nanocrystals. According to the method of Seo et al. [9], we impregnated 1.00 g of fumed silica (Sigma) with 0.25 g Co(NO$_3$)$_2$·6H$_2$O in 50 mL ethanol and sonicated it for 1 h. After removal of ethanol and drying at 80°C, we ground the powder and typically used 0.50 g for methane CVD in a tube furnace. We heated the sample in H$_2$ flow to reach 800°C for 5 min and then subjected it

to methane flow of $600 \, cm^3 \, min^{-1}$ for 5 min. On cooling, we etched the sample with 10% HF in H_2O (80%) and ethanol (10%) to dissolve the silica. We collected the Co/GC nanocrystals by centrifugation and thoroughly washed them.

2.2. Characterization. We characterized the nanocrystals by TEM (JEM-2010, Nippon Tekno Co., Ltd.), Ramanspectroscopy (SPEX1403 micro-Raman spectrometer with a laser excitation of $l = 785$ nm, Spex Co., Ltd.), the elemental composition of nanocrystals was analyzed by Energy Dispersive Spectrdmeter (EDS, JEM-2010, Nippon Tekno Co., Ltd.).

2.3. Synthesis of ^{60}Co–Co/GC Nanocrystals. 1.74×10^8 cpm ^{60}Co–$Co(NO_3)_2$ solution was added into mixture suspension (1 g fumed silica and 0.25 g $Co(NO_3)_2 \cdot 6H_2O$ in 50 mL ethanol) and sonicated it for 1 h. Subsequently, the same synthesis method was operated to synthesize the ^{60}Co-Co/GC nanocrystals. The samples were centrifugated and washed thoroughly until supernatant fluid without radioactive counts. Finally, the yields of products were calculated as

$$y = \frac{C}{C_0} \times 100\% \qquad (1)$$

y: yields of sample; C: radioactive counts in nanocrystals; C_0: radioactive counts in reactants.

2.4. Biodistribution and Excretion Study in Mice. The ^{60}Co–Co/GC nanocrystals were dispersed ultrasonically into PBS solution. Female Kongming White mice weighing 16–20 g were obtained from Laboratory Center for Medical Science, Lanzhou University, Gansu, China. Food and water were provided ad libitum throughout experimental period.

The five groups of mice (eight mice per group) were injected intravenously with 1.86×10^5 cpm/per mouse suspension of ^{60}Co–Co/GC nanocrystals. Five groups were sacrificed at 1, 6, 12, 18, and 24 h, respectively. Their tissues, including the heart, lung, liver, spleen, kidney, stomach, and intestine, were immediately dissected, and feces and urine were collected, respectively. Each tissue was wrapped in foil, weighted, and counted for ^{60}Co count. Distribution in tissues was presented in percent injected dose per gram of wet tissue (% ID/g), which could be calculated by the percent injected dose (tissue activity/total activity dosed) per gram of wet tissue. The excretion of ^{60}Co–Co/GC nanocrystals from mice was investigated by counting ^{60}Co in the urine and feces of mice at different time intervals from 0 to 24 h after dosing. Results were expressed as percent injected dose per gram of wet tissue.

2.5. Hemodynamics. Another nine groups mice (six mice/per group) were injected intravenously with 1.86×10^5 cpm/per mouse ^{60}Co–Co/GC nanocrystals to study hemodynamics, the nine groups were sacrificed at 0, 5, 10, 30, 40 min, 1 h, 6 h, 12 h, 18 h, and 24 h, respectively. 0.1 mL blood was collected immediately to count by gamma counter (BH-2001gamma spectrometry, CNNC).
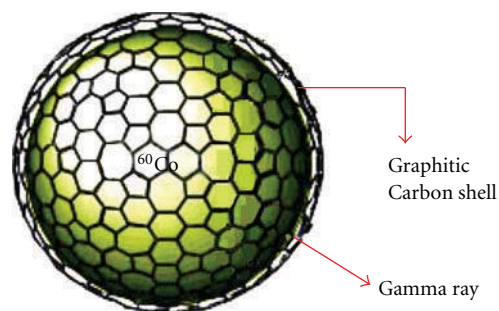

FIGURE 1: The schematic diagram of a ^{60}Co/GC nanocrystal. Note: the single carbon cage denotes the multilayer graphitic carbon shells.

3. Results and Discussion

3.1. Co/GC Nanocrystals. Co/GC nanocrystals have observed clearly from Figure 2, the TEM and HRTEM showed that the diameter of Co/GC nanocrystals was 20.46 ± 3.46 nm, the core diameter of Co nanocrystals was 13.77 ± 2.09 nm, and thickness of cover layer was 4.19 ± 0.82 nm. The elemental composition of nanocrystals were obtained by elemental analysis of EDS to show 25.73 of Co and 73.77% of C, and a little of O (0.33%) found may be from foreign matter such as ethanol or water (Figure 3). This indicated that Co and C in nanocrystals were existed as simple substances. Moreover, Raman spectroscopy was used to identify a graphitic carbon G peak at $\sim 1,600 \, cm^{-1}$ and a disordered D peak at $\sim 1,300 \, cm^{-1}$ (Figure 4), providing evidence for the graphitic shell [9, 10]. Therefore, the results showed that the multilayer Co/GC nanocrystals synthesized were much larger than FeCo/GC nanocrystals in previousreports [9]. Seo et al. have obtained single-layer FeCo/GC nanocrystals, and the diameter of FeCo/GC nanocrystals was smaller [9]. Meanwhile, they impregnated 1 g of fumed silica with different content of mixed metals salts to control diameter of nanocrystals. For example, for 7.2×10^{-4} mol mixed salts (Co/Fe = 3.6×10^{-4} mol), the size of FeCo/GC nanocrystals was ~ 7 nm, but for 1.8×10^{-4} mol mixed salts (Co/Fe = 0.9×10^{-4} mol), the size was ~ 4 nm [9]. In our work, we have selected only $Co(NO_3)_2$ to synthesize Co/GC nanocrystals according to the same method and condition with Seo et al. Therefore, as 8.60×10^{-4} mol Co used in reactants, the diameter of nanoparticles was ~ 20 nm, and the larger Co nanocrystals were embedded into thicker multilayer carbon shells. In other words, relative to Si identified with 1 g in reactants, with increasing of Co from 0.9, 3.6, to 8.6×10^{-4} mol, ~ 4, 7, and 20 nm of metal/GC nanocrystals were formed successively. These seemly indicated that lower concentration or higher dispersion of cobalt salts in reactants would produce smaller diameter of nanocrystals, and concentration of Co could determine diameter of nanocrystals. However, to know how to control thickness of carbon shells of nanocrystals, it was necessary to further study and experiment in next works.

3.2. ^{60}Co-Co/GC Nanocrystals. The ^{60}Co-$Co(NO_3)_2$ was placed into ethanol suspension of reactants and sonicated

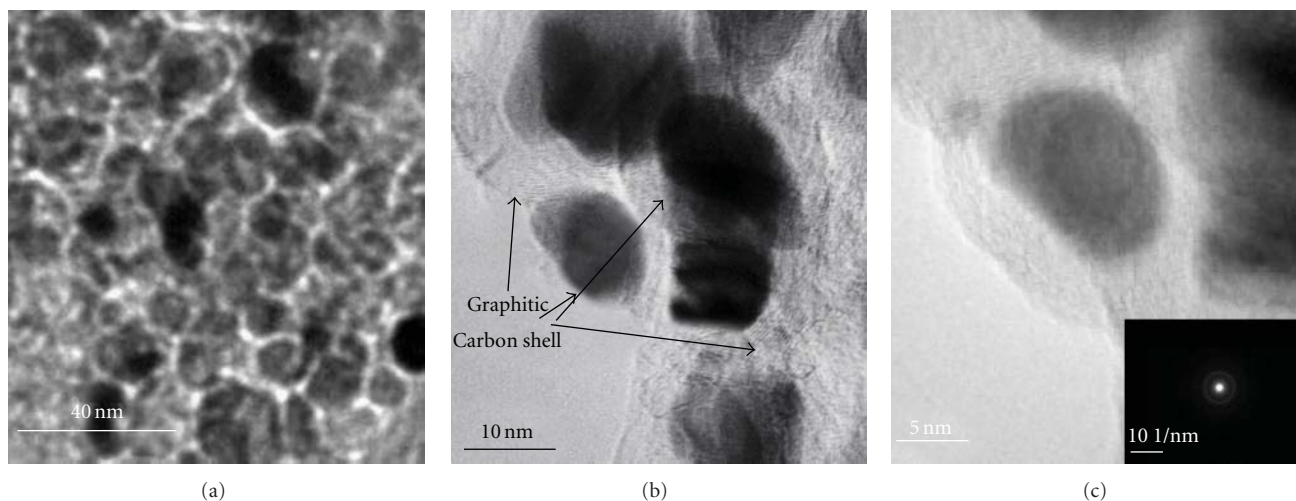(a)   (b)   (c)

FIGURE 2: The TEM and HRTEM images of ^{60}Co-Co/GC nanocrystal; (a): the image of TEM ~20 nm; (b): the image of HRTEM; (c): image of HRTEM and X-ray crystallography; the core of nano Co is ~14 nm; the thickness of cover layer is ~4 nm.
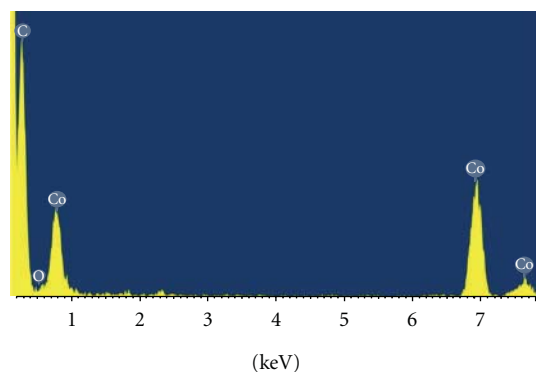

FIGURE 3: The energy dispersive X-ray spectrometer (EDS) of Co/GC nanocrystals, the atomic percentage of C, Co, and O are 73.77%, 25.73%, and 0.33%, respectively.

FIGURE 4: The Raman spectrums (excitation 785 nm) of Co/GC nanocrystals, showing the G and D bands of graphitic carbon.

it for 1 h, then ^{60}Co-Co/GC nanocrystals were prepared according to ditto method. The products were centrifugated and thoroughly washed until radioactive counts cannot be detected in supernatant. Results showed that yield of ^{60}Co-Co/GC nanocrystals was very low and less than 6%, $y = 5.77 \pm 0.23\%$ which indicted that a spot of Co, reduction production by H_2, can be embedded into graphite carbon to make Co/GC nanocrystals *via* methane CVD method. Figure 1 showed schematic diagram of a ^{60}Co/GC nanocrystal, the gamma ray can be emitted and detected by gamma counter, so it will be facilitative to quantify content of nanocrystals in tissues *in vivo*. Meanwhile, after outside graphite carbon shells of nanocrystals functionalized with chemical groups or drug molecules, the nanocrystals with gamma ray can be applied as a new radioactive imaging agent into single-photon emission computed tomography (SPECT).

3.3. Biodistribution in Mice.

A mass of ^{60}Co-Co/GC nanocrystals were accumulated in lung, liver, and spleen

at 1, 6, 12, 18, and 24 h, and highest accumulation in three tissues at 6 h, but low distribution in other tissues at all times. Several studies have implicated endocytosis as a cellular uptake mechanism of nanoparticles [11–13], so it was possible that ^{60}Co-Co/GC nanocrystals from blood were integrated into the phagocytic cells. As macrophages were highly concentrated in the liver and spleen, it could be possible for a large number of ^{60}Co-Co/GC nanocrystals to accumulate there. Therefore, most part of ^{60}Co-Co/GC nanocrystals were accumulated quickly in liver and spleen. The observation, along with the high-level accumulations of ^{60}Co-Co/GC nanocrystals in organs like the liver, spleen, and lungs, suggests that the rapid uptake of the nanotubes was through the mononuclear phagocytes in the reticuloendothelial system (RES) [14]. Such an uptake mechanism involving RES is consistent with the general conception on the fate of nanoparticles *in vivo* [15].

Nanocrystals began to eliminate slowly from lung and liver after 6 h, but there was a gradual increase in spleen from 12 to 24 h (Figure 4). The clearance of ^{60}Co-Co/GC
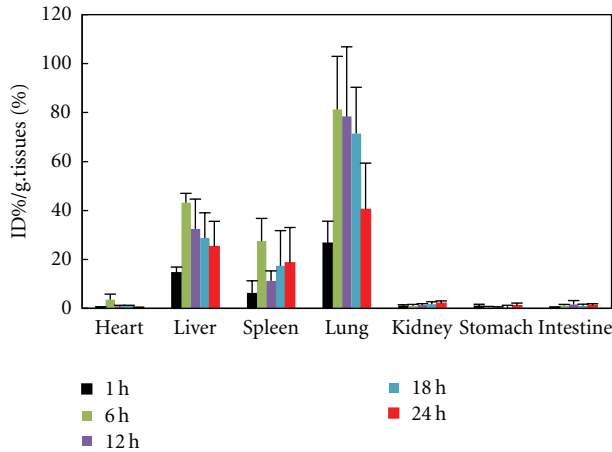
FIGURE 5: The biodistribution of ^{60}Co-Co/GC in different time after injection.

FIGURE 6: The time kinetic carve of ^{60}Co-Co/GC in blood after injection.

TABLE 1: The excretion of ^{60}Co-Co/GC ($n = 6$).

Time/h	Excretion	
	Urine/%	Feces/%
0–6	1.96 ± 0.37	0.40 ± 0.04
6–12	1.06 ± 0.45	0.28 ± 0.02
12–24	3.07 ± 1.70	1.17 ± 0.71
Total	6.09 + 0.74	1.85 ± 0.23

nanocrystals from the lungs may be due to two possible pathways. One is that the nanocrystals are secreted by the alveolar macrophage as mucus through mucociliary transport to leave the lungs. The other is that the interstitial nanocrystals are transferred through the lymph nodes and finally into the spleen. This seems consistent with the observed gradual increase in the uptake by the spleen over the same time period [16] (Figure 5).

The biodistribution of graphite carbon nanoparticles have been massively studied in previous works [14, 15]. It was reported that high biodistribution can be detected in liver and spleen after *i.v.* with fullerenes [14, 15]. Li et al. have studied biodistribution of $C_{60}(OH)_x$ labeled with ^{99m}Tc in mice, and established that most of ^{99m}Tc-$C_{60}(OH)_x$ can accumulated in liver, spleen, and kidney and with higher biodistribution in lung [14]. The biodistribution and metabolism of an endohedral ^{166}Ho$_x$@$C_{82}(OH)_y$ metallo-fullerol were studied in BALB/c mice and Fischer rats and found that high levels of radioactivity has been localized in liver and spleen, and with negligible accumulation in the lung [15]. Compared with our results, although differential sequence of distribution in tissues was observed, basic behavior and fate of fullerene *in vivo* was similar with Co/GC nanocrystals. For some difference, it may be due to size of multilayer ^{60}Co-Co/GC nanocrystals, and further experimental verification and mechanistic elucidation are required.

3.4. Hemodynamics and Excretion Study in Blood. The hemodynamics of ^{60}Co-Co/GC nanocrystals was shown in Figure 6, the results showed that ^{60}Co-Co/GC nanocrystals can be eliminated rapidly from blood and closed to background level in 10 min. It suggested that the clearance time from blood was very short, which may be because that most part of ^{60}Co-Co/GC nanocrystals were detained rapidly in lung, liver, and spleen within short time (Figure 5).

The distribution was still higher and closed to 40, 25 and 18% ID/g in lung, liver and spleen tissues at 24 h. (Figure 5), which indicates that ^{60}Co-Co/GC nanocrystals
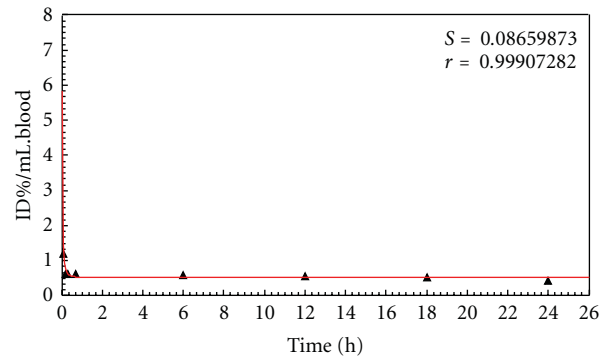
were eliminated hardly from these tissues within 24 h. Meanwhile, few nanocrystals could be detected in blood from 10 min to 24 h, so the nanocrystals can be hardly transported to kidney so as to empty from body *via* urine (Figure 6). We conferred that lower content of blood of nanocrystals was due to high residence in lung, liver, and spleen. Therefore, a few nanocrystals would be transported to other organs, and result in lower distribution in these tissues.

Table 1 showed that excretion of ^{60}Co-Co/GC nanocrystals was very low in 24 h, ~1.96% of nanocrystals were excreted from body *via* urine, and just ~0.4% by feces in 6 h. Total excretion in 24 h was less than 10% *via* urine and feces.

In conclusion, most of ^{60}Co-Co/GC nanocrystals can be retained rapidly in lung, liver, and spleen for short time (Figure 5). Because few ^{60}Co-Co/GC nanocrystals can be detected in blood after 10 min (Figure 6), and then nanocrystals would be transported hardly into other tissues *via* blood circulation. So, to therapy and diagnose target-site of tumor or focus in special organization such as stomach, kidney, and intestines, it would be difficult to selectively localize using external magnetic field in human or animals *in vivo*. Our experimental results were highly consistent with distribution of pristine SWCNTs of Yang et al. [16], and they thought that the different morphology and dispersion characteristics of pristine carbon nanotubes from those of their functionalized counterparts can induce difference in distributions *in vivo*. Therefore, for unfunctionalized and pristine ^{60}Co-Co/GC nanocrystals, it would be indispensable and important to functionalize and modify with chemical method so as to change behavior and fate *in vivo*.

4. Conclusion

The larger sizes of multilayer Co/GC nanocrystals were synthesized successfully in our work; higher biodistribution were observed in lung, liver, and spleen and low biodistribution in other tissues after *i.v.* with ^{60}Co-Co/GC nanocrystals; the clearance from blood was rapid, which was due to high retention of ^{60}Co-Co/GC nanocrystals in three tissues; and the nanocrystals cannot be excreted rapidly by urine and feces from body in 24 h.

Acknowledgment

References

[1] J. M. Bai and J. P. Wang, "High-magnetic-moment core-shell-type FeCo–Au/Ag nanoparticles," *Applied Physics Letters*, vol. 87, no. 5, Article ID 152502, 2005.

[2] U. Hafeli, W. Schutt, J. Teller et al., *Scientific and Clinical Applications of Magnetic Carriers*, Plenum Press, New York, NY, USA, 1997.

[3] C. B. Murray, S. Sun, W. Gaschler, H. Doyle, T. A. Betley, and C. R. Kagan, "Colloidal synthesis of nanocrystals and nanocrystal superlattices," *IBM Journal of Research and Development*, vol. 45, no. 1, pp. 47–56, 2001.

[4] V. F. Puntes, K. M. Krishnan, and A. P. Alivisatos, "Colloidal nanocrystal shape and size control: the case of cobalt," *Science*, vol. 291, no. 5511, pp. 2115–2117, 2001.

[5] D. P. Dinega and M. G. Bawendi, "Eineaus der Losungzuganglicheneue Kristallstruktur von Cobalt," *Angewandte Chemie International Edition*, vol. 111, pp. 1906–1909, 1999.

[6] A. Hütten, D. Sudfeld, I. Ennen et al., "New magnetic nanoparticles for biotechnology," *Journal of Biotechnology*, vol. 112, no. 1-2, pp. 47–63, 2004.

[7] C. Desvaux, C. Amiens, P. Fejes et al., "Multimillimetre-large superlattices of air-stable iron-cobalt nanoparticles," *Nature Materials*, vol. 4, no. 10, pp. 750–753, 2005.

[8] Z. Turgut, J. H. Scott, M. Q. Huang, S. A. Majetich, and M. E. McHenry, "Magnetic properties and ordering in C-coated Fe_xCo_{1-x} alloy nanocrystals," *Journal of Applied Physics*, vol. 83, no. 11, pp. 6468–6470, 1998.

[9] W. S. Seo, J. H. Lee, X. Sun et al., "FeCo/graphitic-shell nanocrystals as advanced magnetic-resonance-imaging and near-infrared agents," *Nature Materials*, vol. 5, no. 12, pp. 971–976, 2006.

[10] F. Tuinstra and J. L. Koenig, "Raman spectrum of graphite," *Journal of Chemical Physics*, vol. 53, no. 3, pp. 1126–1130, 1970.

[11] M. Marsh and H. T. McMahon, "The structural era of endocytosis," *Science*, vol. 285, no. 5425, pp. 215–220, 1999.

[12] S. Mukherjee, R. N. Ghosh, and F. R. Maxfield, "Endocytosis," *Physiological Reviews*, vol. 77, no. 3, pp. 759–803, 1997.

[13] P. Cherukuri, S. M. Bachilo, S. H. Litovsky, and R. B. Weisman, "Near-infrared fluorescence microscopy of single-walled carbon nanotubes in phagocytic cells," *Journal of the American Chemical Society*, vol. 126, no. 48, pp. 15638–15639, 2004.

[14] Q. N. Li, Y. Xiu, X. D. Zhang et al., "Preparation of $^{99m}Tc - C_{60}(OH)_x$ and its biodistribution studies," *Nuclear Medicine and Biology*, vol. 29, no. 6, pp. 707–710, 2002.

[15] D. W. Cagle, S. J. Kennel, S. Mirzadeh, J. M. Alford, and L. J. Wilson, "In vivo studies of fullerene-based materials using endohedral metallofullerene radiotracers," *Proceedings of the National Academy of Sciences of the United States of America*, vol. 96, no. 9, pp. 5182–5187, 1999.

[16] S. T. Yang, W. Guo, Y. Lin et al., "Biodistribution of pristine single-walled carbon nanotubes in vivo," *Journal of Physical Chemistry C*, vol. 111, no. 48, pp. 17761–17764, 2007.

Research Article

Effect of Superhydrophobic Surface of Titanium on *Staphylococcus aureus* Adhesion

Peifu Tang,[1] Wei Zhang,[1] Yan Wang,[1] Boxun Zhang,[1] Hao Wang,[1] Changjian Lin,[2] and Lihai Zhang[1]

[1] *Department of Orthopedics, General Hospital of Chinese PLA, Beijing 100853, China*
[2] *State Key Laboratory for Physical Chemistry of Solid Surfaces Department of Chemistry, College of Chemistry and Chemical Engineering, Xiamen University, Xiamen, Fujian 36100, China*

Correspondence should be addressed to Changjian Lin, linchangjian@sohu.com and Lihai Zhang, zhanglihai@gmail.com

Despite the systemic antibiotics prophylaxis, orthopedic implants still remain highly susceptible to bacterial adhesion and resulting in device-associated infection. Surface modification is an effective way to decrease bacterial adhesion. In this study, we prepared surfaces with different wettability on titanium surface based on TiO_2 nanotube to examine the effect of bacterial adhesion. Firstly, titanium plates were calcined to form hydrophilic TiO_2 nanotube films of anatase phase. Subsequently, the nanotube films and inoxidized titaniums were treated with 1H, 1H, 2H, 2H-perfluorooctyl-triethoxysilane (PTES), forming superhydrophobic and hydrophobic surfaces. Observed by SEM and contact angle measurements, the different surfaces have different characteristics. *Staphylococcus aureus* (SA) adhesion on different surfaces was evaluated. Our experiment results show that the superhydrophobic surface has contact angles of water greater than 150° and also shows high resistance to bacterial contamination. It is indicated that superhydrophobic surface may be a factor to reduce device-associated infection and could be used in clinical practice.

1. Introduction

The number of trauma and aged patients requiring internal fixation devices or joint replacements is increasing steadily. In the USA, about 2 million fracture-fixation devices are inserted annually. Infection is generally the most common serious complication of fixation devices. Although infection of initially inserted internal fixation devices is about 5% [1], such infection is associated with a high potential for chronic osteomyelitis or limb loss, even death. Since cure of infections associated with internal fixation devices commonly requires removal of the infected devices, managements could be rather difficult and quite expensive. The serious medical complications, problematic managements, and economical sequelae of infections associated with internal fixation devices have prompted a keen interest in exploring innovative preventive approaches [2–5].

Mechanism of device-related internal fixation caused by bacteria is very complex, but bacteria adherence on device surfaces is an initial crucial step and a prelude to clinical infection [6]. Many studies show that wettability of surface is one of the reasons of bacteria adherence. Hydrophilic surface (contact angle <90°) attracted most of bacteria such as *Staphylococcus aureus*, *Escherichia coli* [7], whereas hydrophobic surface (contact angle >90°) attracted *Psx. Taiwanensis* and *Staph. epidermidis* and reduced the adherence of bacteria including *D. geothermalis* and *M. Silvanus* [8], *Staphylococcus aureus* [9], and *Streptococcus mutans* [10]. Whether attraction or reduction depends on the type of bacteria and the surface characteristics, in particular contact angle.

Staphylococcus aureus (SA) is the main pathogenic bacteria in the internal fixation-related infection in clinic [6]. How to reduce SA adherence and how to prevent infection most concerned things by orthopaedic surgeons. To surface characteristics, why hydrophobic surface could reduce some bacteria and attract some others? We assume that the degree of hydrophobicity is not enough and being increased to superhydrophobicity (contact angle >150°) could be attributed to the reduction of bacteria adherence

substantially at the interfaces. Common approaches to enhance the degree of hydrophobicity at biomaterial surfaces were raising the surface roughness and modifying low surface energy [11–15]. But both tended not to exhibit water contact angle values more than 150°.

In this work, we used a more facile method to fabricate superhydrophobic surface on the titanium, and we compared with other techniques including etching [16], sol-gel [17], chemical vapor phase deposition [18], and mechanical stretching method [19]. Firstly, anodic oxidation was conducted to generate the nanotube on the titanium surface in the HF acid system, with the surface wettability being moderate hydrophilicity. And then PTES was modified on the surface of the nanotube by layers self-assembly technique, and the superhydrophobic surface with high contact angle was formed. Then we investigated the ability of different surfaces to prevent bacterial adherence *in vitro*.

2. Materials and Methods

2.1. Materials—Substrates. Medical purity titanium was purchased from Zheng tian Co., Ltd in Beijing, China. 1H, 1H, 2H, 2H-perfluorooctyl-triethoxysilane (PTES) used for surface hydrophobic modification was purchased from Degussa Co., Ltd.

2.2. Surface Treatment. At the first step, the purity titanium samples were cut into dimensions of 1 cm $\times$ 2 cm $\times$ 0.2 cm by flame incision machine (Zheng tian Co., Ltd, China). Different sizes of sand papers were used to polish the samples until their surfaces become smooth. Then the polished samples were washed by ultrasonic (90 kHz, output power 90 W), propanone, ethanol, and deionized water, successively.

Secondly, the superhydrophobic nanotube structure TiO_2 film was fabricated through electrochemical oxidation and self-assembled technique. Purity titanium (99.5%) sheets were electrochemically anodized with Pt counterelectrode in 0.5 wt% HF electrolyte under certain voltage for 1 h, rinsed with deionized water, and dried with dry nitrogen stream. The prepared amorphous TiO_2 nanotube films were calcined at 450°C for 2 h to form anatase phase and then treated with a methanolic solution of hydrolyzed 1 wt% 1H, 1H, 2H, 2H-perfluorooctyl-triethoxysilane (PTES, Degussa Co., Ltd.) for 1 h and subsequently heated at 140°C for 1 h to remove residual solvent and promote chemisorption of the SAM. Sample 1 was treated by surface anodic oxidation only (NT), sample 2 was treated by PTES after the anodic oxidation (NTS), and sample 3 was treated by PTES on the surface of titanium (TiS).

2.3. Surface Characterization. The surface morphology of the samples was examined with Hitachi S-4800 Field Emission scanning electron microscope. The samples were pressed slightly and coated with gold. The water contact angles of the samples were measured by First Ten Angstroms dynamic

contact angle analyzer (FTA 200) at ambient temperature with a droplet volume of 0.013 mL.

2.4. Biological Analysis Materials. S. aureus 8325 strain was purchased from Academy of Military Medical Sciences; Luria-Bertani (LB) medium and agar which were used for growing and maintaining bacteria cultures were purchased from Sigma-Aldrich; Osmium tetroxide (OsO_4) was purchased from Simec (Switzerland); Glutaraldehyde was purchased from AGAR (Stansted, UK), Tannin Acid was purchased from Fluka (Buchs, Liechtenstein), and The BacLight RedoxSensor CTC Vitality Kit was purchased from Invitrogen detection technologies (USA).

2.5. Bacterial Culturing and Adhesion. Got 1 mL *S. aureus* 8325-4 into a tube, followed by 5 mL Luria-Bertani (LB) medium (no antibiotics) and placed it on the swing bed overnight (37°C, 250 r.p.m., 12 h) and then stored in 4°C for use. Multiple proportion dilution and plate counting methods were conducted to adjust the density of 1 μL liquid into 1×10^9 cfu/mL. LB mediums were then added into the liquid until the final density of 1×10^6 cfu/mL. Metal samples were placed into the six-well culture dish to be sterilized by γ-ray (25 kGy), and liquid at the density of 1×10^6 cfu/mL was added into every well with 10 mL. Then the dish was put into the incubation case with the relative humidity above 90% at 37°C. Scanning electron microscopy (SEM) and fluorescence microscopy (FM) were conducted after 2 h to 4 h.

2.6. Visualization of S. Aureus on Different Surfaces. After being rinsed with 0.01 M PBS to remove the float bacterium on the surface, the sample was moved into the six-well culture dish and 2.5% glutaraldehyde was added and then kept in the freezer at 4°C overnight. After being washed with 0.01 M PBS (three times for 30 min each), 1% osmic acid was added to fix for 2 h. After being washed with 0.01 M PBS (three times for 30 min each), samples were kept in the 2% Tannin solution. 30 min later, the solution was refreshed, and, after another 30 min, samples were washed with 0.01 M PBS (three times for 30 min each). Then samples were dehydrated by 50% alcohol, 70% alcohol, 90% alcohol and absolute alcohol and had a transition using isoamyl acetate. Visualization with a Hitachi S-4800 Field Emission SEM operated in secondary electron (SE) detection modes.

2.7. Bacterial Adherence and Fluorescence Microscopy Counting. Metal samples were placed into the six-well culture dish to be sterilized by γ-ray (25 k Gy), and liquid at the density of 1×10^6 cfu/mL was added into the wells with 10 mL each. The dish was sealed and put into standard bacteria culture incubator (at a 37°C, humidified, 5% CO_2, and 20% O_2 environment). *S. aureus* 8325 was cultured on the surfaces for prescribed time period (2 and 4 h), washed twice with PBS (0.01 M) to remove any loose or unattached bacteria, and stained with fluorescent redox dye, CTC for 30 minutes at 37°C and protected from light. Bacteria cell counts were then completed using a fluorescence microscope in a field of view of 200 mm $\times$ 200 mm. Colony-forming

(a)

(b)
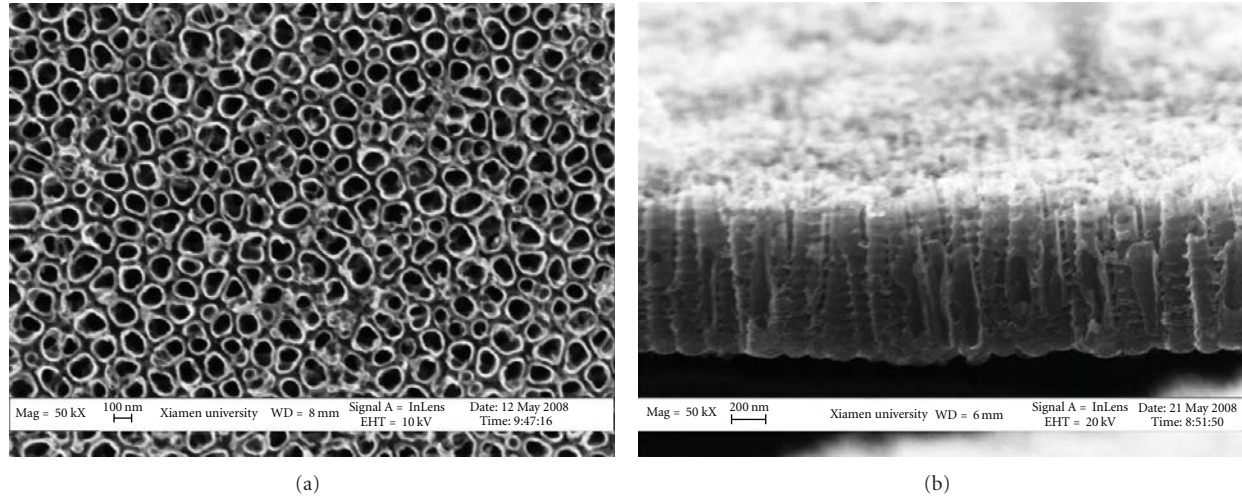
FIGURE 1: SEM images of the nanotube layer formed on titanium in 0.5 wt% HF electrolyte solution at 20 V: (a) top view; (b) cross-section.
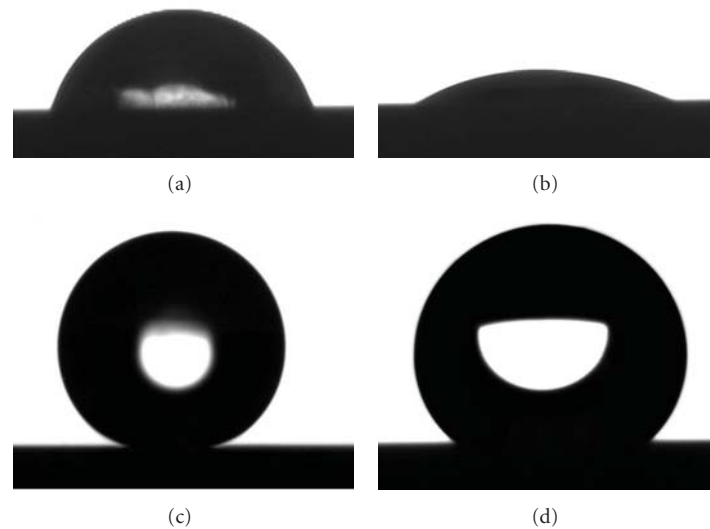

(a)

(b)

(c)

(d)

FIGURE 2: Photographs of water droplet shape on (a) NT film; (b) NT film and the rapid spread and wet the NT film; (c) NTS film, PETS-treated on the surface of nanotube array; (d) TiS film, PETS-treated on the surface of titanium.

units were determined using Image Pro software. Ten fields were averaged for each substrate. Statistical analysis was done using a one-way ANOVA with Tukey's test. Experiments were completed in triplicate and were repeated three times [2].

2.8. Surplus Bacterium Solution Count. Ultraviolet spectrophotometer was conducted to determine the OD value of the bacteria solution that was soaked in the samples at the wave length of 600 nm.

3. Results and Discussion

It is generally believed that what we are able to do is to minimize its deleterious clinical consequences, once an implant infection has developed [20, 21]. However, there is no doubt that prevention represents a main goal. For implant materials, the interface biomaterial surface-surrounding tissue represents the real ground where the battle takes place and where accidental contamination can first develop into colonization [6], and so many routes of surface coating and modification developed. Recently researchers [8–10] report that wettability (hydrophilicity and hydrophobicity) may be a factor of deceasing bacteria adherence on surfaces. But few people discussed the superhydrophobic surfaces of titanium or the effect of bacteria. In this work we have fabricated superhydrophobic nanostructured TiO_2 surfaces with electrochemical and self-assembly method [22], validated the character of superhydrophobicity, and compared with hydrophilic and hydrophobic surfaces on bacteria adherence. In SEM morphology, anodic oxidation was conducted in our solution containing fluorine to generate the regulated
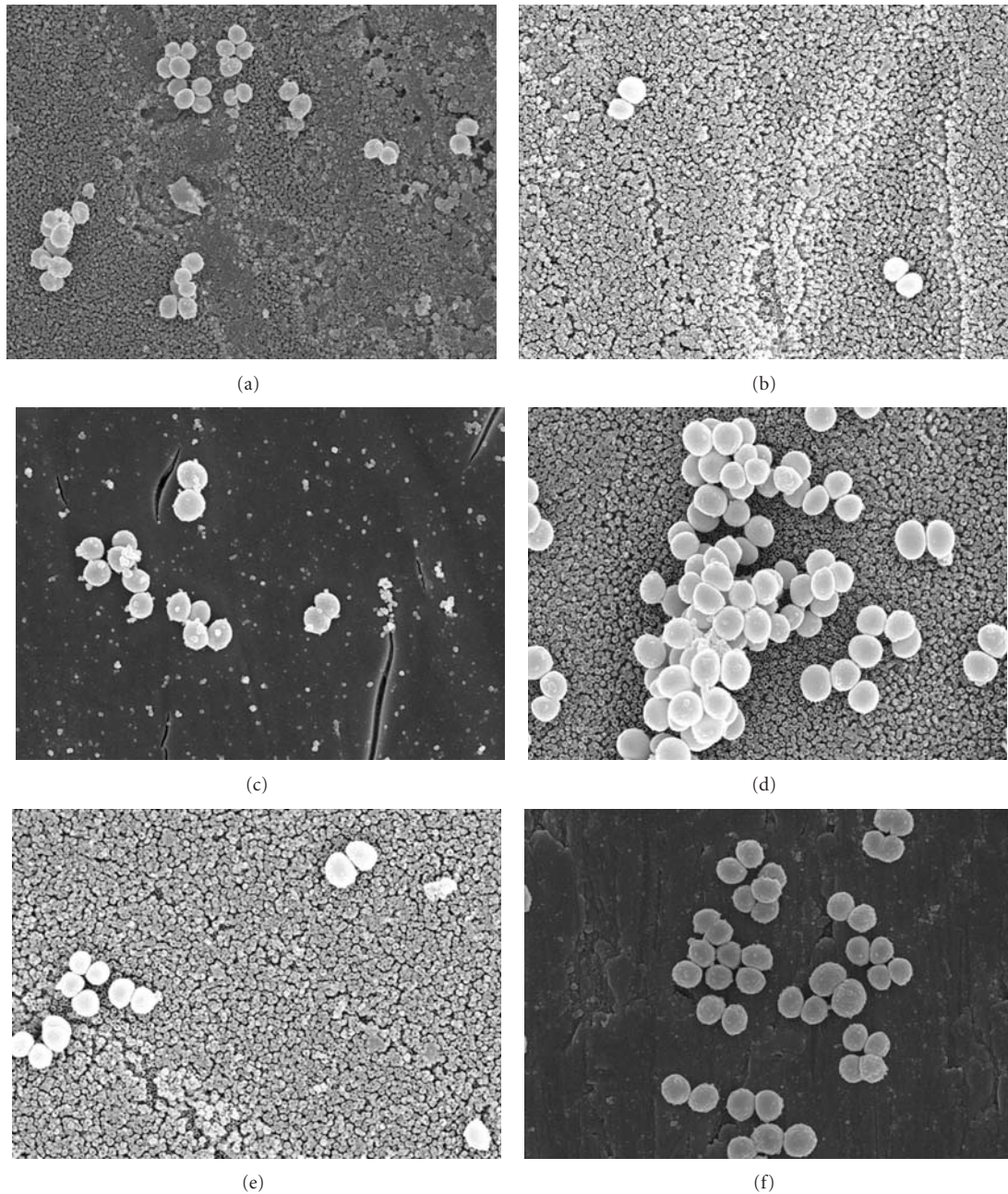
(a)

(b)

(c)

(d)

(e)

(f)

FIGURE 3: SEM images of bacteria colonies after 2 h on (a) NT, (b) NTS, and (c) TiS, and after 4 h on (d) NT, (e) NTS, and (f) TiS (×10 K).

nanotubes array structure on the surface of titanium by the etching of fluoride ion. Figure 1 shows an SEM image of TiO_2 nanotubes with uniform and regular array. This nanotube is about 400 nm long, with an 8 to 10 nm vessel wall and an inner diameter ranging from 80 to 100 nm. There are no difference between nanotube film treated with or without PETS on SEM image.

Electrochemical anodizing is verified to be a convenient and effective method for fabricating nanostructured TiO_2 films with powerful mechanical strength directly on pure titanium (Ti) substrates, compared with sol-gel technique,

sputtering, and chemical vapor deposition [23]. The nanotube created in HF acid system using this way was uniform, thus a rough surface formed, just as Crimes [24] described. A detailed study on crystallization and structural transformation of these nanotube arrays upon thermal annealing is reported elsewhere [25], and the wettability of the rough surface was moderate hydrophilic (the contact angle was 54°) after being calcined forming anatase phase. Figure 2(a) was captured when the water dropped on the surface instantly, and then water rapidly spreads and wets the film due to side penetration of the liquid by capillary
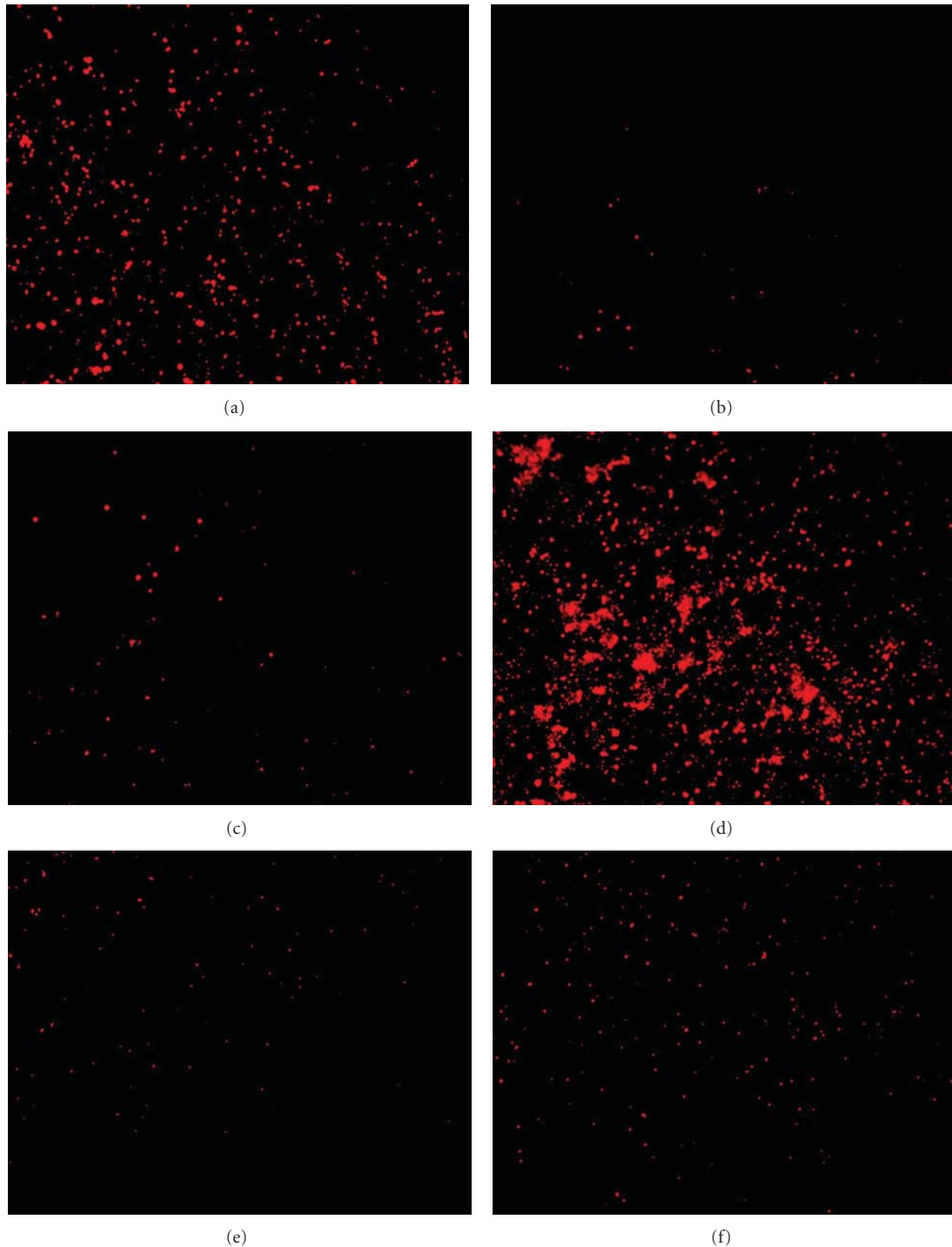
(a)

(b)

(c)

(d)

(e)

(f)

FIGURE 4: Fluorescence microscope images of bacteria stained with CTC after 2 h (a–c) and 4 h (d–f) of culture on NT, NTS, and TiS.

forces [26], showed in Figure 2(b). Figure 2(c) shows that the contact angle of NTS is increased to 156° after it was modified by PETS, which is superhydrophobicity, while the contact angle of TiS is only 133° (Figure 2(d)).

The moderate hydrophilic nanotube films can be fabricated through self-assembly technique, and the hydrophobicity of the films is also improved greatly. It is well known that a flat Surface with low surface energy tends to exhibit

high water contact angle values on the order of 100–120°. However, this is insufficient to produce a water repellent or superhydrophobic surface, which requires a water contact angle larger than 150° [27]. Generally speaking, hydrophobic surfaces can be generated by being roughed and being modified by low-energy materials. Numerous nanotube surfaces increase the surface area and the rough degree and also modify the low surface energy material PTES, in
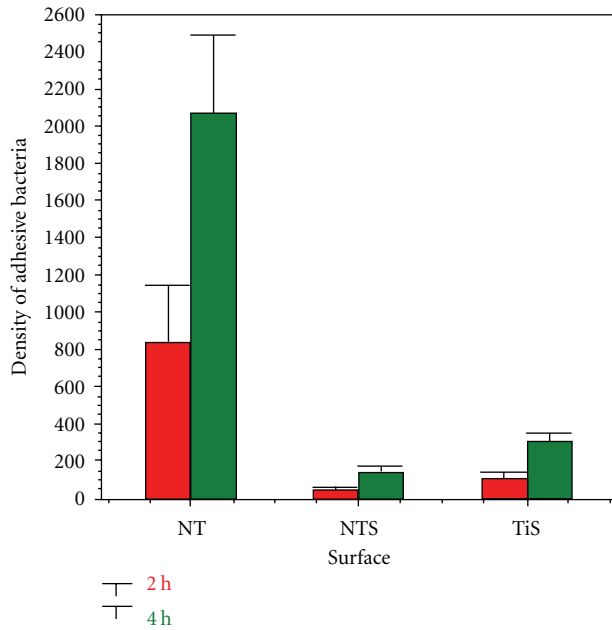
FIGURE 5: Decreased *S. aureus* adhesion on nanotubes self-assembled with PETS (NTS) compared to TiS and NT; NTS ($P < .05$) compared with growth on TiS and NT after 2 h of culture; NTS ($P < .05$) compared with growth on TiS and NT after 4 h of culture.

FIGURE 6: Graph showing OD_{600} of the surplus bacteria solution soaking the tested samples after 2 h and 4 h of culturing. The concentration of *S. aureus* solution was evaluated with the ultraviolet spectrophotometer. The value of OD_{600} is higher than the other two ($P < .05$) at either 2 h or 4 h.

which the lotus leaf effect of superhydrophobic surface was generated.

In this experiment, three kinds of surfaces were created, moderate hydrophilic surfaces (NT), superhydrophobic surfaces (NTS), and hydrophobic surfaces (TiS), which were modified by PETS on flat titanium as a control. In visualization of *S. aureus* on different surfaces (Figures 3(a)–3(f)) are shown the SEM images of bacterial colony formation after 2 h and 4 h of culture on NT, NTS, and TiS, respectively. At 2 h, there were more bacteria on the hydrophilic surfaces (NT, Figure 3(a)) than those on the hydrophobic surfaces (TiS, Figure 3(c)), and in comparison to the superhydrophobic surfaces (NTS, Figure 3(b)), more bacteria were observed on both the surfaces above. Furthermore, bacteria on hydrophobic surfaces, including NTS and TiS, were scattered, while bacteria on hydrophilic surfaces tended to gather. By 4 h, bacteria on the three surfaces all increased and those on the hydrophilic surface (NT, Figure 3(d)) were still more and in clumps compared with the other two (NTS and TiS, Figures 3(e) and 3(f)). The images of SEM showed that the amount of bacteria on superhydrophobic surfaces was less and bacteria were mostly scattered, which indicated that interaction among bacteria was less than that between bacteria and material surfaces. It means that bacteria were not easily adhesive on them. Further studies of CTC dye bacteria indicate that there is an approximately 50%–90% decrease in bacteria colonies on TiS compared to NT and TiS after 4 h of culture. CTC (5-cyano-2, 3-ditolyl tetrazolium chloride) has been used to evaluate the respiratory activity of many bacterial populations derived from environmental sources. Healthy
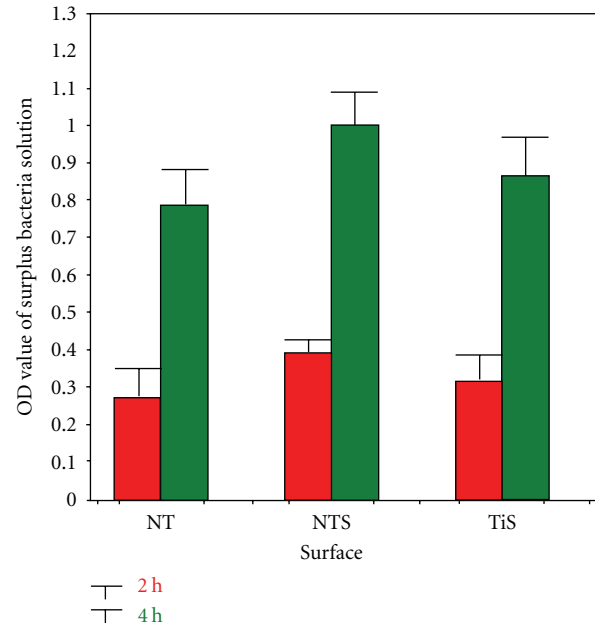
cells respiring via the electron transport chain will absorb and reduce CTC into an insoluble, red fluorescent formazan product. Only live and healthy bacteria could be stained and observed on the surfaces. On the images of fluorescence microscope, the amount of bacteria on hydrophilic surfaces was much more than that on the other two and tended to gather. Once bacteria were in clump, biological membrane could be formed, which kept them away from the effect of body immunity and antibacterial agent, and thus it caused the infection. There was no aggregation of bacteria on the superhydrophobic surface, which suggested that the interaction was tiny and there was little chance to form the biological membrane that was easy to be cleared by body immunity and antibacterial agent. In this way, incidence of infection was decreased [28].

We also tested the OD_{600} value of surplus soaking solution. Figure 4 shows the fluorescence microscopy images of bacteria colonies formed on NT, NTS, and TiS surfaces after 2 h (Figures 4(a)–4(c)) and 4 h (Figures 4(d)–4(f)) of culture. These images suggest that hydrophobic and superhydrophobic surfaces (NTS and TiS) have fewer and smaller bacteria colonies compared to hydrophilic surface (NT). In particular, much less bacteria were again observed by FM on the PETS-coated surfaces compared with the other two. Figure 5 shows the bacteria colony count obtained by Image Pro software. Statistical analysis using one-way ANOVA with Tukey's test showed that the differences between NT and TiS significant ($P < .05$), as were the differences observed between NTS and TiS ($P < .05$). We collected the surplusbacteria solution of tested samples at 2 h and 4 h. And the OD value at the wave length of 600 nm was determined

using the ultraviolet spectrophotometer. Figure 6 shows the changes of OD_{600} of the surplus bacteria solution soaking the samples. Statistic analysis using Tukey's test of the one-way ANOVA showed that the surplus bacteria solution of the superhydrophobic sample was significantly higher than that of the hydrophilic and hydrophobic ones.

Bacteria are in the lag phase 4 h before, according to the growth curve of bacteria. It means that it was not the amount of bacteria that increased but the body that became bigger in this period. So the total number of bacteria in each dish of 2 h or 4 h was the same. As the superhydrophobic surfaces were not profitable for the bacteria adherence, there were more bacteria in the liquid than on the sample surfaces. However, the results in the liquid soaking hydrophilic samples were on the contrary.

4. Conclusion

Electrochemistry anodic oxidation on the titanium surface could generate regulated TiO_2 nanotube array to roughen the surface, while modifing the low surface energy material PTES could easily generate the superhydrophobic surface. Our experiments showed that the amount of bacteria adherence on these surfaces was different. With the contact angle increased, the amount of bacteria decreased. Superhydrophobic surface may decrease the incidence of infection by inhibiting the adherence of *Staphylococcus aureus in vitro*. However, *Staphylococcus aureus* was not totally absent on the superhydrophobic surface; they were less and more scattered compared with those on the hydrophilic and hydrophobic surfaces. So superhydrophobicity was one of the factors affecting bacterial adherence. Further research will focus on the reduction of some other bacteria, such as streptococcus, Gram-negative, on superhydrophobic surface of titanium and the effect *in vivo*.

References

[1] R. O. Darouiche, "Treatment of infections associated with surgical implants," *The New England Journal of Medicine*, vol. 350, no. 14, pp. 1422–1429, 2004.

[2] K. C. Popat, M. Eltgroth, T. J. LaTempa, C. A. Grimes, and T. A. Desai, "Decreased Staphylococcus epidermis adhesion and increased osteoblast functionality on antibiotic-loaded titania nanotubes," *Biomaterials*, vol. 28, no. 32, pp. 4880–4888, 2007.

[3] L. G. Harris, S. Tosatti, M. Wieland, M. Textor, and R. G. Richards, "Staphylococcus aureus adhesion to titanium oxide surfaces coated with non-functionalized and peptide-functionalized poly(L-lysine)-grafted- poly(ethylene glycol) copolymers," *Biomaterials*, vol. 25, no. 18, pp. 4135–4148, 2004.

[4] M. Stigter, K. de Groot, and P. Layrolle, "Incorporation of tobramycin into biomimetic hydroxyapatite coating on titanium," *Biomaterials*, vol. 23, no. 20, pp. 4143–4153, 2002.

[5] K. Vacheethasanee and R. E. Marchant, "Surfactant polymers designed to suppress bacterial (Staphylococcus epidermidis) adhesion on biomaterials," *Journal of Biomedical Materials Research*, vol. 50, no. 3, pp. 302–312, 2000.

[6] C. Davide, M. Lucio, and R. A. Carla, "The significance of infection related to orthopedic devices and issues of antibiotic resistance," *Biomaterials*, vol. 27, no. 11, pp. 2331–2339, 2006.

[7] J. Ji and W. Zhang, "Bacterial behaviors on polymer surfaces with organic and inorganic antimicrobial compounds," *Journal of Biomedical Materials Research—Part A*, vol. 88A, no. 2, pp. 448–453, 2008.

[8] M. Raulio, M. Järn, J. Ahola et al., "Microbe repelling coated stainless steel analysed by field emission scanning electron microscopy and physicochemical methods," *Journal of Industrial Microbiology and Biotechnology*, vol. 35, no. 7, pp. 751–760, 2008.

[9] H. Yang and Y. Deng, "Preparation and physical properties of superhydrophobic papers," *Journal of Colloid and Interface Science*, vol. 325, no. 2, pp. 588–593, 2008.

[10] A. Okada, T. Nikaido, M. Ikeda et al., "Inhibition of biofilm formation using newly developed coating materials with self-cleaning properties," *Dental Materials Journal*, vol. 27, no. 4, pp. 565–572, 2008.

[11] S. A. Kulinich and M. Farzaneh, "Hydrophobic properties of surfaces coated with fluoroalkylsiloxane and alkylsiloxane monolayers," *Surface Science*, vol. 573, no. 3, pp. 379–390, 2004.

[12] H. M. Shang, Y. Wang, K. Takahashi, G. Z. Cao, D. Li, and Y. N. Xia, "Nanostructured superhydrophobic surfaces," *Journal of Materials Science*, vol. 40, no. 13, pp. 3587–3591, 2005.

[13] S. Boduroglu, M. Cetinkaya, W. J. Dressick, A. Singh, and M. C. Demirel, "Controlling the wettability and adhesion of nanostructured poly-(p-xylylene) films," *Langmuir*, vol. 23, no. 23, pp. 11391–11395, 2007.

[14] R. Rioboo, M. Voué, A. Vaillant et al., "Superhydrophobic surfaces from various polypropylenes," *Langmuir*, vol. 24, no. 17, pp. 9508–9514, 2008.

[15] B. Bhushan and Y. Chae Jung, "Wetting study of patterned surfaces for superhydrophobicity," *Ultramicroscopy*, vol. 107, no. 10–11, pp. 1033–1041, 2007.

[16] B. Qian and Z. Shen, "Fabrication of superhydrophobic surfaces by dislocation-selective chemical etching on aluminum, copper, and zinc substrates," *Langmuir*, vol. 21, no. 20, pp. 9007–9009, 2005.

[17] R. Taurino, E. Fabbri, M. Messori, F. Pilati, D. Pospiech, and A. Synytska, "Facile preparation of superhydrophobic coatings by sol-gel processes," *Journal of Colloid and Interface Science*, vol. 325, no. 1, pp. 149–156, 2008.

[18] N. Shirahata and A. Hozumi, "Ultrathin poly(ethylene glycol) monolayers formed by chemical vapor deposition on silicon substrates," *Journal of Nanoscience and Nanotechnology*, vol. 6, no. 6, pp. 1695–1700, 2006.

[19] Z. Cheng and S. H. Teoh, "Surface modification of ultra thin poly (ε-caprolactone) films using acrylic acid and collagen," *Biomaterials*, vol. 25, no. 11, pp. 1991–2001, 2004.

[20] W. Zimmerli and P. E. Ochsner, "Management of infection associated with prosthetic joints," *Infection*, vol. 31, no. 2, pp. 99–108, 2003.

[21] D. M. Allen, "Orthopaedic implant infections: current management strategies," *Annals of the Academy of Medicine Singapore*, vol. 26, no. 5, pp. 687–690, 1997.

[22] Y. Lai, C. Lin, J. Huang, H. Zhuang, L. Sun, and T. Nguyen, "Markedly controllable adhesion of superhydrophobic spongelike nanostructure TiO_2 films," *Langmuir*, vol. 24, no. 8, pp. 3867–3873, 2008.

[23] D. Gong, C. A. Grimes, O. K. Varghese et al., "Titanium oxide nanotube arrays prepared by anodic oxidation," *Journal of Materials Research*, vol. 16, no. 12, pp. 3331–3334, 2001.

[24] Q. Cai, M. Paulose, O. K. Varghese, and C. A. Grimes, "The effect of electrolyte composition on the fabrication of self-organized titanium oxide nanotube arrays by anodic oxidation," *Journal of Materials Research*, vol. 20, no. 1, pp. 230–236, 2005.

[25] O. K. Varghese, D. Gong, M. Paulose, C. A. Grimes, and E. C. Dickey, "Crystallization and high-temperature structural stability of titanium oxide nanotube arrays," *Journal of Materials Research*, vol. 18, no. 1, pp. 155–156, 2003.

[26] A. B. Foraker, R. J. Walczak, M. H. Cohen, T. A. Boiarski, C. F. Grove, and P. W. Swaan, "Microfabricated porous silicon particles enhance paracellular delivery of insulin across intestinal caco-2 cell monolayers," *Pharmaceutical Research*, vol. 20, no. 1, pp. 110–116, 2003.

[27] A. Lafuma and D. Quéré, "Superhydrophobic states," *Nature Materials*, vol. 2, no. 7, pp. 457–460, 2003.

[28] K. Lewis, "Persister cells, dormancy and infectious disease," *Nature Reviews Microbiology*, vol. 5, no. 1, pp. 48–56, 2007.

Research Article

Fabrication of Lateral Polysilicon Gap of Less than 50 nm Using Conventional Lithography

Th. S. Dhahi,[1] U. Hashim,[1] M. E. Ali,[1] N. M. Ahmed,[2] and T. Nazwa[1]

[1] *Institute of Nano Electronic Engineering, Universiti Malaysia Perlis, 01000 Kangar, Perlis, Malaysia*
[2] *School of Physics, Universiti Sains Malaysia, 11800 Penang, Malaysia*

Correspondence should be addressed to Th. S. Dhahi, sthikra@yahoo.com

We report a thermal oxidation process for the fabrication of nanogaps of less than 50 nm in dimension. Nanogaps of this dimension are necessary to eliminate contributions from double-layer capacitance in the dielectric detection of protein or nucleic acid. The method combines conventional photolithography and pattern-size reduction techniques. The gaps are fabricated on polysilicon-coated silicon substrate with gold electrodes. The dimensions of the structure are determined by scanning electron microscopy (SEM). An electrical characterization of the structures by dielectric analyzer (DA) shows an improved conductivity as well as enhanced permittivity and capacity with the reduction of gap size, suggesting its potential applications in the detection of biomolecule with very low level of power supply. Two chrome Masks are used to complete the work: the first Mask is for the nanogap pattern and the second one is for the electrodes. An improved resolution of pattern size is obtained by controlling the oxidation time. The method expected to enable fabrication of nanogaps with a wide ranging designs and dimensions on different substrates. It is a simple and cost-effective method and does not require complicated nanolithography process for fabricating desired nanogaps in a reproducible fashion.

1. Introduction

The present invention relates to a process of forming an electrode with a desired nanogap. The development of a cost-effective, easily performable, and high-throughput technique for the fabrication of such structures is of great interests both for the possibility of increasing the device-packing density and the reduction of power consumption [1]. Such structures have potential applications in the next generation nanoelectronic devices, such as single electron transistors [1], metal/insulator tunnel transistors [2], nanowire transistors [3], nanotube- or nanoparticle-based devices [4, 5]. Chemical and biological nanosensors, biochips, and nanobioelectronics are other applications, which are progressing rapidly [4, 6–9]. The coupling of biomolecules with nanomaterials (nanoparticles, nanotubes, etc.) and nanostructures (e.g., nanoelectrodes, nanotransistors, nanogaps, nanopores, and nanochannels) of compara-ble dimensions might allow the creation of hybrid systems with unique functions and applications [4, 7, 10–16]. Such

functional hybrid systems, originated from the "marriage" of biomolecules and nanoscaled transducers, provide powerful tools, not only for manipulation and detection, but also for the fundamental research of single biological molecule (DNA, immunoglobulins, proteins, and living cells).

The realization of different nanometer-sized structures has been demonstrated by advanced high-resolution nano-lithography techniques, such as electron- or ion-beam lithography, focused ion-beam milling, scanning tunneling or atomic force microscopy, nanoimprint lithography, and different top-down fabrication techniques [17]. Although these techniques provide high resolution in generating different nanostructures, most of them are time-consuming, low-throughput, complicated, and expensive. If conventional photolithography could be applied to form nanometer-sized structures including line and space patterns, it would be highly advantageous. Therefore, recently, some non-conventional techniques in combination with conventional photolithography have been proposed for the preparation of nanoelectrodes, nanogaps, and other nanoscaled devices.
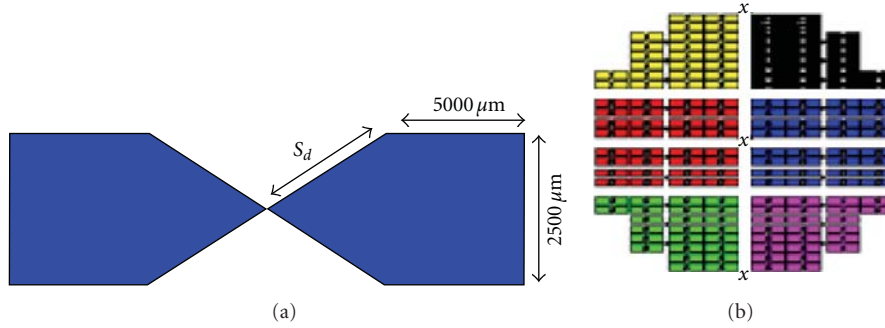
FIGURE 1: Schematic presentation of the first Mask with dimension specification (a) and the actual Mask on chrome glass (b).
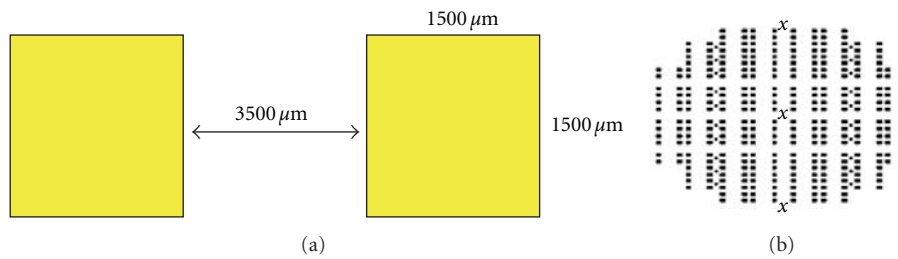

FIGURE 2: Design specification for Mask 2 (a) and the actual Mask on chrome glass (b).

These techniques include, for instance, a photoresist thermal reflow and shrinking [18] or photoresist ashing technique [19], a shadow evaporation process [20], a controlled size reduction using the oxidation of Si [21–23] or laser-assisted electrochemical etching [24], chemical-mechanical polishing [25], the decrease of separation between metallic electrodes by means of an electrodeposition from an electrolyte solution [26], methods that utilize a sidewall structure [27], a self-aligned plasma etching of a silicon dioxide layer and silicon substrate [28], or a lateral, partial anodic oxidation of the side edge of a photolithographically structured metallic film (e.g., Ti) [29], and techniques that use a silicon-on-insulator structure [30].

An alternative solution for the fabrication of self-aligned nanostructures by means of conventional photolithography combined with pattern-size reduction techniques has recently been proposed [31, 32]. The method of the thermal oxidation is displayed by patterning nanostructures with different sizes and layouts on a polysilicon-coated silicon material. The current report demonstrated the preparation of polysilicon nanogaps of less than 50 nm on a Si_3N_4–SiO_2–Si substrate. Less than 50 nm gap is expected to eliminate contributions from double-layer capacitance in the dielectric identification of protein, nucleic acid, or small molecule [33]. A number of methods for fabricating nanogaps have already been established. But our goal is to develop a cost-effective and easily performable fabrication technique that can be applied in batch production. We have proved the suitability of our method in such application by fabricating a gap size of 42 ± 5 nm on silicon substrate in a reproducible manner. Preliminary DA characterization data suggests that

such structure can be used in biomolecule sensing with very low level of current supply.

2. Materials and Methods

2.1. Mask Design. A 100 mm p-type silicon wafer is used as a substrate to fabricate the nanogap structure. We design two masks: one for the polysilicon nanogap and the other for the gold electrode by AutoCAD software. The masks are printed onto a chrome glass surface and purchased from a commercial company (Photonic Pte. Limited, Singapore). We apply dry etching (reactive ion etching (RIE)) to fabricate the gap and wet etching (buffer oxide etching (BOE)) to pattern the electrode structures. The anisotropy of RIE is modeled, and the etching profiles are simulated [34].

Figure 1(a) shows the first Mask for nanogap generation with a length of 5000 μm and a width of 2500 μm. The chrome Mask with actual arrangement of device design is shown in Figure 1(b). It consists of 160 dies with 6 different layouts. The angle length of the end electrode is of 1/6th scale starting from 100 μm to 1100 μm with an increment of 100 μm for each unit of S_d length. This is simply for checking the best angle for the best nanogap formation after the etching process. The symbol S_d refers to the dimension of the side angle of the proposed nanogap. The sharpness of the nanogap proportionates to the dimension of S_d.

Figure 2(a) is a schematic device design of Mask 2 with 1500 μm of length and 1500 μm of width. The distance between the two rectangles is 3500 μm. The actual Mask is shown on the chrome glass Figure 2(b).
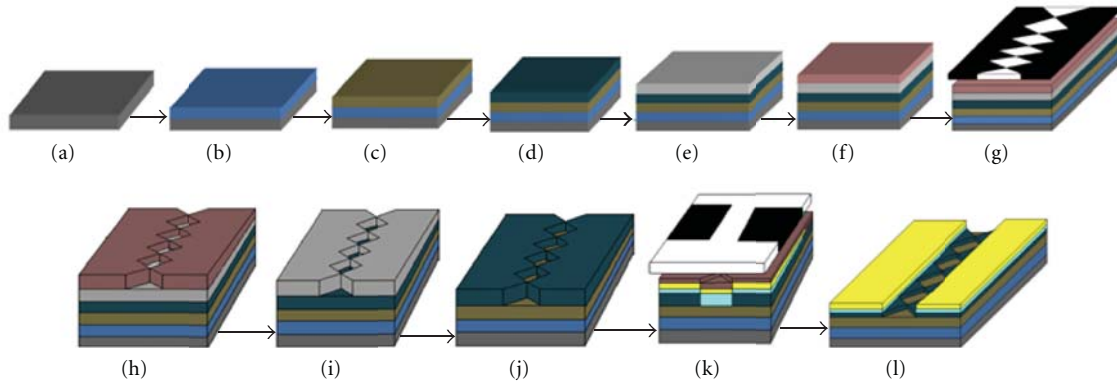
FIGURE 3: The process flow for the fabrication of polysilicon nanogap structure. (a) Silicon wafer starting material; (b) deposit of 50 nm SiO_2 layer; (c) deposit of 150 nm Si_3N_4 layer; (d) deposit of 2000 nm polysilicon layer; (e) deposit of 135 nm Al layer; (f) photoresist coating; (g) Mask 1 exposure; (h) the resist development; (i) wet etching for Al layer; (j) dry etching of polysilicon layer; (k) exposure of Mask 2 after depositing Ti/Au layer; (l) final device after wet etching for the Ti/Au electrode.
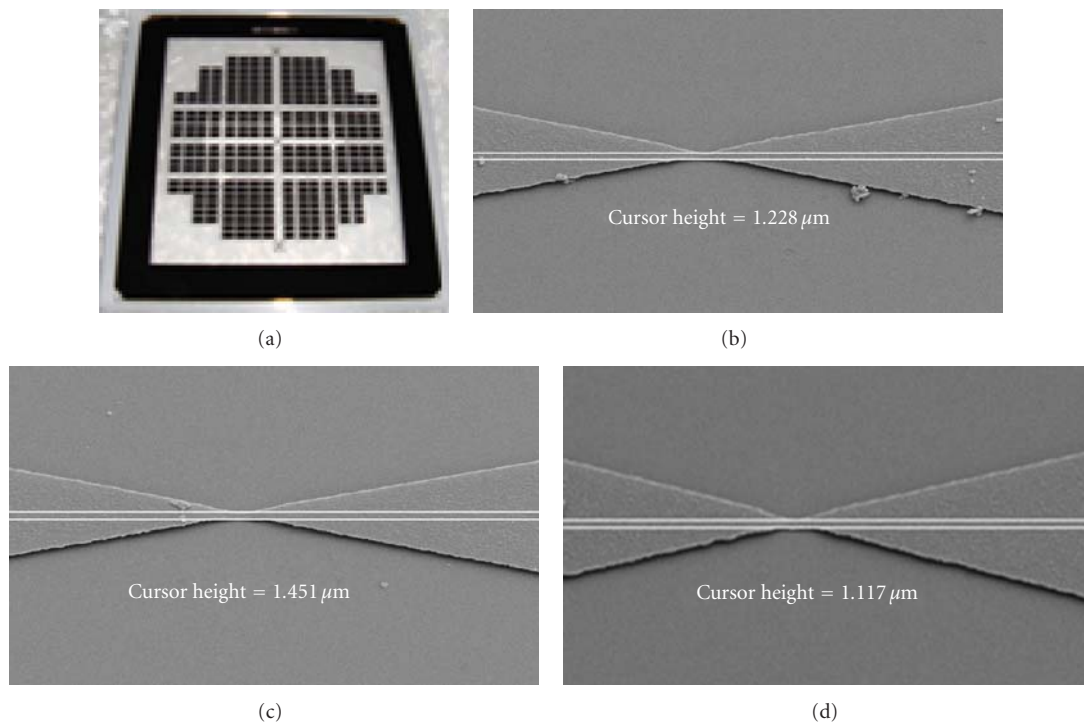

FIGURE 4: Photo Mask used in exposure process (a) SEM images of fabricated polysilicon pattern (b) before (c) after thermal oxidation treatment and (d) at the end of BOE.

2.2. Fabrication of Nanogap Structure.

Figure 3 schematically shows the process flow for the fabrication of gold electrode with desired polysilicon nanogap on silicon substrate. The fabrication is started with the cleaning of the silicon wafer (a), followed by deposition of a 50 nm SiO_2 (b), and 150 nm Si_3N_4 (c), layers by plasma-enhanced chemical vapor deposition (PECVD) equipment. In the next step, a 2000 nm polysilicon layer (d) is deposited by low-power chemical vapor deposition (LPCVD) equipment. After that, a layer of 135 nm aluminum substrate (e) is placed as a hard Mask by physical vapor deposition (PVD) instrument to avoid damage to the polysilicon layer during the etching (RIE) process. The next is the photolithography process. A layer of positive photoresist of 1200 nm thickness (f) is applied on the aluminum substrate, and then exposed to ultraviolet light through Mask 1 (g). Following the development process (h), only the unexposed resist would remain. The wet-etching process of the aluminum layer (i), is performed before removing the resist. Subsequently, the dry-etching process (j), for the polysilicon layer is done to fabricate the nanogap by reduction of gap size. A layer of 150 nm gold substrate is deposited (k), over a 60 nm Ti layer. In the following step, the resist-coating process is applied before exposing Mask 2 and developing the resist, (k). Finally, the wet-etching process of

(a)

(b)

(c)
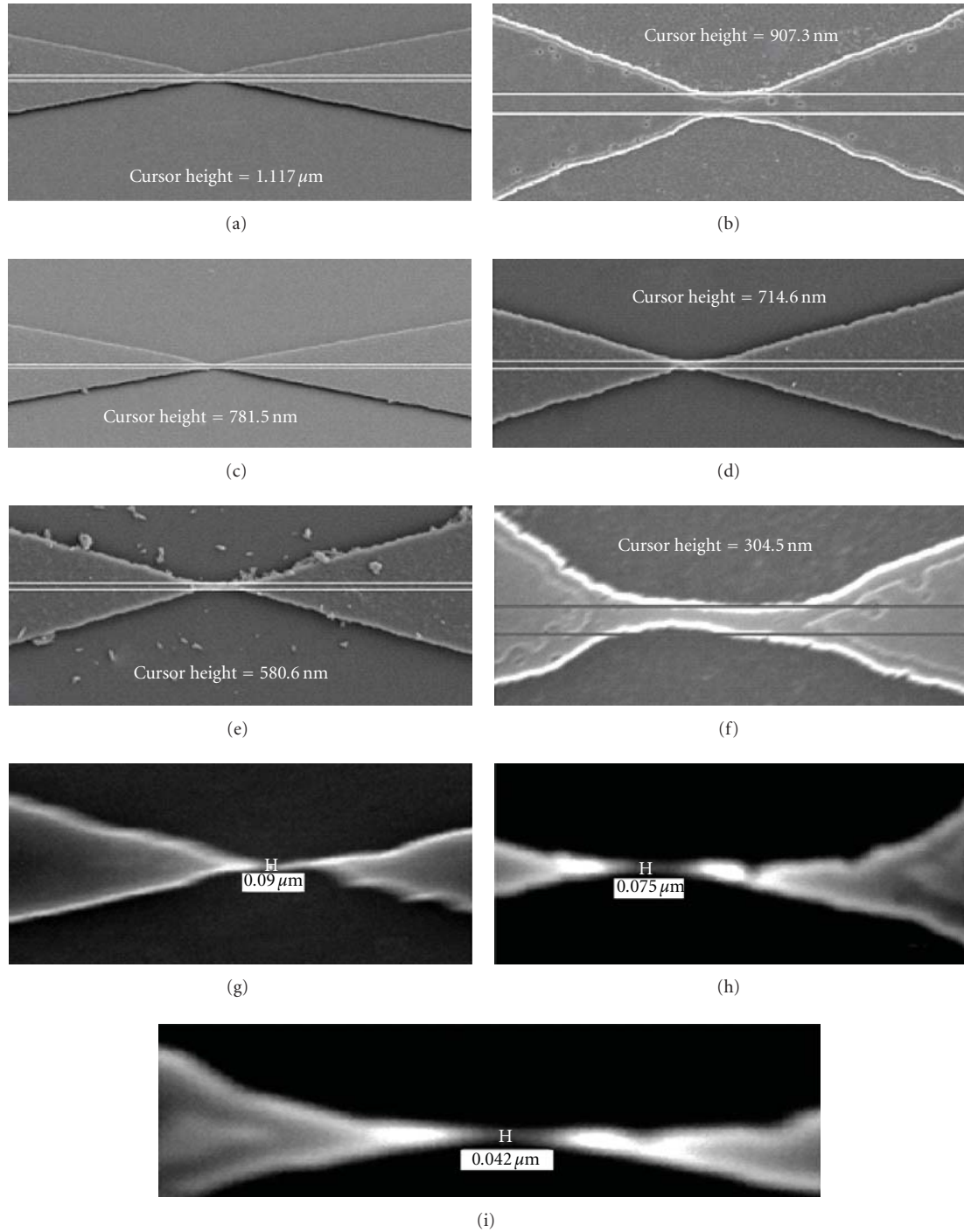

(d)

(e)

(f)

(g)

(h)

(i)

Figure 5: The SEM images of the nanopap structure after etching with BOE solution at the end of each thermal oxidation. Shown are the polysilicon layer at the end of the first to seventh cycles with 15 min of oxidation, from (a) to (g); 7th cycle with 10 min (h), and 5 min (i), of thermal oxidation.

the Ti/Au substrate is performed to obtain the gold electrode with the polysilicon nanogap (l).

Before fabricating the electrode, the aluminum layer is wet-etched and polysilicon layer is dry-etched, using a reactive ion etching (RIE) process with a mixture of tetrafluoromethane (CF_4) and O_2 plasma, according to the Mask layout. The structured polysilicon layer is oxidized at a temperature of $900°C$ in dry O_2 atmosphere to form the oxide layer which is sequentially etched by BOE solution [35]. The oxidation time is varied from 5 to 15 min in each cycle of oxidation and etching depending on the thickness of the polysilicon layer. The prepared structures are optically characterized with a SEM (JOEL) before and after the oxidation process.

2.3. Electrical Characterization. The final device with 90, 75 and 42 nm gap is connected to a dielectric analyzer (Alpha-A High Performance Frequency Analyzer, Novocontrol Technologies, Hundsangen, Germany). Capacitance, permittivity, and conductivity are measured at room temperature with air in the nanogap spaces.

3. Results and Discussion

3.1. Nanogap Fabrication. Figure 4 shows the photo Mask and the SEM cross-sectional view of an original photolithographically patterned polysilicon layer before and after applying the oxidation process. The thickness of the polysilicon layer plays an important role in the stability of the fabricated structure. According to our experience, fabricated structure is frequently broken down if a thin layer of polysilicon (<200 nm) is used. For the current experiment, a polysilicon layer of 2000 nm is chosen because of its higher stability in sequential thermal oxidation and etching. After patterning the polysilicon layer with the designed chrome Mask, the width of the layer at gap location is 1.228 μm (shown by cursor height in Figure 4(b)). Then we apply sequential thermal oxidation and etching in alternation to create a nanogap at the desired position. An oxide layer of silicon dioxide (SiO$_2$) is created on polysilicon layer (Figure 4(c)) by thermal oxidation at 900°C for 15 min [35], and then the fabricated oxide layer is stripped out completely (Figure 4(d)) by the etching process using buffer oxide etching (BOE) solution for 10–15 min [36].

Figures 5(a)–5(i), shows the nanogap structure at the end of each cycle of oxidation and etching. We observe that the polysilicon layer loses its width by 60–280 nm after each cycle of oxidation and etching, depending on the stages of cycles. Thus at the end of the 7th cycle, a 90 nm gap is realized (Figure 5(g)). We then reduce the oxidation time of the structure shown in Figure 5(f) from 15 min to 10 min. After etching with BOE solution for 10–15 min, we found a 75 nm gap (Figure 5(h)). We further reduce the time of oxidation to 5 min to obtain a 42 nm gap (Figure 5(i)). Repetition of the procedures in triplicate experiment generates a nanogap of diameter 42 ± 5 nm showing the feasibility of the method to be used in batch production.

The precise control of nanostructure dimensions is a crucial point for a reproducible fabrication [37]. The pattern size reduction technique can generate an excellent reproducibility by controlling the thickness of oxide layer [35]. Thus, the size of the nanogap structure can be precisely controlled by the careful selection of oxidation time. In order to see the relationship of the pattern-size reduction of the polysilicon layer with oxidation time of the 7th cycle, the thickness of the oxide layer and also the size of the fabricated gap are measured. A plot of layer thickness and oxidation time (Figure 6(a)), demonstrates a proportional relationship. Similar relationship is also observed between nanogap size and oxidation time when they are plotted in a graph (Figure 6(b)). A plot of nanogap size versus oxide layer thickness reveals that gap size is increased over the time of oxidation (Figure 6(c)).
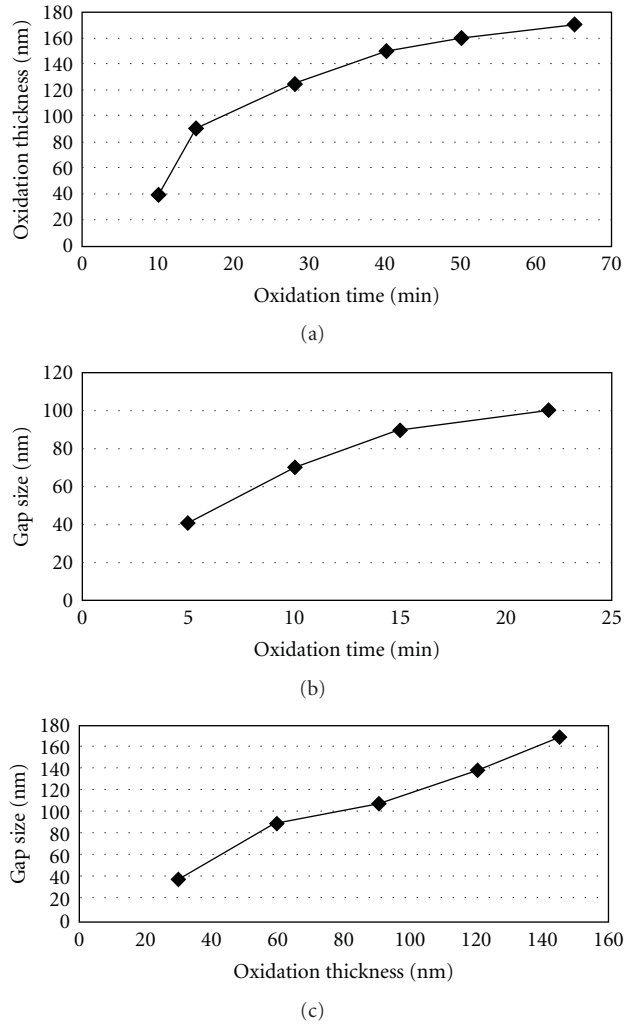

(a)

(b)

(c)

FIGURE 6: The thickness of oxide layer (a) and gap size (b) as a function of the 7th-cycle oxidation time. The relationship of gap size and oxidation thickness is shown in (c).

3.2. Electrical Properties of Fabricated Nanogap Electrodes. Electrical sensing of biomolecules (proteins and nucleic acids) solely relies on the measurement of current and/or voltage to identify target binding [38]. Usually a probe biomolecule is immobilized in the nanogap between the electrode pair, and electrical properties are measured to come up with a decision whether the detection is achieved or not [39]. Detection with low voltage or current is desired as high voltage may burn the anchored biomolecule probes and targets simultaneously, causing the device failure in biological sensing [40]. Gap-size reduction should allow the electrode structure to detect target biomolecule binding with very low supply of current.

Figures 7(a)–7(c), show the capacitance, permittivity, and conductivity parameters of 90, 75 and 42 nm gap electrodes fabricated in the current experiment. An increment of all three parameters, namely, capacitance, (a), permittivity, (b), and conductivity, (c), is achieved with the reduction of gap size. This can be explained with following
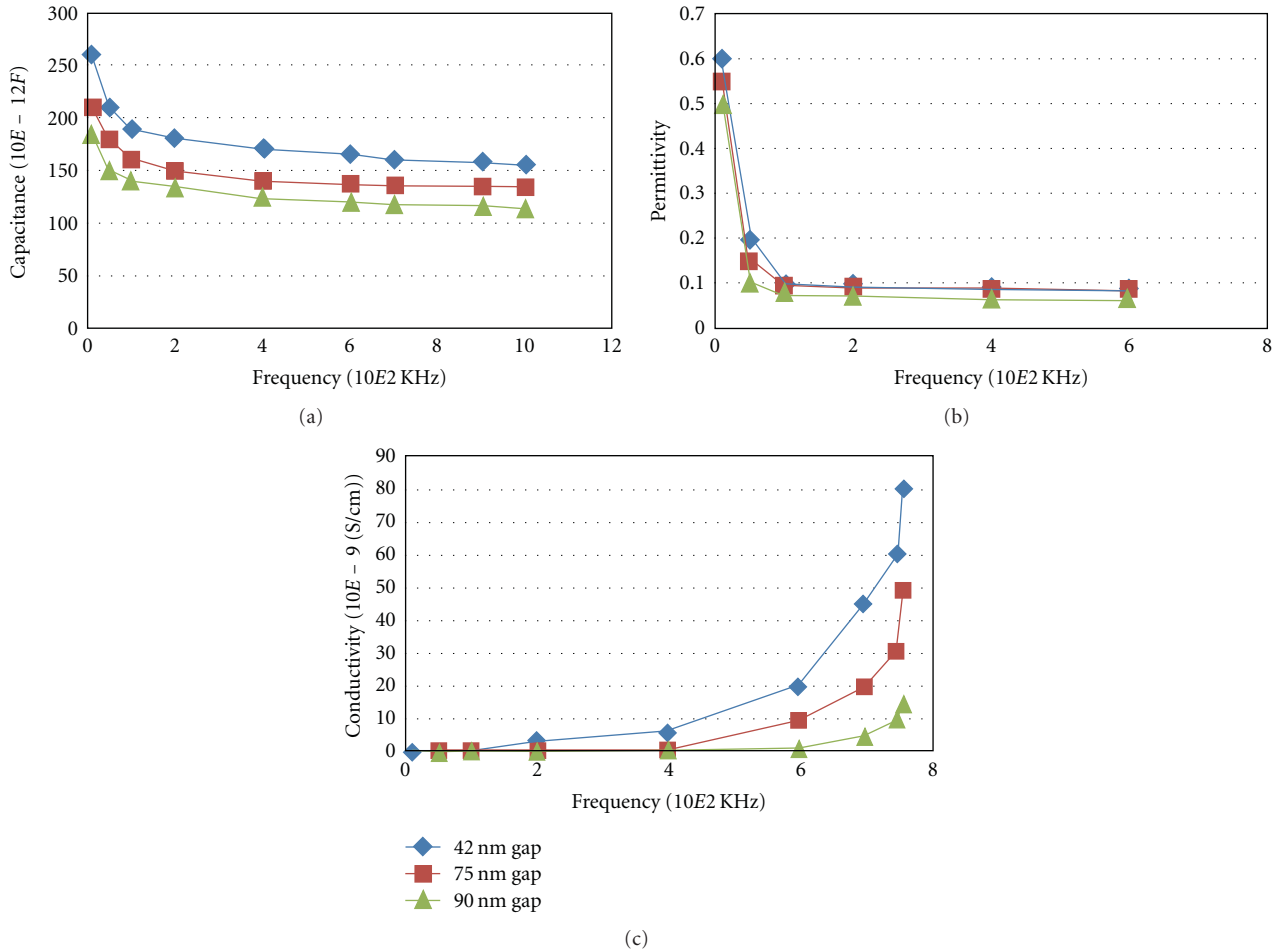
(a)

(b)

(c)

Figure 7: Capacitance (a), permittivity (b), and conductivity (c) profiles of different nanogap electrodes.

simple equation that explains the operating principle of a capacitor:

$$C = \frac{\acute{\varepsilon} * A}{d},$$ (1)

where: $\acute{\varepsilon} = \varepsilon/\varepsilon^\circ$; $\acute{\varepsilon}$: the permittivity; ε°: the permittivity for air in the free space; C: the capacitance value; A: the surface area of the nanogap structure, and d: the size of the gap/distance between the two plates.

Since the gap size, d, is the denominator of the above equation, reduction of gap-size should increased the capacitance of a nanogap capacitor [41]. The equation also reflects that permittivity and capacitance have a linear relationship. Therefore, permittivity enhancement by gap-size reduction is a logical outcome.

Permittivity reflects the index of a material's ability to transmit current without imposing a resistance [42]. On the other hand, conductivity is a measure of a substance capacity to allow the passage of current. Thus, the relation of permittivity, and conductivity is proportional. Therefore, an increment of capacitance, permittivity and conductivity with gap-size reduction suggests that the fabricated nanogap structure can be used in biosensing applications with the minimum supply of power.

Nanogap structures are also implicated to eliminate the formation of electrical double layer between the electrodes in dielectric sensing of proteins and nucleic acids [33]. Dielectric detection of biomolecules is interesting as it is label-free and does not need any reference electrode [43]. In the current experiment, no dielectric measurement is performed as it can be done only after immobilizing the probe biomolecule in the appropriate nanogap. However, our group is working to do it in near future and will be reported in a separate publication.

3.3. Limitation and Efficacy of the Current Method. The current method of fabricating nanogap etches up the surfaces of the plates that separated the gap. More benefit of the desired properties can be realized if integrity of the polysilicon layer can be restored. However, the measurement of capacitance, permittivity, and conductivity clearly reflects certain advantages of the 42 nm gap structure over those of 75 and 90 nms showing its feasible operation with low-current supply. Moreover, the potential of the current method in reproducible fabrication of the desired nanogap has made it a suitable candidate in batch production.

4. Conclusion

A simple method for the fabrication of nanogaps of less than 50 nm in diameter using polysilicon material on a Si–SiO$_2$–Si$_3$N$_4$ substrate is developed. The method combines the conventional lithography and pattern-size reduction techniques to fabricate desired nanogap in a reproducible manner which is essential in batch production. Measurement of several electrical parameters strongly suggests that structure can be used in electrical devices that consume very low level of electricity. The fabricated structure should been abled to detect biomolecules with the minimal supply of electrical current.

Acknowledgments

References

[1] H. Namatsu, Y. Watanabe, K. Yamazaki et al., "Fabrication of Si single-electron transistors with precise dimensions by electron-beam nanolithography," *Journal of Vacuum Science and Technology B*, vol. 21, no. 1, pp. 1–5, 2003.

[2] R. Sasajima, K. Fujimaru, and H. Matsumura, "A metal/insulator tunnel transistor with 16 nm channel length," *Applied Physics Letters*, vol. 74, no. 21, pp. 3215–3217, 1999.

[3] A. Marchi, E. Gnani, S. Reggiani, M. Rudan, and G. Baccarani, "Investigating the performance limits of silicon-nanowire and carbon-nanotube FETs," *Solid-State Electronics*, vol. 50, no. 1, pp. 78–85, 2006.

[4] B. L. Allen, P. D. Kichambare, and A. Star, "Carbon nanotube field-effect-transistor-based biosensors," *Advanced Materials*, vol. 19, no. 11, pp. 1439–1451, 2007.

[5] Y. Ding, Y. Dong, A. Bapat et al., "Single nanoparticle semiconductor devices," *IEEE Transactions on Electron Devices*, vol. 53, no. 10, pp. 2525–2531, 2006.

[6] M. J. Schöning and A. Poghossian, "Bio FEDs (Field-Effect Devices): state-of-the-art and new directions," *Electroanalysis*, vol. 18, no. 19-20, pp. 1893–1900, 2006.

[7] Y. Umasankar and S. M. Chen, "A review on the electrochemical sensors and biosensors composed of nanowires as sensing material," *Sensors*, vol. 8, no. 1, pp. 290–313, 2008.

[8] T. C. Yih and I. Talpasanu, *Micro- and Nano-Manipulations for Biomedical Applications*, Artech-House, London, UK, 2008.

[9] A. Poghossian and M. J. Schöning, "Silicon-based chemical and biological field-effect sensors," in *Encyclopedia of Sensors*, C. A. Grimes, E. C. Dickey, and M. V. Pishko, Eds., pp. 463–534, American Scientific Publishers, Stevenson Ranch, Calif, USA, 2008.

[10] J. Tang, E. P. de Poortere, J. E. Klare, C. Nuckolls, and S. J. Wind, "Single-molecule transistor fabrication by self-aligned lithography and in situ molecular assembly," *Microelectronic Engineering*, vol. 83, no. 4–9, pp. 1706–1709, 2006.

[11] G. J. Zhang, J. H. Chua, R. U. E. Chee et al., "Highly sensitive measurements of PNA-DNA hybridization using oxide-etched silicon nanowire biosensors," *Biosensors and Bioelectronics*, vol. 23, no. 11, pp. 1701–1707, 2008.

[12] G. Sigalov, J. Comer, G. Timp, and A. Aksimentiev, "Detection of DNA sequences using an alternating electric field in a nanopore capacitor," *Nano Letters*, vol. 8, no. 1, pp. 56–63, 2008.

[13] J. Gun, M. J. Schöning, M. H. Abouzar, A. Poghossian, and E. Katzd, "Field-effect nanoparticle-based glucose sensor on a chip: amplification effect of coimmobilized redox species," *Electroanalysis*, vol. 20, no. 16, pp. 1748–1753, 2008.

[14] C. Y. Tsai, Y. H. Tsai, C. C. Pun et al., "Electrical detection of DNA hybridization with multilayer gold nanoparticles between nanogap electrodes," *Microsystem Technologies*, vol. 11, no. 2-3, pp. 91–96, 2005.

[15] X. Liang and S. Y. Chou, "Nanogap detector inside nanofluidic channel for fast real-time label-free DNA analysis," *Nano Letters*, vol. 8, no. 5, pp. 1472–1476, 2008.

[16] Y. H. Cho, S. W. Lee, T. Fujii, and B. J. Kim, "Fabrication of silicon dioxide nanochannel arrays without nanolithography for manipulation of DNA molecule," *Microelectronic Engineering*, vol. 85, no. 5-6, pp. 1275–1277, 2008.

[17] Y. Chen and A. Pepin, "Nanofabrication: conventional and nonconventional methods," *Electrophoresis*, vol. 22, no. 2, pp. 187–207, 2001.

[18] C. C. Meng, G. R. Liao, and S. S. Lu, "Formation of submicron T-gate by rapid thermally reflowed resist with metal transfer layer," *Electronics Letters*, vol. 37, no. 16, pp. 1045–1046, 2001.

[19] K. S. Kim, K. N. Lee, and Y. Roh, "Formation of nanometer-scale structures using conventional optical lithography," *Thin Solid Films*, vol. 516, no. 7, pp. 1489–1492, 2008.

[20] T. Ishida, M. Horikawa, M. Nakano, Y. Naitoh, K. Miyake, and W. Mizutani, "Field effect of self-assembled organic multilayer in nanogap electrode; current oscillation behaviour at room temperature," *Japanese Journal of Applied Physics*, vol. 44, no. 12–15, pp. L465–L468, 2005.

[21] Y. K. Choi, J. I. Zhu, J. Grunes, J. Bokor, and G. A. Somorjai, "Fabrication of sub-10-nm silicon nanowire arrays by size reduction lithography," *Journal of Physical Chemistry B*, vol. 107, no. 15, pp. 3340–3343, 2003.

[22] S. Hashioka, H. Tsuritani, T. Obata, M. Kadosaki, S. Fujiki, and K. Tanino, "Fabrication technique for preparing nanogap electrodes by conventional silicon processes," *Japanese Journal of Applied Physics*, vol. 44, no. 6, pp. 4213–4215, 2005.

[23] Y. H. Cho, S. W. Lee, B. J. Kim, and T. Fujii, "Fabrication of silicon dioxide submicron channels without nanolithography for single biomolecule detection," *Nanotechnology*, vol. 18, no. 46, Article ID 465303, 2007.

[24] R. Juhasz and J. Linnros, "Silicon nanofabrication by electron beam lithography and laser-assisted electrochemical size-reduction," *Microelectronic Engineering*, vol. 61-62, pp. 563–568, 2002.

[25] C. Lee, E. H. Yang, N. V. Myung, and T. George, "A nanochannel fabrication technique without nanolithography," *Nano Letters*, vol. 3, no. 10, pp. 1339–1340, 2003.

[26] A. F. Morpurgo, C. M. Marcus, and D. B. Robinson, "Controlled fabrication of metallic electrodes with atomic separation," *Applied Physics Letters*, vol. 74, no. 14, pp. 2084–2086, 1999.

[27] K. H. Chung, S. K. Sung, D. H. Kim et al., "Nanoscale multi-line patterning using sidewall structure," *Japanese Journal of Applied Physics*, vol. 41, no. 6, pp. 4410–4414, 2002.

[28] G. Georgiev, M. Müller-Wiegand, A. Georgieva, K. Ludolph, and E. Oesterschulze, "Lithography-free fabrication of sub-100 nm structures by self-aligned plasma etching of silicon dioxide layers and silicon," *Journal of Vacuum Science and Technology B*, vol. 21, no. 4, pp. 1361–1363, 2003.

[29] S. Hashioka, T. Mogi, and H. Matsumura, "Novel nano-fabrication technique with low edge roughness," *Japanese Journal of Applied Physics*, vol. 42, no. 6, pp. 4169–4172, 2003.

[30] S. Strobel, K. Arinaga, A. Hansen, and M. Tornow, "A silicon-on-insulator vertical nanogap device for electrical transport measurements in aqueous electrolyte solution," *Nanotechnology*, vol. 18, no. 29, Article ID 295201, 2007.

[31] J. Platen, A. Poghossian, and M. J. Schöning, ""Microstructured nanostructures"—nanostructuring by means of conventional photolithography and layer-expansion technique," *Sensors*, vol. 6, no. 4, pp. 361–369, 2006.

[32] A. Poghossian, J. Platen, and M. J. Schöning, "Towards self-aligned nanostructures by means of layer-expansion technique," *Electrochimica Acta*, vol. 51, no. 5, pp. 838–843, 2005.

[33] D. D. Carlo, H. Kang, X. Zeng, K.-H. Jeong, and L. P. Lee, "Nanogap-based dielectric immunosensing," in *Proceedings of the 12th International Conference on Solid State Sensors, Actuators and Microsystems*, pp. 1180–1180, IEEE, Boston, Mass, USA, June 2003.

[34] H. Spelthahn, A. Poghossian, and M. J. Schöning, "Self-aligned nanogaps and nanochannels via conventional photolithography and pattern-size reduction technique," *Electrochimica Acta*, vol. 54, no. 25, pp. 6010–6014, 2009.

[35] H. Xiao, *Introduction to Semiconductor Manufacturing Technology*, Prentice Hall, Upper Saddle River, NJ, USA, 2001.

[36] V. K. Rathi, M. Gupta, and O. P. Agnihotri, "The dependence of etch rate of photo-CVD silicon nitride films on NHF content in buffered HF," *Microelectronics Journal*, vol. 26, no. 6, pp. 563–567, 1995.

[37] C. Laslau, Z. Zujovic, and J. Travas-Sejdic, "Theories of polyaniline nanostructure self-assembly: towards an expanded, comprehensive Multi-Layer Theory (MLT)," *Progress in Polymer Science*, vol. 35, no. 12, pp. 1403–1419, 2010.

[38] T. G. Drummond, M. G. Hill, and J. K. Barton, "Electrochemical DNA sensors," *Nature Biotechnology*, vol. 21, no. 10, pp. 1192–1199, 2003.

[39] X. Chen, Z. Guo, G.-M. Yang et al., "Electrical nanogap devices for biosensing," *Materials Today*, vol. 13, no. 11, pp. 28–41, 2010.

[40] S. Kyu Kim, H. Cho, H. J. Park, D. Kwon, J. Min Lee, and B. Hyun Chung, "Nanogap biosensors for electrical and label-free detection of biomolecular interactions," *Nanotechnology*, vol. 20, no. 45, Article ID 455502, 2009.

[41] M. Yi, K. I. H. Jeong, and L. P. Lee, "Theoretical and experimental study towards a nanogap dielectric biosensor," *Biosensors and Bioelectronics*, vol. 20, no. 7, pp. 1320–1326, 2005.

[42] A. A. Saif and P. Poopalan, "Effect of the film thickness on the impedance behavior of sol-gel Ba 0.6Sr0.4TiO3 thin films," *Physica B*, vol. 406, no. 6-7, pp. 1283–1288, 2011.

[43] C. Berggren and G. Johansson, "Capacitance measurements of antibody-antigen interactions in a flow system," *Analytical Chemistry*, vol. 69, no. 18, pp. 3651–3657, 1997.

Research Article

Fabrication of Coated-Collagen Electrospun PHBV Nanofiber Film by Plasma Method and Its Cellular Study

Jafar Ai,[1] Saeed Heidari K,[2] Fatemeh Ghorbani,[3] Fahimeh Ejazi,[3] Esmaeil Biazar,[4] Azadeh Asefnejad,[3] Khalil Pourshamsian,[4] and Mohamad Montazeri[5]

[1] Department of Tissue Engineering, Faculty of Advanced Technologies, Tehran University of Medical Sciences, Tehran, Iran
[2] Clinical Proteomics Research Center, Faculty of Paramedical Sciences, Shahid Beheshti University of Medical Sciences, Tehran, Iran
[3] Department of Biomaterial, Faculty of Biomedical Engineering, Science and Research Branch-Islamic Azad University, Tehran, Iran
[4] Department of Chemistry, Islamic Azad University-Tonekabon Branch, Tonekabon, Iran
[5] Faculty of Medical Sciences, Babol University of Medical Sciences, Iran

Correspondence should be addressed to Esmaeil Biazar, e.biazar@tonekaboniau.ac.ir

Background. Tissue engineering is defined as the designing and engineering of structures to rebuild and repair a body damaged tissue. Scaffolding Poly Hydroxy Butyrate Valerate (PHBV) has shown good biocompatibility and biodegradable properties. Nanofibers have improved the performance of biomaterials, and could be considered effective. One of the important methods for designing nanofiber scaffold is the electrospinnig method. In this study, PHBV nanofibers were well designed and then, modified with the immobilized collagen via the plasma method. The samples were evaluated by ATR-FTIR, SEM, contact angle, and, finally, cell culture. *Results.* ATR-FTIR structural analysis showed the presence of collagen on the nanofiber surfaces. The SEM images showed the size average of nanofibers as to be about 280 nm; that increased with a collagen coating up to 300 nm. Contact angle analysis showed 67 degree for uncoated nanofibers and 56 degree for coated nanofibers. Cellular investigations (USS cells) showed better adhesion and cell growth and proliferation of coated samples than uncoated samples. *Conclusions.* In this work, the PHBV nanofibers with a size average about 280 nm were designed. Nanofibers were successfully coated with collagen via the plasma methods. These collagen-coated nanofibers could be used well for tissue engineering.

1. Introduction

Poly Hydroxy Butyrate Valerate (PHBV) is a biomaterial that is used in a variety of applications including surgical sutures, wound dressing, drug delivery, and tissue engineering. This is due to its specific properties such as good biocompatibility, biodegradability, and nontoxicity as well as its piezoelectricity features. However, this material is a hydrophobic polyester which should be modified with other materials until it improves its cell adhesion and hydrophilicity properties [1–5]. It has been generally accepted that extracellular matrix mimics may improve the attachment, proliferation, and viability of the cultured cells [6]. Electrospinning has been rapidly developed into a technique to prepare nanofibers with the diameter ranging from tens of nanometers to several microns [7–9]. The electrospun fibrous mats also show extremely high surface area and large porosity. Besides, the fibrous structure of the electrospun mats may mimic the extracellular matrix. It is well known that the collagen is a natural extracellular matrix component of nearly every tissue such as bone, skin, tendon, and ligament. Fiber diameters of the electrospun nanofibrous mats even approach that of collagen fiber bundles, between 50 and 500 nm [9]. Therefore, during the last few years, many works considering the tissue engineering of electrospun nanofibers have been reported. Most recently, electrospun nanofibers were prepared by Yang et al. and were applied in neural tissue engineering [10]. Although the presented nanofibers may mimic the morphologies of extracellular matrix to some extent, some modifications are still required to create a friendly environment for the cells attachment, proliferation, and functions such as communications. Some natural materials such as collagen

and fibronectin and some peptides have been reported as scaffold modifiers [11, 12]. Controlling surface properties is very important for the high performance of adhesion. Biomaterials wettability is an important factor in the surface modification of materials. Surface modification of hydrophobic polymer surfaces can be achieved by wet (acid, alkali), dry (plasma), and radiation treatments (ultraviolet radiation and laser) [13–16]. Nonthermal and low-pressure plasma have been used in a series of surface treatment applications. The majority of plasma-assisted technologies are based on low-pressure processes [17]. The treatment of polymeric materials with plasma is a frequently used technique to accomplish surface modifications that affects chemical composition as well as surface topography. Moreover, microwave discharges are routinely employed in the processing of materials to deposit films as well as coatings [18, 19]. In this study, the USS cells were used. The USSCs were first isolated from the umbilical cord blood in 2003 by Jager et al., and their differentiation capacity for transplantation was evaluated [20]. Kogler et al. (2004) also evaluated these cells for cytokine production. The USSCs are pluripotent, and also they are considered as the rare cell populations in umbilical cord blood. They have a high potential to proliferate and differentiate; thus, they are considered as valuable sources in cell therapy [21]. The USSCs are CD45−, the adherent and HLA class II-negative stem cells with a long telomerase. Moreover, these cells possess a unique cytokine profile and have a high percentage of productions associated with self-renewing factors. In spite of other cord blood-derived mesenchymal cells, differentiated only into osteoblasts, chondrocytes, adipocytes [22], and neurons [21], the USSCs have the differentiation potential into osteoblasts, chondrocytes, blood cells, neurons, hepatocytes, and heart tissues under ex vivo conditions [21]. This cell expresses different factors, including adherent cells, growth factors, and various cytokines such as SCF, VEGF, GM-CSF, M-CSF, TGF-1, IL-6, G-CSF, LIF, Flt3 ligand, TPO, HGF, SDF-1, IL-15, IL-12, IL-8, and IL-1, [22]. In this study, the coated collagen PHBV nanofibers were obtained through the plasma method. The samples were evaluated by ATR-FTIR, SEM and the contact angle as well as the cell culture with USSCs.

2. Materials and Methods

2.1. Nanofiber Preparation.
A poly (3-hydroxybutyrate-co-3-hydroxyvalerate) PHBV containing 5 mol% of 3-hydroxyvalerate with 680,000 molecular weight was purchased from Sigma Chemical Co. 2,2,2-trifluoroethanol (TFE) to prepare PHBV solution was also purchased from Sigma-Aldrich Chemicals and was used as received without further purification. An electrospinning apparatus used in this study was prepared by the Asia Nanomeghyas Company (Iran). The PHBV was dissolved at determined concentration in TFE. The PHBV solution (2%w) in a glass syringe was controlled by the syringe pump. A positive high voltage source through a wire was applied at the tip of the syringe needle. In this situation, a strong electric field was generated between the PHBV solution and a collector. When the electric field reached a critical value with increasing voltage,
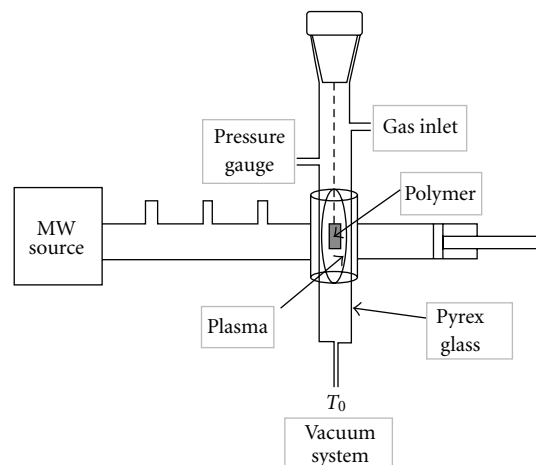

Figure 1: Experimental setup of microwave plasma.

the mutual charge repulsion overcame the surface tension of the polymer solution and the electrically charged jet was ejected from the tip of a conical shape as the Taylor cone. Ultrafine fibers were formed by the narrowing of the ejected jet fluid as it underwent increasing surface charge density due to the evaporation of the solvent. The electrospun PHBV nanofibrous mat was carefully detached from the collector and was dried in vacuo for 2 days at room temperature to remove solvent molecules completely. The used parameters for this nanofibers preparation can be seen in Table 1.

2.2. Plasma Treatment.
In our current experimental observation, we used a microwave plasma source to modify the surface of the polystyrene samples. The microwave plasma has significant advantage over other techniques like Radio Frequency Glow Discharge (RFGD), frequently used in polymer surface modifications. Microwave sources could be operated at low pressures (10^{-3} to 10^{-1} mbar), which reduced the risk of gas phase contamination during processing. Moreover, the plasma properties could be controlled conveniently by adjusting the microwave power. Hence, the surface modification of this polymer became important. In this paper, we have demonstrated the effect of microwave plasma on the surface property of PHBV nanofibers with active gas (oxygen) at different times. Before exposure, the nanofibers were cut into 1×1 cm sections. Then, they were placed within the ethanol solution for 24 hours to eliminate pollution and fats on the films. After removing the films from the solution, they were well washed in distilled water. The samples were placed in the plasma chamber and exposed to oxygen gas during 30 and 60 sec. The irradiated samples were investigated by structural analysis and microscopic and cellular investigations at times. The plasma surface treatment was reached in the microwave-induced plasma with a surface wave at 100 W. The experimental setup has been shown in Figure 1.

2.3. Collagen Immobilization.
Collagen (type I, from bovine Achilles tendon, purchased from Sigma) was immobilized onto the nanofiber surface based on the following protocol.

TABLE 1: Used parameters for nanofibers preparation.

Syringe Diameter (mm)	Dram speed (rpm)	Injected speed (mL/min)	Syringe tip distance to deram (mm)	Voltage (kv)	Temperature (°C)	Time (h)
17	1000	2	75	20	30	7

A weighted amount of the plasma modified nanofibrous mat was rinsed with acetic acid buffer solution (50 mM, pH: 5). Then, the radiated mat was submerged into the collagen solution (15 mg/mL in acetic acid solution, 50 mM, pH: 5) and was shaken gently for 2 h at 50°C. The obtained samples were placed inside a vacuum oven so that they would fully lose humidity.

2.4. Fourier Transmission Infrared Spectroscopy.

The samples were examined by FTIR (Bruker-Equinox 55; Bruker Optics, Billerica, Mass) before and after adjustment. The samples were scratched into powder and were produced as capsules using KBr and, then, were put to investigation.

2.5. Scanning Electron Microscopy.

The surface characteristics of various modified and unmodified films were studied by scanning electron microscopy (SEM; Cambridge Stereoscan, model S-360; Cambridge Instruments, Wetzlar, Germany) to analyze the changes in the surface morphology. The films were first coated with a gold layer (Joel fine coat, ion sputter for 2 hours) to provide surface conduction before their scanning.

2.6. Contact Angle Analysis.

The sample surfaces static contact angles were investigated by a contact-angle-measuring device (Krüss G10; Krüss, Matthews, NC) following the sessile drop method.

2.7. Cellular Analysis

2.7.1. Culture and Isolation of the USSC from Fresh Umbilical Cord Blood.

After consent from mothers, their umbilical cords were obtained from the cord vein. Only 40% of the cord blood samples contained USSCs. The mean age of donors was 28 years. After collecting the samples, the red blood cells were lysed using ammonium chloride (NH_4CL) and the isolation procedure continued by Ficoll. Then the samples were rinsed twice with sterile phosphate-buffered saline (pH 7.4). After centrifuging, the resultant cells were placed in Dulbecco's modified Eagle's medium (DMEM) low glucose, which had been enriched with 100 nmol dexamethasone, 10% fetal bovine serum (FBS), penicillin, and streptomycin. The first medium exchange process was done for 24 hours, then every 4 days. When 80% of the flask surface area was covered by the cells, the cells were passed by using 0.25% trypsin and ethylenediaminetetraacetic acid (EDTA). The USSCs were regularly expanded on the culture medium; and the 37°C temperature and 5% of CO_2 were required for the growth. The USSCs were first trypsinized and counted. The tubes, containing 10^5-10^6 cells, were incubated on a rocker rotator for 10 to 6 hours and centrifuged at 1000 rpm

for 6 minutes, and 3% human serum was added to cell deposition thereafter. The resultant mixture remained at room temperature for 30 minutes. The cells were again centrifuged as above, and the PBS was added to the cell deposition. The cell mixture was passed through a nylon mesh, and then 100 μL of cells was added to each tube with the following antibodies: anti-CD90, anti-CD105, anti-CD166, anti-CD45, anti-CD73, and anti-CD34. Next, they were kept at 4°C out of light for 45 minutes. After washing, the cells were fixed in 100 μL of 1% paraformaldehyde. Finally, the flow cytometric analysis was carried out. The karyotype analysis was performed on USSC. The first and last passages were chosen for karyotype analysis. The cells were first placed in an incubator with 0.1 μg/mL colcemid for 3 to 4 hours. Next, they were trypsinized, and 0.075 of M KCL solution was added. The cells were incubated with 5% CO_2 at 37°C for 20 minutes. In the next stage, methanol and acetic acids in ratio of 1 : 3 were added for fixing the samples. Finally, the cells were scattered over the slide surface, and the chromosomes were subjected to karyotype analysis.

2.7.2. Cell Culture Study on the Polymer Surface.

The tissue culture polystyrenes (TCPSs) as control samples were well cleaned and sterilized by the autoclave method. Individual samples were placed in Petri dishes using a sterilized pincer; the USSC suspension was transferred to a flask (25 cm) containing DMEM, 2 mML-glutamine, penicillin (100 μL/mL), streptomycin (100 μL/mL), and FBS 10%. The suspension was then placed in an incubator (5% CO_2, 37°C). The USSCs were proliferated in the flask and were washed using the PBS. Then the trypsin enzyme/EDTA was added to the flask (37°C), and the flask was incubated for 2 minutes. The culture media (FBS/DMEM) was added to the flask, and the cells were gently pipetted. The cell suspension was transferred to a falcon tube (15 mL) and centrifuged (1410 rpm) for 5 minutes. The solution was removed and the precipitation was transferred to a new flask (75 cm) for reculturing. Pieces of cell culture (1 × 1 cm) from the petri dish (control) and the main sample were placed individually in one of the Petri dish wells by using a sterilized pincer. 100,000 cells/well were seeded into a 24-well culture plate removed by pipette and poured onto the control and the main samples. Then all samples were placed in Memmert incubator at 37°C for 48 hours and studied using a ceti microscope (Wolf Laboratories, UK). Cell proliferation was determined by the MTT assay for viable cell numbers. The MTT tetrazolium compound was reduced by living cells in a colored formazan product that was soluble in the tissue culture medium. The quantity of formazan product was directly proportional to the number of viable cells in the culture. The assays were performed by
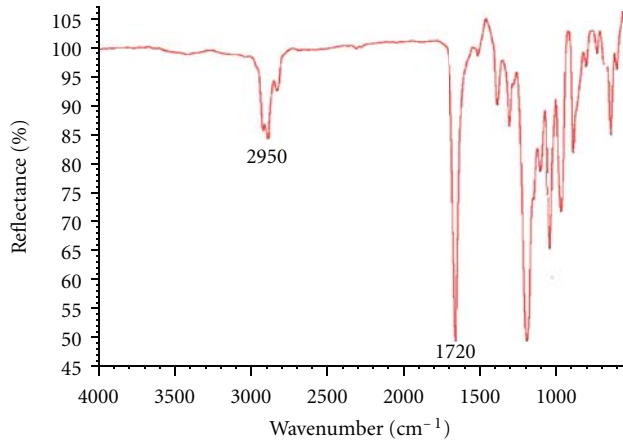
Figure 2: FTIR analysis of uncoated nanofiber film.

Figure 3: FTIR analysis of collagen film.

adding 20 μL of MTT solution (Sigma-Aldrich) and 200 μL of fresh medium to each well after aspirating the spent medium and incubating at 37°C for 4 hours with protection from light. Colorimetric measurement of formazan dye was performed at a wavelength of 570 nm using a Rayto microplate reader.

3. Results

3.1. FTIR Results. The results, from the ATR-FTIR spectrum of the uncoated nanofiber sample, the collagen film, and the nanofiber sample modified with collagen, have been shown in Figures 2–4. In Figure 2, the strong band in 1720 cm^{-1} has been shown to be related to the C=O group. The stretching band in 800–975 cm^{-1} has been shown to be related to the –C–O–C–O group, and the stretching band in 2800–3000 cm^{-1} has been shown to be related to the –CH$_3$ groups.

Figure 3 illustrates the ATR-FTIR spectra of collagen film. The spectra show the strong band in 1720 cm^{-1} as related to the C=O group and stretching bands in 2900–3000 cm^{-1} as related to the –CH$_3$ groups. The stretching bands in 3318 cm^{-1} and 3746 cm^{-1} are related to the OH and NH groups.

Figure 4 also shows the strong band in 1720 cm^{-1} as related to the C=O group, the stretching band in 800–975 cm^{-1} as related to the –C–O–C– group, and the stretching bands in 2800–3000 cm^{-1} as related to the –CH$_3$ groups. The stretching bands in 3429 cm^{-1} and 3783 cm^{-1} are related to the OH and NH groups due to the presence of collagen.

3.2. SEM Investigations. Figures 5 and 6 show the electron microscopy images of the uncoated and the coated nanofibers with collagen in different magnifications. Figure 5 shows the nanofiber mat prepared by the electrospinning method of different magnifications ((a) 5000×, (b) 10000× and, (c) 20000×).

Figure 6 shows the collagen-coated nanofiber mat prepared by the electrospinning method of different magnifications ((a) 5000×, (b) 10000×, and (c) 20000×).

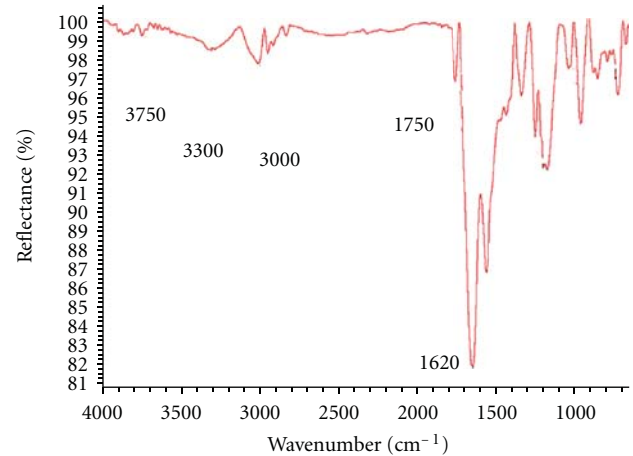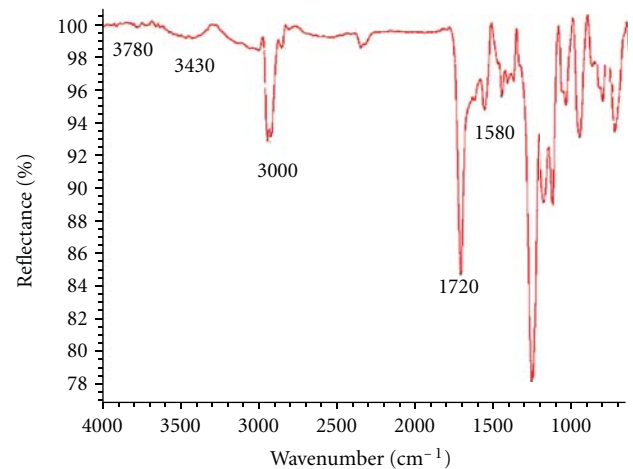Figure 4: FTIR analysis of coated nanofiber film.

Table 2: Contact angle for uncoated and coated collagen nanofibers.

T (°C)	PHBV nanofiber θ (deg)	Coated collagen nanofiber (treated plasma at 30 s) θ (deg)	Coated collagen nanofiber (treated plasma at 60 s) θ (deg)
25	67 ± 3.2°	58 ± 1.9°	56 ± 1.2°

3.3. Contact Angle Results. Table 2 shows the contact angle obtained for the uncoated and the coated collagen nanofibers. The contact angles of 67° and 56–58° were obtained for the uncoated and the coated nanofibers, respectively. The 10° difference in the contact angle, obtained for the 2 samples, shows a better hydrophilicity of the collagen-coated nanofibers than the uncoated nanofibers.

3.4. Cellular Study. Table 3 shows the MTT assay for TCPS (control), the uncoated nanofiber, and the coated collagen nanofiber samples by plasma in different times. The results showed a high viability for the samples of the uncoated
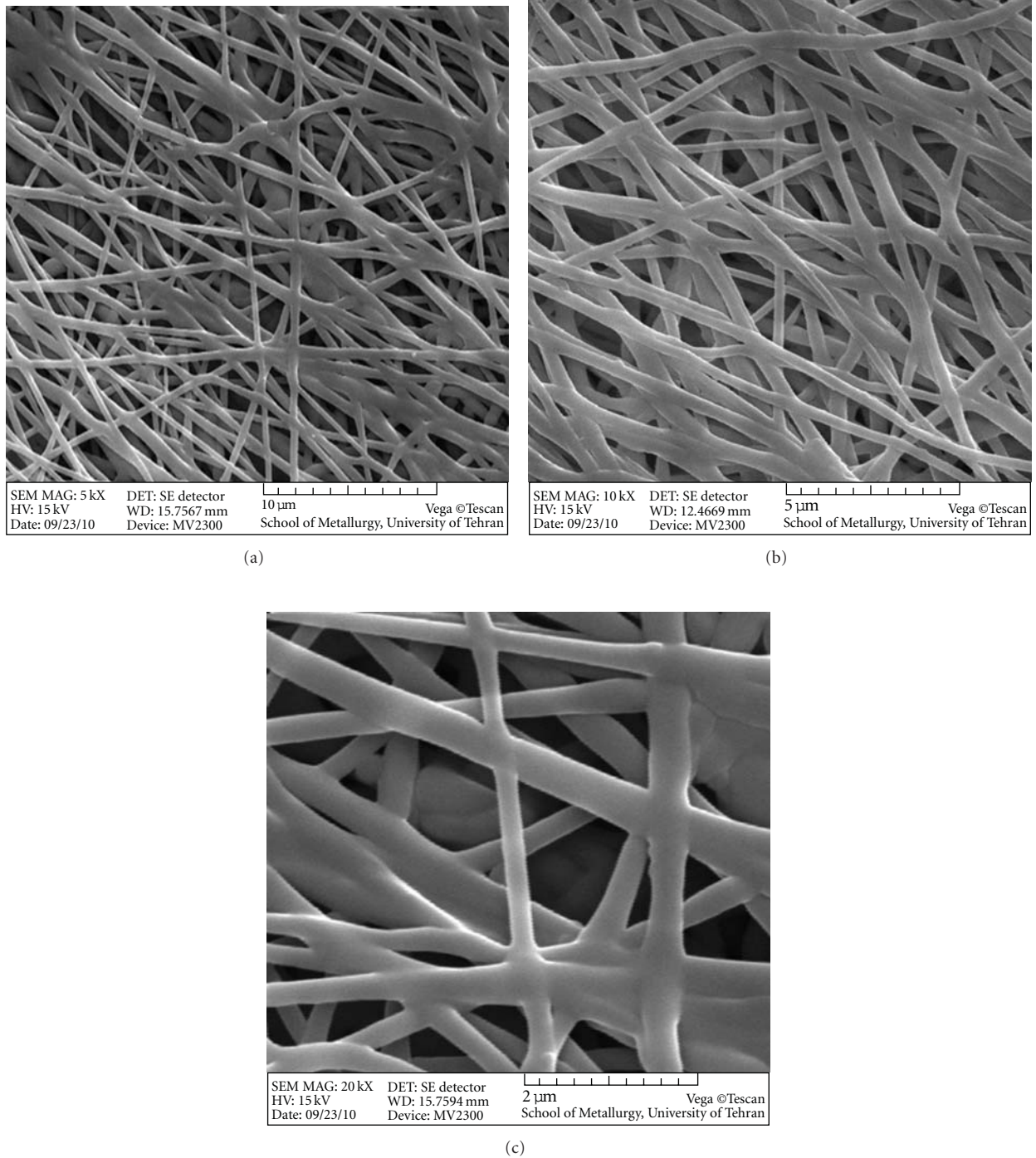
(a)

(b)

(c)

FIGURE 5: SEM images of PHBV nanofibers in different magnifications ((a) 5000×, (b) 10000×, and (c) 20000×).

nanofiber and the collagen-coated nanofiber by plasma in the different times of 30 and 60 seconds (112, 130, and 164% resp.). Figure 7 shows images of the cell culture on the nanofibers and the control sample. Image (a) is related to the control sample and images (b), (c), and (d) are related to the uncoated nanofiber and the collagen-coated nanofiber by plasma in the different times of 30 and 60 s.

4. Discussion

ATR-FTIR structural analysis showed successfully the presence of collagen on the nanofiber surfaces. The smooth and homology nanofibers have been clearly shown in the figures. The size average was obtained for the normal nanofibers to be about 280 nm. The smooth and homology
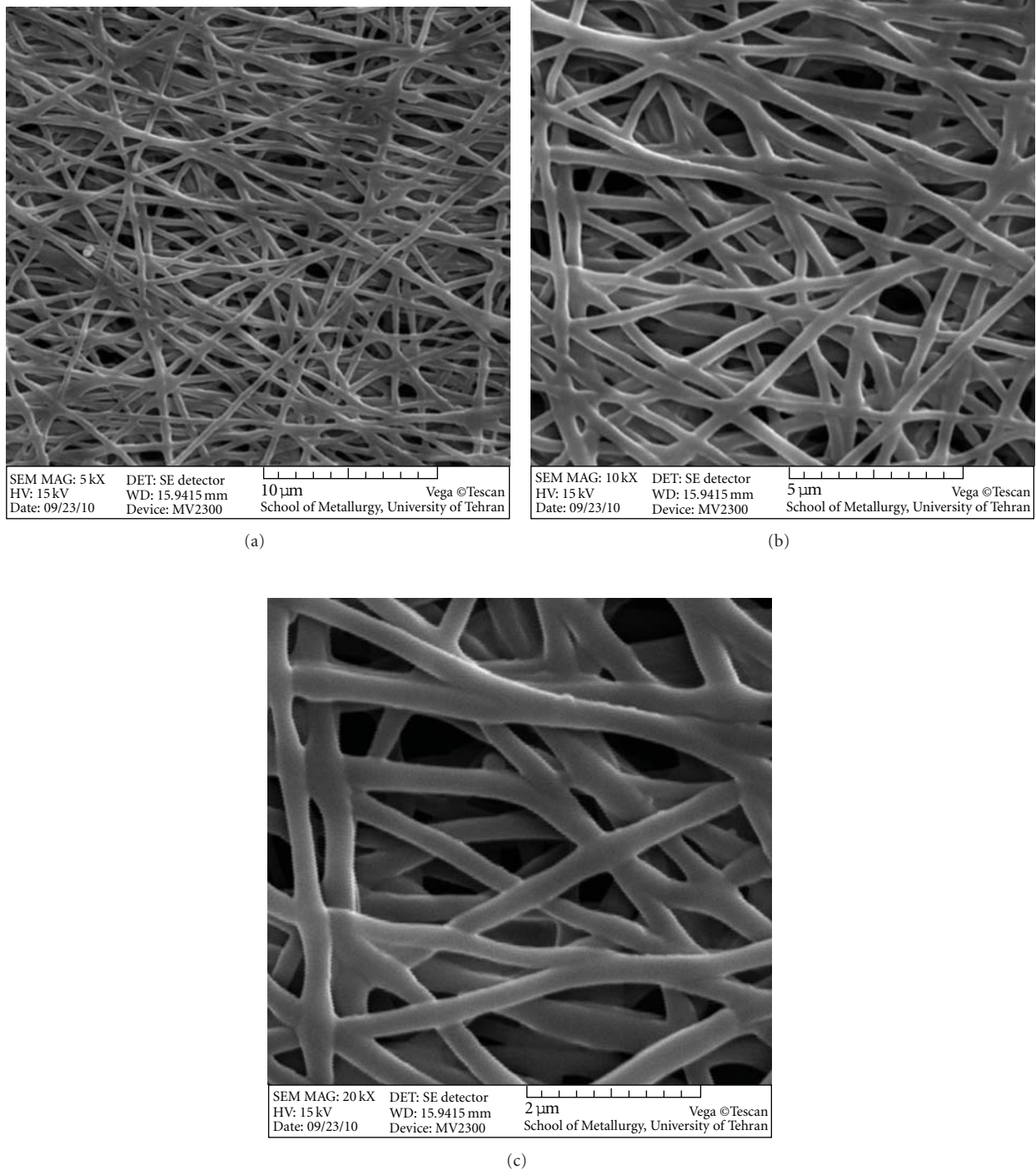
SEM MAG: 5 kX | DET: SE detector
HV: 15 kV | WD: 15.9415 mm
Date: 09/23/10 | Device: MV2300
10 µm
Vega ©Tescan
School of Metallurgy, University of Tehran

(a)

SEM MAG: 10 kX | DET: SE detector
HV: 15 kV | WD: 15.9415 mm
Date: 09/23/10 | Device: MV2300
5 µm
Vega ©Tescan
School of Metallurgy, University of Tehran

(b)

SEM MAG: 20 kX | DET: SE detector
HV: 15 kV | WD: 15.9415 mm
Date: 09/23/10 | Device: MV2300
2 µm
Vega ©Tescan
School of Metallurgy, University of Tehran

(c)

FIGURE 6: SEM images of coated collagen PHBV nanofibers in different magnifications ((a) 5000×, (b) 10000×, and (c) 20000×).

modified nanofibers have been clearly shown in the figures. The size average was obtained for the modified nanofibers to be about 400 nm, whose increasing is due to collagen coated on the PHBV surfaces. The 10° of difference in the contact angle, obtained for the two samples (normal and modified nanofibers), shows a better hydrophilicity of the collagen-coated nanofibers than of the uncoated nanofibers.

The results showed a high viability for the samples of the uncoated nanofiber and the collagen-coated nanofiber by plasma in the different times of 30 and 60 second but the collagen-coated nanofiber by plasma in 60 s showed a better viability than the uncoated nanofiber and the radiated sample in 30 s. Also, these samples caused more cells to proliferate. Cellular images showed well growth in
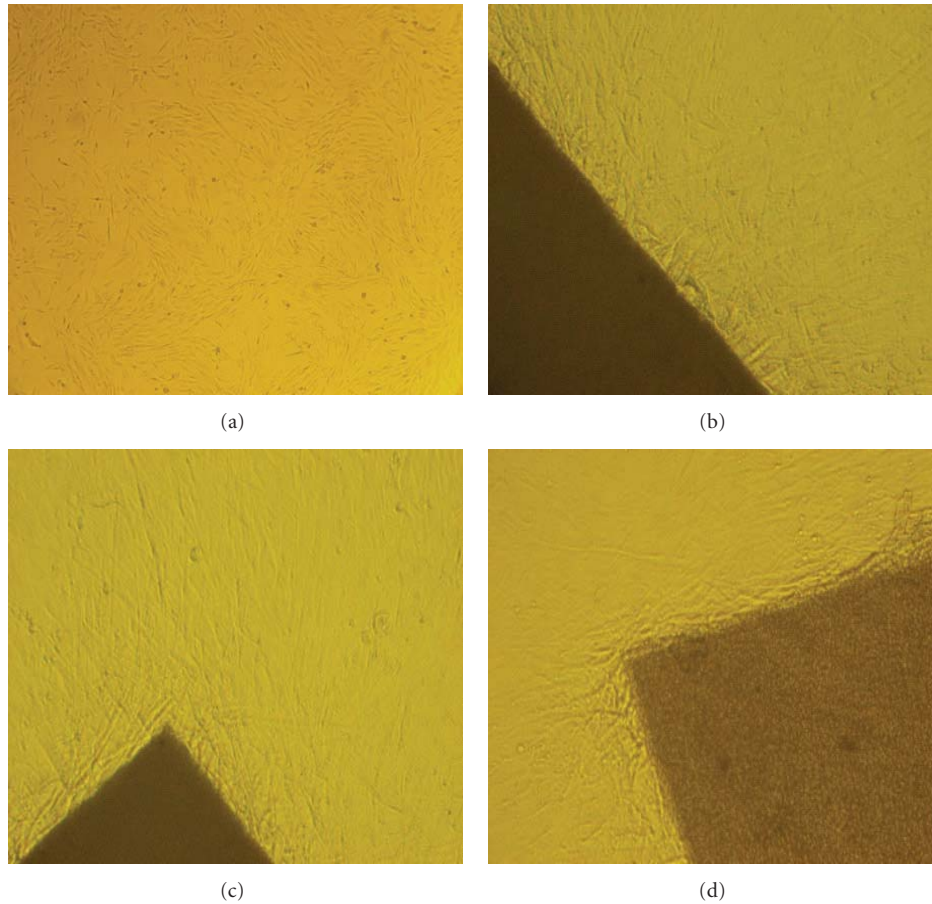
FIGURE 7: USS cell growth on the samples. (a) Control (TCPS), (b) uncoated nanofiber, (c) coated nanofiber (modified by plasma, 30 s), and (d) coated nanofiber (modified by plasma, 60 s).

TABLE 3: MTT analysis of the samples.

Sample	λ (nm)	Viability %
TCPS	606	100
PHBV nanofiber	677	112
PHBV nanofiber (coated collagen nanofiber by oxygen plasma) (30 seconds)	792	130
PHBV nanofiber (coated collagen nanofiber by oxygen plasma) (60 seconds)	999	164

the vicinity of nanofibers especially the collagen-coated nanofiber.

5. Conclusions

PHBV nanofibers with an average size of about 280 nm were designed and successfully coated with collagen by the plasma methods shown in the analysis. A 10° difference in the contact angle, obtained for the 2 samples, showed a better hydrophilicity of the collagen-coated nanofibers than the uncoated ones. Cellular investigations showed better adhesion, growth, and viability in the collagen-coated nanofibers than in the uncoated nanofibers. These collagen-coated nanofibers could be used well for tissue engineering.

References

[1] S. F. Williams, D. P. Martin, D. M. Horowitz, and O. P. Peoples, "PHA applications: addressing the price performance issue I. Tissue engineering," *International Journal of Biological Macromolecules*, vol. 25, no. 1–3, pp. 111–121, 1999.

[2] J. Liu, B. Zhao, Y. Zhang, Y. Lin, P. Hu, and C. Ye, "PHBV and predifferentiated human adipose-derived stem cells for cartilage tissue engineering," *Journal of Biomedical Materials Research—Part A*, vol. 94, no. 2, pp. 603–610, 2010.

[3] W. Meng, SE. Y. Kim, J. Yuan et al., "Electrospun PHBV/collagen composite nanofibrous scaffolds for tissue engineering," *Journal of Biomaterials Science, Polymer Edition*, vol. 18, no. 1, pp. 81–94, 2007.

[4] A. Ndreu, L. Nikkola, H. Ylikauppilar, N. Ashammakhi, and V. Hasirci, "Electrospun biodegradable nanofibrous mats for tissue engineering," *Nanomedicine*, vol. 3, no. 1, pp. 45–60, 2008.

[5] G. Torun Köse, F. Korkusuz, A. Özkul, S. Ber, H. Kenar, and V. Hasirci, "Tissue engineering of bone using collagen and PHBV matrices," *Technology and Health Care*, vol. 10, no. 3-4, pp. 299–301, 2002.

[6] C. Gerard, C. Catuogno, C. Amargier-Huin et al., "The effect of alginate, hyaluronate and hyaluronate derivatives biomaterials on synthesis of non-articular chondrocyte extracellular matrix," *Journal of Materials Science: Materials in Medicine*, vol. 16, no. 6, pp. 541–551, 2005.

[7] D. Li and Y. Xia, "Electrospinning of nanofibers: reinventing the wheel?" *Advanced Materials*, vol. 16, no. 14, pp. 1151–1170, 2004.

[8] Z. M. Huang, Y. Z. Zhang, M. Kotaki, and S. Ramakrishna, "A review on polymer nanofibers by electrospinning and their applications in nanocomposites," *Composites Science and Technology*, vol. 63, no. 15, pp. 2223–2253, 2003.

[9] L. A. Smith and P. X. Ma, "Nano-fibrous scaffolds for tissue engineering," *Colloids and Surfaces B: Biointerfaces*, vol. 39, no. 3, pp. 125–131, 2004.

[10] F. Yang, R. Murugan, S. Wang, and S. Ramakrishna, "Electrospinning of nano/micro scale poly(l-lactic acid) aligned fibers and their potential in neural tissue engineering," *Biomaterials*, vol. 26, no. 15, pp. 2603–2610, 2005.

[11] T. Ito, T. Nakamura, K. Suzuki et al., "Regeneration of hypogastric nerve using a polyglycolic acid (PGA)-collagen nerve conduit filled with collagen sponge proved electrophysiologically in a canine model," *International Journal of Artificial Organs*, vol. 26, no. 3, pp. 245–251, 2003.

[12] T. A. Kapur and M. S. Schoichet, "Chemically-bound nerve growth factor for neural tissue engineering applications," *Journal of Biomaterials Science, Polymer Edition*, vol. 14, no. 4, pp. 383–394, 2003.

[13] H. W. Lu, Q. H. Lu, W. T. Chen, H. J. Xu, and J. Yin, "Cell culturing on nanogrooved polystyrene petri dish induced by ultraviolet laser irradiation," *Materials Letters*, vol. 58, no. 1-2, pp. 29–32, 2004.

[14] V. Roucoules, F. Gaillard, T. G. Mathia, and P. Lanteri, "Hydrophobic mechano chemical treatment of metallic surfaces. Wettability measurements as a means of assessing homogeneity," *Advances in Colloid and Interface Science*, vol. 97, no. 1–3, pp. 177–201, 2002.

[15] K. M. Hay, M. I. Dragila, and J. Liburdy, "Theoretical model for the wetting of a rough surface," *Journal of Colloid and Interface Science*, vol. 325, no. 2, pp. 472–477, 2008.

[16] U. Kogelschatz, "Dielectric-barrier discharges: their history, discharge physics, and industrial applications," *Plasma Chemistry and Plasma Processing*, vol. 23, no. 1, pp. 1–46, 2003.

[17] A. I. Kuzmichev, "Ion plasma sources based on a microwave oven," *Instruments and Experimental Techniques*, vol. 37, pp. 648–653, 1994.

[18] V. Asmussen, "electron cyclotron resonance microwave discharge for etching and thin film deposition," *Journal of Vacuum Science & Technology*, vol. 7, pp. 883–889, 1989.

[19] C. Takahashi, Y. Jin, K. Nishimura, and S. Matsuo, "Anisotropic etching of Si and WSiN using ECR plasma of SF-CF gas mixture," *Japanese Journal of Applied Physics*, vol. 39, no. 6, pp. 3672–3676, 2000.

[20] M. Jager, M. Sager, A. Knipper et al., "In vivo and in vitro bone regeneration from cord blood derived mesenchymal stem cellsIn-vitro- und in-vivo-knochenregenerierung durch mesenchymale stammzellen aus dem nabelschnurblut," *Orthopade*, vol. 33, no. 12, pp. 1361–1372, 2004.

[21] G. Kogler, S. Sensken, J. A. Airey et al., "A new human somatic stem cell from placental cord blood with intrinsic pluripotent differentiation potential," *Journal of Experimental Medicine*, vol. 200, no. 2, pp. 123–135, 2004.

[22] G. Kogler, T. F. Radke, A. Lefort et al., "Cytokine production and hematopoiesis supporting activity of cord blood-derived unrestricted somatic stem cells," *Experimental Hematology*, vol. 33, no. 5, pp. 573–583, 2005.